A NUMERICAL STUDY INTO THE BEHAVIOUR OF MONOPILED FOOTINGS IN SAND FOR OFFSHORE WIND TURBINES

By

Behrang Pedram

MEng.

This thesis is presented for

the degree of Doctor of Philosophy at

THE UNIVERSITY OF WESTERN AUSTRALIA

Achieving International Excellence

School of Civil and Resource Engineering

September 2015

LETTER OF TRANSMITTAL

I hereby declare that, except where specific reference is made to the work of others, the contents of this dissertation are original and have not been submitted in whole or in part for consideration for any other degree of qualification at this, or any other, university.

Behrang Pedram
September 2013

ABSTRACT

As demand for renewable energy sources increases, foundation systems that are capable of withstanding higher load capacities are required to generate more energy per structure. One such approach for wind powered generators is to construct a hybrid system that increases the lateral load capacity of the entire foundation. The proposed hybrid structure consists of a hollow pile/tower firmly attached to a circular footing.

It has been discussed that for this proposed hybrid structure to be beneficial, its stiffness and ultimate lateral capacity must be higher than that of a single pile/tower. Additionally, the bending moments acting on the pile section under the ground for the piled footing structure must be smaller than that of a single pile/tower.

A few scholars have discussed that the hollow pile/tower controls the initial behaviour of the proposed hybrid structure and benefits of the bearing plate were clear after the structure had rotated during their testing programme in a sand deposit, concluding that the stiffness of the hybrid structure was similar to the stiffness of the monopile at small displacements.

In the first section of this thesis, equations that have been developed for short elastic piles embedded in an elastic soil medium are upgraded using 20 noded elements and an equation has been developed for calculating the horizontal displacement of a restrained elastic pile.

In this thesis, the lateral capacity of monopiles, un-piled footings and piled footing structures installed in sand are explored. The behaviour of the structures were investigated through 3-dimensional finite elements analysis and a series of small-scale centrifuge model tests conducted by Harloe (2010). In the numerical models constructed for comparison purposes with the test results, the pile/towers were treated as an elasto-plastic material (with strain hardening) and the soil was idealised using the Mohr-Coulomb constitutive model with a linear and parabolic increase in the soil modulus.

As there were close agreements between the test results and the FE predictions, it was clear that the ultimate lateral capacity and the stiffness of the hybrid structures were higher than that of a monopile. It was evident that the stiffness of the hybrid structures were higher than of a monopile from the initial point; this was also confirmed by the centrifugal tests. It was also demonstrated that the stiffness of the un-piled footing structure, used as a wind turbine, was higher than that of a monopile at low displacements; this point was also confirmed by the small-scale centrifuge tests. Moreover, from the results of the FE analysis, it was obvious that the initial behaviour of the hybrid structure was totally controlled by the bearing plate and not by the pile/tower.

From the results of the numerical models and the centrifugal tests, it was apparent that the ultimate lateral capacity of the un-piled footing structures used as wind turbines, which are installed at shallow depths in a sand deposit, could be accurately calculated by a combination of the limit equilibrium equations and the equations used for VHM loadings. In addition, it was illustrated that for the un-piled footing structures resting close to the ground level in a sand deposit, the overturning capacity could also provide a reasonable estimate to the ultimate lateral capacity of the structure.

The bending moments generated on the hollow bar used in the centrifuge tests as pile/towers for the monopile and the piled footing structures were extracted from their corresponding FE models and demonstrated that the hybrid structure produced smaller values for the pile section embedded in the sand deposit.

For the final section of the thesis, a parametric study was conducted by constructing numerical models for monopiles, piled footings and un-piled footing structures embedded in soft and stiff sand deposits. In these models, the pile/towers were considered as elasto-plastic (with no strain hardening) and the soil was idealised using the Mohr-Coulomb constitutive model. From the results of this study, it was clear that the stiffness of a monopile could be enhanced in excess of 40% by constructing a footing at the ground level with a radius and thickness of 10 m and 2.99 m respectively. The stiffnesses were checked at a tower displacement of 0.2 times the pile diameter (D_{pile}) for the structures installed in the soft and stiff sand media. Although the footing's size was adjusted for a pile diameter of 4.6 m, it was evident that by changing the pile dimensions for the monopiles and the hybrid structures with their nominated footing, the stiffness of the hybrid structure at a tower displacement of $0.2D_{pile}$ would still be higher than of a monopile structure in excess of 38%.

From the results of the parametric study, it was apparent that for monopiles and piled footings, which have high eccentricities the effect of the soil modulus and the soil friction angle, are very small on the overall behaviour of the structures. Evidently, that the soil parameters did not affect the ultimate lateral capacity of the monopiles and the piled footing structures, while as the soil became stiffer the stiffness of the structures increased. In all investigated cases, the difference in the stiffness for each individual structure (monopiles or piled footings) installed in two different soil groups (loose & dense) was less than 15% at a tower displacement of $0.2D_{pile}$.

For the hybrid structure, it was illustrated that by embedding the footing into the surrounding soil the stiffness and the ultimate lateral capacity of the structure would not be affected. Moreover, it was demonstrated that by adopting a shorter pile length for the hybrid structure compared to a monopile, a higher stiffness and ultimate lateral capacity could be sustained for the hybrid structure, as the footing controls the initial behaviour of the hybrid structure.

For pile/tower structures used as wind turbines embedded in sand deposits, it was illustrated that the solution chart generated by Broms (1964) for calculating the ultimate lateral capacity of a long pile embedded in a sand deposit was more accurate compared to the chart produced by Fleming et al. (1992) and the method adopted by Zhang et al. (2005). It was also clear that the accuracy of the chart produced by Fleming et al. (1992) and the method adopted by Zhang et al. (2005) dropped significantly, when the pile/tower structure was embedded in a dense sand deposit.

ACKNOWLEDGEMENTS

I would like to thank my supervisors and my parents for their assistance in completing this thesis. Pursuing this work was an interesting and unforgettable journey. I would also like to thank my colleagues who made the working environment pleasant for me during this period.

The text is edited for language and consistency by “Edit-A-word” editing service.

TABLE OF CONTENTS

LIST OF FIGURES

LIST OF TABLES

NOMENCLATURE

γ ..... Shear strain
A ..... Cross-sectional area of the structure
a ..... Pivot point of pile
A´ ..... Effective area
a_n ..... Water particle acceleration
A_p ..... Pile cross sectional area
A_{wave} ..... Total wave acceleration
B ..... Foundation width
C_M ..... Inertia coefficient
C_s ..... Shape coefficient
C_u ..... Undrained shear strength
D ..... Pile diameter
D_f ..... Foundation embedment depth
D_p ..... Pile diameter
D_r ..... Relative density
E ..... Young's modulus of elasticity
E_s ..... Soil Young's modulus of elasticity
e_{max} ..... Maximum void ratio
e_{min} ..... Minimum void ratio
E_p ..... Modulus of elasticity of the pile
E_{soil} ..... Soil modulus of elasticity
f ..... Unit skin friction
f ..... Frequency
F ..... Side shear resistance
F_{cd} ..... Coefficient for depth factor
F_{ci} ..... Load inclination factor
F_{cs} ..... Coefficient for shape factor
F_{qd} ..... Coefficient for depth factor
F_{qi} ..... Load inclination factor
F_{qs} ..... Coefficient for shape factor
f_{uH} ..... Flexibility coefficient
f_{uM} ..... Flexibility coefficient
$F_{\gamma d}$ ..... Coefficient for depth factor
$F_{\gamma i}$ ..... Load inclination factor
$F_{\gamma s}$ ..... Coefficient for shape factor
$f_{\theta H}$ ..... Flexibility coefficient
$f_{\theta M}$ ..... Flexibility coefficient
G_s ..... Shear modulus
H ..... Horizontal load

H_f..... Ultimate lateral capacity of the pile or $Q_{u(g)}$
I ..... Second moment of inertia
$I_{u(z)}$ ..... Turbulence intensity
K_h ..... Lateral subgrade modulus
K_{HH} ..... Pile head stiffness coefficient
K_{HM}..... Pile head stiffness coefficient
K_{MH}..... Pile head stiffness coefficient
K_{MM} ..... Pile head stiffness coefficient
K_o ..... Earth pressure coefficient at rest
K_p ..... Passive earth pressure
L ..... pile length
L/D ..... Slender ratio
L_0 ..... Initial length
L_a ..... Active length of the an elastic pile
L_e ..... Effective pile length or L´
M ..... Moment load
m_E ..... A multiplier used for increasing the soil modulus
M_{max}..... Maximum moment
M_y..... Plastic moment of the material or M_p
N..... Gravity scale factor
N^*_c..... Coefficient for calculating the end bearing capacity
N^*_q ..... Coefficient for calculating the end bearing capacity
N^*_σ ..... Bearing capacity factor for piles
N_c..... Bearing capacity factor due to cohesion
N_q ..... Bearing capacity factor due to surcharge
N_γ..... Bearing capacity factor due to self-weight
P ..... Force (N)
P ..... Pile circumference
$P_{ab\&bc}$ .... Limiting pressures
P_{Max}..... Maximum earth pressure
P_u ..... Force per unit length of the pile
P_z ..... Vertical load on the pile
Q..... Frontal soil resistance for a pile
q´ ..... Effective vertical stress
Q_b ..... End bearing capacity
q_c..... average cone resistance
Q_s..... Skin friction
Q_{ult} ..... Ultimate capacity (shallow foundation)
R ..... Radius of footing
r_i..... Inner pile radius

r_o ..... Outer pile radius
S ..... Degree of saturation
$S_{(f)}$ ..... Spectral energy density
t..... Pile wall thickness
u..... Horizontal displacement of the pile head
U..... Wind speed
U_0 ..... 1 hour mean wind speed
U_z..... Mean wind speed
V..... Vertical load
V_{Max} ..... Maximum vertical load
V_n ..... Particle velocity
V_{struc}..... Velocity of the structure
V_{wave} ..... Water velocity
Z ..... Depth into ground
α..... None-homogeneity factor
α_t ..... Correction factor
β..... Load inclination
γ..... Unit weight
γ' ..... Effective unit weight
δ..... Soil-pile friction angle
ΔL..... Incremental pile length
ε..... Strain
ε_p..... Volumetric strain
θ..... Angle at which foundation rotated at ground level
$\xi_{a,n}$..... Wave amplitude
ρ..... Density
ρ_{AIR} ..... Mass density of air
σ..... Total stress
σ'_0 ..... Mean effective normal ground stress
$\sigma'_{average}$ .. Average vertical stress used for piles
σ_{yield} ..... Yield stress of the pile material
τ ..... Shear stress
υ_s..... Poisson ratio of the soil
ϕ..... Friction angle
ϕ′ ..... Effective friction angle
ϕ'_c ..... Effective critical friction angle
ϕ'_{peak} ..... Peak effective friction angle
ψ ..... Soil dilation angle
ω ..... Angular speed of centrifuge

CHAPTER 1 INTRODUCTION

1.1 OUTLINE

As the global population increases, the demand for energy arises. On the contrary, many countries are concerned about the amount of fossil carbon fuels available for the future generations. Renewable energies are a solution to this problem as they decrease the amount of carbon emissions released into the environment. Renewable energy comes in different forms such as solar power (energy derived from the sun), wind and wave power, biomass (using plant energy), biofuel and geothermal energy (heat captured from the earth at volcanically active locations). During these last few decades, there has been a lot of research and advancements made on the methods of extracting and utilising these energies from the environment.

One of the most promising of these renewable energies is wind power. Wind turbines generally capture the wind energy, transforming it to electricity. Constructing wind turbines onshore takes a lot of space and causes noise pollution. To solve these problems and take advantage of stronger wind flows, engineers began constructing wind farms offshore.

Offshore wind farms may consist of dozens of turbines that are usually constructed in a grid formation, as illustrated in Figure 1-1. Constructing wind farms offshore allows the turbines to benefit from higher wind speeds at sea but the cost of their construction is higher than onshore wind turbine farms. Most offshore wind farms are constructed in shallow water depths (between 15 m to 35 m) in different types of soil media.

The costs of the foundation of Rejsby Hede wind farm in Denmark was 6% of the totals projects costs, while for the Danish offshore wind farm constructed at Tunoe Knob, the foundation cost was around 23% of the total project cost (Krohn, 2002). A report by Department of Trade and Industry (DTI) (2001) calculated that the foundation costs for an offshore wind turbine could be up to 30% of the total cost of the structure. One way to decrease the construction costs is to design an efficient foundation, which can be easily constructed and installed on site. An efficient foundation is dependent on the structural strength and the surrounding soil, so a robust design requires a single foundation that can be installed at multiple locations with different loading patterns and different soil types surrounding the site.

As shown in Figure 1-2, the vertical load acting on a wind turbine is relatively low in comparison to the lateral load applied. This comparison is usually made with other types of offshore structures similar to jack-up drilling units, also illustrated in Figure 1-2. The lateral load imposed on a wind turbine is generated from the action of environmental forces, which can cause significant cyclic loadings. These cyclic loadings can cause large fluctuation in moment to horizontal load ratio over time (Byrne et al., 2003).

During the installation phase of offshore wind turbines, periods of bad weather can be encountered at sea. During these phases, no work can be performed and this can significantly

increase the overall installation costs. Therefore, it is logical to decrease the number of wind turbines in a farm but to increase the output per structure.

The trend is to install fewer but larger wind turbines in a farm. This means that the loads acting on the structure and consequently the foundation will increase, and so the foundations have to be designed so that they do not fail under the large lateral forces and moments acting on them. This has encouraged researchers to look for new foundation types, which can withstand higher lateral and vertical loads.

If a single foundation is proposed, that can withstand high lateral forces during operation and it is economical, the high costs involved in offshore installation phase can be waived and substantial cost savings can be made. To come-up with a new design offshore foundation, extensive research on site and in the laboratory is required. This research is aimed to investigate a new proposed offshore foundation for wind turbines in shallow waters with the aid of small-scale centrifuge tests and finite element analysis.

1.2 FOUNDATIONS

Different foundation types have been used for constructing wind turbines in the last few decades. It is obvious that a foundation must be able to withstand the loads acting on it and to avoid total failure. In addition, from a structural point of view the displacements must fall within the serviceability criteria.

Figure 1-3 illustrates different parts of a wind turbine. In Figure 1-3, number 1 is the foundation, number 2 is the main tower, number 3 is the nacelle, number 4 is the rotor and number 5 is the hub. Wind turbines might fail in regards to problems associated with their nacelle, as shown in Figure 1-4. These problems are electrical and are not relevant to this study.

The bending moments acting on the tower can cause complete failure of the structure, as illustrated in Figures 1-5 and 1-6. This type of failure is common in single pile/tower structures; and has been investigated in this thesis.

Overturning is another common type of failure in wind turbines involving a tower and a footing at the ground level (un-piled footings). In these structures, the ultimate lateral capacity of the entire structure is controlled by the overturning moment generated at the toe of the footing. Figures 1-7 and 1-8 each illustrate a failed wind turbine comprising of a footing and a tower used for onshore purposes. These structures initially illustrate a stiff behaviour when they are laterally loaded but their ultimate resistance is small compared to the ultimate lateral capacity of a single pile. The behaviour of these foundations (un-piled footings) is also investigated in this thesis.

In designing wind turbines one needs to be attentive of not only the performance and loading conditions but also it is important to consider the behaviour of the structure's foundation. Numerical packages available for design purposes focus on the loading conditions and not on the foundation behaviour. The design criteria are set to decrease fatigue on the structure as wind turbines are under high cyclic loadings during their lifespan. From a geotechnical point of view, it is important to investigate the soil behaviour under cyclic loading for these structures, as the

soil surrounding the foundation degrades and can cause total failure (Anderson et al. 1988 & 2008).

In investigating the foundation, it is important to consider an accurate soil model and that is because wind turbine farms are constructed on vast areas of land and so the soil deposit might significantly change under each structure. It is a usual practice to adopt a uniform soil material when constructing numerical models, this might not be the case in reality, and so the variability of the soil on site must be considered when a wind turbine farm is to be constructed. This indeed requires drilling boreholes at different locations on the proposed site or conducting CPTs (Cone Penetrometer Tests) during the site investigation period.

Different foundation types are available for offshore wind turbines. The most common foundations used in practice are monopiles (single piles), rafts, caissons, skirted foundations, tripods and gravity structures (bucket foundation). Figure 1-9 illustrates three foundation types used in practice for shallow waters. Either piles or suction caissons are suitable for tripods in practice, as both structures can resist the imposed lateral loads.

In deeper waters, anchored systems are used for floating constructions, as the cost of constructing a foundation sitting at the ground level can be extremely high. Figure 1-10 is a schematic illustration of wind turbines installed in deep waters with the aid of different anchoring systems.

A brief overview of some structures used in practice for constructing offshore wind turbines will be provided in the upcoming sections.

1.2.1 Monopile (single pile)

Single piles or monopiles are the most common foundation type used in offshore and onshore designs for wind turbines. These structures are mainly constructed from steel and have a typical diameter of 4 to 6 metres, a length of 10 m to 40 m and a thickness of 40 to 60 mm.

These structures can withstand horizontal forces by bending while supporting the vertical load transmitted by the structure. These structures are well suited for different types of soil media and their slender ratio (length to diameter) can be adjusted so that they can withstand large horizontal forces.

The guidelines provided by the American Petroleum Institute (API) (2007) for laterally loaded piles is on the background of the *p-y* curves which essentially considers the soil medium as a series of infinitely close independent elastic springs. Winkler originally proposed this method in 1876. As discussed by Poulos & Davis (1980) the continous nature of the soil medium in this method is ignored and the pile reaction at a point is simply related to the deflection at that point.

The details of Winkler's method will be discussed in Chapter 3 and in Chapter 6 by conducting, a parametric study in it will be demonstrated that the soil properties of sand (the friction angle and the Young's modulus) for a laterally loaded pile for a wind turbine is of marginal importance. It seems that the ultimate lateral capacity of a single pile embedded in a cohesionless material is mainly controlled by the pile's dimensions (thickness and diameter) and not by the soil's properties.

Monopiles are well suited for wind turbines (for onshore and offshore cases) and satisfy the displacement and rotation design criteria. The main disadvantage to these structures is their high installation costs which are generated from using a very large hammer to drive the piles to their required depth. The costs of pile driving for offshore structures are much higher than onshore cases, as specialised vessels and barges are employed for their installation. Figure 1-11 illustrates an offshore wind turbine under construction.

1.2.2 Raft foundations

Raft foundations are constructed at the base (ground level) of onshore and offshore wind turbines; these structures consist of a shallow raft and a tower with blades and nacelle installed on top of the tower. Figure 1-12 illustrates a raft foundation during the construction of an onshore wind turbine. These structures are mainly controlled by their overturning capacity and must be large and heavy enough to withstand the lateral loads acting on the wind turbine.

Usually there are no tensile forces acting between the soil and the raft when these structures are laterally loaded and therefore, to overcome this problem in onshore cases, sometimes micro piles are constructed around the outer rim of the footing. This decision is usually made based on the costs of installation and the available budget.

Raft foundations are large and heavy and are usually constructed on strong soil deposits, so that the soil medium can withstand the weight of the structure. In offshore cases, these structures are usually constructed in shallow waters (less than 25 m) and are very susceptible to overturning, as illustrated in Figures 1-7 and 1-8.

For offshore cases, shallow rafts are constructed onshore and are transferred by vessels to their proposed locations. This in fact reduces the costs of installations but as mentioned, they are very susceptible to overturning. The behaviour of this structure will also be investigated in this thesis.

1.2.3 Single Caisson

These foundations are very similar to short chunky piles as they are hollow pipes constructed from steel. These hollow tubes are open at bottom and closed on the top. The installation procedure is to position the cylinder (caisson) at the bottom of the sea; this will allow the caisson to be partially embedded under its own self-weight. In the second stage, water is pumped from the caisson and generating a differential pressure across the caisson, which pushes the foundation further into the soil medium.

Figure 1-13 is a side view of caissons. These structures are not well suited to withstand tensions and as discussed by Houlsby et al. (2005) these foundations need to become very large in deep wasters, which is not economical in practice.

1.2.4 Tripods and tetrapods

Figure 1-14 illustrates tripod foundations for offshore wind turbines. These foundations are positioned at the seabed level and are supported by piles or caissons. These foundations are well

suited for deep waters where high moments act at the ground level. If caissons are used to secure these structures to the ground, the foundation might be vulnerable to tensile forces.

Tetrapods are four legged structures and are more resilient in respect to tripods (3-legged structures) as discussed by Houlsby et al. (2005). Tripods have a simplified shape in respect to tetrapods and they use less material (they also use three caissons during their installation phase while tetrapods need four).

1.3 RESEARCH OBJECTIVES

The aim of this thesis is to investigate the behaviour of a hybrid foundation consisting of a single pile/tower and a circular footing embedded in a sand medium. This offshore foundation is encouraging for water depths of 10 to 30 m. If the proposed structure is to be successful, its stiffness must be higher than that of a single pile and also it's ultimate lateral capacity needs to be higher than that of a raft foundation and a single pile structure. A schematic illustration of this foundation is presented in Figure 1-15.

A 3D elastic model (pile and soil) with reflective symmetry was constructed and equations have been derived for capturing the behaviour of the hybrid structure in a purely elastic soil medium. Moreover, these equations have all been derived with the aid of 20 noded elements.

Harloe (2010) conducted small-scale centrifuge tests in medium dense sand at The University of Western Australia (UWA) to investigate the behaviour of the proposed hybrid structure, monopiles and shallow un-piled footing foundations. The details of the testing programme and the results will be discussed in Chapter 4.

The focus of this research is on constructing 3D numerical models by the aid of ABAQUS (V6.7 Dassault Systèmes, 2007) for the proposed hybrid structure, shallow rafts (un-piled footings) and monopiles. These models are constructed to confirm the test results obtained by Harloe (2010) at UWA. The results of these tests and the FE models will be compared to conclude how the hybrid structure behaves in respect to a monopile and an un-piled footing foundation. The lateral responses of these structures have also been investigated for when an excess vertical load is applied to the structures. The very last scenario is in fact for when an upgrade is essential for the structures.

In the last chapter, a parametric study has been conducted to investigate the effects of different parameters on the lateral response of the hybrid structure and a single pile. These parameters include the thickness and diameter of the footing (or the bearing plate) the dimensions of the pile and the soil properties, those are the friction angle and the soil's modulus of elasticity.

1.4 THESIS OUTLINE

The thesis is constructed of seven chapters and an appendix. An overview of the six chapters is given below:

Chapter 2 provides an overview of the relevant literature. In this chapter, concepts and findings of different scholars on piles and raft foundations are discussed and their results will be used for comparison purposes with the data captured from the centrifuge tests and the FE results in the upcoming chapters.

Chapter 3 contains a literature review on different methods of calculating the lateral capacity of a single pile (elastic) embedded in an elastic soil medium. An elastic model is constructed in this chapter by the aid of ABAQUS and a parametric study has been conducted to evaluate the benefits of using a bearing plate at the ground level for a monopile. The results obtained from different scholars who have worked on elastic soil and piles are illustrated, and equations have been derived for calculating the lateral displacement of a single pile with a free and fixed head.

Chapter 4 describes the tests conducted by Harloe (2010) on single piles, monopiled footings and footings in the beam centrifuge at UWA. These small-scaled models were embedded in commercial silica sand during the testing programme. The details of each individual test are discussed in this chapter.

Chapter 5 contains 3D numerical models, which were constructed for comparison purposes with the test data obtained in the beam centrifuge (that is the results of Chapter 4). In the numerical models a Mohr-Coulomb soil criteria has been adopted in conjunction with an elsto-plastic property for the pile/towers involved in the testing programme. Moreover, for comparison purposes four extra numerical models containing monopiles, piled footings and single footings were constructed. In addition to the numerical models constructed for comparison purposes with the test data a small parametric study was also conducted at the end of this chapter.

Chapter 6 presents a detailed parametric study on the behaviour of monopiled footing structures to investigate the significance of the footing's dimensions (thickness and diameter) and the embedment depth in two different soil types. In addition, the behaviour of the monopile and a nominated monopiled footing structure was investigated by conducting a parametric study on the friction angle and the soil's modulus of elasticity. The pile's length, thickness and diameter were also changed for both structures to illustrate how much the stiffness and the ultimate capacity of the structures are altered when these parameters are changed. In addition, all the results obtained for the monopiles have been compared with the solutions available in the literature (discussed in Chapter 2).

Chapter 7 summarises the key conclusions from this research and provides recommendations for future study.

Figure 1-1. An offshore wind farm (www.graysharboroceanenergy.com)

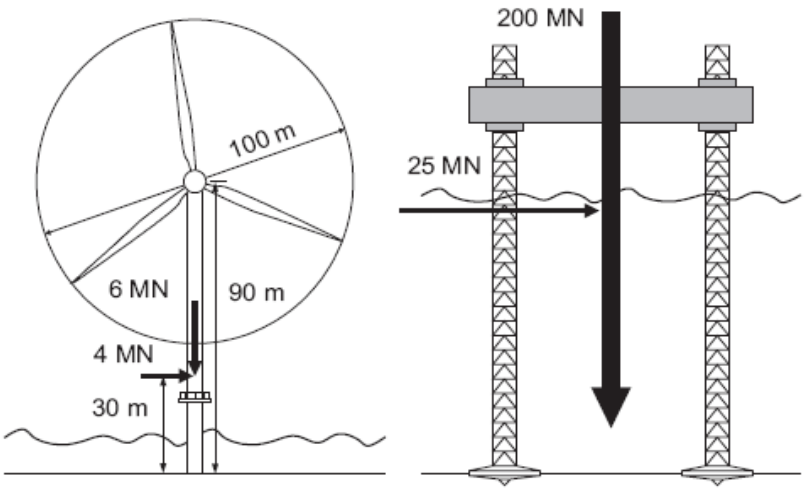

Figure 1-2. Typical loads on an offshore wind turbine (left) and a mobile jack-up drilling unit (right) (Bienen et al. 2006; Byrne et al. 2003)

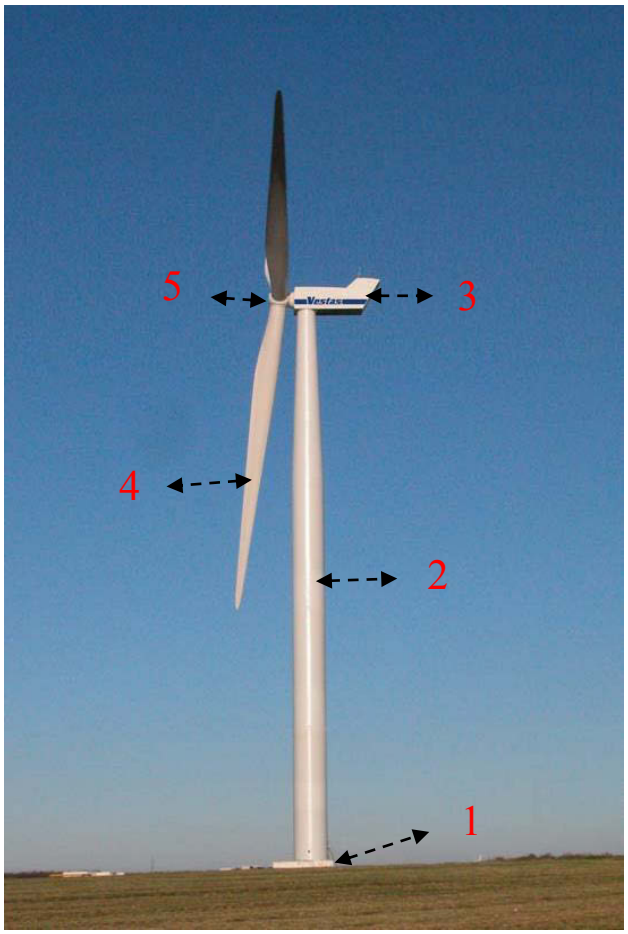

Figure 1-3. Different segments of a wind turbine (The wind turbine's photo was adopted from Vestas-V120)

Figure 1-4. Failure of a wind turbine associated with electrical problems (Photo courtesy of Stuart McMahan, adopted from www.newscientist.com)

Figure 1-5. Failure of a wind turbine in respect to the bending moments acting on the tower (Photo courtesy of Brian Hulke)

Figure 1-6. Failure of a wind turbine's tower in Wyoming, 1/Feb/2011 (Photo courtesy of Eric Nielsen)

Figure 1-7. Failure of a wind turbine comprising of a tower and a footing (photo courtesy of Con-tech systems Ltd)

Figure 1-8. Failure of a wind turbine due to overturing of the structure (photo courtesy of Con-tech system Ltd)

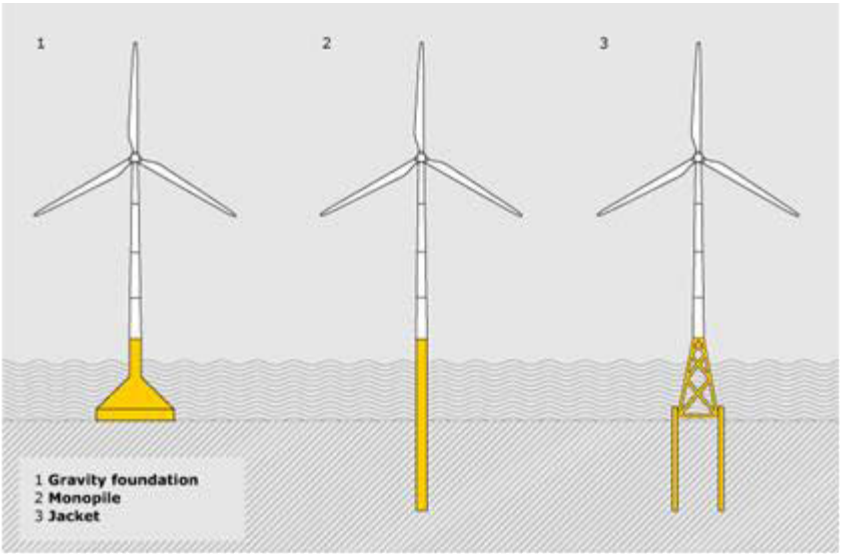

Figure 1-9. Three different types of foundations used in shallow waters. From (left to right) is a gravity foundation, monopile and a jacket foundation (Courtesy of Züblin)

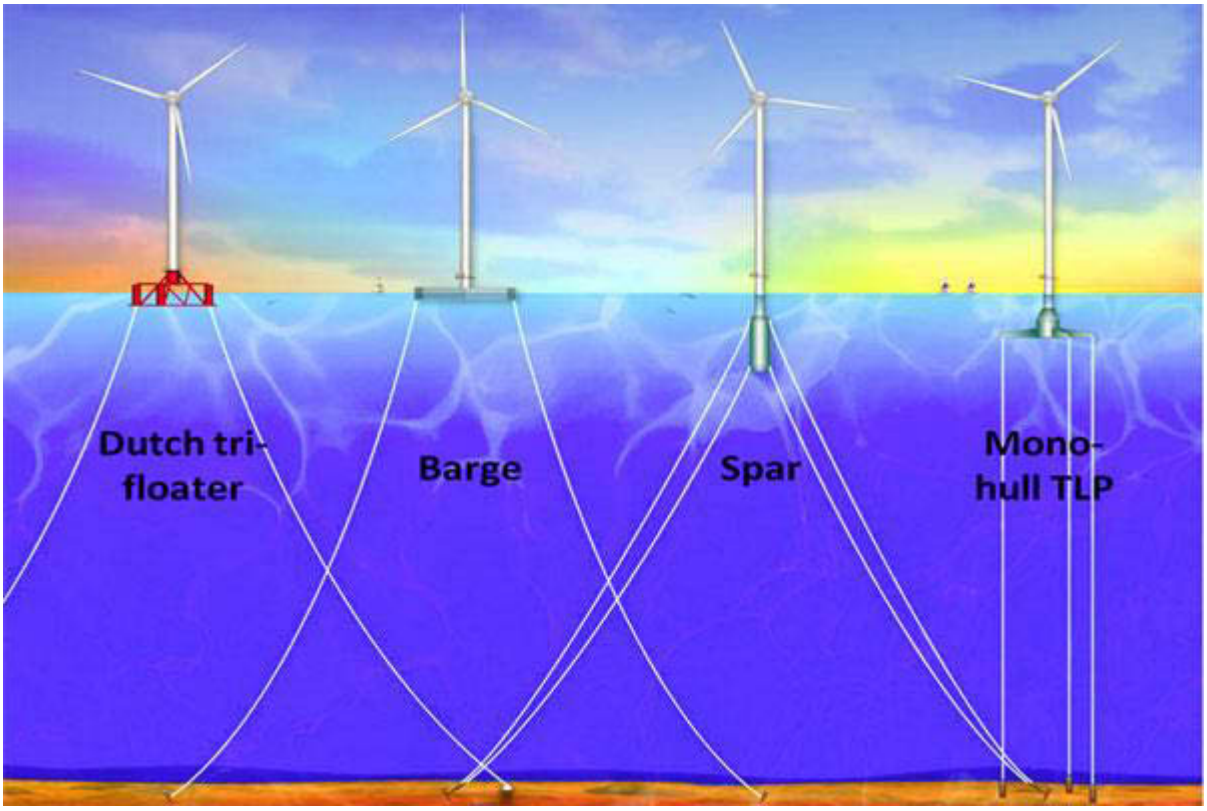

Figure 1-10. Wind turbines installed in deep waters with the aid of anchoring systems (Courtesy of UCSD)

Figure 1-11. Installation of a monopile for an offshore wind turbine (www.hornsrev.dk)

Figure 1-12. An onshore raft foundation for a wind turbine during construction (www.johnrsweet.com)

Figure 1-13. Side view of caissons (www.noed.com.cn)

Figure 1-14. Tripods used for offshore wind turbines (Photo courtesy of Trianel Ltd)

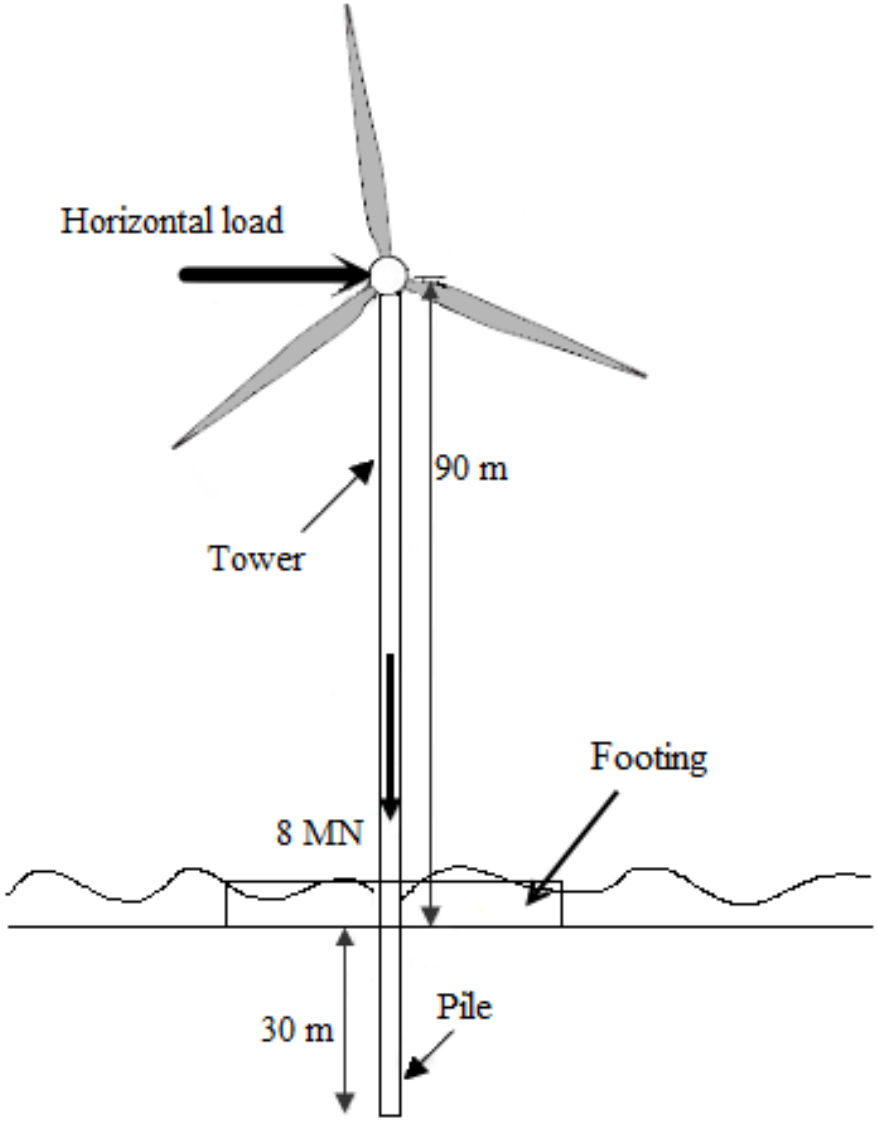

Figure 1-15. A schematic illustration of an offshore piled footing structure

CHAPTER 2 LITERATURE REVIEW

2.1 INTRODUCTION

An overview of the literature relevant to this study is provided in this chapter. The existing methods and ideas are discussed and summarised in the previous chapter. The discussions will mainly focus on deep and shallow foundations embedded in sand deposits.

The ideas and methods, which are commonly used in practice for calculating the ultimate capacity of deep and shallow foundations in sands, have been discussed. In addition, different methods for calculating the ultimate lateral capacity of a single pile embedded in a sand deposit are summarised in the previous chapter. At the end of the chapter, the literature available on the proposed hybrid structure (piled footing) has also been discussed.

2.2 GENERAL LITERATURE

For a wind farm to be economical a capacity of around 100 MW is necessary (Senders 2009). Two main wind farms, which were constructed in Europe, are the Horns Rev wind farm in Denmark and the Egmond aan zee wind farm in the Netherlands. Both wind farms have individually a total output of over 100 MW and their foundations were constructed by monopiles.

The Egmond aan zee wind farm was the first large wind farm built in the North Sea off the Dutch coast in 2006. The wind farm is around 10-15 km from shore and is made-up of 36 wind turbines, each with a capacity of 3 MW. This amount of energy is roughly enough to provide renewable electricity for more than 100,000 households. Each wind turbine was approximately 600 m apart from each other. The pile/towers in this wind farm were constructed from steel and were driven 30 m into the seabed. Each pile roughly weighs around 250 tons and has a diameter of 4.6 m with a plate thickness of 50 mm to 60 mm. After driving each pile into the seabed (with their head standing above the seabed level), a transition piece with a length of around 25 m with a diameter of 4.3 m was placed on the pile. Attached to the transition piece are work platforms, ladders and a berthing facility for boats. An inflatable grout seal was used to grout the space between the pile and the transition piece. The grout is designed to close gaps of a few centimetres and simultaneously resist an internal pressure of few bars. Grouting the space above the grout seal with cement resulted in a very strong joint between the transition piece and the monopile. The hub height (the height above the sea level) was around 70 m and the total area covered by the wind farm is 27 km^2. Figure 2-1 illustrates a single wind turbine from the Egmond aan zee wind farm with the transition piece in place.

The Horns Rev wind farm was built in 2002 and is located on the west coast of Denmark in a region called Blåvandshuk. This wind farm consists of 80 wind turbines, which each have a turbine capacity of 2 MW. The hub height from the sea level is 90 m and the total turbine's height (that is the height of the tower and pile together) is 115 m. The rotor diameter for each wind turbine is 80 m and the weight of the super structure is around 259 tons. The pile diameter

and thickness of each wind turbine is 4 m and 50 mm respectively. The depth of the water at the site is around 6-14 m and the distance between each turbine is around 560 m. After the steel piles were installed by, a pile driver located on a barge to a depth of around 25 m below the ground level the turbines were placed on top of the tower by the aid of a crane constructed on a vessel. The wind turbines were connected to an offshore station by submersible cables and then the offshore station was connected to an onshore power transmission grid through another set of underwater cables. Many technical failures were reported almost a year after completion, many of which were attributed to manufacturing problems, salt in the air affecting the electrical components and weather conditions. It is worth noting that the cost of constructing the Egmond aan zee wind farm was around 200 million EUR while the cost of Horns Rev wind farm was around 270 million EUR.

The trend in practice is mainly to construct fewer but larger wind turbines with higher output per structure, leading to an increase in the forces acting on the foundation and so new types of structures are being investigated to accommodate the increase in the forces for future designs.

New foundation types are proposed in recent years, as these new structures are investigated in regards to the high forces and moments acting on them. Wind turbine foundations must be able to withstand high moments acting at the ground level; this requires that all new proposed structures to be extensively studied before they can be constructed for utilisation for onshore and offshore cases. Before adopting any new structure in practice, it is important that each structure is tested in regards to the acting forces and moments, which a wind turbine might experience. To check how a new structure might behave under different loading regimes, centrifuge tests, onshore tests and numerical stimulations can be conducted to illustrate the benefits of a new proposed structure.

As discussed by Byrne et al. (2003) the costs of an offshore wind turbine foundation could account for 35% of the total installation costs. This amount can be substantially reduced by simplifying the foundation installation and by considering a consistent foundation, which can withstand vertical loads and high moments at the ground level.

Wind turbines should primarily be designed for fatigue performance and stiffness as their design is more critical under serviceability and cyclic loading compared to their ultimate capacity (Houlsby et al., 2005a). Hence, it is important to understand the behaviour of the structure under lateral force versus lateral displacement for different proposed structures. To come up with such a response from the structure it is essential to have a clear understanding of different types of loads and their magnitudes acting on the structure.

2.3 LOADS ACTING ON A WIND TURBINE

Det Norske Vertitas (DNV) (2004 & 2007) categorises the loads acting on a wind turbine. These loads are as follows:

1. Permanent loads: they are controlled by the self-weight of the structure and the permanent equipment, which are installed on the main body or the tower (the nacelle, hub and rotor).

2. Variable loads: they contain the weight of structures, which might be used to investigate and check the structure during its serviceability life span. These loads can contain weights from personnel to operational cranes set on the structure.
3. Environmental loads: they include hydrodynamic, aerodynamic and earthquake loads.

Hydrodynamic and aerodynamic loads (environmental loads) impose cyclic loading on offshore structures. The horizontal and moment loadings generated on offshore wind turbines are mainly due to the action of environmental loads. Phenomena such as earthquake, snow, ice and earth movement can also induce extreme loads on the structure. Tides and variations in hydrostatic pressure can also introduce high amount of forces and moments on the structure.

In reality, the variable loads acting on the structure for a wind turbine are not significant compared to the weight of the structure and the environmental loads, therefore many researches do not consider them in the analysis or in tests.

The self-weight of the structure in this thesis is considered as the weight of the structure acting above the foundation level (this is similar to the concept of Byrne et al. 2003). In fact, the self-weight of the structure acts eccentric in regards to the centre of the pile in wind turbines, this eccentricity can increase the acting moments at the level of the foundation. The eccentricity is mainly due to the weight of the hub, nacelle and the rotor, which are located offset from the centre of the structure.

2.3.1 Hydrodynamic loads

The wave loads applied to an offshore structure are dynamic in nature but can be adequately represented by their static equivalents for shallow depths of water (API, 2007). For deeper waters, a load analysis involving a dynamic action of the structure will be appropriate, as the platform tends to be more flexible.

Currents are usually considered as uniform flow fluids with a velocity that is a function of the vertical coordinate without any acceleration. Several equations are provided for calculating the current velocity at a certain depth. Equation 2-1 is a straightforward equation provided by Soulsby (1997) for calculating the current velocity at different depths.

$$V_{\text{current(at depth z)}} = \begin{cases} V_{\text{current-ref}} \left(\dfrac{z}{0.32 z_w}\right)^{\frac{1}{7}} & \text{For } 0 < z \leq 0.5 z_w \\ 1.07 V_{\text{current-ref}} & \text{For } 0.5 z_w < z \leq z_w \end{cases} \quad \textbf{2-1}$$

In the above equation, $V_{current}$ is the current velocity at a certain depth (z) while z_w is the water depth.

The wave characteristics of a specific location are calculated over a period of three hours and are called wave spectrums or the sea state. Two wave spectra are often used in practice are the JONSWAP and the Pierson Moskowitz wave spectrum.

The Pierson-Moskowitz spectrum (PM) is expressed as in Equation 2-2. $S_{PM(\omega)}$ is a standard wave spectra which makes use of the significant wave height (H_s) and the mean zero-crossing wave period (T_z).

$$S_{PM(\omega)} = \frac{A_a}{\omega^5} \exp\left[\frac{-B}{\omega^4}\right] \quad \textbf{2-2}$$

In equation 2-2, A_a and B_b are as follows:

$$A_a = \frac{4\pi^3 H_s^2}{T_Z^4}$$

$$B_b = \frac{16\pi^3}{T_z^3}$$

H_s and T_z in A_a and B_b equations are the significant wave heights and the mean zero crossing wave period respectively. ω is also the angular frequency.

The JONSWAP wave spectrum can be expressed as in Equation 2-3 (Ochi 1979).

$$S_{JS(\omega)} = \frac{1}{\pi^2 8}\frac{H_s^2 K_b^4 K_Y}{T_P^4}\left(\frac{2\pi}{\omega}\right)^5 \exp\{\frac{-1}{\pi}\left(\frac{2\pi K_b}{\omega T_p}\right)^4\}\{Y^{\exp\left\{\frac{-(\omega-\omega_p)^2}{2M^2\omega_p^2}\right\}}\} \quad \textbf{2-3}$$

In equation 2-3, the constants are empirical and are as follows:

$Y = 3.3$

$T_p = K_L T_z$

$K_b = 1.4085$

$K_L = 0.327\, e^{-0.315M} + 1.17$

$K_Y = 1 - 0.285 \ln M$

$\omega_p = 2\pi/T_P$

$M = M_a = 0.07$ for $\omega < \omega_p$

$M = M_b = 0.09$ for $\omega \geq \omega_p$

Both the Pierson-Moskowitz and JONSWAP wave spectrums express the sea state in an angular frequency state and to transfer them to a wave time series they must be changed to a discrete form. To do so, the area under the graph for a given band width of ω_n for the spectrum (S) is calculated from Equation 2-4.

$$S_{\omega_n} = \frac{1}{\Delta\omega}\int_{\omega_n - \Delta\omega}^{\omega_n + \Delta\omega} S(\omega) d\omega \quad \textbf{2-4}$$

The surface elevation above the mean water level, ξ can be calculated in the time region as in equation 2-5.

$$\xi = \sum_{n=1}^{N_w} \xi_{a,n} \cos(\omega_n t + \varepsilon_n) \quad \textbf{2-5}$$

In the above equation ω_n is the angular frequency, $\xi_{a,n}$ is the wave amplitude and ε_n is the phase shift. The amplitude is derived from Equation 2-6.

$$S_{(\omega_n)} \Delta\omega = 0.5\, \xi_{a,n}^2 \quad \textbf{2-6}$$

The next step is to calculate the wave velocity (V_{wave}, horizontal) for an irregular wave at a depth of z_w but before that V_n that is the particle velocity of an individual regular Airy wave has to be determined by Equation 2-7.

$$V_n(z,t) = \xi_{a,n}\omega_n \frac{\cosh(k_n(z+z_w))}{\sinh(k_n z_w)} \sin(\omega_n t + \varepsilon_n) \quad \textbf{2-7}$$

In Equation 2-7, K_n can be determined by iteration through the dispersion relationship by considering $\frac{\omega_n^2}{g \tanh(k_n z_w)}$ equal to K_n.

The V_{wave} at a certain depth is determined by Equation 2-8.

$$V_{wave}(z,t) = \sum_{n=1}^{N_w} V_n(z,t) = \sum_{n=1}^{N_w} \xi_{a,n}\omega_n \frac{\cosh(K_n(z+z_w))}{\sinh z_w} \sin(\omega_n t + \varepsilon_n) \quad \textbf{2-8}$$

Moreover, the water particle acceleration can be determined as in Equation 2-9.

$$a_n(z,t) = \xi_{a,n}\omega_n^2 \frac{\cosh(k_n(z+z_w))}{\sinh(k_n z_w)} \cos(\omega_n t + \varepsilon_n) \quad \textbf{2-9}$$

By the aid of the last equation, the total wave acceleration can be calculated as in Equation 2-10.

$$A_{wave}(z,t) = \sum_{n=1}^{N_w} a_n(z,t) = \sum_{n=1}^{N_w} \xi_{a,n}\omega_n^2 \frac{\cosh(K_n(z+z_w))}{\sinh(K_n z_w)} \cos(\omega_n t + \varepsilon_n) \quad \textbf{2-10}$$

As discussed by API (2007) the hydrodynamic loads acting on a structure can be calculated by the Morison equation, which is an empirical equation. Equation 2-11 illustrates an extended version of this equation as the force per unit length for a vertical structure.

$$q_{hydro}(x,z,t) = \frac{\pi}{4}\rho_w C_M A_{wave} D^2 - \frac{\pi}{4}\rho_w (C_M - 1) D^2 A_{wave} + 0.5\rho_w C_D D |V_{wave} - V_{strcu}|(V_{wave} - V_{struc}) \quad \textbf{2-11}$$

In this equation, ρ_w is the unit weight of water, C_M is the inertia coefficient, D it the diameter of the structure, $A_{structure}$ is the acceleration of the structure, A_{wave} is the acceleration of water (as in Equation 2-10), V_{wave} is the water velocity (as in Equation 2-8), V_{struc} is the velocity of the structure and C_D is the drag coefficient.

Some of the coefficients in Equation 2-11 are constants, which have been experimentally evaluated by different researchers. For example, a value of 0.7 has been adopted by DNV (2004) for the drag coefficient (C_D) when dealing with a circular cylinder and a value of 2.0 has been suggested for the inertia coefficient (C_M) by a few researchers.

2.3.2 Aerodynamic loads

As discussed by the API (2007), wind forces are mainly exerted on the section of the structure, which are above the sea level. Wind speed is mainly classified as:

1. Gusts that usually last for less than one minute.
2. Steady wind speeds that last for longer than one minute.

In practice, the wind data must be collected from an elevation of at least 10 m above the sea level for a specified duration of time (usually one hour). For determining the appropriate design wind speed for a normal offshore condition the following points must be considered:

1. The frequency of occurrence of the wind speed from various directions for each month or season must be specified.
2. The guest speed associated with sustained wind speed must be evaluated.
3. The persistence of sustained wind speeds above the specified thresholds for each month or season.

For extreme wind speeds, the following points must be considered:

1. The date of occurrence, magnitude of gusts, sustained wind speeds and the wind directions.
2. The projected number of occasions during the specified life of the structure when sustained wind speeds from specified directions should exceed a specific lower bound wind speed.

These points are considered as wind criteria for design purposes and must be collected before any structure is constructed offshore.

Wind loads are also similar to wave loads and are dynamic in nature, but in shallow waters, some structures might behave in a static fashion. In deeper waters, wind loads are significant and should be studied in detail (a dynamic analysis is required). For a dynamic analysis, the knowledge of the wind turbulence, intensity, spectra is usually required. Some of these items addressed below.

Wind speed value is only meaningful if qualified by its elevation and duration. For strong wind conditions the design wind speed u (z, t) (ft/s) at a height of z (ft) above the sea level for and averaging time period of t(s) [where $t \leq t_0$; t_0 = 3600sec] is given by Equation 2-12.

$$u(z,t) = U(z)[1 - 0.4 \times I_u(z) \times \ln(\frac{t}{t_0})] \quad \textbf{2-12}$$

U(z) in the above equation is the mean wind speed at a level of z (ft) for a duration of 1 hour and is calculated by equation 2-13.

$$U(z) = U_0 \left[1 + C \ln\left(\frac{z}{32.8}\right)\right] \quad \textbf{2-13}$$

In Equation 2-13, $C = 5.73 \times 10^{-2} \times (1 + 0.0457\, U_0)^{0.5}$ and $I_u(z)$ in Equation 2-12 [turbulence intensity] at a height of z is given by Equation 2-14.

$$I_U(z) = 0.06\,[1 + 0.0131\, U_0] \times \left(\frac{z}{32.8}\right)^{-0.22} \quad \textbf{2-14}$$

U_0 is the 1 hour mean wind speed at 32.8 ft (10 m) above the sea level.

The above equations are usually used for wind profiles and gusts. For dynamic wind behaviour, the following wind spectrum (Equation 2-15) may be used for the energy density of longitudinal wind speed fluctuations.

$$S(f) = \frac{3444\left(\frac{U_0}{32.8}\right)^2 \times \left(\frac{z}{32.8}\right)^{0.45}}{(1 + f^0)^{\frac{5}{3n}}} \quad \textbf{2-15}$$

Where f^0 is calculated as in Equation 2-16.

$$f^0 = 172\, f \left(\frac{z}{32.8}\right)^{\frac{2}{3}} \left(\frac{U_0}{32.8}\right)^{-0.75} \quad \textbf{2-16}$$

Where

n = 0.468 (in Equation 2-15)

S (f) = spectral energy density

f = frequency (Hz)

z (ft) = height from sea level

U_0 = 1 hour mean wind speed at 32.8 ft (10 m) above the sea level

To calculate the wind drag force on an object Equation 2-17 can be used.

$$F = \frac{\rho_{AIR}}{2} u^2 C_s A \quad \textbf{2-17}$$

In Equation 2-17, F is the wind force, ρ_{AIR} is the mass density of air, C_s is a shape coefficient, A is the area of the object and u is the wind speed.

The values of C_s (shape coefficient) for different shapes are as below:

Beams and sides of a building = 1.5

Cylindrical sections = 0.5

Overall projected area of a platform = 1.0

It must also be noted that wind pressure and resulting forces may be determined from wind tunnel tests conducted on a representative model too.

For a wind turbine, the aerodynamic loads on the blades are of a great importance. Different theories like the blade element and the blade element momentum theory are used for calculating the forces acting on a wind turbine. These theories were not investigated in this thesis, as the load (the aerodynamic force) is located at the nacelle's level for a wind turbine.

During the testing programme in the beam centrifuge, the loads were applied to the top of the towers and so in the constructed numerical models in Chapter 5 a displacement is introduced to the tower's head to investigate the structure's response.

2.3.3 General comments

Byrne et al. (2003) estimated that the vertical load acting on a 90 m high offshore wind turbine (3.5 MW) is to be around 6 MN and the horizontal load is in a range of 4 MN. They also estimated that the overturning moment at the foundation level would be around 120 MNm. Byrne et al. (2003) point out that the loads acting on an offshore wind turbine could substantially vary as they are not only dependent on the size of the structure but also on where they are located.

Senders et al. (2009) calculate the horizontal force acting on an 86.6 m tetrapod offshore wind turbine between 0.4 to 1.2 MN depending on the gusts that might occur every 50 years. They also calculate the vertical load acting on the foundation to be around 7 MN for a tetrapod and 6.6 MN for a tripod in a water depth of 25 m. Their calculations reveal that the maximum overturning moment at the foundation level for a tetrapod is 155 MNm, of which 58 MNm is made from the hydrodynamic load and 97 MNm is from the aerodynamic load. They also point out that the hydrodynamic load is located at almost 2/3 of the crest height and the aerodynamic load is located at the nacelle's level.

The proposed hybrid structure (piled footing) studied in this thesis is suitable for shallow waters (up to a depth of 10 m) and so the main load acting on this structure will be the aerodynamic load, which is located at the nacelle's level. In Chapters 4, 5 and 6 the loads applied to the proposed structure are at the nacelle's level. As mentioned in the previous section, for shallow waters the wind load can also behave in a static fashion (API 2007) and so during the testing programme a monotonic load was applied to the tower's head, while the numerical models were all displacement controlled.

2.4 DEEP FOUNDATIONS (PILES)

Piles are mainly members constructed from steel, concrete or timber. They are considered as deep foundations (embedment depth or $D_f > 4$ m) and the cost of constructing and installing them is usually higher than shallow foundations. Below is a list of some situations that pile foundations are required (Vesic, 1977).

1. When the upper soil medium is susceptible to settlement (compressible) or it is too weak to support the loads transferred from the structure. In these cases, piles are used to transfer the loads to a stronger soil medium (like the bedrock) or to gradually transfer the loads to the soil (floating piles). This is illustrated in Figure 2-2 (a) and (b).

2. Piles are used to resist horizontal loads by bending and meanwhile supporting the vertical load applied to them from the superstructure. This situation can arise in retaining structures or offshore foundations, which are subjected to high hydrodynamic and aerodynamic loadings, as illustrated in Figure 2-2 (c).
3. Piles can be used when the upper soil medium is collapsible (loess) or expansive (Montmorillonite). This is because these types of soils can cause considerable damage if the foundation is rested on top of them as illustrated in Figure 2-2 (d).
4. Piles can be used to resist uplift forces in offshore environments similar to caissons, this is illustrated if Figure 2-2 (e).
5. If there is erosion at the ground surface the baring capacity of the soil will significantly decrease for shallow foundations while long piles will not be very much affected by erosion at the ground level as shown in Figure 2-2 (f).

Figure 2-2 illustrates the five above situations which pile foundations are required for supporting the superstructure.

2.4.1 Types of piles

There are different ways to categories piles in practice:

a. Classification by material
   1 Steel
   2 Concrete
   3 Timber
b. Classification by effect of installation
   1 Driven or high displacement piles
   2 Low displacement piles
   3 None-displacement piles
c. Classification by method of installation
   1 Driven
   2 Driven tube filled with concrete
   3 Bored piles
   4 Composite piles
   5 Screwed piles (Atlas)
   6 Pushed
   7 Vibrated

2.4.2 Classification by material type

2.4.2.1 Steel piles

Steel piles are mainly pipe piles or H-section piles. Pipe piles can be driven by an open or closed end. In the case of driven pipe piles, they can be filled by concrete after they have been driven into their calculated location. When piles are driven into strong datum (gravel and soft rock) the pile can be fitted with a driving point or shoe to ease the driving process and to protect the pile's

toe. Figure 2-3 illustrates two different types of driving points or driving shoe used for pipe piles in practice.

Piles used for offshore wind turbines in practice are open-ended pipe piles constructed from steel, which are driven into the soil medium and are not filled by concrete, as illustrated in Figure 2-4. These driven piles can have different lengths and thicknesses. It must also be pointed out that epoxy is usually used as a coating on piles installed in organic soils and environments to avoid corrosion of the pile section.

2.4.2.2 Concrete piles

These piles can be divided into precast and cast in situ piles. The precast concrete piles are prepared by the usual reinforcement material and can be square or octagonal in cross section. The reinforcement is used to enable the pile to resist bending moments during transportation as concrete is not able to withstand tension (brittle material). Figure 2-5 illustrates two types of precast concrete piles, a square and an octagonal pile section with their reinforcements.

Cast in situ piles are built on site by boring a hole into the ground and then filling it by concrete. These piles might be cased or uncased and can contain a pedestal at their bottom as illustrated in Figure 2-6. In these piles, a pedestal or a hammer is dropped to the bottom of the pile while the concrete is still fresh.

Cased piles with reinforcements can also be constructed on site. In these piles, after the ground has been bored to the desired depth by an auger (as shown Figure 2-7) a case is driven into the ground, the casing might be gradually withdrawn as concrete is being powered or the cavity can be filled with the case in place. As illustrated in Figure 2-8, reinforcement cages are also lowered into the cavity to increase the tension capacity of concrete.

Figure 2-9 is a schematic illustration of a continous flight augur system for pilling with the machine involved in the process. In this method, concrete is poured down the auger at the desired depth while the auger is gradually pulled out of the ground.

2.4.2.3 Timber piles

These piles are made of tree trunks and their maximum length is between 10-20 m. A timber must be straight and without defects if it is to be used as a pile. The American Society of Civil Engineers classifies timber piles into three groups:

1. Class A is piles, that are able to carry heavy loads; the minimum diameter of the toe must be 356 mm.
2. Class B are used for medium loads and the toe diameter should be in the range of 305-330 mm.
3. Class C are used only for temporary constructions and the minimum butt diameter must be 305 mm.

In all above cases, the pile tip diameter must not be less than 150 mm. When driving timber piles a shoe must be used at the tip of the pile to avoid damaging the cross section. In addition, a cap

must be used at the pile's head during the driving and installation phase as the hammer can also crush the wooden fibres.

2.4.3 Classification by method of installation

2.4.3.1 Driven piles

When large diameter piles are driven into loose soils, they will push the soil sideways as the pile head advances and this will cause compaction in the soil surrounding the pile. Concrete piles (precast) and closed ended pipe piles are considered as high displacement piles.

2.4.3.2 Low displacement piles

H-sections and steel tube piles are considered as low displacement piles. Piles used for offshore wind turbines are steel tube piles and can be considered, as low displacement piles when there base is open.

2.4.3.3 None-displacement piles

If a hole is bored initially, then concreted, the soil is not significantly disturbed and so the pile is termed a non-displacement pile (Figure 2-8). It is clear that these piles cause very small displacements within the soil and so the state of stress does not significantly alter around the pile.

2.5 EQUATIONS FOR ESTIMATING THE AXIAL LOAD CAPACITY OF SINGLE PILES

2.5.1.1 Introduction

As illustrated in Figure 2-10 the ultimate capacity of a single pile consists of two parts. One part is due to the friction between the pile and the surrounding soil, which is called skin friction or shaft friction, and the other is due to the end bearing at the base or tip of the pile. In Figure 2-10, Q_f represents the side friction while Q_b is the base resistance. If the skin friction is greater than 80% of the end bearing capacity, the pile is considered a friction pile while if the reverse is the case, the pile will be considered as an end bearing pile. In the case of floating piles, the end bearing of the pile is usually neglected.

In coarse-grained soils the load transfer to the adjacent soil along the side of the pile is almost linear with depth, that is higher loads are at the top and lower loads are at the bottom. For fine-grained soils, the load transfer has nonlinear decreases with depth. Figure 2-11 illustrates how the skin friction is transferred to the soil in a fine and coarse-grained soil.

If the skin friction is to be mobilised, a vertical displacement of 5-10 mm is required between the pile and the soil. However, the base resistance is mobilised when the pile tip has moved about 10%-25% of the pile diameter (or width). The lower range (10%) is for driven piles while the upper limit (25%) is for bored piles. As illustrated in Figure 2-11, the end bearing resistance is mobilised when slip or failure zones similar to shallow foundations are formed at the tip of the pile. This indicates that the skin friction is mobilised at about one-tenth of the displacement

required to mobilize the end bearing resistance. Vesic (1977) illustrated this point for pipe piles in dense sand while Randolph (2003) illustrates the same concept for a bored pile.

Figure 2-12 illustrates the results of Randolph et al. (2003) for a 0.8 m bored pile with a length of 20 m. The response of the pile's base, shaft and its total response is indicated in the figure. From the figure, it is clear that the shaft's capacity is mobilised at around 4 MN while the base response is still rising for displacements of over 80 mm. They also note that when the pile's shaft capacity has been reached (fully mobilised) the stiffness of the pile-soil system is only controlled by the pile's base and from that point on the displacements start to increase rapidly. It is also interesting to note that if the ultimate capacity of the pile is considered to be 7 MN the skin friction is carrying 60% of that load. At around a working load of 3.5 MN the skin friction carries almost 95% of the load. As previously discussed, in the case of offshore wind turbines the vertical load on the structure due to the weight of the nacelle, hub and the rotor is a small fraction of the ultimate vertical capacity of the pile and so the skin friction generated between the soil and the steel pipe must carry the applied vertical load.

When piles are driven (as in the case of offshore piles) into loose granular materials, the soil around the pile's shaft tends to densify and this will increase the relative density and the friction angle of the soil surrounding the pile. On the other hand, in dense material, the pile driving process loosens the sand around the pile's shaft and so the critical shear strength ($\phi_{critical}$) parameters must be used for calculating the skin friction generated between the pile and the surrounding soil (Budhu 2007).

In case of loose granular material for driven piles, the peak friction angle (ϕ_{peak}) can be used for the skin friction generated between the soil and the pile or as reported by Kishida (1967) Equation 2-18 can be used.

Kishida assumes that the diameter of the compacted zone around the pile is 7D (D is the pile diameter) from the centre of the pile. As discussed by Poulos & Davis (1980) when ϕ_1 (the initial friction angle of the soil) is equal to 40° there will be no changes in the relative density due to pile driving. It must also be pointed out that Equation 2-18 is well suited for calculating the end bearing capacity of a single pile driven into loose sand (Poulos et al .1980).

$$\phi_2^{'} = \frac{\phi_1^{'} + 40°}{2} \qquad \textbf{2-18}$$

Many studies have been conducted on how to calculate the skin friction and the base resistance of piles in different soils. In the upcoming sections, a few of these methods are briefly explained.

2.5.2 Estimating the base resistance of piles

There are different approaches for calculating the base resistance of a single pile embedded in sand or clay. A few available methods, which are commonly used in practice, have been briefly explained in the upcoming sections.

2.5.2.1 Estimating the base resistance of a single pile by Meyerhof's method

Meyerhof (1976) observed that the end bearing capacity of a single pile (Q_b) embedded in a sand deposit increases with depth of embedment up to around L/D = 0.5 where D is the pile diameter and L is the length of the pile. This point is illustrated in Figure 2-13. In most cases, the ratio of L/D is higher than 0.5 and so the maximum end bearing can be considered for a pile embedded in a sand layer.

Equation 2-19 provides an estimate of the end bearing capacity of a single pile installed in a cohesionless material. In this equation, A_p is the area of the pile and q' is the effective vertical stress at the level of the pile's tip.

$$Q_b = A_p q' N_q^* \quad \textbf{2-19}$$

The values of N_q^* are related to the friction angle of the soil, as illustrated in Figure 2-14.

The value of Q_b in Equation 2-19 must be less than the limiting value of $A_P q$ were q is calculated as in Equation 2-20.

$$q = 50\, N_q^* \tan\phi' \quad \textbf{2-20}$$

It is clear that if the calculated value in Equation 2-19 is higher than the value calculated in Equation 2-20 the limiting value (that is Equation 2-20) will be considered as the end bearing capacity of the single pile in a cohesionless soil.

From Figure 2-14 for a saturated undrained clay (friction angle = 0 that is a Tresca failure criterion) N^*_c will be equal to 9. The ultimate end bearing capacity of a single pile embedded in a clay layer will be equal to $9C_uA_p$ (C_u is the undrained shear strength of the soil and A_p is the area of the pile section). This recommendation is suitable for a total stress path calculation (TSP) in undrained clays.

2.5.2.2 Estimating the base resistance of a single pile by Janbu's method

In 1976, Janbu proposed Equation 2-21 for calculating the base resistance of a single pile embedded in sand or a clay layer.

$$Q_p = A_p\left(C_u N_c^* + q' N_q^*\right) \quad \textbf{2-21}$$

In Equation 2-21, the form of the soil failure at the pile's tip is shown in the insert of Figure 2-15 with the values of η' between 75° for soft clays to 105° for dense sandy soils. It is clear that in sands (C_u = 0, an effective stress path, ESP) Equation 2-21 will reduce to Equation 2-19. Moreover, the values of N_q* and N_c* are related to the friction angle of the soil as illustrated in Figure 2-15.

The values of N_q* and N_c* can also be calculated from Equations 2-22 and 2-23. Instead of using Figure 2-15, Equation 2-22 can be directly used with considering $\lambda' \leq \pi/3$ for soft fine-grained soils and $\lambda' \leq 0.58\pi$ for dense, coarse-grained soils and overconsolidated fine-grained soils.

$$N_q^* = (\tan\phi' + \sqrt{(1+\tan^2\phi')^2}\,(e^{2\lambda'\tan\phi'}) \quad \textbf{2-22}$$

$$N_C^* = \left(N_q^* - 1\right)\cot\phi \quad \textbf{2-23}$$

The value of N_c* in Equation 2-23 is calculated through adopting the value of N^*_q in Equation 2-22.

For an effective stress path, calculation (ESP) in a clay layer Equation 2-21 can also be used. For this case, the value of C_u must be equal to zero and the value of N^*_q can be calculated from Equation 2-22 with the lower values of λ' for soft clays and higher values for overconsolidated clays.

2.5.2.3 Estimating the base resistance in sands by Coyle and Castello's method

In 1981, Coyle and Castello proposed Equation 2-19. This was based on analysing large-scale field load tests for driven piles in sand. q' in this equation is the effective vertical stress at the pile's tip and A_p is the pile's cross sectional area. The values of N_q* are illustrated in Figure 2-16 and are related to the friction angle and the slender ratio (L/D, where L is the pile's length and D is the pile's diameter) of the pile.

2.5.2.4 Estimating the base resistance in sands by Berezantzev's method

Berezantzev et al. (1961) proposed an equation as in the form of Equation 2-19 with the values of N_q' illustrated in Figure 2-17. They used a correction factor α_t in respect to the friction angle of the soil and the slender ratio of the pile to calculate the correction factor, as illustrated in the inset diagram of Figure 2-17. After calculating the correction factor (α_t) the value of N_q' is read through the friction angle of the soil. The value of N_q* (used in Equation 2-19) will be equal to the correction factor times N_q'.

2.5.2.5 Estimating the base resistance of a single pile by Vesic's method

Vesic (1977) proposed a method estimating the end bearing capacity of a single pile based on the theory of expansion of cavities. Equation 2-24 is the equation proposed by Vesic.

$$Q_b = A_p q_p = A_p(C_u N_c^* + \sigma_0' N_\sigma^*) \quad \textbf{2-24}$$

σ_0' is the mean normal ground effective stress at the level of the pile point and it is equal to equation 2-25 with $K_0 = 1 - \sin\phi'$ and q' equal to the effective vertical stress at the pile's tip.

$$\sigma_0' = \left(\frac{2K_0 + 1}{3}\right) q' \quad \textbf{2-25}$$

N_σ^* is calculated by Equation 2-26 with N_q^* determined from Figure 2-18.

$$N_\sigma^* = \frac{3N_q^*}{(1+2K_0)} \quad \textbf{2-26}$$

N_C^* in equation 2-24 is calculated by Equation 2-27 were N_q^* can be read from Figure 2-18.

$$N_C^* = (N_q^* - 1)\cot\phi \quad \textbf{2-27}$$

If an effective stress path (ESP), were considered for calculating the base resistance, of a single pile in clay or a sand layer, applying Equation 2-19 would be much more suitable for the calculating the base resistance. For such a case the value of N_q* is calculated by Equation 2-28 with the value of I_{rr} equal to Equation 2-29.

$$N_q^* = \frac{3}{3-\sin\phi'}\{\exp[\left(\frac{\pi}{2}-\phi'\right)\tan\phi']\tan^2(\frac{\pi}{4}+\frac{\phi'}{2})I_{rr}^{\frac{\frac{4}{3}\sin\phi'}{1+\sin\phi'}} \quad \textbf{2-28}$$

$$I_{rr} = \frac{I_r}{I_r\varepsilon_p + 1} \quad \textbf{2-29}$$

In Equation 2-29, the value of $I_r = \frac{G_S}{C+q'\tan\phi'}$ with G_s equal to the shear modulus of the soil, C is the cohesion (when dealing with sands or and ESP it can be neglected), q′ is the effective vertical stress at the pile's tip, ε_p is the volumetric strain and ϕ' is the effective friction angle of the soil. For the case of dense sands or saturated soils where there is no volume change, I_r and I_{rr} will be equal (the volumetric strain will also be equal to zero, $\varepsilon_p = 0$). After calculating I_{rr} from Equation 2-29 the value of N_q* can be calculated and its value can be used in Equation 2-19.

On the other hand, if a total stress path (TSP) is to be considered for the soil layer it would be appropriate to only consider the end bearing capacity equal to $N_c^*(C_u)_{base}$. The value of N_c* can be considered as 9 or it can be calculated by $6.44\ \ln(C_u)_{base} - 0.63[\ln(C_u)_{base}]^2 - 7.55$ (Skempton 1959). The value of C_u in Skempton's equation is the average undrained shear strength over two pile diameters below the base.

2.5.2.6 Estimating the base resistance of a single pile by API (2007) recommendations

API (2007) provides Equation 2-19 for calculating the base resistance of a single pile embedded in a sand deposit. Their recommended values for N_q* are illustrated in Table 2-1.

It must be pointed out that the limiting end bearing capacity values in Table 2-1 is equal to N_q* times the effective vertical stress at the piles tip. API (2007) has also mentioned that the strength values increase with increasing the sand fractions and decreases when the silt fractions are increased, this is clear from the sand-silt category in Table 2-1. It is also clear that there has been no recommendation made for the first row of Table 2-1, which is for loose sands and medium dense silts. The relative density description for each soil type recommended by API (2007) is illustrated in Table 2-2.

Relative density	Soil Description	End bearing Factor N_q*	Limiting unit end bearing value (MPa)
Very loose loose loose Medium Dense Dense	Sand Sand Sand-Silt Silt Silt	Not Applicable	Not Applicable
Medium Dense	Sand-Silt	12	3
Medium Dense Dense	Sand Sand-Silt	20	5
Dense Very Dense	Sand Sand-Silt	40	10
Very Dense	Sand	50	12

Table 2-1. Design parameters for cohesionless soils (API 2007)

Description	Relative Density %
Very loose	0 – 15
Loose	15 – 35
Medium dense	35 – 65
Dense	65 – 85
Very Dense	85 - 100

Table 2-2. The definition for the relative density descriptions (API 2007)

2.5.2.7 Estimating the base resistance of a single pile by CPT correlations

The cone penetration was originally developed to estimate the end bearing capacity of single piles. The unit end bearing capacity (that is $q'N_q$* in Equation 2-19) has been observed to vary from $0.4q_c$ to $0.9q_c$ (q_c is the cone resistance of the CPT) as in Figure 2-19. Lehane et al. (2005) provides a value of $0.6q_c$ for the unit end bearing capacity of a closed ended pile driven in an offshore strong foundation layer.

Fleming et al. (1983) calculates the unit end bearing capacity of a single pile by averaging the tip cone values over an influence zone of 8-pile diameter above the pile base and 2-pile diameter below the pile base, as illustrated in Figure 2-20. The average cone resistance is calculated as in Equation 2-30.

$$q_b = \frac{q_{c1} + q_{c2} + 2q_{c3}}{4} \qquad \textbf{2-30}$$

In Equation 2-30 q_{c1} is the average value of the cone resistance over 2 pile diameter below the base, q_{c2} is the minimum cone resistance over two pile diameter below the pile base and q_{c3} is the

average of the minimum cone resistance values lower than q_{c1} over eight pile diameters above the pile's base.

Nordlund (1963) recommended an average value of q_c over a depth of three pile diameters above the pile base and two pile diameters below the base, as illustrated in Figure 2-20.

2.5.3 Estimating the skin friction of single piles in sand

The skin friction of a single pile can be estimated from equation 2-31.

$$Q_s = \sum p\Delta Lf \qquad \textbf{2-31}$$

In this equation, p is the perimeter of the pile, ΔL is an incremental pile length and f is the unit skin friction resistance at a certain depth.

Similar to the end bearing capacity of single piles embedded in sand the frictional resistance (f in Equation 2-31) of a single pile increases with depth up to around 15 to 20 times the pile diameter and after that depth, it remains constant. This has been illustrated in Figure 2-21.

For depths between 0 to 15 or 20 pile diameter the skin friction is calculated as in Equation 2-32 with the values of K_s equal to 1 - sinϕ′ for bored piles, 1.8(1 - sinϕ′) for high displacement driven piles and for low displacement piles a value of 1.4 (1 – sinϕ′) can be adopted (Poulos 2009).

$$Q_s = \int_0^{15-20D} p\ \sigma'_{at\ 15-20D}\ K_s \tan\delta\, dz \qquad \textbf{2-32}$$

The values of δ can range between 0.5ϕ′ to 0.8ϕ′ depending on the soil and the pile's material. In Equation 2-32, p is the pile's perimeter, D is the pile's diameter and σ′ is the effective vertical stress at a depth of 15 or 20 pile diameter.

As illustrated in Figure 2-22 Meyerhof (1976) provided a chart for calculating the values of K_s tanδ in Equation 2-32 for different types of piles used in practice. In this figure, ϕ'_1 is the angle of internal friction prior to installation of the pile. As discussed in Section 2.5.1.1 the friction angle of the soil can be influenced by the pile's installation process.

When using Equation 2-31 f (K_s tanδ) is calculated up to 15-20D (that is actually the integral in Equation 2-32) and then its value will not change for the rest of the pile's length.

2.5.3.1 Coyle and Castello's method for calculating the skin friction in sands

In regards to the discussion made in Section 2.5.2.3, Coyle and Castello proposed Equation 2-33 for calculating the skin friction for piles embedded in a sand medium.

$$Q_s = \left(K\sigma'_{average}(\tan 0.8\phi')\right)pL \qquad \textbf{2-33}$$

In this equation $\sigma'_{average}$ is the average vertical stress between the head and the tip of the pile, p is the pile's perimeter, L is the total length of the pile, ϕ′ is the effective friction angle of the soil and K is the earth pressure coefficient. The value of K in Equation 2-33 is related to the slender ratio (L/D) of the pile and the friction angle of the soil, as illustrated in Figure 2-23.

2.5.3.2 Estimating the skin friction of a single pile by CPT results

By calculating an average value for the sleeve resistances results obtained from a CPT test, the skin friction of a single pile can be calculated. The average sleeve resistance from a CPT test will be equal to the value of f in Equation 2-31. Therefore, it is clear that to calculate the skin friction of the pile, the average value of the sleeve resistance calculated from the CPT must be multiplied by the perimeter of the pile and by the embedment length. This method provides a very crude estimate of the skin friction of the pile (Budhu 2007).

For coarse-grained soils, the unit skin friction of a single pile can be calculated by Equation 2-34, which was originally proposed by Vesic (1977) or by Equation 2-35, which was suggested by Jardine et al. (1998).

$$f = 0.11\exp(-3\tan\phi'_c)q_c \quad \textbf{2-34}$$

$$f = \sigma'_{rc}\tan\phi_i \quad \textbf{2-35}$$

In Equation 2-34, ϕ'_c is the effective critical friction angle of the soil and q_c is the average value of the cone resistance over the entire length of the pile. In Equation, 2-35 σ_{rc}' is equal to equation 2-36.

$$\sigma'_{rc} = 0.029 q_c \left(\frac{\sigma'_{z0}}{p_a}\right)^{0.13} \left(\frac{h}{R^*}\right)^{-0.38} \quad \textbf{2-36}$$

In Equation 2-36 σ'_{z0} is the effective vertical stress at the pile's base, P_a is the atmospheric pressure, h is the depth from the pile base to the depth at which the shaft friction is considered, ϕ_i is the interface friction angle and R^* is the radius of a closed ended pipe pile. In the case of open-ended piles R* will be equal to $(R_0^2 - R_i^2)^{0.5}$ were R_0 is the outer radius and R_i is the inner radius of the pile.

2.5.3.3 General comments

For open ended and H-piles similar to Figure 2-24 the effect of the soil plug should be considered on the entire cross section area of the pile. For the case of the H-piles, the area will be $d_1 d_2$ (d_1 and d_2 are illustrated in Figure 2-24) and the circumference will be equal to $2(d_1+d_2)$.

For on plugged piles the area will be equal to the pile's annulus. As discussed by API (2007) there are situations where a pile can be driven in to the soil in an unplugged condition but can act as a plugged pile under static loading conditions.

As discussed by Lehane et al. (2005) the variability in capacity predictions in sands exceed those for piles embedded in clays. Das (1999) has also discussed this point, illustrating that the values of the ultimate base resistance of a single pile installed in a sand layer can vary over 400% depending on which theory and equation is used.

Meyerhof (1976) provided the results of several field load tests on long piles. He calculated the end bearing capacity for the tested piles and plotted the results against Equations 2-19 and 2-20;

his results are plotted in Figure 2-25. In this figure, q_l (the dashed line) is his predicted values from EquationS 2-19 and 2-20. It is clear that for a provided friction angle the ultimate point resistance of a single pile can extremely deviate from the theory.

API (2007) notes that cementation will increase the end bearing capacity of a single pile but it can result in loss of lateral pressure and a decrease in the frictional capacity of the pile.

As mentioned in Section 2.5.1.1, Poulos & Davis (1980) use Equation 2-18 for calculating the soil's friction angle for a driven single pile. After calculating the corrected friction angle they use it to come up with a value of N_q* for the base resistance of the driven pile. For the skin friction, they adopt Equation 2-37 and mention that the mean of the values, which is the friction angle prior to, and subsequent to driving has to be used for calculating the value of $K_s \tan\phi'$ in Equation 2-32. In Equation 2-37, ϕ'_1 is the initial friction angle of the soil.

$$\phi' = 0.75'\phi_1 + 10 \qquad \textbf{2-37}$$

2.5.4 Frictional resistance in clays

In this thesis, the focus is on cohesionless material but at this point, a very short description of how the skin friction of a single pile embedded in a clay layer is calculated will be discussed.

There are mainly three methods for calculating the skin friction of a single pile embedded in a clay layer:

1. λ method: this method was proposed by Vijayvergiya and Focht (1972). They assume that the soil displacement, which is caused by pile driving, generates a passive lateral pressure at a depth below the ground surface and so they proposed Equation 2-38 for calculating the skin friction resistance for a single pile embedded in a clay layer. In this equation P is the circumference of the pile, L is the pile's length, σ′ is the mean effective vertical stress for the entire embedment length, C_u is the mean undrained shear strength of the soil and λ is related to the piles embedment length and its value can be read from Figure 2-26.

$$Q_s = P\,L\,\lambda\,(\sigma' + 2C_u) \qquad \textbf{2-38}$$

2. α method: in this method the skin friction resistance of a single pile embedded in a clay layer is calculated as Equation 2-39. In this equation C_u is the undrained shear strength of the soil (ϕ = 0, Tresca failure criterion) and α is read off Figure 2-27. If the undrained shear strength of the soil is less than 50 kPa (normally consolidated clays), α will be equal to one. Equation 2-39 can simply be used for a layered soil as well. To use this equation for a layered soil, the shear strength for each soil layer has to be calculated separately with it's α value and also the length of pile installed each layer has to be measured. The summation of the skin friction of each pile segment (in each layer) will be equal to the total skin friction of the pile.

$$Q_s = \alpha C_u P L \quad \textbf{2-39}$$

3. β method: this method was originally generated for offshore structures embedded in clays. The unit skin friction in this method is calculated by Equation 2-40.

$$f = \beta \sigma' \quad \textbf{2-40}$$

In this equation, σ′ is the average effective vertical stress for a certain length of a pile embedded in a clay layer. In addition, β is equal to (1- $\sin\phi_R$) $\tan\phi_R$ for a normally consolidated soil while for an over consolidated soil it will be equal to (1 – $\sin\phi_R$) $\tan\phi_R$ (OCR) $^{0.5}$. In both cases, ϕ_R is the drained friction angle for the remolded clay. For a layered soil, the unit skin friction has to be calculated for each soil layer and then the length of each section must be multiplied by the calculated value from Equation 2-40. The summation of all the unit skin frictions together will provide the ultimate skin friction of the pile (with considerations made towards the pile's perimeter).

2.6 ULTIMATE LOAD ANALYSIS FOR LATERALLY LOADED PILES

2.6.1 Introduction

Almost all installed piles are subjected to lateral loads. As discussed in Section 1.1, wind turbines are under extreme lateral loads. Lateral loading on a single pile can be divided into active and passive loads.

Active loading is generated by the action of external loads while passive loading is due to the movement of the soil, which can subject the pile to bending stresses. In this thesis, the main concern is on the active loading of a single pile.

In the design of piles for lateral loading, an adequate safety factor must be adopted in respect to the ultimate lateral failure of the structure. In addition, the deflection of the structure under working loads must be within an acceptable range for the proposed structure.

For onshore cases where piles are under extreme lateral loadings, raking piles (angled piles) are installed by ensuring that the resultant load acts along the axis of the pile. This practice is very expensive and so it is common to rely on the lateral capacity of vertical piles for carrying the horizontal forces.

As discussed by Broms (1964), when a single pile is laterally loaded, the normal stresses in front of it will increase while there will be a decrease in the stresses behind it. The soil in front of the pile will tend to move radially away from the pile while the soil behind the pile will move radially towards the pile. As illustrated in Figure 2-28 the soil in front of the pile will fail by forming a wedge while the soil behind the pile will probably separate from the pile foundation. At shallow depths, the soil behind the pile will fail by separation from the pile's head but for higher depths, the soil will fail by flowing radially around the pile and not by separation.

As illustrated in Figure 2-29 a single pile may fail by rotation at a point near its toe (pivot point), while a long pile will form a plastic hinge at some depth below the surface. In the case of short piles, passive pressure will develop behind the pile while in long piles, only the upper part of the pile will undergo significant displacements and it will form a plastic hinge at a level below the ground surface. These pressures are illustrated in Figure 2-30 for a short and a long pile.

When a pile is restrained in a cap three different collapse modes are possible, as illustrated in Figure 2-31. Short piles will fail by translation with forming no hinge (similar to a rigid body), longer piles (intermediate length) will tend to fail by forming a plastic hinge at the level of the pile's cap and long piles will fail by forming plastic hinges at the level of the pile's cap and at a distance below the pile.

As mentioned by Fleming et al. (1992) it is customary to consider the surrounding soil around a pile as a rigid plastic material. By this consideration, the profiles of the limiting pressures will be similar to Figure 2-30.

From Figure 2-30 for a short pile, it is clear that the moments can be calculated at point B (at the pivot point) and it is also clear that the calculated value must be less than the plastic moment of the pile. The horizontal and moment equilibrium equations for Figure 2-30a are as in Equations 2-41 and 2-42 respectively.

$$H_f = P_{ab} - P_{bc} = \int_0^h P_{ab}\,dz - \int_h^l P_{bc}\,dz \qquad \textbf{2-41}$$

$$M_u = H_f(e + h) = P_{ab}(h - l_{ab}) + P_{bc}(l_{bc} - h) \qquad \textbf{2-42}$$

For a given value of P_{ab} and P_{bc} (limiting pressures), the two above equations can be solved for H_f and h (the unknown depth of rotation). It must also be noted that for short piles the assumption is that the soil fails before the failure of the pile itself.

For a uniform distribution of soil resistance, Poulos et al. (1980) provides Figure 2-32. In this figure two different types of soil resistance ($\overline{P}_u$) have been considered, one is for a uniform soil distribution and the second is for a linearly varying distribution with zero at the ground level (in this chart H_u is the ultimate horizontal load). The value of $\overline{P}_u$ for the linearly varying distribution in Figure 2-32 can be considered as $3K_p\sigma_v'$, were K_p is the passive earth pressure and σ_v' is the vertical effective stress at half way along the pile's length (Broms 1964 assumption). Also in this figure, L is the length of the pile under the ground; e is the length of the pile standing above the ground level (eccentricity) and d is the pile diameter.

As discussed by Brinch Hansen (1961) for any soil resistance distribution with depth the centre of rotation can be determined by trial and error in a way that the resulting moments at the point of application (point B in Figure 2-30) for the load distributions equal to zero. After determining the centre of rotation, the ultimate lateral resistance can be determined by the horizontal equilibrium equation.

As previously mentioned for a long pile, a plastic hinge is usually generated at the point of maximum bending moment (at this point the shear force is zero). Point B in Figure 2-30 b is the

location of the maximum bending moment generated on a single long pile. In these piles, the moments have to be considered at point B with ignoring the pressures beneath this point. As in the previous case, the bending moment value must be equal or less than the plastic moment of the material. In addition, from the horizontal equilibrium equation, H_f must be equal to P_{ab} (Figure 2-30 b). This can be summarised as in Equation 2-43 were M_p is the plastic moment of the material and all the nomenclatures are illustrated in Figure 2-30 b.

$$H_f(e + h - (h - l_{ab}) = H_f(e + l_{ab}) = M_p \quad \textbf{2-43}$$

Therefore, from Equation 2-43 it is apparent that the lateral capacity of a long pile is primarily governed by the pile characteristics (that is, the yield moment of the pile section controls the lateral capacity of a single long pile).

As previously mentioned, at failure, a wedge of soil is pushed ahead of the pile and the limiting pressure acting on the pile will be close to K_p (passive earth pressure) times the local vertical effective stress of the soil but at greater depths a much larger limiting pressures may develop. In respect to the maximum limiting force per unit length of the pile, several scholars have adopted different approaches to estimate the maximum lateral capacity of a single pile. In the upcoming sections methods adopted by Broms (1964), Fleming et al. (1992), Meyerhof (1995), Zhang et al. (2005) and API (2007) will be discussed. Winkler's method and the elastic solutions, which are discussed by Poulos et al. (1980) and Carter et al. (1992), will be summarised in Chapter 3.

2.6.2 Broms method

Broms (1964) provided solutions to the ultimate lateral capacity of short and long single piles embedded in sands and clays. His charts for short piles in sands and clays are illustrated in Figure 2-33. For long piles, he provides Figure 2-34. As can be seen he also considers restrained and free-headed piles in his proposed charts. For the short pile cases embedded in a sand deposit, the charts are straightforward with considering Equation 2-44 as the passive earth pressure.

$$K_p = \tan^2\left(45 + \frac{\phi}{2}\right) = \frac{1 + \sin\phi}{1 - \sin\phi} \quad \textbf{2-44}$$

As noted by Broms (1964) the effective unit weight of the soil (γ' kN/m^3) must be used in all his proposed charts if the soil is submerged under water.

The eccentricity (e) in his charts is the height of the pile above the ground level and L, D, C_u and $Q_{u(g)}$ are the pile length (under the ground), pile diameter, shear strength of the soil (for clays) and the ultimate lateral capacity of the pile respectively.

It is clear from the charts that in short piles the L/D ratio (the slender ratio) is an important factor for deriving the ultimate lateral capacity of a single pile, this ratio is also important in the elastic analysis for short piles embedded in an elastic medium (Carter et al .1992).

Broms solutions for long piles are similar to the short pile cases. M_y in Figure 2-34 is equal to the yield moment of the pile section and it can be calculated as in Equation 2-45.

$$M_y = \frac{\sigma_{yield} * I}{\frac{D}{2}} \quad \textbf{2-45}$$

In Equation 2-45, σ_{yield} is the yield stress of the pile material, I is the moment of inertia of the pile section along its strong axis and D is the pile diameter (Equation 2-45 is in fact the flexure equation).

When solving a problem in practice both the short and long pile charts developed by Broms (1964) should be checked.

Broms also provides the deflection of the pile's head under different working loads, as shown in Figure 2-35 for sands and clays. In these figures, η and β are as in Equations 2-46 and 2-47 respectively.

$$\eta = \sqrt[5]{\frac{n_h}{E_p * I_p}} \quad \textbf{2-46}$$

$$\beta = \sqrt[4]{\frac{KD}{4E_P * I_P}} \quad \textbf{2-47}$$

The values of n_h for sands have been provided by different researchers and some proposed values are tabulated in Table 2-3. E_p , I_p , x_0 and Q_g in the above equations and in Figure 2-35 are the modulus of elasticity of the pile, the moment of inertia of the pile section, the allowable deflection of the pile's head and the working load respectively.

n_h values for sands (kN/m^3)	
Dry or moist sand	
Loose sand	1800-2200
Medium dense sand	5500-7000
Dense sand	15000-18000
Submerged sand	
Loose sand	1000-1400
Medium dense sand	3500-4500
Dense sand	9000-12000

Table 2-3 Proposed N_h values for sands

The value of K for clays in Figure 2-35 (b) is calculated as in equation 2-48.

$$K = \frac{\text{Pressure } (\frac{kN}{m^3})}{\text{displacement}} \quad \textbf{2-48}$$

In most cases, geotechnical engineers are provided by the amount of deflection that a structure is allowed to undertake. In such cases, the Q_g, which is the working load, has to be calculated from the allowable deflection, which the structure can handle (using Figure 2-35).

In deriving the charts for long and short piles driven in sands, Broms (1964) suggests that the net limiting force per unit length of the pile increases as in Equation 2-49. In this equation, D is the pile diameter and σ'_v is the effective vertical stress at any point along the pile's depth.

$$P_u = 3K_p\sigma'_vD \quad \textbf{2-49}$$

Broms considered equation 2-49 based on empirical evidence from predicted and observed ultimate load tests conducted on single piles. As discussed by Broms (1964) and Fleming et al. (1992) the calculated values by Broms charts usually underestimates the lateral capacity of a single pile.

Broms (1964) makes a few assumptions in his analysis; a few of them are listed below:

1. He does not consider the active pressure acting at the back of the pile.
2. The shape of the pile section does not have any influence on the ultimate lateral resistance of a single pile.

Figure 2-36 illustrates different types of pile failure, soil reaction and bending moments generated on a short and long single pile embedded in a sand deposit (H_u in these figures is equal to the ultimate lateral capacity of the pile which was previously shown by $Q_{u(g)}$). For the case of a short pile embedded in a sand layer the calculated moments at the piles toe will provide Equation 2-50 (this equation is derived from the soil reaction diagram proposed by Broms).

$$Q_{u(g)} = \frac{0.5\gamma D}{e + L}L^3K_p \quad \textbf{2-50}$$

The figures generated by Broms for short and long piles embedded in a sand layer were produced by Equation 2-50. From the bending moment diagram of a long pile, illustrated in Figure 2-36 it is clear that the maximum bending moment is located at a depth of f below the ground surface. By considering the moments at point f, Equation 2-51 is derived and it can be used to calculate the maximum horizontal force at depth f below the ground surface.

$$Q_{u(g)} = \int_0^f 3\gamma D\, K_p y dy = \frac{3}{2}K_p f^2 \gamma D \quad \textbf{2-51}$$

Form Equation 2-51 the value of f (the location of the maximum bending moment) can be calculated, and that will be equal to Equation 2-52.

$$f = 0.82\sqrt{\frac{H_u}{K_p D\gamma}} \quad \textbf{2-52}$$

Form the maximum bending moment's location the maximum moment can be calculated as in Equation 2-53.

$$M_{max} = Q_{u(g)}\left(e + \frac{2}{3}f\right) \quad \textbf{2-53}$$

As mentioned by Broms (1964) the value of $Q_{u(g)}$ in Equation 2-53 has to be calculated from Equation 2-50 and if the value of $M_{max} > M_{yield}$ (in Equation 2-53) then the pile is considered as a long pile and the value of $Q_{u(g)}$ has to be calculated from Equation 2-51 with taking $M_{max} = M_{yield}$. The graphs provided by Broms for long and short piles were plotted in respect to this procedure.

For the restrained piles, Broms assumes that at the level of the cap (top level) the moment restraint is at least M_y. Figure 2-37 illustrates the different failure modes of a restrained pile with their soil reactions and bending moment diagrams for short and long piles.

For short restrained piles, the horizontal equilibrium provides Equation 2-54. Broms plots the results of this equation in respect to the dimensionless parameters L/D in Figure 2-33 (a).

$$Q_{u(g)} = 1.5L^2 K_p \gamma D \quad \textbf{2-54}$$

The maximum moment can also be calculated as in Equation 2-55.

$$M_{max} = \frac{2}{3}Q_{u(g)}L \quad \textbf{2-55}$$

If $M_{max} > M_{yield}$ then the pile can be considered as an intermediate pile length with a hinge formed between the cap and the pile. For this scenario, the horizontal equilibrium will be equal to Equation 2-56.

$$F = \left(\frac{3}{2}\gamma D L^2 K_p\right) - Q_{u(g)} \quad \textbf{2-56}$$

Now the moments have to be considered in respect to the toe of the pile with considering F from Equation 2-56. Equation 2-57 provides the values of the maximum moment at depth f with the consideration that it is equal to the yield moment of the material. In addition, in this equation $Q_{u(g)}$ is calculated from Equation 2-51.

$$M_{yield} = \left(0.5\gamma D L^3 K_p\right) - Q_{u(g)}L \quad \textbf{2-57}$$

As previously illustrated, all analysis results from Broms (1964) calculations are plotted in his dimensionless charts for short and long piles in sands and clays.

2.6.3 Meyerhof's method

Meyerhof (1995) has also provided solutions for laterally loaded piles at the ground level for clays and sands. He considers a pile long when $K_r < 0.01$, K_r is equal to Equation 2-58.

$$K_r = \frac{E_p * I_p}{E_s * L^4} \quad \textbf{2-58}$$

When working in sands he considers an equivalent soil modulus for the cohesionless material (E_s). In the above equation E_p is the modulus of elasticity of the pile's material, I_p is the moment of inertia of the cross section of the pile and L is the pile's embedment length.

For short piles ($K_r > 0.01$), the ultimate lateral capacity of a single pile embedded in sand can be calculated as in Equation 2-59. Similar to Broms (1964) method, the effective unit weight of the soil must be used for submerged sands. In this equation, γ is the unit weight of the soil, D is the pile diameter and L is the length of the pile under the ground.

$$Q_{u(g)} = 0.12\gamma DL^2 K_{br} \quad \textbf{2-59}$$

The value of $Q_{u(g)}$ calculated in Equation 2-59 must be smaller than $0.4p_1DL$,where p_1 is equal to $40N_q\tan\phi$ (kPa) and $60N_q\tan\phi$ (kPa) for a Menard pressuremeter and a self-boring full displacement pressure meter respectively (N_q is the bearing capacity factor used in shallow foundations). The value of K_{br} in Equation 2-59 is related to the friction angle of the soil and the slender ratio of the pile, as illustrated in Figure 2-38.

The maximum moment for a short pile embedded in a sand layer is equal to Equation 2-60.

$$M_{max} = 0.35Q_{u_{(g)}}L < M_{yield} \quad \textbf{2-60}$$

M_{yield} in the above equation is calculated as in Equation 2-45.

For long piles embedded in a sand layer, Meyerhof uses Equation 2-59, but he uses $L_{effective}$ instead of L; were $L_{effective}$ is related to L by Equation 2-61

$$\frac{L_e}{L} = 1.65K_r^{0.12} \leq 1 \quad \textbf{2-61}$$

For calculating K_r in equation 2-61, L must be used and not L_e.

The maximum moment for a long pile is calculated as in Equation 2-62 , where Q_g is the working load applied at the ground level and K_r is as in Equation 2-58.

$$M_{max} = 0.3K_r^{0.2}Q_g \leq 0.3Q_g \quad \textbf{2-62}$$

For short piles installed in a clay layer Meyerhof provides Equation 2-63. This equation provides the ultimate lateral capacity of a single pile embedded in a clay layer. As in the previous cases, D is the pile diameter and L is the pile length.

$$Q_{u(g)} = 0.4C_uK_{cr}DL \quad \textbf{2-63}$$

As in the case of sands, the calculated value in Equation 2-63 must be smaller than $0.4p_1DL$. The values of K_{cr} are illustrated in Figure 2-39. The values of p_1 are estimated from the limit pressure meter in clays and can be related to the C_u of the soil depending on the type of pressure meter used in practice.

For the maximum bending moment of the pile embedded in a clay layer, Meyerhof (1995) provides Equation 2-64.

$$M_{max} = 0.22LQ_{u(g)} \leq M_{yield} \quad \textbf{2-64}$$

M_{yield} can be calculated as in Equation 2-45.

For long piles in clays, Meyerhof uses Equation 2-63 with an effective length calculated as in equation 2-65 and K_r calculated as in Equation 2-58.

$$\frac{L_{effective}}{L} = 1.5K_r^{0.12} \leq 1 \quad \textbf{2-65}$$

The maximum moment for a long pile embedded in a clay layer is equal to Equation 2-66. In this equation, Q_g is the working load applied at the ground level and L is the pile's length.

$$M_{max} = 0.3K_r^{0.2}Q_gL \leq 0.15Q_gL \quad \textbf{2-66}$$

2.6.4 Fleming's method

Fleming et al. (1992) provides solutions for the ultimate lateral capacity of single piles in sands and clays similar to Broms method. They use the centrifuge data collected by Barton (1983) to generate empirical equations and charts similar to Broms (1964) solutions.

In sands, they mention that the limiting lateral effective force per meter length of the pile is taken as in EquationS 2-67 and 2-68.

$$P_u = K_pD\sigma'_v \qquad \text{if } z \leq 1.5D \quad \textbf{2-67}$$

$$P'_u = K_p^2D\sigma'_V \qquad \text{if } z \geq 1.5D \quad \textbf{2-68}$$

K_p is as in Equation 2-44, σ_v' is the vertical effective pressure at depth z and D is the pile diameter. Both equations in Equations 2-67 and 2-68 are empirical. On the background of these two equations Fleming et al. (1992) provides charts similar to Figure 2-40 for short and long piles in sands and Figure 2-41 for short and long piles embedded in clays.

As discussed in Section 2.6.1 short single piles (without a cap) fail by rotation about a point close to the toe and on the other hand short piles with caps fail by translation or by generating a plastic hinge between the cap and the pile; the last is actually how an intermediate pile length with a cap fails. In Figures 2-40 and 2-41, the solid lines are used to predict the ultimate lateral capacity of a single pile (free-headed) and the dashed lines are used for calculating the ultimate lateral capacity of a restrained pile.

For short piles without a cap, similar to Broms solutions the dimensionless factor L/D (length over pile diameter) and the e/D (pile's head eccentricity over pile diameter) are the controlling factors for determining the ultimate lateral capacity of a single pile. These graphs were generated in respect to the type of failure which takes place within the pile's section and so for short and

intermediate pile lengths Figures 2-40(a) and 2-41(a) must be used and on the other hand, for long piles (restrained or free-headed) graphs (b) in those figures must be used.

The none-dimensional value $\frac{M_P}{K_P^2 \gamma D^4}$ is used for sands with M_p calculated as in Equation 2-45. H in Figures 2-40 and 2-41 is the ultimate lateral capacity of the pile and it has been calculated in a non-dimensional manner. For short restrained piles embedded in a sand layer depending on weather, the structure will translate or form plastic hinge (intermediate pile lengths) different dashed lines in Figures 2-40 (a) and 2-41(a) can be used.

Similar to Broms (1964), in the method adopted by Fleming et al. (1992), when dealing with saturated sands the effective unit weight of the soil must be used (γ' kN/m^3).

For single piles embedded in clays Fleming et al. (1992) provides the net lateral force per unit length as in Equations 2-69 to 2-71.

$$P_u = 2\tau_u D \qquad \text{at } z = 0 \text{ (ground level)} \qquad \textbf{2-69}$$

$$P_u = \left(2 + \frac{7}{3}\frac{z}{D}\right)\tau_u D \qquad \text{when } z \leq 3D \qquad \textbf{2-70}$$

$$P_u = 9\,\tau_u D \qquad \text{when } z \geq 3D \qquad \textbf{2-71}$$

In Equations 2-69 and 2-70, the lateral capacity at shallow depths is similar to the formation of passive wedges in retaining walls and that is suchlike Broms concept. At higher depths, (three times the pile diameter), the failure mechanism is similar to the lateral load required to push a circular cylinder into clays, which was studied by Randolph and Houlsby (1984).

From Figure 2-41 the lateral load capacity of a single pile (short and long) embedded in a clay layer can be calculated with only consideration towards the shear strength (τ kPa, they also sometimes call it the τ_u analysis or the total stress path method) of the soil. In Figure 2-41 instead of τ_u the value of C_u (the undrained cohesion) must be used (this is also the case for Equations 2-69 to 2-71).

As in the case of short piles embedded in sands the slender ratio (L/D, pile length over pile diameter) is a critical non-dimensional factor for piles embedded in a clay layer. For short restrained piles embedded in a clay layer (similar to the sand case) depending on the failure type (translational or by forming a plastic hinge for the intermediate pile lengths) different dashed lines in Figure 2-41(a) have to be used in conjunction with the calculated values of L/D for a short restrained pile.

It is a conventional practice to apply a safety factor in the range of 2-3 to the ultimate lateral capacity of the pile (H in these diagrams).

2.6.5 Zhang's method

Zhang et al. (2005) proposes a method for calculating the ultimate lateral resistance of a single pile in regards to the frontal soil resistance and the side shear resistance in cohesionless soils. In

their method the ultimate resistance of the soil is considered and not the ultimate resistance of the pile, so their method is applicable to both flexible (long) and rigid (short) piles. They also check their method in respect to lab and field pile tests and illustrate that the proposed method is accurate for calculating the ultimate lateral capacity of a single pile.

As illustrated in Figure 2-42 the soil resistance is constructed of the frontal and side shear resistance (Briaud and Smith 1983 and Smith 1987) and so the ultimate resistance of the soil against the pile is equal to the summation of the forces, as in Equation 2-72. In this equation, F is ultimate lateral shear resistance acting on the sides of the pile and Q is the ultimate frontal soil resistance.

$$P_u = Q + F \quad \textbf{2-72}$$

They proposed two equations for calculating the values of Q and F; they are as in Equations 2-73 and 2-74. In these equations D is the pile diameter or width, P_{max} is the maximum earth pressure in front of the pile (at $\theta = 0°$), τ_{max} is the maximum side shear resistance which acts at $\theta = \pm 90°$ and ς and μ are shape factors to account for the nonuniform distribution of the lateral and shear drag forces.

$$Q = \mu P_{max} D \quad \textbf{2-73}$$

$$F = \varsigma \tau_{max} D \quad \textbf{2-74}$$

They adopt the values of μ and ς from Briaud and Smith (1983). The adopted values are illustrated in Table 2-4. These shape factors are only related to the pile's shape.

Pile shape	μ	ς
Circular	0.8	1.0
Square	1.0	2.0

Table 2-4. Shape factors adopted by Zhang et al. (2005)

After defining the values of Q and F by Equations 2-73 and 2-74, they mention that the ultimate lateral capacity of a single pile can be calculated by Equation 2-75.

$$P_{ultimate} = (\mu P_{max} + \varsigma \tau_{max}) D \quad \textbf{2-75}$$

For the value of P_{max} they adopt Fleming's equation (Equation 2-68) and for τ_{max} they adopt Equation 2-76, which is similar to the ultimate shear resistance in soil's. API (1991) has also proposed this equation for calculating the shear resistance along a pile embedded in a soil medium.

$$\tau_{max} = K\,\gamma'\,z\,\mathrm{Tan}\delta \qquad \textbf{2-76}$$

In Equation 2-76, K is related to the lateral earth pressure (it is the ratio of horizontal to vertical effective stress), z is the embedment depth, γ' is the effective unit weight of the soil and δ is the interface friction angle between the pile and the soil.

For the values of K, they recommend charts from Kulhawy et al. (1983 and 1991), as illustrated in Table 2-5. For the values of δ, they also recommend tabulated values form Kulhawy (1991), which are illustrated in Table 2-6.

Pile type and method of construction	K
Pile-jetted	(0.5-0.7)K_0
Pile-small displacement, driven	(0.7-1.2)K_0
Pile-large displacement, driven	(1.0-2.0)K_0
Drilled shaft-build using dry method with minimal side wall disturbance and prompt concreting	(0.9-1.0)K_0
Drilled shaft-slurry construction with good workmanship	(0.9-1.0)K_0
Drilled shaft-slurry construction with poor workmanship	(0.6-0.7)K_0
Drilled shaft-casing method below water table	(0.7-0.9)K_0

Table 2-5. Values of K recommended by Kulhawy et al. (1983 and 1991)

Pile type	δ
Rough concrete	1.0ϕ'
Smooth concrete	(0.8-1.0)ϕ'
Rough steel	(0.7-0.9)ϕ'
Smooth steel	(0.5-0.7)ϕ'
Wood	(0.8-0.9)ϕ'
Drilled shaft built using dry method or with temporary casing and good construction techniques	(1.0)ϕ'
Drilled shaft built with slurry method	(0.8-1.0)ϕ'

Table 2-6. Values of δ recommended by Kulhawy et al. (1983 and 1991)

For the frontal and side shear resistance they adopt Prasad and Chari's (1999) soil resistance distribution to calculate the ultimate lateral capacity of a single pile. They argue that the reason for choosing Prasad and Chari's method is that they have not considered any soil resistance at the point of rotation of the pile. The last point is clearly illustrated in Figure 2-43.

From Figure 2-43, the ultimate lateral capacity (H_u in the figure) of a single pile can be calculated by the two equilibrium equations, which are as in Equations 2-77 and 2-78. It is clear that

Equation 2-77 is the equilibrium equation for the horizontal forces while Equation 2-78 is the moment equilibrium equation.

$$Q_{u(g)} = \int_0^L p_u D dz = \int_0^L (\mu P_{max} + \varsigma \tau_{max}) D dz \quad \textbf{2-77}$$

$$Q_{u(g)} e = \int_0^L p_u D z dz = \int_0^L (\mu P_{max} + \varsigma \tau_{max}) D z dz \quad \textbf{2-78}$$

In the above equations, e is the eccentricity and L is the length of the pile under the ground. It must be noted that a is equal to the depth of rotation of the pile under the ground and it is illustrated in Figure 2-43.

They provide Equations 2-79 and 2-80 for calculating the depth of the pivot point and the ultimate lateral capacity of a single pile embedded in a cohesionless soil respectively.

$$a = \frac{[-(-0.567L + 2.7e) + (5.307L^2 + 7.29e^2 + 10.541eL)^{0.5}}{2.1996} \quad \textbf{2-79}$$

$$Q_{u(g)} = 0.3\left(\mu K_p^2 + \varsigma K \tan\delta\right)\gamma' a D(2.7a - 1.7L) \quad \textbf{2-80}$$

Using the two above equations, they calculate the ultimate lateral capacity of centrifugal model tests conducted by Barton et al. (1983) and field tests conducted on rigid piles. Their predicted results were in a very good agreement with the centrifugal tests conducted by Barton et al. (1983), as illustrated in Figure 2-44.

2.6.6 API (2007)

For calculating the ultimate lateral capacity of a single pile embedded in a sand deposit, API (2007) adopts Borgard and Matlock's (1980) method. Reese et al. (1974) originally suggested this method with considering a wedge type of failure at the ground surface and a plane-strain failure mode for higher depths. They provide Equations 2-81 and 2-82 and mention that Equation 2-81 can be used for calculating the ultimate lateral capacity of a single pile at shallow depths while Equation 2-82 is suitable for higher depths. In these two equations K_a is the active earth pressure, K_0 is the earth pressure coefficient at rest, ϕ' is the effective friction angle of the soil, α is the angle defining the shape of the wedge and β is the angle of breakage of the soil with respect to the horizontal direction ($45° + \phi'/2$). In addition, D is the pile diameter, z is the embedment depth and γ' is the effective unit weight of the soil.

$$P_u = \gamma' z \left[D\left(K_p - K_a\right) + z\left(K_p - K_0\right)\sqrt{K_p}\tan\alpha + zK_0\sqrt{K_p}\left(\frac{1}{\cos\alpha} + 1\right)\tan\phi'\sin\beta\right] \quad \textbf{2-81}$$

$$P_u = \gamma' z D\left(K_p^3 + K_0 K_p^2 \tan\phi' - K_a\right) \quad \textbf{2-82}$$

If the two equations are graphed in respect to the depth of the pile (z), the plots will intersect at a point (Z_c). For depths higher than Z_c Equation 2-81 shall be used while for depths below the intersection point Equation 2-82 can be used.

Borgard and Matlock (1980) removed some parts of Equations 2-81 and 2-82. In addition, they considered some parts of those equations as constants (this did not introduce too much error). This procedure enabled them to provide Equations 2-83 and 2-84, which are only related to the friction angle of the soil.

Equation 2-83 is used for determining the lateral capacity of a single pile near the ground surface while Equation 2-84 is used for deeper depths. The values of C_1, C_2 and C_3 are illustrated in Figure 2-45. In the proposed equations P_u (or $Q_{u(g)}$) is the ultimate lateral resistance, z is the embedment depth, γ' is the effective unit weight of the soil and D is the pile diameter.

API (2007) also proposes Equations 2-83 and 2-84 for calculating the ultimate lateral capacity of a single pile embedded in a sand deposit.

$$P_u = (C_1 z + C_2 D)\gamma' z \quad \textbf{2-83}$$

$$P_u = C_3 \gamma' z D \quad \textbf{2-84}$$

API (2007) also proposes the usage of the *p-y* curves for calculating the lateral soil resistance and deflection for piles embedded in sands. They provide Equation 2-85 for calculating the lateral deflection of a single pile under working loads.

$$P = AP_u \tanh\left[\frac{Kz}{P_u A} y\right] \quad \textbf{2-85}$$

In equation 2-85, P_u is the ultimate lateral capacity at depth z (as in Equations 2-83 and 2-84), z is the embedment depth, y is the lateral deflection of the pile and K can be related to the relative density of the soil or the effective friction angle of the material as in Figure 2-46. In Equation, 2-85 A is a factor that takes account of the effects of cyclic loading. API (2007) provides Equation 2-86 for static loading and adopts a value of 0.9 for cyclic loading for a single pile.

$$A = \left(3.0 - 0.8\frac{z}{D}\right) \geq 0.9 \text{ for static loading} \quad \textbf{2-86}$$

2.7 THE INFLUENCE OF VERTICAL LOADS ON THE LATERAL RESPONSE OF SINGLE PILES EMBEDDED IN SANDS

Karthigeyan et al. (2006) conducted a parametric study to evaluate the increase in the lateral capacity of single piles embedded in different types of sand deposits in regards to the application of a vertical load. The parametric study was conducted by the aid of a program called GEOFEM3D, which was developed by one of the authors and was validated before initiating the study.

The validity of the numerical package was verified by back calculating the response of two pile load test data from two different published cases, one was in respect to a short rigid pile and the second case was for a long flexible pile. They compare their results with the data published by Karasev et al. (1977) for a rigid pile and for the long pile case, they back analyse the results

obtained by Comodromos (2003). For the long pile case they also conduct an analysis with FLAC 3D to illustrate that the generated package provides acceptable results.

For their three-dimensional models, they consider the pile material as linear elastic while the soil was idealised using the Drucker-Prager perfectly plastic constitutive model. Based on symmetry only half of the model was constructed (all their models had reflective symmetry) as illustrated in Figure 2-47. They meshed their model with 20-node isoparametric brick elements (used on the pile and the soil body) and the interface between the pile and the sand was modelled using 16-node joint elements with zero thickness to represent slip and separation between the pile and the soil. They note that the accuracy of the mesh density on the entire model was checked by several trials until the displacements did not change with more refinement of the mesh. Figure 2-47 also illustrates their adopted dimensions and the generated mesh on the soil block for the numerical models.

They choose two different types of sands for their parametric study. One soil was considered loose with the following parameters:

ϕ' (friction angle of the soil) = 30°, Ψ (dilation angle) = 0°-10°, γ (unit weight of the soil) = 18 kN/m^3, ν (Poisson's ratio) = 0.3, K_0 (earth pressure at rest) = 0.5 and E_{soil} = 20 MPa (a constant soil modulus was used in their analysis).

The second soil sample in the FE analysis was considered as dense sand, with the following soil properties:

ϕ' (friction angle of the soil) = 36°, Ψ (dilation angle) = 0°-12°, γ (unit weight of the soil) = 20 kN/m^3, ν (Poisson's ratio) = 0.3, K_0 (earth pressure at rest) = 0.42 and E_{soil} = 50 MPa (a constant value was adopted).

The dimensions and properties of the concrete pile used in their study were as follows:

A square shaped pile with dimensions of 1200 mm by 1200 mm, pile's length equals to 10 m, Young's modulus equals to 25 GPa and the Poisson's ratio is equal to 0.15.

In their analysis, the vertical load on the pile's head was applied in two different ways. In the first case, the vertical load and the horizontal displacements were applied simultaneously to the pile's head. This case was called the SAVL case (Simultaneously Applied Vertical and Lateral loads). For the second case, the vertical loads were applied prior to the lateral displacements. During applying the lateral displacements to the pile's head in the second case, the vertical loads were kept constant. This case was called the VPL case (Vertical load Prior to Lateral load).

Before initiating their study, they define the ultimate vertical load (V_{ult}) capacity of a single pile by a separate analysis. Then they apply a ratio of that ultimate vertical load to the pile's head with a lateral displacement imposed on the pile's head for both cases.

The response of the pile under combined loading was investigated for when the vertical loads were equal to zero (only lateral loading), $0.2V_{ult}$, $0.4V_{ult}$, $0.6V_{ult}$ and $0.8V_{ult}$. In addition, they plot

their results in respect to lateral deflection (mm) versus lateral load (kN) for the pile's head. Their results are illustrated in Figures 2-48 and 2-49 for the SAVL and the VPL cases respectively.

As can be seen from Figures 2-48 and 2-49 the vertical load has only a marginal influence on the lateral response of the piles in the case of loose sands (that is for both the SAVL and the VPL cases). From Figures 2-48 and 2-49, it is also clear that the influence of the vertical load on the lateral response of a single pile is more significant in dense sand compared to loose sand. From Figure 2-49, it is also apparent that in the case of the VPL loading the significance of the vertical load on a single pile embedded in dense sand is much more pronounced compared to the results obtained from the SAVL case.

They also introduce a quantity named Percentage Improvement in lateral Capacity (PIC) to measure the influence of the vertical loads on the lateral response of the piles in the proposed loose and dense sands. The PIC was defined as in Equation 2-87, were LCWV is the Lateral load Capacity With Vertical load and LCNV is the Lateral load Capacity under a pure lateral load.

$$\mathrm{PIC} = \frac{\mathrm{LCWV} - \mathrm{LCNV}}{\mathrm{LCNV}} \times 100 \qquad \textbf{2-87}$$

They record the PIC values at deflections of 0.1B and 0.05B (B is the pile's width) for different values of the vertical load which were a fraction of the ultimate vertical capacity of the pile and produce Tables 2-7 and 2-8.

Vertical load in terms of V_{ult}	Lateral load at deflection of 0.05B		PIC at deflection of 0.05B		Lateral load at deflection of 0.1B		PIC at deflection of 0.1B	
	Loose	Dense	Loose	Dense	Loose	Dense	Loose	Dense
0	273	453	-	-	354	641	-	-
0.2	275	461	+0.7	+1.7	361	668	+1.9	+4.2
0.4	277	470	+1.4	+3.7	363	698	+2.5	+8.9
0.6	280	478	+2.5	+5.5	354	714	0.0	+11.4
0.8	278	484	+1.8	+6.8	330	718	-6.8	+12.0

Table 2-7. PIC values with respect to different vertical load levels for the SAVL case

Vertical load in terms of V_{ult}	Lateral load at deflection of 0.05B		PIC at deflection of 0.05B		Lateral load at deflection of 0.1B		PIC at deflection of 0.1B	
	Loose	Dense	Loose	Dense	Loose	Dense	Loose	Dense
0	317	453	-	-	398	641	-	-
0.2	326	486	+2.8	+7.3	410	678	+3.0	+5.8
0.4	334	547	+5.3	+20.7	420	740	+5.5	+15.4
0.6	346	591	+9.1	+30.4	434	801	9.0	+24.9
0.8	362	631	+14.2	+39.3	453	857	+13.8	+33.7

Table 2-8. PIC values with respect to different vertical load levels for the VPL case

From Table 2-7 it is clear that there is a decrease in the lateral load capacity for the SAVL cases when the vertical loads are beyond $0.6V_{ult}$ (at lateral deflections of 0.1B) for both sands. On the other hand, all the values increase in the case of a VPL loading scenario and that is for both the loose and dense sands.

They argue that the influence of the vertical loads on the lateral response of piles is more prominent for dense sands than loose sands. The reasons for this difference can be further assessed through factors such as friction angle, soil's modulus of elasticity and the soil's dilation angle.

Figure 2-50 illustrates the influence of the soil's modulus of elasticity and the effects of the friction angle on the response of the pile under pure lateral loading. In this figure, the pile is under a vertical load of $0.6V_{ult}$. They mention that the difference in the PIC values were significant due to the presence of the vertical loads for different friction angles, however the behaviour was found to be nearly the same for a soil with a constant friction angle of 36° with different soil's modulus of elasticity's (20 MPa and 50 MPa).

They also investigate the influence of the dilation angle on the lateral capacity of a single pile embedded in a sand deposit. The value of the dilation angle was changed from zero to $\phi/3$ (that will be 10° for the loose sand and 12° for the dense sand). They plot their results in respect to the PIC value as illustrated in Figure 2-51. From this figure, it is clear that the PIC values are much smaller for loose sands compared to the dense sand.

They also investigate the influence of the slender ratio (L/B, with B equal to the pile's breadth) for a single pile under different vertical loads. Their results are illustrated in Figure 2-52. In this figure, B is equal to the pile's breadth for a square pile with dimensions of 600 mm by 600 mm and with varying lengths of 5 m, 10 m and 15 m. They conducted their analysis for a pure lateral load (vertical load equal to zero) and under the influence of a vertical load equal to $0.6V_{ult}$. From Figure 2-52, it is clear that lateral capacity of a single pile increases as L/B increases (that is for all possible cases). It is also clear that the influence of the vertical load on the lateral response of the pile decreases as the slender ratio of the pile increases (this is the case for both types of lateral loading, that is the SAVL and VPL cases). They also mention that the influence of the vertical load on piles with lower slender ratios is higher than pile's with high slender ratios.

It must be pointed out that in this study because the pile material was elastic (without a yield point) the soil failure was considered in all generated figures. In addition, the pile's head was at the ground level, which allowed the soil to fail within an acceptable deflection appointed for the pile's head. As it will be illustrated in Chapters 5 and 6 this is not the case for pile/towers which have a high eccentricities (height above the ground level) similar to offshore wind turbines.

2.8 BEARING CAPACITY OF SHALLOW FOUNDATIONS

2.8.1 Introduction

Shallow foundations by definition are structures that have an embedment depth of less than or equal to the width of the foundation (Terzaghi, 1943). Later investigators have suggested that

foundations with an embedment depth (D_f) equal to 3 to 4 times the width of the foundation can also be considered as shallow foundations.

Similar to deep foundations, these structures should not collapse under the conceivable loading conditions and the settlement of the structure must be within the tolerable limits. In the case of shallow foundations, usually the settlement criteria governs the structure design.

The nature of the bearing capacity failure in soils is dependent on the stiffness of the soil. Figure 2-53 illustrates a strip foundation with a width of B located on three different soil mediums; the load versus settlement graph of the structures has also been illustrated in the figures.

Figure 2-53(a) illustrates a foundation resting on a stiff soil medium, when the load on the foundation passes the collapse load (Q_{ult}) the soil surrounding the structure will suddenly fail and the failure surface will extend to the ground surface. The value of Q_{ult}, which causes the soil to fail, is referred to the ultimate bearing capacity of the foundation. The collapse load in a dense soil is termed the general shear failure as the shear planes are fully developed.

Figure 2-53(b) illustrates a foundation resting on sand or clayey soil with medium compaction. In this type of failure, the shear planes are not fully developed and they do not extend to the ground surface by the amount of q_{u1} (Vesic 1973 calls q_{u1} the first failure load). If the shear failures are to be extended to the ground surface an extra load has to be applied to the structure, which brings the load up to the value of Q_{ult} illustrated in Figure 2-53(b).The value of Q_{ult} is called the ultimate bearing capacity and beyond this point, the settlement of the structure will be large. This type of failure, which occurs in medium dense soils, is usually called the local shear failure.

Figure 2-53(c) illustrates a structure supported by a loose soil. In this type of failure, the failure surface will not extend to the ground surface and will be confined to the surfaces of the rigid wedge. This failure is called the punching shear.

2.8.2 Terzaghi's bearing capacity equations

Terzaghi (1943) derived bearing capacity equations based on Prandtl's (1920) failure mechanism. He assumed the following:

1. The soil was considered as semi-infinite, homogeneous, isotropic, weightless and rigid-plastic.
2. The embedment depth of the foundation is smaller than the width of the footing.
3. Only a general shear failure occurs.
4. The shear strength above the footing level was negligible and it was not considered in the calculations.
5. The base of the footing was considered rough.
6. The angle of the wedge generated beneath the footing was equal to the soil's friction angle (Vesic, 1973 finds out that the angle is more likely to be equal to $45° + \phi'/2$).

Using the equilibrium analysis, Terzaghi calculated the ultimate bearing capacity in the form of Equation 2-88 (this equation is only for a strip foundation, a 2D case).

$$q_u = cN_c + q'N_q + 0.5\gamma'BN_\gamma \quad \textbf{2-88}$$

In Equation 2-88, c is the cohesion, γ' is the effective unit weight of the soil, q' is the effective vertical stress at the level of structure's footing and N_c, N_q, N_γ are the bearing capacity factors and are only related to the soil's friction angle.

The bearing capacity factors can be calculated as in Equations 2-89 to 2-91 for a strip foundation.

$$N_c = \cot\phi' \left[\frac{e^{2\left(\frac{3\pi}{4} - \frac{\phi'}{2}\right)\tan\phi'}}{2\cos^2\left(\frac{\pi}{4} + \frac{\phi'}{2}\right)} - 1 \right] \quad \textbf{2-89}$$

$$N_q = \left[\frac{e^{2\left(\frac{3\pi}{4} - \frac{\phi'}{2}\right)\tan\phi'}}{2\cos^2\left(\frac{\pi}{4} + \frac{\phi'}{2}\right)} \right] \quad \textbf{2-90}$$

$$N_\gamma = 0.5\left(\frac{K_0}{\cos^2\phi'} - 1\right)\tan\phi' \quad \textbf{2-91}$$

The ultimate bearing capacity of a square and circular foundation can also be calculated by Equations 2-92 and 2-93 respectively.

$$q_u = 1.3cN_c + q'N_q + 0.4\gamma'BN_\gamma \quad \textbf{2-92}$$

$$q_u = 1.3cN_c + q'N_q + 0.3\gamma'BN_\gamma \quad \textbf{2-93}$$

Terzaghi also proposed equations for calculating the ultimate bearing capacity of foundations, which exhibit a local shear failure. His proposed equations for a strip, square and circular foundations are as in Equations 2-94 to 2-96 respectively.

$$q_u = 0.66cN'_c + q'N'_q + 0.5\gamma'BN'_\gamma \quad \textbf{2-94}$$

$$q_u = 0.867cN'_c + q'N'_q + 0.4\gamma'BN'_\gamma \quad \textbf{2-95}$$

$$q_u = 0.867cN'_c + q'N'_q + 0.3\gamma'BN'_\gamma \quad \textbf{2-96}$$

The values of N'_c, N'_q and N'_γ are calculated by the bearing capacity equations (2-89 to 2-91) but the friction angle has to be replaced by $\tan^{-1}(2/3\tan\phi')$ in the bearing capacity equations.

In the case of offshore foundations were the soil is totally submerged under water the effective unit weight of the soil has to be used in the bearing capacity equations with the effective stress considered at the base of the footing (that is $q' = \gamma' D_f$).

2.8.3 The general bearing capacity equation

The ultimate bearing capacity equations derived by Terzaghi do not address the cases of a rectangular footing and as previously mentioned they do not take into account the shearing

resistance of the soil above the footing. In addition, the equations derived by Terzaghi are not suitable for inclined loadings on the foundation.

To overcome the problems with Terzaghi's equations Meyerhof (1963) proposed Equation 2-97.

$$q_u = cN_cF_{cs}F_{cd}F_{ci} + q'(N_q - 1)F_{qs}F_{qd}F_{qi} + 0.5\gamma' BN_\gamma F_{\gamma s}F_{\gamma d}F_{\gamma i} \quad \textbf{2-97}$$

In this equation, c is the cohesion, q′ is the effective stress at the base of the foundation, γ′ is the effective unit weight of the soil and B is the width of the foundation (for a circular foundation B is equal to the diameter of the circular foundation, Das 1999 & Budhu 2007). F_{cs}, F_{qs}, $F_{\gamma s}$ are the shape factors, F_{cd}, F_{qd}, $F_{\gamma d}$ are the depth factors and F_{ci}, F_{qi}, $F_{\gamma i}$ are the load inclination factors.

It must be pointed out that some scholars do not consider the cohesion in Equation 2-97. They argue that the cohesion and the friction angle are not mobilised at the same shear strain levels (cohesion is mobilised at smaller shear strains while the friction angle is mobilised at much larger shear strain values). Thus, as shear strains develop under the foundation during loading, c and ϕ would not be mobilised simultaneously (Budhu, 2008). To overcome the problem they adopt their parameters based on effective and total stress paths. This was also the case for deep foundations embedded in clay layers.

The values of the shape, depth and inclination factors used in Equation 2-97 are illustrated in Table 2-9.

Factor	Relationship	Source
Shape factors L is the length and B is the width of the foundation (B>L)	$F_{cs} = 1 + (B/L)(N_q/N_c)$	De Beer (1970) Hansen (1970)
	$F_{qs} = 1 + (B/L)\tan\phi'$	
	$F_{\gamma s} = 1 - 0.4(B/L)$	
Depth factors		Hansen (1970)
When $D_f/B < 1$	$F_{cd} = 1 + 0.4(D_f/B)$	
	$F_{qd} = 1 + 2\tan\phi'(1-\sin\phi')^2(D_f/B)$	
	$F_{\gamma d} = 1$	
When $D_f/B > 1$	$F_{cd} = 1 + 0.4\tan^{-1}(D_f/B)$ (in radians)	Hansen (1970)
	$F_{qd} = 1 + 2\tan\phi'(1-\sin\phi')^2\tan^{-1}(D_f/B)$	
	$F_{\gamma d} = 1$	
Inclination factors		Meyerhof (1963); Hanna and Meyerhof (1981)
β is the inclination of the load on the foundation with respect to the vertical	$F_{ci} = F_{qi} = (1 - \beta/90°)^2$	
	$F_{\gamma i} = (1 - \beta/\phi)^2$	

Table 2-9. Shape, depth and inclination factors used in the bearing capacity equation

The value of N_q in Equation 2-97 is calculated by Equation 2-98. In this equation, ϕ'_{peak} is the effective peak friction angle of the soil.

$$N_q = e^{\pi \tan\phi'} \tan^2\left(45° + \frac{\phi'}{2}\right) \quad \textbf{2-98}$$

Many equations have been proposed for calculating N_γ in Equation 2-98. Some of these equations are illustrated in Table 2-10.

Vesic (1973)	$N_\gamma = 2(N_q + 1)\tan\phi'$
Meyerhof (1976)	$N_\gamma = (N_q - 1)\tan(1.4\phi')$
Davis and Booker (1973) The friction angle is in radians	[rough footing] $N_\gamma = 0.1054\exp(9.6\phi')$
	[smooth footing] $N_\gamma = 0.0663\exp(9.3\phi')$
Ueno et al. (1998) The friction angle is in radians	$N_\gamma = 0.477\exp(6.52\phi')$ [rough footing]

Table 2-10. The commonly used bearing capacity factors

The equations derived by Davis and Booker (1973) in Table 2-10 were originally obtained by curve fitting their theoretical results by Poulos et al. (2002). The equation given by Ueno et al. (1998), Table 2-10 were also obtained by curve fitting their theoretical results.

When using the bearing capacity equations the effective peak friction angle of the soil could be used for calculating the shape, depth and inclination factors. As plain strain conditions were used in developing the bearing capacity equation, the effective peak friction angle must be calculated from a plane strain test (a shear box test or a simple shear test). The effective peak friction angles calculated by a triaxial apparatus are generally less than the peak friction angles calculated in a plane strain test. Equation 2-99 can be used to convert the effective peak friction angle calculated in a triaxial apparatus to the effective peak friction angle of a plane strain test.

$$(\phi'_{peak})_{plain\ strain} = 1.125(\phi'_{peak})_{triaxial} \quad \textbf{2-99}$$

Vesic (1973) discussed that considering a peak plain strain friction angle for the soil might help resolve the differences between theoretical and experimental results for long rectangular foundations. However, this is not the case for square and circular foundations. It must be mentioned that Budhu (2007) uses a peak plain strain friction angle for all shallow foundations. Ko and Davidson (1973) concluded that when plane strain friction angles are used in the bearing capacity equations for rough footings in dense sands the bearing capacity of the structure can be seriously overestimated. Moreover, Powrie (1997) discusses that using a critical soil friction angle might be more reliable than using the peak friction angle of the soil in the bearing capacity equations. In Chapter 5, it will be illustrated that a critical soil friction angle for the centrifuge tests will provide a reasonable estimate for the ultimate capacity of the un-piled footing structures embedded in the silica sand.

The ultimate net bearing capacity is calculated by Equation 2-97 but if the ultimate gross bearing capacity is required, the stress at the base of the foundation (that is $\gamma' D_f$) has to be added to that equation if the foundation is embedded in the soil layer.

The allowable bearing capacity is also the value calculated in Equation 2-97 divided by a safety factor and summed with the stress acting at the base of the structure if the foundation is embedded in the soil layer.

2.8.4 Eccentric loads

In many scenarios, the foundations are subjected to moments in addition to the vertical loads acting on them, as illustrated in Figure 2-54. In these cases, the location of the resultant vertical load can be adjusted so that it would not coincide with the centroid of the footing. The distance of the resultant vertical load from the centroid is called eccentricity. The applied moments acting on a shallow foundation at the ground level can be converted to a vertical resultant load acting at a specified eccentricity by Equation 2-100.

$$e_B = \frac{M_y}{V_n} \text{ and } e_L = \frac{M_x}{V_n} \quad \textbf{2-100}$$

In these equations, V_n is the vertical load, M_x and M_y are the moments about the x and y-axis respectively. e_B and e_L are the eccentricities in the direction of the breadth and length of the foundation respectively, as illustrated in Figure 2-55.

Meyerhof (1953) proposed a method called the effective area method for determining the ultimate load that a soil can sustain against bearing capacity failure for foundations that are subjected to vertical and moment loadings. In the proposed procedure, the moment acting on the footing is compensated by giving an eccentricity to the location of the vertical load acting on the footing. If the moment is acting in one direction, an eccentricity can be introduced to the location of the vertical load in the direction of the breadth or length depending on the direction of the acting moment. If for example an eccentricity is introduced to the direction of B (breadth) the effective dimension will now be equal to B′= B – 2e (with L′= L). If the eccentricity was introduced to the length of the footing then L′ = L - 2e and the value of B′ = B.

When calculating the bearing capacity factors, the values must be calculated in respect to B′ and L′ (the effective dimensions) if a moment has been introduced to the foundation.

For calculating the total ultimate load that a foundation can sustain, the calculated value from Equation 2-97 must be multiplied by the effective area of the structure if a moment is acting on the footing (that is B′× L′, this case is for when two moments are acting in the x and y directions).

When dealing with a circular footing the effective area can be calculated as in Equation 2-101. In this equation, D is the diameter of the foundation and e is the eccentricity.

$$A' = \frac{D^2}{2}\left[\cos^{-1}\frac{2e}{D} - \frac{2e}{D}\sqrt{1-\left(\frac{2e}{D}\right)^2}\right] \quad \textbf{2-101}$$

2.8.5 Combined loading

The equations provided in the previous sections for shallow foundations do not consider applying the vertical, horizontal and moment loads simultaneously acting on a shallow foundation. In addition, the expressions given in Equation 2-97 apply linear superposition to a problem, which is nonlinear (Gottardi et al. 1993).

To consider a vertical load, horizontal load and moment acting on a shallow foundation a three-dimensional analysis is necessary. The usual method for combined loadings for footings is to consider a yield surface or a failure surface, which considers a safe combination of loading inside the yield surface. This approach has also been used for anchors and spudcans used to support offshore platforms at UWA.

Taiebat and Carter (2000) provided a yield surface for combined loading of a circular shallow foundation positioned on fine grain soils (clays) while Houlsby and Purzin (1999) provide a failure envelope for a strip foundation based on a two dimensional finite element analysis.

The equation provided by Taiebat and Carter (2000) is in the form of Equation 2-102. In this equation $(V_n)_u$ is the ultimate vertical load, M_u is the ultimate moment capacity and H_u is the ultimate horizontal load capacity. The values of V_n, M and H are the vertical load, moment and shear force applied to the structure.

$$f = \left(\frac{V_n}{(V_n)_u}\right)^2 + \left\{\frac{M}{M_u}\left(1 - 0.3\frac{HM}{H_u M_u}\right)\right\}^2 + \left(\frac{H}{H_u}\right)^3 - 1 = 0 \quad \textbf{2-102}$$

They provide the values of $(V_n)_u$, M_u and H_u as follows:

$$(V_n)_u = (5.7 \text{ to } 6)Ac_u \quad \textbf{2-103}$$

$$M_u = 0.8ADc_u \quad \textbf{2-104}$$

$$M_u = 0.89ADc_u \quad \textbf{2-105}$$

$$H_u = 0.71Ac_u \quad \textbf{2-106}$$

In the above equations, C_u is the shear strength of the soil, A is the cross sectional area of the footing and D is footing's diameter.

Equation 2-104 is only for a vertical load and moment case while Equations 2-105 and 2-106 are for a horizontal load and moment case only. They also conclude that the value f in Equation 2-102 must be less than one if the foundation is to be safe.

Gottardi et al. (1993) discusses that a footing resting on a sand deposit will illustrate a parabolic expression in V-H plane, which can be expressible in the form of Equation 2-107. They also

conduct tests at 1 g level and conclude that the value of β_1 in the latest equation is equal to tanδ (with δ equal to the soil footing interface friction angle) and β_2 equal to one. From the lasts equation it is also clear that the values have been normalised in respect to the maximum vertical load that the soil can sustain (V_{max}).

$$\frac{H}{V_{max}} = \beta_1 \frac{V}{V_{max}} \left\{ 1 - \left(\frac{V}{V_{max}} \right)^{\beta_2} \right\} \quad \textbf{2-107}$$

For the V-M plane, they mention that again a parabolic function will describe the yield surface successfully. They provide Equation 2-108 for the V-M plane and they again normalise the values by the value of V_{max}.

$$\frac{M}{BV_{max}} = 0.4 \frac{V}{V_{max}} \left(1 - \frac{V}{V_{max}} \right) \quad \textbf{2-108}$$

In the above equation, B is equal to the breadth or diameter of the footing and V is the vertical load applied on top of the footing.

For the M-H plane they consider a central ellipse with a slight rotation (clockwise rotation angle = 12.7°) and provide Equation 2-109.

$$82.16 \left(\frac{M}{BV_{max}} \right)^2 + 34.19 \left(\frac{H}{V_{max}} \right)^2 - 22.81 \left(\frac{M}{BV_{max}} \right) \left(\frac{H}{V_{max}} \right) - 0.58 = 0 \quad \textbf{2-109}$$

In the above equation, the values of M, B, H and V_{max} are the moment, breadth or diameter of the footing, the horizontal force and the maximum vertical load on the structure. This equation has also been normalised in respect to V_{max}.

The three-dimensional interaction surfaces in the general space (VHM) are illustrated in Figure 2-56. It must be noted that Equations 2-107 to 2-109 are the yield surfaces for a failed footing resting on a sand deposit.

Govoni et al. (2010) and Gourvenec et al. (2008) conducted centrifuge tests at UWA on footings embedded in silica sand and compared their results with equations provided by Gottardi et al. (1993). They confirm the "rugby ball" shape of the yield surface in three-dimensional load space but they each encounter discrepancies in their results compared to the 1 g tests conducted by Gottardi et al. (1993).

Gourvenec et al. (2008) illustrates and concludes that the moment capacities of the footings tested in the centrifuge are higher than the predicted values at by Gottardi et al. (1993) equation. She also mentions, "The embedment depth causes an increase in the normalised peak moment and the peak moment is mobilised at higher vertical loads" this statement was made compared to Gottardi's equations derived at 1 g level. Govoni et al. (2010) has also argued that the embedment depth can significantly enhance the normalised yield surface (for the moment capacity) in the centrifuge tests; this might be because of passive and active pressures developed around the footing as it translates horizontally.

Govoni et al. (2010) also mentions that the footing size might contribute to the size of the yield surfaces. If this is the case, the maximum moment could be seriously affected by the size of the footing. It also seems that the largest footing diameter used (up to the date of writing this thesis) to capture the yield surfaces in a three-dimensional plane was around 5 m.

2.9 EMBEDDED RETAINING WALLS WITH A STABILISING BASE

From a 2-dimensional approach, a piled footing structure was expected to behave similar to a retaining wall with a stabilising platform, this structure is illustrated in Figure 2-57 (a) and (b). The retaining wall with a stabilising platform is similar to half a piled footing structure under a plain strain situation.

As discussed by Powrie et al. (2007) a retaining wall can be supported by a short horizontal platform known as the stabilising base, which can be attached rigidly to the front of the wall at the ground level or below it.

Powrie et al. (2007) conducted four centrifuge tests on embedded retaining walls with a stabilising base. Two out of four tests were carried out in Leighton Buzzard sand and the other two were conducted in Speswhite Kaolin clay. The plain strain models were subjected to 94 g acceleration in the centrifuge.

Two sets of tests were conducted on the proposed sand, in the first case the wall embedment was 85 mm (equal to 8 m in a prototype) and in the other case the wall's embedment depth was 42.5 mm (equal to 4 m in a prototype). The stabilising base was projected 42.5 mm from the wall in both cases. A schematic cross section of the retaining wall with the dimensions adopted for the two tests are illustrated in Figure 2-57 (a) and (b). They mention that the adopted values for the tests conducted on the retaining walls; those are the retaining walls height and the lengths of the stabilising base were chosen in respect to another study conducted by Powrie and Chandler (1998).

Powrie and Chandler (1998) perform a series of numerical analysis with a program called CRISP and illustrate that the optimal length of the stabilising base must be around 50% of the walls embedment depth. In this study they also mention that the optimal platform length was determined based on economic factors and wall displacement reduction sighted from the results obtained from the program.

The model wall and the stabilising base in the centrifuge tests were constructed as one piece by Aluminium alloy (LM25 TF) with a uniform thickness of 7.3 mm. They also coat the wall and the stabilising base with epoxy resin; this increased the thickness to 10 mm.

Sand samples in the centrifuge were prepared by raining sand from a hopper into the strongbox with the strongbox on its back and the wall bolted to the backplate. The average dry density of the sand was 1626 kg/m^3 and 1635 kg/m^3 for the two the tests conducted on the sand deposit (the tests were called LB8 and LB4). The strong box was then rotated back to vertical and the excavated profile was formed by removing sand using a full-width nozzle attached to a vacuum cleaner, suspended a short distance above the current sand surface. They then unbolt the wall

from the backplate and the excavated sand was replaced by a flexible PVC bag filled to the level of the retained soil surface with zinc chloride solution of the same mass density as the saturated sand. They prepared the sample by this method (direction of deposition to be parallel to the line of the wall) so that the relative vertical and horizontal stiffness would be influenced but the effect on the soil strength would be negligible.

They used pore water pressure transducers for the sand model, which were suspended in place using fishing lines as the sand was poured around them. They also strain gauge each wall with up to nine gauges with two sets used on the stabilising base for capturing the bending stresses acting on the stabilising platform.

They mention that the soil settlement behind the wall was similar to the horizontal wall movement in the sand tests. They also mention that the movements (in the sand cases) were much smaller than the tests conducted on the clay deposit. The reason for the smaller movements recorded in the sand tests were that the sand had a greater stiffness (compared to the clay) and it was less onerous to ground water conditions.

The bending moments measured from the stabilising platform in both tests conducted in the sand deposit corresponded closely to a triangular bending pressure distribution, which increased form zero at the root of the stabilising base to 160-228 kPa at the tip in test LB4 and 256-532 kPa in test LB8. In addition, they mention that the 'sand walls surrounding the embedded retaining wall were remote from collapse'.

As illustrated in Figure 2-58 the restoring moment generated due to the presence of the bearing pressure on the underside of the stabilising platform is the main mechanism for which the platform reduces the wall movement. The bearing pressure on the underside of the stabilising base provides a surcharge on the soil in front of the wall, which increases the passive force applied to the wall and thus it reduces the total wall movement. In addition, the shear forces generated between the soil and the platform reduces the wall movement.

2.10 TESTS CONDUCTED ON PILED FOOTING STRUCTURES

The concept of using a monopile with a footing at the ground level was originally proposed by Dixon (2005), Figure 2-59 is a schematic illustration of the proposed hybrid structure. Stone et al. (2007) conducts tests at 1 g level to show the benefits of this type of structure compared to a single pile (monopile). In their study, they also identified the vertical capacity of the hybrid structure during their testing programme.

Stone et al. (2007) conducted tests in a dense uniform sand with an 11 mm diameter solid Aluminium pile and a 50 mm diameter thick fibreboard footing (the thickness of the footing was 6 mm) at 1 g level. During their testing programme, the vertical load was applied at a rate of 0.02 mm/s through a strain controlled frame load to the structures (monopiles and monopiled footings) to identify the vertical capacity of the structures. In regards to the maximum vertical capacity of the structures, they conclude that the hybrid foundation's vertical capacity is equal to the sum of

its individual components. They also mention that the piled footing's failure mechanism was observed to be symmetric, as the footing did not rotate.

For the combined loading tests, Stone et al. (2007) applies loads directly to the circular footing to provide the vertical load on the structure while the lateral load was applied through a wire and a pulley system at a rate of 0.02 mm/s to the hollow pipe. The lateral load was applied at a height of 36 mm above the ground level to the structures. As illustrated in Figure 2-60 the combined foundation has a greater stiffness compared to a monopile and so it undergoes smaller displacements. They conclude that the degree of restraint provided by the circular footing depends on its size, the embedment depth into the ground and the soil's density.

Stone et al. (2010) conducts tests in the centrifuge at a level of 50 g on monopiles, piled footings and footings to investigate the response of each structure under lateral loading. The dry sand used in their study had a minimum and maximum void ratio of 0.61 and 1.06 respectively. The sand had also a critical state friction angle of 32°-33°. For their centrifuge tests, they use an open-ended steel tube with a thickness and length of 0.5 mm and 19 mm respectively. The footing used in the centrifuge tests was made out of Aluminium and had a diameter and thickness of 100mm and 5 mm respectively. The footing used in the tests also had a clamping arrangement so that its location could be adjusted on the pile's body during the testing procedure. For the tests conducted on the monopiles, they keep the footings of the ground level at a height of 20-25 mm. This was in fact, done by clamping the footing to the pile's body.

They mention that air pluviation created samples with a unit weight of 13.7 kN/m^3, void ratio of 0.89 and a relative density of 39%. The sample was then poured into a strong box and located on the centrifuge. They installed the piles by pushing them into the sand by hand to 80% of their depth and then for the final part they used light tapping with a hammer to drive the pile to the desired depth of installation.

For the piled footing tests, they mention that the bearing plate was in firm contact with the soil surface and the vertical loads were applied through dead weights placed directly on the bearing plate. The lateral load was applied to the model foundations by a steel wire looped around the pile and connected to a load actuator at a height of 30 mm (1.5 m) above the ground level.

Table 2-11 is a summary of the centrifuge tests conducted by Stone et al. (2010). In this table, the vertical load on the structure was considered without the self-weight of the foundation.

Test ID	*Test type*	*Pile embedment (mm)*	*Vertical load (N)*
FV	Footing only vertical push	n/a	n/a
PV	Vertical loaded pile only	200	n/a
PL1	Laterally loaded pile only	180	600
HL1	Monopiled footing	180	600
HL2	Monopiled footing	180	1100
HS1	Monopiled footing	50	600

Table 2-11. Summary of centrifuge tests conducted by Stone et al. (2010)

For identifying the vertical capacity of the footing, that is test FV in Table 2-11 they used a 50 mm diameter plate instead of the 100 mm diameter bearing plate which was originally used in the piled footing tests. The results of their vertical tests are illustrated in Figure 2-61. As they mention, the vertical capacity of the large footing is considerably higher than of the monopile.

Stone et al. (2010) plots the results of the combined vertical and horizontal loadings through plots of lateral load versus lateral displacement, as illustrated in Figure 2-62. This figure illustrates the results of two monopiled footings and a monopile with a vertical load of 600 N. As shown in Table 2-11, test HS1 is for a monopiled footing with a short pile under a vertical load of 600 N.

Stone et al. (2010) concludes that the foundation plate provides a degree of moment restraint to the pile head through the soil reaction on the underside of the bearing plate. They also point out that the initial behaviour of the monopiled footing was controlled by the behaviour of the pile but as the foundation rotates, the lateral stiffness of the monopiled footing is governed by the moment restraint provided by the bearing plate. This last point was derived from Figure 2-62 because it is clear that the initial stiffness of the monopile (PL1) and the monopiled footing (HL1) are the same in this figure (for small displacements). They also mentioned that the response of the monopiled footing (that is its stiffness) is mainly controlled by the initial contact between the bearing plate and the soil. From Figure 2-62, it is clear that the embedment depth of the pile has a significant influence on the lateral response of the monopiled footing. In addition, they note that a gap between the soil and the bearing plate can eliminate any influence of the bearing plate and consequently affecting the response of the hybrid structure.

The tests conducted in the centrifuge by Stone et al. (2010) do not really represent a realistic scenario. One of the main problems with their tests is the location of the applied lateral loads to the structures. As previously mentioned, the lateral loads were applied at 30 mm above the ground level, which is equivalent to 1.5 m in a prototype. The force at 1.5 m above the ground level will indeed generate very small moments at the ground level and this is inconsistent with the results and findings of Byrne et al. (2003). The second problem with these tests is that the dead weights were placed directly on the bearing plate for the monopiled footing tests while they had to be located on the pile's body or on the pile's head. Placing the weights on the footing during the tests will cause the load to be completely transferred to the footing rather than to the pile and this can result in a very high stiffness for the structure. The third problem is that the

horizontal loads in Figure 2-62, which were applied to the structures, are much smaller to those experienced by offshore wind turbines (Byrne et al. 2003). The low-recorded lateral load during the testing procedure might be due to the height at which the lateral load was applied to the structures.

The inconsistencies in the tests conducted by Stone et al. (2010) seriously affected their conclusions. As can be seen from Fiugres 2-60 and 2-62 the results are not matching. In the 1 g tests (Figure 2-60) the piled footing structure's stiffness was higher than of a monopile from the very initial point while in the centrifuge tests (Figure 2-62) the initial stiffness of both structures are exactly the same up to a displacement of around 1mm.

Lehane et al. (2010) investigated the response of a monopile, monopiled footing and a footing in kaolin clay. Their tests were conducted in the beam centrifuge at UWA at an acceleration level of 200 g. They used a T-bar test to assess the shear strength of the soil at various depths; the changes in the shear strength with depth are illustrated in Figure 2-63.

Table 2-12 summarises the six tests conducted in the beam centrifuge in the kaolin clay. The piles in the tests were constructed out of Aluminium alloy with a diameter of 19 mm. The footings in the tests had diameters of 60 mm and 75 mm and were constructed out Aluminium alloy too. The third footing used in the tests had a diameter of 75 mm but incorporated a 12 mm skirt around its outer periphery. They discuss that the later was used to investigate the potential influence of suction underneath the platform on the tension side of the pile. All footings involved in the tests were embedded around 4 ± 1 mm into the clay before the tests were conducted. The lateral load was applied at a height of 30 m (in a prototype) to the structures during the testing procedure. This height ensured that the ratio of moment to the horizontal force was within the range experienced by offshore wind turbines as discussed by Byrne et al. (2003).

They plotted the test results in graphs of lateral force versus lateral displacement (the lateral displacement was divided by the pile's diameter in the original paper). Figure 2-64 illustrates the results of the six tests. They discuss that the lateral capacity of a single pile is at least ten times greater than of a single footing case and the initial stiffness of all three structures seems to be very close to each other. They note that the higher stiffness of the footing with a solid pile can be attributed to the higher flexure rigidity (EI) of the pile compared to the flexible pile.

Figure 2-65 illustrates the bending moments acting on the pipe pile for test number two (single pile) and test number three (pile with a footing) inferred from the strain gauges used on the structures during the testing procedure.

Test number	Foundation geometry	Prototype dimensions (m)	Max H applied (N, model ≡ MN, prototype
1	Pipe pile with 60 mm diameter footing	D_{pile} = 3.8 m $D_{footing}$ = 12 m	220N ≡ 8.8 MN
2	Pipe pile	D_{pile} = 3.8 m $D_{footing}$ = 12 m	230 ≡ 9.2 MN
3	Pipe pile with 75 mm diameter footing	D_{pile} = 3.8 m $D_{footing}$ = 12 m	220N ≡ 8.8 MN
4	Solid pile with 75 mm diameter footing	D_{pile} = 3.8 m $D_{footing}$ = 12 m	295N ≡ 1.8 MN
5	Pipe pile with skirted 75 mm diameter footing	D_{pile} = 3.8 m $D_{footing}$ = 12 m	220N ≡ 8.8 MN
6	75 mm diameter skirted footing	D_{pile} = 3.8 m $D_{footing}$ = 12 m	21N ≡ 0.83 MN

Table 2-12. Details of centrifuge tests conducted in the kaolin clay (Lehane et al., 2010)

If a piled footing structure is to be used in practice instead of a single pile the stiffness of the proposed structure has to be higher than of a single pile while its bending moments must be smaller than of a monopile. From Figures 2-64 and 2-65 it is clear that the stiffness of the proposed structure in a clay deposit is not very much different from a single pile and also the bending moments acting on both structures do not illustrate a considerable gap.

To back up their findings Lehane et al. (2010) also conducted a 3D analysis with Plaxis 3D Foundations to calculate the response of tests number two, three and six (Table 2-12). They model the hollow pile as a solid pile with an equivalent flexure rigidity and the soil was modelled as an elastic perfectly plastic material with a friction angle of zero (Tresca criterion). The shear strength of the soil was taken as the best estimate of the T bar tests conducted in the centrifuge (S_u (kPa) = 7.5 + 1.75Z (m)). They also considered the Young's modulus to be constant for the soil, and it was equal to 8 MPa. In addition, a Poisson's ratio of 0.49 was considered for the undrained clay. The FE predictions for the three tests are illustrated in Figure 2-66.

They concluded that for a clay deposit with undrained shear strength of around 20 kPa at the ground surface the contribution to stiffness, ultimate capacity and the bending moment for a piled footing with a footing diameter equal to four times the pile's diameter was insignificant. They also discuss that the proposed structure could be more successful in deposits with a greater surface stiffness and strength (similar to stiff sand deposits).

2.11 CONCLUSION

In this chapter, the behaviour of deep and shallow foundations was discussed. Methods available in the literature for estimating the ultimate axial capacity and lateral capacity of piles were discussed in Sections 2.5 and 2.6 respectively. In Section 2.7 the influence of vertical load on the lateral capacity of single piles embedded in sands was also discussed. It was clear that the vertical

load did not significantly contribute to an increase in the lateral load capacity of a single pile embedded in sand deposit. In Chapters 5 and 6, the methods illustrated for calculating the ultimate lateral capacity of a sing pile embedded in a sand layer will be used for comparison purposes with the FE and the test results conducted in the centrifuge.

In Section 2.8, the ultimate capacity of footings under centric, eccentric and combined loading was discussed. The bearing capacity equation and the equation adopted by Gottardi et al. (1993) will be combined for calculating the ultimate capacity of single footings embedded in a sand deposit in Chapters 5 and 6.

In Section 2.9, it was discussed that from a 2-dimensional approach, a piled footing was expected to behave similar to a retaining wall with a stabilising platform. It was clear that the optimal length of the stabilising base must be at least around 50% of the walls embedment depth. This point will be further investigated by constructing numerical models in Chapter 6.

In Section 2.10, a review of the tests conducted on piled footing structures embedded in sands and clays was presented. It was clear that a very limited number of tests are conducted on this newly proposed structure. As discussed in Chapter 1, for a newly proposed structure it is extremely important to investigate the structures behaviour in detail through tests or numerical modelling. For instance, the effects of the pile and footing diameter, pile length, pile thickness, the footing's thickness and its embedment depth must be investigated in different soils. In Chapters 5 and 6, centrifuge tests and numerical models will be constructed to illustrate the benefits of using this structure in practice.

Figure 2-1. Egmond aan zee wind farm located in the North Sea (www.trelleborg.com)

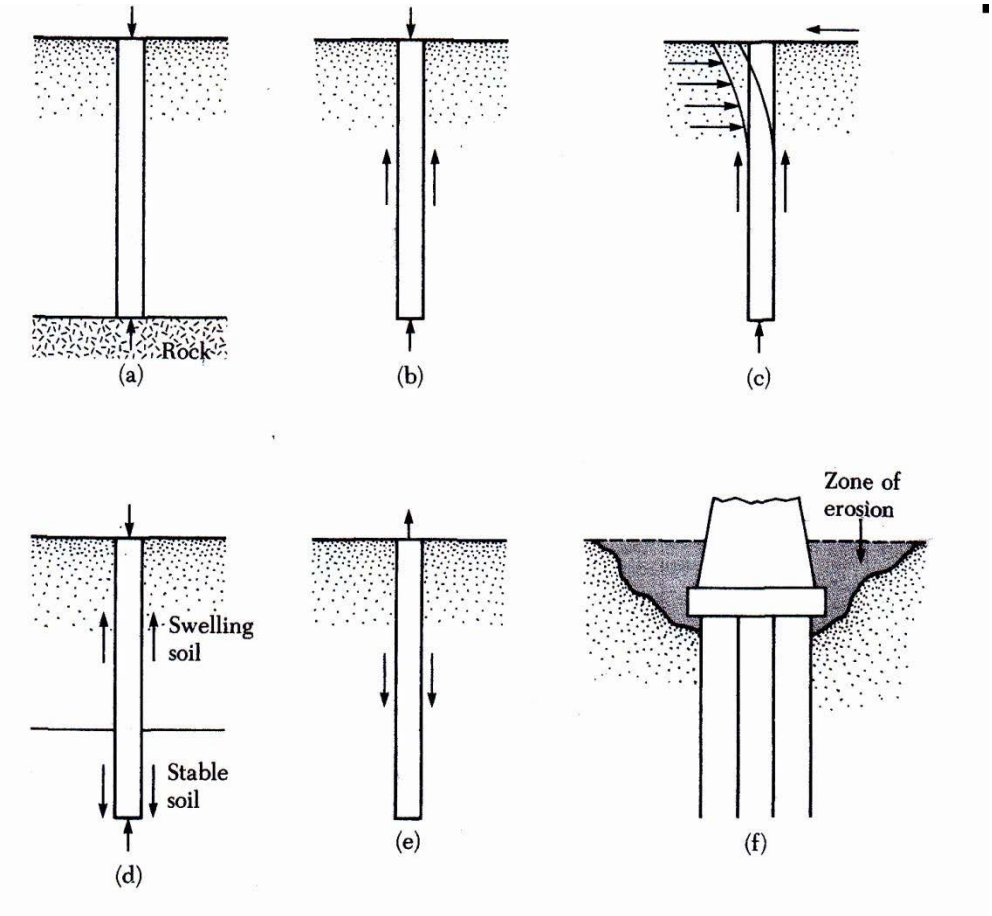

Figure 2-2. Conditions were pile foundations can be used in practice (after Das 1999)

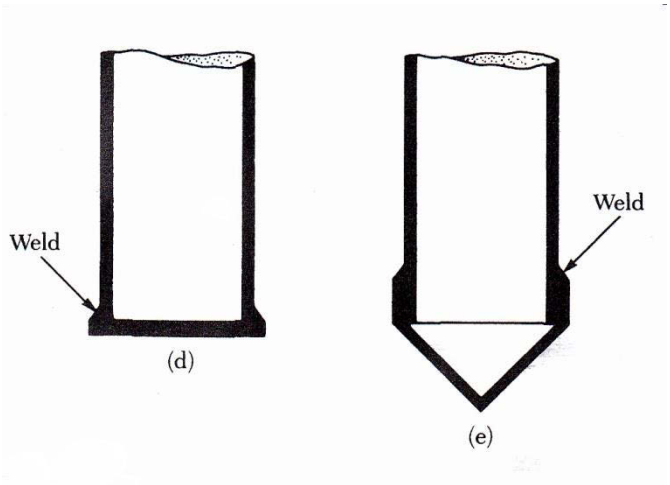

Figure 2-3. Two different types of driving shoes used in practice (after Das 1999)

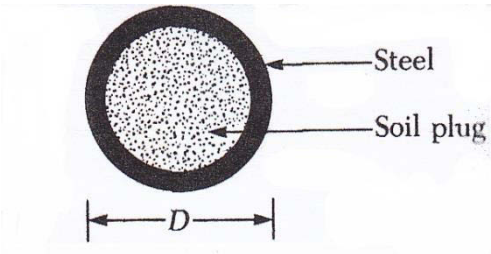

Figure 2-4. An open ended steel pipe pile with the soil plug (after Das 1999)

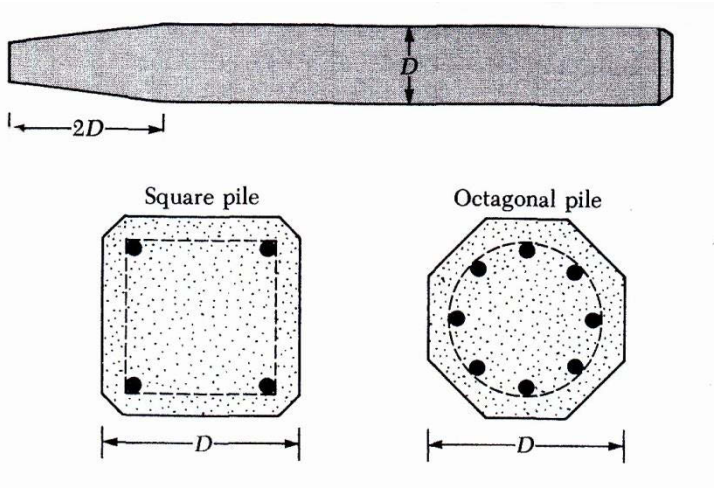

Figure 2-5. Precast piles with reinforcements (after Das 1999)

Figure 2-6. A single pile with a pedestal at its base (www.franki.com.au)

Figure 2-7. An auger used on site for pile installation (Photo courtesy of Duncan Priestley Civil Engineering)

Figure 2-8. A single pile with a case and reinforcements under construction (Photo courtesy of Duncan Priestley Civil Engineering)

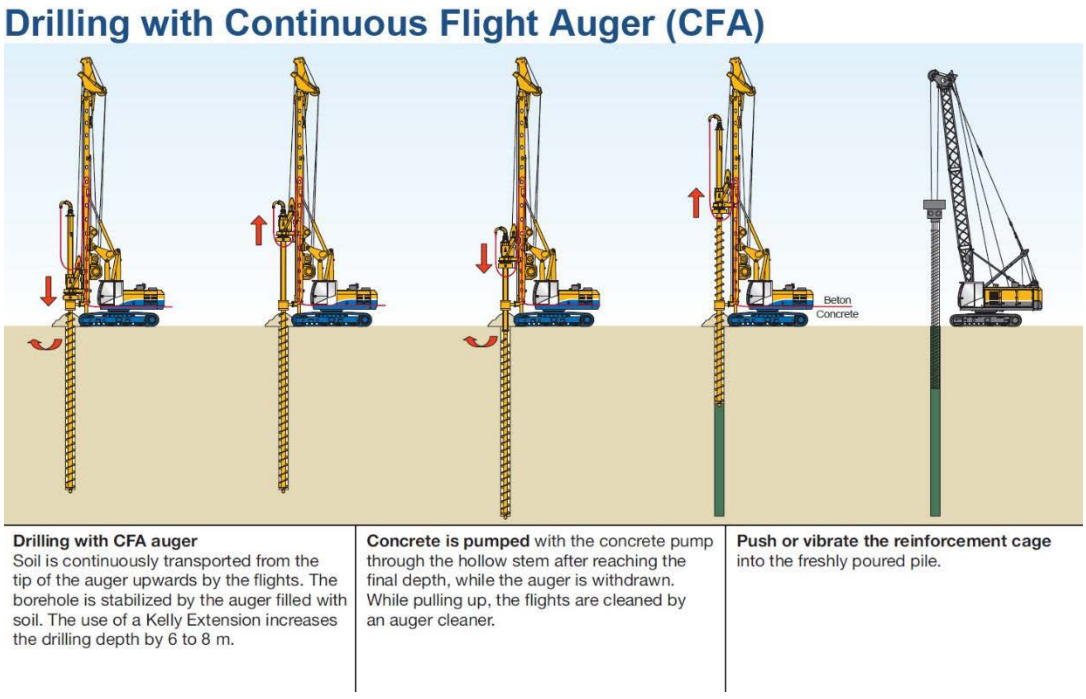

Figure 2-9. A flight auger system for piling (www.bauerpileco.com)

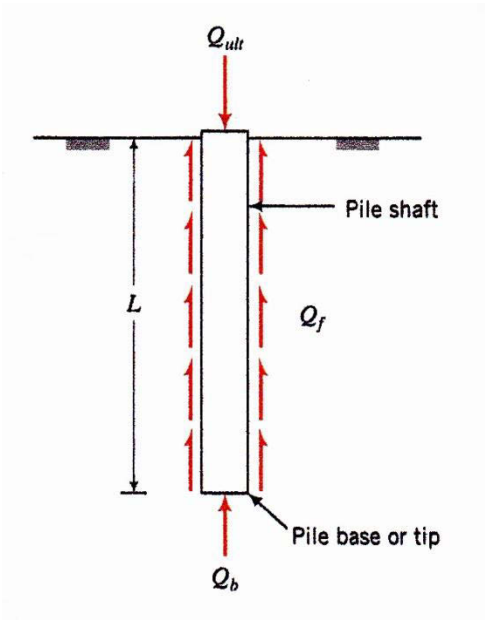

Figure 2-10. Pile shaft and base resistance (after Budhu 2007)

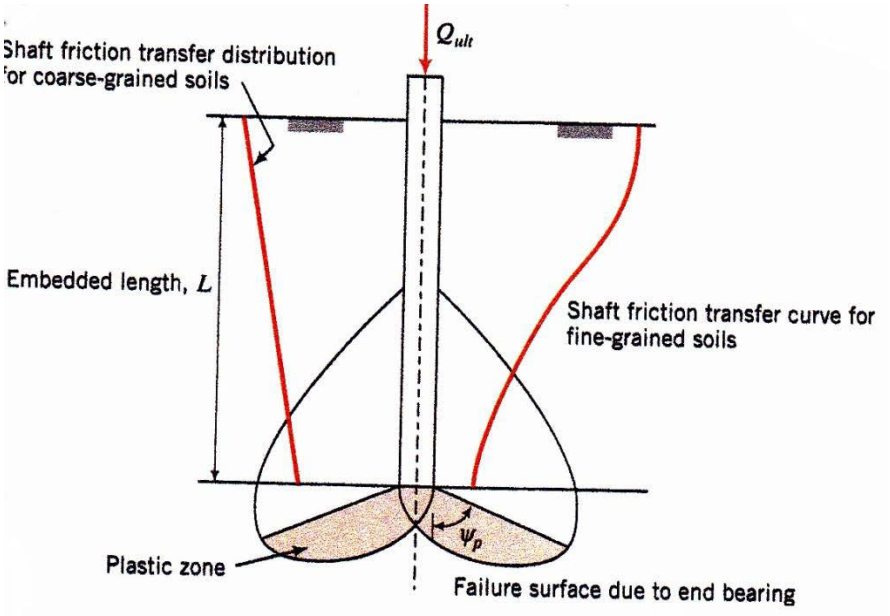

Figure 2-11. Load transfer characteristics for a single pile in coarse and fine-grained soils (after Budhu 2007)

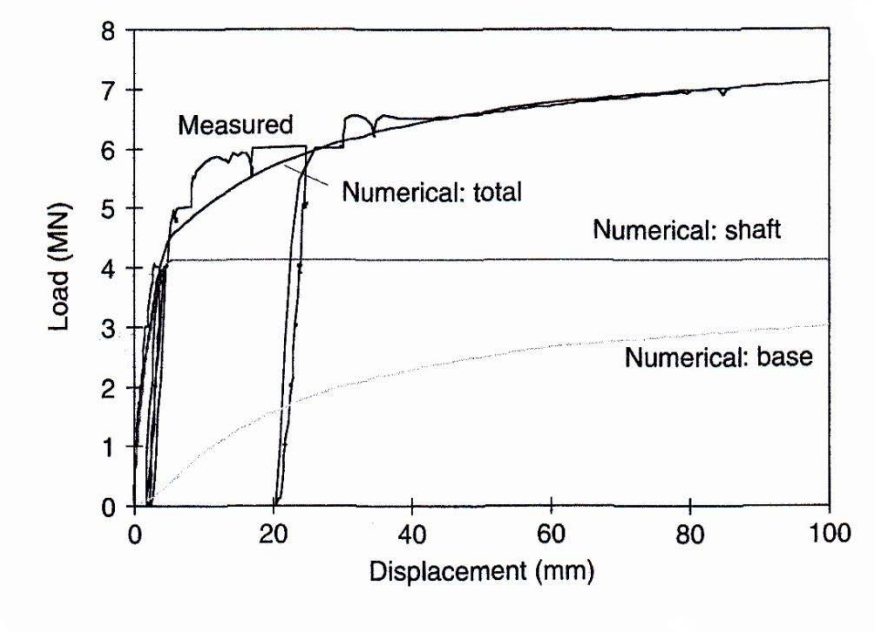

Figure 2-12. The load settlement response of a single pile (after Randolph 2003)

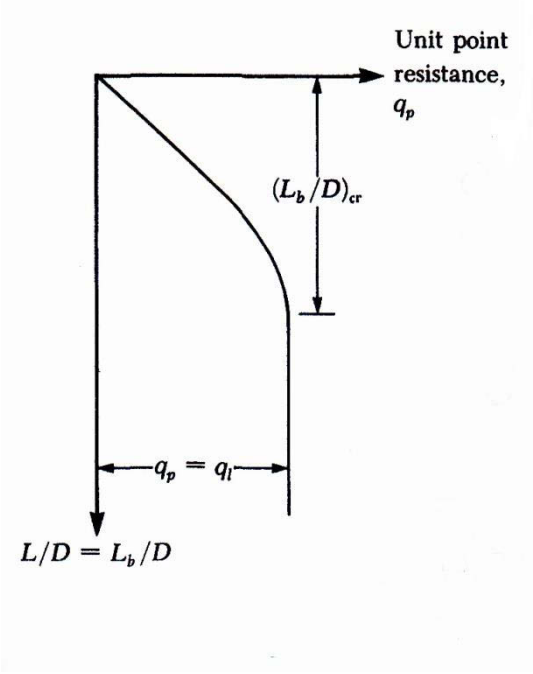

Figure 2-13. Variation of unit point resistance in sand (after Das 1999)

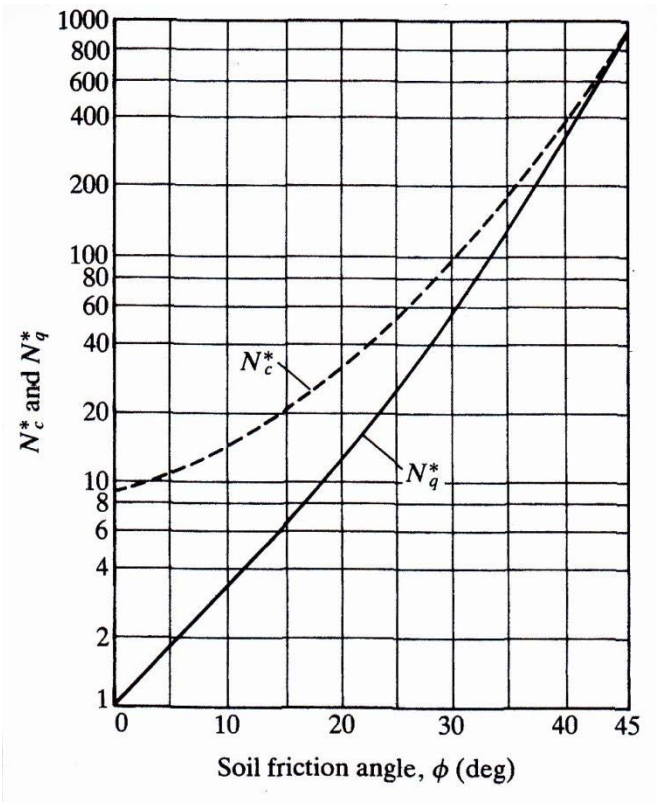

Figure 2-14. The variation in N_c^* and N_q^* with the friction angle of the soil (after Meyerhof 1976)

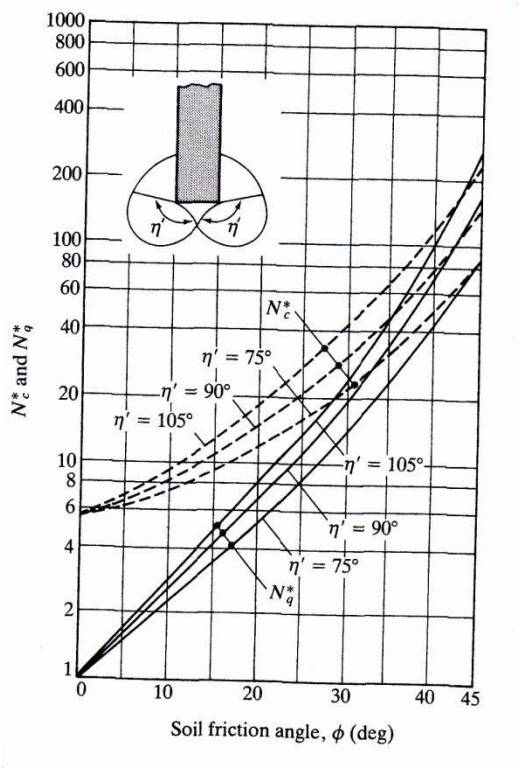

Figure 2-15. Janbu's bearing capacity factors (after Janbu 1976)

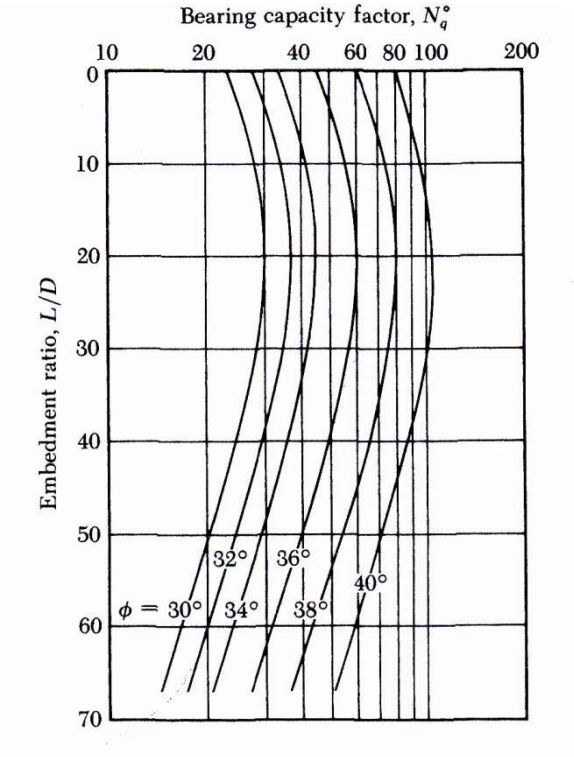

Figure 2-16. The bearing capacity factors proposed by Coyle and Castello (1981)

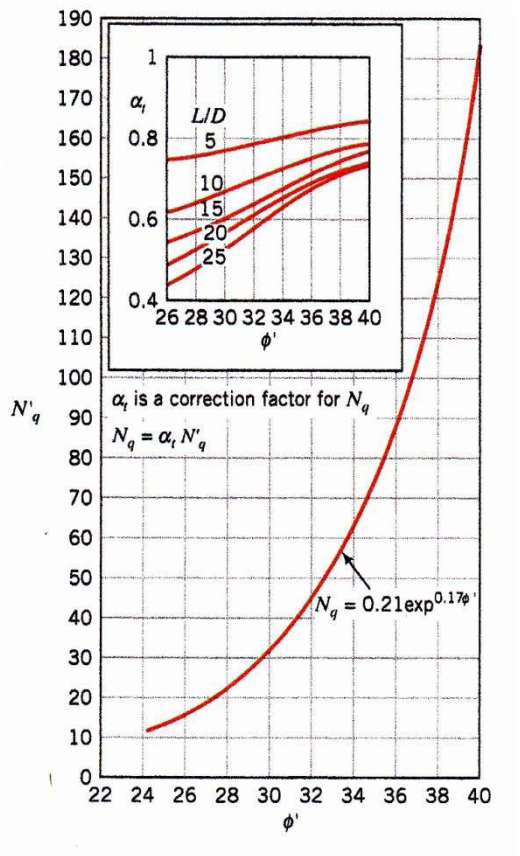

Figure 2-17. N_q' values proposed by Berezantzev et al. (1961)

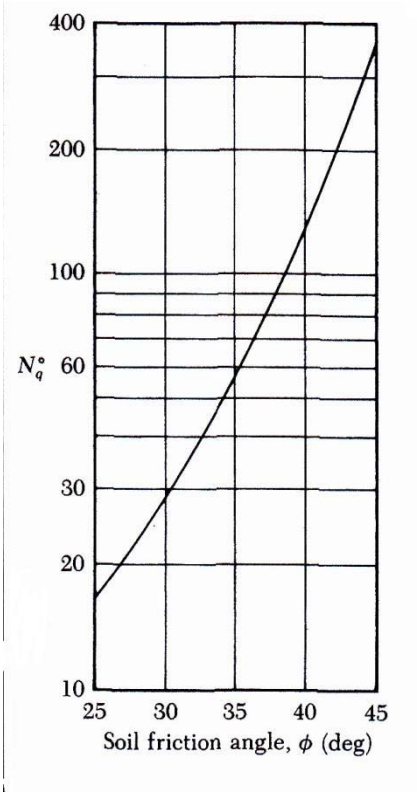

Figure 2-18. Vesic's bearing capacity factor

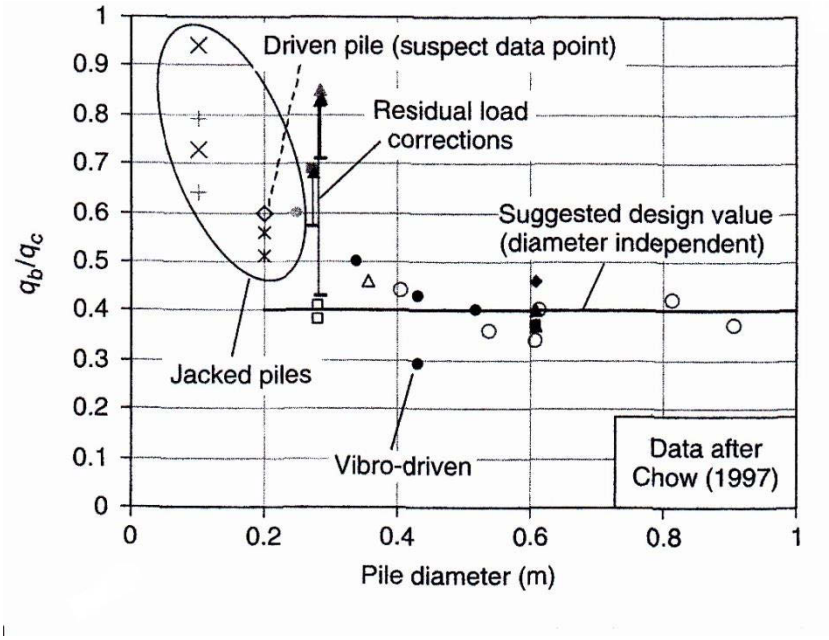

Figure 2-19. Normalized end bearing resistance for driven close ended piles (annotation by Randolph 2003)

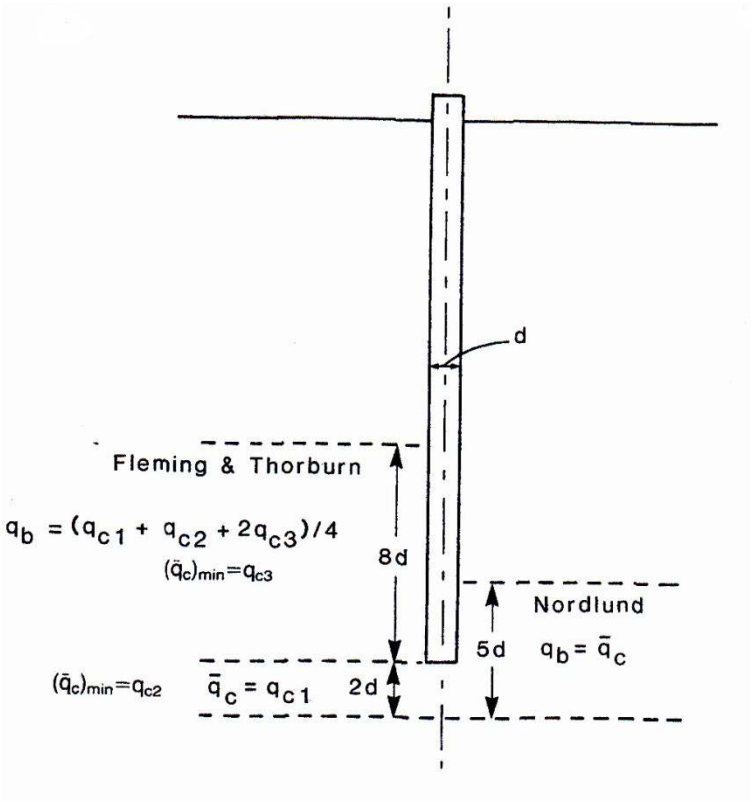

Figure 2-20. Different averaging methods to determine the end bearing pressure from CPT results (after Fleming et al. 2009)

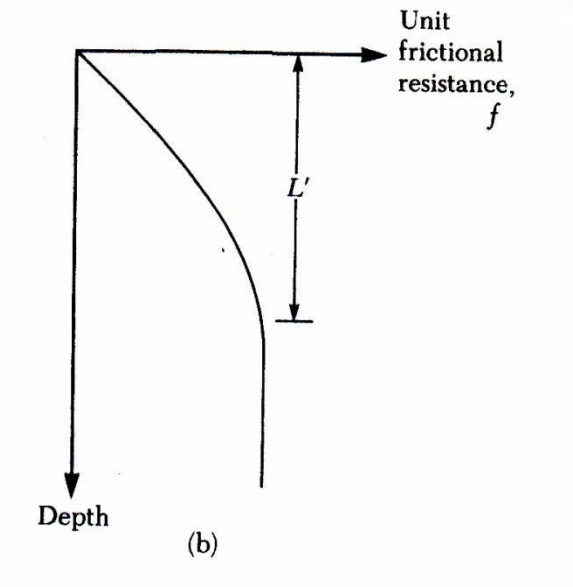

Figure 2-21. The change in the unit frictional resistance for piles embedded in sand (after Das 1999)

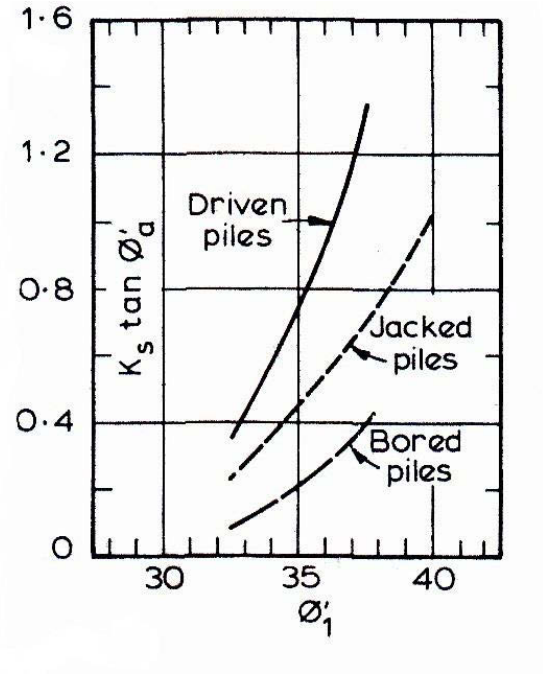

Figure 2-22. Values of $K_s \tan\phi'$ proposed by Meyerhof (1976)

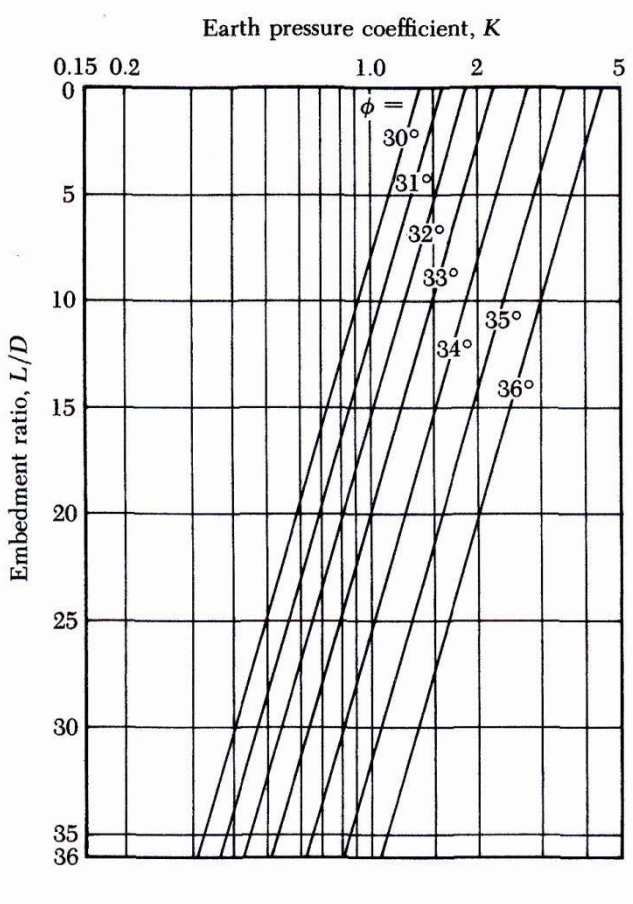

Figure 2-23. Variation of K with L/D (after Coyle and Castello, 1981)

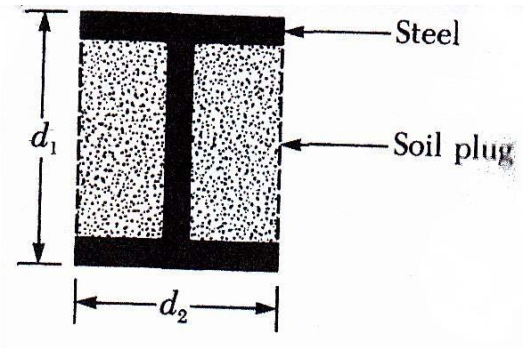

Figure 2-24. An H-pile section used as a pile (after Das 1999)

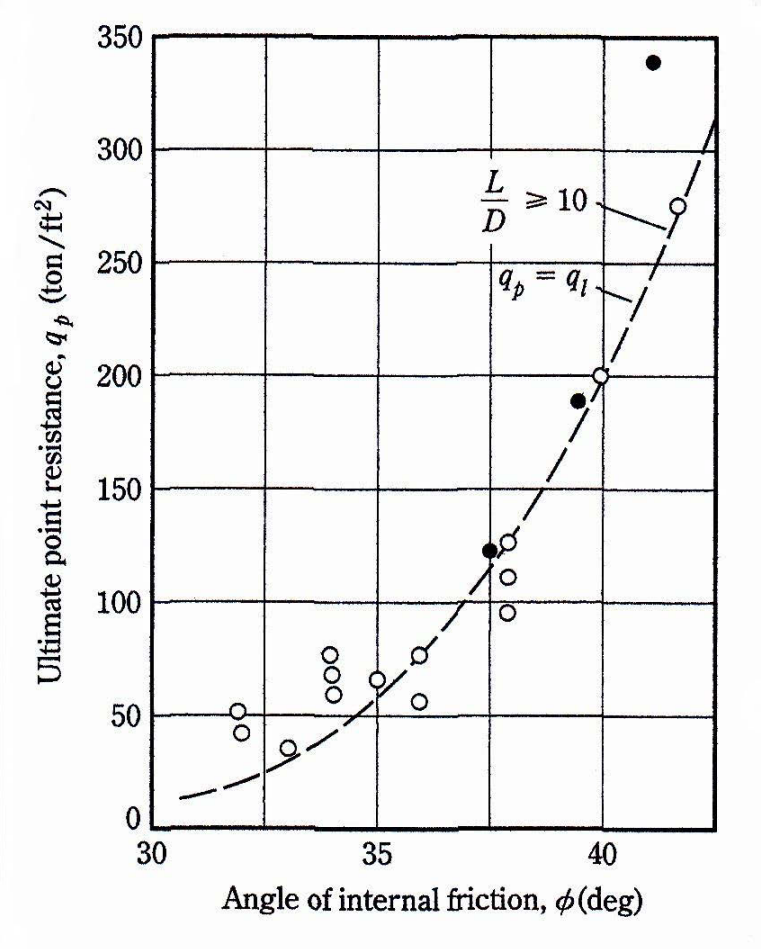

Figure 2-25. Ultimate point resistance for driven piles in sand (after Meyerhof 1976)

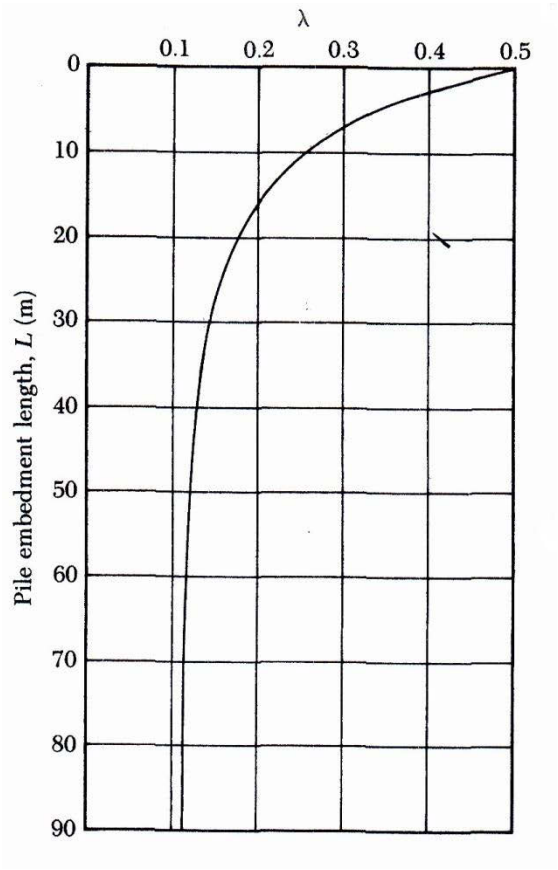

Figure 2-26. Variation of λ with the pile's embedment length (after McClelland 1974)

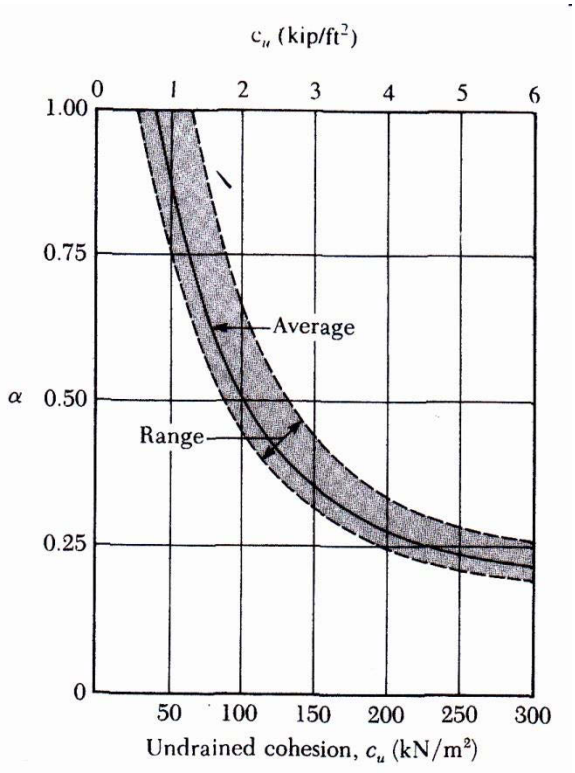

Figure 2-27. Variation of α with the undrained cohesion (after Das 1999)

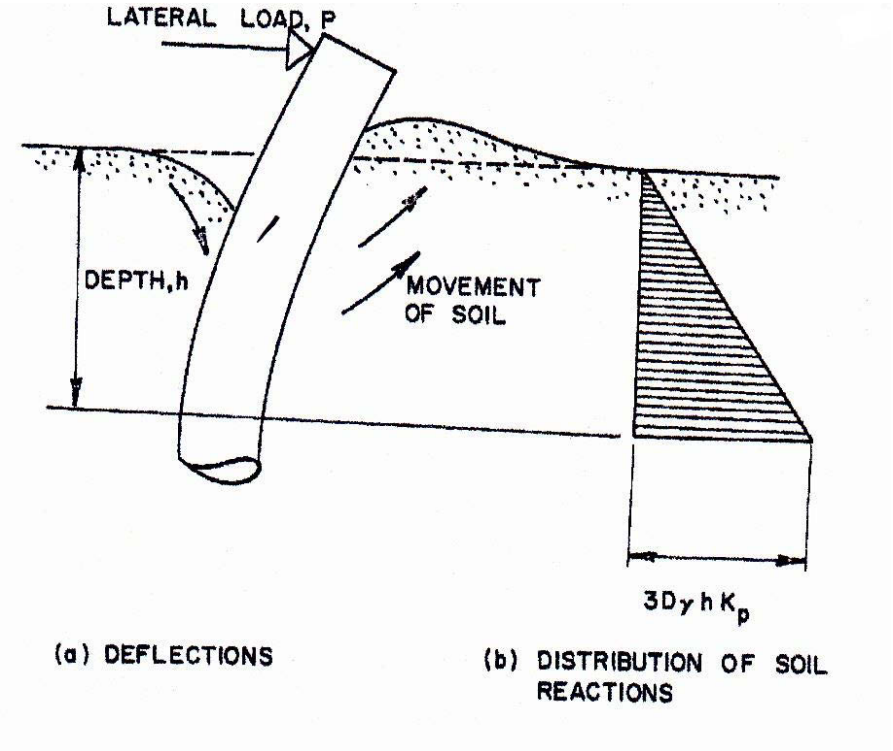

Figure 2-28. The failure mechanism in a single pile (after Broms 1964)

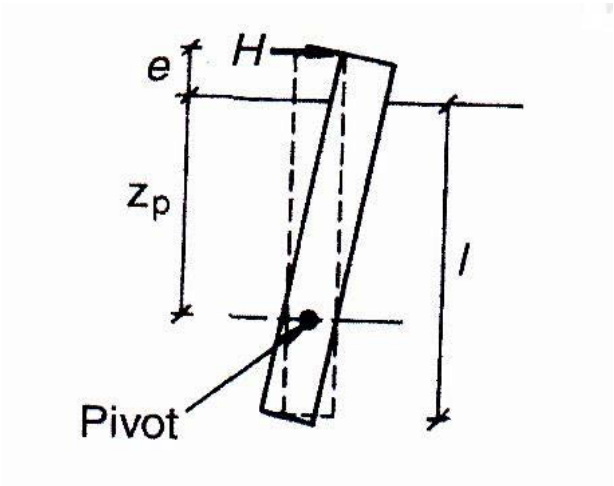

Figure 2-29. The rotation of a short pile at its pivot point (after Broms 1964)

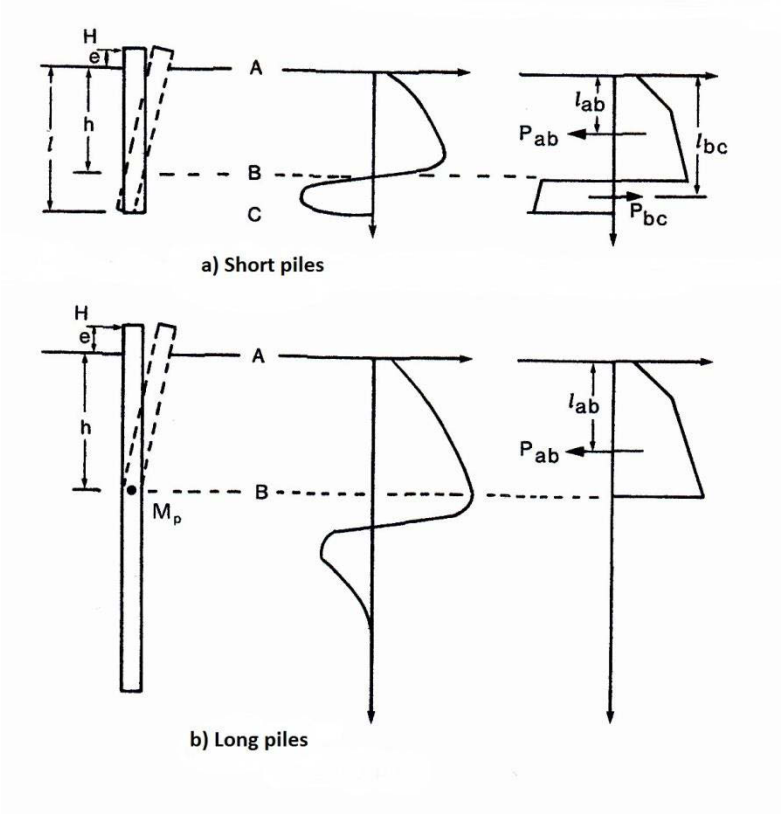

Figure 2-30. The variation of soil resistance along laterally loaded piles, a) short pile b) long pile (after Fleming et al. 2009)

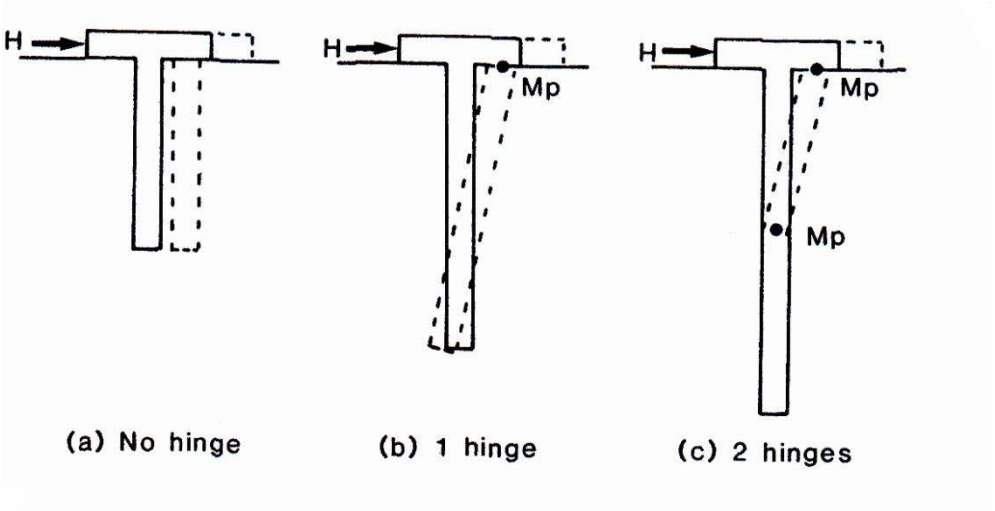

Figure 2-31. Failure modes for laterally loaded piles with a cap (after Fleming et al. 2009)

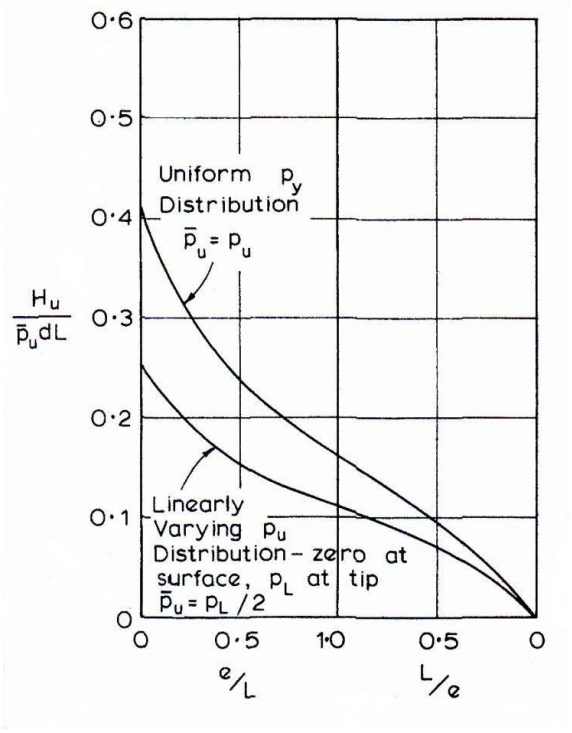

Figure 2-32. The variation of soil distribution pressure (after Poulos et al., 1980)

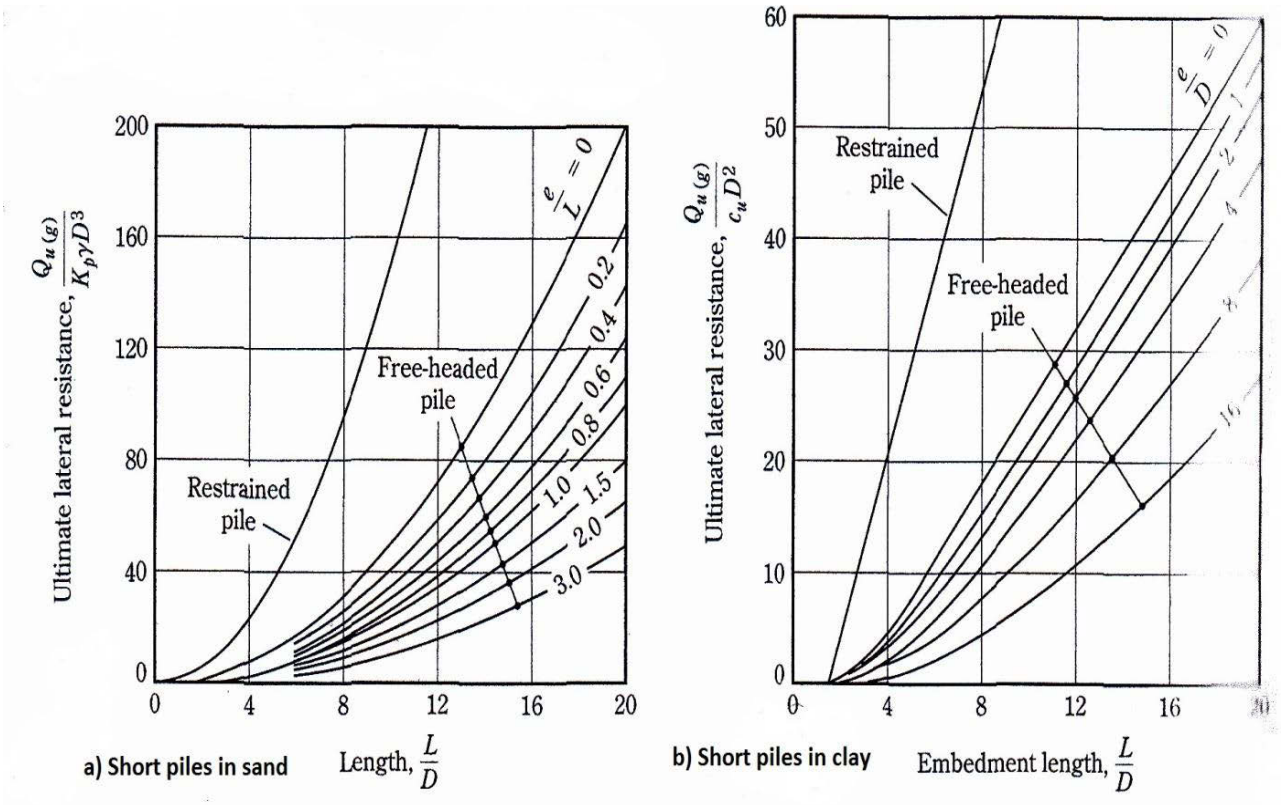

Figure 2-33. Broms charts for calculating the ultimate resistance of short piles embedded in (a) sand (b) clay

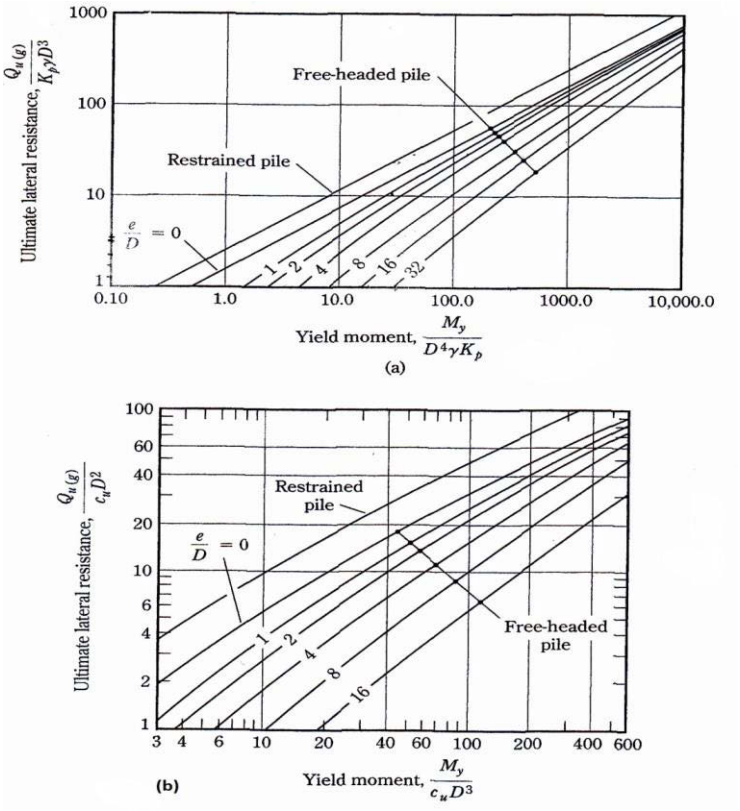

Figure 2-34. Broms charts for calculating the ultimate resistance of long piles embedded in (a) sands (b) clays

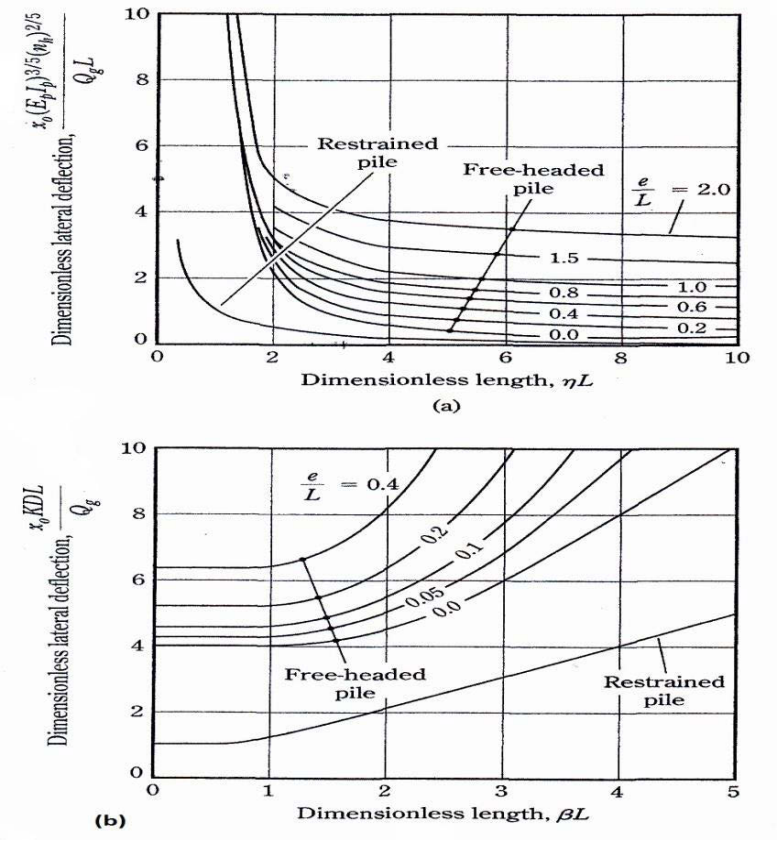

Figure 2-35. Broms charts for estimating the pile's head deflections (a) in sands (b) in clays

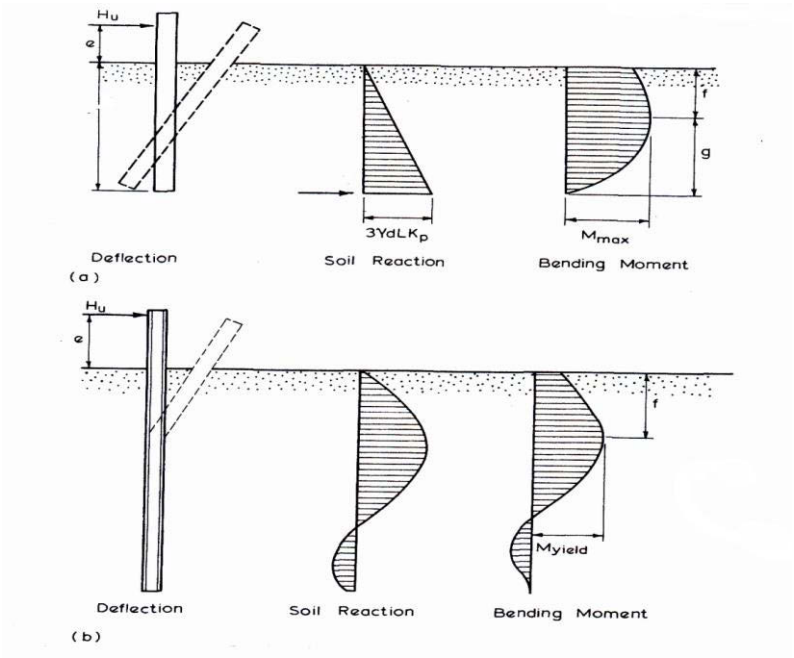

Figure 2-36. The behaviour of free headed piles in cohesionless material (a) short piles (b) long piles (after Broms 1964)

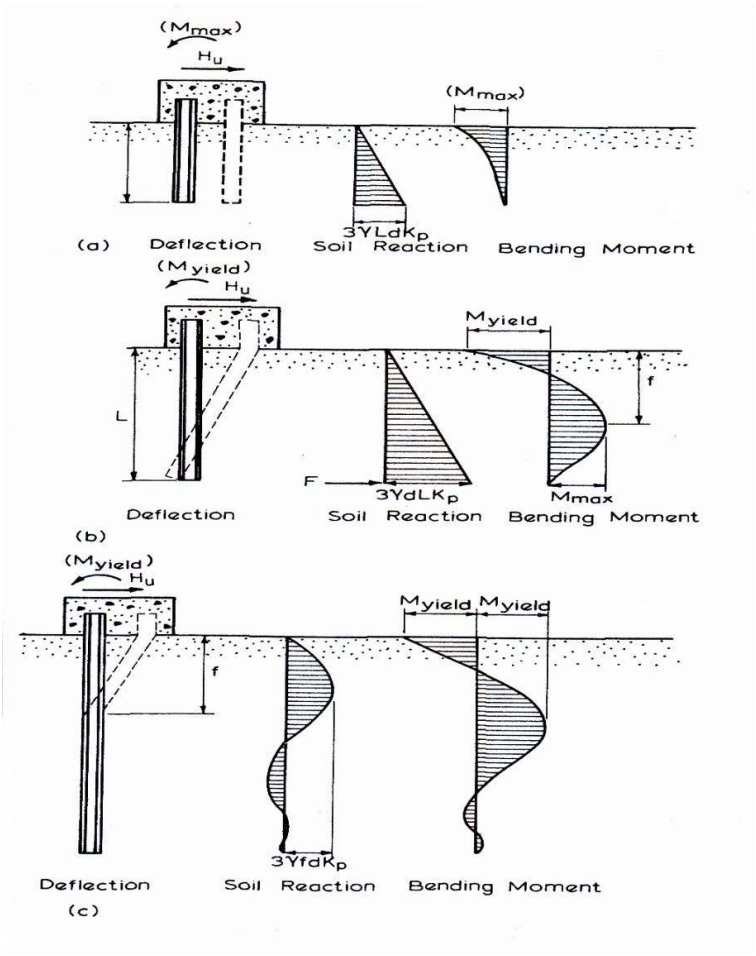

Figure 2-37. The behaviour of restrained piles in sand (a) short (b) intermediate (c) long (after Broms 1964)

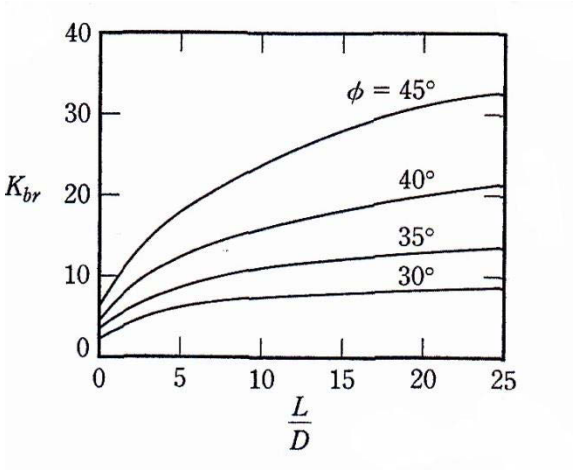

Figure 2-38.Variation of the resultant net soil pressure coefficient (after Meyerhof 1995)

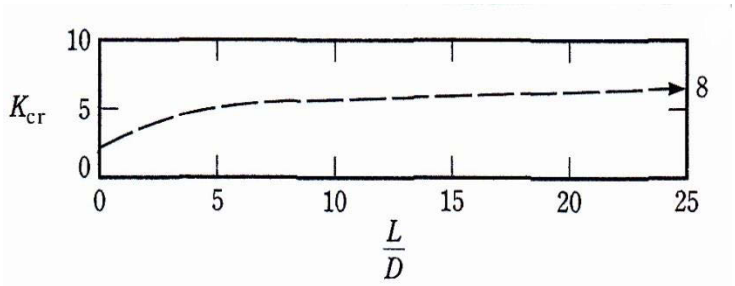

Figure 2-39. Variation of K_{cr} for clays (after Meyerhof 1995)

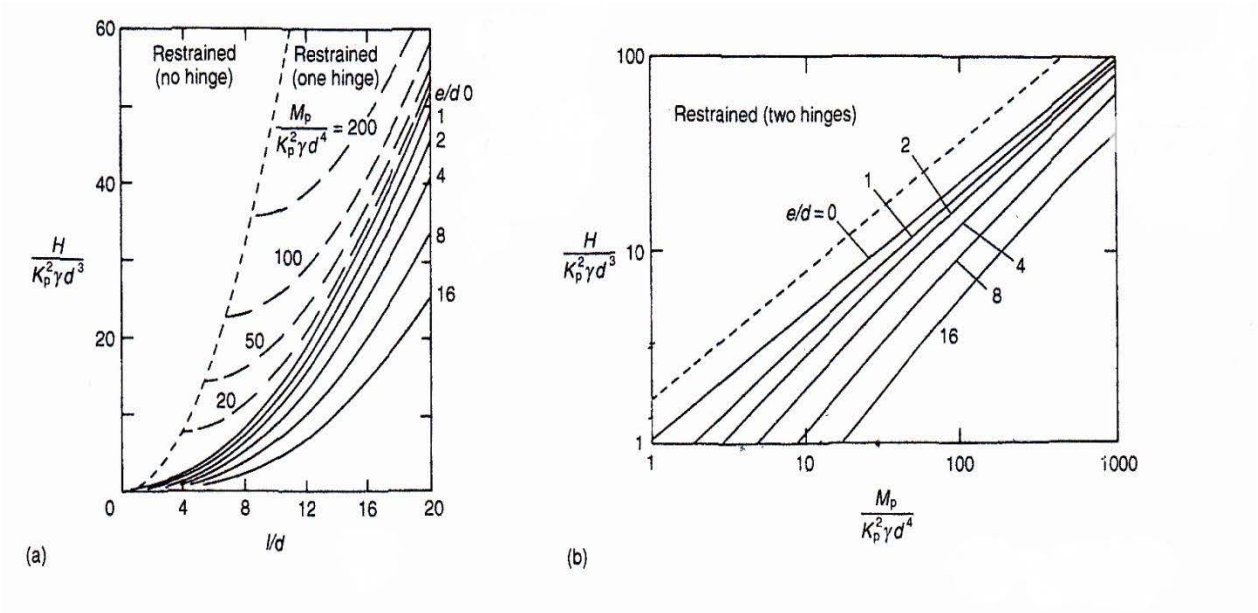

Figure 2-40. Charts for calculating the ultimate resistance of piles in sands (a) short piles (b) long piles (after Fleming et al. 1992, republished by Powrie 1997)

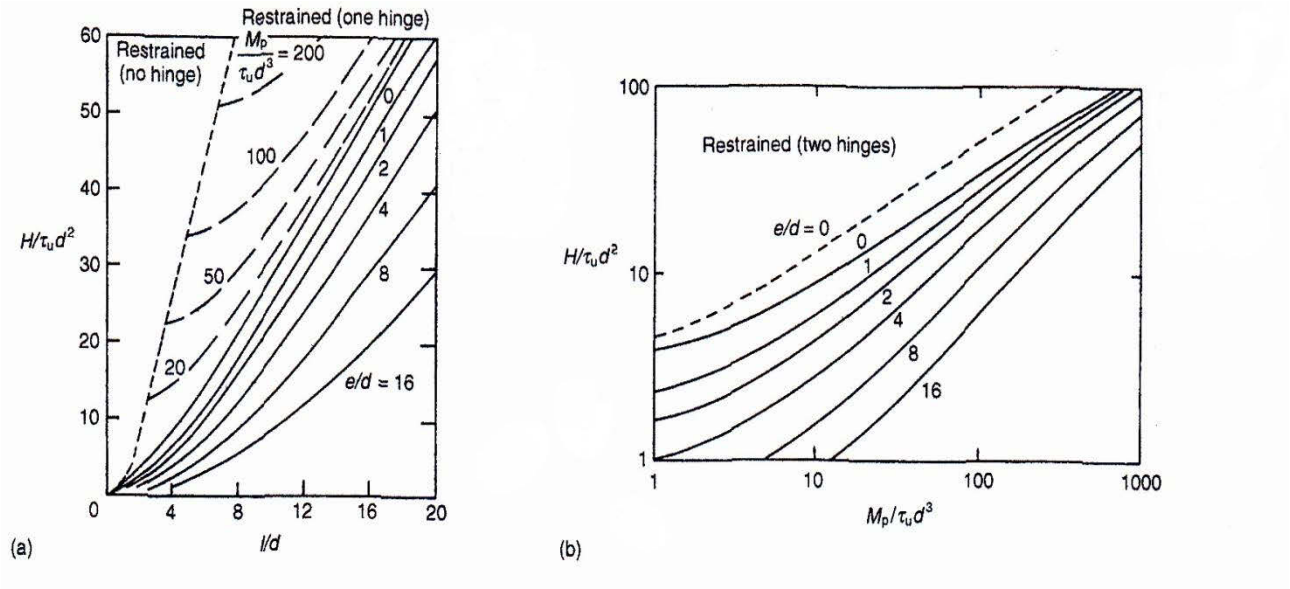

Figure 2-41. Charts for calculating the ultimate resistance of a single pile in clay (a) long piles (b) short piles (after Fleming et al. 1992, republished by Powrie 1997).

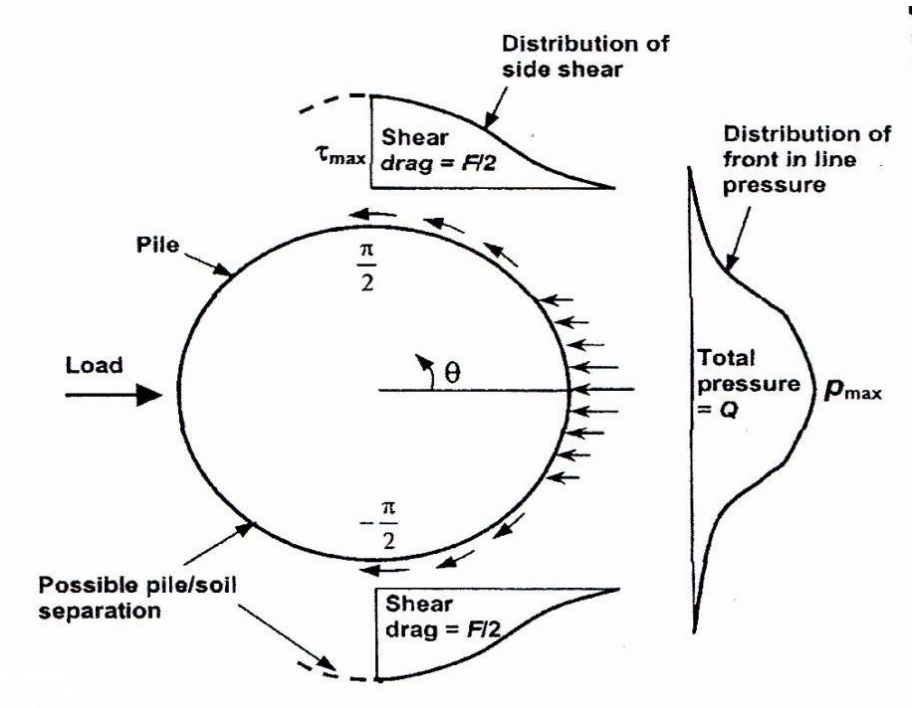

Figure 2-42. Distribution of earth pressure and side shear around a single pile (after Smith, 1987)

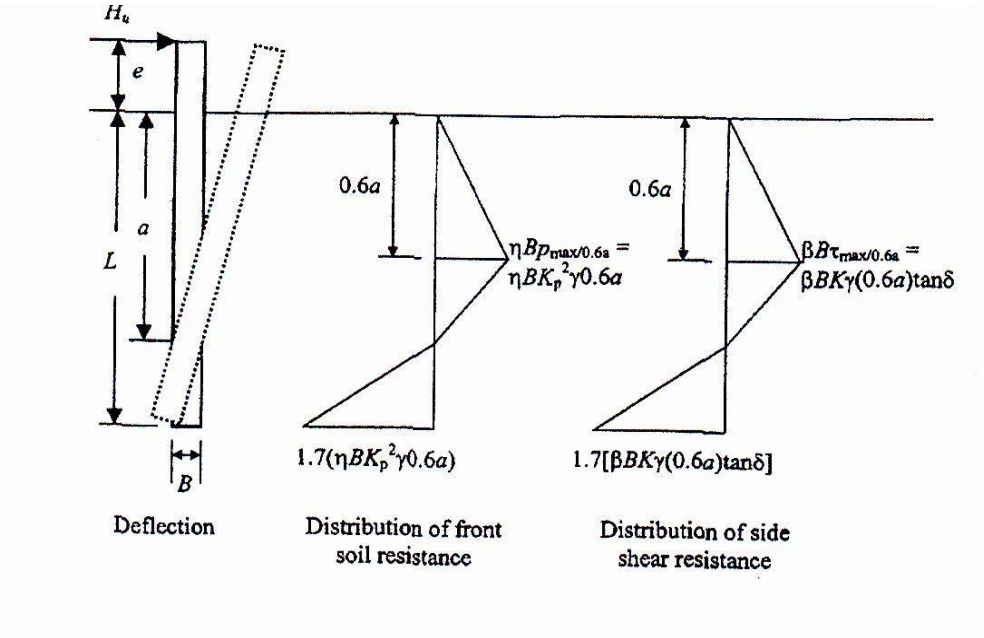

Figure 2-43. Distribution of frontal and side shear resistance (after Zhang et al. 2005)

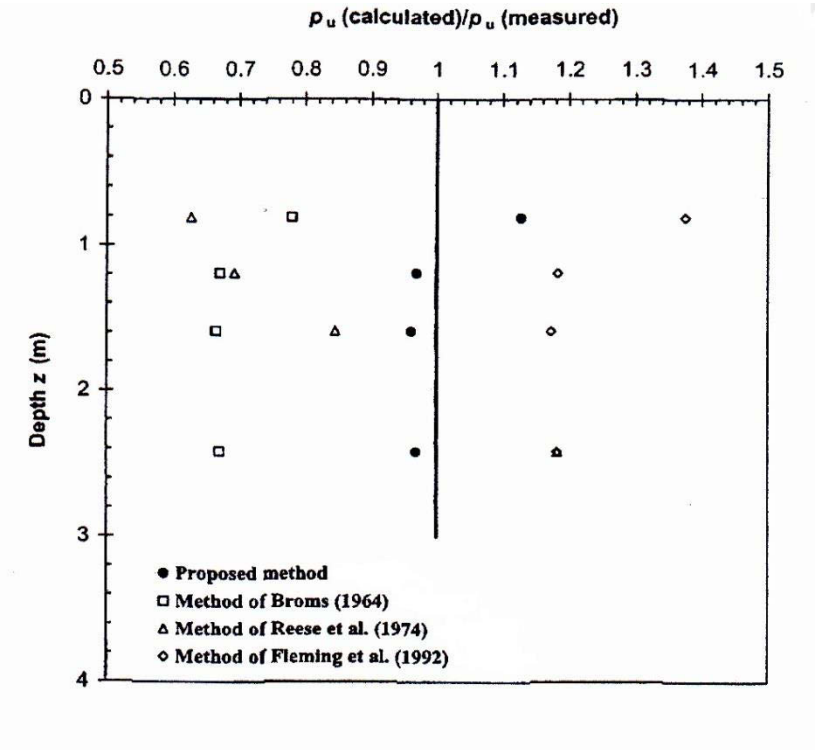

Figure 2-44. Comparison of the ultimate lateral resistance of Barton and Finn centrifugal tests with different proposed methods (after Zhang et al. 2005)

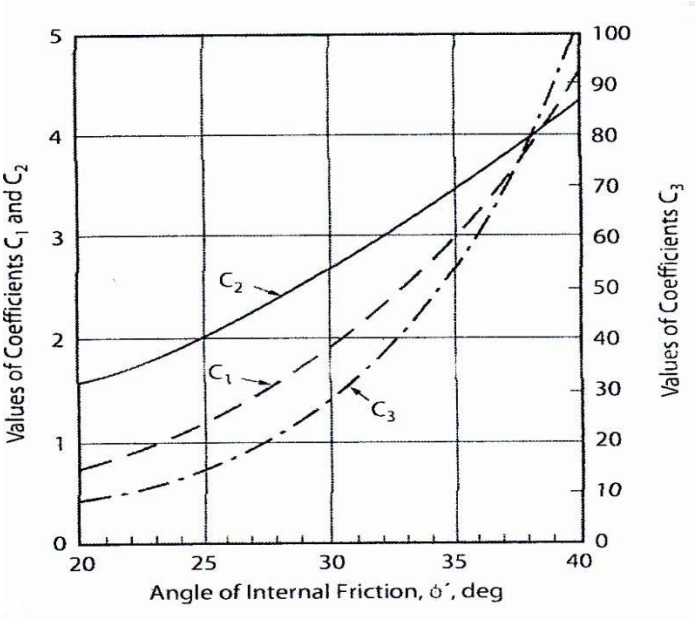

Figure 2-45. Values of C_1, C_2 and C_3 adopted by API (2007)

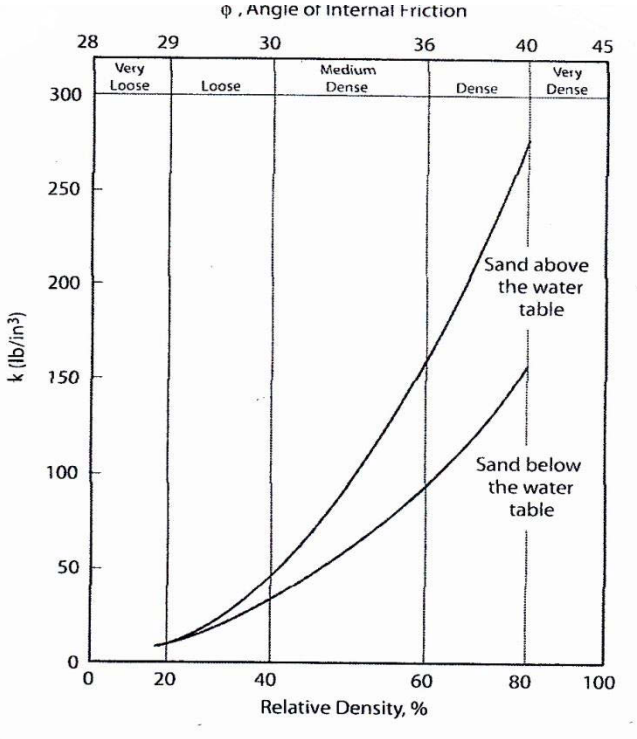

Figure 2-46. The adopted values of K by API (2007)

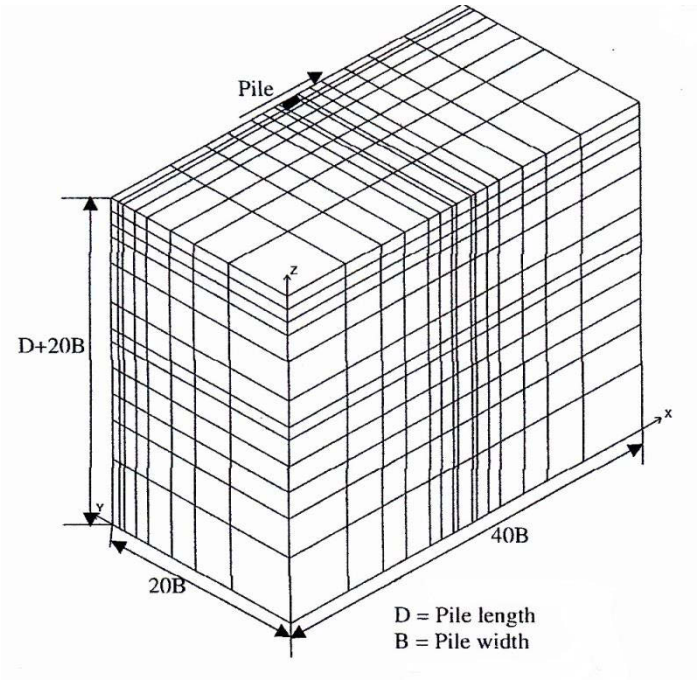

Figure 2-47. The three-dimensional model constructed by Karthigeyan et al. (2006)

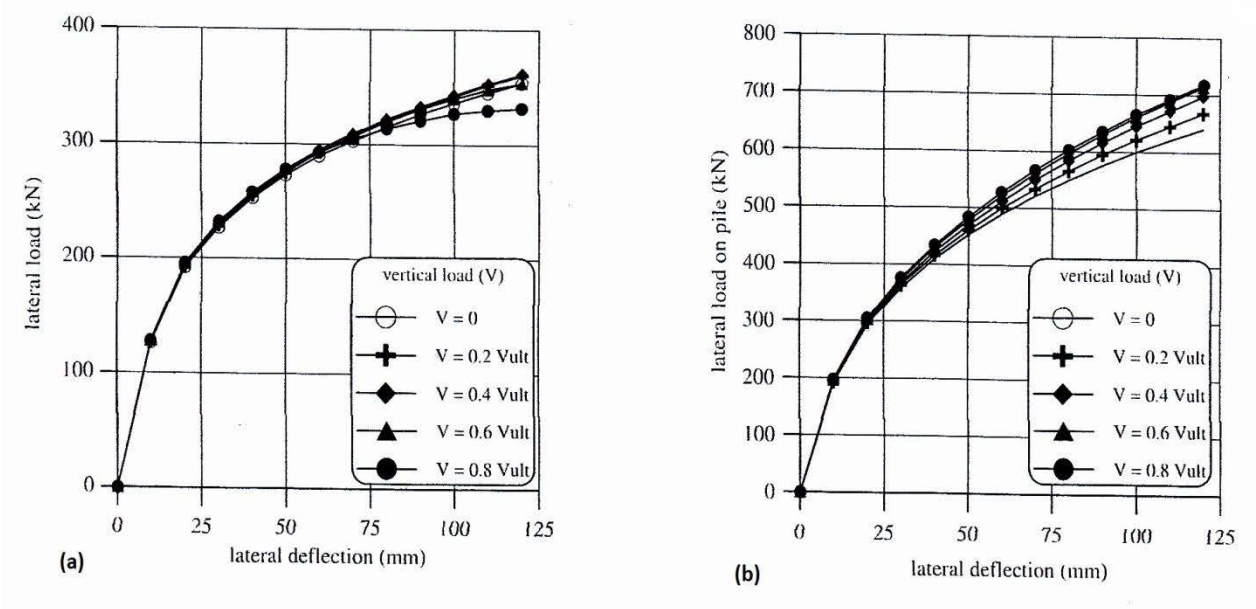

Figure 2-48. Lateral load deflection of a pile for the SAVL case (a) loose sand (b) dense sand (after Karthigeyan et al. 2006)

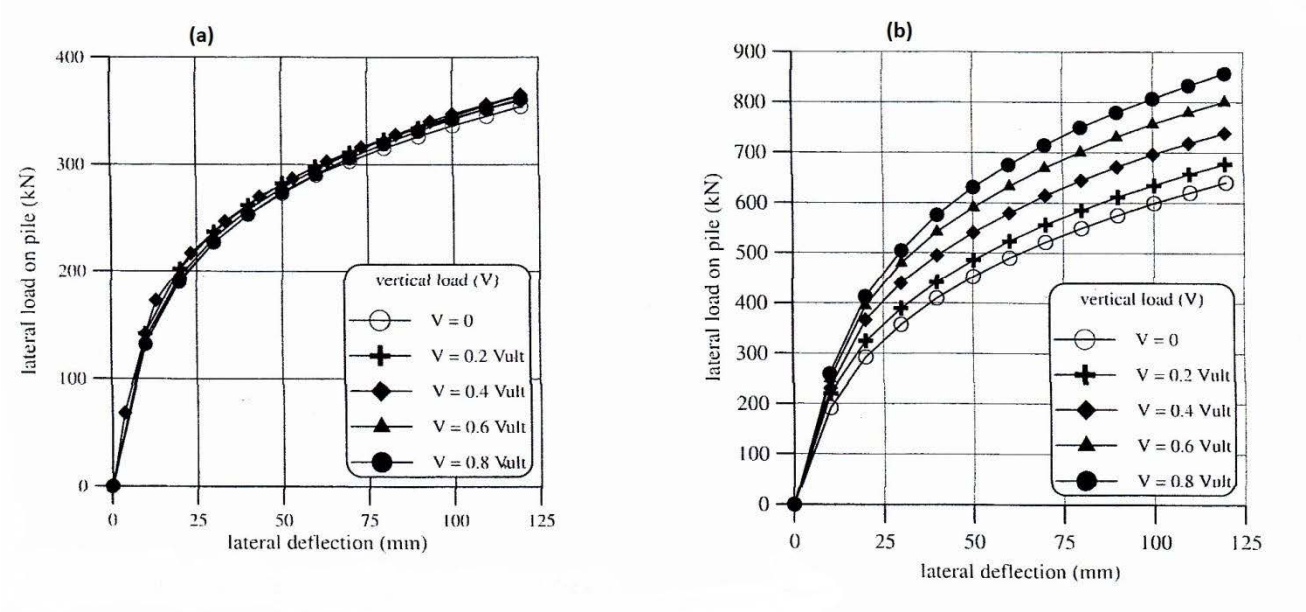

Figure 2-49. Lateral load deflection of a single pile for the VPL case (a) loose sand (b) dense sand (after Karthigeyan et al. 2006)

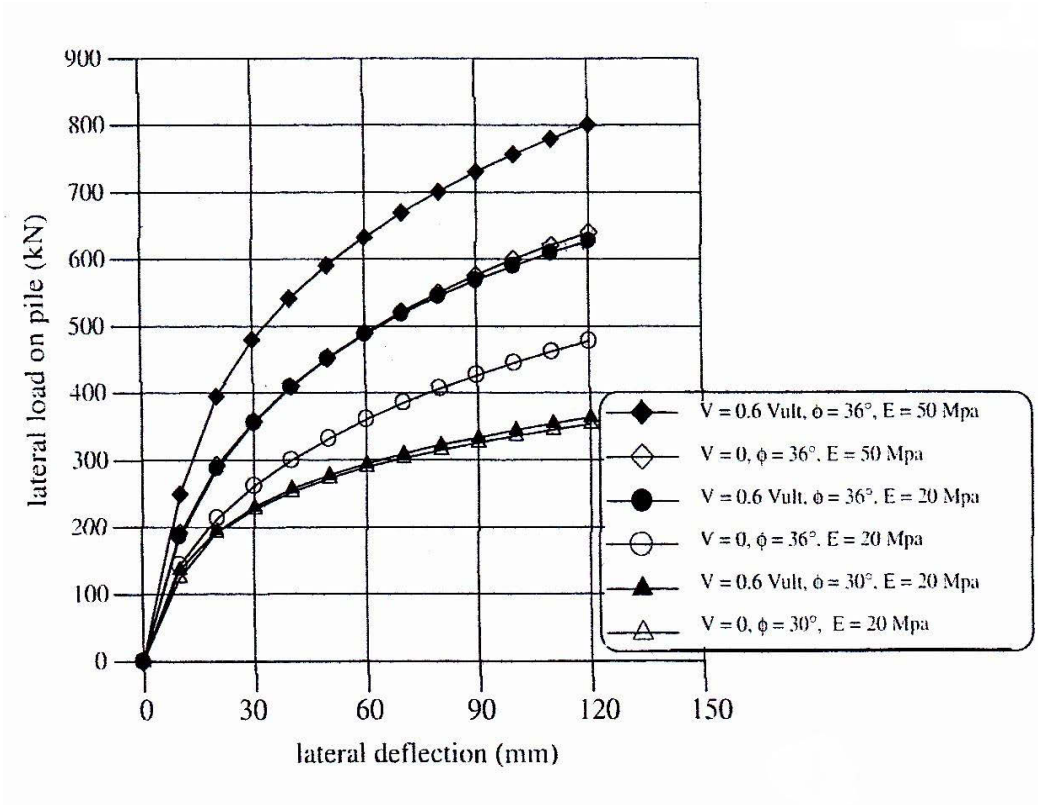

Figure 2-50. Influence of vertical load on the lateral response of a single pile with different soil modulus and friction angles (after Karthigeyan et al. 2006)

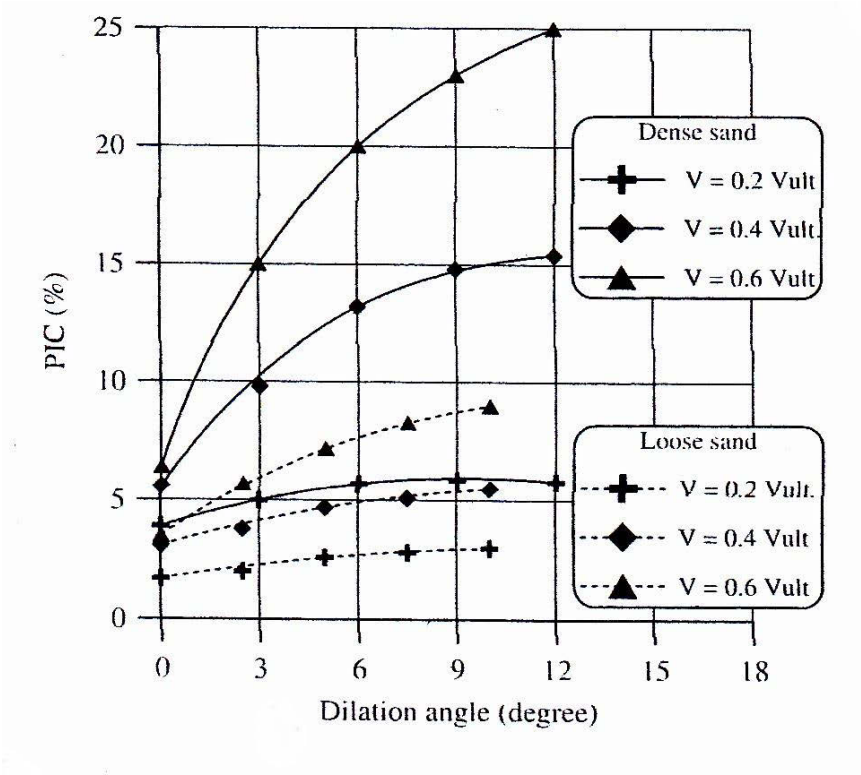

Figure 2-51. Influence of dilation angle on PIC of pile in dense and loose sands (after Karthigeyan et al. 2006)

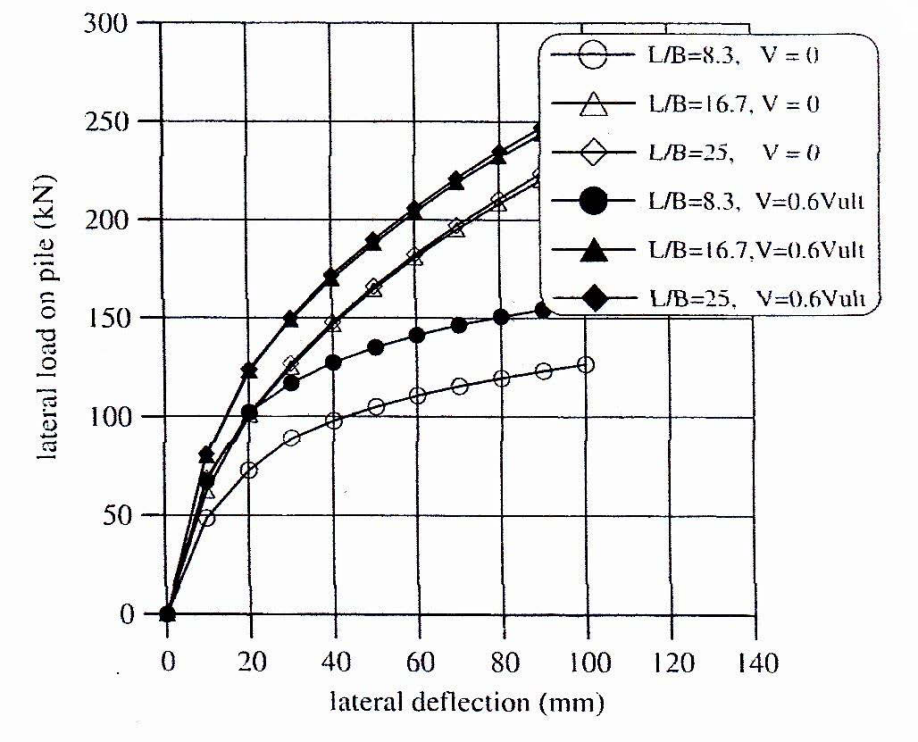

Figure 2-52. Influence of vertical load on the lateral response of piles with different slender ratios (after Karthigeyan et al. 2006)

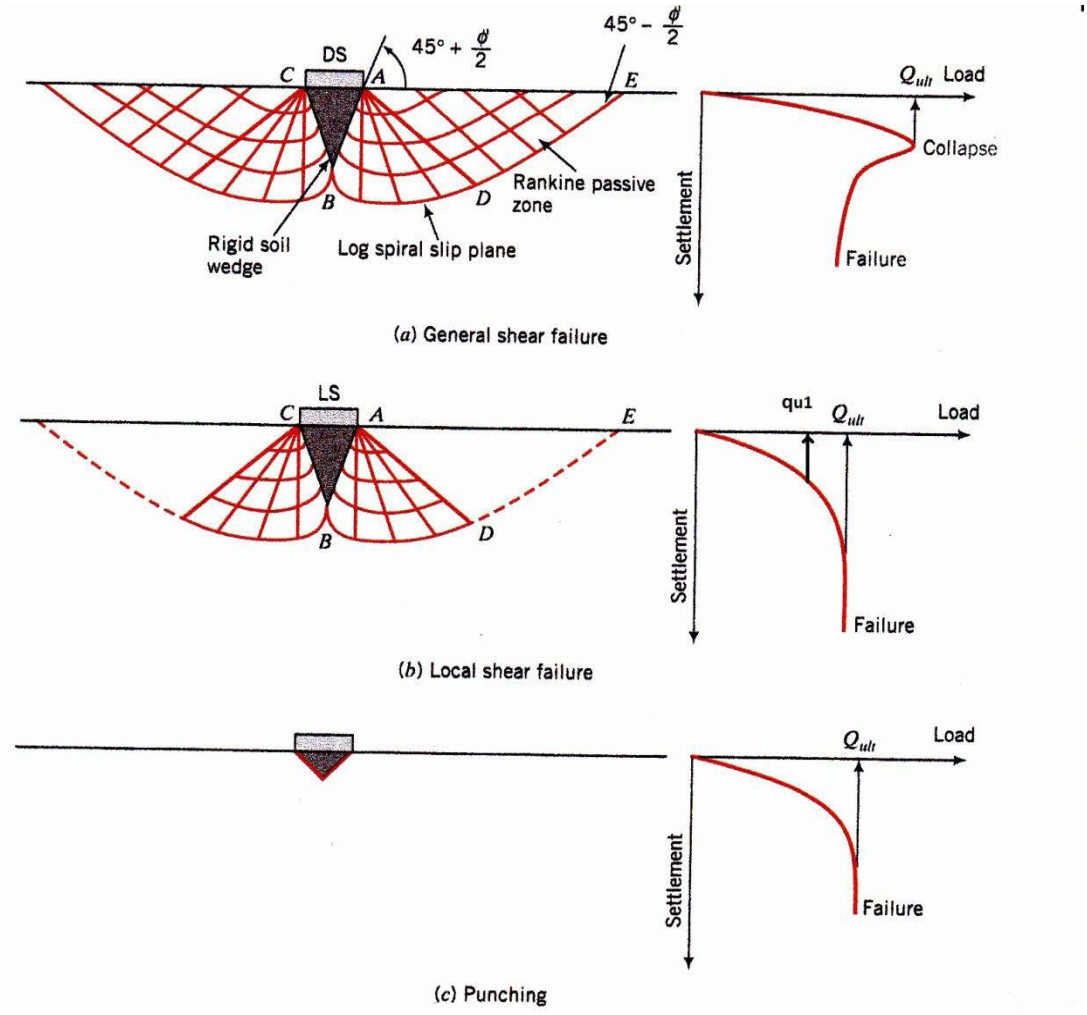

Figure 2-53. Failure mechanisms in three different soil types for shallow foundations (after Budhu 2007)

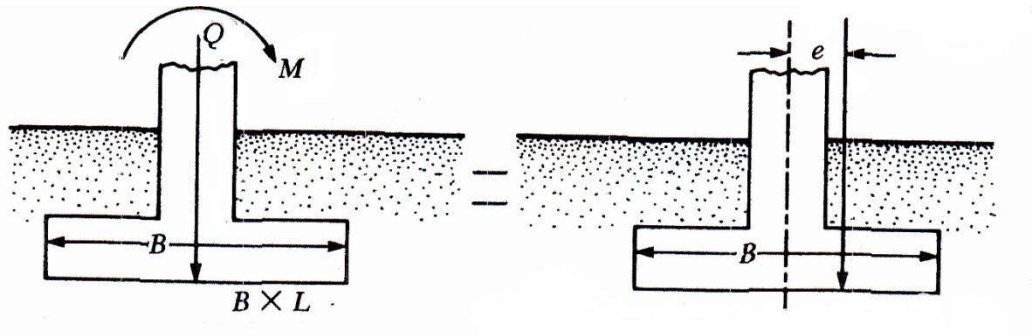

Figure 2-54. An eccentrically loaded foundation, which is equivalent to a foundation with moment acting on it (after Das 1999)

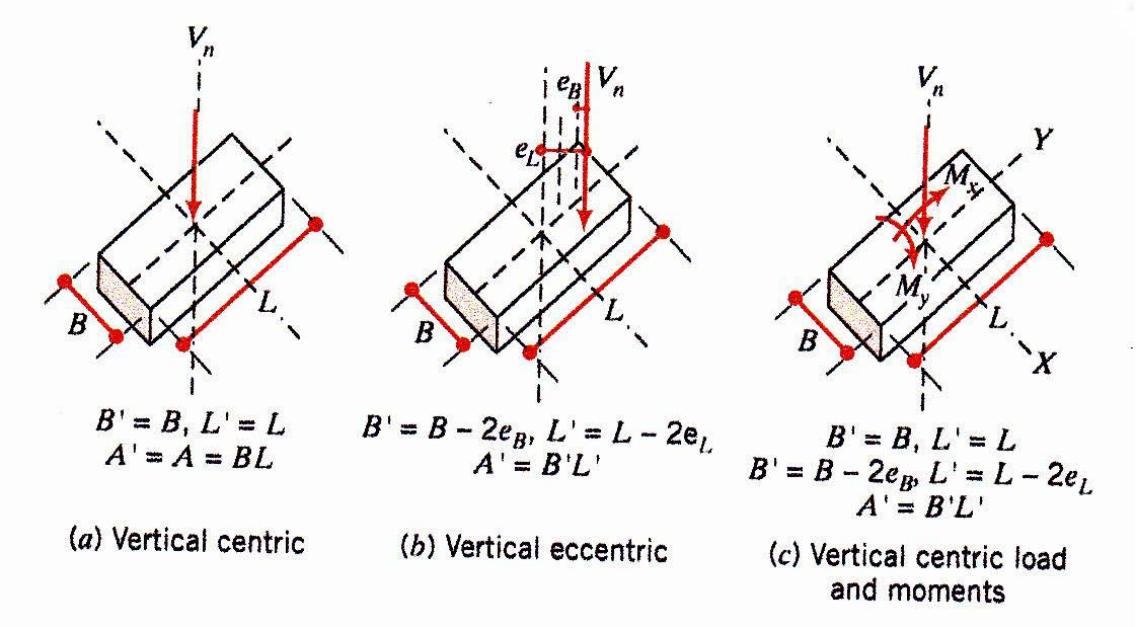

Figure 2-55. Different possible types of loading on a shallow foundation (after Budhu 2007)

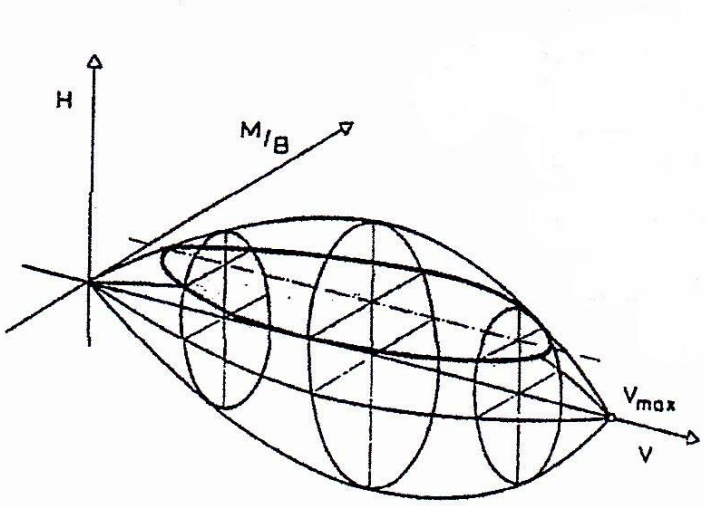

Figure 2-56. Three-dimensional interaction surface for a VHM space (after Gottardi 1993)

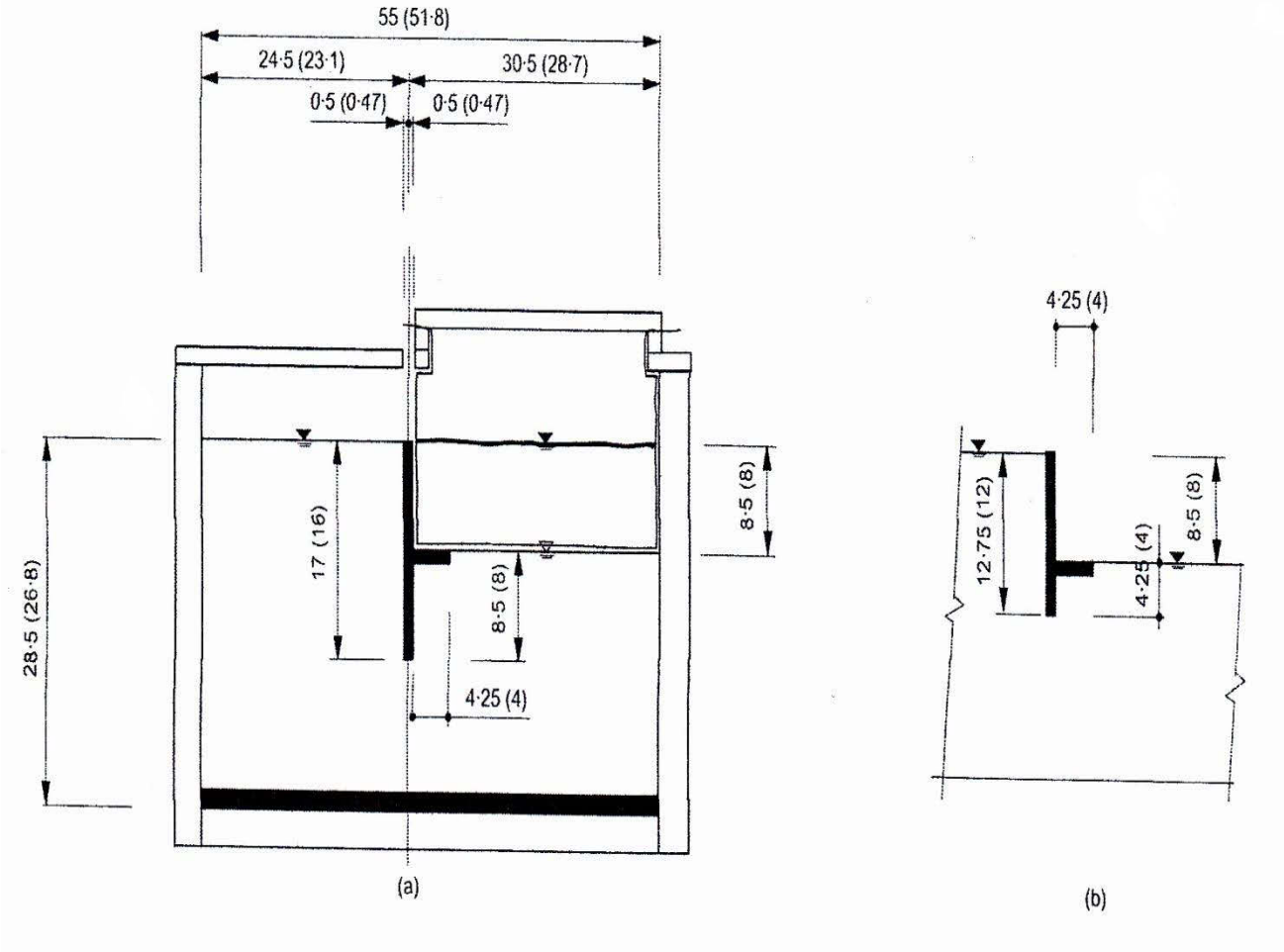

Figure 2-57. Schematic cross section of a retaining wall with a stabilising platform (after Powrie et al. 2007)

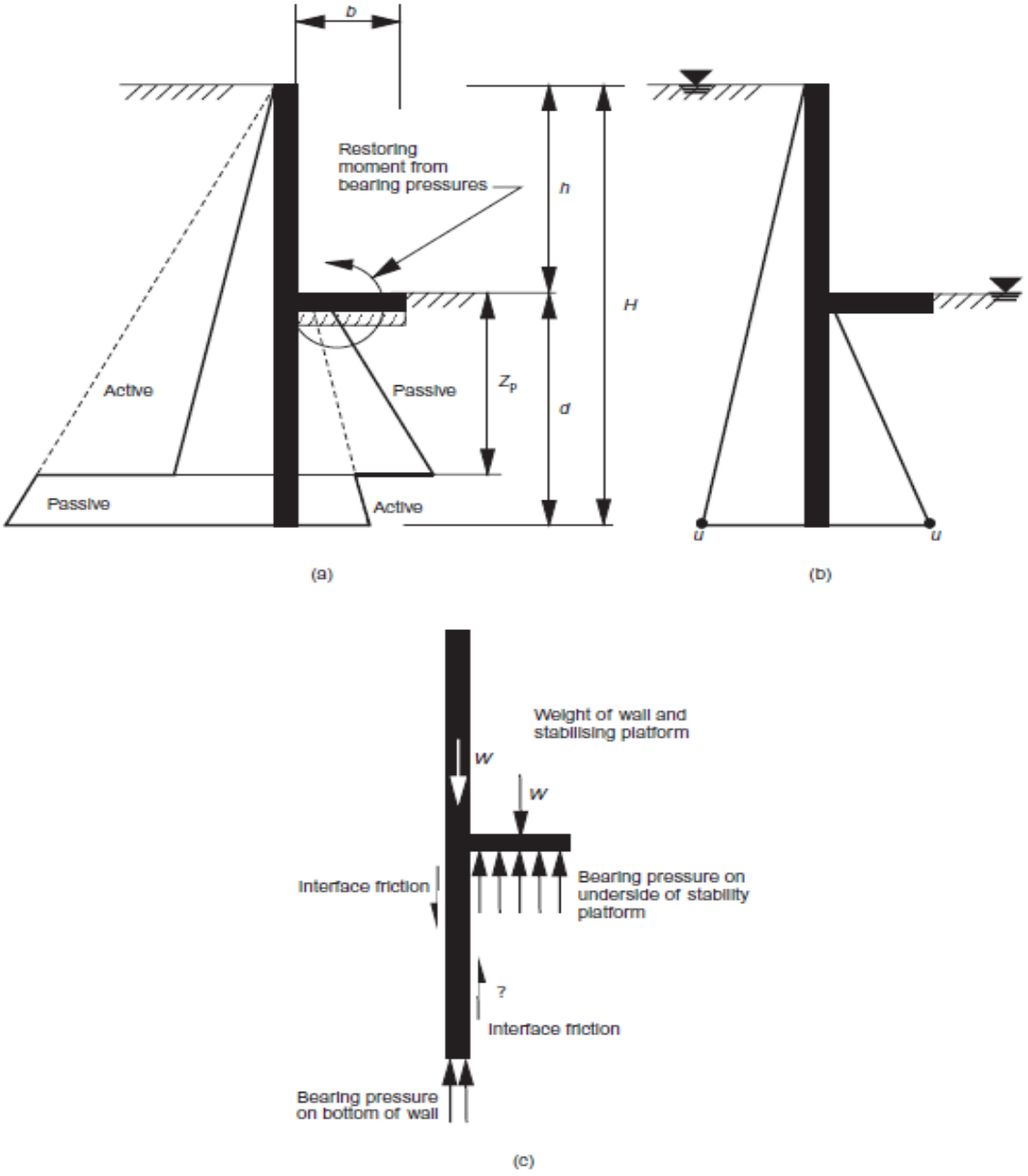

Figure 2-58. Idealized stress distribution for an embedded retaining wall with a stabilising base (a) horizontal effective stresses (b) pore water pressures acting on the structure (c) vertical forces (after Powrie eat al. 2007)

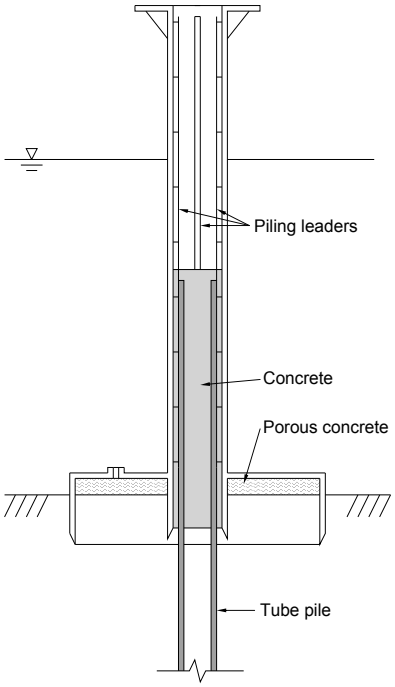

Figure 2-59. A schematic illustration of a monopiled footing (Dixon 2005)

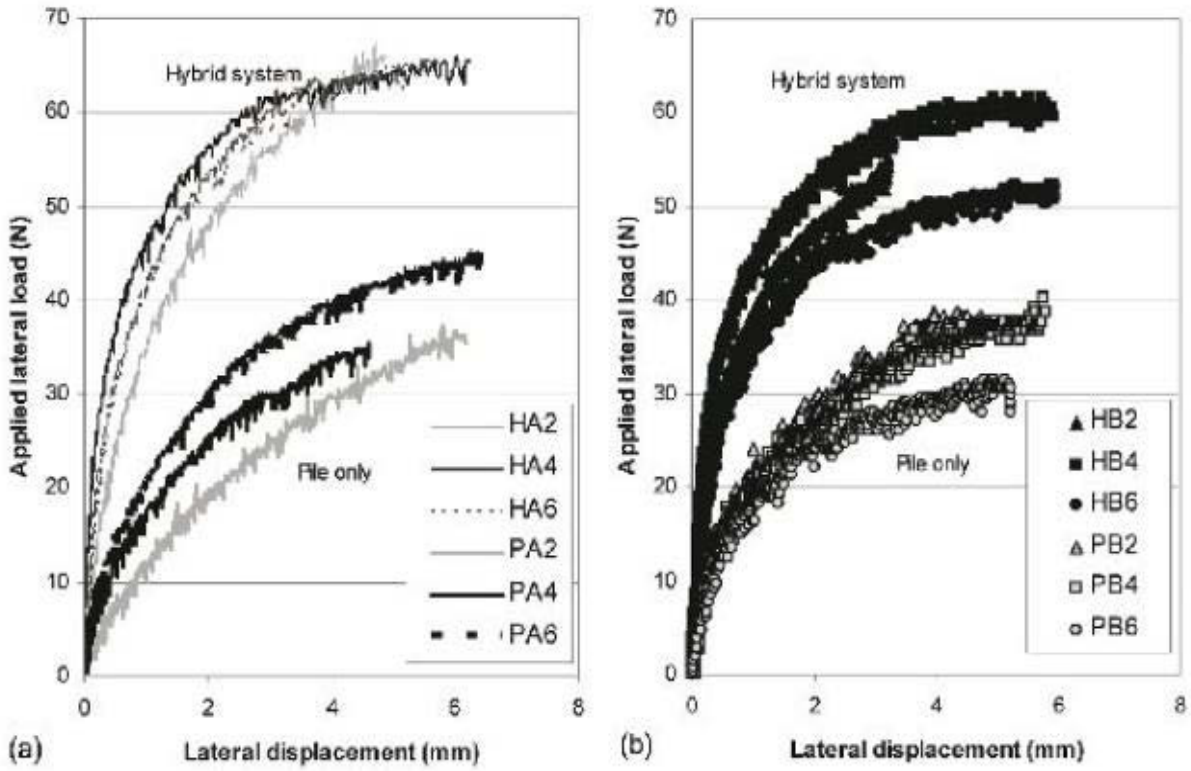

Figure 2-60. Lateral load vs. lateral displacement for monopiled footing structures compared to monopiles (a) results read from 6 mm elevation (b) results read from 36 mm elevation (after Stone et al. 2007)

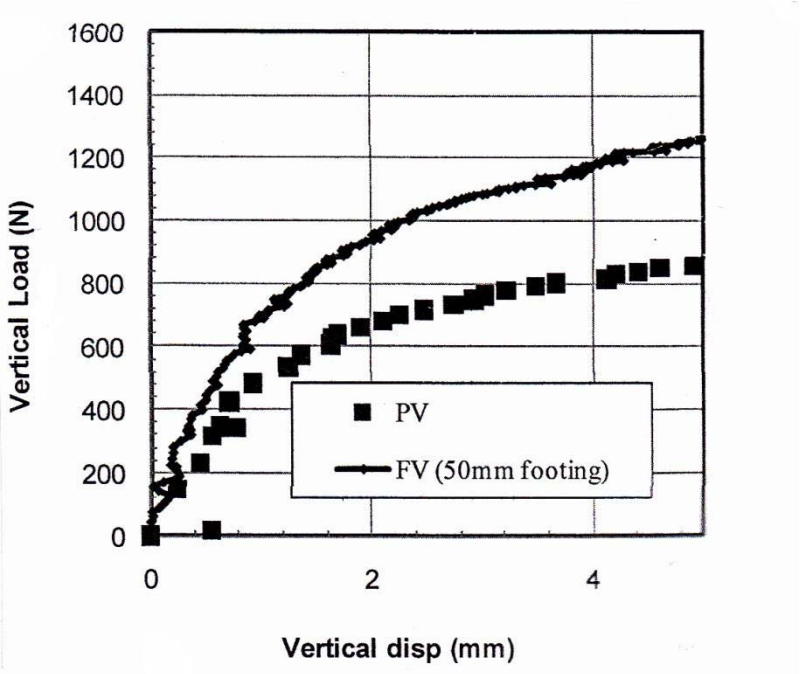

Figure 2-61. Vertical load versus vertical displacement for a 50 mm diameter plate (FV) and a single pile (PV) (after Stone et al. 2010)

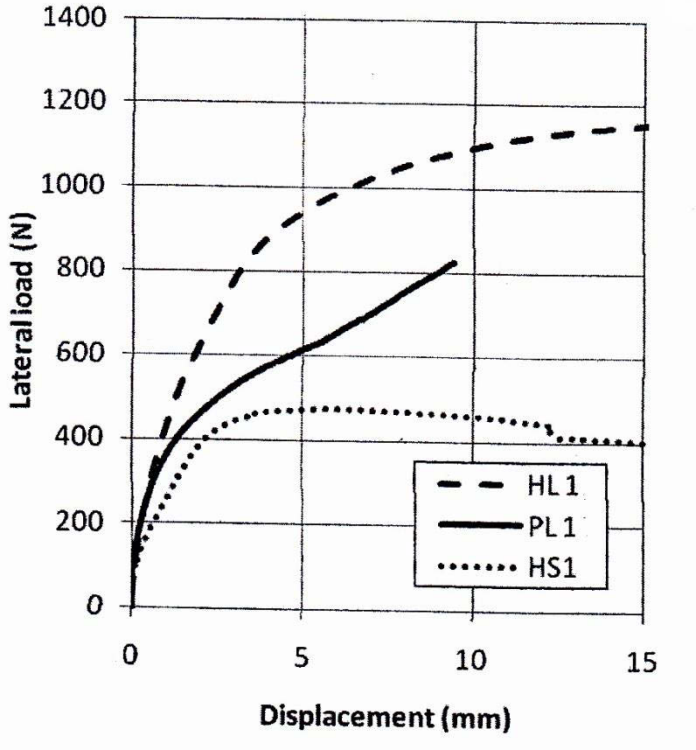

Figure 2-62. Lateral load versus lateral displacements for monopiled footing (HL1), single pile (PL1) and a monopiled footing with a short pile (HS1) (after Stone et al. 2010)

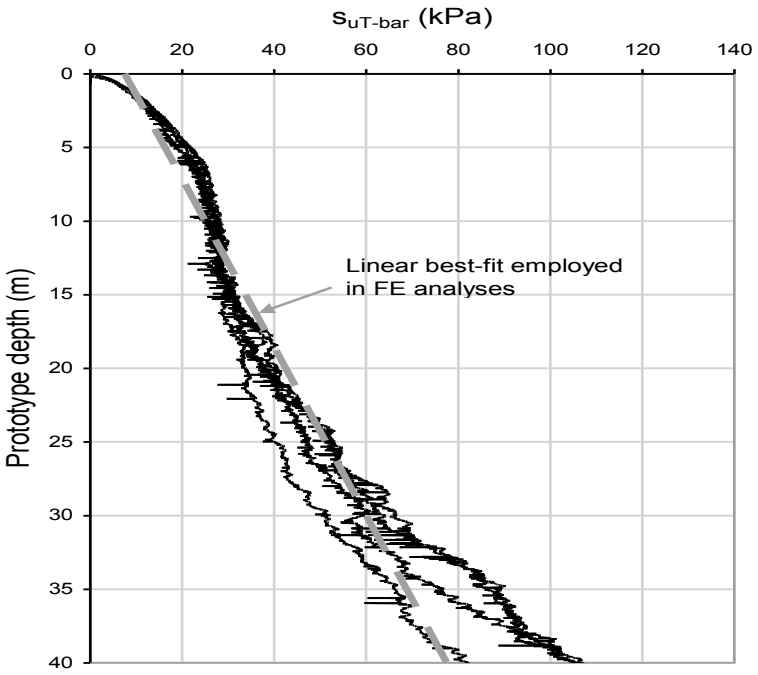

Figure 2-63. Profile of the T-bar tests for measuring the undrained shear strength of the clay in the centrifuge (after Lehane et al. 2010)

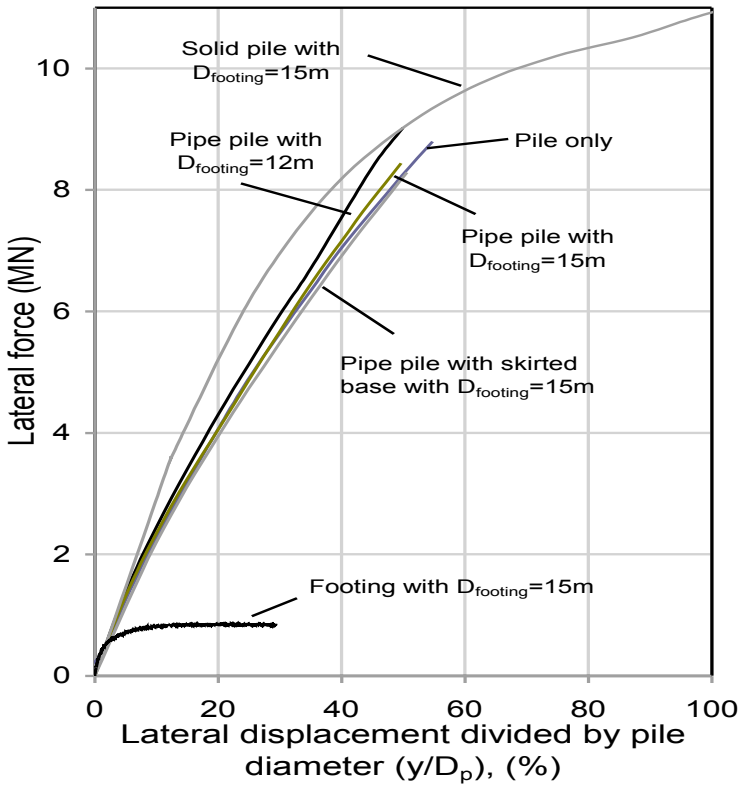

Figure 2-64. Lateral load-displacement response for the proposed structures in the centrifuge (after Lehane et al. 2010)

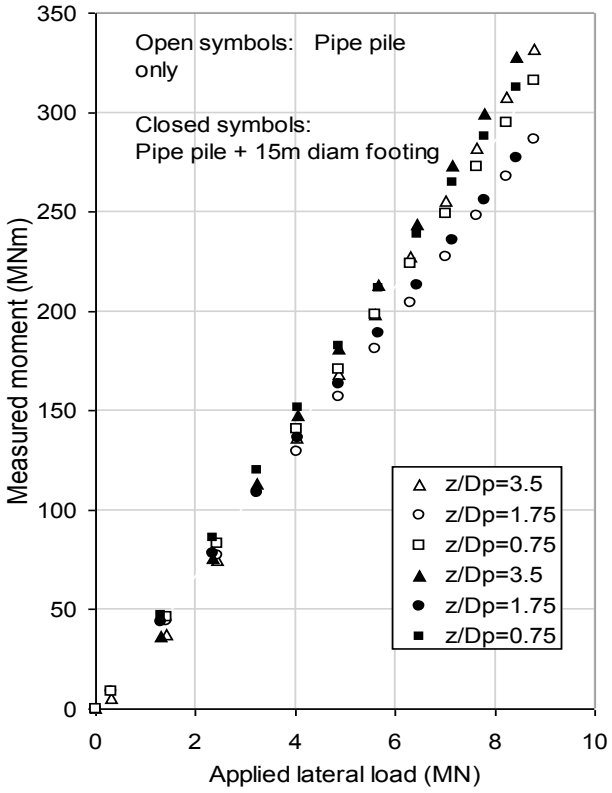

Figure 2-65. Measured bending moments in the centrifuge for tests number two and three (after Lehane et al. 2010)

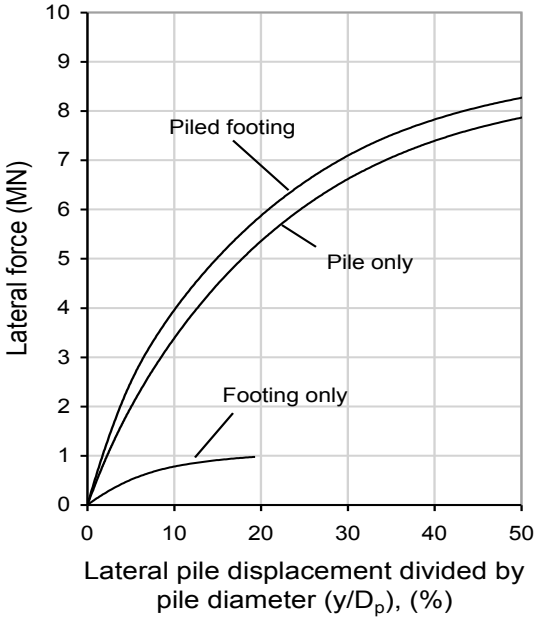

Figure 2-66. Plaxis 3D predictions for the response of three different types of foundations (after Lehane et al. 2010)

CHAPTER 3 ELASTIC ANALYSIS

3.1 INTRODUCTION

In this chapter, a literature review on the elastic beam method for calculating the horizontal displacement of a pile's head, its rotation and the depth of the maximum moment along the pile's length is discussed. Following the elastic beam method there will be a discussion on methods of calculating the pile's head displacement, rotation and the maximum moment along the pile's body for a single pile embedded in an elastic soil medium.

In the second part of this section, an elastic model is constructed and the accuracy of the model is tested in respect to the equations provided by different scholars. At the end, equations are derived for calculating the displacement and rotation of a free-headed short pile embedded in an elastic soil medium. In addition, an equation is derived for calculating the lateral displacement of a restrained pile embedded in a homogenous elastic soil medium.

3.2 ELASTIC BEAM ON ELASTIC FOUNDATION METHOD

In this method, the pile is considered as an elastic beam, which is attached to discrete springs. Thus, the displacement of one spring has no effect on any other spring, as illustrated in Figure 3-1. In this way, the model greatly simplifies the mathematical analysis at the expense of neglecting the continuity of the soil.

Winkler originally generated this model and it is useful for soil profiles, which are highly inhomogeneous because of their complex layering. This model is also useful in coming to an understanding of the dynamic response of pile groups (Pender, 1993).

The basic structural mechanics for a laterally loaded section of an embedded pile can be derived from the free body diagram illustrated in Figure 3-2. In this figure, the lateral load deflection of a pile is considered only in the Y direction and the shear deflections are negligible.

Taking the moments about point O in Figure 3-2 (right), with considering the moments to be positive in the counter clockwise direction will provide us with equation 3-1.

$$(\mathrm{M} + d\mathrm{M}) - \mathrm{M} + \mathrm{P_z}dy - \mathrm{V}dz + pdz\frac{dz}{2} = 0 \qquad \textbf{3-1}$$

Neglecting the second derivative in the last part of the above equation and rearranging will give Equation 3-2. $\mathrm{P_z}$ in this equation is the vertical load.

$$\frac{d\mathrm{M}}{dz} + \frac{dy}{dz}\mathrm{P_z} - \mathrm{V} = 0 \qquad \textbf{3-2}$$

Differentiating the above equation with respect to z will give Equation 3-3.

$$\frac{d^2\mathrm{M}}{dz^2} + \frac{d^2y}{dz^2}\mathrm{P_z} - \frac{d\mathrm{V}}{dz} = 0 \qquad \textbf{3-3}$$

The value of $d^2\mathrm{M}/dz^2$ in the above equation is equal to $\mathrm{E_pI_p}d^4\mathrm{y}/dz^4$ and the value of $d\mathrm{V}/dz$ is equal to P (where P is equal to –ky). $\mathrm{E_p}$ is the piles modulus of elasticity, $\mathrm{I_p}$ is the second moment of area of the pile and y is the pile deflection or soil compression.

Using the values of $d^2\mathrm{M}/dz^2$ and $d\mathrm{V}/dz$ and substituting them into Equation 3-1 will provide us with Equation 3-4.

$$\mathrm{E_pI_p}\frac{d^4\mathrm{y}}{dz^4} + \frac{d^2\mathrm{y}}{dz^2}\mathrm{P_z} + \mathrm{ky} = 0 \qquad \textbf{3-4}$$

The above equation is the governing equation for a laterally loaded elastic pile. The above equation does not include side shear, and as mentioned $\mathrm{P_z}$ is the vertical load acting on the pile's head.

Equation 3-4 can be solved by different methods (Finite difference or boundary element method) with assumptions made on the value of k in respect to the soil's response.

In the elastic beam on elastic foundation method, the value of k (the soil stiffness) is equal to the lateral subgrade modulus $\mathrm{K_h}$ of the soil. $\mathrm{K_h}$ is the ratio of the horizontal soil reaction per unit area to the lateral soil displacement. The determination of $\mathrm{K_h}$ is often difficult and expensive so usually empirical relations are used from the results of SPT and CPT in practice.

Form Table 2-3 the values of the modulus of subgrade reaction ($\mathrm{K_h}$, $\mathrm{FL^{-2}}$) can be calculated. The value of $\mathrm{K_h}$ is usually assumed constant with depth for fine-grained soils and linearly increasing with depth for coarse-grained soils.

The values in Table 2-3 can be referred as the coefficient of subgrade reaction ($\mathrm{FL^{-3}}$) or they are in fact the slope of the variation of $\mathrm{K_h}$ with depth. In the following equations, the value of $\mathrm{n_h}$ has been considered for cohesionless material (that is a linear increase for $\mathrm{K_h}$ with depth) while for cohesive soils the value of $\mathrm{K_h}$ are directly calculated by an equation provided by Vesic (1961) and it will be assumed that it will be constant.

Winkler's solutions for cohesionless material are expressed in terms of the following parameter:

$$\mathrm{T} = \sqrt[5]{\frac{\mathrm{E_pI_p}}{\mathrm{n_h}}} \qquad \textbf{3-5}$$

In the above equation, $\mathrm{n_h}$ is the coefficient of subgrade reaction (as in Table 2-3), $\mathrm{E_p}$ is the Young's modulus for the pile material and $\mathrm{I_p}$ is the second moment of area of the pile section.

If the pile's length is greater than 5T, the pile can be considered as a long pile. For piles that are shorter than 2T the pile is considered a rigid pile.

The solutions to Equation 3-4 are as in Equations 3-6 to 3-10. In these equations $\mathrm{E_p}$, $\mathrm{I_p}$ are the modulus of elasticity and the moment of inertia of the pile section respectively. $\mathrm{A_x}$,$\mathrm{B_x}$, $\mathrm{A_\theta}$, $\mathrm{B_\theta}$,

A_m, B_m, A_v, B_v, $A_{p'}$ and $B_{p'}$ are coefficients. U_z, θ_z, M_z, V_z and P'_z are the pile deflection, slope of the pile, moment of the pile, shear force on a pile and soil reaction at any depth respectively. Q_g and M_g are the working horizontal and moments acting at the ground level on the pile's head respectively.

The values of all coefficients for long piles have been provided in Figure 3-3. The first column of this table provides the values of Z, which are the nondimensional depths and are equal to the depth of interest (under the ground), divided by the value of T calculated in Equation 3-5.

$$U_z = A_x \frac{Q_g T^3}{E_p I_p} + B_x \frac{M_g T^2}{E_p I_p} \quad \textbf{3-6}$$

$$\theta_z = A_\theta \frac{Q_g T^2}{E_p I_p} + B_\theta \frac{M_g T}{E_p I_p} \quad \textbf{3-7}$$

$$M_z = A_m Q_g T + B_m M_g \quad \textbf{3-8}$$

$$V_z = A_v Q_g + B_v \frac{M_g}{T} \quad \textbf{3-9}$$

$$P'_z = A_{p'} \frac{Q_g}{T} + B_{p'} \frac{M_g}{T^2} \quad \textbf{3-10}$$

For example, at the depth of zero (at the ground level), the value of z/T will be equal to zero and the coefficients will be equal to the values in the first row of Figure 3-3. Equations 3-6 to 3-10 are suitable for cohesionless material where there is a linear increase in the value of the lateral subgrade modulus.

For cohesive soils, Davison and Gill (1963) provide Equation 3-11 and 3-12 for calculating the horizontal displacement and moments at any depth along the pile's body.

$$U_z = A'_x \frac{Q_g R^3}{E_p I_p} + B'_x \frac{M_g R^2}{E_p I_p} \quad \textbf{3-11}$$

$$M_z = A'_m Q_g R + B'_m M_g \quad \textbf{3-12}$$

In the above equations A'_x, B'_x, A'_m and B'_m are coefficients illustrated in Figure 3-4. The value of R in the above equations can be calculated as in equation 3-13. The value of K_h in Equation 3-13 can be calculated by Equation 3-14 (Vesic 1961). In these equations E_p, I_p, E_s, D and υ_s are the modulus of elasticity of the pile material, the moment of inertia of the pile section, soil's modulus of elasticity, pile diameter and the soil Poisson's ratio respectively.

$$R = \sqrt[4]{\frac{E_p I_p}{K_h}} \quad \textbf{3-13}$$

$$K_h = 0.65 \sqrt[12]{\frac{E_s D^4}{E_p I_p}} \frac{E_s}{1 - \upsilon_s^2} \quad \textbf{3-14}$$

In Figure 3-4, the value of Z is nondimensional and is equal to z/R, where z is the depth of interest and R is as in Equation 3-13.

In addition, the value of Z_{max} in Figure 3-4 is calculated as in Equation 3-15 with L equal to the piles length and R equal to Equation 3-13.

$$Z_{max} = \frac{L}{R} \quad \textbf{3-15}$$

3.3 THE *P-Y* ANALYSIS

The *p-y* curve method is similar to the elastic beam on elastic foundation method except that the k parameter (soil stiffness) in Equation 3-4 is not a constant nor increases linearly with depth. A nonlinear relationship between the soil resistance and soil displacement is assumed along the pile's length. The nonlinear relationships have been obtained from the results of well-instrumented laterally loaded piles.

It must be pointed out that both the elastic beam on elastic foundation method and the *p-y* curves do not consider the continuity and soil shearing resistance, as they were originally developed by considering discrete springs. Another drawback to these methods is that the spring modulus of the model is dependent on the size of the foundation.

3.4 THE ELASTIC APPROACH FOR CALCULATING THE DEFLECTIONS OF A SINGLE PILE

In this approach, the pile and the soil body are considered as a continuous medium with calculating the stress strain behaviour from constitutive models. These methods are usually appropriate for small strain levels and the effects of pile and soil yielding cannot be obtained from this approach.

Poulos (1971a) presents solutions for the lateral deflection of a pile head in the form of charts for a single pile embedded in an elastic soil medium. Randolph (1981), Davies and Budhu (1987) and Carter et al. (1992) provide equations for calculating the lateral deflection and rotation of a single pile head in an elastic medium (these equations do not require solution charts).

In this section, initially the method employed by Poulos (1971a) which can also be found in Poulos & Davis (1980) is summarised. Moreover, the equations used for calculating the lateral

deflection of a single elastic pile embedded in an elastic soil medium developed by other scholars will also be discussed in the upcoming sections.

3.4.1 Solution charts for a floating pile embedded in uniform soil

The problem involves a pile embedded in an elastic soil medium as illustrated in Figure 3-5. The pile's length is equal to L; it carries a moment (M) and a lateral load (H) at the ground level. A load applied at any eccentricity (distance from the ground level) can be replaced with an equivalent moment and lateral force acting at the ground level on the pile's head.

For a constant soil modulus with depth (similar to over consolidated clays), the ground line deflection p of a free head pile can be expressed as in Equation 3-16. In this equation, the values of I_{pH} and I_{pM} are presented in the charts shown in Figures 3-6 and 3-7 respectively.

$$p = \frac{H}{E_s L} I_{pH} + \frac{M}{E_s L^2} I_{pM} \qquad \textbf{3-16}$$

As mentioned by Poulos et al. (1980) the value of υ_s (the soil Poisson's ratio) for deriving Figures 3-6 and 3-7 were equal to 0.5 (this is also illustrated in both figures); however υ_s has relatively little influence on the solutions.

The rotation of the pile head θ is calculated by Equation 3-17. The influence factors $I_{\theta H}$ and $I_{\theta M}$ are given in Figures 3-7 and 3-8 respectively.

$$\theta = \frac{H}{E_s L^2} I_{\theta H} + \frac{M}{E_s L^3} I_{\theta M} \qquad \textbf{3-17}$$

The value of K_R in the charts provided by Poulos et al. (1980) is equal to Equation 3-18. In this equation E_p, I_p, E_s and L are the modulus of elasticity of the pile, the second moment of inertia of the pile cross section and the length of the pile under the ground respectively.

$$K_R = \frac{E_p I_p}{E_s L^4} \qquad \textbf{3-18}$$

For a pile that has a fixed head (i.e. cast into a foundation or cap so that it does not rotate, Das 1999 and Poulos 2009) the ground line deflection is given by Equation 3-19. The value of I_{pF} is given in Figure 3-9 while the value of F_{pF} is illustrated in Figure 3-10.

$$p = \frac{H}{E_s L} I_{pF} \Big/ F_{PF} \qquad \textbf{3-19}$$

In Figure 3-10 the value of H is equal to the horizontal load applied to the pile's head at the ground level while H_u as previously discussed can be equal to $P_y DL$ (D is the pile's diameter and L is the embedded depth of the pile). P_y can be considered as the yield pressure halfway along the embedded part of the pile and by considering Broms (1964) solutions that will be equal to $3K_p\sigma'_v$ (K_p is the passive earth pressure and σ'_v is the effective vertical stress at halfway along the pile's embedded depth).

3.4.2 Solution charts for floating piles in soils with a linearly increasing modulus

Poulos et al. (1980) provides charts for piles embedded in sands and normally consolidated clays with considering the soil's modulus to increase linearly with depth. Assuming a constant soil modulus for these types of soils can lead to unacceptable inaccuracies so they assume that the soil modulus increases linearly with depth from zero at the ground surface, and at any depth, the soil's Young's modulus is equal to Equation 3-20. The value of N_h in this equation can be read of Table 2-3.

$$E_s = N_h Z \quad \textbf{3-20}$$

The ground line deflection and rotation can be calculated by Equations 3-21 and 3-22.

$$p = \frac{H}{N_h L^2}\frac{I'_{pH}}{F'_p} + \frac{M}{N_h L^3}\frac{I'_{PM}}{F'_p} \quad \textbf{3-21}$$

$$\theta = \frac{H}{N_h L^3}\frac{I'_{\theta H}}{F'_\theta} + \frac{M}{N_h L^4}\frac{I'_{\theta M}}{F'_\theta} \quad \textbf{3-22}$$

In the above equations I'_{pH}, I'_{pM}, $I'_{\theta H}$ and $I'_{\theta M}$ can be read from Figure 3-11 to Figure 3-13 and the values of F'_p and F'_θ are given in Figures 3-14 and 3-15 respectively. The value of K_N in the figures is equal to Equation 3-23, where E_p, I_p, N_h and L are the modulus of the pile material, the moment of inertia of the pile section, the rate of increase in the soil's modulus of elasticity and the pile's length under the ground respectively.

$$K_N = \frac{E_p I_p}{N_h L^5} \quad \textbf{3-23}$$

For a fixed head pile, the ground line deflection is as in Equation 3-24.

$$p = \frac{H}{N_h L^2} I'_{pF} / F'_{pF} \quad \textbf{3-24}$$

In the above equation, the values of I'_{pF} and F'_{pF} are illustrated in Figures 3-16 and 3-17 respectively.

As previously mentioned, the value of H/H_u is the ratio of the applied horizontal force to the yield pressure halfway along the embedded length of the pile. That is $H_u = 3K_p\sigma'_v DL$, where K_p is the passive pressure, D is the pile diameter, L is the length of the pile under the ground and σ'_v is the effective vertical stress at halfway along the pile's embedded depth.

3.4.3 Solution charts for calculating the maximum moments in a single pile

Poulos and Davis (1980) provide charts for calculating the maximum moments generated in a pile for a purely elastic soil medium and a soil with an increasing modulus of elasticity.

For a horizontally loaded pile in a constant elastic soil medium, Figure 3-18 was proposed for calculating the maximum moment acting on the pile section. In this figure, the value of K_R is

equal to Equation 3-25 and H and L are the horizontal force acting on the pile's head at the ground level and the pile length underground respectively.

$$K_R = \frac{E_p I_p}{E_s L^4} \quad \textbf{3-25}$$

As discussed by Poulos & Davis (1980) the location of the maximum moment is typically between 0.1L to 0.4L below the ground surface (with L equal to the length of the pile under the ground); this is for a homogenous soil. The larger depths for the maximum bending moment are usually for stiffer piles.

For a pile with a fixed head (i.e. pile with a cap) embedded in a purely elastic soil the value of the maximum moment occurs at the pile head where the restraint is provided and its value can be calculated by Figure 3-19. As in the pile case the value of K_R, H and L are required for this figure. As illustrate in Figures 3-18 and 3-19 these solutions are for a Poisson's ratio of 0.5 but as discussed by Poulos and Davis (1980), Pender (1993) and Davis and Budhu (1986) the value of υ_s does not significantly alter the results.

For a free head pile, embedded in a soil with varying soil modulus the maximum moment generated by a horizontal load is illustrated in Figure 3-20. As in the case of a pile embedded in a purely elastic soil the maximum moments, occur at a depth of around 0.1L to 0.45L below the ground level.

For a fixed headed pile embedded in an elastic soil medium with a linearly increasing soil modulus the maximum moment is calculated by Figure 3-21.

As mentioned by Poulos & Davis (1980) the maximum values of the moments for a linearly varying soil modulus with depth are greater than for a uniform soil modulus, and that is the case for the free headed and fixed headed piles as well.

3.4.4 Equations for calculating the lateral deflection of a long single pile embedded in an elastic soil medium

In this method instead of using influence factors adopted by Poulos & Davis (1980) in the form of charts, a set of equations can be solved simultaneously for calculated the pile's head displacement and rotation at the ground level for an elastic soil and pile.

The equations are as follows:

$$u = f_{uH}H + f_{uM}M \quad \textbf{3-26}$$

$$\theta = f_{\theta H}H + f_{\theta M}M \quad \textbf{3-27}$$

In the above equations H is the applied horizontal force, M is the applied moment at the ground level and f_{uH}, f_{uM}, $f_{\theta H}$ and $f_{\theta M}$ are flexibility coefficients. U and θ are also the pile's head displacement and rotation respectively.

From the reciprocal theorem, the values of $f_{\theta H}$ and f_{uM} must be equal.

The values of the flexibility coefficients change depending on the adopted soil's modulus of elasticity for long piles and short piles embedded in an elastic soil medium. The flexibility coefficients are functions of the soil and pile's modulus of elasticity, the Poisson's ratio, the pile diameter and the pile length (the latter is only for short piles).

The flexibility coefficients are obtained from the results of boundary element or finite element calculations on a solid circular pile section embedded in an elastic soil medium. For other cross sections, an equivalent E_p is obtained by Equation 3-28. In this equation r is equal to width of the proposed pile section while $(E_p I_p)_{actual}$ are the modulus of elasticity and the moment of inertia of the cross section of the proposed pile.

$$E_P = \frac{(E_P I_P)_{actual}}{0.25\pi r^4} \quad \textbf{3-28}$$

Two eccentricity terms have been introduced for a single pile loaded with a shear and moment acting at the ground level. These eccentricity terms are illustrated in Equations 3-29 and 3-30.

$$e = \frac{M}{H} \quad \textbf{3-29}$$

$$f = \frac{M}{DH} \quad \textbf{3-30}$$

In the above equations D, H and M are the pile diameter, the horizontal force and moment acting at the ground level respectively.

In the upcoming equations it has been found that once the length of the pile exceeds some critical value additional length makes negligible difference to the calculated deformations (similar to the elastic beam on an elastic foundation method). The effective length is defined as the depth, which the lateral deflections are one thousand of the head deflection (Kuhlemeyer 1979 and Randolph 1981).

As shown in Figure 3-22 three different soil modulus with depth can be considered for and elastic soil medium. A constant soil modulus is usually appropriate for over consolidated clays. A linear increase in the soil modulus is more suited to normally consolidated clays and cohesionless soils at moderate strain levels. Finally, the parabolic increase in the soil modulus is well suited for sands at small strain levels.

The values of the flexibility coefficients and the active length of an elastic pile change depending on the distribution of the Young's modulus with depth for the proposed soil.

3.4.4.1 Constant soil modulus with depth

Davis and Budhu (1986) provide Equation 3-31 for the active length of a single pile embedded in an elastic soil medium with a constant soil modulus. In this equation, D is the pile diameter and K equals to the ratio of the pile's modulus of elasticity to the soil's modulus ($K = E_p/E_s$).

$$L_a = 0.5DK^{0.36} \quad \textbf{3-31}$$

As previously discussed, if the length of a single pile embedded in an elastic soil medium (with a constant soil modulus) is greater than L_a the pile is considered long and Equations 3-32 to 3-34 are valid for the flexibility coefficients.

$$f_{uH} = \frac{1.3K^{-0.18}}{E_s D} \quad \textbf{3-32}$$

$$f_{uM} = f_{\theta H} = \frac{2.2K^{-0.45}}{E_s D^2} \quad \textbf{3-33}$$

$$f_{\theta M} = \frac{9.2K^{-0.73}}{E_s D^3} \quad \textbf{3-34}$$

The location of the maximum moment in the pile section is given by Equation 3-35 and the magnitude of the maximum moment is obtained from Equation 3-36.

$$L_{M_{max}} = 0.4L_a \quad \textbf{3-35}$$

$$M_{max} = I_{MH} DH \quad \textbf{3-36}$$

In the above equations L_a is the active length of the pile, D is the pile diameter and H is the horizontal force acting on the pile's head. The value of I_{MH} can be calculated as in Equation 3-37 with considering Equations 3-38 and 3-39.

$$I_{MH} = aK^b \quad \textbf{3-37}$$

$$a = 0.12 + 0.24f + 0.1f^2 \quad \textbf{3-38}$$

$$b = \exp(-1.3 - 0.34f) \quad \textbf{3-39}$$

In the above equations, the value of f is as in Equation 3-30.

It must also be noted that if the value of I_{MH} is greater than six, the maximum moment is equal to the moment acting at the pile's head.

Davis and Budhu also provide Equations 3-40 and 3-41 for calculating the displacement of a fixed head pile in an elastic soil medium (i.e. cast into a foundation or cap so that it does not rotate Das 1999 & Poulos 2009).

$$u_F = f_{FH} H \quad \textbf{3-40}$$

$$f_{FH} = \frac{0.8K^{-0.18}}{E_s D} \quad \textbf{3-41}$$

In the above equations H is the horizontal force, D is the pile diameter, E_s is the soil modulus of elasticity and K is equal to E_p/E_s.

The maximum moment acting on a fixed headed pile can be calculated as in Equation 3-42 with considering Equation 3-43.

$$M_F = -I_{MF} H D \quad \textbf{3-42}$$

$$I_{MF} = 0.24K^{0.27} \quad \textbf{3-43}$$

For a fixed headed pile in a constant soil modulus the assumption in deriving Equation 3-42 and 3-43 is that the pile head rotation is equal to zero. When calculating the displacements of a fixed headed pile there is no need to use Equations 3-26 and 3-27 as only the displacement of the pile's head can be calculated by Equations 3-40 and 3-41.

In section 3.5.2, flexibility coefficients will be derived for long piles embedded in a homogenous soil. In addition, an equation will be derived for calculating the lateral displacement of a single fixed headed pile embedded in soil medium with a constant Young's modulus.

3.4.4.2 Linearly variation of soil modulus with depth

Budhu and Davis (1987 and 1988) provide the flexibility coefficients required for calculating the lateral displacement and rotation of a single pile embedded in an elastic soil medium with a linearly increasing soil modulus.

For the case were the modulus of elasticity increases as in Equation 3-44 with m considered as the rate of increase in the Young's modulus and D taken as the pile diameter the stiffness ratio can be calculated as in Equation 3-45 (E_p is the modulus of elasticity of the pile section).

$$E_s = mD \quad \textbf{3-44}$$

$$K = \frac{E_p}{mD} \quad \textbf{3-45}$$

Budhu and Davis provide values of m for sands in respect to the relative density of the soil. As discussed by Pender (1993) these values are well suited for static loading of piles and they are not appropriate for dynamic loading in loose saturated sands.

The active length of a single pile embedded in a linearly increasing soil modulus is calculated as in Equation 3-46.

$$L_a = 1.3DK^{0.22} \quad \textbf{3-46}$$

As in the previous case, if the length of a single pile is longer than the value of L_a the pile is considered as a long pile and increasing the length will not significantly affect the displacement and rotation of the pile's head.

The flexibility coefficients are calculated as in Equations 3-47 to 3-49.

$$f_{uH} = \frac{3.2K^{-0.33}}{mD^2} \quad \textbf{3-47}$$

$$f_{uM} = f_{\theta H} = \frac{5.0K^{-0.55}}{mD^3} \quad \textbf{3-48}$$

$$f_{\theta M} = \frac{13.6K^{-0.77}}{mD^4} \quad \textbf{3-49}$$

In the above equations, m is the rate of increase in Young's modulus with depth (with the units of MPa), D is the pile diameter and K is calculated as in Equation 3-45.

The location of the maximum moment is calculated as in Equation 3-50, which is similar to Equation 3-35.

$$L_{M_{max}=} 0.41\, L_a \quad \textbf{3-50}$$

The maximum moment along the pile section is calculated from Equations 3-51 and 3-52 with the values of a and b equal to Equations 3-53 and 3-54 respectively. In the last two equations, the value of (f) is equal to Equation 3-30.

It must be noted that if the value of I_{MH} in Equation 3-52 is greater than eight, a value of eight is used in Equation 3-51.

$$M_{max} = I_{MH}DH \quad \textbf{3-51}$$

$$I_{MH} = aK^b \quad \textbf{3-52}$$

$$a = 0.6f \quad \textbf{3-53}$$

$$b = 0.17f^{-0.3} \quad \textbf{3-54}$$

The above equations are for free-headed piles. For a fixed headed pile, Equations 3-55 and 3-56 are used for calculating the displacement of the pile's head.

Similar to the case of a constant Young's modulus adopted for the soil, Equations 3-26 and 3-27 are not required for a fixed headed pile, as only the displacement can be calculated.

$$u^F = f_{FH}H \quad \textbf{3-55}$$

$$f_{FH} = \frac{1.35K^{-0.33}}{mD^2} \quad \textbf{3-56}$$

The fixing moment for a fixed headed pile can be calculated by Equations 3-57 and 3-58. In these equations, D is equal to the pile diameter, H is the horizontal force acting on the pile's head at the ground level and K is equal to Equation 3-45.

$$M^F = -I_{MF}HD \quad \textbf{3-57}$$

$$I_{MF} = 0.37K^{0.22} \quad \textbf{3-58}$$

3.4.4.3 Parabolic variation of soil modulus with depth

For a parabolic variation of soil modulus with depth, the stiffness ratio must be calculated at a certain depth of interest as in Equation 3-59. In this equation, E_{sD} equals to the Young's modulus of the soil at depth D and E_p is the pile's modulus of elasticity.

$$K = \frac{E_p}{E_{sD}} \quad \textbf{3-59}$$

The active length of the pile lies between the values given by Equations 3-31 and 3-46 (that is the uniform soil modulus and the linear variation in the soil modulus for when E_{sD} = mD).

The flexibility coefficients were derived by Gazetas (1991) and are given in Equations 3-60 to 3-62. In these equations, D is the pile diameter, E_{sD} is the soil modulus at the depth of interest and K is equal to Equation 3-59.

$$f_{uH} = \frac{2.14K^{-0.29}}{E_{sD}D} \quad \textbf{3-60}$$

$$f_{uM} = f_{\theta H} = \frac{3.43K^{-0.53}}{E_{sD}D^2} \quad \textbf{3-61}$$

$$f_{\theta M} = \frac{12.16K^{-0.77}}{E_{sD}D^3} \quad \textbf{3-62}$$

For a parabolic increase in the soil modulus there is no simple equation for the magnitude and position of the maximum moment.

3.4.5 Equations for calculating the lateral deflection of a short single pile in a purely elastic soil medium

Carter and Kulhawy (1992) provide equations for a short pile embedded in a constant soil modulus. For a pile to be considered short the following inequality must be satisfied.

$$L_r \leq (0.05 \text{ to } 0.07)D\left(\frac{E_p}{E_s}\right)^{0.5} \quad \textbf{3-63}$$

In the above equation E_p is the modulus of elasticity of the pile, E_s is the modulus of elasticity of the soil and D is the pile diameter.

In the case of short piles embedded in a constant soil modulus, the slender ratio (L/D, L is the pile length and D is the pile diameter) is an important factor in calculating the flexibility coefficients.

Equations 3-64 to 3-66 give the flexibility coefficients for a short pile embedded in a constant soil modulus.

$$f_{uH} = \frac{0.7\left(\frac{L}{D}\right)^{-0.33}}{E_s D} \quad \textbf{3-64}$$

$$f_{uM} = f_{\theta H} = \frac{0.4\left(\frac{L}{D}\right)^{-0.88}}{E_s D^2} \quad \textbf{3-65}$$

$$f_{\theta M} = \frac{0.6\left(\frac{L}{D}\right)^{-1.67}}{E_s D^3} \quad \textbf{3-66}$$

By using the above equations with Equations 3-26 and 3-27, the lateral deflection and rotation of a short pile embedded in an elastic soil medium can be estimated.

A short pile deforms in a rigid manner and the point of rotation or the pivot point (a) for such piles can be calculated as in Equation 3-67.

$$\frac{a}{D} = \frac{0.3\left(\frac{L}{D}\right)^{-0.33} + 0.5f\left(\frac{L}{D}\right)^{-0.88}}{0.5\left(\frac{L}{D}\right)^{-0.88} + 0.3f\left(\frac{L}{D}\right)^{-1.67}} \quad \textbf{3-67}$$

In the above equation L is the pile's length, D is the pile diameter and f can be calculated as in equation 3-30.

3.4.6 Intermediate pile lengths in a soil with a constant modulus of elasticity

For pile lengths, which stand between Equations 3-31 and 3-63, Carter and Kulhawy (1992) suggest an estimate for calculating the deflection of the pile's head. They state that the displacement of the pile head can be calculated as 1.25 times either the lateral displacement of a rigid pile with the slender ratio as in the actual pile, or the displacement of a flexible pile with the same (E_p/E_s) for the actual pile.

Carter and Kulhawy (1992) do not make any suggestions on the amount of rotation for an intermediate pile length embedded in a constant soil modulus.

3.4.7 Pile head stiffness matrix

The pile head stiffness matrix is determined by inversion of the two by two matrix of the flexibility coefficients, which is equal to Equation 3-68.

$$\begin{bmatrix} K_{HH} & K_{HM} \\ K_{MH} & K_{MM} \end{bmatrix} = \frac{1}{(f_{uH}f_{\theta M} - f_{uM}^2)} \begin{bmatrix} f_{\theta M} & -f_{uM} \\ -f_{\theta H} & f_{uH} \end{bmatrix} \quad \textbf{3-68}$$

K_{HH}, K_{HM}, K_{MH} and K_{MM} are the pile head stiffness coefficients. As in the flexibility coefficients, the values of K_{MH} and K_{HM} for the stiffness matrix must be equal.

The displacement and rotation of a free head pile can be calculated as in Equation 3-69.

$$\begin{bmatrix} H \\ M \end{bmatrix} = \begin{bmatrix} K_{HH} & K_{HM} \\ K_{MH} & K_{MM} \end{bmatrix} \begin{bmatrix} \Delta h \\ \Delta\theta \end{bmatrix} \quad \textbf{3-69}$$

In the above equation H, M, Δh, $\Delta\theta$ are the horizontal force or the shear force acting on the pile head, the moment acting at the ground level on the pile, the horizontal displacement of the pile's head and the rotation of the pile head (in radians).

The values of K_{HH} and K_{MH} can be calculated when a unit horizontal displacement is applied to the pile head with zero rotation in a numerical model. In addition, the values of K_{HM} and K_{MM} are calculated by applying a unit rotation to the pile head with zero horizontal displacement.

3.5 AN ELASTIC MODEL WITH A CONSTANT YOUNG'S MODULUS

In this section, numerical models have been constructed with the aid of the commercially available software ABAQUS V6.7 (Dassault Systèmes, 2007). The models consist of single piles and piled footing structures, which are embedded in an elastic soil medium with a constant Young's modulus.

In the upcoming sections, the components of the models will be described and equations will be derived for calculating the lateral displacement and rotation of a long and short pile embedded in a purely elastic soil medium. In addition, an equation is derived for calculating the displacement of a fixed headed pile with the assumption that the rotation of the pile head is zero.

3.5.1 Constructed numerical models with a constant Young's modulus

3.5.1.1 Introduction

The constructed models in this section (single piles and piled footings) all have reflective symmetry and the soil body is made-up of two components. The reason for having two components to the soil body is that the area close to the structures must have a finer mesh and so the soil body was divided into two components with two different mesh densities.

In the case of the single piles, the pile was constructed so that its head was exactly at the ground level. In the piled footing models, the footing height was 3m (in all cases) and it was embedded to a depth of 0.6 m below the ground surface.

Figure 3-23 to Figure 3-25 illustrates the three components used to construct the numerical models for the single pile cases. For the piled footing structures, the soil body further from the structure is as in Figure 3-23, but the soil section close to the pile and the footing were cut extruded so that the footing could be embedded into the soil body, as illustrated in Figure 3-26. The pile and footing constructed for the piled footing structures are illustrated in Figures 3-27 and 3-28 respectively.

It must be pointed out that the footings had to be partitioned at 0.6 m from their base so that they could be tied to the soil body. In addition, the piles in the piled footing cases were partitioned so that they could be tied to the footings in the interaction module. The partition generated on the pile section for the piled footing structures is illustrated in Figure 3-28.

The piles in the single pile and piled footing structures were also partitioned form their centre so that the moment acting on the pile's head could be applied to the structure as a couple moment. The partitions generated on the piles are also illustrated in Figures 3-25 and 3-28.

3.5.1.2 The dimensions and the material properties for the numerical models

In respect to the discussions made in Sections 3.4.4.1 and 3.4.5, three different pile lengths were considered for the numerical models. The first type were the long piles, which they all satisfy Equation 3-31. In fact, their lengths were longer than the proposed equation and they were constructed out of high strength concrete and steel.

The long concrete piles had a diameter of 3 m and 4 m and were considered as full and circular. The lengths of these concrete piles were all 40 m and they had a modulus of elasticity of 29 GPa. The pile dimensions and the soil Young's modulus adopted for each pile section is illustrated in Table 3-1. The Poisson's ratios for the soils were also equal to 0.49.

The long steel piles were actually hollow circular piles, which their equivalent modulus was calculated by Equation 3-28 so that the cross section would be equivalent to a full circular pile with a diameter equal to the original diameter of the hollow pile. The pile diameters were 3 m, 4 m and 5 m with lengths varying between 30 m and 40 m, as illustrated in Table 3-2. The adopted pile lengths (30 m and 40 m) for the steel piles were higher than the values calculated by Equation 3-31. In Table 3-2, the original thicknesses of the hollow steel piles have been provided too.

A set of short concrete piles were also constructed which satisfied the inequality in Equation 3-63. These piles had diameters of 5 m and 6 m and their lengths varied between 5 to 15 m. In addition, these piles all had a modulus of elasticity equal to 29 GPa and were originally considered as full circular piles. The dimensions and the soil Young's modulus for the adopted piles are illustrated in Table 3-3.

The third set of piles had lengths between Equations 3-31 and 3-63 (intermediate pile lengths). These piles were also solid concrete piles with diameters of 5 m and 6 m. The pile dimensions and the material properties are all illustrated in Table 3-4. These piles were also considered as full and circular.

For the piled footing structures, the long, short and the intermediate piles were used with different footing sizes tied to them. It must be pointed out that because the piles used for offshore wind turbines have large diameters; the constructed piles in the numerical models all had diameters greater than 3 m.

Table 3-5 provides the dimensions and the soil Young's modulus used for the long steel piles used in the piled footing structures. The piles used in the piled footing models had the same dimensions as in Table 3-2 (they were originally hollow steel piles). For the large pile diameters (4 m and 5 m), only a footing with a diameter of 10 m was used in the numerical models. For the smaller pile diameter, two different footing diameters (10 m and 20 m) were used in the constructed models.

For the long solid concrete piles, two different footing diameters (15 m and 25 m) were used, as illustrated in Table 3-6. The pile dimensions and the soil properties for these pile-footing structures were as in Table 3-1.

The intermediate pile lengths, which were constructed out of concrete, were also used as hybrid structures. Table 3-7 illustrates the pile and footing dimensions with the soil Young's modulus used in the numerical models. The piles used for these analyses were all solid circular piles with a Young's modulus of 29 GPa.

Table 3-8 provides the dimensions and the soil Young's modulus for the piled footing structures with short concrete piles. As can be seen two different footing dimensions were adopted for the hybrid structure for the numerical models. The pile dimensions and soil properties were adopted from Table 3-3.

Pile Diameter (m)	L(pile) m	E(pile) GPa	E(soil) MPa
3	40	29	10
3	40	29	50
3	40	29	100
4	40	29	10
4	40	29	50
4	40	29	100

Table 3-1. The dimensions and soil properties adopted for the long single solid concrete piles

Pile Diameter (m)	L(pile) m	E(soil) MPa	Equivalent E(pile) GPa	Original thickness (mm)
3	40	10	10.45	20
3	40	50	10.45	20
3	40	100	10.45	20
3	30	10	10.45	20
3	30	50	10.45	20
3	30	100	10.45	20
4	40	10	11.73	30
4	40	50	11.73	30
4	40	100	11.73	30
4	30	10	11.73	30
4	30	50	11.73	30
4	30	100	11.73	30
5	40	10	6.32	20
5	40	50	6.32	2
5	40	100	6.32	20
5	30	10	6.32	20
5	30	50	6.32	20
5	30	100	6.32	20

Table 3-2. The dimensions and soil properties adopted for the long single hollow steel piles in the numerical models

Pile Diameter (m)	L(pile) m	E(soil) MPa	E(pile) GPa
5	10	10	29
5	10	30	29
5	15	10	29
5	5	10	29
5	5	30	29
6	5	10	29
6	5	30	29
6	10	10	29
6	10	30	29
6	15	10	29

Table 3-3. The dimensions and soil properties adopted for the short solid single concrete piles

Pile Diameter (m)	L(pile) m	E (soil) MPa	E((pile) GPa
5	15	30	29
5	25	30	29
5	25	10	29
6	15	30	29
6	25	10	29
6	25	30	29

Table 3-4. The dimensions and soil properties adopted for the intermediate pile lengths

Pile Diameter (m)	Footing Diameter (m)	L(pile) m	E(soil) MPa	E(pile) GPa
3	10	40	10	10.45
3	10	40	50	10.45
3	10	40	100	10.45
3	10	30	10	10.45
3	10	30	50	10.45
3	10	30	100	10.45
3	20	40	10	10.45
3	20	40	50	10.45
3	20	40	100	10.45
3	20	30	10	10.45
3	20	30	50	10.45
3	20	30	100	10.45
4	10	40	10	11.73
4	10	40	50	11.73
4	10	40	100	11.73
4	10	30	10	11.73
4	10	30	50	11.73
4	10	30	100	11.73
5	10	40	10	6.32
5	10	40	50	6.32
5	10	40	100	6.32

Table 3-5. The dimensions and soil properties adopted for the piled footing structures with long hollow steel piles

Pile Diameter (m)	Footing Diameter (m)	L(pile) m	E(soil) MPa	E(pile) GPa
3	15	40	10	29
3	15	40	50	29
3	15	40	100	29
3	25	40	10	29
3	25	40	50	29
3	25	40	100	29
4	15	40	10	29
4	15	40	50	29
4	15	40	100	29
4	25	40	10	29
4	25	40	50	29
4	25	40	100	29

Table 3-6. The dimensions and soil properties adopted for the piled footing structures with long solid concrete piles

Pile Diameter(m)	Footing Diameter (m)	L(pile) (m)	E(soil) MPa	E(pile) GPa
5	15	15	30	29
5	25	15	30	29
5	15	25	30	29
5	25	25	30	29
5	15	25	10	29
5	25	25	10	29
6	15	15	30	29
6	25	15	30	29
6	15	25	10	29
6	25	25	100	29
6	25	25	300	29
6	15	25	300	29

Table 3-7. The dimensions and soil properties adopted for the piled footing structures with intermediate concrete piles

Pile Diameter(m)	Footing Diameter (m)	L(pile) (m)	E(soil) MPa	E(pile) GPa
5	15	10	10	29
5	15	10	30	29
5	25	10	10	29
5	25	10	30	29
5	15	15	10	29
5	25	15	10	29
5	15	5	10	29
5	15	5	30	29
5	25	5	10	29
5	25	5	30	29
6	15	5	10	29
6	15	5	30	29
6	25	5	10	29
6	25	5	30	29
6	15	10	10	29
6	15	10	30	29
6	25	10	10	29
6	25	10	30	29
6	15	15	10	29
6	25	15	10	29

Table 3-8. The dimensions and soil properties adopted for the piled footing structures with short solid concrete piles in the numerical models

3.5.1.3 The step, interaction, boundary condition and mesh module generated for the numerical models

As the constructed models were only for an elastic analysis, one-step was required for the piles and piled footing models in the numerical analysis. The assembled pile and piled footing structures are illustrated in Figures 3-29 and 3-30 respectively.

In all numerical models the parts (the soil body, pile and footing) were tied to each other with considerations made towards the mesh density for each part instance. As previously mentioned, the soil body consisted of two parts, which were tied to each other. Figures 3-31 and 3-32 illustrates the interaction between the inner and the outer part of the soil body in the numerical models.

In the single pile and piled footing models, the pile was tied to the inner soil body as illustrated in Figures 3-33 and 3-34. In the piled footing structures, the footing was tied to the pile's head and to the inner soil body. Figures 3-35 and 3-36 illustrate the interaction between the inner soil body

and the footing in the piled footing structures. In addition, Figures 3-37 and 3-38 illustrate the interaction between the footing and the pile section for the piled footing structures.

As all models contained reflective symmetry, three boundary conditions were required for each model. The base of all models was restricted from moving in the vertical direction, as illustrated in Figure 3-39. The radial boundary condition restricted any movements in the horizontal directions, as illustrated in Figure 3-40. The third boundary condition imposed on the pile and piled footing structures were to restrict any movement in the direction out of the plane, as illustrated in Figure 3-41. The latest is to satisfy the boundary condition for models with reflective symmetry.

All constructed models were displacement controlled rather than load controlled. This required a boundary condition to be imposed on the pile's head for each model. To use Equation 3-69 it was necessary to impose a horizontal displacement on the pile's head (for both the pile and piled footing structures) and to restrict it to move in the vertical direction. Figure 3-42 illustrates the pile in a piled footing model with the imposed horizontal displacement. To avoid any local deformation to the pile's head the displacement was imposed on the entire cross section area of the pile head rather than on a single point. After the analysis was completed, the horizontal reaction forces were calculated for the pile head and the moments were calculated by reading the reaction forces in the vertical direction and multiplying them with their distance from the centreline of the pile. In addition, because the value of the displacement to the pile head was introduced as a boundary condition its value was known and the rotation was equal to zero as no rotation was allowed for the pile head. This calculation provides the values of K_{HH} and K_{MH} in Equation 3-69.

The datum coordinate system used to calculate the couple moment acting on the pile's head in the numerical models for the piles and piled footing structures are illustrated in Figures 3-43 and 3-44 respectively.

To calculate the values of K_{HM} and K_{MM} couple moments were applied to the pile head. For the pile and the piled footing structures it was essential to apply the boundary condition as a moment (as a function) to the pile head with restricting it from moving horizontally. Figure 3-45 illustrates the boundary conditions acting on the pile head in a piled footing structure. The displacement was applied as a function so that it would not generate local deformation and it would correctly represent a moment acting on the pile head. After the analysis was completed, the reaction forces in the horizontal direction provided the value of H while the values of M were calculated by multiplying the reaction forces in the vertical direction by their distance from the centreline of the pile. The values of Δh for this case was equal to zero and the values of $\Delta\theta$ were calculated from the vertical displacement of the corner of the pile head. By conducting this analysis, the values of K_{HM} and K_{MM} were calculated from Equation 3-69.

The mesh generated on a nominated pile and piled footing structure is illustrated in Figures 3-46 and 3-47 respectively. As previously mentioned and illustrated in the figures, the soil close to the structures had a finer mesh compared to the soil further away from the pile and the piled footing structure.

The mesh constructed on the soil body for both the single pile and the piled footing structures were from 20-noded quadratic brick elements (C3D20). These elements were also used on the piles constructed in the single pile and the piled footing structures with a reduced integration scheme. The footing in the piled footing structures were also constructed from 20-noded quadratic brick elements with a reduced integration scheme.

The mesh type used on the soil body, the piles and the footings had the highest accuracy compared to any other mesh type (up to the date of writing this thesis). The ability to use such a high accuracy mesh type on all parts of the model was because the soil body was generated as a semicircular shape. This was an advantage for deriving the equations for the short and long piles embedded in a homogenous soil.

3.5.2 Results and discussion

In this section, some of the stiffness coefficient values calculated for the piles and the piled footing structures will be illustrated in tables. In addition, the stiffness coefficients calculated for the piles are all checked in respect to the results of other scholars (Davis et al. and Carter et al.).

The piles head stiffness coefficients for the long solid concrete piles are illustrated in Table 3-9. As previously mentioned, the reciprocal theorem requires that $K_{HM} = K_{MH}$ and this is clearly the case for the obtained results in Table 3-9.

The results of the solid short concrete piles are illustrated in Table 3-10. As expected, the values of K_{HM} and K_{MH} are equal, similar to the long pile cases.

Table 3-11 illustrates the results of the intermediate concrete piles embedded in a homogenous soil.

Pile Diameter (m)	L(pile) m	E(soil) MPa	E(pile) GPa	$K_{HH} \times 10^6$ (N/m)	$K_{MM} \times 10^8$ (Nm)	$K_{HM} \times 10^7$ (N)	$K_{MH} \times 10^7$ (N)
3	40	10	29	184.6	164	-114	-114
3	40	50	29	640	240	-240	-240
3	40	100	29	1100	294	-340	-340
4	40	10	29	240	400	-214	-214
4	40	50	29	900	600	-460	-460
4	40	100	29	1540	716	-640	-640

Table 3-9. The stiffness coefficients calculated for the long solid concrete piles

Pile Diameter (m)	L(pile) m	E(soil) MPa	E(pile) GPa	$K_{HH} \times 10^6$ (N/m)	$K_{MM} \times 10^8$ (Nm)	$K_{HM} \times 10^7$ (N)	$K_{MH} \times 10^7$ (N)
5	10	10	29	240	140	-146	-146
5	10	30	29	698	424	-392	-392
5	15	10	29	280	316	-230	-230
5	5	10	29	152	36.8	-48.6	-48.6
5	5	30	29	450	108	-142.6	-142.6
6	5	10	29	168.8	46.2	-54	-54
6	5	30	29	503.2	136	-160	-160
6	10	10	29	270	187.2	-162	-162
6	10	30	29	784	520	-440	-440
6	15	10	29	320	384	-272	-272

Table 3-10. The stiffness coefficients calculated for the short solid concrete piles

Pile Diameter (m)	L(pile) m	E(soil) MPa	E(pile) GPa	$K_{HH} \times 10^6$ (N/m)	$K_{MM} \times 10^8$ (Nm)	$K_{HM} \times 10^7$ (N)	$K_{MH} \times 10^7$ (N)
5	15	30	29	740	716	-540	-540
5	25	30	29	814	1060	-620	-620
5	25	10	29	346	698	-366	-366
6	15	30	29	860	960	-680	-680
6	25	10	29	420	1008.2	-502	-502
6	25	30	29	1006	1740	-920	-920

Table 3-11. The stiffness coefficients calculated for the intermediate pile lengths

For the case of the long steel and concrete piles the accuracy of the stiffness coefficients were checked in respect to Equations 3-32 to 3-34 (with the aid of Equation 3-68). The results are illustrated in Figures 3-48 to 3-50. This check insured that the calculated stiffness coefficients were in line with the results obtained by Davis and Budhu (1986). It must be pointed out that as the values of K_{HM} and K_{MH} were equal, Figure 3-50 represents the results of both cross term stiffness coefficients.

The results of the short concrete piles were also checked in respect to Equations 3-64 to 3-66 with the aid of Equation 3-68. The results are illustrated in Figures 3-51 to 3-53.

From Figures 3-48 to 3-50, it is clear that the results obtained for the long piles are in a very close agreement with Equations 3-32 to 3-34 derived by Davis and Budhu (1986) while the discrepancies are slightly higher for the short pile cases.

The slightly higher discrepancy in the short piles can be due to the mesh type or the mesh density used in the numerical models. The discrepancy can also be related to whether the models were displacement or load controlled. In the original paper published by Carter & Kulhawy (1992), they do not give any indication on whether the models were displacement or load controlled. As previously mentioned the constructed models in this thesis were all displacement controlled.

Figures 3-54 to 3-56 illustrates the derived flexibility coefficients for the long hollow steel and solid concrete piles. In these charts E_p, E_s and D are the modulus of elasticity of the pile, modulus of elasticity of the soil and the pile diameter respectively. In addition, u, H, M and θ are the displacement (m), horizontal force (kN), moment (kNm) and rotation (rad) acting on the pile's head.

The flexibility coefficients derived for a long pile embedded in a homogenous soil are as in Equations 3-70 to 3-72 ($K=E_{pile}/E_{soil}$).

$$f_{uH} = \frac{1.3K^{-0.18}}{E_s D} \quad \textbf{3-70}$$

$$f_{uM} = f_{\theta H} = \frac{2.0K^{-0.5}}{E_s D^2} \quad \textbf{3-71}$$

$$f_{\theta M} = \frac{11.3K^{-0.73}}{E_s D^3} \quad \textbf{3-72}$$

The above equations are in a very close agreement with Equations 3-32 to 3-34 derived by Davis and Budhu (1986).

Figures 3-57 to 3-59 illustrates the derived flexibility coefficients for the short concrete piles. As in the case of long piles E_p, E_s, D, u, H, M and θ illustrated in these figures are the modulus of elasticity of the pile, Young's modulus of the soil, pile diameter, pile head displacement (m), horizontal force (kN), moment (kNm) and rotation (rad) acting on the pile's head respectively.

As all models were displacement controlled, the value of u was known and the value of H could be calculated as a reaction force acting on the pile's head for the horizontal displacement case. As previously mentioned the moment (M) was also applied as a displacement with a function and so the reaction forces could be extracted for each node on the pile's head and the values were multiplied by their distance from the centreline of the pile. The rotation (θ) was also calculated from the vertical displacement of the pile's head corner.

The equations derived for the short piles are as follows:

$$f_{uH} = \frac{0.64\left(\frac{L}{D}\right)^{-0.6}}{E_s D} \quad \textbf{3-73}$$

$$f_{uM} = f_{\theta H} = \frac{0.25\left(\frac{L}{D}\right)^{-1.46}}{E_s D^2} \quad \textbf{3-74}$$

$$f_{\theta M} = \frac{0.66\left(\frac{L}{D}\right)^{-1.96}}{E_s D^3} \quad \textbf{3-75}$$

The above equations are in line with Equations 3-64 to 3-66 derived by Carter and Kulhawy (1992).

As mentioned by Carter and Kulhawy (1992) the derived equations for the flexibility coefficients for short piles embedded in a homogenous soil are accurate for slender ratios between 1 and 10, that is $1 < L/D \leq 10$. As can be seen from Table 3-10 and Figures 3-57 to 3-59 appropriate results can also be obtained for slender ratios equal an slightly lower than one.

The accuracy of the derived equations for the short piles and equations proposed by Carter and Kulhawy (1992) are checked by two examples at this point.

Example 1

A reinforced concrete pile with a diameter of 0.5 m and a length of 1 m is embedded in a homogenous soil with a Young's modulus of 20 MPa. If the pile's modulus of elasticity is equal to 25 GPa and the horizontal force acting on the pile's head is equal to 1470.790 kN, find the lateral displacement of the pile's head (no moment is acting on the pile).

The pile length satisfies Equation 3-63 so it is a short pile and Equations 3-64 to 3-66 can be used to calculate the flexibility coefficients.

$f_{uH} = 5.57\times10^{-8}$

$f_{uM} = f_{\theta H} = 4.35\times10^{-8}$

$f_{\theta M} = 7.54\times10^{-8}$

With considering the moment equal to zero in Equation 3-26, the displacement of the pile's head will be equal to 0.082 m (82 mm).

Using Equations 3-73 to 3-75 will provide the following flexibility coefficients.

$f_{uH} = 4.22\times10^{-8}$

$f_{uM} = f_{\theta H} = 1.82\times10^{-8}$

$f_{\theta M} = 6.17\times10^{-8}$

With the moment equal to zero and using Equation 3-26, the displacement of the pile head will be equal to 0.062 m (62 mm).

The FE model constructed for Example 1 predicts a value of 0.05 m (50 mm).

Example 2

A reinforced concrete pile with a diameter of 5 m and a length of 10 m is embedded in a homogenous soil with a Young's modulus of 30 MPa. If the pile's modulus of elasticity is equal to 29 GPa and the horizontal force and moment acting on the pile's head are equal to 17.5 MN and 2.12×10^{7} Nm respectively find the lateral displacement and rotation of the pile's head.

The pile length satisfies Equation 3-63 so it is a short pile and Equations 3-64 to 3-66 can be used to calculate the flexibility coefficients.

$f_{uH} = 3.71\times10^{-9}$

$f_{uM} = f_{\theta H} = 2.9\times10^{-10}$

$f_{\theta M} = 5.03\times10^{-11}$

The above values will provide a horizontal displacement equal to 0.071 m (71 mm) and a rotation equal to 0.0061 rad for the pile's head.

Using Equations 3-73 to 3-75 will provide the following flexibility coefficients.

$f_{uH} = 2.81\times10^{-9}$

$f_{uM} = f_{\theta H} = 1.21\times10^{-10}$

$f_{\theta M} = 4.11\times10^{-11}$

The above flexibility coefficients will provide a displacement equal to 0.05 m (50 mm) and a rotation of 0.0029 rad.

The FE model constructed for Example 2 predicts a displacement equal to 0.05 m (50 mm) and a rotation equal to 0.001 rad for the pile's head.

As illustrated in the above examples the derived equations for the short piles are in a closer agreement with the FE predictions.

As discussed by Carter and Kulhawy (1992) they use 8-noded, isoparametric and quadrilateral elements in their investigation. As previously mentioned in this study 20-noded, isoparametric and quadrilateral elements were used to investigate the behaviour of the embedded piles. This could have been a factor in generating the discrepancy between the results. In addition, Carter et al. (1991) does not mention wether their models were load or displacement controlled. If their models were load controlled (rather than displacement controlled), this is another source which could have caused discrepancy between the derived equations and the provided equations by Carter and Kulhawy (1992) (Cook et al. 2002).

It must be pointed out that the flexibility coefficients for the intermediate pile lengths for the single piles did not converge in a manner that a successful regression could be conducted.

Table 3-12 illustrates the results of the piled footing structures for the long solid concrete piles. As can be seen, the values of K_{HM} and K_{MH} are not equal and this was the case for the long hollow steel piles too.

Table 3-13 illustrates the results of the piled footing structures with intermediate pile lengths. As can be seen, the values of K_{HM} and K_{MH} for these structures are equal and this was the case for the cross term coefficients calculated for the short solid concrete piles as well.

By deducing the values of the pile head flexibility coefficients from the flexibility coefficients of the piled footing structures, Equation 3-76 was developed for calculating the lateral displacement of a fixed head pile in a homogenous soil medium. In this equation, $K_{HH,\ PILE}$ is the flexibility coefficient of a long pile, which can be calculated through Equations 3-32 to 3-34 or it can be calculated by Equations 3-70 to 3-72 in conjunction with Equation 3-68.

In Equation 3-76, D is the pile diameter and E_{soil} is the modulus of elasticity of the soil.

$$K_{HH} = K_{HH,\ PILE} + \frac{E_{soil} D^{1.25}}{9} \qquad \textbf{3-76}$$

As in Equation 3-40, the above equation can be used for calculating the lateral displacement of a single pile with the assumption that the pile's head does not undergo any rotation (i.e. cast into a foundation or cap so that it does not rotate, Das 1999 & Poulos 2009). Example 3 and Example 4 compares the results of Equations 3-40 and 3-76 for a fixed headed single pile embedded in a homogeneous soil.

It must be pointed out that the displacement of the pile's head for the piled footing structure is not related to the footing size (radius or thickness) as in Equations 3-40 and 3-76. In addition, an attempt was made to generate an equation for the pile's head rotation for a piled footing structure; unfortunately, the results did not converge in such a manner that a successful regression could be conducted. The reason was that there were outliers and their behaviour could not be followed accurately.

Pile Diameter	Footing Diameter	L(pile) m	E(soil) MPa	E(pile) GPa	$K_{HH} \times 10^6$ (N/m)	$K_{MM} \times 10^8$ (Nm)	$K_{MH} \times 10^7$ (N)	$K_{HM} \times 10^7$ (N)
3	15	40	10	29	240	260	-130	-146
3	15	40	50	29	1020	540	-232	-340
3	15	40	100	29	1860	780	-360	-500
3	25	40	10	29	380	420	-131	-150
3	25	40	50	29	1700	860	-280	-350
3	25	40	100	29	3200	1120	-520	-640
4	15	40	10	29	300	500	-230	-244
4	15	40	50	29	1180	960	-510	-560
4	15	40	100	29	2140	1300	-680	-806
4	25	40	10	29	440	700	-238	-250
4	25	40	50	29	1860	1440	-640	-580
4	25	40	100	29	3250	1840	-710	-920

Table 3-12. Piled footing results for long concrete piles

Pile Diameter	Footing Diameter	L(pile) m	E(soil) MPa	E(pile) GPa	$K_{HH} \times 10^6$ (N/m)	$K_{MM} \times 10^8$ (Nm)	$K_{MH} \times 10^7$ (N)	$K_{HM} \times 10^7$ (N)
5	15	15	30	29	860	1000	-580	-580
5	25	15	30	29	1240	1380	-800	-800
5	15	25	30	29	880	1240	-740	-740
5	25	25	30	29	1260	1600	-820	-820
5	15	25	10	29	360	780	-378	-378
5	25	25	10	29	540	1000	-388	-388
6	15	15	30	29	980	1340	-780	-780
6	25	15	30	29	1340	1760	-840	-840
6	15	25	10	29	434	1140	-540	-540
6	25	25	10	29	880	1280	-600	-600
6	25	25	30	29	1400	2400	-960	-960
6	15	25	30	29	1040	1960	-940	-940

Table 3-13. Piled footing results for intermediate pile lengths

Example 3

A concrete pile with a diameter of 0.5 m and a length of 15 m was installed in a soil with a Young's modulus of 25 MPa. The modulus of elasticity of the pile is 20 GPa and the horizontal shear force and moment acting on the pile's head are equal to 100 kN and 200 kNm respectively.

Find the lateral displacement of the pile's head if the pile is free head and for when it is a fixed headed pile.

The problem will be solved with the equations derived by Davis and Budhu and with the derived equations in this section for long single piles.

From Equation 3-31, it is clear that the pile is a long pile embedded in a homogenous soil.

Equations 3-32 to 3-34 will provide us with the following values:

$f_{uH} = 3.12\times10^{-8}$

$f_{uM} = f_{\theta H} = 1.74\times10^{-8}$

$f_{\theta M} = 2.24\times10^{-8}$

By using Equation 3-26 and 3-27, the horizontal and rotation of a single free-headed pile is equal to 0.0065 m (6.5 mm) and 0.006 rad respectively.

For a fixed headed pile, Equation 3-40 can be used to calculate the displacement of the pile head. The displacement for the fixed headed pile will be equal to 0.0019 m (1.9 mm) which is smaller than the value obtained for a free-headed pile.

By using Equations 3-70 to 3-72, the coefficients can be calculated as follows:

$f_{uH} = 3.12\times10^{-8}$

$f_{uM} = f_{\theta H} = 1.13\times10^{-8}$

$f_{\theta M} = 2.75\times10^{-8}$

These values in conjunction with Equations 3-26 and 3-27 will provide a displacement and rotation equal to 0.0053 m (5.3 mm) and 0.006 rad respectively.

From equation 3-76, the displacement of a fixed headed pile is calculated to be equal to 0.002 m (2 mm) which is smaller than a single pile case.

It is apparent that there is a very close agreement between the results obtained from Equations 3-32 to 3-34 and Equations 3-70 to 3-72 for calculating the displacements and rotation of a long free-headed single pile. In addition, the results of Equation 3-76 are in line with the results obtained from Equation 3-40 for calculating the displacement of a fixed headed pile embedded in a homogenous soil.

Example 4

Repeat Example 3 for a fixed head pile with considering a pile a diameter of 3 m and a constant soil modulus of 40 MPa.

Equation 3-40 predicts the pile head displacement to be equal to 0.21 mm while Equation 3-76 estimates a value of 0.28 mm for a fixed head pile.

3.6 CONCLUSION

In this chapter, detailed literature review on free and fixed headed pile structures was discussed. Methods available for calculating the lateral deflection and rotation of a single pile were discussed through using charts and equations. The flexibility coefficients calculated by different scholars for long and short piles were provided for different distribution of soil modulus of elasticity.

The stiffness coefficients for long, short and intermediate concrete and steel piles were calculated by conducting an FE analysis. From the stiffness coefficients, the flexibility coefficients were calculated for long and short piles embedded in different constant modulus of elasticities. It was evident that the coefficients were similar to the equations provided by prvious scholars for long and short piles. The difference calculated in the values of the flexibility coefficients compared to other scholars were slightly higher for short pile structures embedded in a uniform soil modulus of elasticity. Furthermore, an equation was derived for calculating the lateral displacement of a long fixed pile head structure (with no rotation) by the aid of the stiffness coefficient of a long pile embedded in a uniform soil modulus.

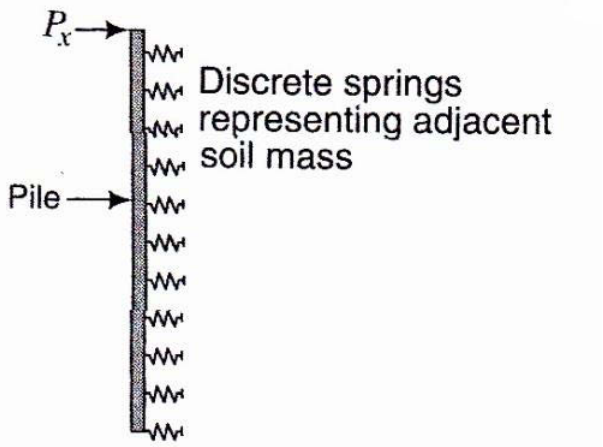

Figure 3-1. Simulation of the soil mass as a set of discrete springs (after Budhu 2007)

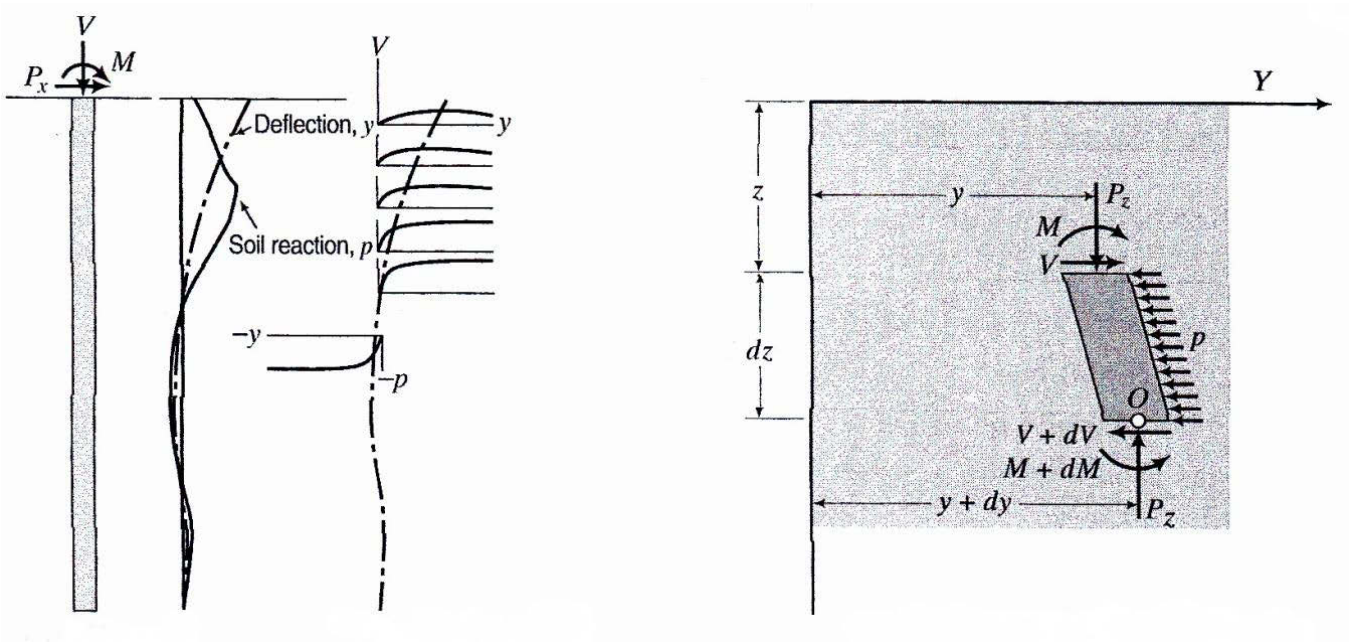

Figure 3-2. Pile soil response to lateral, vertical and moment loading (left). The free body diagram of a pile section under combined loading (right) (after Budhu 2007)

Z	A_x	A_θ	A_m	A_v	A'_p	B_x	B_θ	B_m	B_v	B'_p
0.0	2.435	−1.623	0.000	1.000	0.000	1.623	−1.750	1.000	0.000	0.000
0.1	2.273	−1.618	0.100	0.989	−0.227	1.453	−1.650	1.000	−0.007	−0.145
0.2	2.112	−1.603	0.198	0.956	−0.422	1.293	−1.550	0.999	−0.028	−0.259
0.3	1.952	−1.578	0.291	0.906	−0.586	1.143	−1.450	0.994	−0.058	−0.343
0.4	1.796	−1.545	0.379	0.840	−0.718	1.003	−1.351	0.987	−0.095	−0.401
0.5	1.644	−1.503	0.459	0.764	−0.822	0.873	−1.253	0.976	−0.137	−0.436
0.6	1.496	−1.454	0.532	0.677	−0.897	0.752	−1.156	0.960	−0.181	−0.451
0.7	1.353	−1.397	0.595	0.585	−0.947	0.642	−1.061	0.939	−0.226	−0.449
0.8	1.216	−1.335	0.649	0.489	−0.973	0.540	−0.968	0.914	−0.270	−0.432
0.9	1.086	−1.268	0.693	0.392	−0.977	0.448	−0.878	0.885	−0.312	−0.403
1.0	0.962	−1.197	0.727	0.295	−0.962	0.364	−0.792	0.852	−0.350	−0.364
1.2	0.738	−1.047	0.767	0.109	−0.885	0.223	−0.629	0.775	−0.414	−0.268
1.4	0.544	−0.893	0.772	−0.056	−0.761	0.112	−0.482	0.688	−0.456	−0.157
1.6	0.381	−0.741	0.746	−0.193	−0.609	0.029	−0.354	0.594	−0.477	−0.047
1.8	0.247	−0.596	0.696	−0.298	−0.445	−0.030	−0.245	0.498	−0.476	0.054
2.0	0.142	−0.464	0.628	−0.371	−0.283	−0.070	−0.155	0.404	−0.456	0.140
3.0	−0.075	−0.040	0.225	−0.349	0.226	−0.089	0.057	0.059	−0.213	0.268
4.0	−0.050	0.052	0.000	−0.106	0.201	−0.028	0.049	−0.042	0.017	0.112
5.0	−0.009	0.025	−0.033	0.015	0.046	0.000	−0.011	−0.026	0.029	−0.002

Figure 3-3. Coefficients for long piles embedded in cohesionless soils (after R.J. Woodwood et al. 1972)

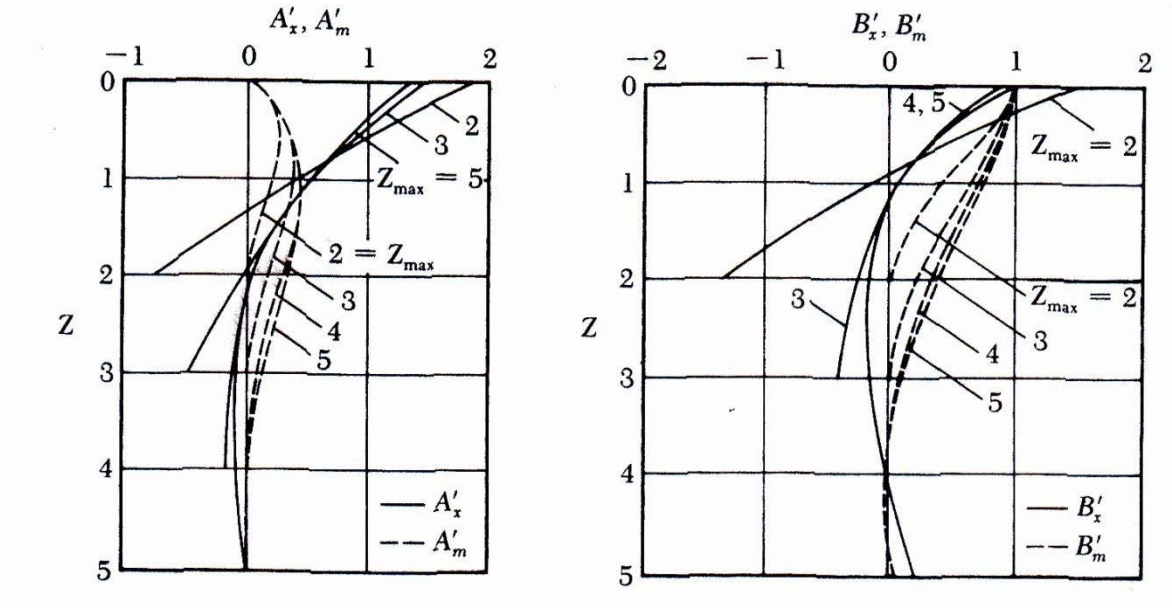

Figure 3-4. Coefficients for elastic piles in cohesive soils (after Davisson and Gill, 1963)

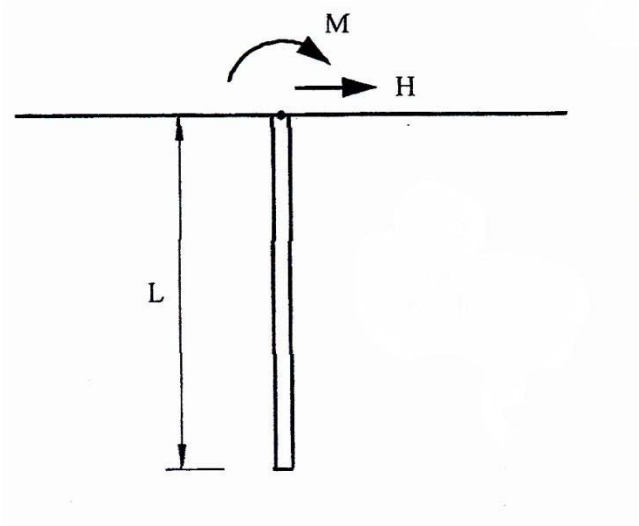

Figure 3-5. A laterally loaded pile

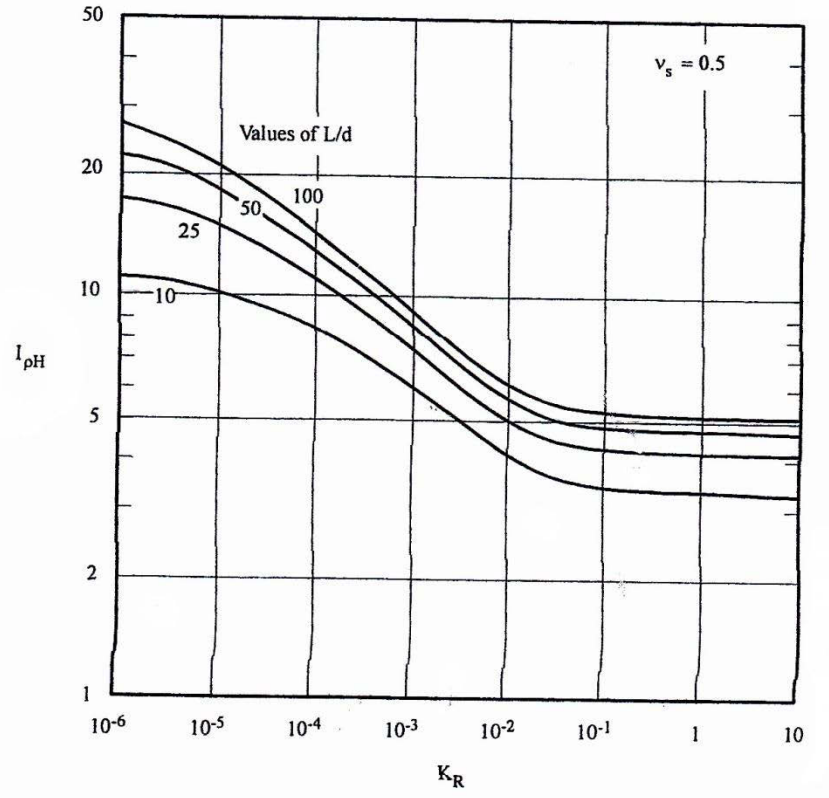

Figure 3-6. Values of I_{pH} for a free head pile embedded in a homogenous soil (after Poulos et al. 1980)

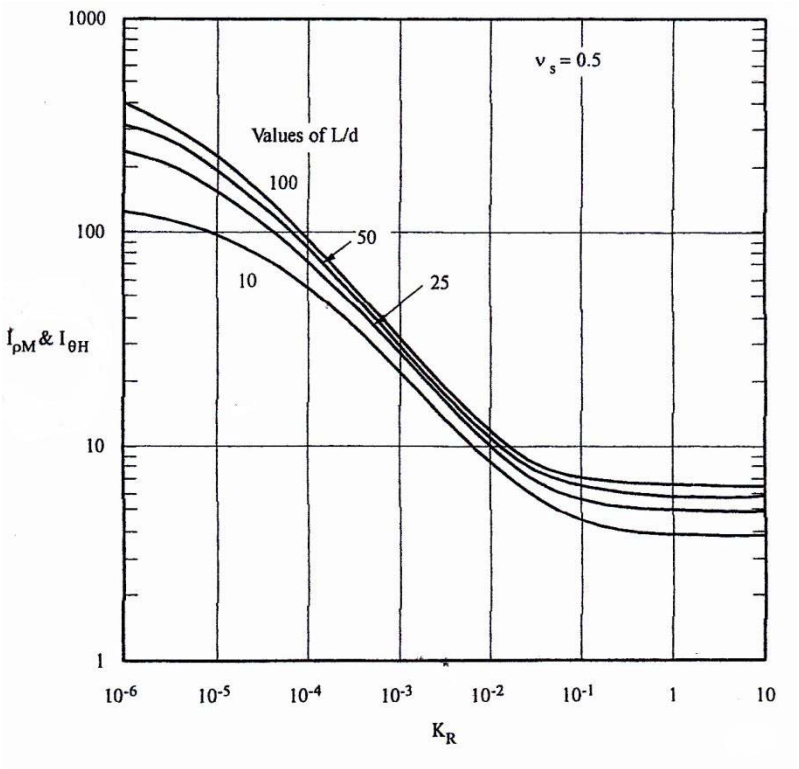

Figure 3-7. Values of $I_{\theta H}$ and I_{pM} for a free head pile embedded in a homogenous soil (after Poulos et al. 1980)

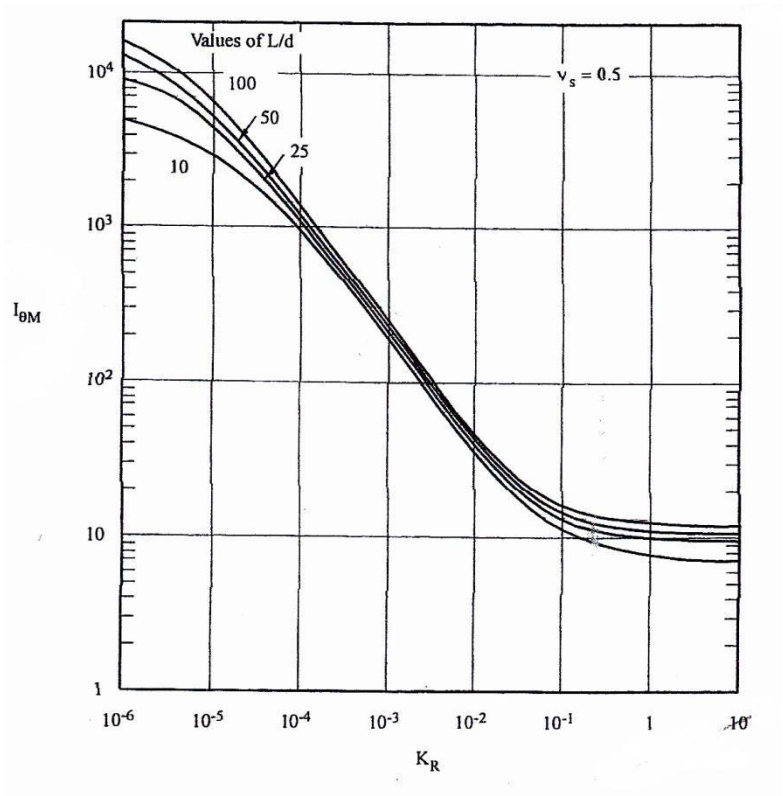

Figure 3-8. Values of $I_{\theta M}$ for a free head pile embedded in a homogenous soil (after Poulos et al. 1980)

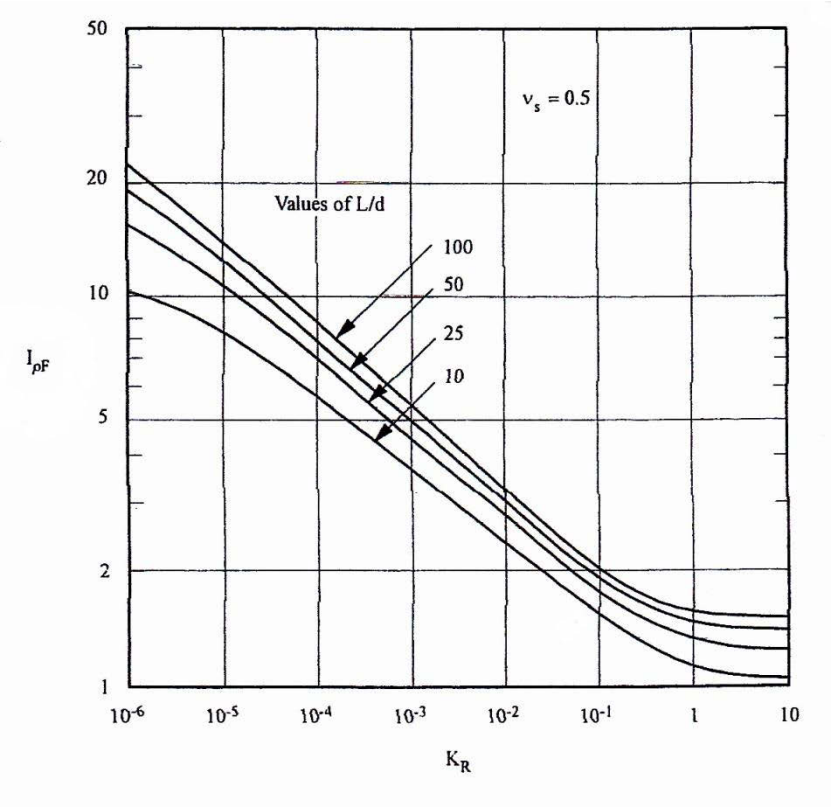

Figure 3-9. Values of I_{pF} for a fixed head pile embedded in a homogenous soil (after Poulos et al. 1980)

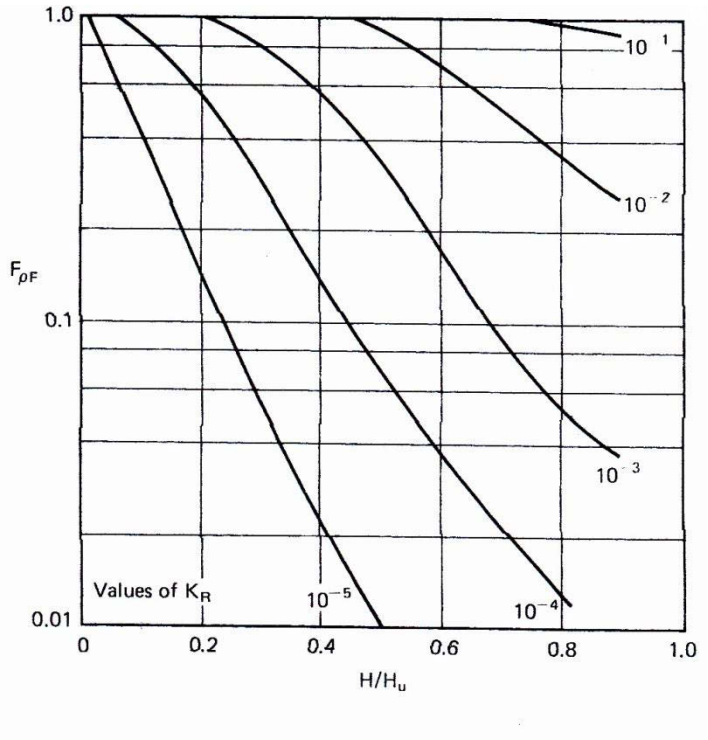

Figure 3-10. Values of F_{pF} for a fixed head pile in a uniform soil modulus (after Poulos et al. 1980)

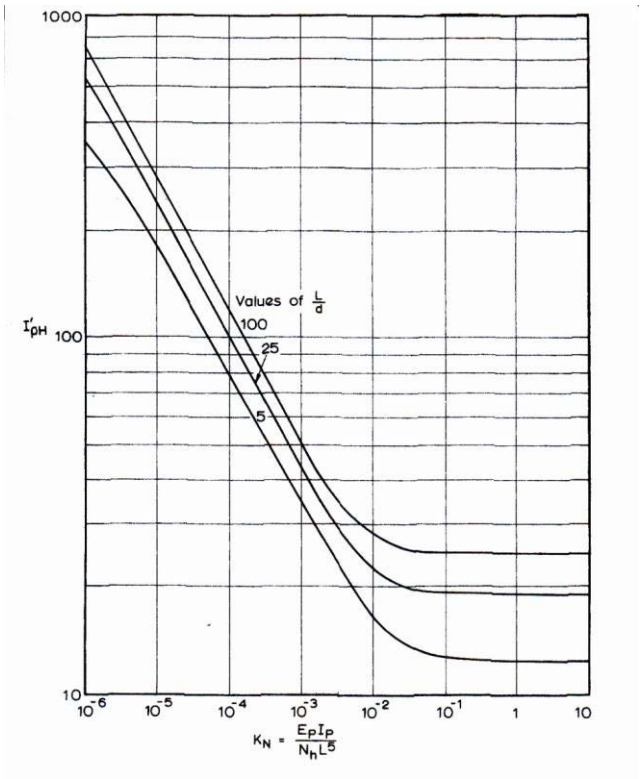

Figure 3-11. Values of I'_{pH} for free head floating piles with a linearly varying soil modulus (after Poulos et al. 1980)

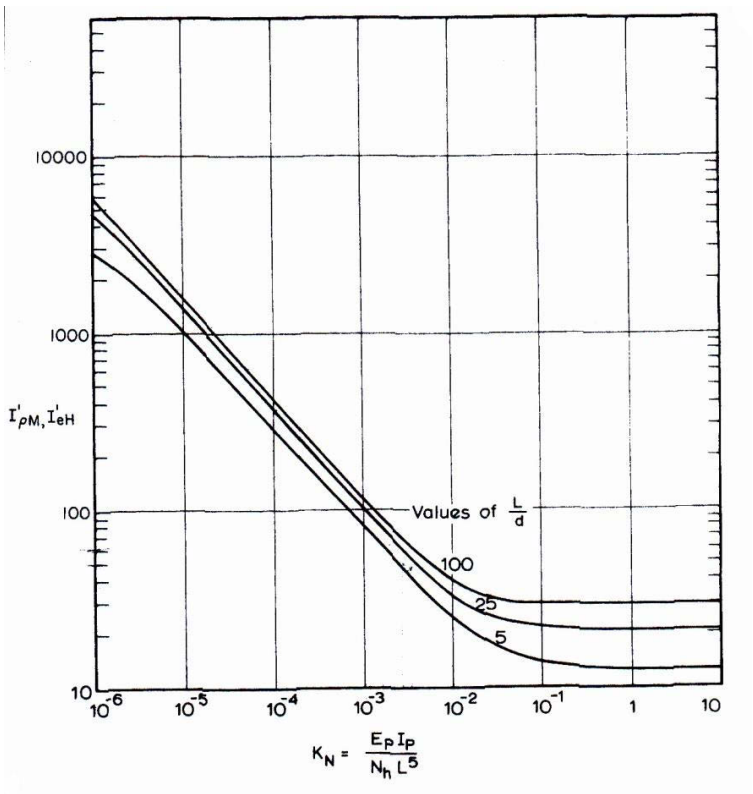

Figure 3-12. Values of I'_{pM} and $I'_{\theta H}$ for free head floating piles with a linearly varying soil modulus (after Poulos et al. 1980)

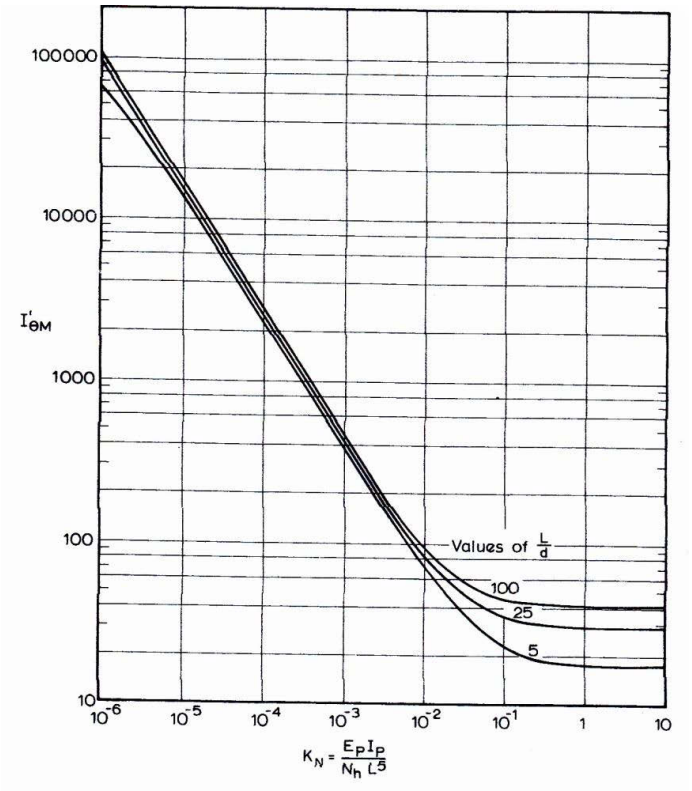

Figure 3-13. Values of $I'_{\theta M}$ for free head floating piles with a linearly varying soil modulus (after Poulos et al. 1980)

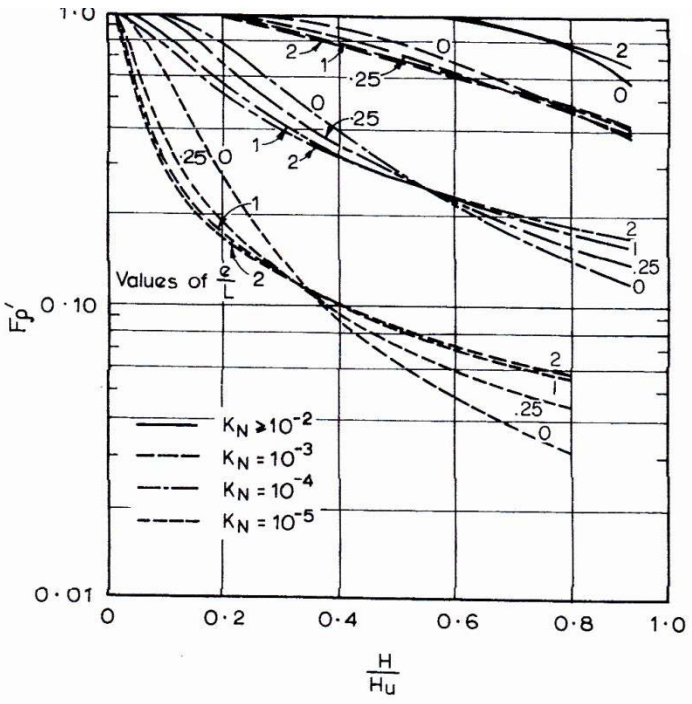

Figure 3-14. Values of F'_p for free head floating piles with linearly varying soil modulus (after Poulos et al. 1980)

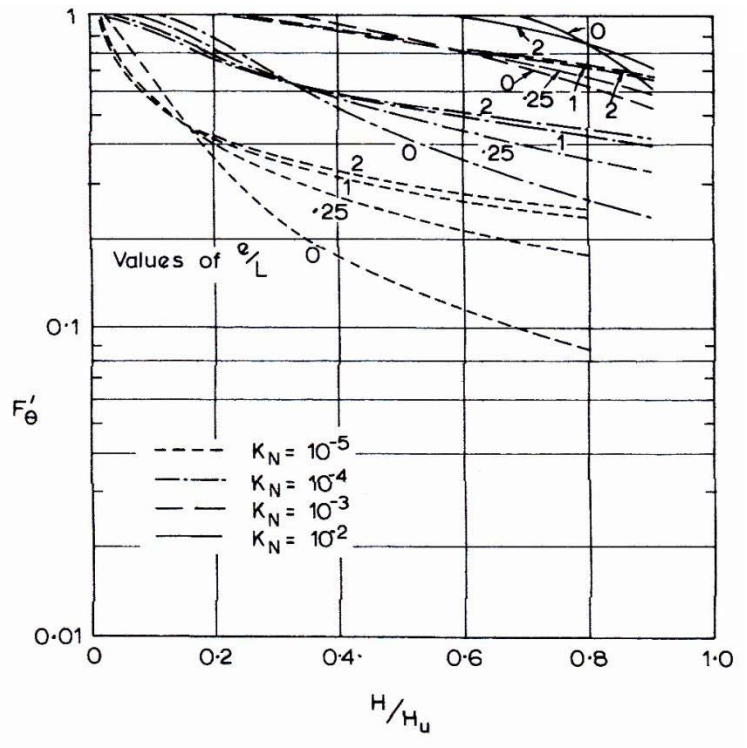

Figure 3-15. Values of F'_θ for free head floating piles with linearly varying soil modulus (after Poulos et al. 1980)

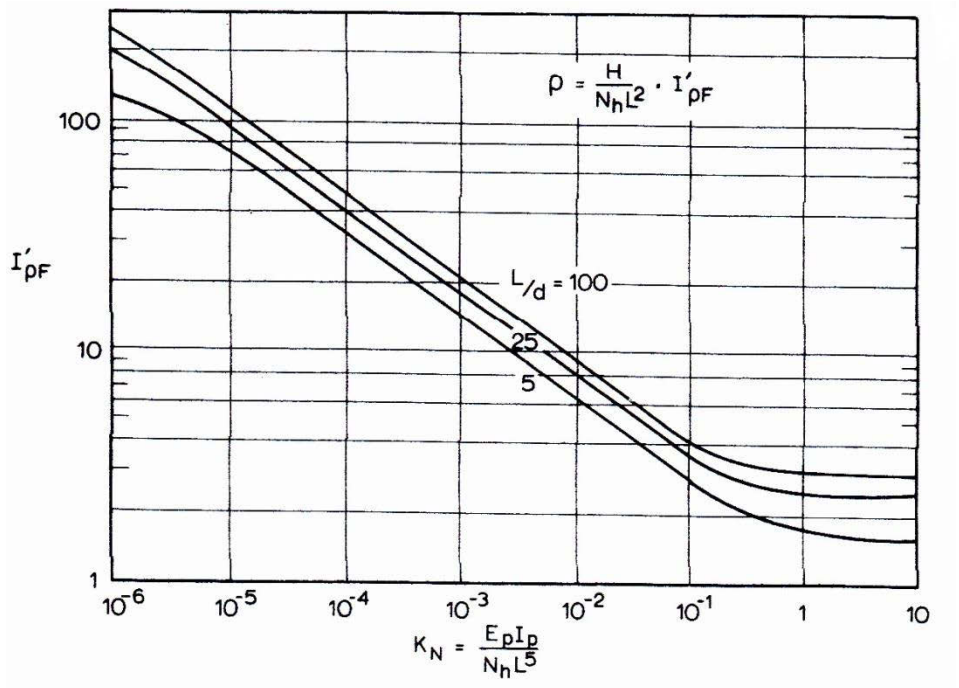

Figure 3-16. Values of I'_{pF} for fixed head floating piles with linearly varying soil modulus (after Poulos et al. 1980)

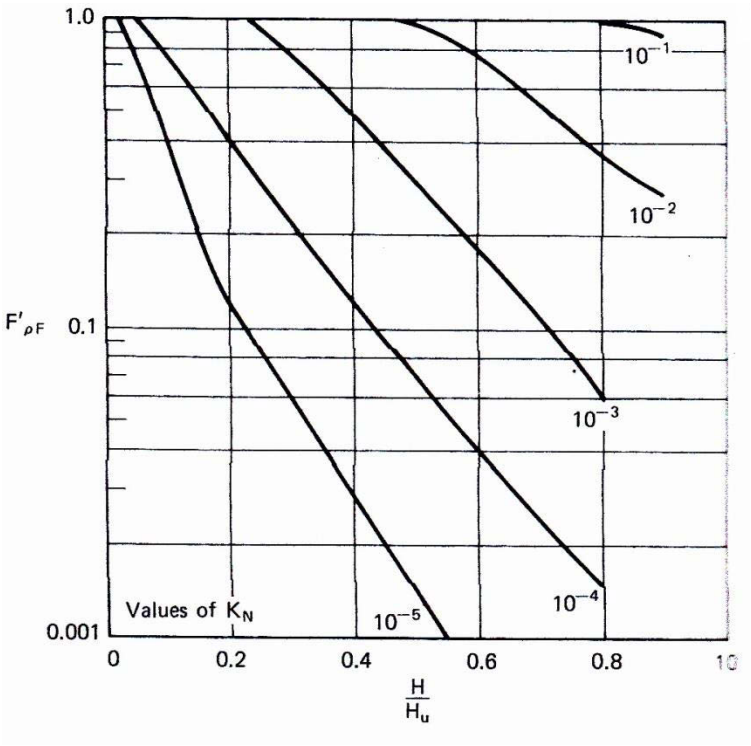

Figure 3-17. Values of F'_{pF} for fixed head floating piles with linearly varying soil modulus (after Poulos et al. 1980)

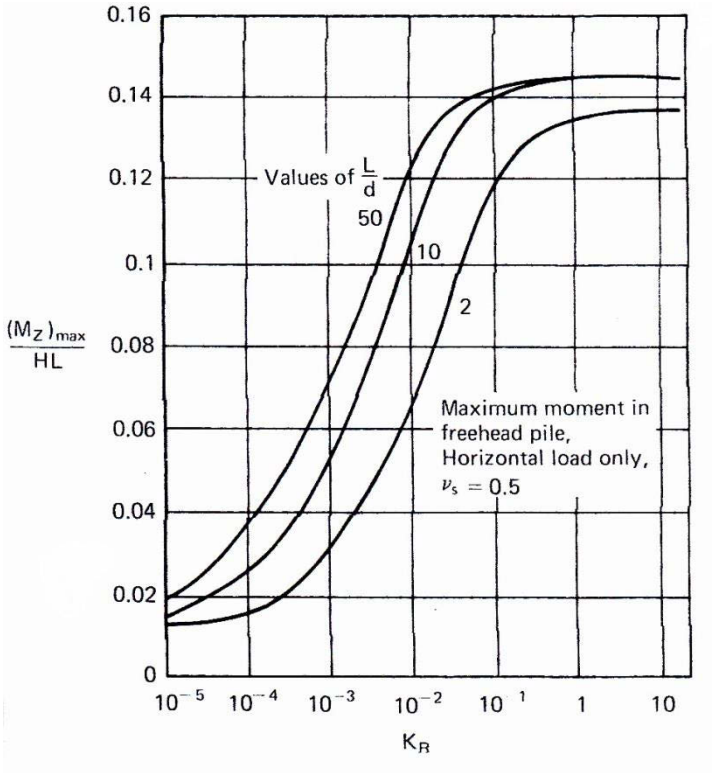

Figure 3-18. Maximum moments generated in a free head pile for a homogenous soil (after Poulos et al. 1980)

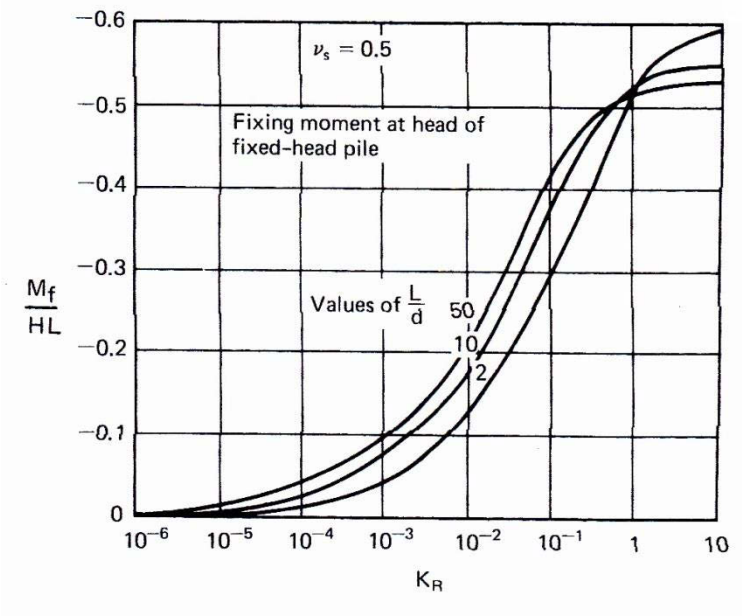

Figure 3-19. Fixing moments for a fixed head pile (after Poulos et al. 1980)

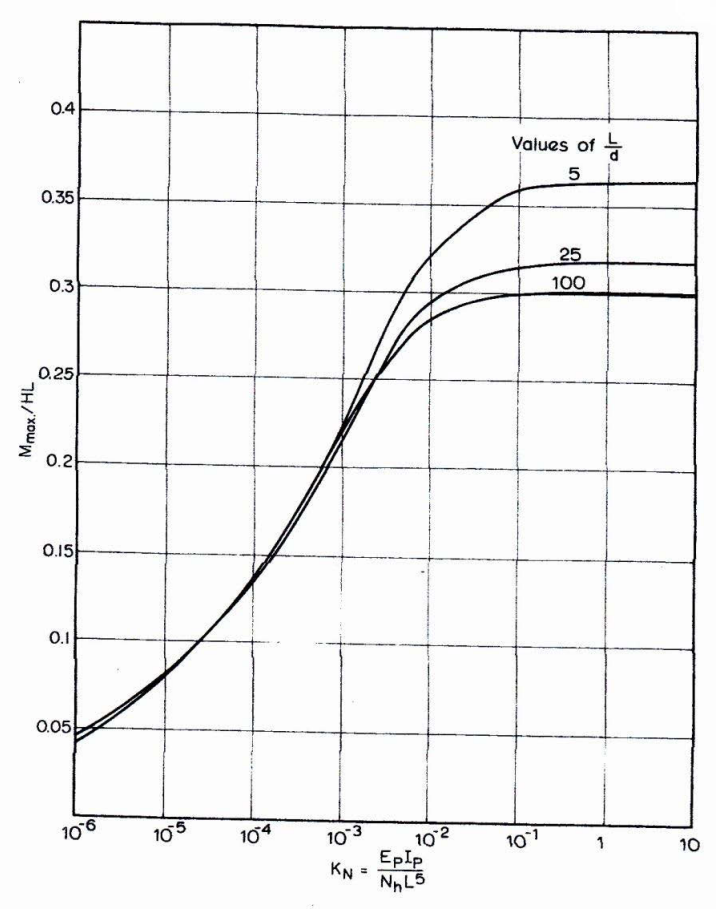

Figure 3-20. Maximum moment in a free head pile in a linearly varying soil modulus (after Poulos et al. 1980)

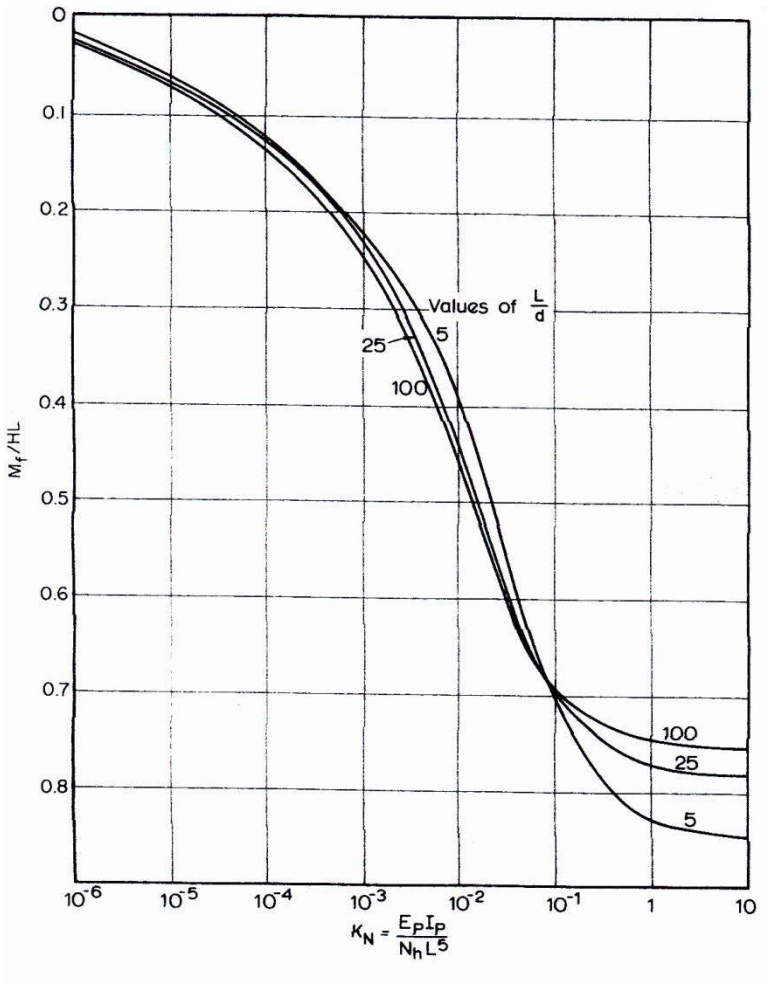

Figure 3-21. Fixing moment in a fixed head pile with a linearly increasing soil modulus (after Poulos et al. 1980)

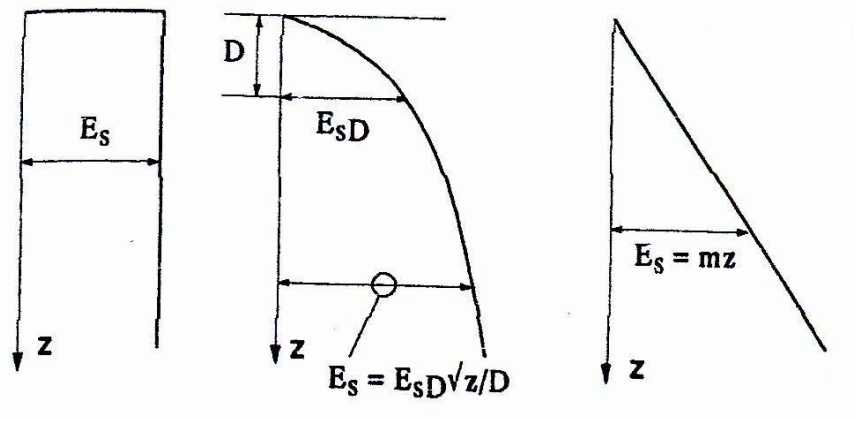

Figure 3-22. Distribution of Young's modulus with depth (from left to right; constant, parabolic and linear) (after Pender 1993)

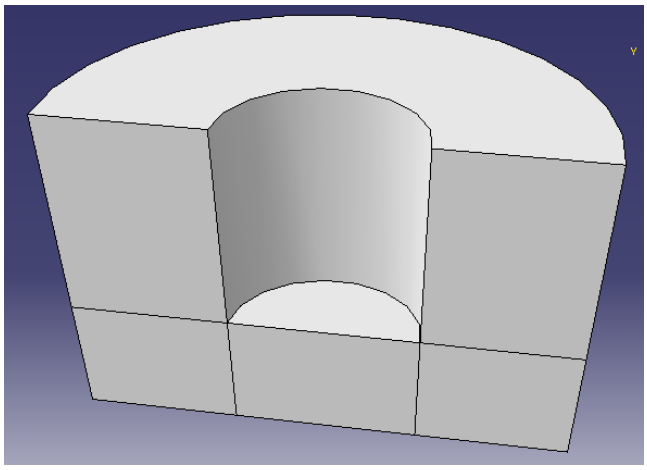

Figure 3-23. The soil body further from the structure

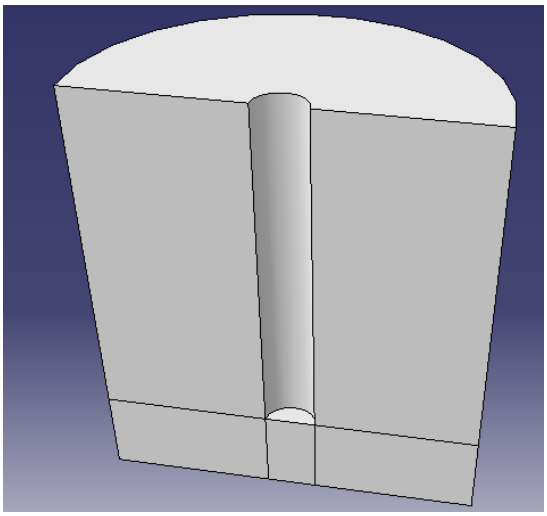

Figure 3-24. The soil body close to the single pile

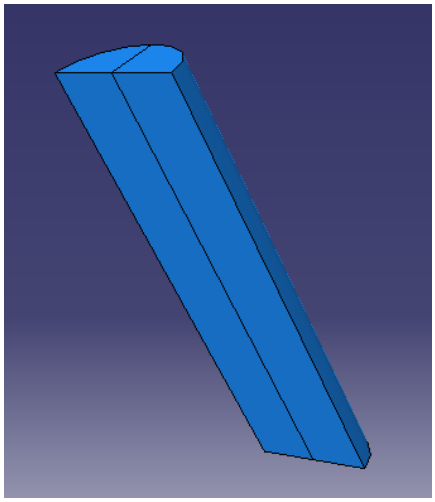

Figure 3-25. The pile constructed for the single pile models

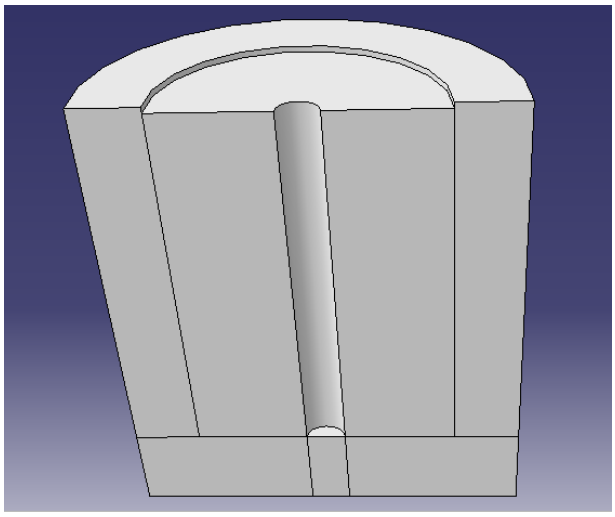

Figure 3-26. The soil body close to the piled footing structure

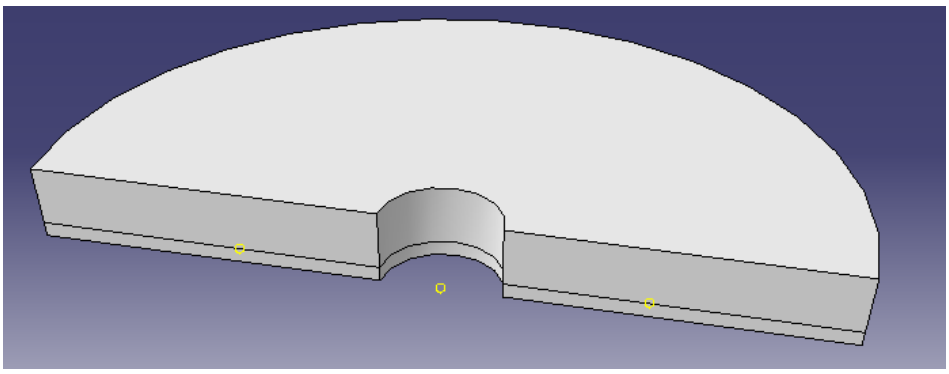

Figure 3-27. The footing constructed for the piled footing structures

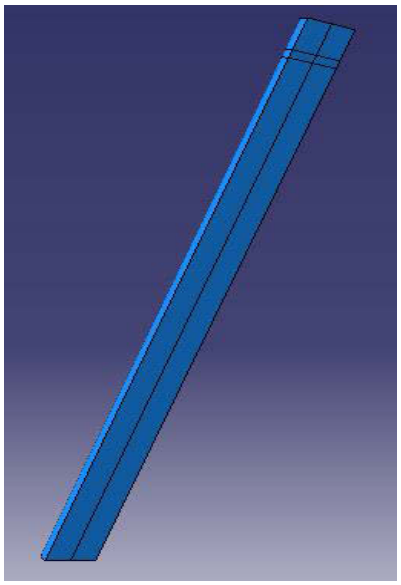

Figure 3-28. The pile used in the piled footing structures

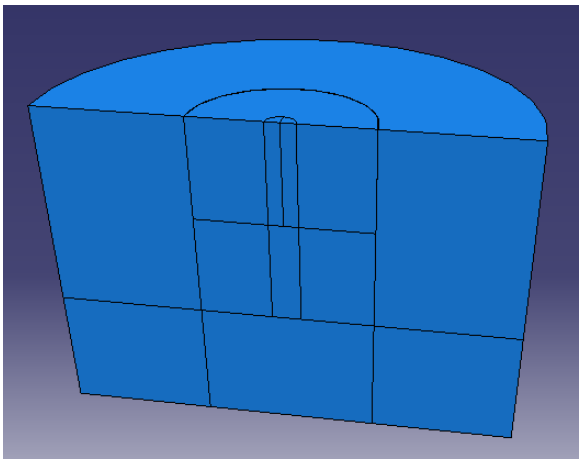

Figure 3-29. A single pile structure in the numerical models

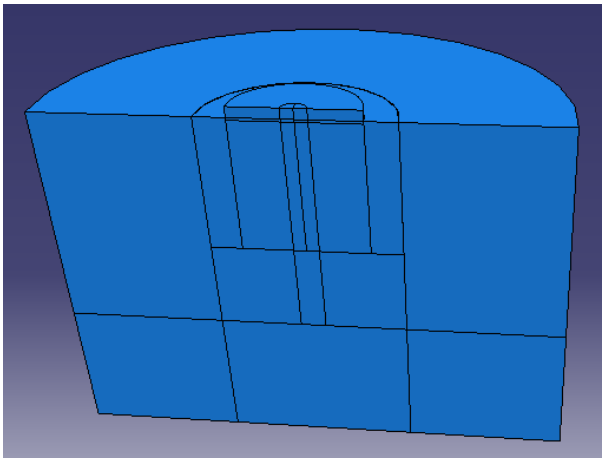

Figure 3-30. The piled footing structure in the numerical models

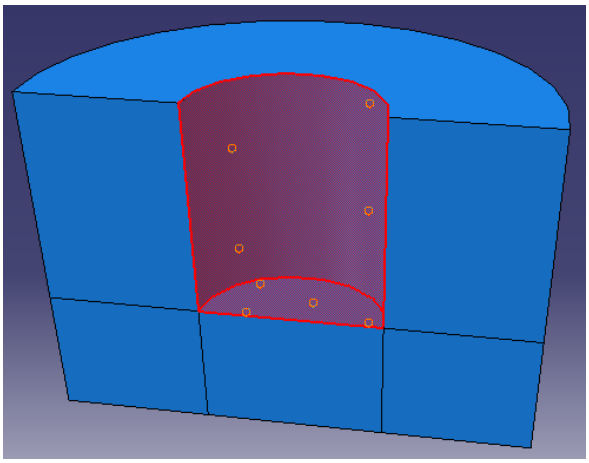

Figure 3-31. The outer segment of the soil body

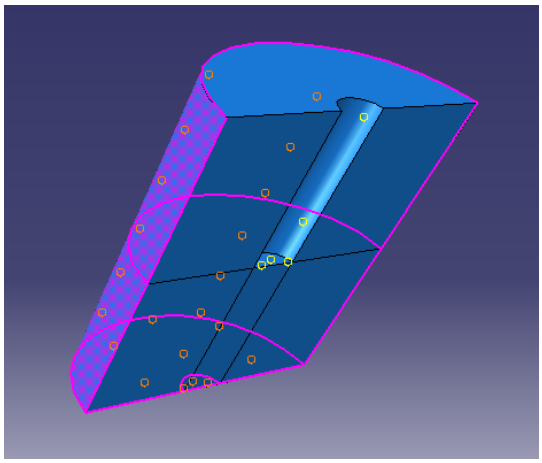

Figure 3-32. The inner segment of the soil body

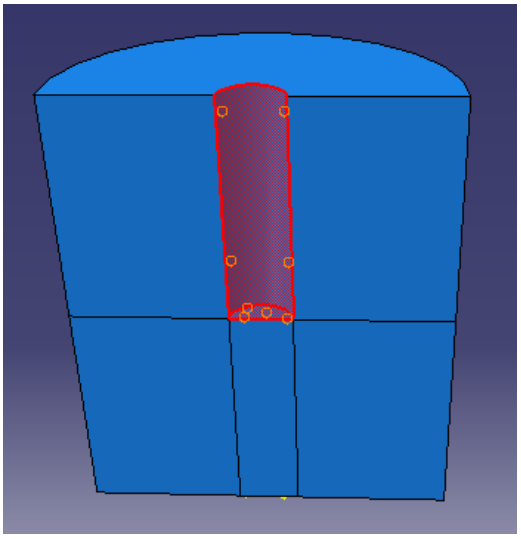

Figure 3-33. The location of the inner soil body interacting with the pile

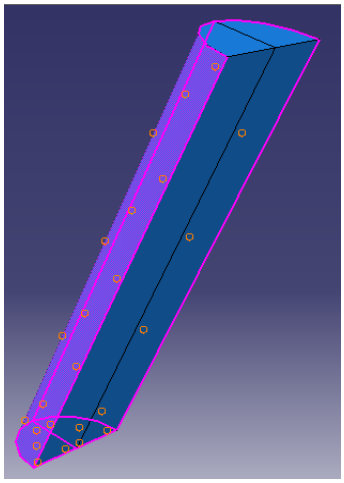

Figure 3-34. The location of the pile section interacting with the inner soil body

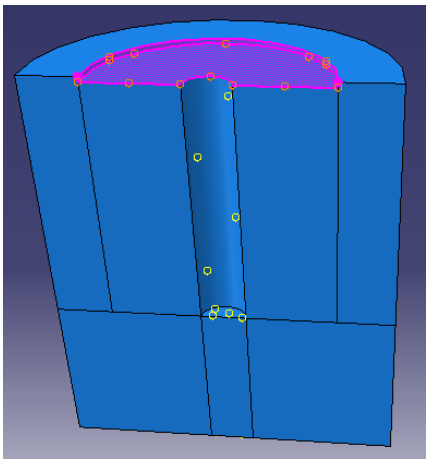

Figure 3-35. The location on the inner soil body interacting with the base of the footing

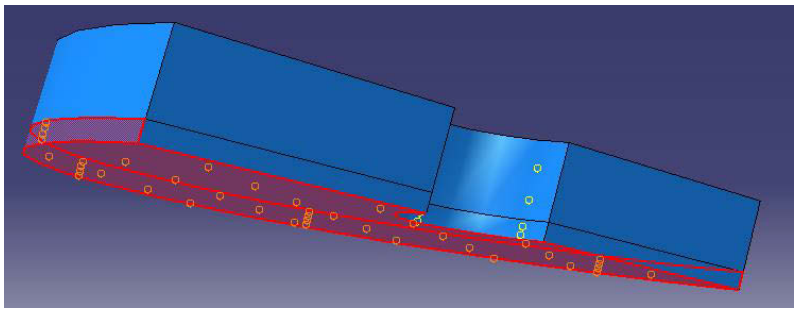

Figure 3-36. The base and sides of the footing interacting with the inner soil body

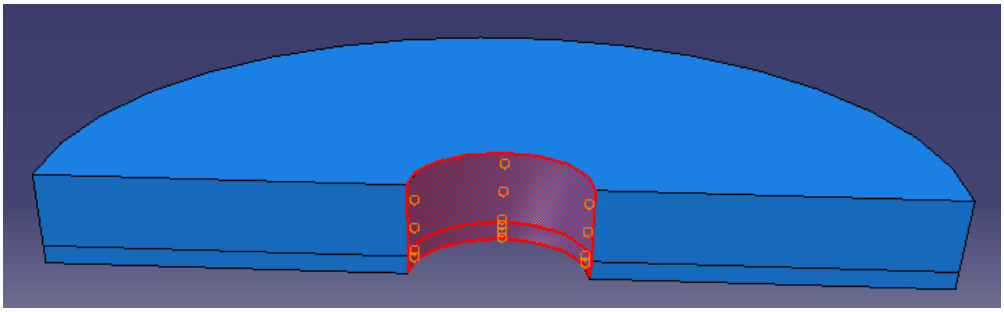

Figure 3-37. The location chosen on the footing to interact with the pile section

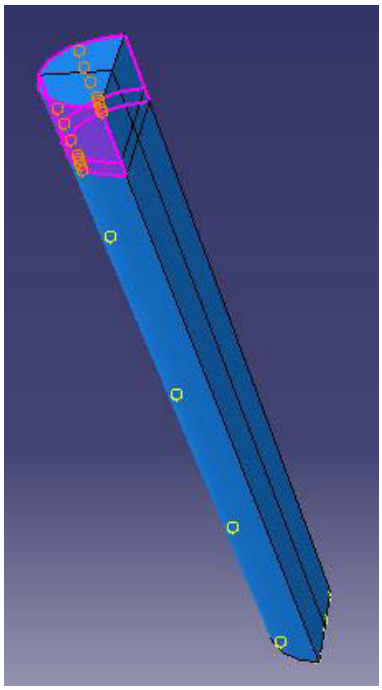

Figure 3-38. The location on the pile section interacting with the footing

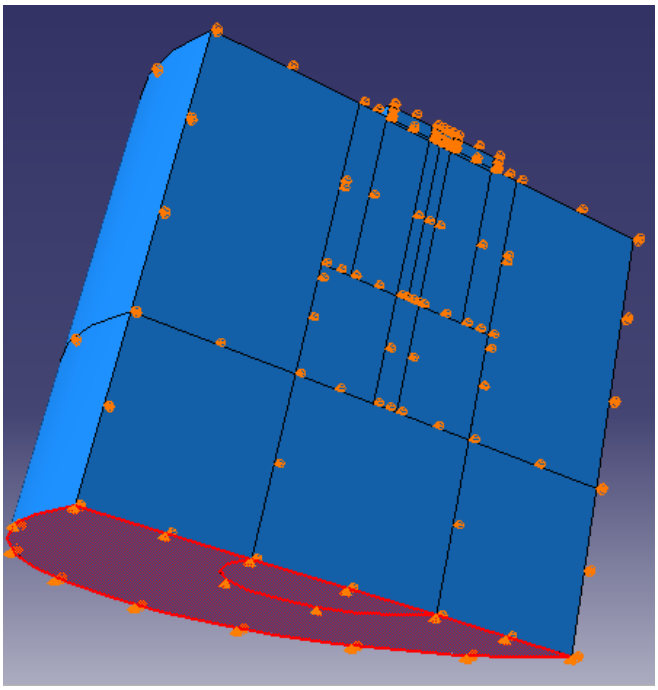

Figure 3-39. The base of all models was restricted to move in the vertical direction

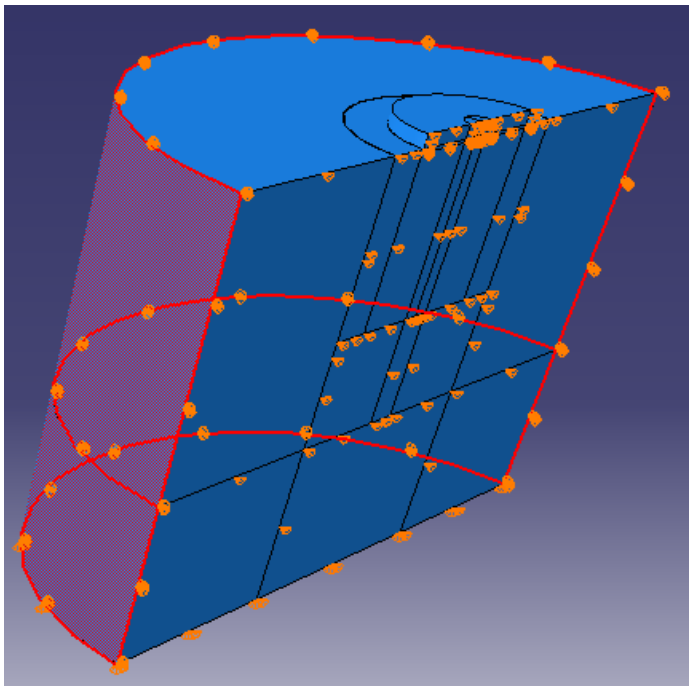

Figure 3-40. The sides of the soil body were restricted to move in the horizontal directions

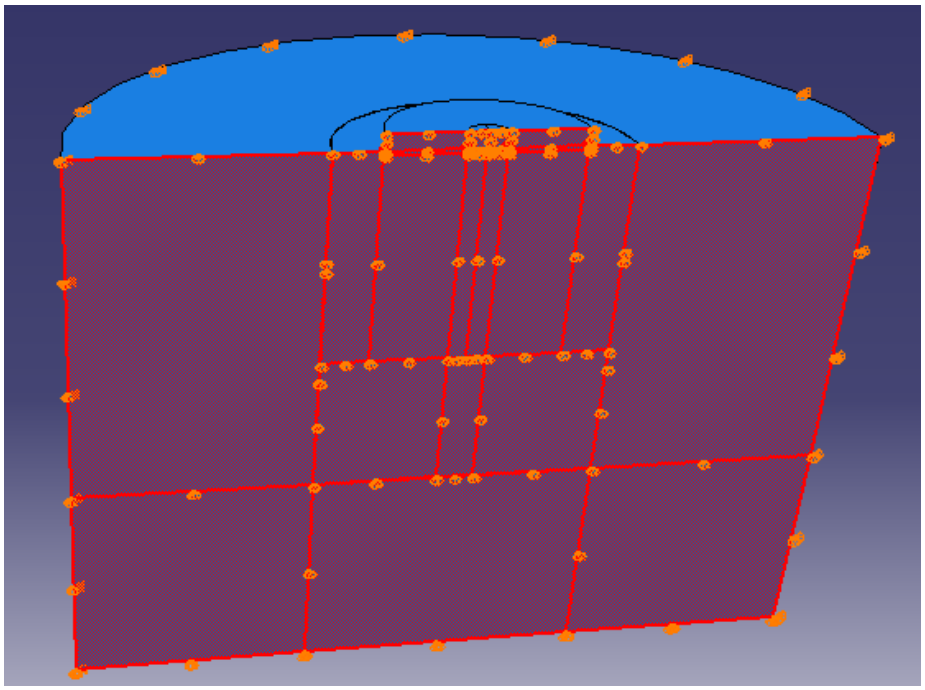

Figure 3-41. The front face of the model was restricted to move in the direction out of the plane

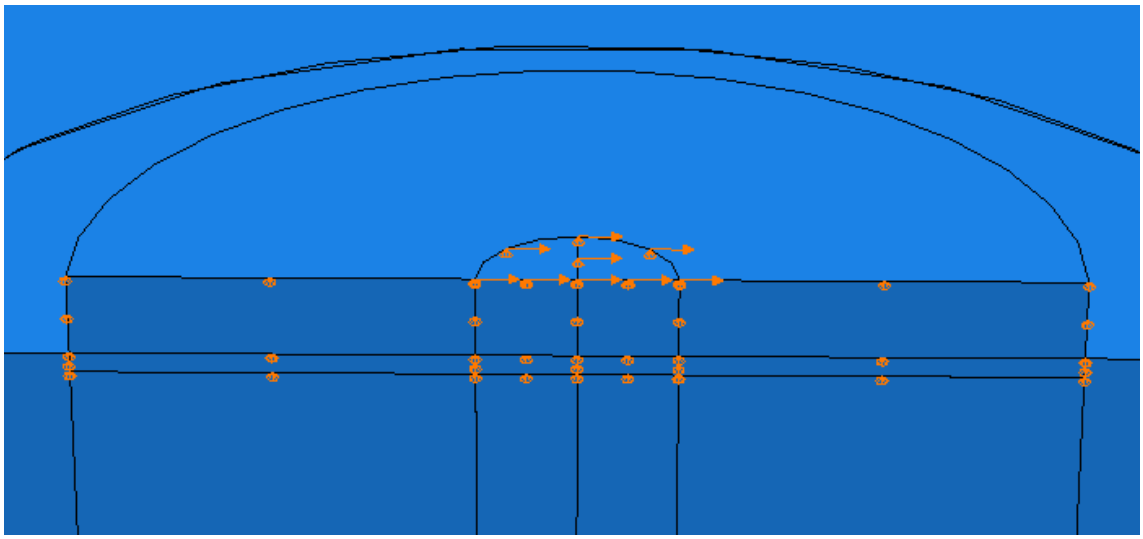

Figure 3-42. The horizontal displacement applied to the pile head

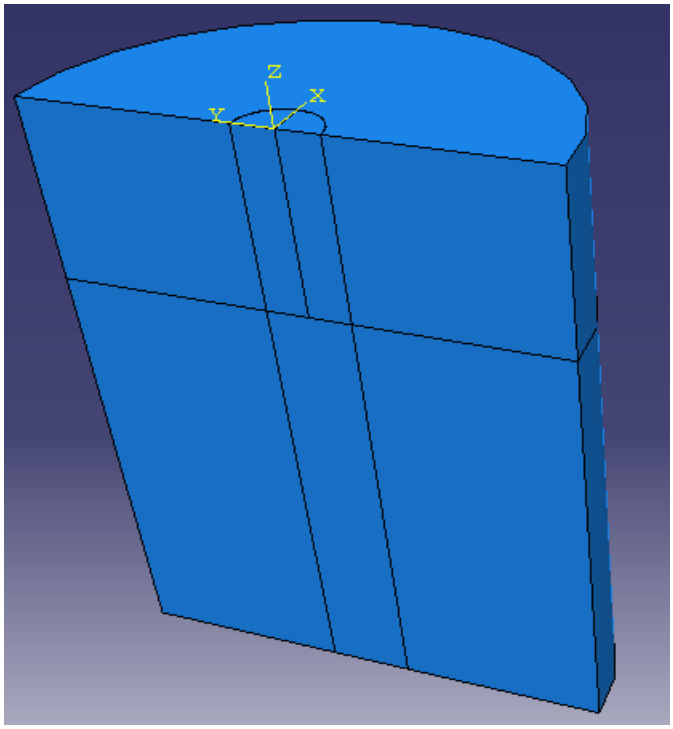

Figure 3-43. The location of the datum coordinate system on the pile structures

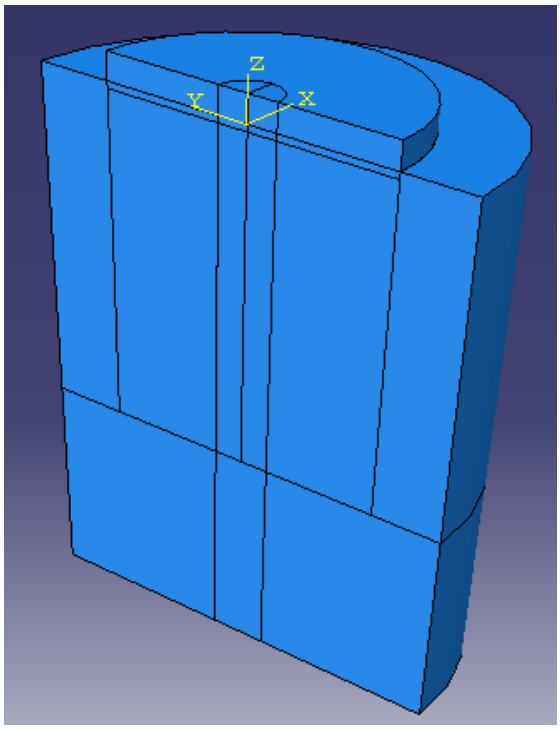

Figure 3-44. The location of the datum coordinate system on the piled footing structures

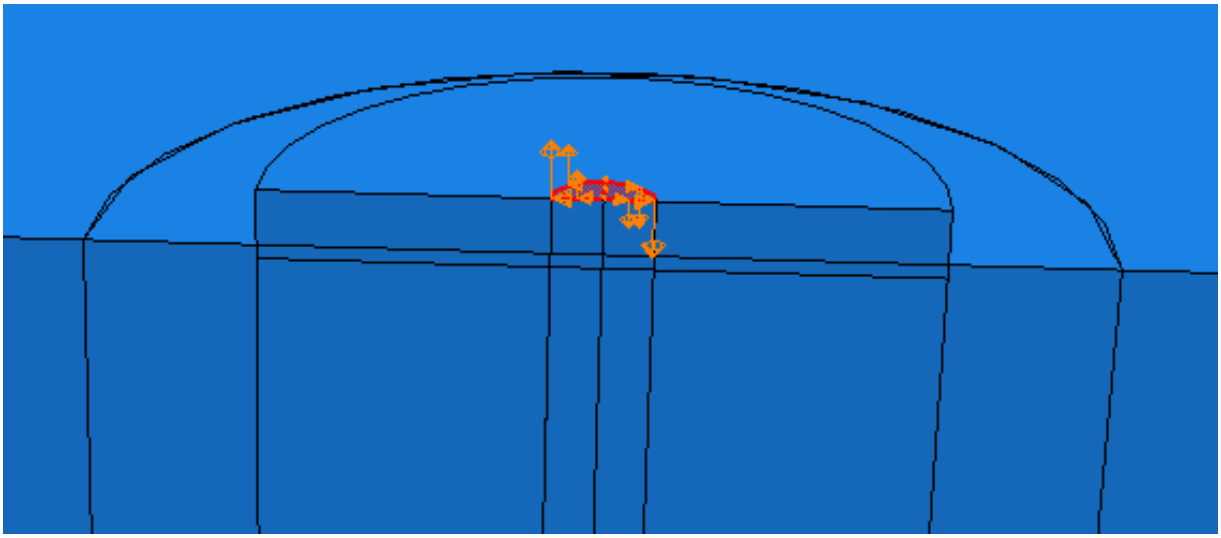

Figure 3-45. The moment was introduced to the pile's head through a function

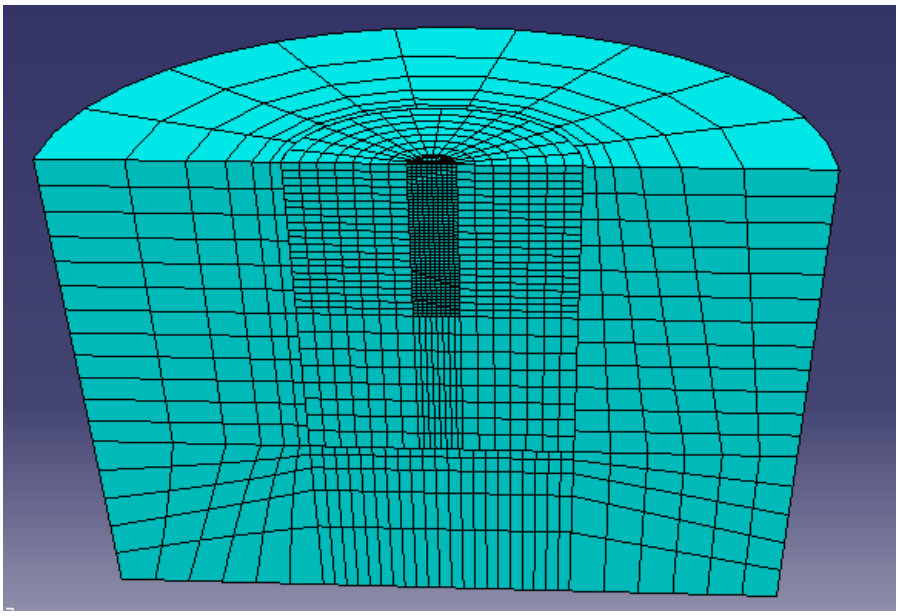

Figure 3-46. The mesh generated for the pile structure

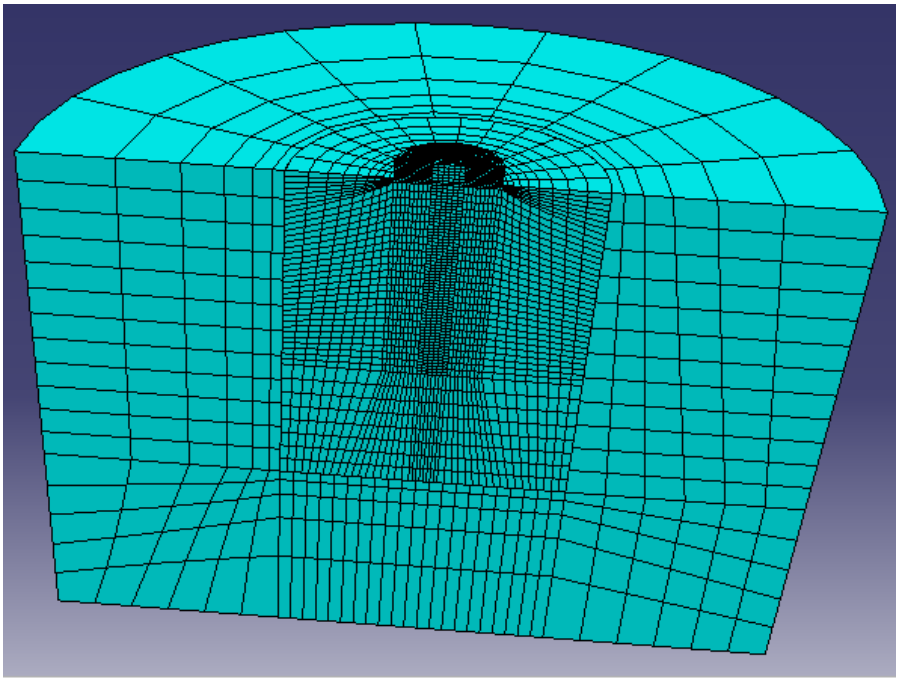

Figure 3-47. The piled footing structure with its generated mesh

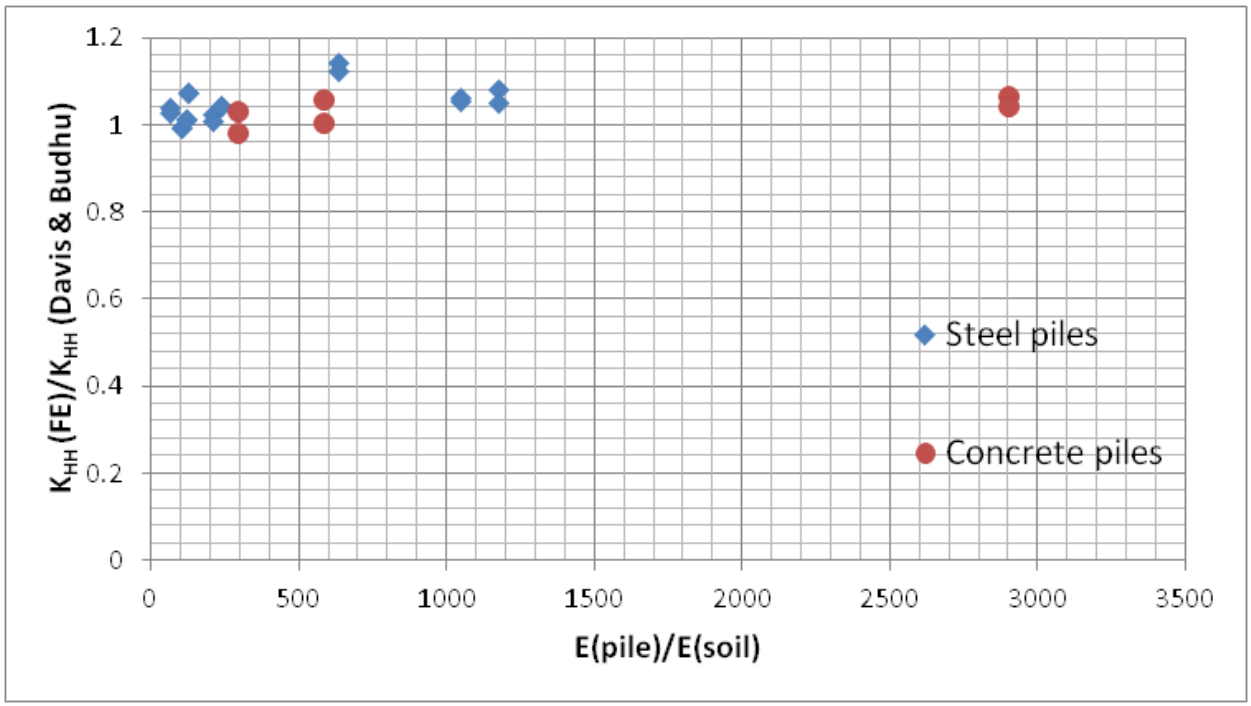

Figure 3-48. The accuracy of the K_{HH} values calculated from the numerical models (long piles)

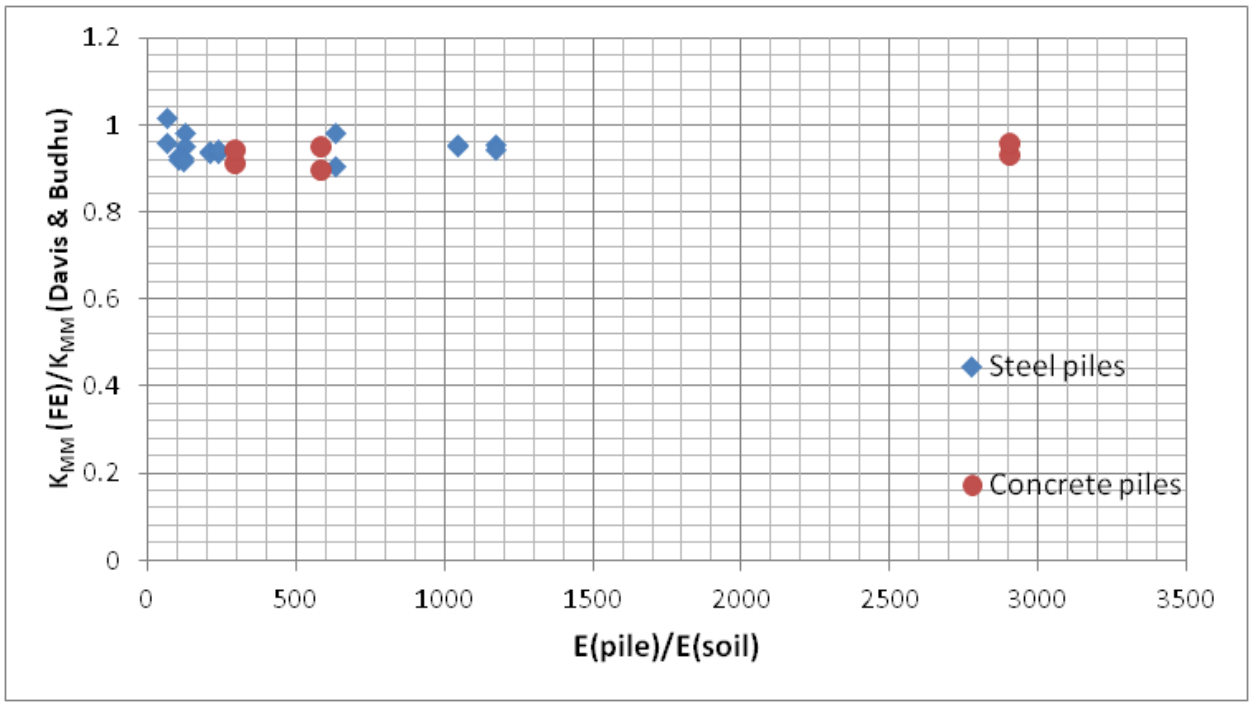

Figure 3-49. The accuracy of the K_{MM} values calculated from the numerical models (long piles)

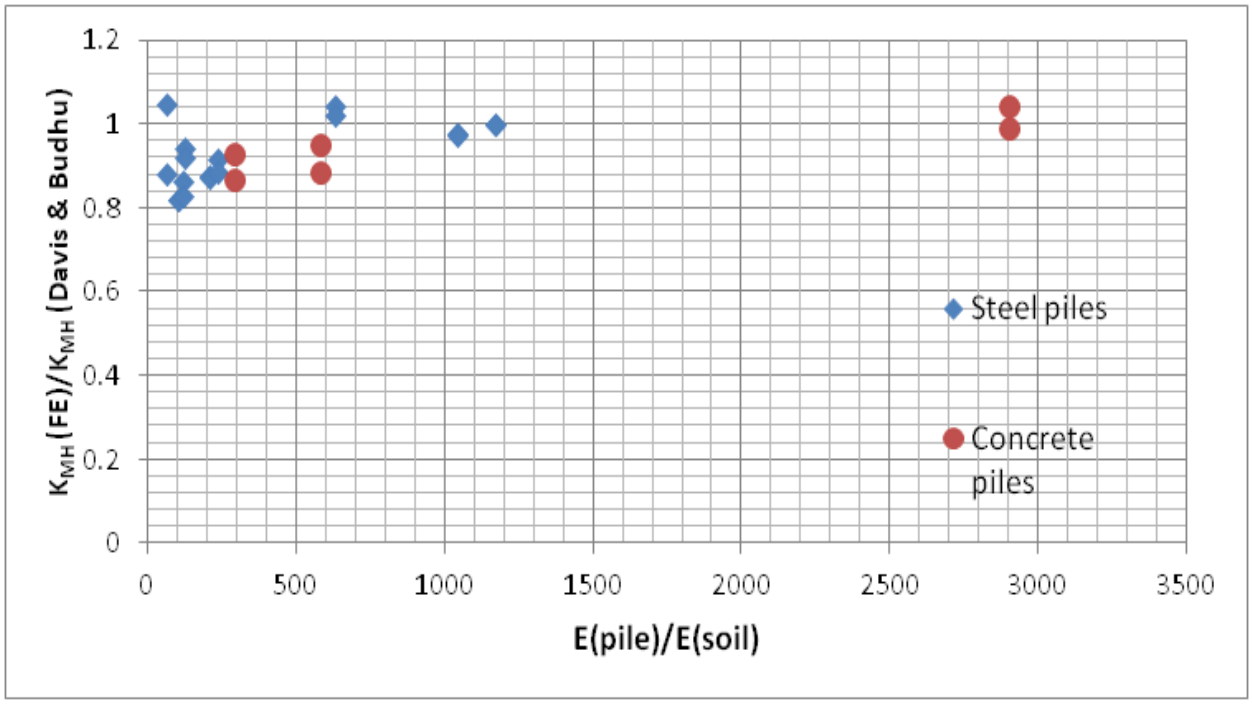

Figure 3-50. The accuracy of the K_{MH} and K_{HM} values calculated from the numerical models (long piles)

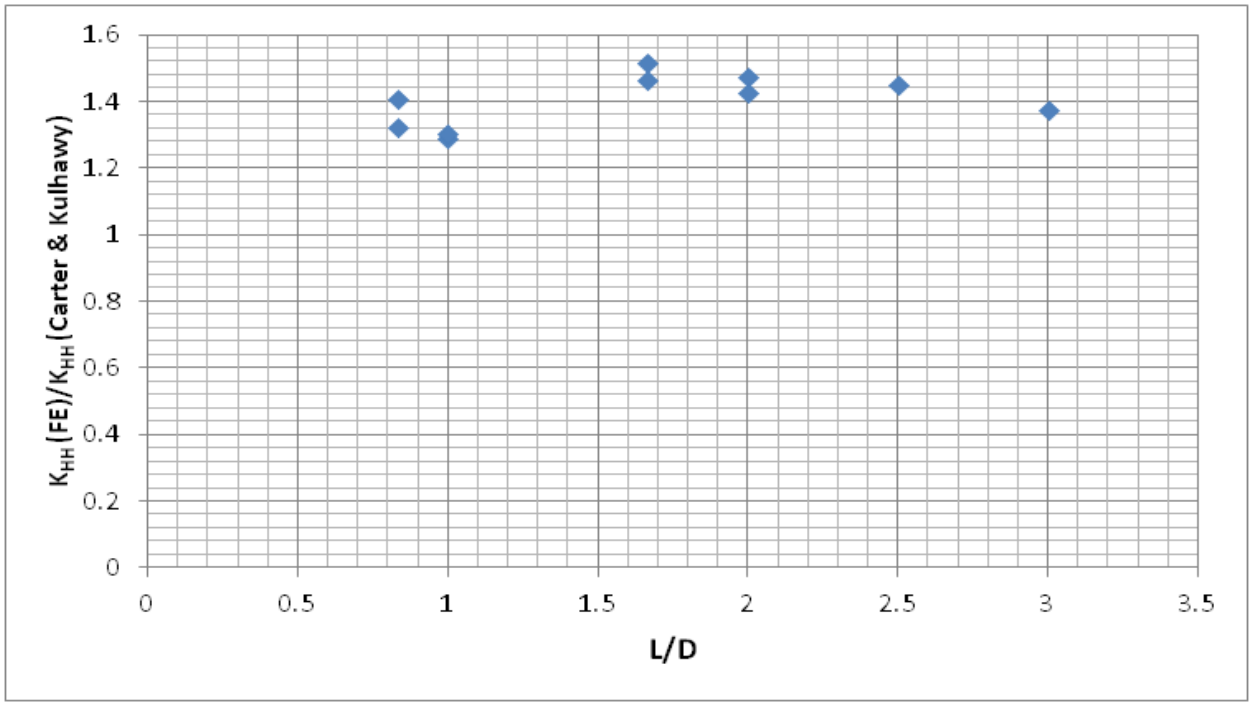

Figure 3-51. The accuracy of the K_{HH} values calculated from the numerical models (short piles)

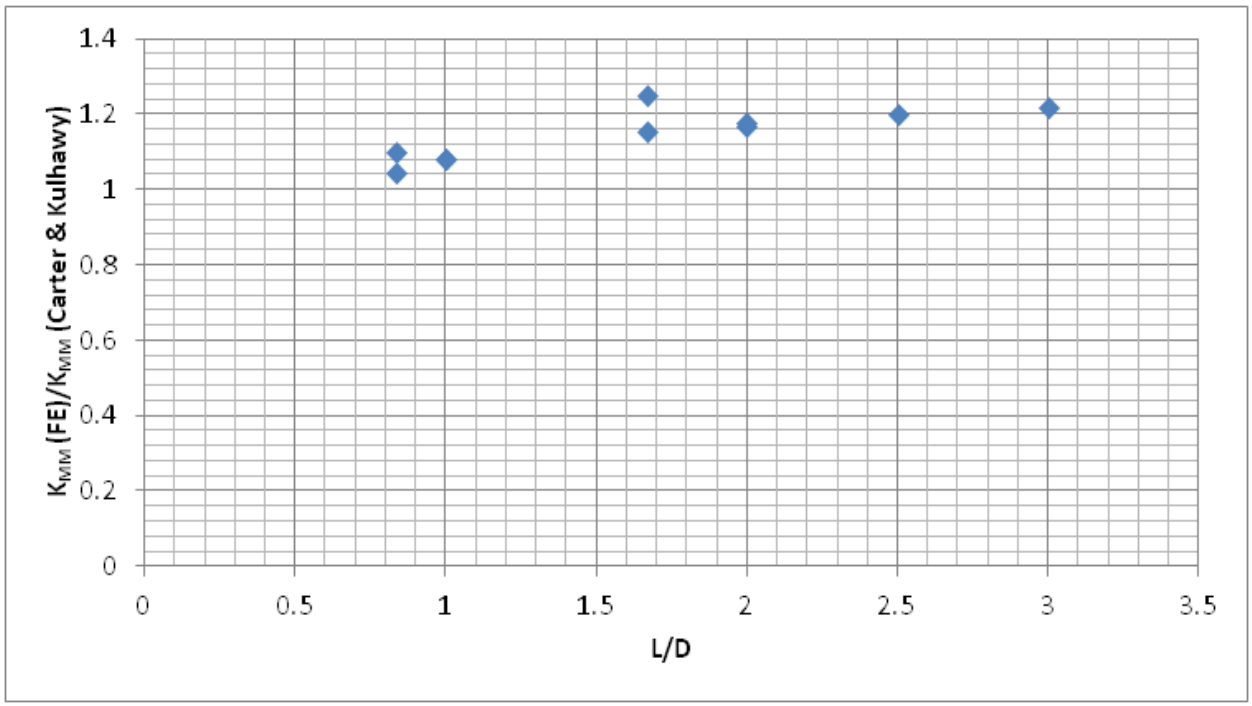

Figure 3-52. The accuracy of the K_{MM} values calculated from the numerical models (short piles)

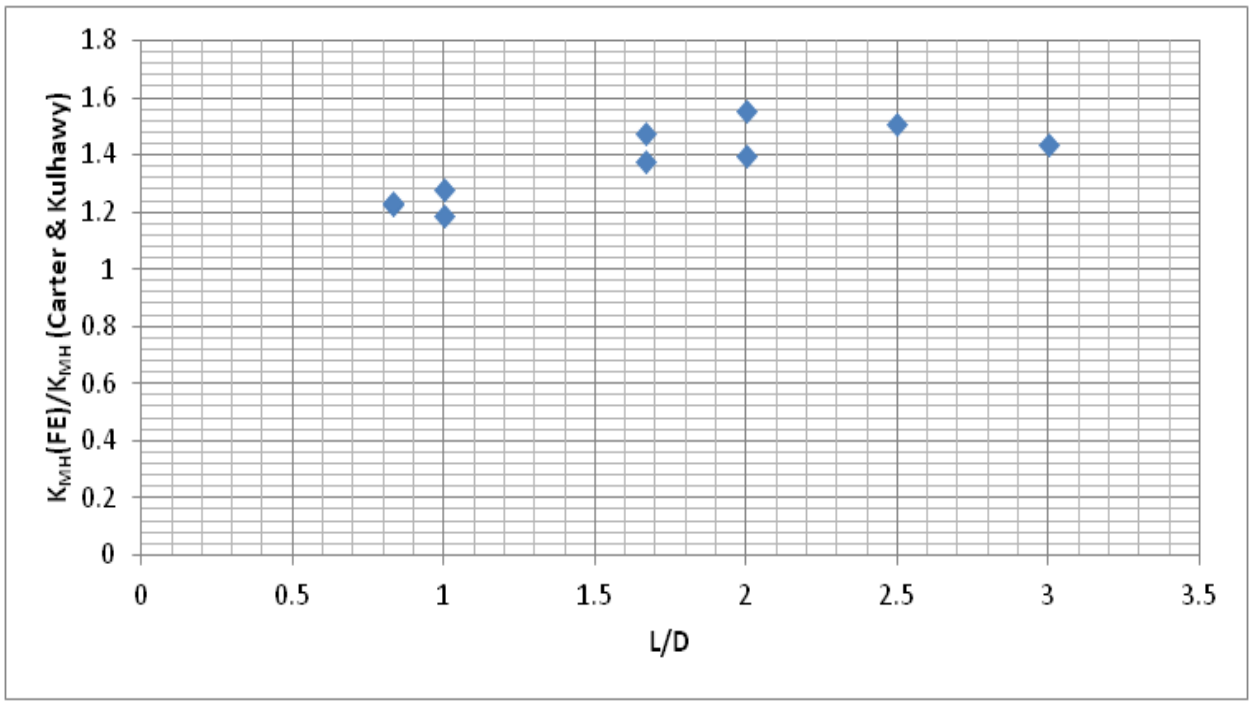

Figure 3-53. The accuracy of the K_{MH} and K_{HM} values calculated from the numerical models (short piles)

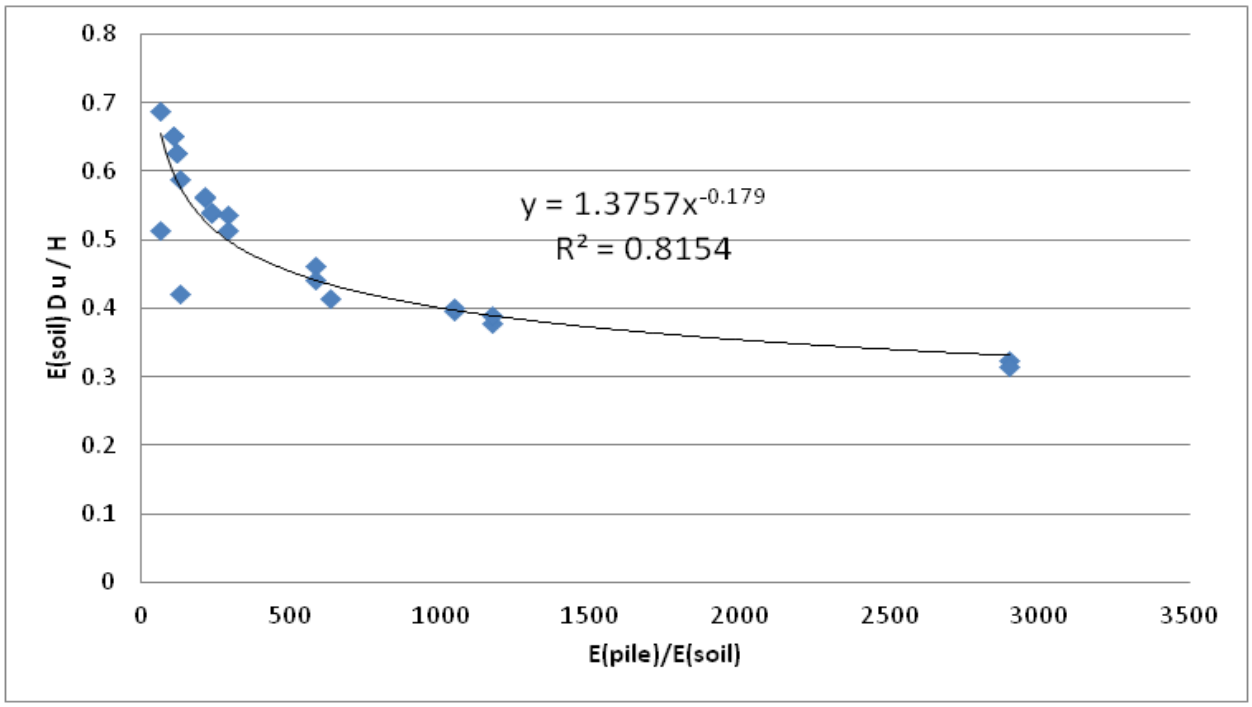

Figure 3-54. The value of f_{uH} calculated for a long pile embedded in a homogeneous soil

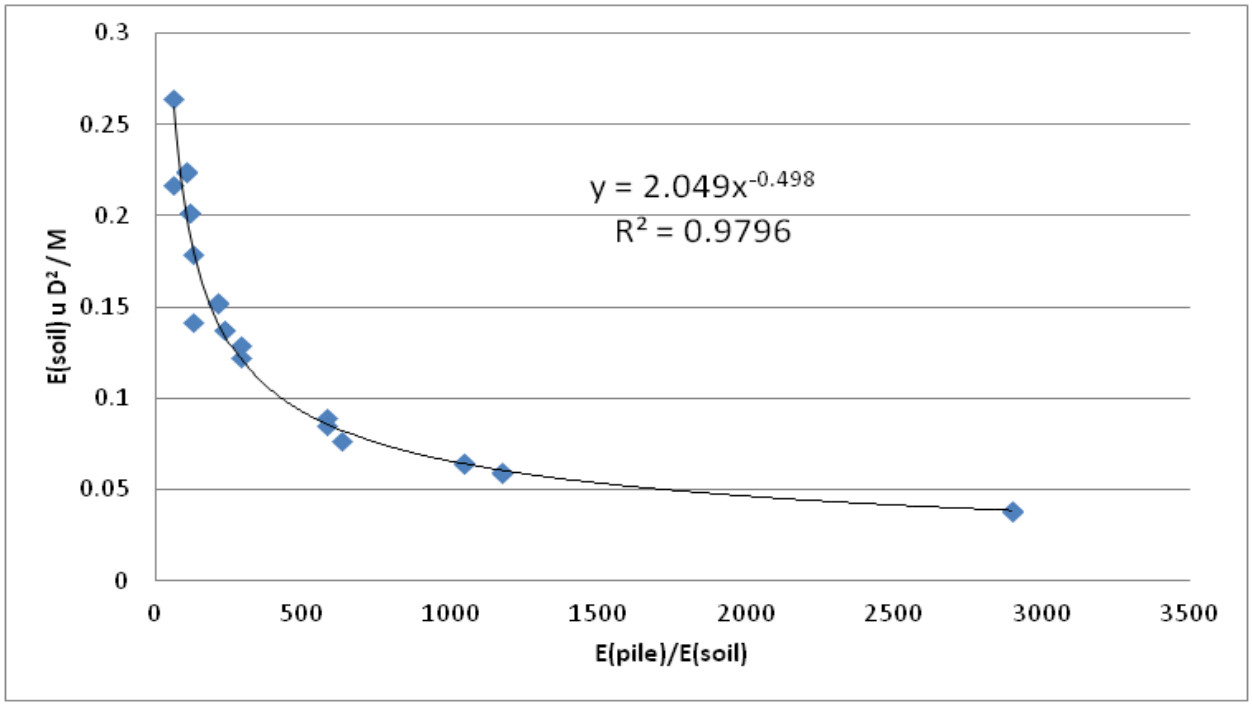

Figure 3-55. The values of f_{uM} and f_{0H} calculated for a long pile embedded in a homogeneous soil

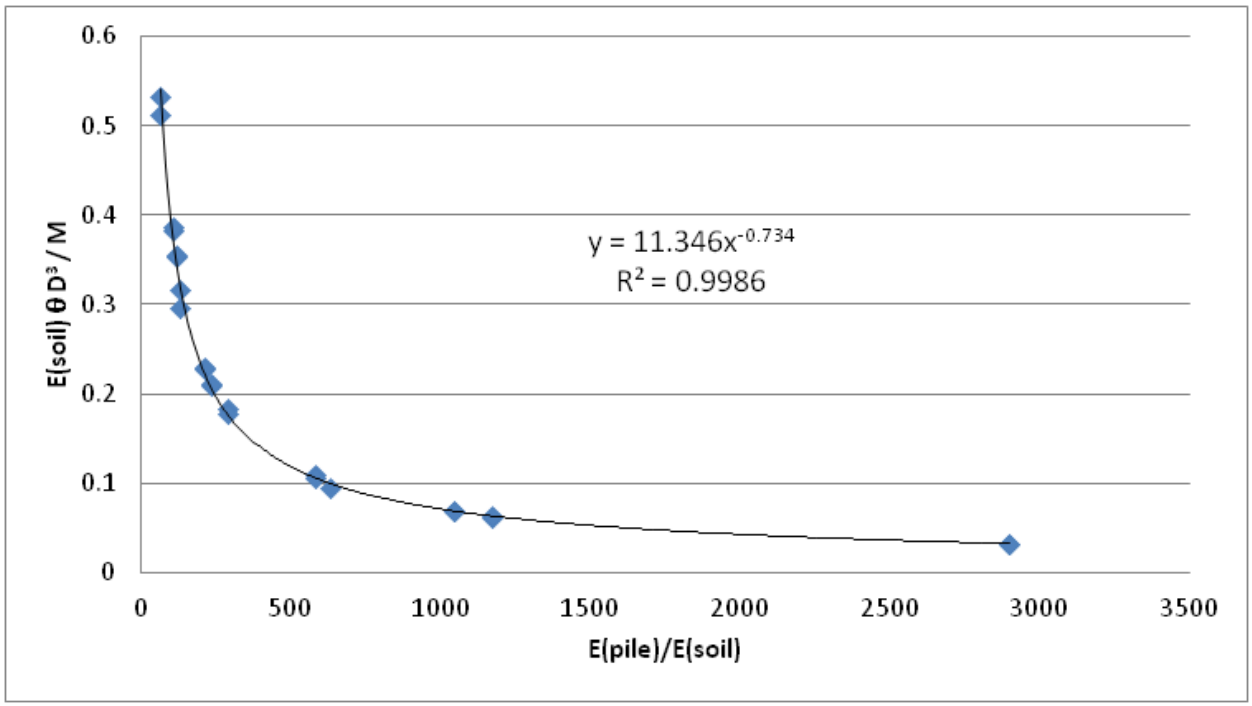

Figure 3-56. The value of $f_{\theta M}$ calculated for a long pile embedded in a homogenous soil

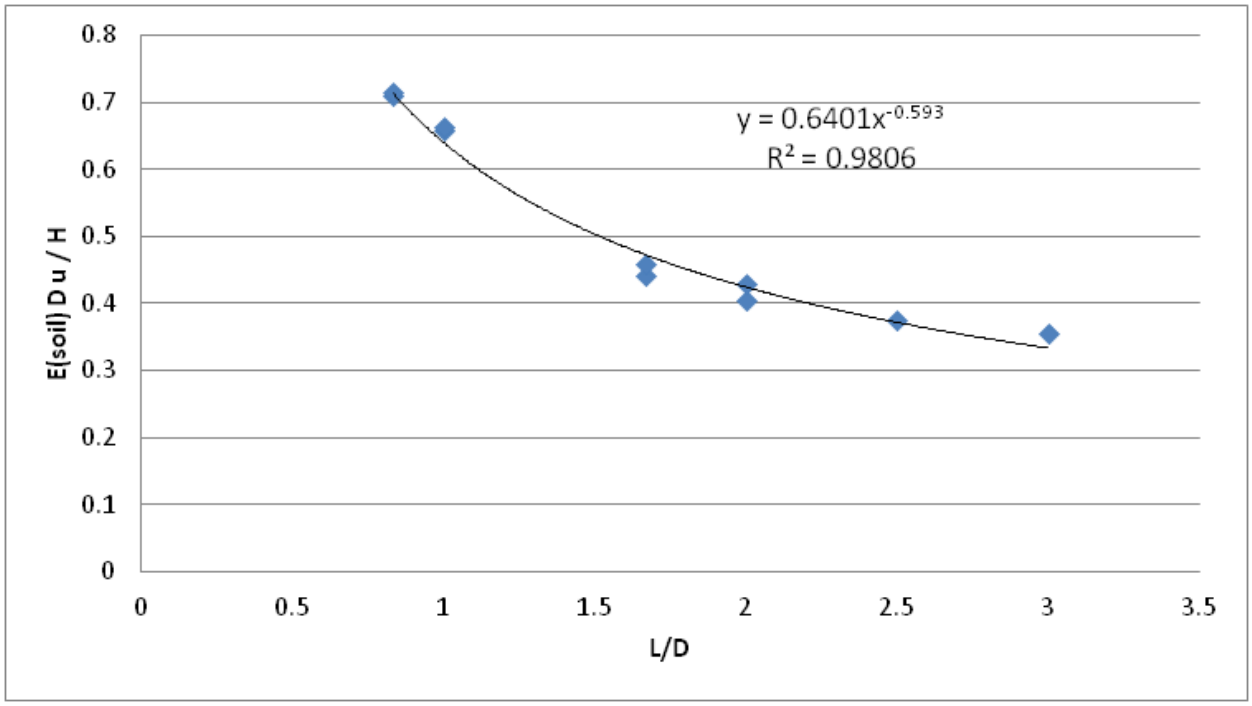

Figure 3-57. The value of f_{uH} calculated for a short pile embedded in a homogenous soil

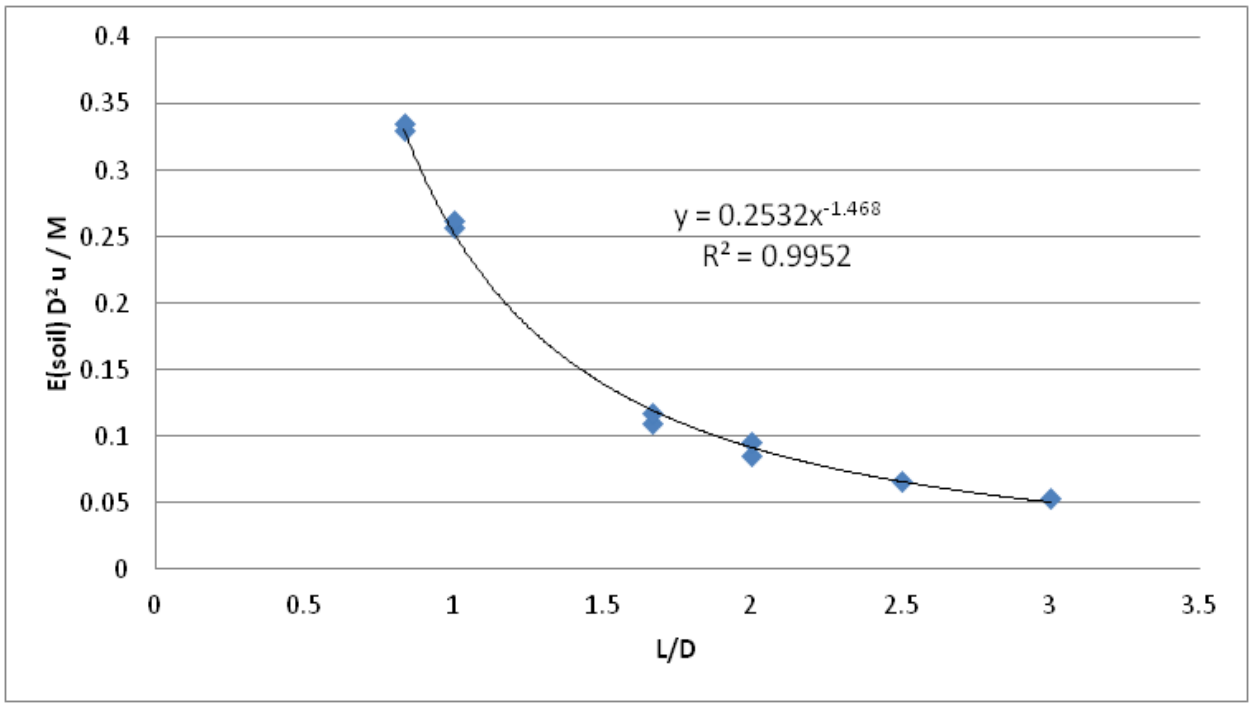

Figure 3-58. The values of f_{uM} and $f_{\theta H}$ calculated for a short pile embedded in a homogenous soil

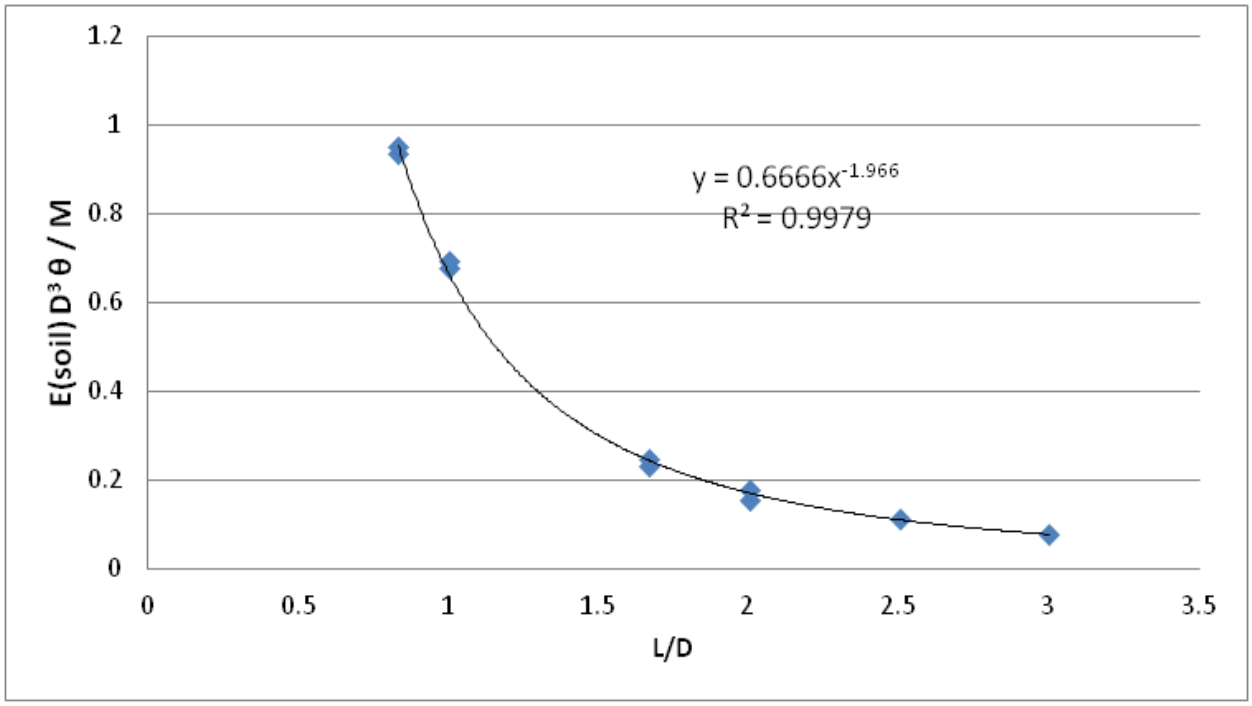

Figure 3-59. The value of $f_{\theta M}$ calculated for a short pile embedded in a homogenous soil

CHAPTER 4 CENTRIFUGE MODELLING

4.1 INTRODUCTION

As discussed in Chapter 2 almost all pile foundations are subjected to some kind of horizontal loading from the structure that they are supporting. These lateral loads can be introduced to the pile's head by the action of the wind on a building or by the wave action on a platform in an offshore foundation, which is supported by piles. All wind turbine tower foundations are affected by the wind action, which can cause large lateral loadings on the pile supporting the blades. As previously discussed, wind turbines do not carry high vertical loads but they must be able to carry significant lateral loads, which are imposed on them by the action of wind.

In this chapter, an overview of the centrifuges available at UWA will be provided and later in the chapter, the details and results of the tests conducted in the centrifuges on monopiles, piled footings and single footings with towers will be discussed. It must be mentioned that the tests and the photos in this chapter are all adopted from Harloe (2010).

At the end of the chapter, the results of the monopiles, piled footings and un-piled footings with towers will be compared to see whether the lateral response of a monopile can be enhanced by the presence of a footing at the ground level in a saturated sand medium.

4.2 PURPOSE OF CENTRIFUGE MODELLING

4.2.1 Introduction

Physical modelling by a centrifuge is a valuable way to investigate the basic mechanics of collapse and deformation. The physical modelling results can also be used to validate numerical models. This is due to the low cost of performing these tests in a similar prototype stress environment. Full-scale tests are probably the best way to validate the failure mechanics but these kinds of tests are usually expensive and are not economical. To overcome the problems of replicating full-scale tests, geotechnical centrifuge results are valuable because the actual field stress levels can be properly simulated at the model scale (Murff, 1996).

In some countries like Japan, physical modelling techniques are used directly in design while in other countries this might not be the case. Centrifuges are particularly useful in studying systems such as slopes, dams, embankments, tunnels, offshore structures, consolidation, bearing capacity of foundations, stability of retaining walls, liquefaction, contaminant migration and frost heave under static and dynamic loads. Apparatus have been developed to construct embankments, drive piles into the soil, load foundations and to simulate an excavation process while the model is in flight in a centrifuge (in rotation).

Transducers are usually used to measure the soil movements and the pore water pressures for samples in flight. Axial loads, bending moments in piles and retaining walls are usually measured by the means of load cells or strain gauges arranged in an appropriate bridge network. Usually

miniature video cameras are used to record the progress of a centrifuge test and to determine the displacements from black marker beads embedded in the visible face of the model.

Small-scale physical modelling at 1 g level can provide misleading results as the stresses due to the soil self-weight are very small compared to the field. Because the soil's behaviour is dependent on the stress history and the stress path, which the soil has followed, the stress-strain relationships at 1 g tests do not correctly replicate the behaviour in the field. To overcome such problems, tests can be conducted at a scale of $1/N$ in a centrifuge with a radial acceleration of N times the normal gravity.

Most centrifuges used to test geotechnical models compromise of a rotating arm, which is balanced by the mean of a counterweight. The model itself is within a strong box located at the end of the rotating arm. Centrifuges used in geotechnical modelling can vary in dimensions from radii of a few centimetres to around 10 m.

Small-scale centrifuges are usually constructed to study the mechanism of collapse in small-scale models at very high accelerations. Usually in these centrifuges, there is not room for installing instruments to measure the pore water pressures and the stresses within the soil.

During centrifuge testing, it is usual practice to use the same soil as in the prototype construction. This means that the ratio of the dimension of the structure (e.g. the width or the length of a foundation or the depth of an excavation) to the typical particle size D_{50} is N times smaller in the model than in the prototype.

As discussed by Powrie (1997) sometimes the particle size may be too large in comparison with the feature, that is being tested. One example of this situation is when a 1m thick resistive layer is to be constructed within a landfill cap, at a scale of 1:40, the layer would only be 25 mm thick in the centrifuge test. It was argued that it is not clear whether the rupture following the settlement of the landfill depends on the differential settlement relative to the thickness of the capping layer, or it is related to the differential settlement of the individual particle size. If the latter is the case, centrifuge tests using a soil in which the particle size has been reduced by a factor of N is necessary. This will indeed change the soil properties (manly the permeability which is of a great importance in landfill design) and considerably affect the results. In such cases, a number of tests at different scales must be carried out to establish the maximum scale factor at which similar results will be obtained, and to do so the material in the model must be as in the prototype. This procedure in practice is called "*modelling of the models"*.

Clays are usually consolidated to a known equilibrium state before the changes in stress comprising from the actual test are imposed. For investigating the collapse mechanism in an undrained fashion, the centrifugal acceleration might be increased gradually to initiate the rapid collapse of a clay model with uniform shear strength. It is recommended that low permeability clays must be used to ensure that any changes in volume (and the undrained shear strength) which might occur during the gradual increase in centrifugal acceleration are insignificant.

However, there have been many successful tests conducted by centrifuges but it must be noted that in many cases some important aspects of soil behaviour are neglected or inadequately considered by the use of simple methods.

As discussed by Powrie (1997) every adopted modelling method will depend on a number of factors. These can include the nature of the problem, which is under investigation, the purpose of the tests and the constraints on time and cost.

To compare the lateral capacity of monopiles, piled footings and un-piled footings embedded in a sand deposit, a set of tests were conducted in the beam centrifuge at UWA on commercial silica sand.

In this chapter, a brief description of the centrifuge modelling principles is provided followed by a complete and extensive description of the tests conducted on different proposed structures. Further details on centrifuge modelling are available in Taylor (1995).

4.2.2 Principles of centrifuge modelling

When conducting physical modelling for geotechnical purposes it is important to generate the body forces properly on the proposed structure. It is also important to simulate the stress and strain between the model and the prototype accurately.

In centrifuge modelling, the model dimensions have been reduced by a factor of N (where N is the centrifugal acceleration) and the self-weight of the model must be increased by the same factor. N can be derived from Equation 4-1.

$$N = \frac{\omega_c{}^2 \mathrm{R}}{\mathrm{g}} \qquad \textbf{4-1}$$

In the above equation, ω_c is the angular velocity and R is the radius of the machine.

The main scaling relationships between the model and the prototype are listed in Table 4-1.

For example, if the strong box in the centrifuge is 1 m^3 and the proposed sand has a unit weight of 10 kN/m^3, at the level of 1 g the initial vertical stress at the base of the container will be 10 kN/m^3 while at 100 g the vertical stress at the base of the container will be 100 times greater (1 MPa). This corresponds to a sample sitting at 100 m below the ground surface in a prototype scenario.

Another example can be made for the time required for clay to consolidate in a centrifuge test. If a clay sample consolidates after 2 years in practice (prototype) it will only take the sample to consolidate in 105 minutes and 7.2 seconds at a level of 100 g.

From Table 4-1 it is clear that for calculating the forces in a centrifuge test they have to be scaled up to N^2 while for converting the mass a scaling factor of N^3 is required.

Quantity	Model	Prototype
Length	1	N
Volume	1	N^3
Density	1	1
Force	1	N^2
Stress	1	1
Moment	1	N^3
Strain	1	1
Displacement	1	N
Area	1	N^2
Mass	1	N^3
Frequency(dynamic tests)	1	N
Acceleration	1	1/N
Velocity	1	1
Time (consolidation)	1	N^2
Time (creep)	1	1
Time (dynamic)	1	N

Table 4-1. Centrifuge model scaling relationships

4.2.3 The Beam centrifuge facility at UWA

The beam centrifuge at UWA is an Acutronic Model 661centrifuge and has a maximum payload of 200 kg with a maximum acceleration of 200 g. The maximum angular velocity when spinning at the maximum acceleration (200 g) is 340 rpm. A photograph of the beam centrifuge is given in Figure 4-1.

The machine has a working radius of 1.8 m and the strong box are located on a platform which is balanced by counterweights at the other end of the cross beam. The counter weights can be adjusted in accordance with the weight of the strong box.

The machine is located in a concrete chamber room with an air conditioning facility. The air conditioning is to keep the chamber's temperature constant during the testing procedure.

Tests in the beam centrifuge are conducted in a strong box, which is constructed from Aluminium, as shown in Figure 4-2. The strong box has an internal plan of 390 mm by 650 mm with a height of 325 mm. Drainage holes have been designed at the base of the box so that the amount of soil saturation can be controlled during the test. An external standpipe is connected to the strongbox as shown in Figure 4-3, this standpipe has been connected to the box to maintain and control the water level in the sample during the testing procedure.

An electrical actuator has been developed at UWA for conducting tests in the beam centrifuge while the sample is in-flight. As previously discussed, different types of tests, such as loading piles in soils, pulling anchors and loading footings can be conducted in the strong box with the aid of this actuator while the sample is in-flight.

The actuator available at UWA is able to move vertically and horizontally and its maximum speed along the strongbox is 3 mm/s. The maximum vertical and horizontal load capacity of the actuator is 6.5 kN and 2 kN respectively. The actuator can move either by a load or displacement criteria mainly specified by the user's requirements. Figure 4-4 illustrates the actuator resting on the strongbox before conducting a test.

An in-flight computer that is located on top of the central platform of the centrifuge maintains connection between the centrifuge and the user and it is connected to a data logging computer in the control room. More details on the UWA centrifuges can be found in Randolph et al. (1991).

4.3 TESTS CONDUCTED IN THE CENTRIFUGE

Eight tests were conducted in the beam centrifuge at a level of 175 g to compare the lateral capacity of monopiles, piled footings and un-piled footings for wind turbines embedded in a sand layer. Table 4-2 illustrates the tests conducted in the beam centrifuge; more details of every individual test will be discussed through the chapter.

Test Number	Foundation Geometry	Prototype Dimensions
Test number 1	Monopile	$D_{pile\ (outer)}$ = 3.3 m, $D_{pile\ (inner)}$ = 3 m and L_{pile} = 35 m
Test number 2	Un-piled footing	D_{pipe} = 3.3 m and L_{pipe} = 34.4 m
Test number 3	Piled Footing	$D_{pile\ (outer)}$ = 3.3 m, $D_{footing}$ = 17.5 m and L_{tower} = 35 m
Test number 4	Un-piled footing	$D_{pile\ (outer)}$ = 3.3 m, $D_{footing}$ = 17.5 m and L_{tower} = 34.4 m
Test number 5	Piled Footing	$D_{pile\ (outer)}$ = 3.3 m, $D_{footing}$ = 17.5 m and L_{tower} = 35 m
Test number 6	Piled Footing	$D_{pile\ (outer)}$ = 3.3 m, $D_{footing}$ = 17.5 m and L_{tower} = 35 m
Test number 7	Un-piled footing	$D_{pile\ (outer)}$ = 3.3 m, $D_{footing}$ = 17.5 m and L_{tower} = 34.4 m
Test number 8	Monopile	$D_{pile\ (outer)}$ = 3.3 m, $D_{pile\ (inner)}$ = 3 m and L_{pile} = 35 m

Table 4-2. Tests conducted in the centrifuge

4.3.1 Sample preparation

Fine commercial silica sand was poured evenly into the beam's centrifuge strongbox. The surface of the sand was vacuumed to make sure that there was no indentation at the ground level, as shown in Figure 4-3. The sand was saturated by pumping water into the strong box. The total mass of the strong box and the saturated soil was 225 kg.

The strong box and the soil were installed on the centrifuge's platform and water was pumped into the soil for the whole duration of the tests. This ensured that the soil was saturated while the

tests were conducted. Before starting the tests, the soil was allowed to consolidate while the centrifuge was in-flight, and more soil had to be added to the strong box.

4.3.2 The equipment dimensions

As shown in Table 4-2 eight tests were conducted in the beam centrifuge to capture the behaviour of monopiles, piled footings and un-piled footings. Figure 4-5 is a schematic illustration of the location of each test conducted in the centrifuge's strongbox. Consideration was given to the location of each test so that they would not interact with each other.

For the single pile tests, the pile/towers were installed by hammering them to the required depth at 1 g level with a guide plate secured to them. The guide plate was used to ensure that the piles would be installed vertically, as shown in Figure 4-6 (right). All pipe piles were installed to a depth of 200 mm (equivalent to 35 m in a prototype) with an average of 250 light taps on the pipe's head.

Table 4-3 illustrates the dimensions of the Aluminium pipes used as piles in the centrifuge tests, which are reported by Harloe (2010).

	Model in centrifuge (mm)	Prototype (m)
Pile outer diameter	19	3.3
Pile inner diameter	17	3
Pile length	387	67.725
Pile length under the ground	200	35
Load application above ground	150	26.3

Table 4-3. The pipe's dimensions used as piles in the centrifuge tests (reported by Harloe 2010)

For the tests, the footings were initially pushed into the sand at 1 g level to a depth of 2 +/- 1, (equivalent to 0.35 m in a prototype), as illustrated in Figure 4-7. Three different footings were used throughout the tests conducted in the centrifuge. All three footings are illustrated in Figure 4-8. The footing dimensions are summarised in Table 4-4.

	Thickness (mm)	Diameter (mm)	Prototype Diameter (m)
Footing 1	15	100	17.5
Footing 2	15	60	10.5
Footing 3	10	40	7

Table 4-4. Footing dimensions used in the centrifuge tests

For the piled footing cases, the footings were initially pushed into the sand similar to the un-piled footing cases and then the pile/towers were hammered into the soil with the metal guide attached to them.

In the case of the piled footing tests, a collar was used to attach the piles securely to the footing during the tests, as shown in Figure 4-9. The collar's dimensions are illustrated if Figure 4-10. In

all piled footing cases only footing number one (100 mm in diameter, Table 4-4) was installed at the ground level to capture the behaviour of the hybrid structure.

Eight tests were conducted in the strongbox as shown in Figure 4-5 but only seven results are available and they will be discussed later. Test number 2 in Table 4-2 could not be completed and it was used as a guide for the other single footing tests.

4.3.3 Soil characteristics

Three miniature CPTs were conducted on the soil when the centrifuge was in-flight. The locations of the CPTs are illustrated in Figure 4-5. The CPTs were conducted to capture the characteristics of the sand in-flight. The CPT results are illustrated in Figure 4-11. The relative density was calculated by Equation 4-2 [Schneider et al. (2006)].

$$D_r = \sqrt{\frac{\frac{q_c}{\sigma'_v}}{250}} \qquad \textbf{4-2}$$

Figure 4-12 illustrates the relative density of the sand in-flight calculated by Equation 4-2. The relative density of the soil calculated by CPT1 is slightly higher than one, which in fact is not acceptable. Results of CPT2 and CPT3 look profound as the relative density of the soil increased with depth and they are less than one. It must be pointed out that the relative density of CPT3 at a depth of 1.4 mm in a prototype scenario was also above one and it was ignored. As there is limited space in the strong box, the CPTs were conducted close to the pile structures to provide a close estimate of the soil stiffness near the structures.

4.3.4 Lateral and Horizontal loads applied on the proposed structures

For the single piles, hybrid structures (piled footings) and the un-piled footing cases, the horizontal load application point was 150 mm above the ground level (26.25 m in a prototype scenario). The horizontal load was applied to the pipe's head by the actuator discussed in Section 4.2.3. Figure 4-13 illustrates the actuator and the hybrid structure before conducting the test. A displacement-controlled method was adopted for applying the horizontal forces on all proposed structures.

The vertical loads on the proposed structures consisted of the lever arm's mass, collar, screws and the load application piece (as previously mentioned the vertical loads on the structure are the loads, which act above the foundation level in this thesis). Figure 4-14 illustrates the load application piece with the screws used during the testing programme.

To study the behaviour of the hybrid structure and the un-piled footings under higher load applications, in tests Number Six and Seven (Table 4-2) footings number two and three were installed on the tower during the tests to increase the load acting on the structures. As illustrated in Figure 4-15, the footings; were securely attached to the hollow pipe during the testing programme.

As discussed, the extra load applied to the structures by footings number two and three were not applied directly on top of the footings, this was the case for the piled footing and the un-piled footing structures.

Table 4-5 provides the vertical and lateral loads, which were imposed on the structures during the testing programme. The vertical forces were arranged in respect to the loads, which a real wind turbine might encounter in practice.

The vertical loads acting on tests number six and seven are clearly higher than other cases, and that is due to the weight of the extra footings, which were installed on those structures during the testing procedure.

It must be noted that the Aluminium bars (pile/towers) used in these tests were recycled from another set of tests conducted on pile/towers in the beam centrifuge. The initial tests conducted on the pile/towers were conducted in a Kaolin clay. More details and the mechanical properties of the Aluminium bar are provided in Section 5.3.

Test	*Foundation type*	*Vertical Load*		*Horizontal Load*	
		Model (N)	Prototype (MN)	Model (N)	Prototype (MN)
1	Monopile	0.98	5.3	314.5	9.6
2	Footing (Not completed)	1.7	9.3	103.6	3.2
3	Piled Footing	1.2	6.5	573.2	17.6
4	Un-piled footing	1.1	5.9	97.1	3.0
5	Piled Footing	1.2	6.4	524.6	16.1
6	Piled Footing	2.5	13.2	684.8	21.0
7	Un-piled footing	2.4	12.7	161.5	5.0
8	Monopile	1.2	6.5	360.2	11.0

Table 4-5. Vertical and lateral loads applied to the structures in the centrifuge tests (after Harloe 2010)

4.4 TEST RESULTS

In this section, the details of the eight tests mentioned in Section 4.3.4 will be further discussed and their results will be provided.

4.4.1 Monopile test (Test Number One)

In this test, a single pipe (19 mm in diameter) was driven to a depth of 200 mm and bent to failure while the centrifuge was in-flight. The vertical load on the pipe was mainly due to the structural elements, which were required to be installed on the pipe for the duration of the test. These parts included the load application piece, screws and the weight of the collar sitting on the

pipe's body, as illustrated in Figure 4-16. Figure 4-17 illustrates the pile/tower, collar and the application piece attached to the pipe before conducting the test in the centrifuge.

The mass of the attached components (without the weight of the lever arm) was 74.1 g. This mass included the mass of the collar, the load application piece and the screws; this mass was directly attached to the hollow pipe.

The mass of the screws and the load application piece illustrated in Figure 4-14 was 42.3 g (this mass is present in all eight tests). The vertical forces acting above the foundation level was adjusted to be between 5 to 6 MN (this included the weight of the collar and the pipe's lever arm), which is in line with the results of Byrne et al. (2003).

The test result is illustrated in Figure 4-18, as can be seen the pipe has yielded at around 9 MN. The yield of the hollow pipe occurred beneath the ground level and it was at a depth of 7 m beneath the mudline for a prototype. Figure 4-19 illustrates the yield point of the pile/tower with the attached collar after the test was completed in the centrifuge.

4.4.2 Un-piled footing test (Test Number Two)

In this test, a footing was attached to a solid pipe (tower) and a monotonic lateral force was applied to the pipe's head. The force versus displacement curve for this structure was also plotted but not up to the failure point due to mechanical problems, this point will be further discussed in Section 5.6 with the aid of Figure 5-113. Figure 4-20 shows the structure, which includes the solid tower, the load application piece and the footing located in the centrifuge before conducting the test.

The mass of the screws and the application piece on the pipe was recorded as 42.3 g (if the pipe's mass is included this value will rise to 177.5 g, which is equivalent to a weight of 1.7 N).

This test was unfortunately not successful and only a small part of the forces versus displacement curve was generated, which is illustrated in Figure 4-21. This test was merely used as a guide to the other two footing tests (tests number four and seven).

4.4.3 Piled footing test (Test Number Three)

In this test, a 19 mm diameter pipe was used in conjunction with the 100 mm Aluminium footing (footing number one in Table 4-4). As in the monopile cases, the hollow pipe was embedded to a depth of 200 mm by hammering and the footing was manually installed to a depth of 2 mm $\pm$ 1 mm which was firmly attached to the pile/tower. The dimensions of the pipe and the footing are as in Tables 4-3 and 4-4 respectively. Figure 4-6 illustrates the hybrid structure and the installation process of the pipe after the footing was initially installed to its required depth.

As illustrated in Figure 4-22 the hybrid structure's weight was controlled by the weight of the screws, the load application piece, a collar and a cap resting on top of the tower. The recorded mass (including the lever arm) was 122.3 g, which generates a force of 1.2 N. This load generates a vertical force of 6.43 MN on the structure in a prototype scenario. In addition, this force was

acting above the foundation level in the proposed hybrid structure and the load application piece was positioned at 150 mm above the ground level, as illustrated in Figure 4-23.

Figure 4-24 illustrates the force versus displacement curve for this test. As illustrated in Figure 4-25, the yield point on the Aluminium pipe occurred at around 8.2 m above the footing level in a prototype scenario (or 10.8 m above the ground level). This height is in fact corresponding to a point just above the attached collar in the test.

4.4.4 Un-piled footing test (Test Number Four)

Figure 4-26 illustrates the footing used in the beam centrifuge to capture the behaviour of an un-piled footing with a tower in respect to a monotonic lateral force. This test is similar to test number two but instead of a solid pipe, which was used in that test, the tower was board so that the weight of the entire structure would be reduced.

The pipe's length (tower) was 197 mm, which is equivalent to 34.475 m in a prototype. For this test, the pipe was drilled with a 15 mm drill bit up to a depth of 132 mm from the top of the solid lever arm. This in fact reduces the weight of the proposed structure and that is important in calculating the over turning moment and the ultimate capacity of the structure.

Figure 4-27 shows the drilled pipe, which was used in the footing tests. Tests number four and seven in the centrifuge where conducted with the same drilled pipe illustrated in Figure 4-27.

The lateral load in the centrifuge test was applied at 150 mm above the ground level on the drilled pipe (equivalent to 26.25 m in a prototype). The vertical load at 1 g level acting above the footing level was calculated to be 1.1 N (this value was calculated from the weight of the screws, the load application piece and the pipe). This load was equivalent to 5.9 MN in a prototype scenario and it was acting above the footing level during the test.

After the test was completed, it was observed that the footing had rotated about its axis and had been pushed into the surrounding soil in the direction of the applied load as shown in Figure 4-28. The footing was embedded to a depth of 0.7 m (in a prototype) in the direction of the applied load (it was initially embedded at a depth of 0.35 m).

The force versus displacement curve for this test is illustrated in Figure 4-29.

4.4.5 Piled footing test (Test Number Five)

The weights acting in this test were identical to test number three. The weight of the load application piece, the screws, the collar and the lever arm's mass above the foundation was 122.3 g. This weight generates a force equal to 6.4 MN in a prototype.

The main difference between this test and test number three is that before monotonically loading the piled footing structure to failure in this test the structure was loaded laterally ten times from 0 MN to 15.3 MN before it was loaded to failure. Introducing a one-way cyclic loading to the structure usually softens the soil surrounding the structure and this can cause failure at lower lateral loads (Anderson et al. 1988 & 2008).

Figure 4-30 illustrates the result of test number five. The yield point on the pile/tower was observed to be around 5.3 m below the ground level and the base of the pile (at the ground level) was laterally displaced by 0.8 m.

Figure 4-31 illustrates the Aluminium bar after the test was completed in the centrifuge.

4.4.6 Piled footing test (Test Number Six)

This test is similar to test number three, but in this particular case, the vertical force was increased. As illustrated in Figure 4-32 the two footings (footings number two and three, Table 4-4) were firmly attached to the pipe's body just above the collar.

The total mass of the structure above the footing level was calculated to be 251.7 g and that generates a force equal to 13.2 MN in a prototype. In this test the application piece, the screws, two footings (footing number two and three), the collar and the cap were all attached to the hollow tower during the test.

Footings number two and three (Table 4-4) were securely attached to the tower's body during the testing programme. Footing number one was used at the base of the hybrid structure (acting as the bearing plate for the entire structure). As in test number three, footing number one was embedded into the silica sand (2 mm $\pm$ 1 mm, which is equivalent to 0.35 m in a prototype) while footing number two was at the level of the collar and footing number three was resting on top of it.

Figure 4-33 illustrates the proposed structure in the centrifuge strongbox before conducting the test. In this test, the main goal was to study the behaviour of a piled footing structure under an increased vertical load.

The load versus displacement graph for this test is illustrated in Figure 4-34.

4.4.7 Un-pile footing test (Test Number Seven)

This test is similar to test number four, but footings number two and three where attached to the tower as illustrated in Figure 4-35. In this figure the load application piece, screws and the footings are illustrated.

Footings number two and three were used to increase the vertical load on the footing during the testing programme. Footing number one was used at the base of the foundation similar to all other tests.

The total mass of the structure above the footing level was 242.2 g, which is equivalent to 12.7 MN for a prototype. It must be noted that the tower used in this test was exactly the same pipe, which was used in test number four, shown in Figure 4-27. This pipe is 19 mm in diameter and 197 mm in length.

The result of this test is illustrated in Figure 4-36. By comparing this figure and Figure 4-29, it is clear that the lateral force at failure has increased by 2 MN when the vertical force on the structure was increased. Similar to test number four the footing (footing number one, Table 4-4)

rotates about its axis during the testing procedure and it was embedded to a depth of 0.9m after the test was completed while it was initially embedded to a depth of 0.35 m.

4.4.8 Monopile test (Test Number Eight)

This test is identical to test number one. The only difference is that in this test a cap was present for the duration of the test, as shown in Figure 4-37. Similar to test number one the screws, the load application piece and the collar were attached to the pipe's body during the testing procedure. The mass of the cap was recorded as 24.5 g, which is equivalent to 1.28 MN in a prototype. Figure 4-38 illustrates the result obtained from the experimental test conducted on this proposed structure.

The cap was introduced in this test to study how the pile structure would behave laterally under an increase in the vertical load.

The yield point on the pile for this test was around 3.5 m below the ground level. After the test was completed, the base of the pile had a lateral displacement of 0.8 m in a prototype.

4.4.9 Water level heights during the centrifuge tests

For all tests which footing number one (Table 4-4) was present at the ground level, the water level was adjusted so that it would be around the top of the footing level, as illustrated in Figure 4-39. This was also the case for tests number one and eight (monopiles) though footing number one was not present during these tests.

All tests were conducted with the water level standing above the ground surface because realistically the foundation (the bearing plate) in a prototype scenario would be submerged underwater.

4.4.10 Lateral and vertical loads imposed on the structures in the centrifuge tests

As discussed in Chapter 2, Byrne et al. (2003) provides the maximum lateral loads, which might act on a wind turbine during its life expectancy. On the background of his work and experience gained from other previous works (similar to Senders et al. (2009)), the maximum vertical forces acting on the wind turbine towers for the eight conducted tests were adjusted so that they would be in a range of 6 to 7 MN (Table 4-5). This was not the case for tests number six and seven were the vertical load was doubled to illustrate how the structures behave under an excess vertical load. In addition, the vertical loads in the piled footings and un-piled footing tests were not directly applied onto the footings.

As previously discussed, applying a vertical load directly on the footing can generate very high lateral forces, which might not correctly replicate the situation in practice. The tabulated horizontal forces in Table 4-5 for the monopiles and the piled footing cases are in fact equal to the yield point of the hollow pipe used in the tests.

4.4.11 Comparing the test results

Figure 4-40 compares the results of tests number one (monopile with a vertical load of 5.3 MN) with test number eight (monopile with a vertical load of 6.5 MN). It is clear that the stiffness of both structures is similar.

The higher yield point in test number eight is only because the monopile in this test has experienced a higher level of strain hardening (this will be further discussed in Sections 5.3 and 5.4.3.5). At this stage, it can be mentioned that by using the Broms (1964) solution for long piles in sands the yield point of the monopile can be calculated as 8.94 MN, which is consistent with the results of test number one.

Figure 4-41 illustrates and compares the results of the monopile (test number one), un-piled footing (test number four) and piled footing (test number three) structures tested in the centrifuge. From these results, it is clear that the stiffness of the hybrid structure is higher than that of a monopile from the initial point. It is also clear that at low displacements, the stiffness of the un-piled footing is closer to the stiffness of the hybrid structure and it is higher than the stiffness of the monopile.

As discussed in Section 2.10, the derived conclusion that the stiffness of the piled footing is higher than of monopile from the initial point is not similar to the results obtained by Stone et al. (2010) in the centrifuge tests at a level of 50 g. On the other hand, this conclusion is in a closer agreement with the results obtained by the tests conducted in 2007 by Stone et al. at 1 g level.

From the test results illustrated in Figure 4-41, it is clear that the lateral capacity of a single pile can be increased in excess of 50% if a foundation plate is positioned at the ground level to support the pile and the tower.

Figure 4-42 compares the results of the piled footing tests in the centrifuge (tests number three, five and six). It is clear that the stiffnesses of the three structures are in a close agreement with each other. In addition, the piled footing structure in test number five fails at a lower lateral load compared to test number three. As discussed in Section 4.4.5 this test was cycled from 0 MN to 15.3 MN ten times before it was monotonically loaded to failure, so its maximum lateral load was expected to be smaller than the results obtained from test number three.

Figure 4-43 illustrates the results of tests number six (piled footing) and seven (un-piled footing) conducted in the centrifuge. These two tests were conducted with footings numbers two and three attached to their towers (the vertical load was increased in these tests to range of 12.7 MN to 13.2 MN). It is clear that the initial stiffness of the un-piled footing is similar to the stiffness of the hybrid structure at small displacements.

For comparison purposes, test number one (monopile) has been included in Figure 4-44. It is clear that the initial stiffness of the un-piled footing is higher than the stiffness of the monopile structure at low displacements. Although the vertical load on the monopile in test number one is not in the range of tests, number six and seven it will be illustrated in Chapter 5 that increasing

the vertical load on a monopile does not significantly alter the horizontal capacity of the structure (this was also discussed in Chapter 2, with respect to the results of Karthigeyan et al. 2006).

It was important to define how the stiffness of the three strucutres (single pile, piled footing and footing) would initially behave during lateral loading and how much the lateral capacity would increase if a hybrid structure were used; numerical models were constructed with ABAQUS similar to the tests conducted in the beam centrifuge at UWA. This would also provide independent validation that the test results were accurate and the derived conclusions were acceptable.

It must also be noted that as discussed in Section 4.4.4 the thickness of the tower in the un-piled footing tests was not consistent with the thickness of the monopile and the piled footing structures used in the centrifuge tests (as the tower was drilled with a 15 mm drill bit). Moreover, the last 65 mm (11.37 m in a prototype) of the tower was solid and these factors could have affected the results as the weight on a footing structure can significantly affect the stiffness of a single footing structure in overturning. In Chapter 5, all tests have been replicated by constructing their numerical models with ABAQUS and the discrepancies in the tests have been waived by constructing four extra models for comparison purposes.

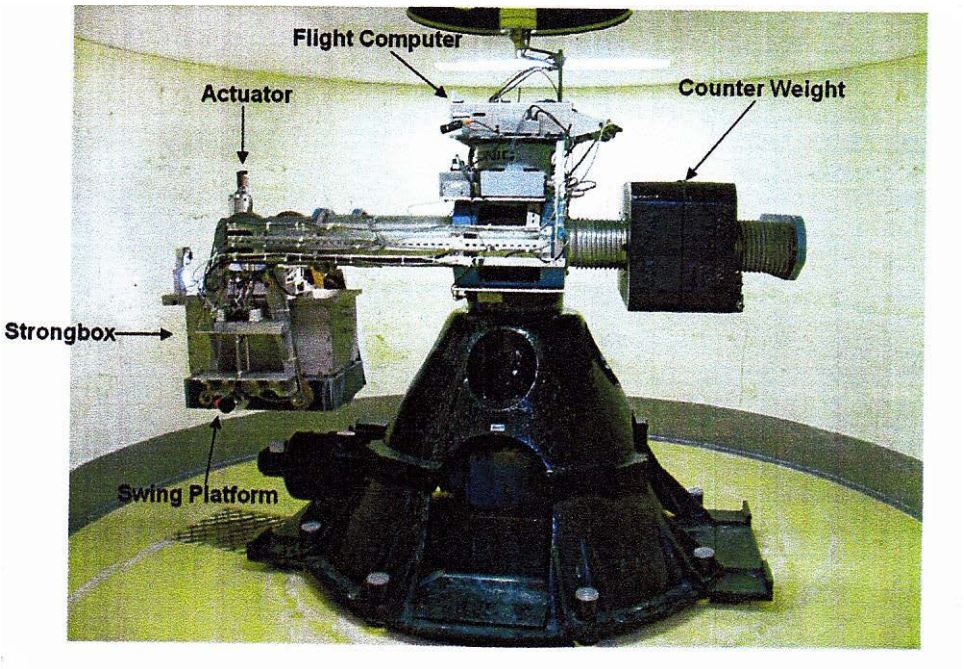

Figure 4-1. The geotechnical beam centrifuge at UWA

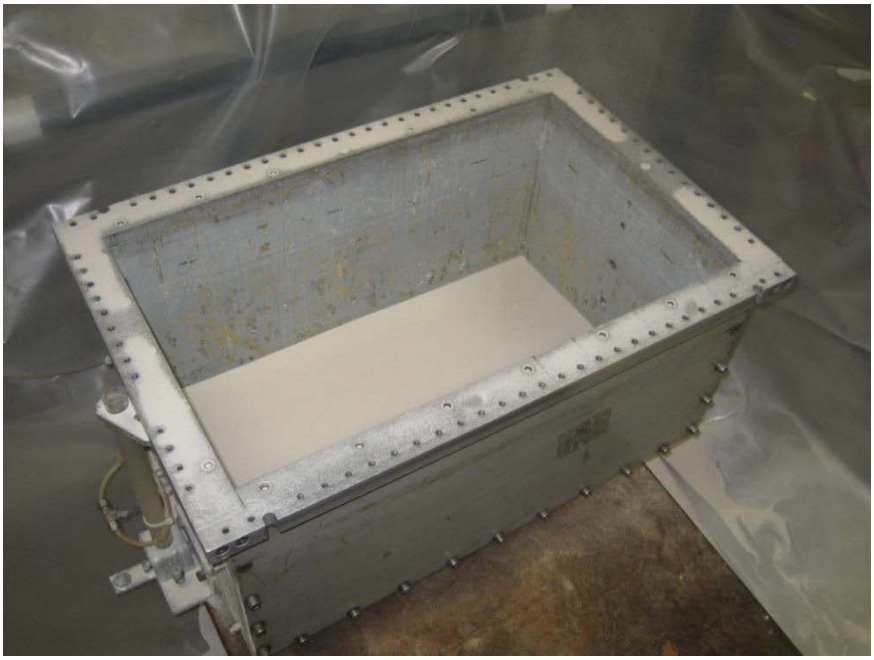

Figure 4-2. The strongbox used on the beam centrifuge (after Harloe 2010)

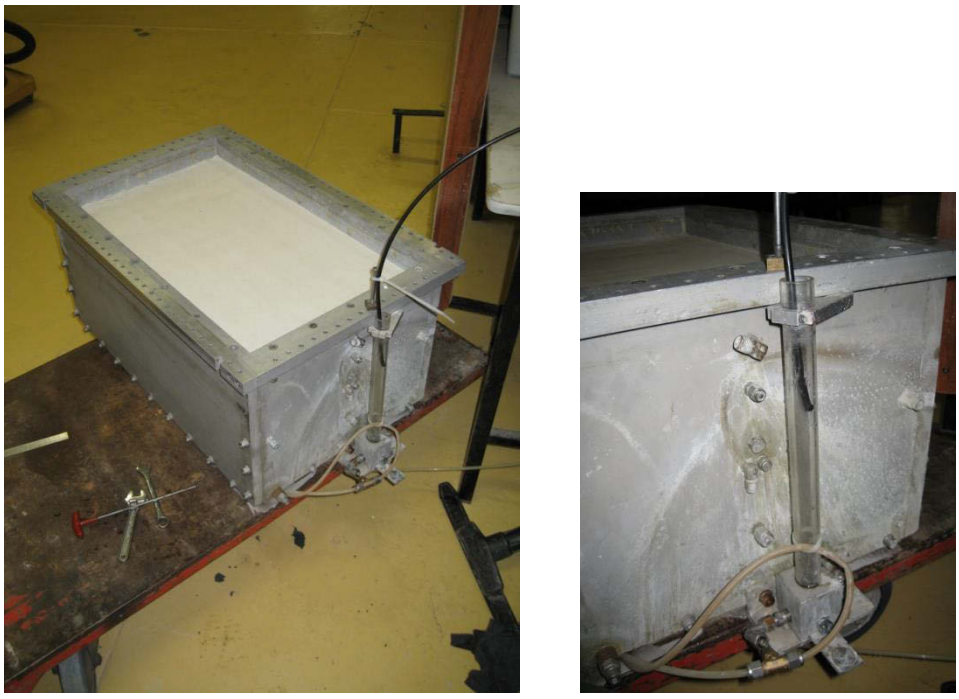

Figure 4-3. The beam strong box with its standpipe (after Harloe 2010)

Figure 4-4. Motor driven actuator located on top of the strongbox (after Harloe 2010)

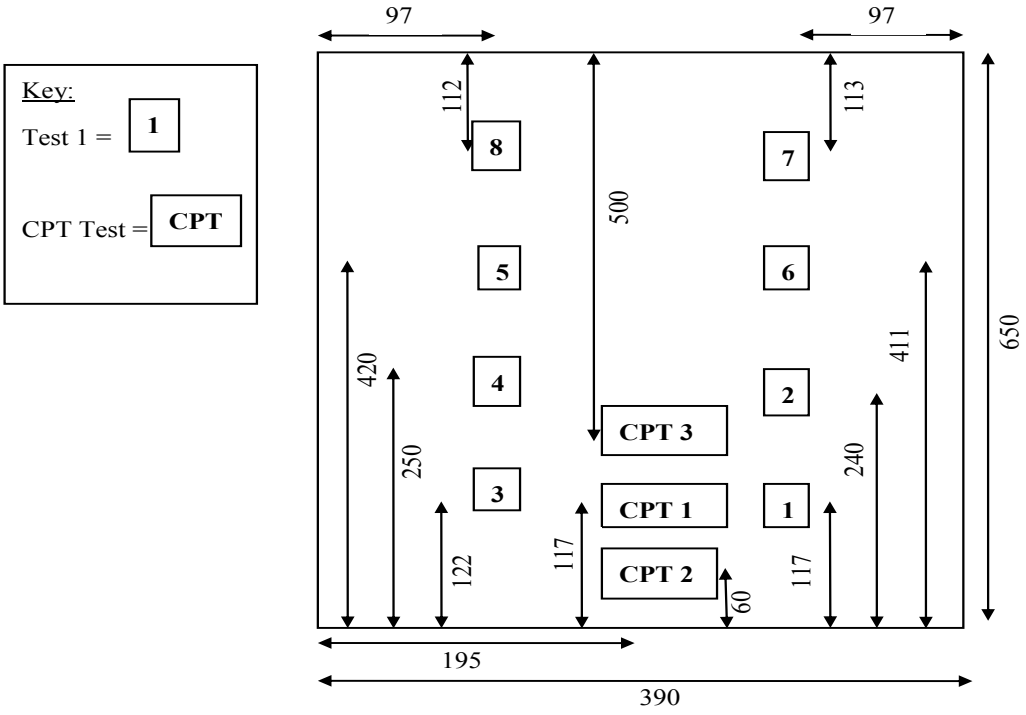

Figure 4-5. A schematic illustration of each test conducted in the centrifuge (after Harloe 2010)

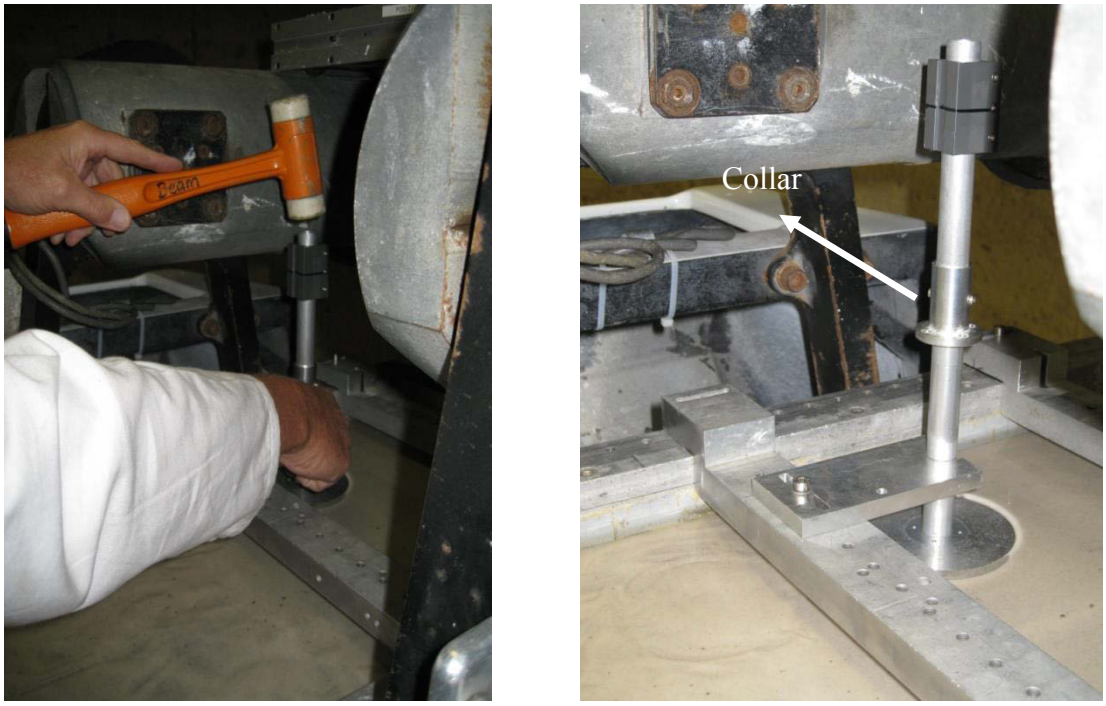

Figure 4-6. All piles were hammered to the required depth with a secured plate in place (after Harloe 2010)

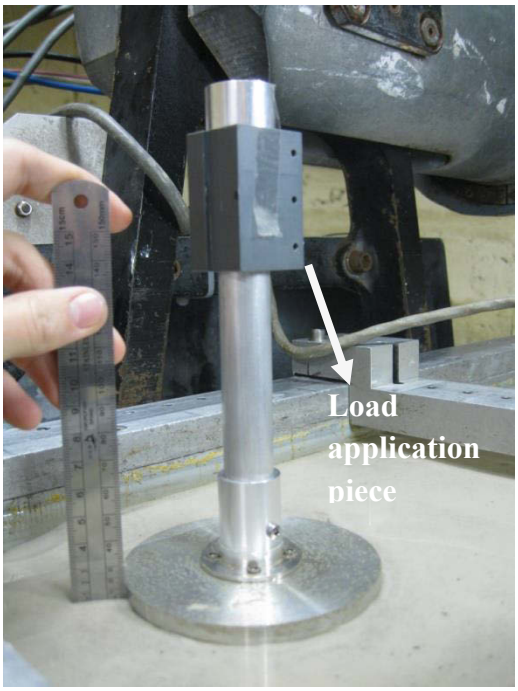

Figure 4-7. The footings in the tests were initially pushed into the sand to a depth of 2 mm ± 1 mm (after Harloe 2010)

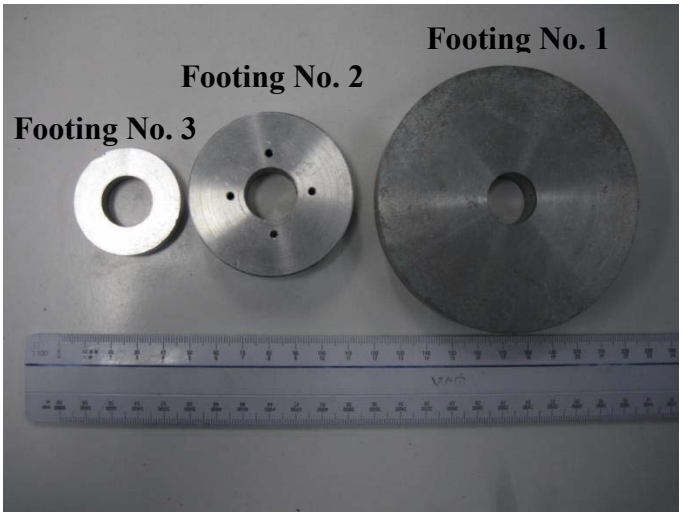

Figure 4-8. The three footings used in the centrifuge tests (from right to left are footings number one, two and three) (after Harloe 2010)

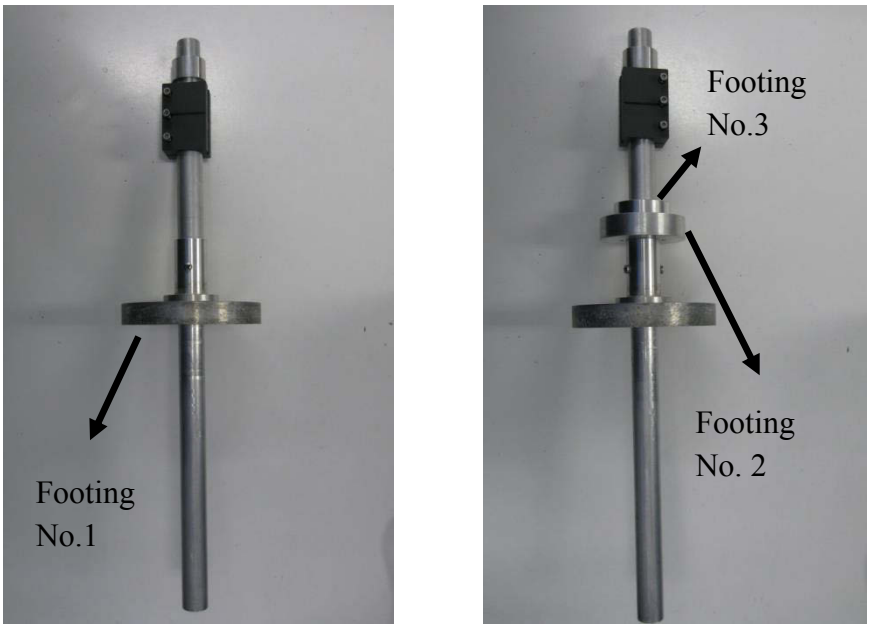

Figure 4-9. Two piled footing structures with their attached collar (after Harloe 2010)

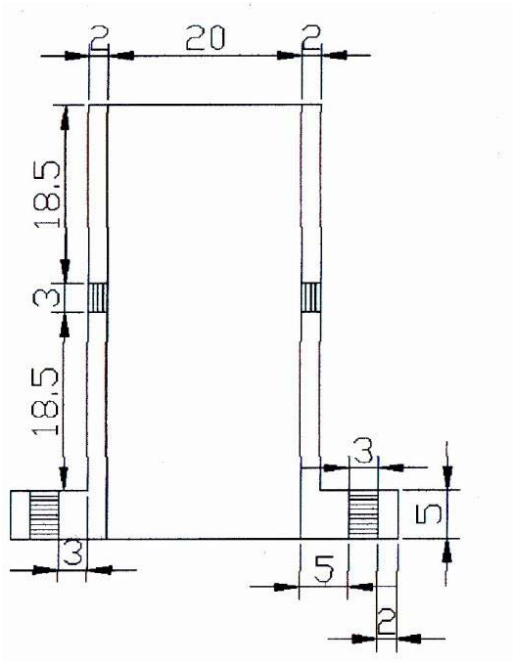

Figure 4-10. The dimensions of the collar used in the tests (after Patel 2009)

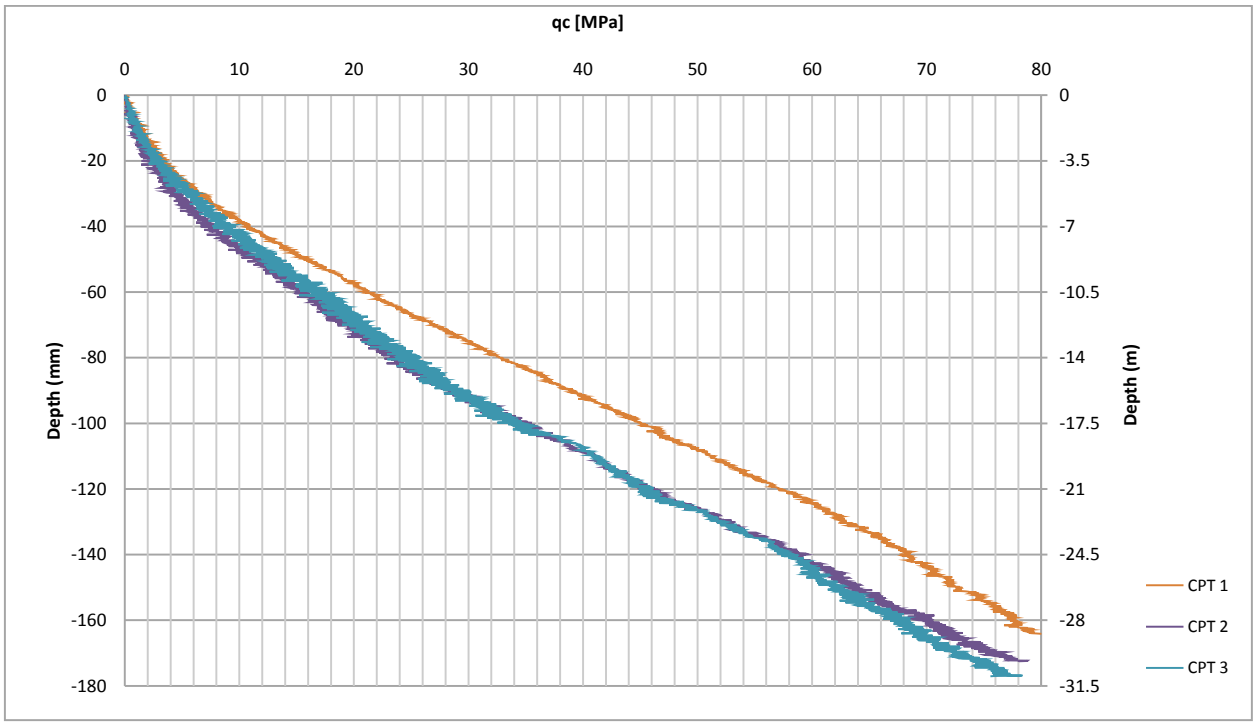

Figure 4-11. The results of the cone penetrometers tests (after Harloe 2010)

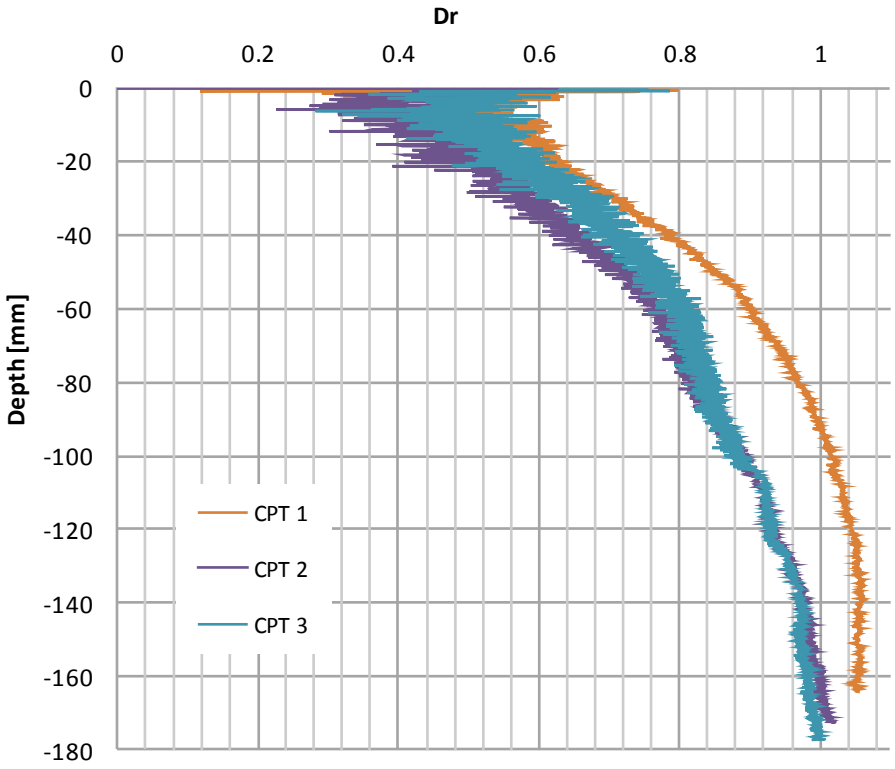

Figure 4-12. The relative density of the sand in-flight (after Harloe 2010)

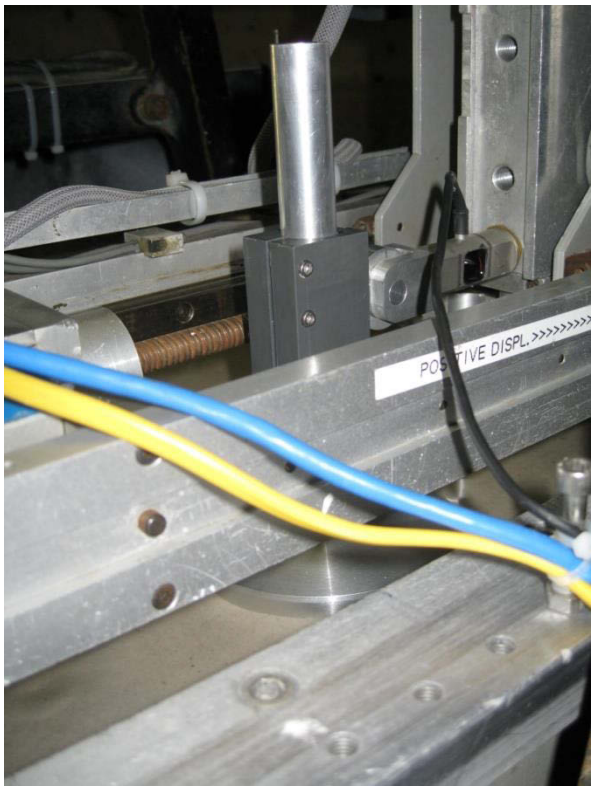

Figure 4-13. The actuator attached to the hybrid structure before conducting the test (after Harloe 2010)

Figure 4-14. The load application piece with the screws used during the tests (after Harloe 2010)

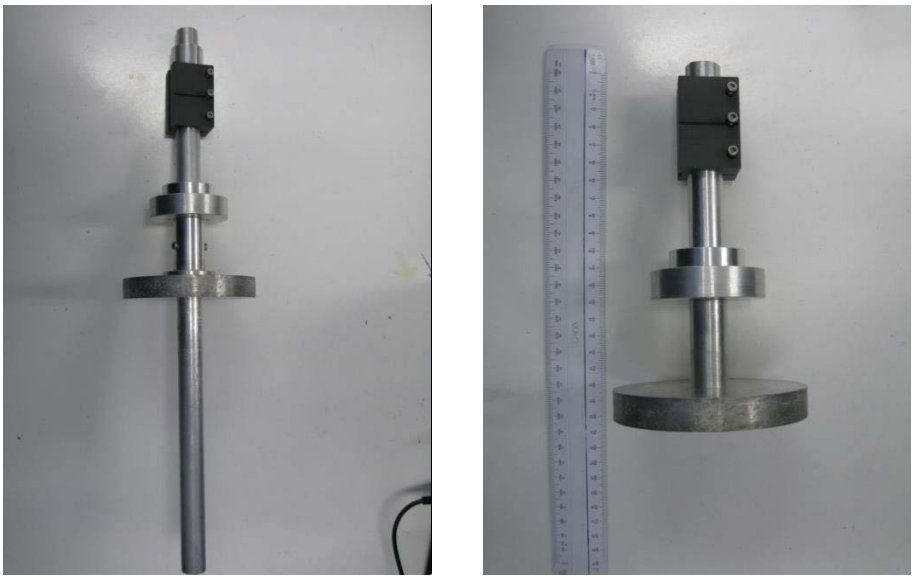

Figure 4-15. Footings number two and three were used to increase the vertical loads on the single footing and the hybrid structure during the tests (Table 4-4) (after Harloe 2010)

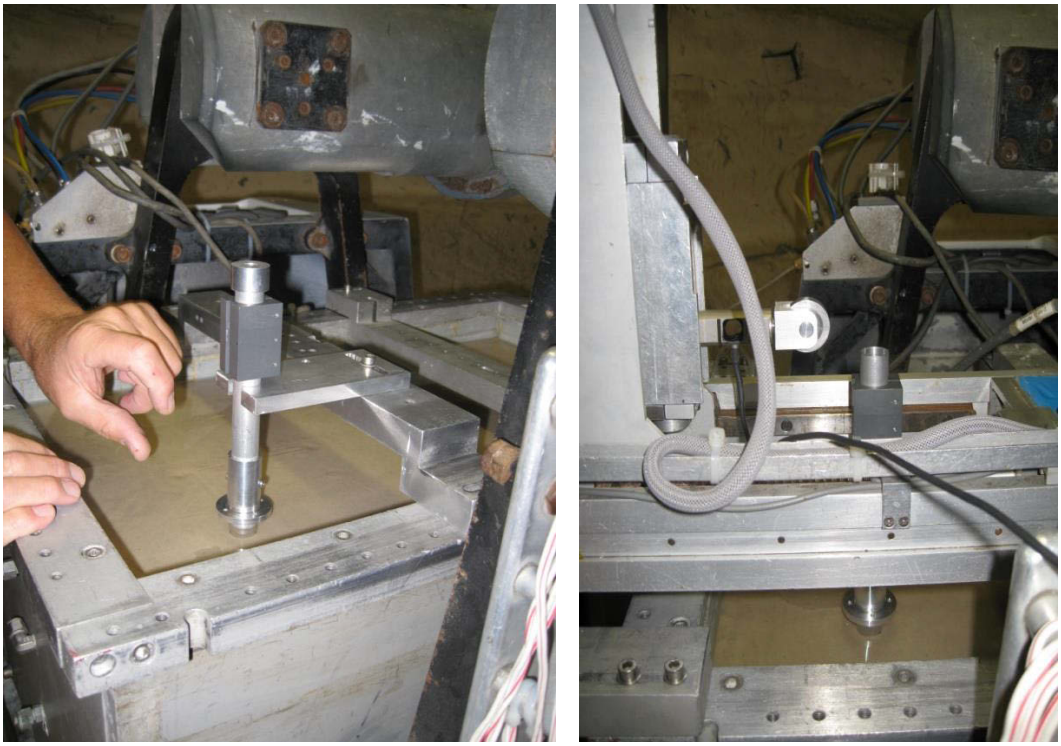

Figure 4-16. Test number one (monopile) with the attached collar (after Harloe 2010)

Figure 4-17. The hollow pipe with the collar and the load application piece (test number one) (after Harloe 2010)

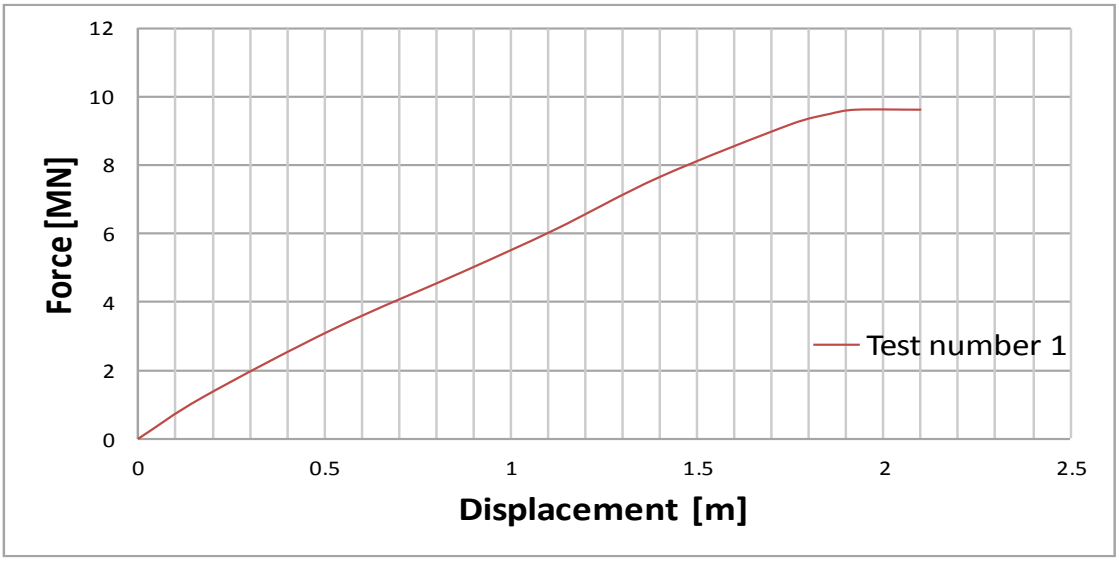

Figure 4-18. The results of test number one (Single pile) (after Harloe 2010)

Figure 4-19. The yielded aluminium bar (test number one) (after Harloe 2010)

Figure 4-20. Test number two, the footing and the solid tower used during the testing programme (after Harloe 2010)

Figure 4-21. Results of test number two (Single footing) (after Harloe 2010)

Figure 4-22. The hybrid structure used in test number three (after Harloe 2010)

Figure 4-23. The location of the load application piece in test number three (Piled footing structure) (after Harloe 2010)

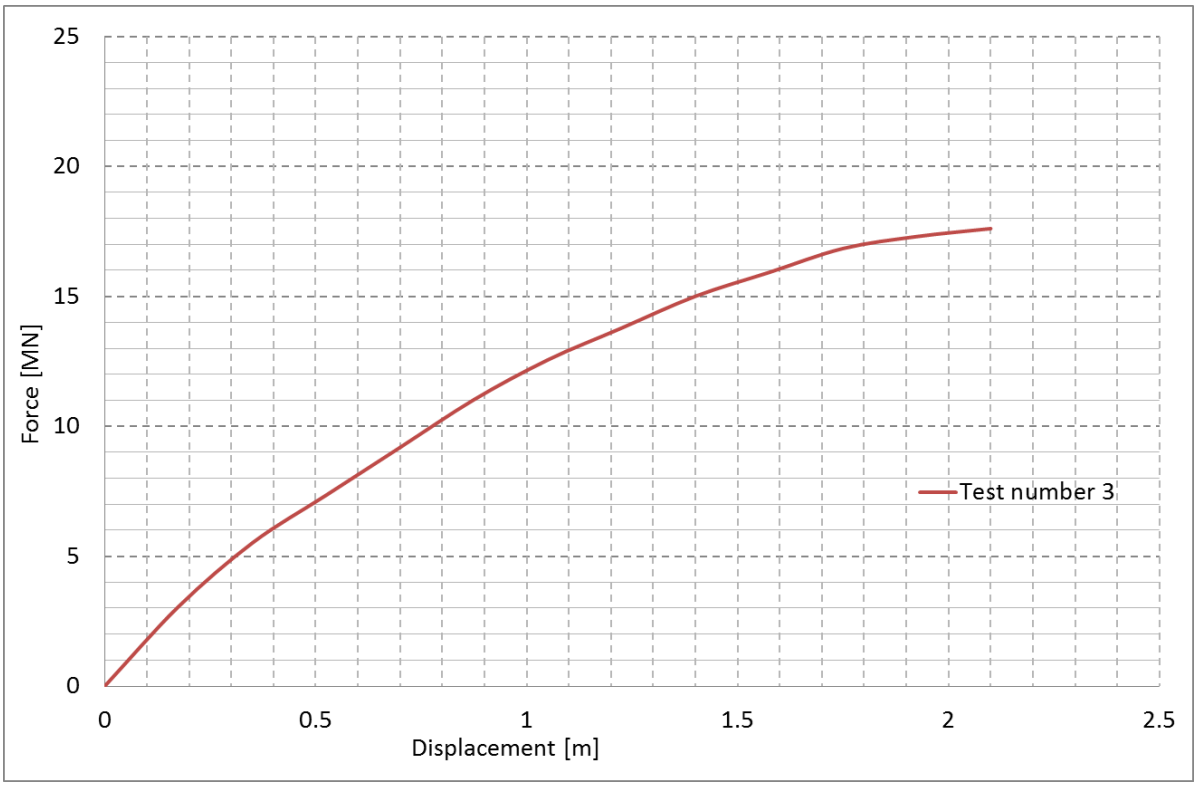

Figure 4-24. Results of test number three (Piled footing structure) (after Harloe 2010)

Figure 4-25. The yielded aluminium bar after test number three was completed (after Harloe 2010)

Figure 4-26. The single footing test (test number four) (after Harloe 2010)

Figure 4-27. The drilled pipe used in tests number four and seven (after Harloe 2010)

Figure 4-28. The rotated footing after test number four was completed (after Harloe 2010)

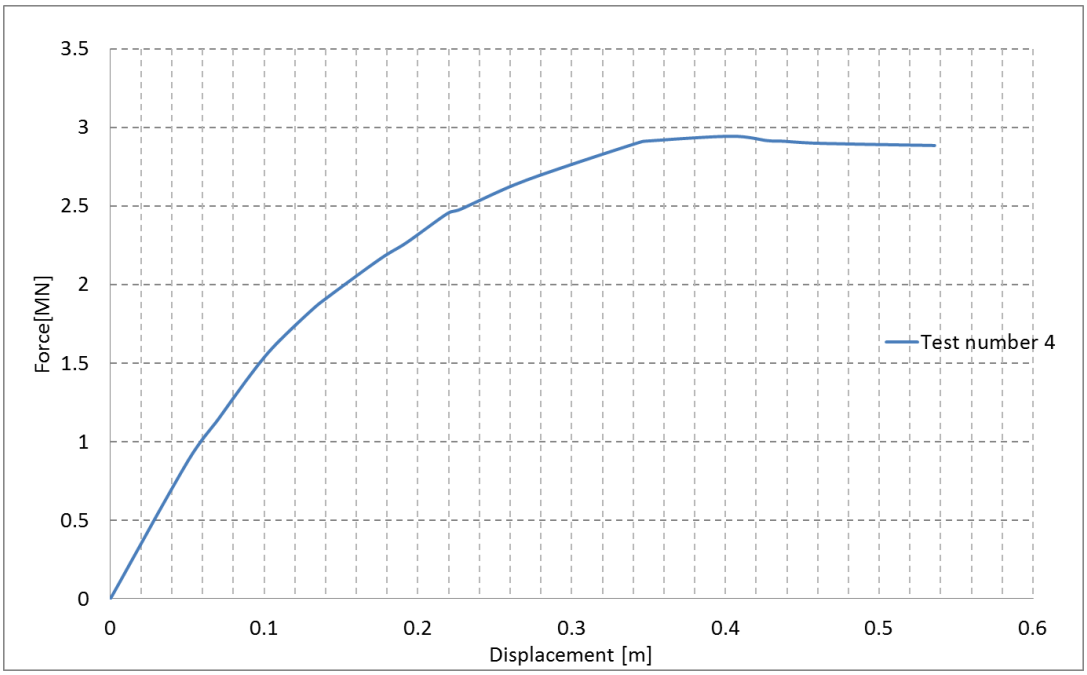

Figure 4-29. Force versus displacement curve for test number four (Single footing) (after Harloe 2010)

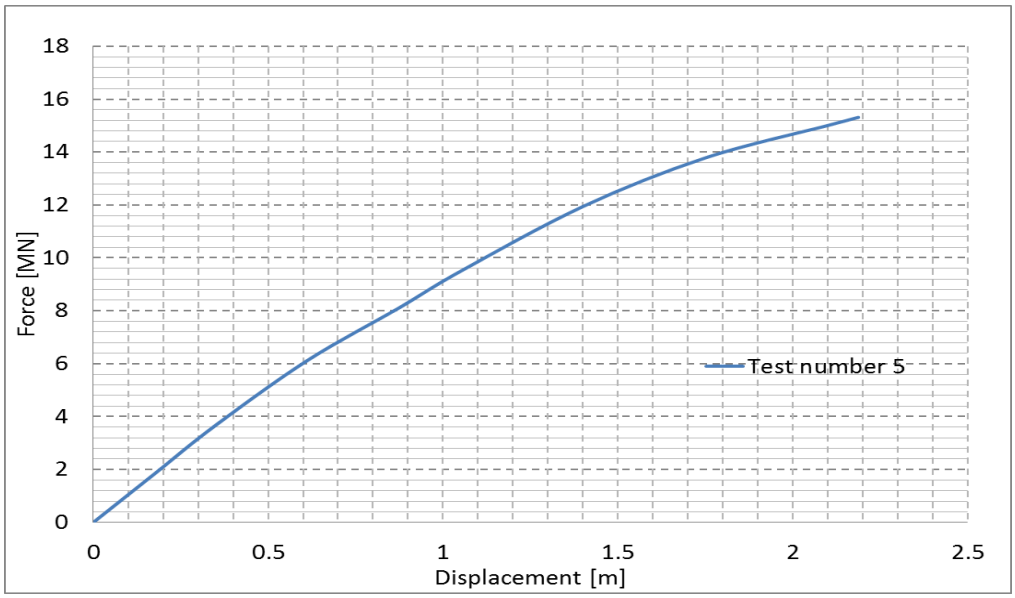

Figure 4-30. Force versus displacement curve for test number five (Piled footing structure) (after Harloe 2010)

Figure 4-31. The yielded pile after test number five was completed (after Harloe 2010)

Figure 4-32. The proposed piled footing structure (test number six) (after Harloe 2010)

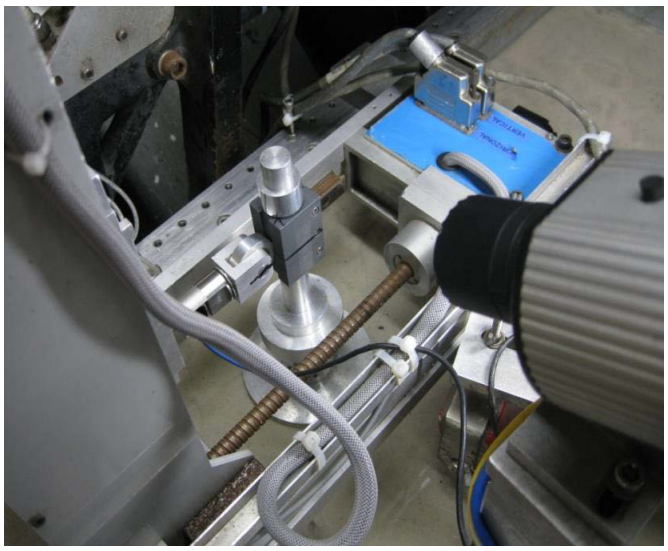

Figure 4-33. The piled footing structure installed in the silica sand (test number six) (after Harloe 2010)

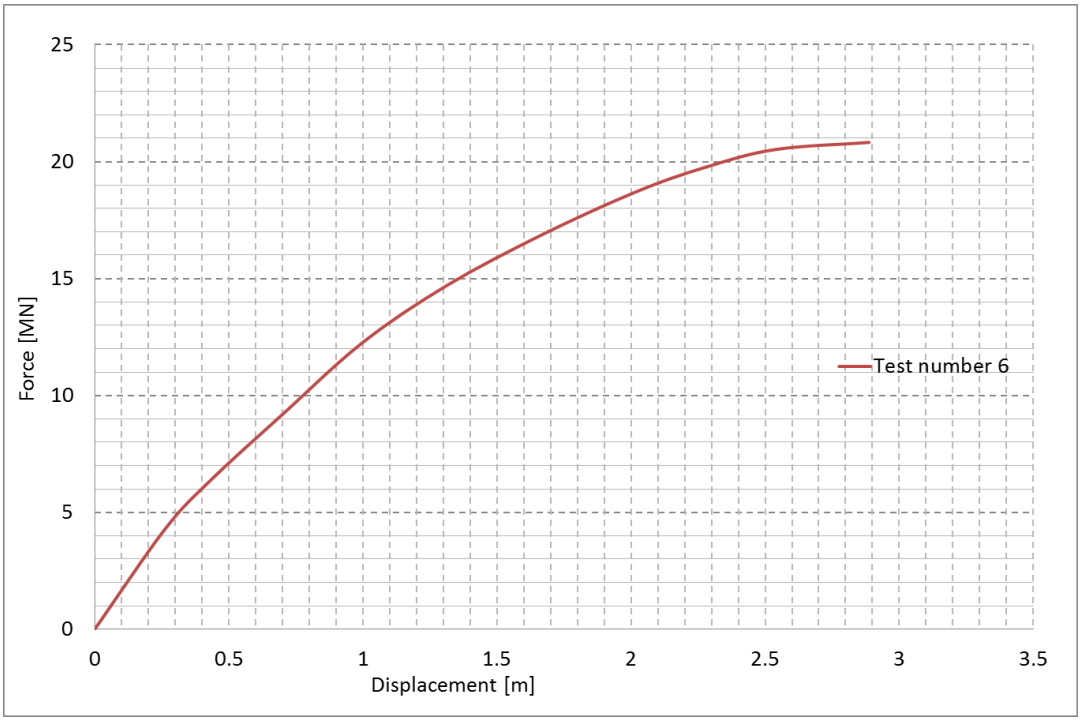

Figure 4-34. Load versus displacement graph for test number six (Piled footing structure) (after Harloe 2010)

Figure 4-35. The single footing structure in test number seven (Single footing) (after Harloe 2010)

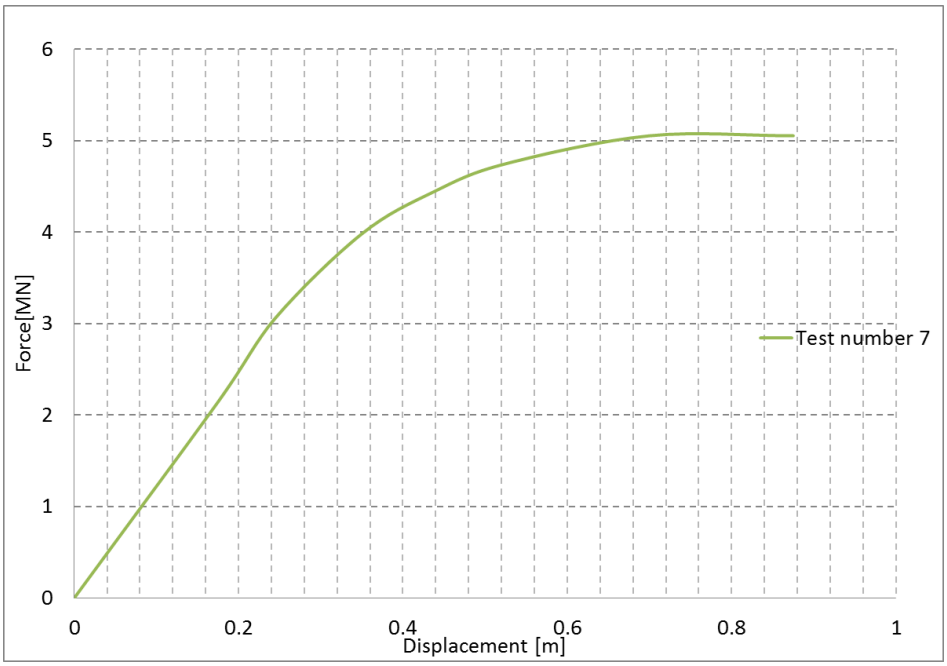

Figure 4-36. The results of test number seven (Single footing structure) (after Harloe 2010)

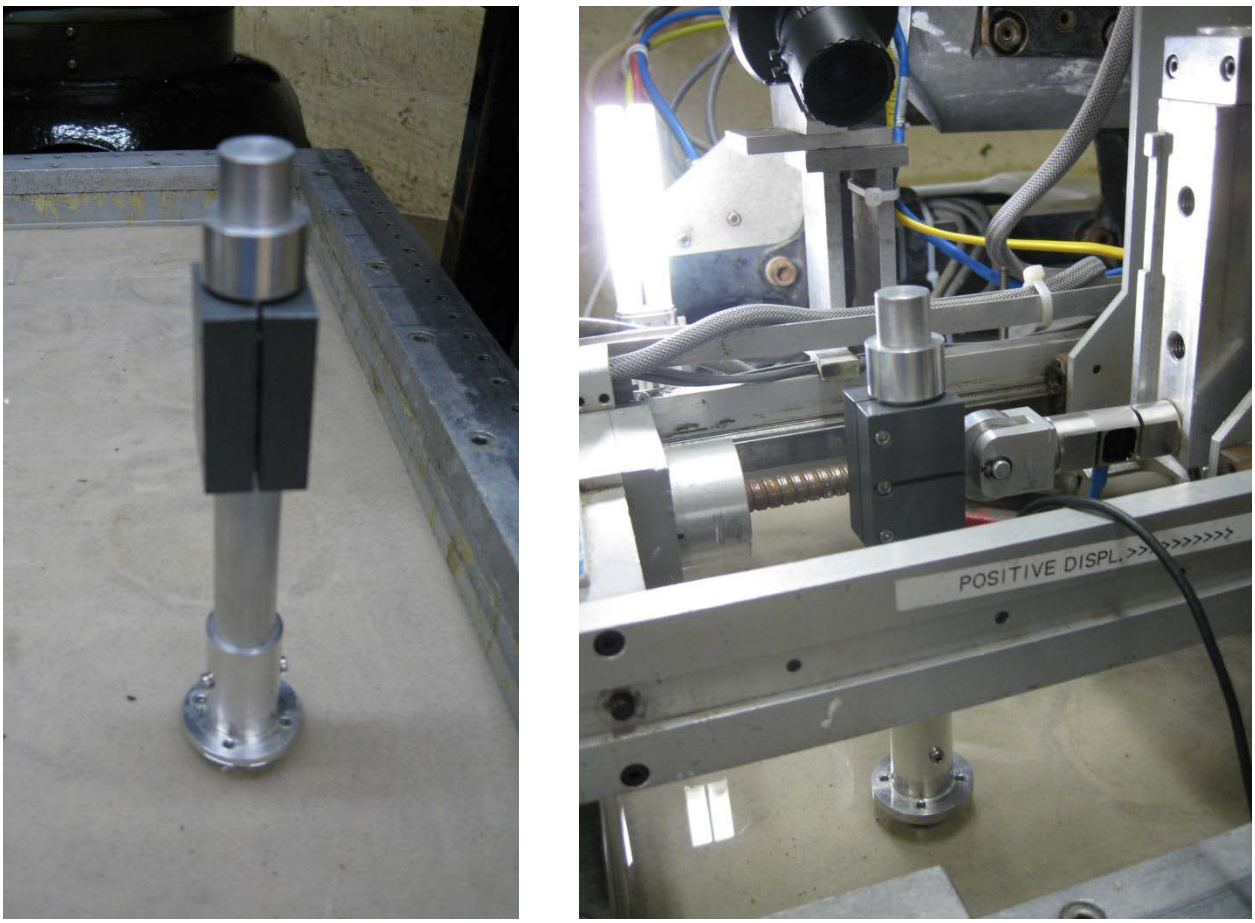

Figure 4-37. Test number eight (Single pile) installed in the centrifuge strongbox (after Harloe 2010)

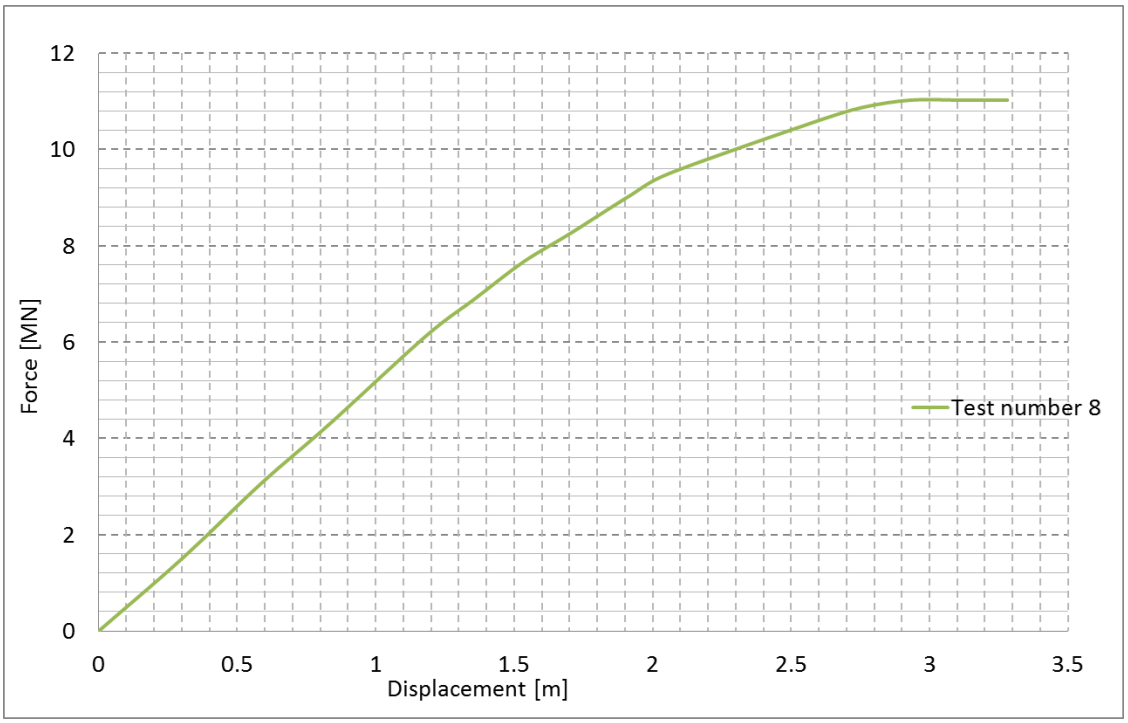

Figure 4-38. Force versus displacement graph for test number eight (Single pile) (after Harloe 2010)

Figure 4-39. The water level was at the level of the bearing plate during the tests (after Harloe 2010)

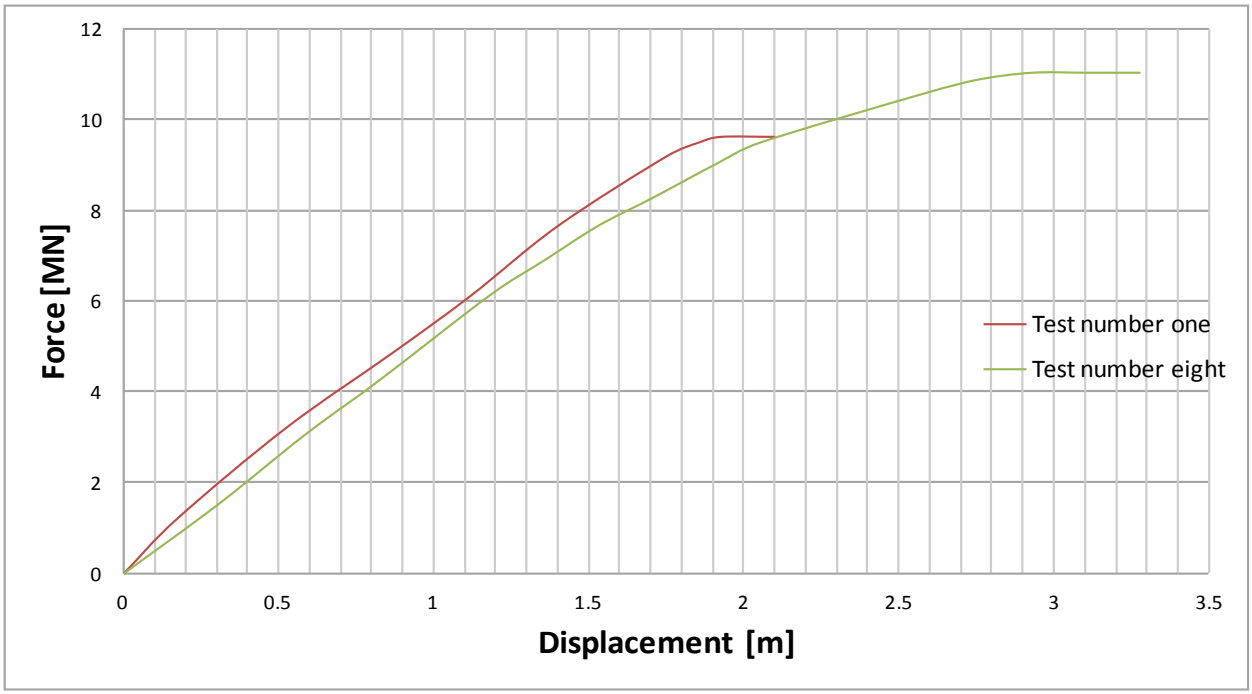

Figure 4-40. Results of the monopile tests conducted in the centrifuge (after Harloe 2010)

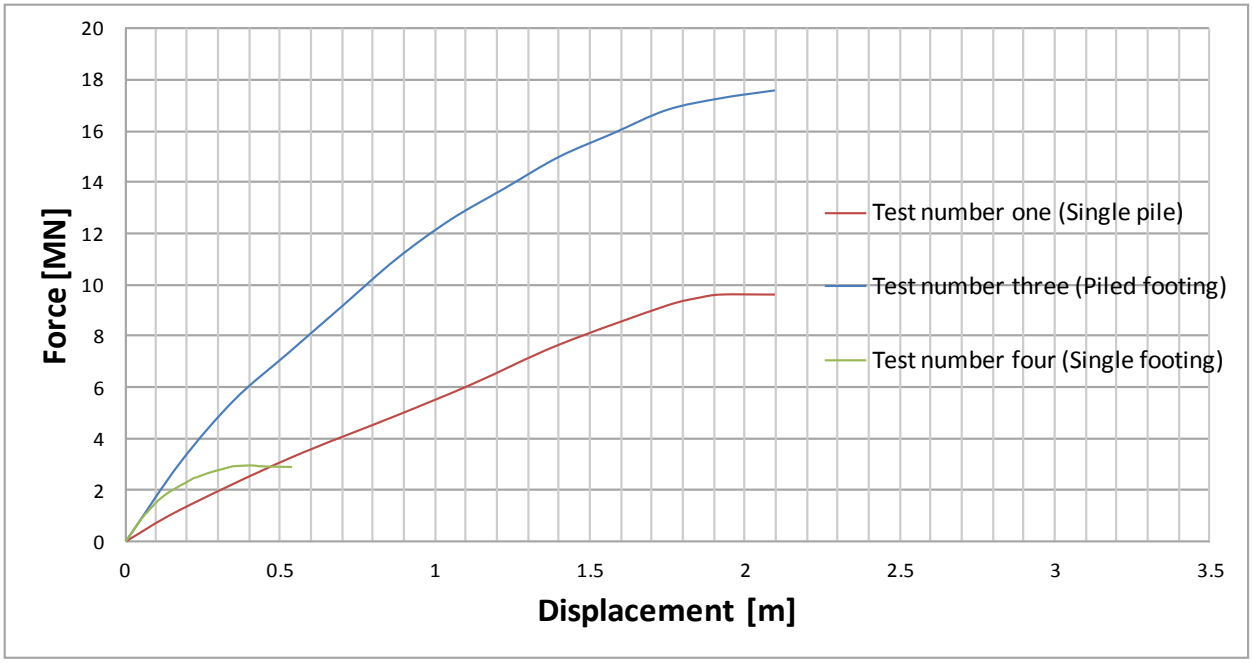

Figure 4-41. Comparing the results of tests number one, three and four conducted in the centrifuge (after Harloe 2010)

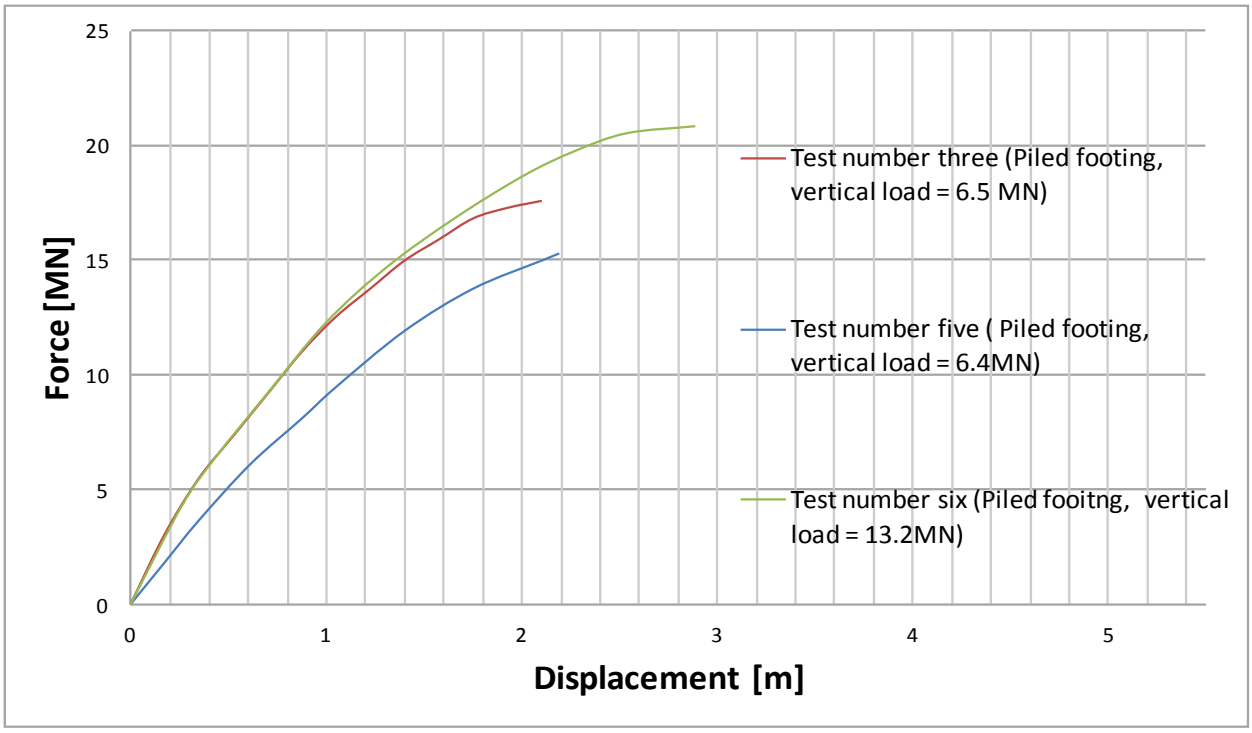

Figure 4-42. Comparing the piled footing tests conducted in the centrifuge (after Harloe 2010)

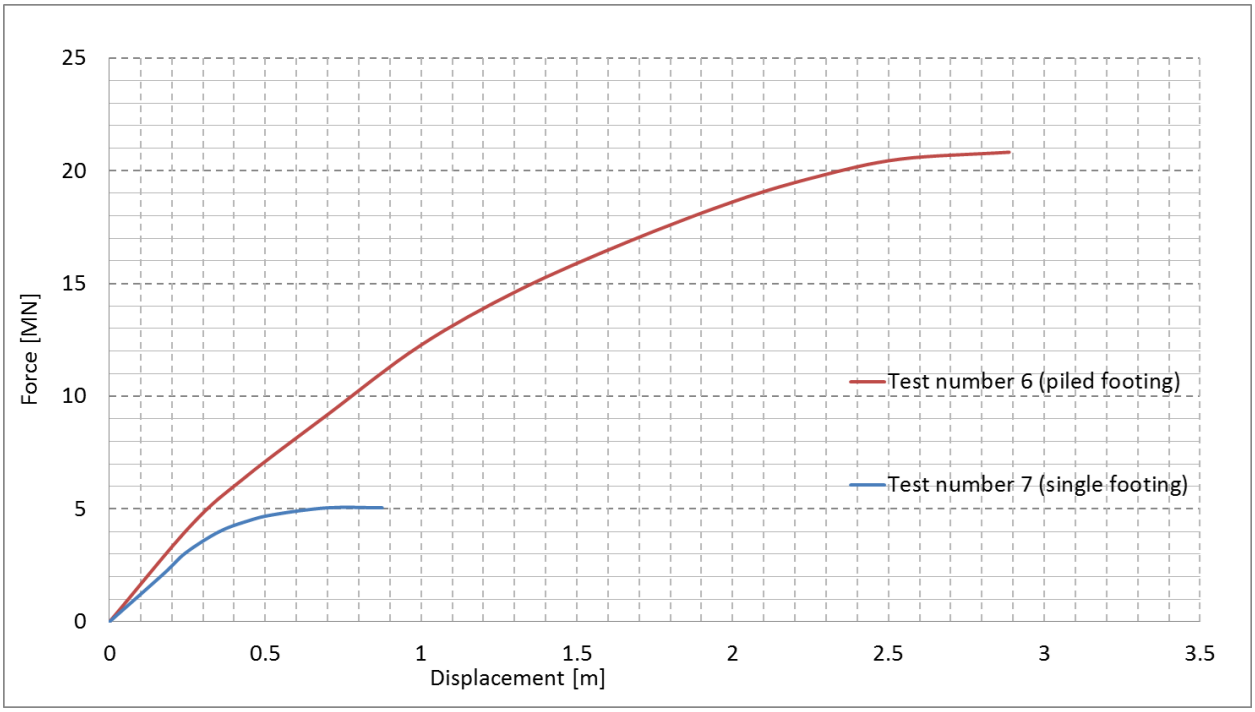

Figure 4-43. Results of tests number six and seven (vertical loads are in the range of 12.7 MN to 13.2 MN) (after Harloe 2010)

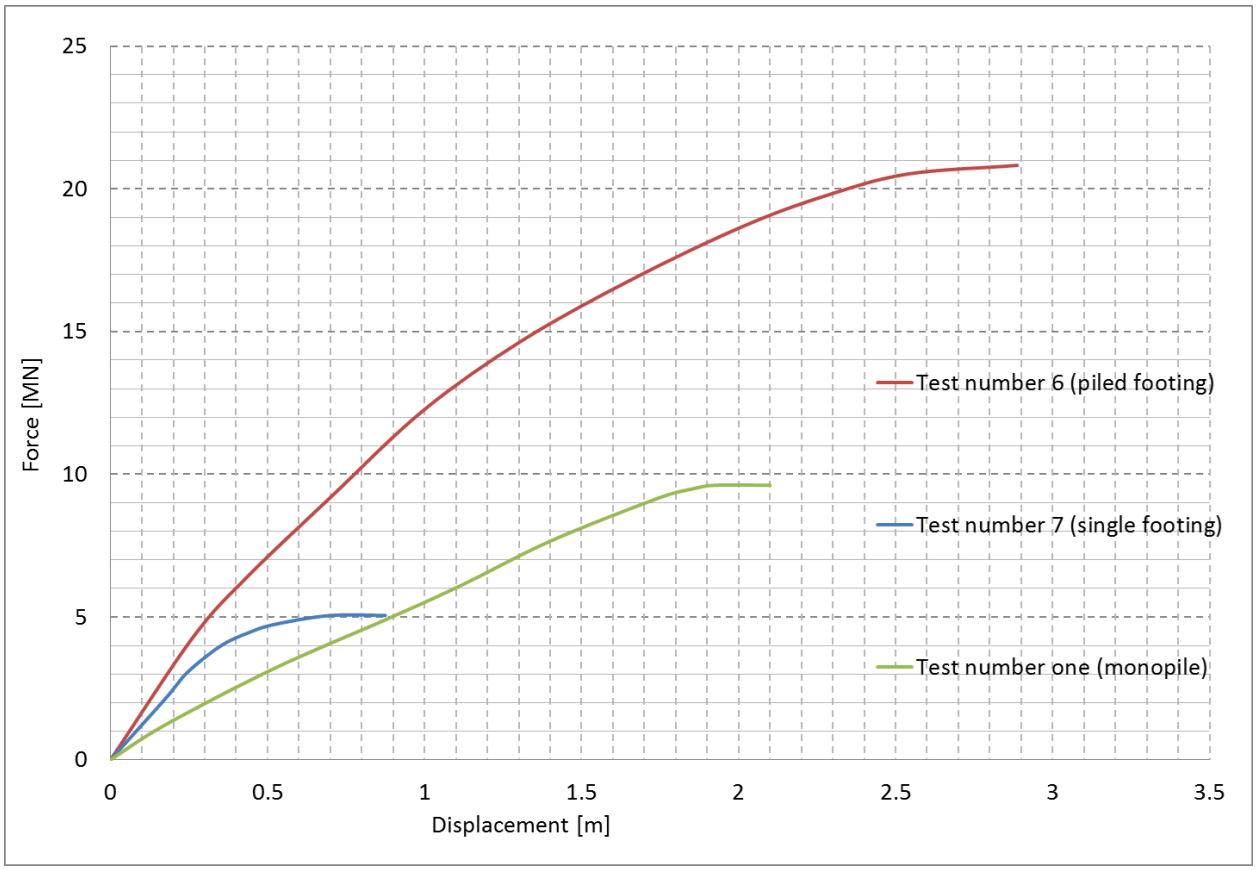

Figure 4-44. Comparing the results of the piled footing, single footing and the monopile structure (after Harloe 2010)

CHAPTER 5 THE CONSTRUCTED NUMERICAL MODELS

5.1 INTRODUCTION

In this section, an overview of the three dimensional models constructed for the eight tests conducted in the beam centrifuge described in Chapter 4 will be presented. The numerical predictions are individually compared with the test results and at the end, the results of the monopiles, piled footings and the un-piled footings will be compared and further discussed. The commercially available software ABAQUS 6.7 (Dassault Systèmes, 2007) was used to construct all the numerical models in this chapter. The main goal was to replicate the conditions in the beam centrifuge tests as closely as possible so that comparisons could be made between the tests and the numerical predictions. This would also ensure that the results of the tests described in Chapter 4 were accurate and acceptable. It must be noted that the results of Chapters 4 and 5 were published in: Increased performance of monopiles when combined with footings for tower foundations in sand (2014). *Journal of Geotechnical and Geoenvironmental Engineering (ASCE),* Vol. 140, No. 7.

Before deliberating on the constructed numerical models, the mechanical properties of the Aluminium bar and the soil used in the tests discussed in Chapter 4 will be considered in the upcoming sections.

5.2 THE MECHANICAL PROPERTIES OF THE SILICA SAND

As discussed in Section 4.3.3, the relative density of the silica sand used in the centrifuge tests was in the range of medium to dense. This assumption was made in regards to the CPT results illustrated in Figure 4-12 (considering only the results of CPT2 and CPT3, as discussed in Section 4.3.3).

The mechanical properties of the silica sand used in the beam centrifuge are given in Table 5-1 (Dyson, 1999).

Saturated unit weight (kN/m^3)	e_{max}	e_{min}	e	Poison ratio (ν)	G_s	Friction angle (critical)	Dilation angle	Cohesion (kPa)
19.92	0.76	0.49	0.55 – 0.6	0.3	2.65	32°	6°- 8°	0

Table 5-1 Characteristics of the Silica sand used in the beam centrifuge (after Dyson 1999)

Gourvenec et al. (2008) also adopted the soil properties represented in Table 5-1 for their numerical models constructed with ABAQUS. In her paper, she adopted tests conducted on the same silica sand in the drum centrifuge at UWA, as discussed in Section 2.8.5.

The relative density of the silica sand can be calculated by Equation 5-1. The relative density will be in the range of 60% to 77% depending on the in situ void ratio of the soil (e).

$$D_r = \frac{e_{max} - e}{e_{max} - e_{min}} \quad \textbf{5-1}$$

$$\gamma = \frac{(G_s + Se)\gamma_w}{1 + e} \quad \textbf{5-2}$$

The unit weight of the sand was calculated by Equation 5-2 and was equal to 19.92 kN/m^3. In Equation 5-2, S = 1 and e = 0.6. The degree of saturation was considered to equal unity because the soil was fully saturated during the testing procedure and the void ratio prior to testing was considered as the average of e_{max} and e_{min} of the soil. From the assumptions, it is clear that the effective unit weight of the soil will be equal to 10 kN/m^3.

The soil properties used in the numerical models were as in Table 5-1 with the effective unit weight of the soil considered for the numerical models. The effective unit weight of the soil was used in the numerical models because the soil during the testing procedure in the beam centrifuge was totally submerged under water. It must also be highlighted that a very small value for the cohesion was necessary for software to initiate the analysis (1 kPa).

For the Poisson ratio (ν), a value of 0.32 had to be adopted because Equation 5-3 was used for all numerical models. In this equation K_0 (lateral earth pressure at rest) was calculated as in Equation 5-4 (empirical equation provided by Jaky 1948) and it was equal to 0.47 (for $\phi' = 32°$) and the dilation angle in all numerical models was equal to 6° which is inline with the results of Table 5-1.

$$K_0 = \frac{\nu}{1 - \nu} \quad \textbf{5-3}$$

$$K_0 = 1 - \sin(\phi') \quad \textbf{5-4}$$

As discussed in Chapter 3 it is conventional to adopt a linear increase in the Young's modulus (E_{soil}) with depth for normally consolidated clays and sand deposits. On the other hand, a constant Young's modulus is well suited for overconsolidated clays in finite element modelling. As discussed by Pender (1993) at small strain levels a parabolic distribution of Young's modulus is also appropriate for sand deposits.

Booker et al. (1985) assumed a parabolic function similar to Equation 5-5 for the soil's modulus of elasticity.

$$E = m_E Z^{\alpha} \quad \textbf{5-5}$$

In Equation 5-5, m_E is considered as a constant value and α is a non-homogeneity factor, which can vary between zero to one (Gibson soil) as shown in Figure 5-1. For α between zero to one, equation 5-5 can represent cohesionless soils at small strains.

A linear increase in the soil's modulus is relevant for sands at moderate and high strain levels. In fact, at high strain levels the soil stiffness will decrease. The concept is illustrated in Figure 5-2. It is clear that when the strain levels are higher within the soil, the soil stiffness decreases and when the strain levels decreases the modulus of elasticity, the shear modulus and the bulk modulus will all increase.

To investigate the behaviour of the proposed structures and to capture the test results conducted in the beam centrifuge, two different variations of soil modulus of elasticity with depth were considered. Equations 5-6 and 5-7 were proposed for capturing the test results conducted in the centrifuge. To increase the modulus of elasticity in the numerical models for the soil body a Python script was used in conjunction with MATLAB [the Python script is given in Appendix A]. The latest equations were adopted on the basis of the relative density of the proposed sand (Figure 4-12). The (m_E, the multipliers) value in Equation 5-6 was fitted to match the lateral pile response and it approximately equates with $E_{soil} = 1.4q_c$.

$$E_{soil}\,(\text{kPa}) = 1500\,Z\,(\text{m}) \quad \textbf{5-6}$$

$$E_{soil}\,(\text{kPa}) = 4000\,Z^{0.7}\,(\text{m}) \quad \textbf{5-7}$$

In the above equations, Z is the depth in metres from the ground level. When using equation 5-6 a very small initial value for the modulus of elasticity had to be used so that the software could initiate the calculations (5 kPa).

Equation 5-7 was adopted in respect to the results of CPT3 (Figure 4-12) with considering the relative density to be very small at the ground surface. The heterogeneity parameter in Equation 5-7 is similar to the value adopted by Gourvenec et al. (2008) who conducted tests in the centrifuge on the same silica sand. Gourvenec mentions that a value of 0.7 was back calculated by trial and error using ABAQUS and this value clearly fits well with the results of CPT3 (Figure 4-12). It must be mentioned that as the pile lengths beneath the ground were 35 m, the adopted moduli of elasticity had to appropriately fit with the CPT results within that region.

A Mohr-Coulomb failure criterion was adopted for the saturated soil used in the tests conducted in the beam centrifuge. The adopted values are illustrated in Table 5-2.

Effective unit weight (kN/m^3)	Dilation angle	Friction angle	Poisson's ratio	In situ earth pressure	Elastic modulus (kPa)
10	6°	32°	0.32	0.47	Eq. 5-6 and Eq. 5-7

Table 5-2 Summary of soil parameters adopted for the finite element analyses

The values tabulated in Table 5-2 are also in a close agreement with the values adopted by Gourvenec et al. (2008) for the same silica sand used in their centrifuge tests.

5.3 THE MECHANICAL PROPERTIES OF THE ALUMINIUM BAR USED IN THE CENTRIFUGE TESTS

Aluminium, Magnesium and Copper are metals that do not exhibit a distinctive yield point beyond the elastic range, as shown in Figure 5-3. The usual practice is to define a nominal yield stress at a specific strain. Normally a 0.2% strain is chosen on the abscissa and then from that point a line parallel to the initial slope of the curve (that is parallel to the modulus of elasticity) is drawn until it touches the stress strain graph of the material. The point of intersection between the line parallel to the modulus of elasticity and the stress strain curve of the material will be the nominal yield stress of the metal, as shown if Figure 5-3. This graphical procedure in practice is called the offset method.

A major problem with the tests conducted in the beam centrifuge was that the Aluminium pipes used as pile/towers were in fact recycled from a previous set of experiments conducted on clays. It is clear that the metal would have strain-hardened due to recycling of the bars. This would indeed increase the yield point and the elastic region of the metal while the ductility would have decreased. In other words, the metal had a smaller plastic region than it had in its original state, as illustrated in Figure 5-4.

The pile/towers used in the centrifuge tests were constructed from Aluminium alloy 6060-T5. This alloy is common in Australia and New Zealand and therefore there is little data available for this alloy from the ASM (American Society of Materials) and www.matweb.com. The best way to obtain the mechanical properties of the bar was to directly contact the supplier and to request the mechanical properties of the Aluminium bar (Moaveni 2008).

The characteristics of the Aluminium bar are illustrated in Table 5-3.

Density	2700 kg/m^3
Modulus of Elasticity	69.5 GPa
Proof stress	185 MPa
Shear strength	140 MPa

Table 5-3 Physical properties of the Aluminium alloy (6060-T5)

To make sure that there were no manufacturing defects within the bars, two sets of tests were conducted. Both tests were carried out to identify the stiffness (modulus of elasticity) of the bar. The Baldwin testing machine at UWA was used to carry out both tests.

Figures 5-5 and 5-6 illustrate both bars used in the tests. The first test (Figure 5-5) was similar to a cantilevered beam while the second test was similar to a simply supported beam (Figure 5-6). For the first test (cantilever beam) the strain gauges were cemented very close to the fixed support, so very high moments were generated, and a false reading was recorded for the stiffness of the bar (the recorded stiffness was indeed very high). The results of this test were unacceptable and were disregarded.

As illustrated in Figure 5-6 the load applied by the Baldwin machine was applied at two points on the bar, which had an equal distance from both ends of the Aluminium bar (this was carried out by the aid of a stiff segment resting between the bar and the load application point from the Baldwin machine).

As shown in Figure 5-6 the simply supported bar used for calculating the stiffness was strain gauged at its centre. The Baldwin machine measured the amount force (kN) that was applied to the pipe and its subsequent displacements. The machine also recorded the amount of strain in volts from the attached strain gauges, which in fact had to be transferred to dimensionless values by using constant multipliers. These multipliers were related to the type of the strain gauges cemented on the pipe's body. Similar to the previous test, for generating the stress versus strain graph for the material, the moment acting on the bar at the strain gauge level was calculated and then by using the flexure equation, ($\sigma = \frac{My}{I}$) that moment was transferred to stress. Figure 5-7 shows the stress versus strain graph for the Aluminium bar. As illustrated in Figure 5-7 the modulus of elasticity of the bar was calculated to be equal to 69.7 MPa.

As can be seen, the modulus of elasticity of the material calculated from the test was in very close agreement with the value provided in Table 5-3. The proof stress in Table 5-3 is the yield stress of the metal obtained from the offset method.

For the numerical models, the modulus of elasticity and the initial yield strength of the bar was equal to 69.5 GPa and 185 MPa respectively. As previously mentioned, the bars would have strain hardened due to many tests conducted on them and so the yield stress of the material would have increased and some permanent and unrecoverable strain would have accumulated in the material's physical property.

Table 5-4 shows all the physical properties adopted in ABAQUS for the Aluminium bars used in the testing programme.

Density above water	2700 kg/m^3
Density under water	1700 kg/m^3
Modulus of Elasticity	69.5 GPa
Poison ratio	0.35
Initial Yield strength	185 MPa
Secondary Yield strength	250 MPa
Permanent strain	0.005

Table 5-4 Physical properties of the Aluminium bar used in the numerical models

To apply strain hardening to a structure in ABAQUS the values of true stress and true strain must be used. Equations 5-8 and 5-9 are conventionally used (Boresi et al. 2003 and Ugural et al. 2003) to calculate the true strain and stress values from the Engineering strain and stresses. In Equations 5-8 and 5-9, ε and σ are the engineering strains and stresses respectively.

$$\varepsilon_{true} = \int_{L_0}^{L} \frac{dL}{L} = \ln \frac{L}{L_0} = \ln(1+\varepsilon) \quad \textbf{5-8}$$

$$\sigma_{true} = \frac{P}{A} = \sigma \frac{L}{L_0} \quad \textbf{5-9}$$

As illustrated in Figure 5-8 the true and the engineering stresses and strains are actually the same in the elastic region (up to the yield point) but in the plastic region the stresses begin to deviate due to the decrease in the cross sectional area of the specimen. The latest point ensured that a value of 185 MPa could be used for the initial yield strength of the material. From Figure 5-8, it is also clear that the maximum deviation between the Engineering and the true stress and strains are within the necking region for a specified material.

After measuring the Engineering stress and strains, their values must be converted to the true values using Equations 5-8 and 5-9 and then the values can be used in ABAQUS. Unfortunately, the Baldwin machine was only able to record the strain values from the cemented gauges for the elastic region and consequently the stress versus strain graph could only be generated for the elastic section for the material.

The secondary yield stress was calculated by increasing the initial yield stress by around 30%. The norm of practice is to increase the initial yield stress in a range of 25% to 50% (Ugural et al. 2003). The value of 30% was chosen to make sure that the material would not get close to its rupture point (the ultimate yield stress of the material). The permanent strain was chosen in respect to stress versus strain graphs of Aluminium (Hibbeler 2005) and by trial and error using ABAQUS.

It must be mentioned that for the pipe section, which was submerged under the water a density of 1.7 kg/m^3 was assigned to the material while for the section above the water level a density of 2.7 kg/m^3 was considered for the Aluminium bar in the numerical models.

To model the footings used in the tests, Table 5-4 was used without considering the yield stresses of the material. As discussed in Section 4.4.9, in the centrifuge tests, the water level was standing at around 10 mm (1.75 m in a prototype) above the bearing plate (footing number one Table 4-4). So in fact, when modelling the pile footing and the un-piled footing cases with footing number one used at the ground level only the submerged density (1.7 kg/m^3) of the footing had to be considered, as the whole footing was under water during the testing programme.

5.4 NUMERICAL MODELS CONSTRUCTED FOR THE CENTRIFUGE TESTS

5.4.1 The soil body characteristics in the constructed numerical models

To mimic the tests conducted in the centrifuge, a soil block with the dimensions of 200 × 200 × 100 (m) (the 100 m was the height of the soil block) were considered for the all numerical models in ABAQUS. The boundaries of the soil block were considered far from the structures so that the effects of the boundaries would be minimal on the end results. As discussed by Logan et al.

(2011) for footings on soils the influence of the footing becomes insignificant when the horizontal distance of the model is almost four to six times the width (or diameter) of the footing while the vertical distance should be taken as four to ten times the width of the footing. It must be noted that none of the constructed models in this section contained reflective symmetry.

Three different types of soil blocks were generated to capture the results of the eight tests conducted in the beam centrifuge. The soil block dimensions were all the same but as shown in Figures 5-9 to 5-11 they contained different types of cuts so relevant structures related to each test could be installed within them.

As shown in Figures 5-9 and 5-10 the length of the pile beneath the ground was considered 35 m (equal to 200 mm in the centrifuge tests with an acceleration of 175 g). As illustrated in Figures 5-10 and 5-11 the footing embedment depth for the piled footing and the un-piled footing structures were equal to 0.35 m (2 mm in the tests) and so the soil was cleaved on its upper surface to host the footings.

For all three-soil blocks, the material properties were considered as in Table 5-2. As in the case of all numerical packages, ABAQUS is able to mesh each selected part by itself. Unfortunately, because the proposed soil body had a cubic shape, the software could only use four noded linear tetrahedral elements (Q4) to mesh the soil block. To overcome this problem, the proposed soil bodies were all partitioned as shown in Figures 5-9 to 5-11 so that brick elements could be used within the soil block too. Further discussion on the mesh type for the soil block will be provided in Section 5.4.1.2.

5.4.1.1 Boundary conditions

The boundary conditions imposed on the soil bodies for all numerical models were similar to each other. The base of all numerical models was restricted from movement in all directions and so a complete fixity was imposed on the base of the models, as illustrated in Figure 5-12.

For the sidewalls of the soil block, only movement in the vertical direction was permitted. That is in fact because horizontal displacements must become negligible far from the load application point. The boundary condition imposed on the sidewalls of the soil block hosting the un-piled footing is illustrated in Figure 5-13.

5.4.1.2 Element selection for the mesh

As previously discussed in Section 5.4.1, the soil body was partitioned in such a way that using four noded linear tetrahedral elements (Q4) could be partially avoided.

The soil body constructed for all models contained two different types of meshes. As illustrated in Figure 5-14 the middle part of the cubic soil body contained linear tetrahedral elements (ABAQUS names them C3D4) while the outer part of the soil body was meshed by eight noded brick elements which ABAQUS names them C3D8R elements. It must be noted that all elements involved were three-dimensional solid stress elements.

For the brick elements on the soil body a reduced integration with an hourglass control scheme was adopted. Changing the reduced integration method on the soil body did not have any significant effect on the predicted results by ABAQUS, so to decrease the computational time a reduced integration scheme was adopted for the brick elements on the soil body.

It must be noted that using a cubic soil body restricts the user from adopting any higher order elements on any other part instances (footings and pile/tower) in the generated models. So in fact, only linear elements were used for all part instances constructed in the numerical models. This restriciton was because of compatibility issues in regards to mesh generation between different segments of the models. The mesh generated for each part instance for different models will be further discussed in the upcoming sections.

As discussed by Cook et al. (2002) and Logan et al. (2011) the problems associated with constant-strain triangle elements (CST) and bilinear quadrilateral elements in a plane strain case are transferred to the 3D situations as well.

The major problems with the CST elements are shear locking and problems associated with bending. As shown in Figure 5-15, Cook et al. (2002) applied a pure bending to a cantilever beam and expected a linear variation in σ_x from the outer section up to the neutral axis (as in the beam theory). From Figure 5-15, it is clear that σ_x remains constant with depth and the stress is independent of $\varkappa$ (displacement). In addition, they mentioned that the result of τ_{xy} displays a wave pattern as illustrated in Figure 5-15.

Another problem associated with CST elements, which is indeed transferred to tetrahedral elements (Q4) in a three dimensional scenario, is shear locking. As shown by Cook et al. (2002) in Figure 5-16 if the lower left element of the bar is chosen from the beam under pure bending with considering two degrees of freedom and using Equation 5-10 with considering $x_2 = a$ and $x_3 = 0$ for the proposed element we obtain $\varepsilon_x = u_2/a$, $\varepsilon_y = 0$ and $\gamma_{xy} = v_2/a$.

Equation 5-10 is indeed the strain displacement [B] matrix for a CST element.

$$\begin{bmatrix} \varepsilon_x \\ \varepsilon_y \\ \gamma_{xy} \end{bmatrix} = \begin{bmatrix} \frac{-1}{x_2} & 0 & \frac{1}{x_2} & 0 & 0 & 0 \\ 0 & \frac{x_3 - x_2}{x_2 y_3} & 0 & \frac{-x_3}{x_2 y_3} & 0 & \frac{1}{y_3} \\ \frac{x_3 - x_2}{x_2 y_3} & \frac{-1}{x_2} & \frac{-x_3}{x_2 y_3} & \frac{1}{x_2} & \frac{1}{y_3} & 0 \end{bmatrix} \begin{bmatrix} u_1 \\ v_1 \\ u_2 \\ v_2 \\ u_3 \\ v_3 \end{bmatrix} \quad \textbf{5-10}$$

As can be seen, the element is displaying a transverse shear strain (γ_{xy}), which in fact does not exist. This parasitic shear absorbs energy and so some of the energy that must go into bending is lost. This causes the elements to be stiff and the resulting deformation is smaller than the actual values. The described phenomenon that occurs in CST elements is called shear locking and it is inherited by the linear tetrahedral elements (Q4) in a three-dimensional analysis as well. The only way to improve the accuracy of the results for these elements is by increasing the mesh density, but as mentioned by Cook et al. (2002) and Logan et al. (2011) the accuracy of the results for these elements converge to the exact solutions very slowly.

Another problem with these tetrahedral elements is that they can cause volumetric locking if high Poisson ratios are used. In fact, for rubberlike materials (or as in the case of saturated clays), where the Poisson ratio is close to 0.5, these elements can lock and become immovable. This excessive stiffness is usually referred to as locking in finite element analysis.

To avoid the effects of the spurious shear stress, a very dense mesh was considered for the centre of the soil block and, as discussed by Cook et al. (2002), an under integration method was adopted for the mesh generated on the outer parts of the soil block (this also reduced the computational time). Cook et al. (2002) discusses that using an under integration scheme reduces or eliminates the parasitic shear strain which is developed in four noded quadrilateral elements and this will be further investigated in the upcoming sections.

5.4.1.3 The mesh density on the soil blocks

Six numerical models were generated by ABAQUS to capture the test results conducted in the beam centrifuge at UWA. In addition to these models, four other models were required for comparison purposes as there were small discrepancies within the conducted tests. The details of each model and their results will be further discussed in the upcoming sections but as previously mentioned only a complete square shaped block of soil was used to mimic the strong box for all tests conducted in the centrifuge. The mesh types on the rectangular block for all models were the same but with different number of elements and nodes as the un-piled footing structures required a slightly denser mesh around their footing region. It must be reminded that a very dense mesh was used for the central segment of the soil block for all soil models.

The total number of elements (hexahedral and tetrahedral) and the number of nodes used in each model will be further discussed in the upcoming sections.

5.4.1.4 The mesh density on the soil body for the monopiles and the piled footing structures

The soil block used for modelling tests number one, three, five, six and eight (Table 4-2) adopted the following mesh density:

Total number of elements: 83503

Total nodes: 38611

Linear hexahedral elements (C3D8R): 24000

Linear tetrahedral elements (C3D4): 59503

5.4.1.5 The mesh density on the soil body for the un-piled footing structures

For tests number two, four and seven (Table 4-2) the mesh density around the footing had to be increased. That is in fact because in this structure the soil failure controlled the structure's behaviour. The mesh density on the soil block for the three footing structures was as follows:

Total number of elements: 86457

Total nodes: 39170

Linear hexahedral elements (C3D8R): 24000

Linear tetrahedral elements (C3D4): 62457

As discussed by Cook et al. (2002) the same problems associated with bilinear rectangle (Q4) elements in a two dimensional case will be transferred to a three dimensional linear hexahedral element (Q8). In a two dimensional case a linear hexahedral element (Q4) will exhibit parasitic shear during bending. In addition, the accuracy of four noded quadrilaterals elements can be improved by adding incompatible modes or by under integrating the element stiffness matrix. These procedures may even eliminate the parasitic shear strain for stress analysis elements. They also mention that for non-uniformly spaced side nodes an under integration scheme can provide more accurate results. In addition, using low order quadrature rules may introduce other spurious problems like the softening effect and this is because some of the polynomial terms vanish at Gauss points for a low order rule and so they do not contribute to strain energy.

As previously mentioned, for the linear tetrahedral elements, the only way to increase the accuracy of the results was to use a dense mesh on the inner segment of the soil block. In regards to the conclusions made by Cook et al. (2002), an under integration with an hourglass control scheme was adopted for the linear hexahedral elements in the soil block but as previously mentioned this would not seriously affect the results of the analysis as these element were far from the load application point. On the other hand, adopting a reduced integration scheme on the pile/tower structure for the piles and the piled footings did affect the results, this will be further discussed in the upcoming sections.

5.4.2 Summary of the constructed models for the tests conducted in the centrifuge

As previously discussed in Section 4.4, eight tests were conducted in the beam centrifuge by Harloe (2010) to investigate the behaviour of different proposed structures under a monotonic lateral load at UWA. To capture the test results with ABAQUS six models similar to the tests were required for comparison purposes. Table 5-5 illustrates a summary of the constructed models, as previously mentioned, in this table the vertical loads (VL) were considered from above the foundation level.

As discussed in Section 4.4.2, test number two (Table 5-5) was not completed but the numerical model for this test will be constructed and its result are compared with the result of the section of the test, which was obtained during the testing programme. The result of test number two (not completed) will also be compared with the results of models number four and seven (Table 5-5).

Test number	*Model number with the applied vertical load*	*Type of structure*
Test number one (VL=5.3 MN)	Model number one	Monopile
Test number two (VL=9.3 MN)	Model number two	Un-piled footing
Test number three (VL=6.5 MN)	Model number three	Piled footing
Test number four (VL=5.9 MN)	Model number four	Un-piled footing
Test number five (VL=6.4 MN)	Model number three	Piled footing
Test number six (VL=13.2 MN)	Model number five	Piled footing
Test number seven (VL=12.7 MN)	Model number six	Un-piled footing
Test number eight (VL=6.5 MN)	Model number one	Monopile

Table 5-5 Summary of the constructed models and the conducted tests in the centrifuge

As discussed in Sections 4.4.4 and 4.4.7 during the testing procedure for the un-piled footing cases the solid bar was not completely drilled and its thickness was not equal to the thickness of the pipes used in the monopile and the piled footing structures. During the testing programme, the last 65 mm (equivalent to 11 m) of the pipe used in the un-piled footings was full and so this will indeed increase the vertical load on the footing and that can alter the results, as vertical loads can seriously affect the capacity of the footing structures. In addition, during the testing procedure on the monopile and the piled footing structures, a collar was used around the pipe's body. This will indeed affect the stiffness of the structure and the outcome of the results.

To overcome the discrepancies in the tests, three extra models were generated with a uniform pipe thickness and no collar attached to the pile and the piled footing structures. In addition, one extra model was generated to investigate the behaviour of the monopile structure with extra loads attached to it (the loads were applied by attaching footings to the tower, as in the case of the tests). The latest model was constructed for comparison purposes with tests number one and eight (monopiles) conducted in the centrifuge to illustrate how much the lateral capacity of a single pile will raise under the effects of a vertical load. Table 5-6 presents the four extra models constructed for comparison purposes. The vertical loads (VL) in this table were considered from above the foundation level, similar to Table 5-5.

Model number	*Test number*	*Type of structure*
Model number seven (VL = 12.5 MN)	No test data	Monopile
Model number eight (VL = 3.75 MN)	No test data	Un-piled footing
Model number nine (VL = 3.75 MN)	No test data	Piled footing
Model number ten (VL = 3.8 MN)	No test data	Monopile

Table 5-6. The four numerical models generated for comparison purposes

5.4.3 Model number one corresponding to tests number one and eight conducted in the centrifuge (Monopiles with VL = 5.3 & 6.5 MN)

This model was constructed of the soil body, a pile/tower and a collar resting on the tower's body. The results of tests number one (monopile, VL = 5.3 MN) and eight (monopile, VL = 6.5 MN) conducted in the centrifuge are illustrated in Figure 4-40. As previously mentioned, these two tests are very similar to each other. The only difference between the two tests is that in test number eight a cap was present on top of the Aluminium tower.

From Figure 4-40, it is clear that the weight of the cap on the pile/tower's head in test number eight (monopile, VL = 6.5 MN) does not significantly influence the stiffness of the structure in comparison to test number one (monopile, VL = 5.3 MN). As previously discussed, the major difference between the two test results is in fact in the yield point of the pipe. As discussed, the pipes would have definitely strain hardened during the testing programme and that is because they had all been used in another set of tests conducted in the centrifuge. Therefore, the difference between the two test results is only due to the amount of strain hardening which has occurred in each individual pipe. Due to this point, only one numerical model was necessary to capture both tests. In the constructed numerical model, the weight of the cap acting on the pile/tower head during test number eight (monopile, VL= 6.5 MN) was transferred to a stress and its value was applied to the pile's head (the cap itself was not constructed for the numerical models).

For test number one, the mechanical properties of the pile/tower are illustrated in Table 5-4 but for test number eight it will be illustrated that a higher yield point was required. It seems that this problem (having a higher yield stress) was only the case for test number eight and so the values of Table 5-4 were all well suited for other tests conducted in the centrifuge.

The strain hardening of the bar will be further discussed in Sections 5.4.3.4 and 5.4.3.5.2.

5.4.3.1 The pile/tower and collar's geometry and mechanical properties

The pipe's dimensions were provided in Table 4-3 and it was also mentioned that the pipe was embedded 200 mm (equal to 35 m in a prototype) in to the silica sand. So as shown in Figure 5-9 the soil was cut to a depth of 35 m to host the pile's body.

The total length of the pile/tower was equal to 67.725 m and it was constructed out of a three-dimensional deformable body with an outer diameter of 3.3 m. The pile/tower was cut extruded with an inner diameter of 3 m, as it was hollow, as illustrated in Figure 5-17.

Four partitions were constructed on the pile's body. The first partition was constructed at a height of 35 m from the base of the pile, the second partition was constructed at a height of 2.6 m (equal to 15 mm in the centrifuge tests) above the ground level, and that was because the pipe was totally submerged under water up to height of 37.6 m from its base.

The first partition on the pile/tower was to tie the pile to the soil block. The second partition, which was located at 37.6 m above the pile's base, was only used to apply the buoyant unit

weight to the pile region, which was above the ground level; this is because the mentioned region was submerged during the testing programme.

The third and fourth partitions on the pile/tower were to tie the collar to the tower's body at the desired location. The collar was positioned at around 30 mm (equal to 5.25 m in a prototype) above the ground level during the tests (number one and eight) conducted in the centrifuge, as shown in Figure 4-16. The total distance between the two generated partitions on the tower's body was equal to 7.875 m and that is equal to the total height of the collar used during the tests, as illustrated in Figure 4-10.

It must be mentioned that all partitions constructed on the pile/tower body where by setting datum points at the required locations and then partitioning the section by the aid of those points.

The material properties chosen for the pile/tower section are tabulated in Table 5-4. For the regions below the water level (37.6 m from the bottom of the pile), a buoyant unit weight was assigned to the pile section while for the region above the water level, a value of 2.7 kg/m^3 was assigned for the material density in the constructed numerical models. The two different material properties adopted for the pile/tower has been illustrated in Figure 5-18.

As previously mentioned, the collar's dimensions are illustrated in Figure 4-10. The constructed collar in the numerical models was made-up from one-part instance by revolution and it had a three-dimensional deformable body.

The collar was cut extruded with a circle (diameter of 3.3 m) as shown in Figure 5-19. The total height of the collar in the numerical models was 7.875 m and the outer diameter was equal to 5.075 m (similar to the dimensions of the real collar illustrated in Figure 4-10).

The mechanical properties of the collar were exactly as the material properties assigned to the pile/tower section above the water level and that is because the collar was made out of Aluminium. Therefore, the same material properties as in Table 5-4 were assigned to the collar but without considering the yield stresses, so in fact, the collar was constructed as an elastic material and that is because the stresses acting on the collar were not of a great importance in this study.

5.4.3.2 Assembly, Step and Interaction

Figure 5-20 shows the assembled pile/tower and collar together. Figure 5-21 illustrates the whole structure with the soil body used in the analysis.

Two steps were sufficient for completing the analysis. The first step was for applying the gravity to the entire model and the other was for applying the lateral load to the tower's head. Both steps in the numerical models were static general steps (by adopting this procedure there was no need to use the geostatic sentence in the keyword editor in ABAQUS). However, as previously mentioned, Equation 5-3 was necessary to calculate the Poisson's ratio by the aid of the in situ coefficient of earth pressure.

As a Mohr-Coulomb failure criterion was considered for the soil body, it was essential to select an unsymmetric matrix solver for both steps involved in the analysis. In ABAQUS an unsymmetric matrix solver is necessary for a Mohr-Coulomb failure criterion, if this option is not chosen the model will face converges problems (ABAQUS manual, 2009).

A full Newton scheme was also adopted for the numerical models. In addition, there was no need to change the initial, maximum and minimum increment size values provided by ABAQUS. These values are usually altered if numerical models run into convergence problems, for the constructed numerical models in this chapter none had such problems.

All part instances (footing, pile/tower and the soil block) in the constructed models were tied to each other in accordance with the adopted mesh density for each part instance. As a whole, two tie constraints were necessary for this model, the first tie was between the soil and the pile and the second constraint was between the tower and the collar.

Figure 5-22 illustrates the selected surfaces on the pile section and the soil body, which interacted with each other.

Figures 5-23 and 5-24 illustrate the selected surfaces on the pile/tower section and the collar to interact with each other respectively.

It must be noted that tying the pile to the soil body is similar to considering a rough interface between the two structures.

5.4.3.3 Applied loads, Boundary Conditions and the Generated Mesh

As previously mentioned, gravity was applied to the entire model (all part instance) in a single static general step. The gravity load was created in the first step and was propagated to the second step of the analysis.

As discussed in Section 4.4.9 the water level was standing 15 mm (equivalent to 2.6 m in prototype) above the ground level when the tests were conducted, so a pressure of 25.5 kPa was acting on the ground surface due to the weight of the water. Because the effective stress at the seabed level is zero this water pressure was not introduced to any of the models.

As discussed in Section 4.4.10 the load application piece was installed on the pipe for the duration of the tests (number one and eight). In addition, for test number eight a cap was also present during the testing procedure.

For the numerical model, replicating test number one (monopile, VL = 5.3 MN), where only the load application piece was present during the testing procedure, a pressure load was applied to the pile/tower's head, so in fact the load application piece was not modelled and only its vertical load was transferred as a pressure. For test number eight (monopile, VL = 6.5 MN) the same procedure was adopted and in addition, the cap's weight was also added to the weight of the application piece and then its value was transferred to a pressure load acting on the pile/tower's head. For test number one the force acting on the pile/tower's was equal to 2.2 MN while for test number eight a force equal to 3.5 MN was acting on the tower's head. The pressures present in

the numerical models were equal to 1.49 MPa and 2.3 MPa for tests number one and eight respectively.

Similar to the gravity applied to the model, the pressure generated on the pile/tower's head was created in the first step and it was then propagated to the second step of the analysis. This indeed is because the weights acting on the pile/tower were present from the very start of the testing programme.

Figure 5-25 illustrates the gravity applied to the entire structure with the applied pressure acting on the pile/tower for model number one.

As a whole, three boundary conditions were imposed on the numerical models. Two boundary conditions were acting on the soil body as explained in Section 5.4.1.1 and the third boundary condition was imposed on the tower's head.

In the numerical models, the monotonic horizontal force acting at the tower's head was mimicked by imposing a displacement on it. To do so a boundary condition was imposed on the pile/tower's head rather than a concentrated force. Applying a concentrated force at one or two particular points could have caused extreme localized distortions and so to overcome the problem a boundary condition was imposed to the entire pile/tower's head surface, as illustrated in Figure 5-26.

Cook et al. (2002) states that a displacement solution converges to the exact solution from the "stiffer" side in an average sense. They also mention that the approximate displacements have a higher accuracy compared to the approximate stresses. The latest is because the stresses are calculated from the derivatives of the approximating filed and it is clear that the accuracy of the results will diminish as successive derivatives are made.

To apply a boundary condition on the tower's head in the numerical models a "Set" had to be introduced, this indeed will allow the user to apply any kind of displacements to the predefined set in any particular direction. This will also allow the reaction forces to be read off the predefined set at the end of the calculation.

As discussed in Chapter 4 the monotonic lateral force in the centrifuge tests were applied horizontally to the pile/tower at 26.25 m (in a prototype) above the ground level by the aid of the load application piece attached to the tower's body. In the numerical models, the horizontal boundary condition was applied to the tower's head in the second step of the analysis. Although this would generate slightly higher moments at the ground level in the numerical models, there was no way to apply a boundary condition on the tower's body (its surface) at 26.25 m above the ground level. In addition, in a real scenario the horizontal forces act on the tower's head not on the towers body (discussed in Chapter 2).

By applying a boundary condition to the tower's head, there was no need to use the horizontal loads given in Table 4-5 for the models, that is because the reaction forces would be read off the pile/tower's head and then the results could be compared with the test results. As previously

mentioned the only vertical force, which had to be taken into account for the models is the stress caused by the load application piece and the cap for tests number one and eight.

The collar was meshed by linear tetrahedral elements as shown in Figure 5-27.

The mesh density on the collar was as follows:

Total number of nodes: 120

Total number of linear tetrahedral (C3D4) elements: 307

Linear hexahedral elements were chosen for the pile/tower's body, as illustrated in Figure 5-28.

The mesh density for the pile/tower section is as follows:

Total number of nodes: 2576

Total number of linear hexahedral (C3D8R) elements: 1274

For the mesh generated on the modelled pile/tower, a reduced integration scheme with an hourglass control criterion was selected. As discussed in Section 5.4.1.3 Cook et al. (2002) concludes that the same problems associated with bilinear rectangle (Q4) elements in a two-dimensional case will be transferred to a three-dimensional linear hexahedral element (Q8). In a two dimensional case a linear hexahedral element (Q4) will exhibit parasitic shear during bending. Therefore, it is obvious that for a prescribed bending deformation the bending moment required to produce it would be larger than the correct value. This is similar to the shear-locking problem associated with linear tetrahedral elements. To overcome the problem, a reduced integration scheme was adopted for the pile/tower in the numerical models (the results will also be compared with full integrations in the upcoming sections to illustrate the accuracy of the results).

Figure 5-29 illustrates both the constructed pile/tower and collar attached together in the numerical model and in the experimental test.

As previously mentioned the load application piece and the cap used during the experimental tests were not modelled, but it must be noted that the weight of the cap and the application must not seriously affect the outcome of the results, this will be illustrated in the upcoming sections. Karthigeyan et al. (2006) discussed the latter point; he illustrated that increasing the vertical load does not significantly increase the lateral capacity of a single pile embedded in a sand deposit (Section 2.7).

5.4.3.4 Comparing the monopile test results with the finite element predictions

In this section, the results of tests number one and eight will be compared with the predicted results from the finite element models. These predictions will also be in regards to different soil moduli adopted for the soil body, as discussed in Section 5.4.1.

As previously mentioned, a displacement was introduced to the tower's head as a boundary condition. To generate a force versus displacement graph for each constructed model (similar to

the test results) the reaction forces of all nodes for the pile/tower's head in the direction of the imposed boundary condition had to be summed up and graphed versus the displacement of a single node located on the pile/tower's head. As all nodes associated with the pile/tower head will have the same amount of displacement, one randomly chosen node will be sufficient to predict the displacement. These required procedures can all be handled in ABAQUS's working environment without using any other software. Figure 5-30 illustrates all the nodes associated with the pile/tower head, which were used for plotting the force versus displacement graphs.

As previously mentioned, to initiate the calculations for Equations 5-6 and 5-7 a very small value of E_{soil} was required at the ground level (5 kPa). As the soil, modulus of elasticity (E) at the ground level is usually considered to be zero none of the proposed equations for E_{soil} (Equations 5-6 and 5-7) contained a constant value in their body, this ensures that the soil's modulus of elasticity was very small at the ground level.

After completing step one (gravity load) the amount of settlement in each model was checked so that the model would not have undergone extreme deformations after application of gravity. As previously mentioned, if a geostatic step was used in ABAQUS to apply the gravity load to a model, the deformations (settlement) after completing the proposed step (the geostatic step) had to be extremely small but if a static general step is used (as in this case) the deformations can be neglected if they are not extremely high. Using the static step is similar to constructing a dummy analysis for the in situ stresses in the soil.

As discussed in Section 5.4.3.2 the part instances in all constructed models were tied to each other and so by choosing this option we will avoid any kind of differential settlements that might take place between the pile/tower and the soil. In fact any extraneous, shear stress that might be generated due to the difference of material properties (Young's modulus, Poisson ratio and the unit weight) between the soil and the pile/tower has been avoided by tying the part instances together for all constructed models.

The maximum amount of settlement for a linear increase in the soil's Young modulus was around 230 mm after applying gravity to the entire model; this value was indeed negligible.

It must be noted that there was no significant changes detected in the numerical results between when a pressure load was applied to the tower's head compared to when there was no pressure applied to it and this is in line with the results of Karthigeyan et al. (2006). This means that the weight of the application piece and the cap were not significant enough in the numerical models to change the predicted trend for the monopile case.

Figure 5-31 illustrates the finite element predicted results with E(kPa) = 1500 Z (m) for test number one (monopile, VL = 5.3 MN). As can be seen two different analysis schemes were used for the generated mesh on the pile/tower constructed in the numerical models, one is with a reduced integration scheme and the other is considering a full integration. It is obvious that the remedies discussed by Cook et al. (2002) mentioned in Section 5.4.3.3 are working very well for the constructed model. In these models, only the weight of the application piece was considered.

Figure 5-32 illustrates the results of test number eight and the predicted results obtained from the finite element analysis with E(kPa) = 1500 Z (m) with a reduced integration and a full integration scheme. The weight of the load application piece and the cap was considered in these numerical models. However, the yield stress in the Aluminium bar was higher than the adopted values in Table 5-4, but it is still clear that the remedies discussed by Cook et al. (2002) are acceptable.

To check the effects of the cap's weight over the behaviour of the structure, as previously mentioned, a pressure load equivalent to the weight of the cap was applied to the pile/tower's head from the first step of the analysis. The applied pressure was equal to the weight of the cap divided by the cross sectional area of the hollow pipe. It is clear that this pressure load (from the cap) must not be significant enough to make any considerable contribution to the results obtained from a single pile without a cap (discussed by Karthigeyan et al. 2006). Figure 5-33 illustrates the results obtained from a pile/tower under a monotonic lateral load with and without the weight generated from the cap compared with the results of test number one; these results are for a linear increase in the soil's modulus of elasticity and with a reduced integration scheme. As can be seen, there will be no changes in the predicted results what so ever. This is consistent with the results obtained by Karthigeyan et al. (2006) discussed in Section 2.7.

The FE results with a parabolic increase in the soil modulus are plotted against the results of test number one in Figure 5-34. As in the previous case (a linear increase in the soil modulus), the reduced integration scheme provides a better result compared to a full integration. For this case, the pressure load from the load application piece was applied to the tower's head during the analysis, as this was the case for test number one.

Figure 5-35 illustrates the results of test number eight (monopile, VL = 6.5 MN) and the predicted results obtained from the finite element analysis with a parabolic increase in the soil's modulus of elasticity for a reduced and a full integration scheme.

As in the previous case, the increase in the stiffness of the structure due to the weight of the cap was also investigated with the nominated parabolic modulus of elasticity. As can be seen from Figure 5-36 there is no difference between the results of the laterally loaded pile/tower in test number one when the weight of the cap was present.

From Figures 5-33 and 5-36, it can be concluded that the discrepancy in the results of test number one and eight was entirely related to the amount of strain hardening, which occurred during the testing procedure. In fact, both tests have a very similar stiffness and only the yield point of the material has changed, which was a proof to the strain hardening of the bar during the testing programme.

Figure 4-19 illustrates the deformed pipe's shape at the end of test number one (monopile, VL = 5.3 MN). As shown in this figure and discussed in Sections 4.4.1 and 4.4.8 the hollow pipe in the tests yielded between 3 to 7 m below the ground surface for tests number one and eight respectively.

Due to the higher accuracy attained in the reduced integration scheme only the Von Mises stresses acting on this hollow pile/tower in the FE models will be compared with the test results

(tests number one and eight). Figures 5-37 and 5-38 illustrates the Von Mises stresses with their maximum and minimum values for model numbers one (VL = 5.3 MN) and eight (VL = 6.5 MN) respectively for a linear increase in the soil's modulus of elasticity. The location of the maximum Von Mises stresses starts from just about the ground level and extends to a depth of around 7 m below the ground surface. It is also clear that there is no difference between the maximum stresses acting on the pile/tower section for different pressures acting on it.

Figures 5-39 and 5-40 illustrate the maximum and minimum stress (Von Mises) acting on the pipe/tower with a reduced integration scheme and a parabolic increase in the soil's modulus of elasticity. Form the latest figures it is again clear that the maximum values are the same.

It is interesting to note that the maximum values of the Von Mises stresses between a linear and a parabolic increase in the soil's modulus of elasticity with different stress values are all the same. In addition, the location were these stresses are acting are very similar to each other irrespective of the type of increase in soil's modulus of elasticity. Therefore, it is clear that considering a linear or a parabolic increase in the soil's modulus of elasticity will not significantly affect the lateral capacity of these structures (pile/towers with high eccentricities).

It must also be noted that if the cap present in test number eight (pile with application piece and cap) would increase the lateral capacity of a monopile; the entire graph of that test would have plotted to the left of the single pile's test (pile without a cap, test number one). However, as can be seen in Figure 4-40 this is not the case and so it can be concluded that test number eight has a higher capacity in respect to test number one only due to the effects of strain hardening generated in the Aluminium bar.

It was illustrated that increasing the vertical load on the pile/tower's head (adding the cap pressure) from the first step of the analysis will not increase the ultimate lateral capacity of the pile/tower in a medium to dense sand. In addition, the vertical load generated by the cap acting on a single pile/tower (test number eight) is not sufficient to contribute to the stiffness of the pile in the numerical models. This is also clear in the centrifuge tests as the stiffness of the two structures are in a very close agreement with each other (Figure 4-40).

The accuracy of the FE results constructed for tests number one & eight can be checked in respect to the solutions provided by Broms (1964) and Fleming et al. (1992). In the upcoming sections, this comparison will be illustrated.

5.4.3.5 Broms and Fleming's solutions for calculating the ultimate lateral capacity of the monopiles in the centrifuge tests

In Sections 2.6.2 and 2.6.4, the methods for calculating the ultimate lateral capacity of a single pile by Broms (1964) and Fleming et al. (1992) were discussed respectively. These two methods can be used to evaluate the ultimate lateral capacity of the single pile for tests number one and eight conducted in the centrifuge.

5.4.3.5.1 Broms solution for calculating the ultimate lateral capacity for tests number one and eight

As discussed in Section 2.6 a single long pile under a monotonic lateral load will fail by forming a hinge at some point along its body, this was the case for tests number one and eight conducted in the centrifuge. The latter ensures that the piles were long and so Equations 2-44 and 2-45 provided in Section 2.6.2 in conjunction with Figure 2-34a can be used to calculate the ultimate lateral capacity of the two piles in tests number one an eight conducted in the centrifuge.

By using, the values tabulated in Tables 5-2, 5-4 and 4-3 all the required parameters can be calculated for Figure 2-34a. From Equations 2-44 and 2-45 the passive earth pressure (K_p), was equal to 3.25 while the yield moment (M_y) was equal to 279.44 MNm (using the flexure equation). The following calculation illustrates the required parameters for using Figure 2-34a.

$$\frac{M_y}{D^4 K_p \gamma'} = 72.5$$

$$\frac{e}{D} = 7.96$$

For a free head pile, the ordinate will be equal to 7.65 and so the calculation will follow as below:

$\frac{Q_u}{K_p D^3 \gamma'} = 7.65$ Which gives Q_u = <u>8.94 MN</u>

From Figure 5-33, it is clear that the calculated result is in a very close agreement with test number one and with the FE results for a maximum yield stress of 250 MPa.

5.4.3.5.2 Fleming's solution for calculating the ultimate lateral capacity for tests number one and eight

By using Equations 2-44 and 2-45 provided in Section 2.6.2 with considering Tables 5-2, 5-4 and 4-3 all the required parameters for Figure 2-40b can be calculated. In Figure 2 40b, M_p is equal to M_{yield} and its value was calculated to be equal to 279.44 MNm.

$$\frac{M_p}{D^4 K_p{}^2 \gamma'} = 22.3$$

$$\frac{e}{D} = 7.96$$

For a free head pile, the ordinate will be equal to 2.38 and so the calculation follows as below:

$\frac{H}{K_p{}^2 D^3 \gamma'} = 2.38$ Which gives Q_u or H = <u>9.0 MN</u>

5.4.3.6 Comparing the results for tests number one (VL = 5.3 MN) and eight (VL = 6.5 MN)

From the results of Sections 5.4.3.5.1 and 5.4.3.5.2 the methods provided by Broms (1964) and Fleming et al. (1992) both agree very well with the finite element results and with test number one (monopile, VL = 5.3 MN) conducted in the centrifuge. Due to the discussion made in Section 5.4.3.4 and the calculated values for the ultimate lateral capacity of the single pile, it was clear that test number eight has been under extreme strain hardening during the testing procedure.

It would not be a good practice to use a very high yield stress for the Aluminium bar used in the numerical models. That is because by considering a very high yield point for the metal the material will get close to its rupture point. To avoid the problem only the values adopted in Table 5-4 will be used in the numerical models and only test number one will be used for comparison purposes in the upcoming sections and the result of test number eight will not be discussed here after.

Figure 5-41 illustrates the results of test number one (VL = 5.3 MN) with the FE results with a linear and parabolic increase in the soil's modulus of elasticity. As can be seen for the pile/tower structures, which have high eccentricities considering a linear, or a parabolic increase in the soil's modulus of elasticity does not significantly affect the results. Considering other soil moduli will be further investigated in Chapter 6.

As the pile/tower in the numerical model (number one) was under tension and compression, the stress versus strain graph for this part instance could be plotted. Figure 5-42 illustrates the graph for the pile/tower under tension and compression for a linear increase in the soil modulus of elasticity with a reduced integration scheme. It must be mentioned that in ABAQUS the Mises stress is required if the stress versus strain graph is to be plotted for a part instance which has gone through strain hardening (as in this case). From the latest figure, it is clear that the pile/tower has experienced a strain hardening similar to the values provided in Table 5-4.

5.4.4 Model number two, corresponding to test number two (Un-piled footing, VL = 9.3 MN)

As mentioned in Section 4.4.2, this test could not be completed but an attempt has been made to replicate the test with constructing its numerical model. It must be reminded that this test was conducted by a completely solid Aluminium bar and a single footing embedded 0.35 m in to the silica sand.

The pipe in the test had a diameter of 19 mm and footing number one (Table 4-4) was used at its base. The load application piece was attached to the pipe's body (with no cap) during the test, as illustrated in Figure 4-20.

The soil characteristics adopted for the numerical model was as in Table 5-2. As in the previous case, a parabolic and a linear increase in the soil's modulus of elasticity will be considered for this model too.

This model could not be constructed with a solid pipe due to numerical problems. To overcome the associated problems the pipe was considered as a hollow tube with an equivalent modulus of elasticity and unit weight. The details will be discussed in the upcoming sections.

5.4.4.1 The tower and footing geometries with their mechanical properties

The total length of the tower was 197 mm, which 15 mm of it was inserted into footing number one during the test. This was also the case for tests number four and seven. The total length of the tower in the constructed numerical model was equal to 31.8 m and its outer radius was equal to 1.65 m with an inner radius of 1.3 m.

The footing for this numerical model was constructed without the central hole, as the tower in the test was solid; it was justified to use one solid section for the footing with the material properties of Aluminium as the tower and footing were both constructed out of one material. Constructing the footing without a central whole would decrease the pipes length by 2.6 m.

The outer surface of the footing and its top surface area were partitioned so that it could be tied to the ground surface and to the tower, which was sitting on top of it. As the entire footing was submerged under water, the buoyant unit weight of Aluminium was considered for the footing. In addition, Aluminium's modulus of elasticity was considered for the bearing plate as in Table 5-4.

As the tower in the numerical model was constructed as a hollow section, Equations 5-11 and 5-12 were used for calculating the equivalent modulus of elasticity and density respectively. In the latest equations E is the modulus of elasticity, I is the moment of inertia of the tower, ρ is the density and A is the cross sectional area of the pipe.

The equivalent modulus of elasticity and unit weight calculated for the tower were 113.5 GPa and 69.65 kN/m^3 respectively.

$$(EI)_{Model} = (EI)_{REAL} \quad \textbf{5-11}$$

$$(\rho A)_{Model} = (\rho A)_{REAL} \quad \textbf{5-12}$$

5.4.4.2 Assembly, Step and Interaction

The assembled structure positioned into the soil block is illustrated in Figure 5-43. Two steps were required for the constructed model. The first step involved applying the gravity load to the entire structure while the second step involved applying the monotonic lateral load to the tower's head. Both steps contained an Unsymmetric matrix solver with a full Newtonian solution technique.

Two interactions were necessary for the model. The first tie constraint (interaction) was between the soil and the footing while the second tie constraint was between the footing and the tower.

5.4.4.3 Applied loads, Boundary conditions and the generated Mesh

The gravity load was acting on the entire model during both steps of the analysis and a pressure of 686 kPa was acting on top of the footing (the pressure was from the load application piece and the screws).

Two boundary conditions were imposed on the soil body (discussed in Section 5.4.1.1) and the third was acting on the tower's head.

Only a reduced integration scheme for this model was considered. This was the case for the linear hexahedral elements on the tower and the soil block (its outer parts).

The mesh density on the tower was as follows:

Total number of nodes: 1462

Total number of linear hexahedral elements (C3D8R): 882

The mesh density on the footing is as follows:

Total number of nodes: 240

Total number of hexahedral elements (C3D8R): 140

Figure 5-44 illustrates the un-piled footing structure constructed for the numerical model and the structure used in test number two.

Figure 5-45 illustrates the complete constructed numerical model. In Figure 5-45 the gravity, the pressure applied on the tower and the lateral boundary condition imposed on the tower's head are all illustrated. For this model, it was very important to consider a fine mesh on the soil block around the bearing plate; this point is because the failure of the soil dominates the behaviour of this structure and not the failure of the tower.

5.4.4.4 The finite element predictions

The maximum vertical settlement after applying gravity to the entire model for a linear increase in the soil's modulus of elasticity was around 260 mm, which was negligible.

From Figure 5-46, it is clear that the highest Von Mises stresses have occurred on the pipe just above the bearing plate but it is clear that the soil failure controls the ultimate capacity of this structure. Figure 5-47 illustrates the Von Mises stresses acting only on the soil block (the footing and tower were removed).

The lateral force versus lateral displacement for both soil moduli and the test result are illustrated in Figure 5-48 (as previously mentioned this test was not completed). As can be seen, adopting a linear or a parabolic increase in the soil Young's modulus does not significantly affect the results. As previously mentioned Gourvenec et al. (2008) adopted a parabolic increase in the soil modulus in her centrifuge tests conducted on embedded footings in the same silica sand at UWA.

The FE results can be checked in respect to the overturning capacity of the structure and the equations given by Gottardi et al. (1993) discussed in Section 2.8.

The overturning capacity of the structure can be calculated using Table 5-7 for comparison purposes with the FE results. In practice the overturing capacity of such structures (un-piled footings) are usually considered as the ultimate capacity, which the structure can withstand (Sender 2009).

Component	Length (m)	Thickness (m)	Area (m^2)	Volume (m^3)	Unit weight (kN/m^3)	Weight (MN)
Footing (submerged)	17.5 (diameter)	2.625	240.4	631	16.677 (submerged)	10.52
Bored pipe	31.8	0.35	3.3	105.105	69.65	7.32

Table 5-7. Structural components of model number two

When considering, the weight of the load application piece and the screws and using Table 5-7 the weight of the entire structure was equal to 19.85 MN. Using Equation 5-13 a value of 5 MN was calculated for the ultimate lateral force, which the structure could withstand. This value has a difference of +8.6% with the predicted value provided from the numerical model with a linear increase in the soil Young's modulus. For a parabolic increase in the soil's modulus, the difference was +5.48%.

$$\text{Force}_{\text{ultimate}} = \frac{\text{Total weight of the structure} \times \text{Radius of the footing}}{\text{Total height of the structure}} \quad \textbf{5-13}$$

To check the FE results with the equations provided by Gottardi et al. (1993) and Butterfield et al. (1994) the value of V_{max} in Equation 2-108 was required. It must be mentioned that as the structure was failed under its maximum moment it was justified to use Equation 2-108 for calculating the ultimate capacity of the un-piled footing structure. The value of V_{max} in Equation 2-108 was calculated using the N_γ from Vesic (1973) provided in Table 2-10. This approach was essential, as the maximum vertical capacity of the un-piled footing structure, was not evaluated in any of the centrifuge tests.

For a soil with a friction angle of 32° the ultimate vertical capacity of the un-piled footing structure, was calculated to be equal to 1.71 MPa. The latest value was calculated for a centric loading with considering the diameter = breadth = length (Das 1999 and Budhu 2007). By using the latest value, V_{max} was calculated to be equal to 412.46 MN. The value of V_{max} was used in Equation 2-108 and the ultimate lateral capacity of the structure was calculated to be equal to 3.83 MN. The latest value has a difference of -16.73% and -18.51% with the FE results for a linear and parabolic increase in the soil modulus of elasticity respectively.

As illustrated in Figure 5-48 the predicted stiffness from the test results (up to a displacement of around 0.8 m) seems to be too high compared to the FE predictions. The results of this test will be compared with the results of tests number four and seven to illustrate the accuracy of the results. The latest point has been further discussed in Section 5.6.

5.4.5 Model number three, corresponding to test number three and five (Piled footing structures with VL = 6.5 MN and 6.4 MN)

Model number three was constructed to capture the test results obtained from tests number three (piled footing, VL = 6.5 MN) and five (piled footing, VL = 6.4 MN) conducted in the centrifuge. Tests number three and five were described in Sections 4.4.3 and 4.4.5 respectively.

5.4.5.1 The pile/tower, collar and footing geometries with their mechanical properties

Model number three was made up of the soil block discussed in Section 5.4.1, a pile/tower, collar and footing number one (Table 4-4) sitting 0.35 m below the ground level. The geometry of the pile/tower and the collar were exactly as in test number one (Section 5.4.3.1). The difference was mainly in the location of where the collar was attached to the tower during the testing procedure.

As illustrated in Figure 4-7, footing number one was pushed into the soil (around 2 mm), the collar was securely located on top of the footing and it was firmly attached to the tower. The

footing dimensions were provided in Table 4-4. Figure 5-49 illustrates the constructed numerical model with the prototype dimensions compared with the original structure tested in the centrifuge.

The constructed pile/tower in the numerical model was partitioned at 37.6 m and 45.475 m from its base. The area, which was constructed by partitioning, was for tying the tower to the collar in the numerical model. Similar to model number one, the pile/tower was also partitioned at 35 m from its base. The latest was because the area beneath this partition could be tied to the soil block.

The collar dimensions were provided in Section 5.4.3.1 and it was constructed as one part instance by revolution with a deformable body.

As illustrated in Figure 5-50, footing number one had a height of 2.6 m and three datum points at 0.35 m from its base were used to partition it. The reason for partitioning the footing at the mentioned height was that the footing had to be tied to the soil similar to model number two. Another partitioning was also required on the footing's surface for tying the collar to the required area on top of the footing. The latest partition was sketched on the footing surface with a diameter of 5.075 m, which is equivalent to the total diameter of the collar used during the tests.

As previously mentioned, footing number one was totally submerged under water and so the buoyant unit weight of Aluminium had to be used for the numerical model. The required mechanical values for the footing are listed in Table 5-4 (the yield points were not used for the footing and the collar constructed in the numerical model). It must be pointed out that the collar during the tests was standing above the water level and so there was no need to use its buoyant unit weight.

For the section of the pile/tower, which was submerged under water the buoyant unit weight of Aluminium had to be considered and that height was actually 37.6 m from the pile's base.

5.4.5.2 Assembly, Step and Interaction

Figure 5-51 illustrates the pile/tower, collar and the footing all assembled and located within the soil block.

Two steps were required to complete the analysis, both were considered as static general steps and an Unsymmetric matrix solver had to be used for both steps. In addition, a full Newtonian scheme was considered for the numerical model. The initial, maximum and minimum increment sizes in ABAQUS were unchanged as in the previous models.

Five tie constraints were used for this particular model. The first tie constraint was constructed between the soil and the footing as illustrated in Figure 5-52. The second interaction was between the pile and the soil. The third tie constraint was between the footing and the base of the collar, as shown in Figure 5-53. The fourth constraint was constructed between the pile and the collar, as illustrated in Figure 5-54. The last constraint was between the tower and the footing, as shown in Figure 5-55. These constraints could be constructed because each part instance was partitioned

beforehand and as previously mentioned the tying constraint in ABAQUS is very similar to a rough interaction between two surfaces.

5.4.5.3 Applied loads, Boundary conditions and the generated Mesh

As in models number one and two, the gravity was applied to the entire model in the load module.

As shown in Figure 4-9, during the testing procedure the cap and the load application piece were both present. As in the two previous models, the load generated from the load application piece had to be transferred to a pressure load and applied to the tower's head. For this model, the weight of the cap was also considered (24.5 g) to act as a pressure load on top of the tower. So as a whole, the weight of the cap and the load application piece were summed and changed to a pressure load acting on the tower's head from the first step of the analysis. The total pressure load was equal to 2.3 MPa.

The boundary conditions on the soil's body were exactly as in model number one with the tower's head displaced through an imposed boundary condition. All the loads acting on the constructed numerical model with the imposed boundary condition acting on the tower's head with the generated mesh are illustrated in Figure 5-56.

The mesh density on the pile/tower for this model was as follows:

Total number of nodes: 1380

Linear hexahedral elements (C3D8R): 680

The mesh density on the footing is as follows:

Total number of nodes: 132

Linear hexahedral elements (C3D8R): 66

The mesh density on the collar is as follows:

Total number of nodes: 96

Linear hexahedral elements (C3D8R): 40

As discussed in Section 5.4.3.3 the pile/tower was considered to have a reduced integration scheme with an hourglass control activated on it. In addition, the effects of a non-reduced integration scheme will be investigated for this model too, similar to test number one (the monopile structure, VL = 5.3 MN).

5.4.5.4 Comparing the test results with the finite element predictions

Similar to models number one and two, different soil stiffness's were used for comparison purposes with the test results. The Python script attached in Appendix A was used to increase the soil's modulus of elasticity in the numerical model. In addition, the results of a reduced and full integration scheme were compared with the test results too.

Figure 5-57 illustrates the results of test number three (piled footing, VL = 6.5 MN) and five (piled footing, VL = 6.4 MN) with the predicted FE results for a full and reduced integration scheme with considering E_{soil} (kPa) = 1500 Z (m). It can be seen that the reduced integration scheme is showing a closer trend to the test results and that was also the case for test number one (monopile, VL = 5.3 MN). The discrepancy between test number five and test number three are high because test number five was cycled ten times from 0 MN to 15.3 MN before it was monotonically loaded to failure (Section 4.4.5).

From Figure 5-57, it is clear that the FE predictions are in a very close agreement with test number three (piled footing, VL = 6.5 MN) conducted in the centrifuge. The discrepancies between the results of test number three and five are indeed high and that is the case for the predicted FE results too. It is obvious that the results of test number five (piled footing, VL = 6.4 MN) had to stand lower than the results of test number three and the FE predictions as this test (number five) experienced cyclic loading.

As can be seen in Figure 5-58 for a linear increase in the soil modulus with a reduced integration scheme the maximum vertical displacement after completing the gravity step (the first step) was around 230 mm, which is negligible. It must also be mentioned that the gravity load was applied only in one single step.

The yielded bar after conducting test number three (piled footing, VL = 6.5 MN) was illustrated in Figure 4-25. The yield point was exactly on top of the collar attached to the tower's body, for test number three. This height was equal to 10.2 m above the ground level for a prototype.

The deformed pile/tower from the numerical analysis is illustrated in Figure 5-59 (for a linear increase in the soil modulus and a reduced integration scheme). As can be seen, the maximum Mises stresses in this model occurred just above the attached collar, similar to the results of test number three conducted in the centrifuge.

The predicted results from the FE analysis with a parabolic increase in the soils modulus (E_{soil} (kPa) = 4000 $Z^{0.7}$ (m)) are illustrated in Figure 5-60. From this figure, it is also clear that a reduced integration scheme provides a closer match with the test results, similar to the previous case (a linear increase in the soil modulus).

Figure 5-61 compares the FE predictions for a linear and parabolic increase in the soil modulus of elasticity for test number three (piled footing, VL = 6.5 MN). As can be seen, changing the modulus of elasticity does not significantly affect the results and that is similar to the results of a monopile structure.

The amount of vertical displacement or settlement, which occurred in the model after completing the gravity step for a parabolic increase in the soil modulus with a reduced integration scheme, was around 280 mm and it is in an acceptable range for the constructed model. In addition, similar to a linear increase in the soil's modulus of elasticity the maximum Mises stresses on the bar occurred right above the attached collar.

As the pile/tower in the numerical model was under tension and compression, the stress versus strain graph for this part instance could be graphed. Figure 5-62 illustrates this graph for the pile/tower under tension and compression for a linear increase in the soil modulus of elasticity with a reduced integration scheme used on the structure. From the latest figure, it is clear that the pile/tower has experienced a strain hardening similar to the values provided in Table 5-4.

5.4.6 Model number four, corresponding to test number four (Un-piled footing, VL = 5.9 MN)

As discussed in Section 4.4.4 an un-piled footing with a pipe used as a tower was laterally loaded to failure in this test. The tower was bored to a depth of 132 mm from the top of the pipe with a 15 mm drill bit and laterally loaded to failure in the centrifuge.

For this test, it must be mentioned that the tower was modelled as a completely bored pipe with an equivalent modulus of elasticity and unit weight considered for the solid part in the constructed model. The details of the model and the adopted values are discussed in Section 5.4.6.1.

5.4.6.1 The tower and footing geometries with their mechanical properties

This model was constructed of a solid footing embedded in to the soil with a hollow pipe, which resembled the tower.

The footing was 2.6 m thick (footing number one, Table 4-4) and was partitioned at 0.35 m by the aid of datum points to allow the footing to be tied to the soil in the interaction module. The footing was constructed as a completely solid body without any openings in it, as shown in Figure 5-63. The reason for constructing the footing as one solid part was because the material properties of the bar and the footing were the same and the section of the pipe, which entered the footing, was solid as well. In addition, the footing and the solid section of the pipe were entirely under water so only the submerged unit weight of Aluminium would be assigned to the footing. As in the previous models, only the unit weight and the modulus of elasticity of Aluminium was assigned to the footing involved in the test.

For attaching the tower to the footing, another partition was constructed on the footing's surface and that is shown in Figure 5-63. This partition was constructed by the aid of the sketching device in ABAQUS and as mentioned, it was defined to tie the tower and the solid footing together in the interaction module.

The tower standing on top of the footing during the testing procedure was 182 mm which is equal to 31.85 m in a prototype scenario and was drilled up to 132 mm (23.1 m in a prototype) from the top of the pipe with a 15 mm diameter drill bit (2.62 m in a prototype). The pipe's inner and outer diameters were 19 mm (3.3 m in a prototype) and 15 mm (2.65 m in a prototype) respectively. All the above-mentioned prototype values were used to construct the numerical model by ABAQUS.

There were serious problems trying to model the tower with one part full and the other part drilled. ABAQUS would terminate the analysis prematurely and would not provide any results

for a half drilled pipe. As previously discussed, this was also the case for model number two (un-piled footing, VL = 9.3 MN). To overcome this problem the tower had to be constructed, as a completely drilled pipe and an equivalent value for the modulus of elasticity and its unit weight had to be considered for the hollow segment of the tower in the numerical model, which indeed resembled the solid part in the test.

The tower was partitioned at 23.1 m (from the top), which is in fact the same point were the pipe was drilled up to in the conducted test. By constructing this partition on the tower, two different mechanical properties could be assigned to the tower in the property module. Two other partitions were also used on the body to ease the mesh generation for the software. All partitions on the tower were constructed by using datum points in ABAQUS; the tower is illustrated in Figure 5-64.

The two equivalent mechanical properties were the modulus of elasticity and the unit weight of the material. For changing the modulus of elasticity in practice, they usually equate the flexural rigidity of a hollow pile with the solid pile and then they work out the required modulus of elasticity. The same method was used for this constructed model as well. Equations 5-11 and 5-12 were used to evaluate E_{Model} and ρ_{Model} for the hollow pile section used in ABAQUS from the real solid pile values in the test (similar to model number two, un-piled footing, VL = 9.3 MN).

It must be remembered that the tower was entirely above the water so there was no need to use the buoyant unit weight of Aluminium for the tower's cross section in the model. By using Equations 5-11 and 5-12, the equivalent modulus of elasticity and unit weight were calculated to be 113.5 GPa and 69.651 kN/m^3 respectively for the hollow tower modelled as the solid pipe in the numerical model. By using these two values in the model, the hollow section of the tower in the model must behave similar to a solid section. For the hollow pipe section in the test, which was also modelled as a hollow pipe in the numerical model, the yield stress was as in Table 5-4, although it must be remembered that the soil failure would control the behaviour of this structure and not the structural capacity of the tower.

5.4.6.2 Assembly, Step and Interaction

Figure 5-65 illustrates the assembled structure (the footing and the tower) embedded in the soil block.

As in the previous models, only two steps were required for completing the analysis. One was for applying the gravity and the other was for imposing a boundary condition on the tower's head. Both steps were static general steps and an Unsymmetric matrix solver with a full Newtonian integration scheme was adopted for the entire model. Similar to the previous models there was no need to change the increment sizes adopted by ABAQUS.

Two tie constraints were required for this particular model. One constraint was between the footing and the soil and the second tie constraint was constructed between the tower and the footing.

5.4.6.3 Applied loads, Boundary conditions and the generated Mesh

Two loads were used in constructing this model. The first load was the gravity load, which was acting on the entire model and was constructed in the first step and propagated to the next. As previously discussed in Section 4.4.10, the application piece and the screws were also present during this test, so a pressure load equal to the weight of the application piece and screws was applied to the top of the tower. The pressure on the tower's head (686 kPa) was active in the first step and in the second step of the analysis.

The mesh generated on the tower and the footing with the applied loads is illustrated in Figure 5-45.

The mesh density on the tower is as follows:

Total number of nodes: 2376

Total number of linear hexahedral elements (C3D8R): 1484

The mesh density on the footing is as follow:

Total number of nodes: 300

Total number of linear hexahedral elements (C3D8R): 176

Only a reduced integration scheme with hourglass control was considered for the mesh generated on the footing and the tower in this model, as the soil failure would have controlled the behaviour of this structure.

5.4.6.4 Comparing the test results with the finite element model predictions

After applying the gravity to the entire model with a linear increase in the soil modulus, the observed amount of settlement was around 240 mm. The Von Mises stresses acting on the tower and footing are illustrated in Figure 5-66. From the figure that the high stresses are acting at the base of the tower were it was connected to the footing and that is similar to the results of model number two.

A 'set' was introduced to the tower's head and the reaction forces on that set were all summed for comparison purposes with the test results.

Figure 5-67 shows the test result and the predicted FE result for a linear increase in the soil modulus with a reduced integration scheme used on the tower and the footing. As can be seen, the maximum numerical difference between the FE prediction and the test result was 0.74 MN, which is in an acceptable range (difference less than +25%).

As shown in Figure 5-68 the FE prediction for a parabolic increase in the soil modulus have been graphed with the test result. The amount of settlement after applying the gravity load to the constructed model was around 240 mm. From this figure, it is clear that the maximum numerical difference between the FE prediction and the test result was 1.1 MN (difference of +36.6%) which is slightly above the acceptable range.

Figure 5-69 compares the results of a linear and parabolic increase in the soil's modulus with the test result. It is clear that the structure behaves slightly stiffer as the soil's modulus has increased.

5.4.6.5 Calculating the ultimate lateral capacity of the structure

To ensure that the ultimate lateral capacity of the proposed structure calculated by the FE analysis and the value observed in the conducted test were accurate and believable; the overturning capacity and the ultimate capacity of the structure were checked in respect to the bearing capacity equations (similar to model number two, un-piled footing, VL = 9.3 MN). These calculations would insure that the ultimate capacity values for the laterally loaded structure illustrated in Figure 5-69 were reasonable.

The structure consisted of three components, as shown in Table 5-8. The footing was totally submerged under water and so the submerged unit weight of Aluminium was considered for the footing. It must also be noted that in Table 5-8 for calculating the full section of the tower the equivalent unit weight was considered (using equation 5-12).

In Table 5-8, the equivalent unit weight was used to calculate the weight of the bored pipe resembling the solid section of the tower in the test. If the real unit of Aluminium was considered with the full area of the tower for the bottom section of the pipe, the area would be calculated to be equal to 8.67 m^2 with a volume of 75.93 m^3. Using the actual unit weight of Aluminium with the provided volume would provide us with a weight of 2.01 MN for the full section of the tower, and that is exactly as in Table 5-8.

Component	Length	Thickness	Area	Volume	Unit weight	Weight
Footing (submerged)	17.5 m (diameter)	2.625 m	240.4 m^2	631 m^3	16.67 kN/m^3	10.52 MN
Bored pipe	23.1 m	0.35 m	3.3 m^2	76.23 m^3	26.48 kN/m^3	2.01 MN
Bored pipe (resembling the solid section)	8.75 m	0.35 m	3.3 m^2	28.875 m^3	69.65 kN/m^3	2.01 MN

Table 5-8. Components of the un-piled footing test (test number four)

The total weight of the structure when considering the weight of the screws and the application piece was equal to 16.42 MN. The lever arm's length was equal to the footing's radius, which was 8.75 m. The height of the structure from the ground level was equal to the total height of the tower plus the thickness of the footing, which was equal to 34.47 m. Using Equitation 5-13, the ultimate lateral capacity of the structure was calculated to be 4.1 MN. It is interesting to note that the latest value was exactly equal to the value predicted by the FE model for a parabolic increase in the soil Young's modulus.

The test results can also be checked in respect to Gottardi et al. (1993) and Butterfield et al. (1994) equation discussed in Section 2.8.5 for a footing under a pure moment loading. For using Equation 2-108, the maximum vertical load for the footing was calculated using the bearing

capacity equations discussed in Section 2.8. The value of N_γ was taken from Table 2-10 (Vesic 1973) for a soil with a friction angle of 32°. The value of V_{max} was calculated to be equal to 412.46 MN for the un-piled footing used in test number four (this value was calculated for a centric load). The latest value was used in Equation 2-108 and it provided a maximum horizontal capacity equal to 3.2 MN. The FE results have a difference of +18.75% and +28.12% with the value calculated from Gottardi et al. equation for a linear and parabolic increase in the soil modulus respectively. The value calculated by Gottardi et al. equation has a difference of +8.84% with the test result.

As discussed by Gourvenec et al. (2008) the moments calculated from the FE results are usually higher than the test results conducted in the centrifuge and the results predicted by Gottardi et al. (1993). The predicted value by the FE analysis for a linear increase in the soil Young's modulus was 1.18 times the value calculated by Gottardi et al. equation while the test result was 0.91 times that value.

The average horizontal displacement of the footing with a linear increase in the soil modulus of elasticity at the ultimate capacity was equal to 0.0064 m while the average shear stress acting at the base of the footing was equal to 3.8 MPa.

5.4.7 Model number five, corresponding to test number six (Piled footing structure, VL = 13.2 MN)

As mentioned in Section 4.4.6 this proposed structure comprises of a footing at the ground level a pile/tower, two footings located on the tower and a collar attached to the bearing plate (as illustrated in Figure 4-15 left). The two footings located on the tower were used to increase the weight on the structure and to illustrate how the structure might behave under an increase in the vertical load.

The constructed model for this test and its results will be further discussed in the upcoming sections.

5.4.7.1 The pile/tower, collar and footing geometries with their mechanical properties

The constructed pile/tower for the proposed structure is illustrated in Figure 5-70. As can be seen, the pipe was partitioned at six locations along its body. The first partition is to tie the pile/tower to the constructed ground block up to a height of 35 m from the base of the pile. The second partition was for tying the pile/tower to the bearing plate (footing number one) located at the ground level. The third and fourth partitions on the pipe were for tying the collar to the tower and the fifth and sixth partitions were used for tying the two footings (number two and three) to the tower in the numerical model. The dimensions of the footings and the collar used in this test were provided in Tables 4-4 and 4-10 respectively.

The second part instance for this model was the bearing plate (footing number one) located at the ground level. The footing was partitioned at 0.35 m from its base so that the footing could be tied to the soil block as the footing was embedded into the silica sand up to around 2 mm from its base during the testing programme. The upper face of the footing was also partitioned so that the

collar could be tied to the bearing plate in the interaction module. As previously mentioned the second partition constructed on the footing was made by the aid of the sketching device available in ABAQUS. The footing with all its partitions was illustrated in Figure 5-50.

Footing number two used on the tower for the numerical model is illustrated in Figure 5-71. This part instance was partitioned on its upper and lower surface area. The partition constructed on the upper surface was for tying footing number three to it while the lower partition was for tying the collar to the footing. The lower partition is also illustrated in Figure 5-71 (right picture). The first partition (on top of the footing) had a radius of 3.5 m while the second partition (on the base of the footing) had a radius of 2 m.

Figure 5-72 illustrates footing number three, which was tied to footing number two in the constructed model. No partitions were required for this footing, as its lower surface area was entirely tied to footing number two in the numerical model.

The last part instance constructed for this model was the collar, which is illustrated in Figure 5-19. The collar was constructed as one part instance by revolution and its dimensions were provided in Figure 4-10.

Two material properties were assigned to the pile/tower in the numerical model. The section below the footing was submerged under water while the section standing above the footing was not submerged. The material properties are listed in Table 5-4, it must be noted that the yield points were all considered for the pile/tower section for this numerical model.

Footing number one, which was located at the ground level, was totally submerged under water and so only, the buoyant unit weight of Aluminium was assigned to it with no yield points considered for it.

For the collar, footing numbers two and three the properties of Aluminium were considered without the yield points. Moreover, as all these part instances were located above the water level there was no need to assign the buoyant unit weight of Aluminium to these sections.

5.4.7.2 Assembly, Step and Interaction

The assembled structure is illustrated in Figure 5-73 and it is compared with the proposed structure used in the testing programme.

Two steps were required for completing the analysis. As in the previous models for both steps an Unsymmetric matrix solver, was used with a full Newtonian solution technique. In addition, there was no need to change the initial increment sizes in ABAQUS or to change the “time average force” acting in any of the required steps.

In total, nine tie constraints were used for this model. The first tie was constructed between footing number one and the soil block (similar to other models). The second tie constraint was between the pile and the soil block. The third constraint was between the collar and footing number one. The fourth tie constraint was constructed between the tower and the collar. The fifth constraint was between the collar and the base of footing number two, as illustrated in Figure

5-74. The sixth tie constraint was between footing number two and three, as shown in Figure 5-75. The seventh, eighth and ninth constraints were between the pile/tower and footings number one, two and three.

5.4.7.3 Applied loads, Boundary conditions and the generated Mesh

As in all other constructed models, the gravity load was constructed in the first step of the analysis and it was applied to the entire model. It was then propagated to the second step of the analysis. Similar to other models, the gravity load was applied to the entire model without the need of applying it to different components of the model in different steps. The last point is a technique, which is sometimes incorporated when ABAQUS is not able to apply the gravity to the entire model in one-step.

As discussed in Section 4.4.6 during this test the load application piece and the cap were both present (3.5 MN in a prototype). Therefore, the weight of both components were added and that value was changed to a pressure load which acted on the tower's head in the first and second step of the analysis (2.3 MPa in a prototype).

As a whole, three boundary conditions were imposed on the model. The first two boundary conditions were used on the ground block (discussed in Section 5.4.1) and the third was constructed to displace the tower's head in the second step of the analysis.

The mesh generated on the pile/tower, collar and the footings are illustrated in Figure 5-76.

The mesh density on the pile/tower is as follows:

Total number of Nodes: 1400

Total number of linear hexahedral elements (C3D8R): 690

The mesh density on footing number one is as follows:

Total number of Nodes: 132

Total number of linear hexahedral elements (C3D8R): 66

The mesh density on footing number two is as follows:

Total number of Nodes: 189

Total number of linear tetrahedral elements (C3D4): 626

The mesh density on the collar is as follows:

Total number of Nodes: 96

Total number of linear hexahedral elements (C3D8R): 40

The mesh density on footing number three is as follows:

Total number of Nodes: 98

Total number of linear tetrahedral elements (C3D4): 35

The results of a full and reduced integration scheme on the linear hexahedral elements used on the pile/tower will be investigated in the upcoming sections.

5.4.7.4 Comparing the test result with the finite element predictions

After applying the gravity load to entire model, the maximum amount of settlement was around 250 mm for the model with a linear increase in the soil modulus.

The Von Mises stresses for a linear increase in the soil's modulus with a reduced integration scheme adopted on the pile/tower, footings and the collar are illustrated in Figure 5-77. Figure 5-78 illustrates the Von Mises stresses acting only on the pile/tower for the constructed model.

As can be seen from the latest figures the tower was bent just above footing number three. In addition, there was a high stress accumulation on the pile/tower from around the ground surface to 7 m below the soil. It was mentioned in Section 4.4.6 that the pipe during the test bent at around 7 m below the ground surface, this is consistent with FE predictions for the section of the pile/tower under the ground surface.

The Von Mises stresses acting on the pipe/tower for a linear increase in the soil's modulus with a full integration scheme is illustrated in Figure 5-79. The results are similar but higher stresses were generated when a full integration scheme was used on the pile/tower.

The displacement versus the lateral force graph for the constructed model is illustrated in Figure 5-80. The latest figure was graphed for a linear increase in the soil's modulus of elasticity. As in the previous models the under integration scheme provided closer results to the tests compared to a full integration scheme.

The force versus displacement graph for a parabolic increase in the soil modulus is illustrated in Figure 5-81. Similar to all other cases the under integration scheme provides a closer result compared to the full integration scheme. The maximum amount of settlement after applying the gravity load for a parabolic increase in the soil modulus was around 300 mm (negligible) for a full and an under integration scheme.

Figure 5-82 illustrates the results of a linear and parabolic increase in the soil's modulus of elasticity with a reduced integration scheme. It is clear that adopting a linear or a parabolic increase in the soil's modulus of elasticity does not significantly affect the results for this structure.

5.4.8 Model number six, corresponding to test number seven (Un-piled footing, VL = 12.7 MN)

As shown in Table 5-5 model number six was constructed similar, to test number seven conducted in the centrifuge. This structure was similar to the un-piled footing with a tower (model number four, un-piled footing, VL = 5.9 MN) but footings number two and three were attached to the tower's body. The extra footings were used to increase the weight on the structure, as discussed in Section 4.4.7.

5.4.8.1 The tower and footing geometries with their mechanical properties

This model consists of a tower and three footings. Footing number one was located at the ground level acting as the bearing plate while the other two footings were located on the tower. The tower used in this model was exactly as in model number four described in Section 5.4.6.1.

The tower used in the test was 197 mm tall and the bottom part of the pipe was full (not drilled), which corresponded to 65 mm of the total height of the pipe. It must be mentioned that 15 mm out of this 65 mm of the tower's length, which was not drilled, was resting within footing number one (Table 4-4) similar to test number four.

The same procedure used for constructing model number four (un-piled footing, VL = 5.9 MN) was adopted for this model too. The reason for adopting the same method was that the tower with a drilled and full segment (similar to the test) could not be modelled and so an equivalent modulus of elasticity and unit weight had to be considered for the last 50 mm of the tower.

It must be reminded that 15 mm of the tower in the test was not drilled and it was positioned inside footing number one and submerged under water. This will allow the footing to be constructed without a central hole in its body and a submerged unit weight could be assigned to it. This latest approach was adopted for model number four in Section 5.4.6 too.

The total height of the tower in the constructed model was 182 mm (31.85 m in a prototype) and it was constructed as an empty pipe with three partitions on its body. The first partition was constructed at a height of 50 mm (8.75 m in a prototype) from the bottom of the tower and that was the segment of the tower, which was full (not drilled), this partition allowed to assign an equivalent modulus of elasticity and unit weight to the segment below this partition. Equations 5-11 and 5-12 were used to calculate the equivalent modulus of elasticity and unit weight for the bottom 50 mm of the tower. The equivalent unit weight and modulus of elasticity were 69.651 kN/m^3 and 113.5 GPa respectively.

Two other partitions were also constructed on the tower. They were used for tying the tower to footings number two and three in the model. The first partition had a height of 2.6 m while the second partition was 1.75 m long. These latest heights were equal to the thickness of the footings used in the test (Table 4-4).

The footing used at the base of the tower (footing number one) was partitioned on its upper surface so that it could be tied to the tower in the interaction module.

Footing number two is illustrated in Figure 5-71. This footing was partitioned on its upper surface so that it could be tied to footing number three in the model. Footing number three is illustrated in Figure 5-72. This part instance did not require any partitioning as its lower surface was tied to footing number two in the interaction module.

By constructing footing number one (the bearing plate) in the model as a solid footing (without the central whole), only the submerged unit weight of Aluminium was required for this part instance. All other part instances were standing above the water level and so there was no need to use the submerged unit for any part instances constructed in this model.

5.4.8.2 Assembly, Step and Interaction

Figure 5-83 illustrates the assembled structure compared to the proposed structure used in the centrifuge test.

Two steps were required for completing the analysis. The first step was to apply the gravity to the entire model and the second step was to displace the tower's head under an imposed boundary condition. Both steps required an Unsymmetric matrix solver with a full Newtonian solution technique. As in the previous models, there was no need to change the increment sizes adopted by ABAQUS or the "time average forces" for this numerical model. Changing the time average force during applying the gravity is a technique used for models, which encounter numerical problems when the gravity cannot be applied to a model in ABAQUS.

Five tie constraints were used for this constructed model. The first constraint was between footing number one and the soil block. The second tie constraint was between the tower and footing number one. The third constraint was between footing number three and the tower. The fourth tie constraint was between footing number two and the tower and the fifth tie constraint was between footings number two and three.

5.4.8.3 Applied loads, Boundary conditions and the generated Mesh

Two loads were considered for the constructed model. The first load was the gravity load; it was acting on the entire model. The gravity load was applied to the entire model in the first step of the analysis and then it was propagated to the second step. The second load was acting on the tower's head and it was resembling the weight of the application piece and screws, which were present during the test (2.3 MN in a prototype). The second load was activated in the first step of the analysis and it was propagated to the second step.

As in the previous models, two boundary conditions were imposed on the soil block, while the third boundary condition was imposed on the tower's head. It was also necessary to identify a set for the tower's head before imposing the boundary condition on to it.

The mesh, loads and the boundary conditions applied on the entire structure are illustrated in Figure 5-84.

The mesh density on the tower is as follows:

Total number node: 2376

Total number of hexahedral elements (C3D8R): 1484

The mesh density on footing number one is as follows:

Total number of nodes: 300

Total number of hexahedral elements (C3D8R): 176

The mesh density on footing number two is as follows:

Total number of nodes: 201

Total number linear tetrahedral elements (C3D4): 676

The mesh density on footing number three is as follows:

Total number of nodes: 174

Total number of linear hexahedral elements (C3D8R): 82

5.4.8.4 Comparing the test results with the finite element predictions

The total amount of vertical displacement for the soil and the proposed structure was around 240 mm for a linear increase in the soil Young's modulus of elasticity after applying the gravity load.

Figure 5-85 illustrates the Mises stresses acting on the proposed structure for a linear increase in the soil's modulus of elasticity. Figure 5-86 illustrates the Von Mises stresses acting on the soil block with a linear increase in the soil modulus of elasticity.

The test result and the FE results for a linear increase in the soil's modulus have been plotted in Figure 5-87. As can be seen, the results are in a good agreement with each other while the reduced and full integration scheme used on the structure does not affect the results. The latest is acceptable because in this structure, the soil failure controls the behaviour of the model and not the tower and as previously mentioned, changing the integration scheme on the soil block far from the footing, (the hexahedral elements) would not affect the results too. In fact, the elements close to the structure were all tetrahedral elements and they controlled the failure of the structure.

Figure 5-88 illustrates the test and the FE predictions for a linear and parabolic increase in the soil's modulus of elasticity. From the latest figure, it is clear that adopting a linear or a parabolic increase in the soil modulus does not significantly affect the results.

5.4.8.5 Calculating the ultimate capacity of the structure

As in the case of models number two (un-piled footing, VL = 9.3 MN) and four (un-piled footing, VL = 5.9 MN), the best way to check the results for this model was to calculate the overturning capacity and the ultimate lateral capacity with the equations provided in Section 2.8. By calculating the latest values, the accuracy of the tests and the FE predictions could be checked.

As shown in Table 5-9 the proposed structure was constructed out of five components with footing number one totally submerged under water. Using equation 5-13, the ultimate lateral capacity of the structure was calculated, the result was compared with the test and the FE results.

Component	Length	Thickness	Area	Volume	Unit weight	Weight
Footing (No.1) (submerged)	17.5 m (diameter)	2.625 m	240.4 m^2	631 m^3	16.67 kN/m^3	10.52 MN
Bored pipe	23.1 m	0.35 m	3.3 m^2	76.23 m^3	26.48 kN/m^3	2.01 MN
Bored pipe (resembling the solid section)	8.75 m	0.35 m	3.3 m^2	28.875 m^3	69.65 kN/m^3	2.01 MN
Footing (No.2)	10.5 m (diameter)	2.625 m	86.54 m^2	227.18 m^3	26.48 kN/m^3	6.017 MN
Footing (No.3)	7 m (diameter)	1.75 m	38.46 m^2	67.31 m^3	26.48 kN/m^3	1.78 MN

Table 5-9 Footing test components used for calculating the overturing moment of the structure

The total weight of the structure including the load application piece and the screws was 24.217 MN. The ultimate lateral capacity of the structure was calculated to be equal to 6.1 MN with the aid of Equation 5-13, which is in a good agreement with the test and the FE results. The calculated value has a difference of +5.1% with the value predicted by the FE analysis and has a difference of +21.27% with the test result.

Using the bearing capacity equations discussed in Section 2.8 with N_γ taken from Table 2-10 (Vesic 1973) for a soil with a friction angle of 32° the ultimate vertical load was calculated to be equal to 412.46 MN. The latest value was used in Equation 2-108 and the ultimate horizontal capacity of the structure was calculated to be equal to 4.62 MN. The latest value has a difference of -8.15% and -20.3% with the test and the FE results respectively. As previously mentioned Equation 2-108, can be adopted for the calculation because the un-piled footing structure would fail under a moment loading scenario. As in the case of the previous un-piled footing tests, the FE results were higher compared to the equation provided by Gottardi et al. and the test result, this point was discussed by Gourvenec et al. (2008). The predicted value by the FE analysis was 1.25 times the value calculated by Gottardi's equation while the test result was 1.08 times that value.

5.5 NUMERICAL MODELS CONSTRUCTED FOR COMPARISON PURPOSES

As previously discussed, if the results of the un-piled footing structure was to be compared with the results of the monopile and the piled footing structures, the tower in the un-piled footing cases had to be completely drilled. In fact, one third of the tower was full in the tests while it had to be completely drilled. In addition, the tower should have had a thickness equal to the towers used in the monopile and the piled footing cases if a correct comparison was to be made between the structures. These two points were important because the applied vertical load significantly controls the behaviour of the footing structure and so the stiffness and the ultimate capacity of the un-piled footing could have been affected by considering higher vertical loads acting on the

footing structure. In regards to the monopiles and the piled footing structures, the collar attached to the structures will also affect the stiffness and so it was necessary to remove the collar for these two structures as well. In Table 5-6 models number eight, nine and ten were constructed for these purposes.

Model number seven was also constructed to illustrate that the vertical load does not significantly increase the stiffness nor the ultimate lateral capacity of a single pile embedded in a sand deposit, as discussed in Section 2.7.

The details of the models in Table 5-6 will be discussed in the upcoming sections.

5.5.1 Model number seven (Monopile structure VL = 12.5 MN, no test data available)

This structure was constructed of a pile/tower, collar and two footings located on top of the collar attached to the tower. The reason for constructing this model was to compare its results with the results of model number one (monopile, VL = 5.3 MN), to identify how much the lateral capacity and stiffness of a single pile would improve when the vertical load on the structure was increased.

5.5.1.1 The pile/tower, collar and footing geometries with their mechanical properties

As this model was constructed only for comparison purposes with model number one (monopile, VL = 5.3 MN), the pile/tower's geometry was similar to that model. The pile was embedded 35 m into the soil and it was partitioned at 2.6 m above the ground level to allow the buoyant unit weight of Aluminium to be assigned to that region. Another partition was also required to allow the collar to be tied to the pile similar to model number one and that partition was constructed at a height of 40.25 m from the base of the pile/tower.

The extra weight acting on this model was mainly made-up of footings number two and three, which were sitting on the collar. The two footings (footing number two and three, Table 4-4) were located above the collar. It must also be mentioned that footing number two was located beneath footing number three and they were tied to the tower. As the footing thicknesses were different, the partitions on the tower were adjusted so that the footings could be correctly tied to it at the required locations. The mechanical properties of the pile/tower are illustrated in Table 5-4. It must be mentioned that both the submerged unit weight and the unit weight above the water were assigned to the pile/tower section (similar to model number one, monopile, VL = 5.3 MN) with considering strain hardening for the pile/tower section.

The collar was constructed exactly as in model number one discussed in Section 5.4.3 and it was located 5.25 m from the ground level.

Footing number two, (Table 4-4) contained two partitions. The partitions were constructed by the sketching device available in ABAQUS and were constructed on the outer faces of the footing for tying the collar and footing number three.

Footing number three, (Table 4-4) did not require any kind of partitioning, as it was located on top of footing number two in the model.

As footings number two and three were located above the water level, there was no need to use the submerged unit weight of Aluminium. Only the modulus of elasticity and the Poisson's ratio were considered for both footings constructed in this model, their mechanical properties are listed in Table 5-4. As this model was constructed for comparison purposes with model number one (monopile, VL = 5.3 MN), the weight of the application piece and the screw were considered for this model too.

5.5.1.2 Assembly, Step and Interaction

Figure 5-89 illustrates the assembled structure located in the soil block.

As in the previous cases, the model required two static general steps and an Unsymmetric matrix solver with a full Newtonian scheme.

Six tie constraints were used for this particular model. The first tie was generated between the pile/tower and the collar. The second and third tie constraints were constructed between the pile/tower and footings number two and three respectively. The fourth constraint was between the base of footing number three and the partitioned zone on top of footing number two. The fifth tie constraint was constructed between the collar and the base of footing number two and the last constraint was between the pile and the soil.

5.5.1.3 Applied loads, Boundary conditions and the generated Mesh

As a whole, two loads were applied to the constructed model. The first load considered on the model was the gravity load; this load was generated in the first step of the analysis and was propagated to the next step. The gravity load was successfully applied to the entire model in the first step of the analysis.

The second load was acting on top of the pile/tower similar to model number one (monopile, VL = 5.3 MN). This pressure load was active during step one and step two of the analysis. This load was generated from the load application piece located on the top of the tower (similar to model number one) and it was equal to a pressure of 1.49 MPa acting on top of the tower.

As previously discussed, two boundary conditions were imposed on the ground block while the third was acting on top of the tower's head.

The mesh generated on the pile/tower, collar and the footings is illustrated in Figure 5-90.

The mesh density on the pile/tower is as follows:

Total number of nodes: 2576

Total number of linear hexahedral elements (C3D8R): 1274

The mesh density on the collar is as follows:

Total number of nodes: 120

Total number of linear tetrahedral elements (C3D4): 307

The mesh density of footing number three:

Total number of nodes: 174

Total number of linear hexahedral elements (C3D8R): 82

The mesh density of footing number two:

Total number of nodes: 188

Total number of linear tetrahedral elements (C3D4): 620

As previously mentioned footing number two, had to be partitioned so that the collar and footing number three could be tied to it. These partitions caused restrictions on selecting the mesh type, which could be generated on this particular part instance and so only tetrahedral elements were used on footing number two.

As shown in the previous cases the reduced integration scheme provided closer results to the tests, so in this section where there were no test data available only a reduced integration scheme will be considered for the structure.

5.5.1.4 The finite element predictions

For a linear increase in the soil's modulus of elasticity the amount of settlement after applying the gravity load was slightly less than 240 mm, which was negligible.

Figure 5-91 illustrates the deformed pile with the components attached to it while Figure 5-92 shows the pile/tower without its components. It was clear that the high stress zone started from slightly above the ground level (1 m) and expanded up to around 8 m below the ground surface.

For a parabolic increase in the soil's modulus of elasticity the amount of settlement after applying the gravity load was around 280 mm. The high stress zone in this case also started from around 1 m above the ground level and extended to a depth of 7 m to 8 m below the ground surface, similar to a linear increase for the soil's modulus of elasticity.

As previously mentioned, there was no tests conducted for this particular structure and so its results are only compared with the results obtained from model number one and test number one conducted in the centrifuge. Figures 5-93 and 5-94 illustrate the results obtained from a linear increase in the soil modulus and a parabolic increase respectively.

As expected, there was not a great increase in the ultimate lateral capacity or the stiffness of the pile/tower, although the vertical load on the structure was significantly increased. This is a clear confirmation on the material presented in Section 5.4.3.4, that by increasing the vertical load on a single pile in medium dense sand (friction angle of around 30°) the stiffness of a single pile will not significantly improve.

5.5.2 Model number eight (Un-piled footing structure VL = 3.75 MN, no test data available)

As previously mentioned, the main reason for constructing this model was that the pipe used as the tower in the un-piled footing tests (Table 5-5) was slightly thicker than the pile/towers used in the monopile and the piled footing structures. In addition, the last 65 mm (equal to 11m in a prototype) of the tower was full, this would increase the weight, and that could have changed the capacity and stiffness of the footing structures.

To overcome the problems, the tower's thickness was reduced to the size of the monopile and the piled footing structures and the tower was completely drilled so that a uniform modulus of elasticity and unit weight could be used on the pile/tower structure.

5.5.2.1 The geometries and the mechanical properties

The height of this structure from the top part of footing number one had to be equal to the total height of the tower in the monopile and the piled footing cases, those are models number nine and ten respectively (Table 5-6). In addition, the load acting on top of the towers had to be equal for all structures if a correct comparison was to be made.

The tower for this constructed model was 34.45 m tall, the outer radius was 1.65 m, and it had an inner radius of 1.5 m, similar to the pile/tower used in the piled footing cases (models nine and ten).

Footing number one was positioned at the ground level with an embedment depth of 0.35 m and it was constructed with the central hole (this was not the case for the models used for capturing the tests, as the tower was not completely drilled in those cases). The dimensions of footing number one were provided in Table 4-4.

For the tower section, which was considered, to be above the footing level there was no need to use the buoyant unit weight of Aluminium but for the segment of the tower, which was within the footing a buoyant unit weight was considered for the hollow tower. As the tower was constructed out of Aluminium the mechanical properties of this alloy was used in the numerical model (Table 5-4) with only considering the first yield point of the material (because the soil failure would control the behaviour of this structure using the second yield point was inappropriate).

The footing in this model was considered to be entirely under water and so the buoyant unit weight of Aluminium was considered for footing number one (with no yield points). The soil properties adopted for this model were also as in Table 5-2.

5.5.2.2 Assembly, Step and Interaction

The assembled tower and footing are illustrated in Figure 5-95. From the latest figure, it is clear that the centre of the footing was hollow and that was the case for the tower installed within the footing too.

Two steps were sufficient for this analysis and they both contained an Unsymmetric matrix solver.

Three tie constraints were used for this model. The first constraint was between the footing and the soil, the second was between the footing and the hollow tower and the third was between the hollow tower and the soil. To construct the third tie constraint the soil block for this un-piled footing structure had to be partitioned so that the bottom of the tower could be tied to the soil. Figure 5-96 illustrates the tie constraint between the tower and the soil block and Figure 5-97 shows the tie constraint between the tower and the footing.

5.5.2.3 Applied loads, Boundary conditions and the generated Mesh

Two loads were acting on the proposed model. The first was the gravity load and the second load was acting on top of the tower. The second load was considered to be equal to 2.5 MN, which is in line for a usual weight considered for the hub, nacelle and rotor acing on a wind turbine (Sender 2009). The load was changed to a pressure, which acted on the tower's head during the analysis similar to a real wind turbine case. Similar to all other models three, boundary conditions were sufficient for this model.

The mesh density on the tower was as follows:

Total number of nodes: 2538

Total number of hexahedral elements (C3D8R): 1590

The mesh density on the footing was as follows:

Total number of nodes: 300

Total number of hexahedral elements (C3D8R): 176

5.5.2.4 The finite element results and the ultimate capacity of the structure

After applying the gravity, the maximum amount of settlement for the entire structure was around 240 mm, which was negligible. The Von Mises stresses acting on the tower and the soil block are illustrated in Figures 5-98 and 5-99 respectively.

Figure 5-100 illustrates the results of this model for a linear increase in the soil modulus (E(kPa) = 1500 Z (m)) with a reduced integration scheme. As in the previous cases, the overturing capacity and the ultimate capacity of the structure can be calculated by the aid of the bearing capacity equations provided in Section 2.8.

Component	Length	Thickness	Area	Volume	Unit weight	Weight
Footing (submerged)	17.5 m (diameter)	2.625 m	231.86 m^2	608.63 m^3	16.67 kN/m^3 (submerged)	10.15 MN
Bored pipe	31.825 m	0.15 m	1.48 m^2	47.1 m^3	26.487 kN/m^3	1.24 MN
Bored pipe (submerged)	2.625	0.15	1.48	3.88	16.67 kN/m^3	0.064

Table 5-10. Structural components of model number eight

The weights of the structural component for this model are illustrated in Table 5-10. It must be mentioned that for the submerged footing, its centre was considered hollow and that indeed reduces the area. The weight of the entire structure with the 2.5 MN (rotor, hob and nacelle) was equal to 13.95 MN. Using Equation 5-13, the overturning capacity of the structure was calculated to be equal to 3.54 MN. The latest value has a difference of -1.11% with the predicted results from the FE analysis for a linear increase in the soil modulus of elasticity.

Using the bearing capacity equations discussed in Section 2.8 with N_γ taken from Table 2-10 (Vesic 1973) for a soil with a friction angle of 32° will provide a V_{Max} equal to 397.8 MN. With considering the equation from Gottardi et al. (Equation 2-108), the lateral load can be calculated to be equal to 2.74 MN. The latest value was 1.3 times the calculated value by the FE analysis and has a difference of -23.6% with the numerical result.

5.5.3 Model number nine (Piled footing structure VL = 3.75 MN, no test data available)

This model was constructed for comparison purposes with models number eight (un-piled footing) and ten (monopile). For this model, similar to model number eight, only a linear increase in the soil modulus will be considered with a reduced integration scheme used on the structures. This model was similar to model number three (piled footing, VL = 6.5 MN) but for comparison purposes, the collar on the structure was removed so it would not affect the stiffness of the structure.

5.5.3.1 The pipe and footing geometries with their mechanical properties

The pile/tower in this model had a total length of 69.45 m with 35 m of it below the ground surface. The outer radius of the pile/tower was 1.65 m and its inner radius was 1.5 m similar to the dimensions of model number eight (un-piled footing structure).

The footing for this model was embedded 0.35 m below the ground surface and it was considered to be submerged. The footing had a thickness of 2.6 m and its dimensions were as in Table 4-4 (footing number one).

The material properties used for the pile/tower were as in Table 5-4 with considering the footing as an elastic material.

5.5.3.2 Assembly, Step and Interaction

The assembled structure is illustrated in Figure 5-101. As in the previous cases, two steps were sufficient for the analysis and they were static general steps with an Unsymmetric matrix solver.

Three tie constraints were necessary for the constructed model. The first constraint was between the pile and the soil, the second constraints was between the tower and the footing, and the last constraint was between the footing and the soil block.

5.5.3.3 Applied loads, Boundary conditions and the generated Mesh

Two loads were sufficient for this model, similar to model number eight. The first load was the gravity load while the second was the 2.5 MN load applied to the structure from the rotor, hub and the nacelle. The second load was present from the very first step of the analysis and it was transferred to a pressure acting on top of the tower.

Two boundary conditions were applied to the soil block while the third one was acting on top of the tower.

The mesh density on the pile/tower was as follows:

Total number of nodes: 2604

Number of linear hexahedral elements (C3D8R): 1288

The mesh density on the footing was as follows:

Total number of nodes: 132

Number of linear hexahedral elements: 66

5.5.3.4 The finite elements results

The maximum amount of settlement in the model after applying the gravity load was around 240 mm for a linear increase in the soil modulus (E(kPa) = 1500Z(m)).

From Figure 5-102 it is clear that the high stress zone is acting just above the footing while when the collar was present (model and test number three, Section 5.4.5) the high stress zone was just above the collar, which was acting as a support for the pile/tower section.

The force versus displacement graph for this model is illustrated in Figure 5-103.

5.5.4 Model number ten (Monopile structure VL = 3.8 MN, no test data available)

In this model, the collar attached to the tower's body was removed so that the outcome could be compared with the results of models number eight (un-piled footing) and nine (piled footing).

5.5.4.1 The pile/tower and footing geometries with their mechanical properties

This model consisted of a single pile embedded 35 m into the soil with an outer radius of 1.65 m and an inner radius of 1.5 m. The length of the tower above the ground level was 34.45 m.

As there was no footing present in this model, the water level was considered to be 2.62 m above the mudline, as in the case of the piled footing and the un-piled footing cases.

Two material properties were assigned to the pile/tower as the section of the pipe, which was below the water level, had a buoyant unit weight. The adopted material properties for the pile/tower are as in Table 5-4.

5.5.4.2 Assembly, Step and Interaction

Two steps were sufficient for the analysis. The first step was for applying gravity while the second step was for displacing the tower's head.

As there were only two part instances within the constructed model one-tie constraint was necessary between the pile and the soil block.

5.5.4.3 Loads, Boundary conditions and the generated Mesh

Two loads were acting on this model. The first one was the gravity load and the second one was a 2.5 MN force acting on the tower's head. The load from the nacelle, hub and rotor was transferred to a pressure acting on the tower's head and it was present for the duration of the analysis as in the case of the two previous models (models number eight and nine).

Two boundary conditions were acting on the soil block while the third one was considered on the tower's head. A reduced integration scheme was considered for the pile/tower in the numerical analysis.

5.5.4.4 The finite element results

The amount of settlement for a linearly increasing soil modulus (E(kPa) = 1500 Z (m)) after applying the gravity load was around 230 mm.

The Mises stresses acting on the pile/tower are illustrated in Figure 5-104. The force versus displacement graph for this model is illustrated in Figure 5-105.

The ultimate capacity obtained from the numerical model can be checked in respect to the solutions provided by Broms (1964) and Fleming et al. (1992) discussed in Section 2.6. Using Broms and Fleming's charts, the lateral capacity of the monopile was calculated to be equal to 7.2 MN and 8.3 MN respectively. The ultimate lateral capacity of this structure was calculated to be equal to 9 MN from the FE analysis. The difference between the solution charts provided by Broms (1964) and Fleming et al. (1992) with the FE result were -20% and -7.77% respectively.

5.6 COMPARING THE RESULTS

In this section, the FE and the test results will be compared for deriving conclusions in regards to the behaviour of the monopiles, piled footings and the un-piled footings embedded in a medium dense sand. The FE predictions in this section will be discussed only in regards to a linear increase in the soil's modulus of elasticity with a reduced integration scheme used on the pile/tower. In addition, as the mechanical devices attached to the structures in the centrifuge tests did not allow the vertical loads to be the same, in this section comparisons are made between the structures, which have the closest vertical loads with each other.

Figure 5-106 illustrates the FE and the test results obtained for the monopile (test and model number one, VL = 5.3 MN) and the piled footing structure (test and model number three, VL = 6.5 MN) used in the centrifuge tests. The vertical load acting on these two structures were close to each other (in the range of 5 to 6.5 MN). It is clear that the stiffness of the hybrid structure was

higher than that of a monopile from the initial point. As discussed in Section 2.10 this was one of the problems associated with the tests conducted by Stone et al. (2010) in the centrifuge. From Figure 5-106, it is also clear that the ultimate lateral capacity of the hybrid structure was higher than that of a monopile. The latest point was confirmed by centrifuge tests and by the FE results.

The difference between the stiffness of the FE predictions for the two structures (monopile and piled footing) in Figure 5-106 was +77% at a tower displacement of 1 m. This value was +101% at a displacement of 0.5 m. This clearly illustrates that by using a piled footing structure instead of a monopile the difference in the stiffness can exceed +40%.

Figure 5-107 illustrates the FE prediction and the test results for the piled footing structure in test and model number three (VL = 6.5 MN) compared to the un-piled footing structure in test and model number four (VL = 5.9 MN). In these structures, the vertical load acting above the footing level (footing number one) was between 5.9 to 6.5 MN. As can be seen, at low displacements the stiffness of the two structures were the same. This clearly demonstrates that at low displacements the footing controls the behaviour of the piled footing structure and not the pile structure.

Figure 5-108 illustrates the FE prediction and the test results for the un-piled footing structures in test and model number four (VL = 5.9 MN) with the results of the monopile in model and test number one (VL = 5.3 MN). It is clear that the initial footing's stiffness is higher than that of a monopile; this was the case for the FE and the test results. The main drawback to the footing structure is its ultimate lateral capacity, which was around three times smaller than the monopile's ultimate capacity.

Figure 5-109 illustrates the FE prediction and the test results for the piled footing structures in model and test number five and six (VL = 13.2 MN) with the un-piled footing structure, model number six (VL = 12.7 MN). These structures had the closest vertical loads for comparison purposes. It is again clear that the stiffness of the footing structure embedded in a sand deposit controls the initial stiffness of the hybrid structure. Stone et al. (2010) mentions that the initial behaviour of the structure was controlled by the pile while from the centrifuge tests and the FE results it is clear that this is not the case, and the initial behaviour of the hybrid structure is controlled by the footing installed at the ground level.

Figure 5-110 illustrates the results of the piled footing structure and the un-piled footing structures under a vertical load of 12.7 to 13.2 MN but the FE predictions for a monopile with the two footings attached to its tower (VL = 12.5 MN) has been included in this figure (this model was discussed in Section 5.5.1). It is clear that the initial stiffness of the un-piled footing structure is again higher than the initial stiffness of the monopile. This was also the case for when the structures were under a vertical load of 5 to 6 MN.

The results of the piled footing structures used in the testing programme with their corresponding FE predictions for vertical loads of 6.5 MN and 13.2 MN are illustrated in Figures 5-111 and 5-112 respectively. It is clear that the ultimate lateral capacity of the piled footing structure with a higher vertical load is higher than that for the lighter structure. By comparing the results illustrated in Figures 5-59 and 5-78, the two footings attached to the tower have acted similar to a

support for the piled footing structure. This indeed has caused the results of the piled footing structure with the extra weights (test number six, that is model number five in Table 5-5) to yield higher results than those of model and test number three (piled footing, VL = 6.5 MN).

Figure 5-113 illustrates the un-piled footing results for tests number two (VL= 9.3 MN), four (VL = 5.9 MN) and seven (VL = 12.7 MN). It is clear that by increasing the vertical load on the structure the ultimate lateral capacity of the structure has increased for tests number four (VL = 5.9 MN) and seven (VL = 12.7 MN). The smaller stiffness of test number seven (VL = 12.7 MN) up to a displacement of around 0.2 m can be contributed to mechanical problems, which might have occurred during the testing procedure in the centrifuge. It is also clear that the initial stiffness of test number two (VL = 9.3 MN and not completed) are not acceptable as the vertical load on this structure was smaller than test number seven (VL = 12.7 MN) but as can be seen its stiffness is much higher.

Figure 5-114 illustrates the FE results for the un-piled footing structures. The models were generated for tests number two (VL = 9.3 MN, not completed), four (VL = 5.9 MN) and six (VL = 13.2 MN), which correspond to models number two, four and six respectively (Table 5-5). It is clear that by increasing the vertical load on the structure, the ultimate lateral capacity and the stiffness of the structure has increased. Byrne et al. (2002) also illustrated the importance of the vertical load acting on a footing, which was horizontally loaded in his 1 g tests conducted on a sand deposit.

Figure 5-115 compares the results of models number eight to ten which were constructed to waive the discrepancies within the tests. As can be seen, the stiffness of the piled footing structure (with no collar attached to its tower) is higher than of a monopile structure. In addition, the stiffness of the un-piled footing structure at small displacements is exactly as of a piled footing structure. It must be reminded that for all three structures illustrated in Figure 5-115, the applied vertical load applied on top of the structure was 2.5 MN.

5.7 BENDING MOMENTS

As discussed in Chapter 2, if a piled footing structure is to be used instead of a monopile in practice, it is important that not only the stiffness and the ultimate capacity of the hybrid structure must be higher than of a monopile, but also its bending moments must be smaller than the bending moments generated on a monopile structure.

For comparison purposes the bending moments generated on models number one (monopile, VL = 5.3 MN) and three (piled footing, VL = 6.5 MN) illustrated in Table 5-5 were selected to be compared with each other. For generating the bending moments, it is conventional to embed a wire at the centre of the pile with a given modulus of elasticity, which is a million times smaller than of the pile's elasticity. After the analysis is completed, the bending moments are read off the wire by the aid of the Python script and multiplied by one million. For the proposed pile/tower, which contained an elasto-plastic material and was empty, a wire could not be installed at the centre of the monopile structure. To overcome the problem a very soft material was embedded into the pile and then the modulus of rigidity (EI) of the wire was adjusted with the pile's

material, but the results were not acceptable. Another solution to the problem was to construct a solid pile/tower with an equivalent modulus of elasticity and unit weight and to use a transformation factor (Hibbeler 2005) for the yield stress. In this method, the yield stress of the material is factored by the ratio of the modulus of elasticity between the solid pile/tower and its hollow case. Unfortunately, this method did not work as well and a descent result was not achieved.

To overcome the mentioned problems and to capture the bending moments, the best way was to extract the results manually from the models. The bending moments generated for models number three (piled footing, VL = 6.5 MN) and number one (monopile, VL = 5.3 MN) for different horizontal forces are illustrated in Figures 5-116 and 5-117 respectively.

In Figure 5-118, the results of model number three (piled footing, VL = 6.5 MN) and model number one (monopile, VL = 5.3 MN) have been compared together. From the latest figure, it is clear that for the section of the pile/tower under the ground the bending moments obtained from the piled footing structure were smaller than of the bending moments acting on a monopile structure, although the ultimate lateral force acting on the piled footing structure was higher than of the monopile case. The decrease in the bending moments in the piled footing structure can be attributed to the presence of the footing at the ground level.

The above discussion clearly illustrates the benefits of using a piled footing structure instead of a monopile for an offshore wind turbine.

For model number three (piled footing, VL = 6.5 MN) the rotation of the footing, the average shear stress and the average horizontal displacement of the footing was obtained from the numerical models for different horizontal loads. Table 5-11 illustrates the results, it must be mentioned that the base rotation was calculated by dividing the differential settlement of the bearing plate by its width (diameter).

Lateral force (MN)	Base rotation (rad)	Average shear (MPa)	Average horizontal displacement (m)
14.8	0.00828	7.7	0.032
11.4	0.0058	5.25	0.021
8.5	0.004	3.41	0.013
6.07	0.0026	1.62	0.0083

Table 5-11. The base rotation, average shear and displacement of the bearing plate for model number three

From the above table it is obvious that as the horizontal force increases the base rotation and the average shear and displacements are increasing as well.

It was discussed that the ultimate lateral capacity of the monopiles and the piled footing structures were controlled by their structural capacity. To investigate this point the yield stress of the monopile in model number ten (Table 5-6) was removed and the monopile was laterally loaded. This would illustrate wether the sidewalls along the pile shaft would fail or not. Figure 5-119 illustrates the results, it is clear that the soil was not anywhere close to its failure point and

the ultimate capacity was controlled by the structural capacity of the monopile. Figure 5-120 illustrates the Von Mises stresses acting on the elastic monopile and the soil block.

5.8 A PARAMETRIC STUDY

To investigate the behaviour of the hybrid structure in different soil deposits a parametric study was conducted at this point. A more detailed study has been conducted in Chapter 6.

This study was conducted on a monopile with an outer diameter of 5 m and a length of 30 m. The tower was 70 m long (from the seabed level) and the thickness of the monopile was equal to 60 mm. The pile in this study was constructed out of steel (ASTM-A36) and the footing was constructed out of concrete (M25). The adopted pile dimensions in this study are in the range of the values employed in practice for offshore wind turbines. The mechanical properties of the pile/tower and the concrete are listed in Table 5-12.

Property	Pile (Steel)	Footing (Concrete)
Density above water (ρ)	7800 kg/m^3	2300 kg/m^3
Density under water	6820 kg/m^3	1319 kg/m^3
Modulus of Elasticity (E)	200 GPa	25 GPa
Poisson ratio (ν)	0.32	0.15
Yield strength	250 MPa	-

Table 5-12. The mechanical properties of the pile/tower and the footing

For this study, no strain hardening was considered for the pile/tower constructed in the numerical models and the footing was located at the ground surface. To compensate for the weight of the nacelle, hub and the rotor a surplus load of 2.5 MN was added to the tower's head for all numerical models.

Two soil deposits were considered for this study, one was loose sand and the other was dense. The soil properties are illustrated in Table 5-13. The adopted Young's modulus increased linearly from the ground surface and the Poisson ratio was adjusted in regards to the friction angle of the soils through Equation 5-3.

Property	Loose sand	Dense sand
Effective unit weight (γ')	7 kN/m^3	7 kN/m^3
Friction angle (ϕ)	32°	42°
Young's modulus (E_{kPa})	750 Z (m)	3000 Z (m)
Poisson's ratio (υ)	0.319	0.248
Dilation angle (Ψ)	0°	0°
In situ earth pressure (K_0)	0.47	0.33

Table 5-13. The mechanical properties of the loose and dense sand

Three footings with diameters of 10 m, 20 m and 30 m were considered. The footing thicknesses were taken to be equal to 10% of their diameter. The water level was adjusted to be standing at the height of the footing for all piled footing cases. For the monopile case, the water level was considered 2 m above the ground level (that was the average height of the water level for the footing cases).

The results obtained from the loose and dense sand are illustrated in Figures 5-121 and 5-122 respectively. It is apparent that the stiffness of the hybrid structure was higher than of a monopile even for the smallest footing dimension. Figure 5-123 illustrates the stress versus strain diagram for the monopiled footing with a footing diameter equal to 30 m in dense sand.

From the results of Figures 5-121 and 5-122 it is clear, that a complete parametric study is required if the benefits and the behaviour of a piled footing structure embedded in sand deposits is to be illustrated. This is plausible, because the stiffness of the smallest footing (1 m) embedded in both sand deposits were higher than of a monopile case from the initial point. In regards to the results obtained from Figures 5-121 and 5-122, a detailed parametric study has been conducted in Chapter 6 to evaluate the response of the hybrid structure and monopiles embedded in loose and dense sand medium.

5.9 CONCLUSION

It was illustrated that the stiffness of a piled footing structure with a footing diameter half the length of the pile was higher compared to the results of a monopile embedded in a medium to dense sand deposit. It was clear that the stiffness of the hybrid structure compared to a monopile was also higher form the initial point.

By the aid of the test results, and the FE predictions it was confirmed that the proposed hybrid structure had a stiffness of over 40% compared to the stiffness of a monopile embedded in a medium dense sand deposit. Moreover, the ultimate lateral capacity of the hybrid structure was higher than of a monopile and this was also confirmed by the centrifuge tests and the FE results.

It was evident that the initial stiffness of an un-piled footing with a tower was higher than of a monopile but the ultimate lateral capacity of the monopile was around three times the ultimate capacity of the un-piled footing. In addition, it was illustrated that the initial stiffness of the hybrid structure was equal to the stiffness of the un-piled footing structure. The FE and the test results confirmed the last point and this was a confirmation that the initial behaviour of the hybrid structure was controlled by the bearing plate and not by the pile structure.

The importance of the vertical load for un-piled footing structures under a moment load were illustrated by the FE models. Moreover, it was shown that for such structures the overturing capacity and a combination of the bearing capacity equations with the VHM loading equations for footings provided reasonable answers for calculating the ultimate lateral capacity of an un-piled footing structure. With the aid of the FE models, it was demonstrated that the ultimate lateral capacity of a monopile structure was not significantly affected when the vertical load on the structure was increased.

From the results of the FE models constructed for the monopiles and the piled footing structures, it was successfully demonstrated that the bending moments generated on the piled footing structure (under the ground) with a hollow pile/tower provided smaller values compared to a monopile structure.

From the FE results, it was clear that by changing the soil stiffness from a linear to a parabolic distribution, the results obtained for the monopile and the piled footing structures were not significantly affected. In addition, by constructing a purely elastic pile/tower, it was clear that the structural capacity controlled the ultimate lateral capacity of the monopiles and the piled footing structures (the soil was remote from collapse). In practice, the maximum allowable rotation at the pile head after installation is typically between 0.003 to 0.009 rad (Malhorta 2011).

From the results of a parametric study, it was clear that if the full benefits of the hybrid structure is to be demonstrated a detailed parametric study is required to study all aspects of the proposed structure.

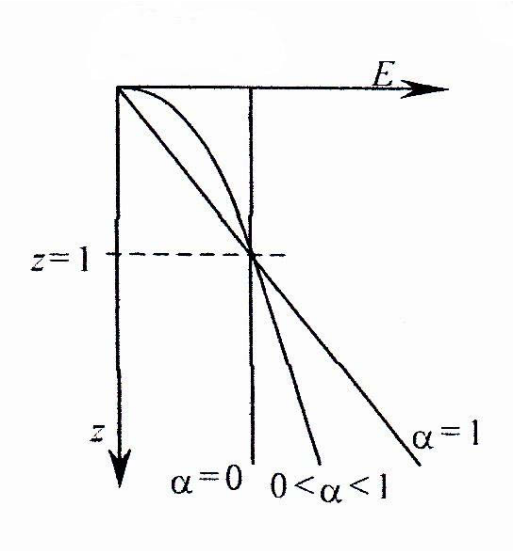

Figure 5-1. Different types of soil moduli adopted for numerical analysis (after Booker et al. 1985)

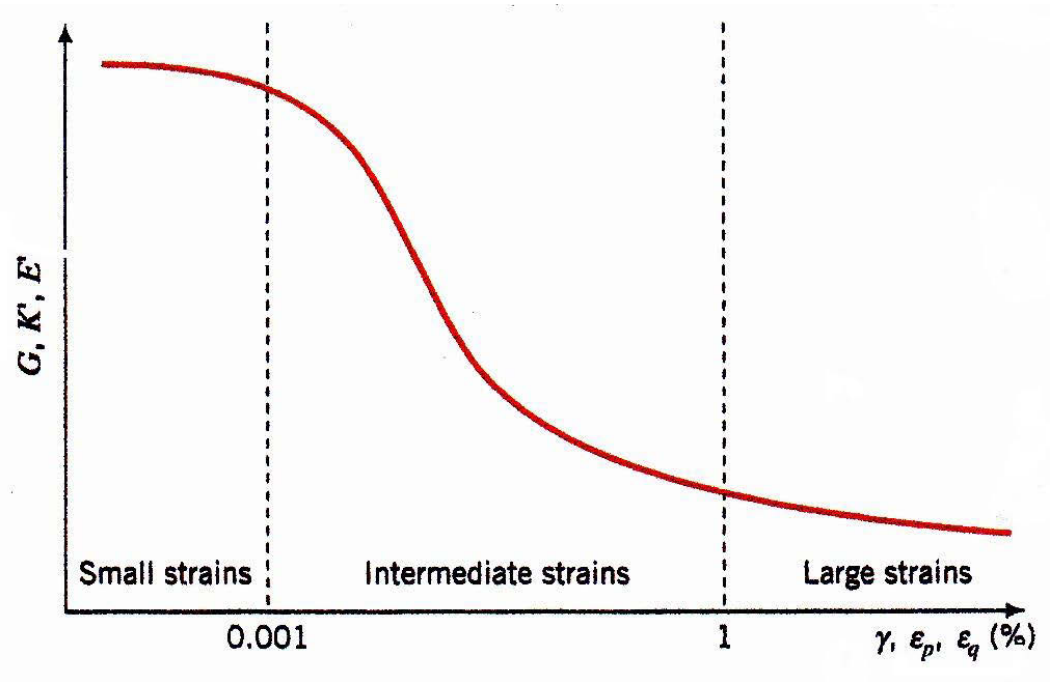

Figure 5-2. A schematic illustration of shear, bulk and soil modulus with strain levels (after Budhu 2007)

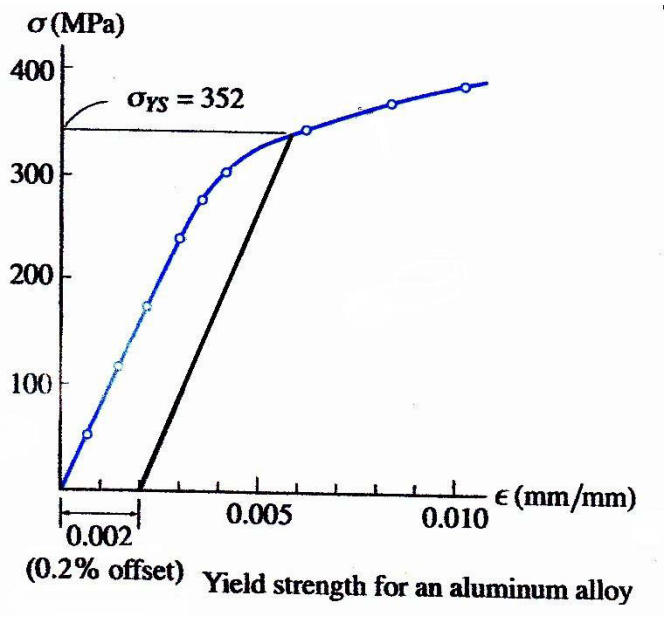

Figure 5-3. Illustration of the yield strength of an Aluminium alloy (after Hibbeler 2005)

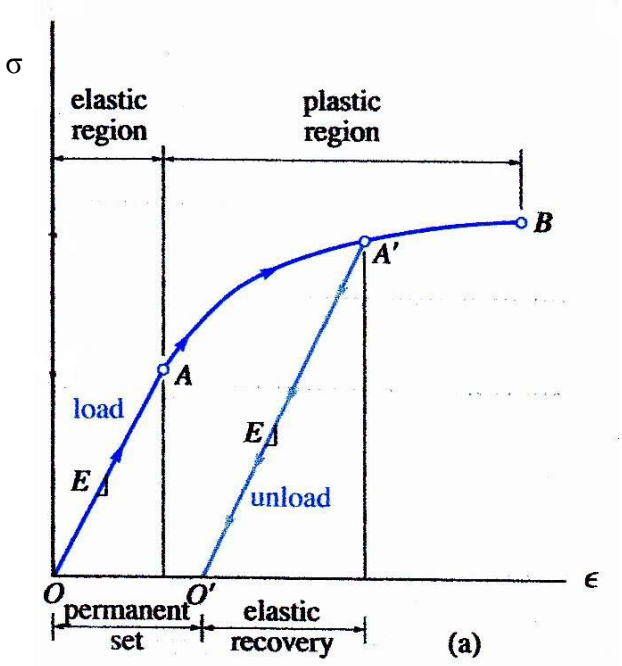

Figure 5-4. Stress versus strain graph illustrating the concept of strain hardening

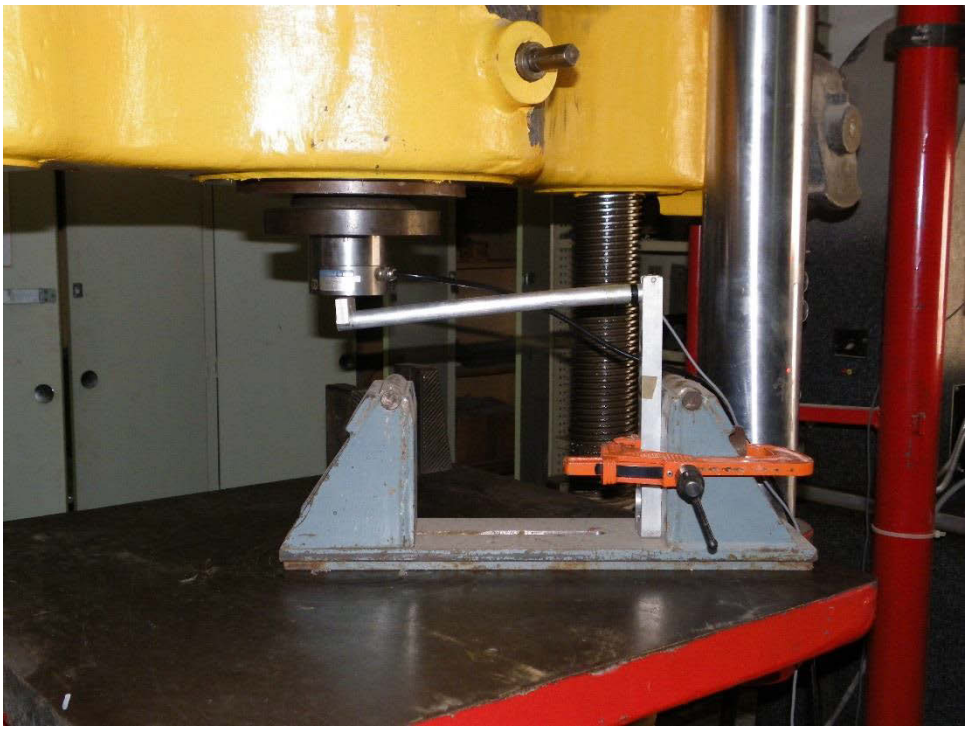

Figure 5-5. The bar used for calculating the stiffness of the material (similar to a cantilevered beam)

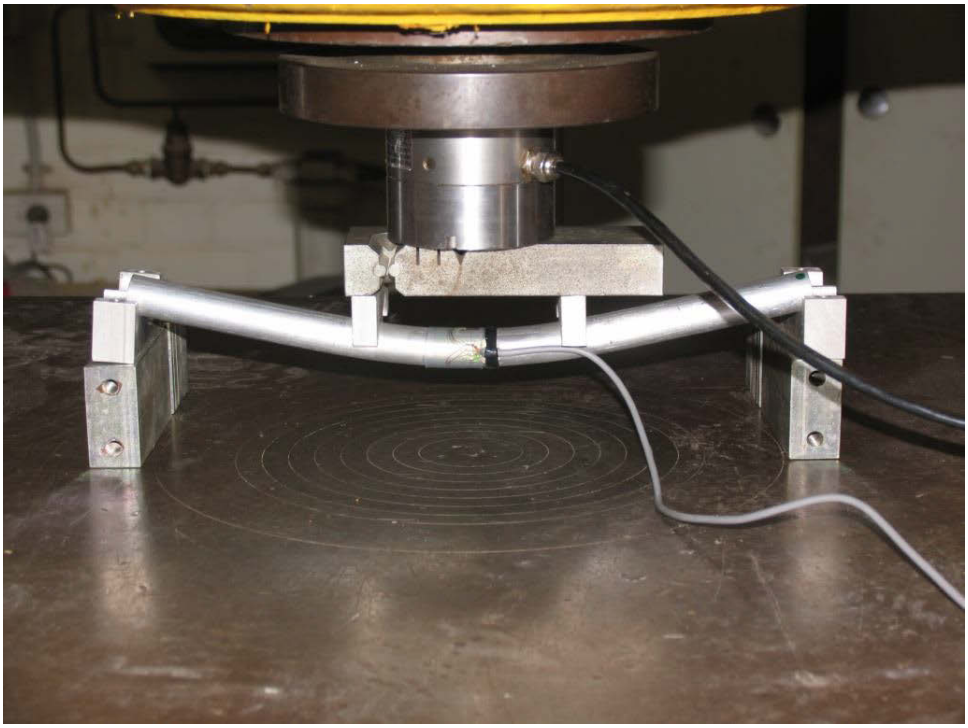

Figure 5-6. The simply supported bar with the attached strain gauges for calculating the Young's modulus of elasticity

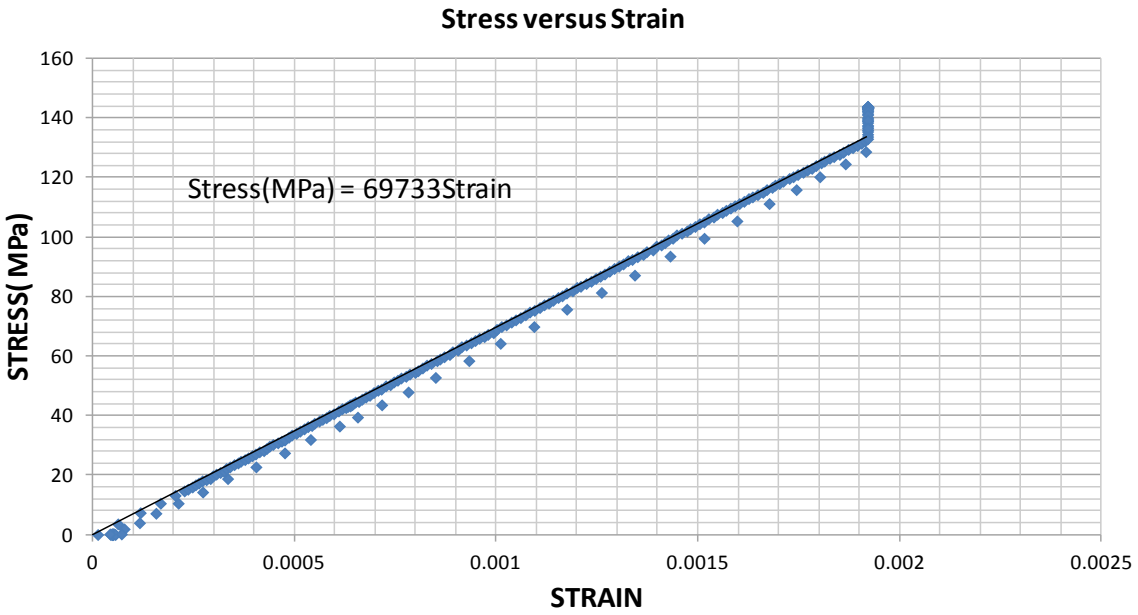

Figure 5-7. Stress versus strain graph for the Aluminium bar used in the centrifuge tests

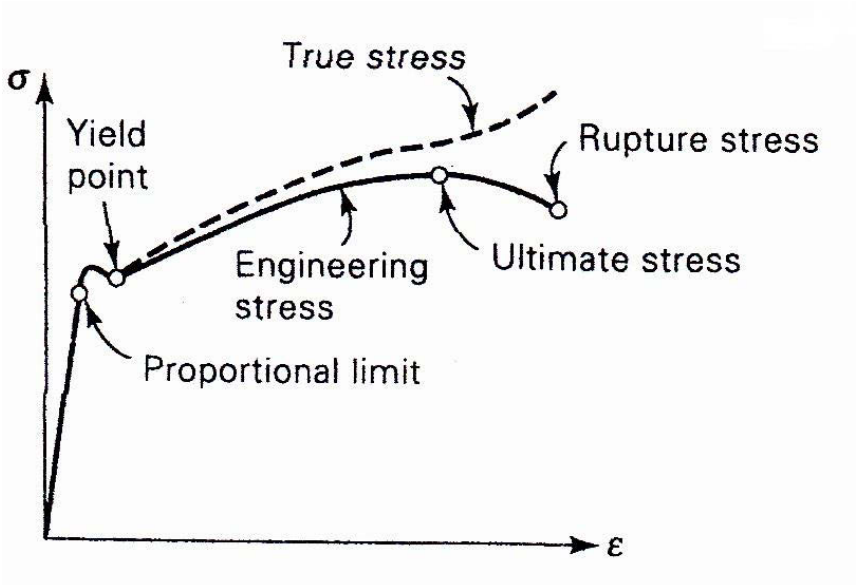

Figure 5-8. A schematic illustration of the stress versus strain graph for a ductile material (after Ugural et al. 2003)

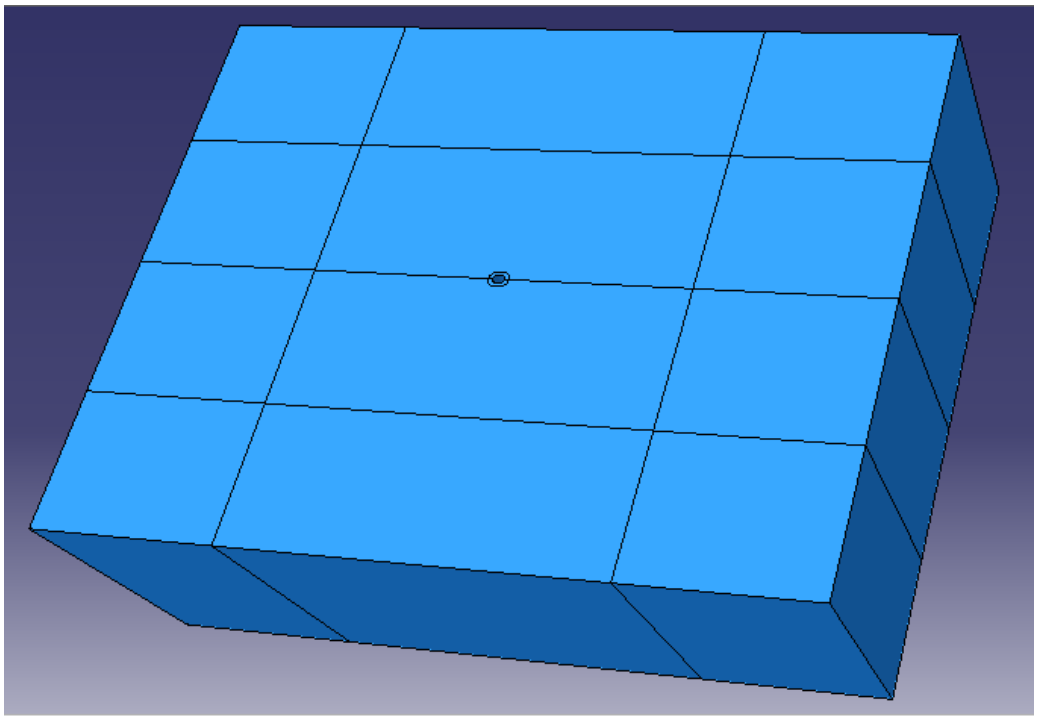

Figure 5-9. The soil block used for the monopile structures

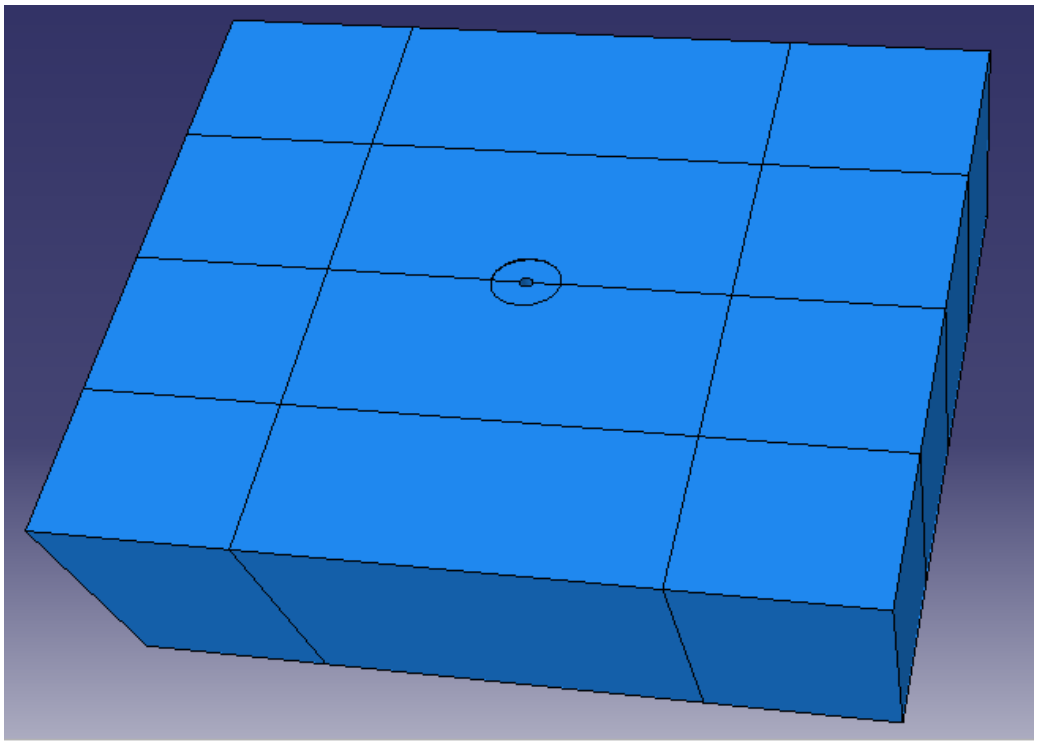

Figure 5-10. The soil block used for the piled footing structures

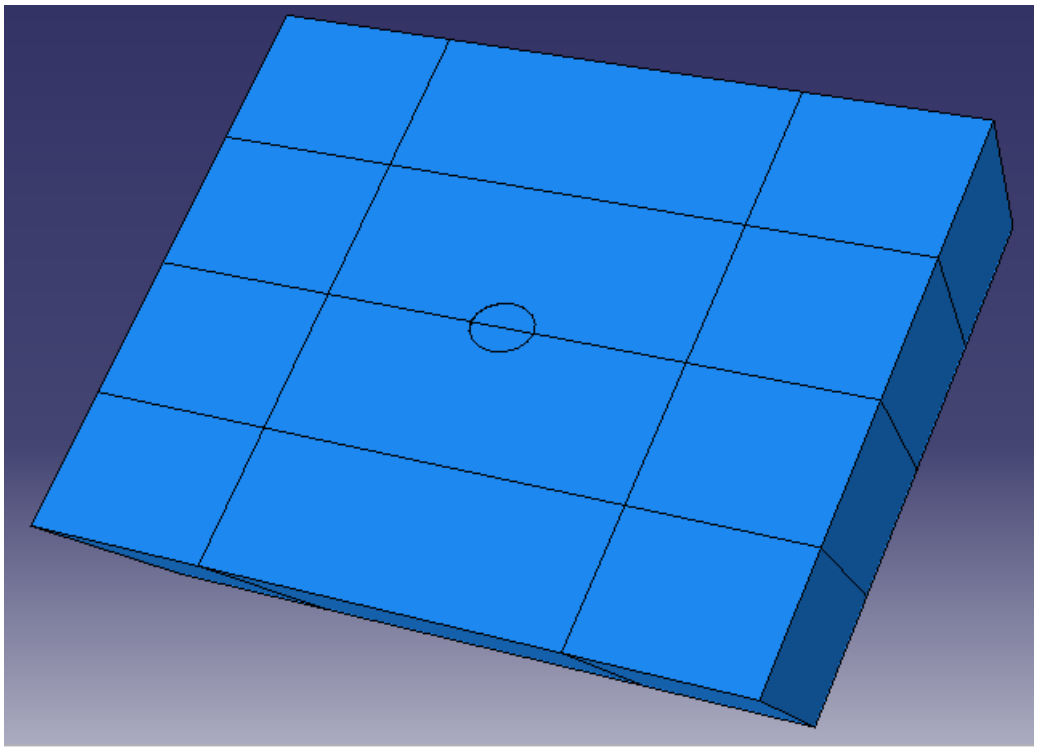

Figure 5-11. The soil block used for the un-piled footing structures

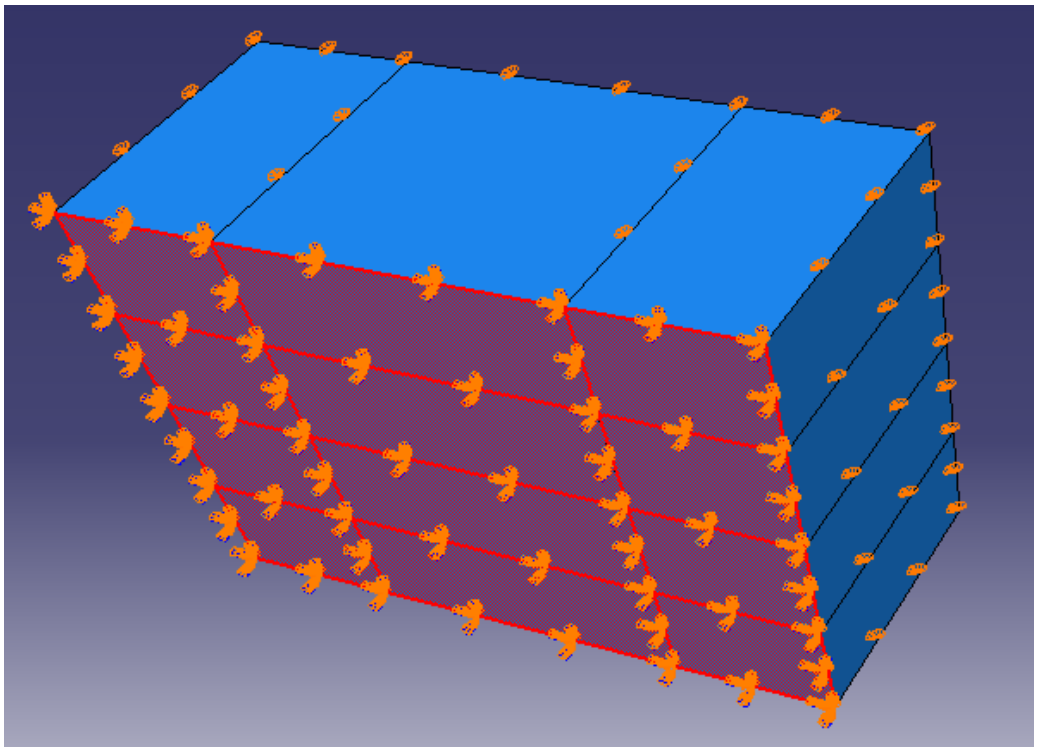

Figure 5-12. The boundary condition imposed on the base of the soil blocks

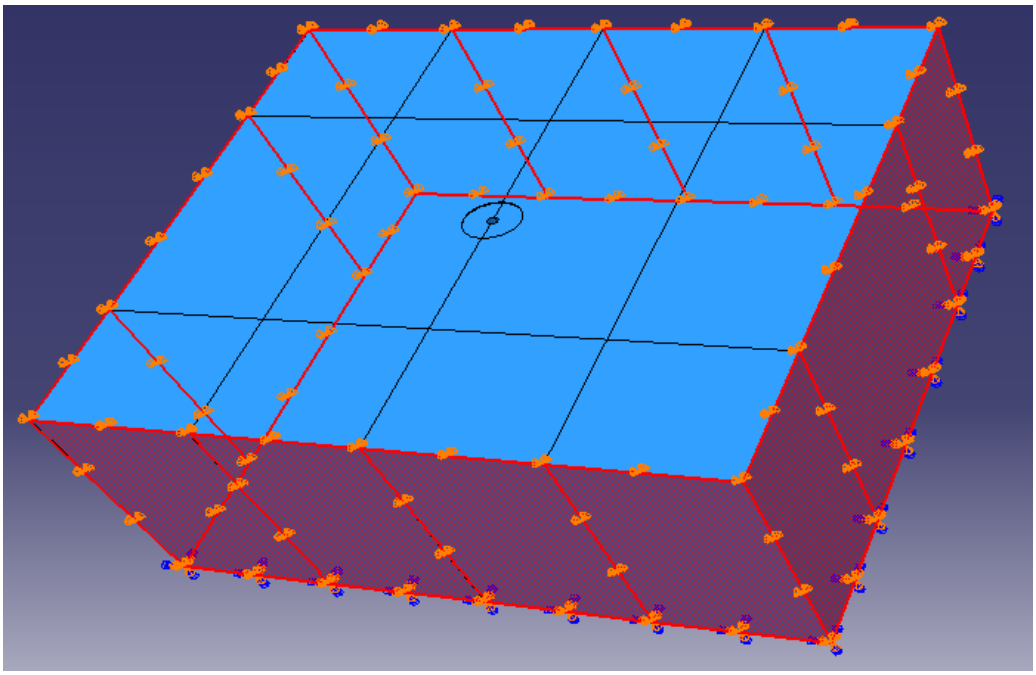

Figure 5-13. The boundary condition imposed on the sides of the soil blocks

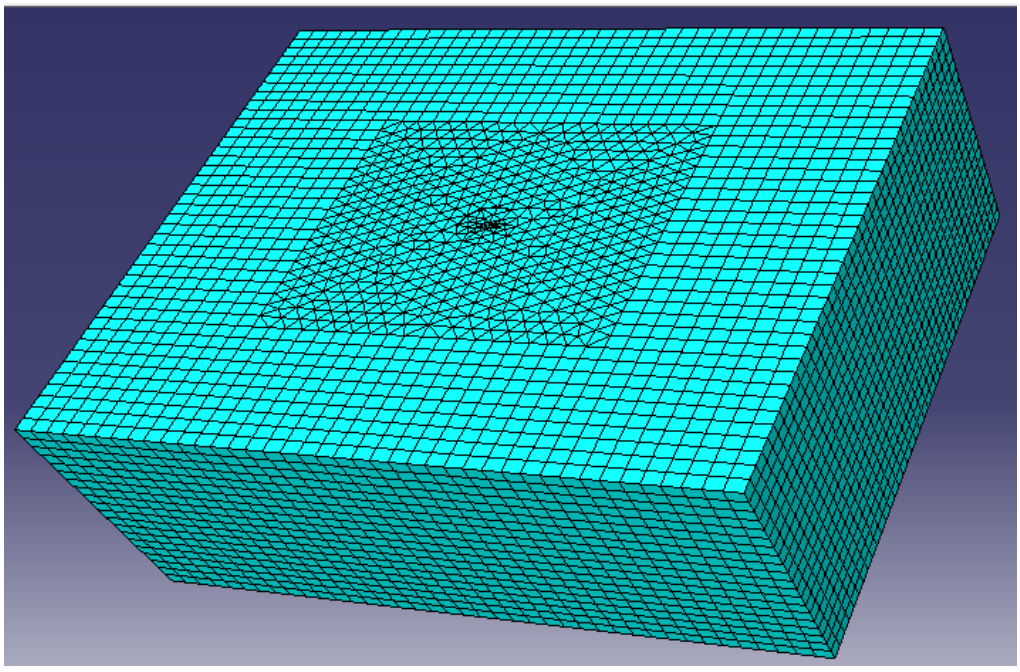

Figure 5-14. The mesh generated on the soil block

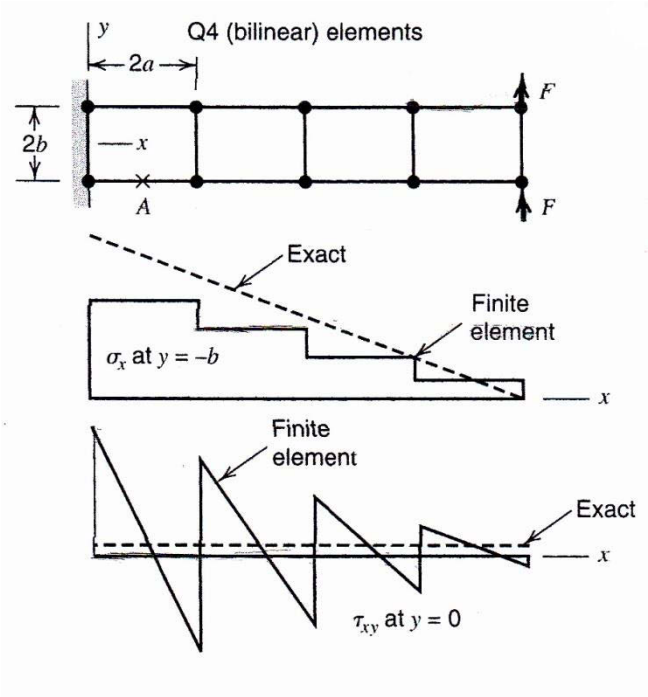

Figure 5-15. A Cantilever beam modelled by Q4 elements (after Cook et al. 2002)

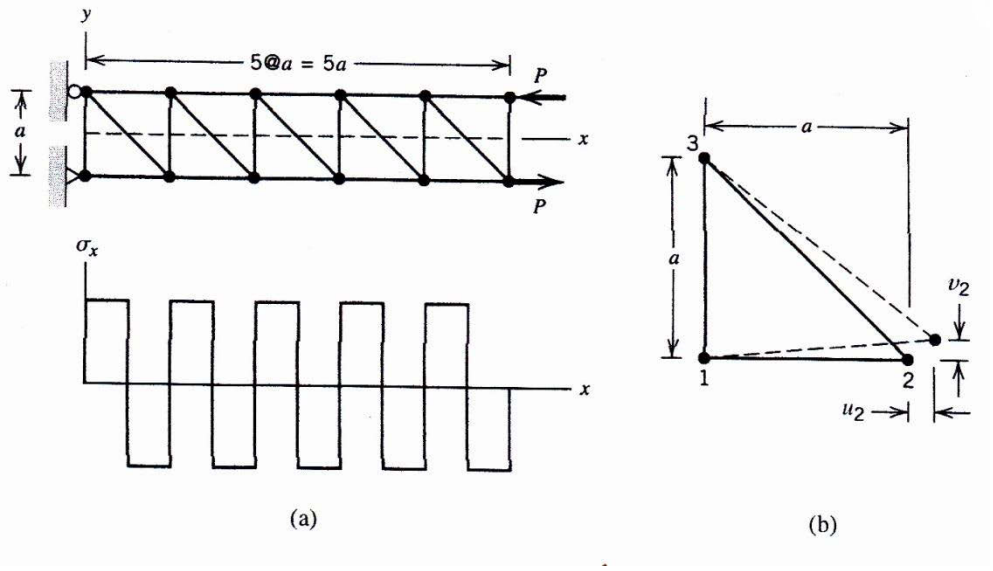

Figure 5-16. The stresses along the ϰ axis in a beam, modelled by CST elements

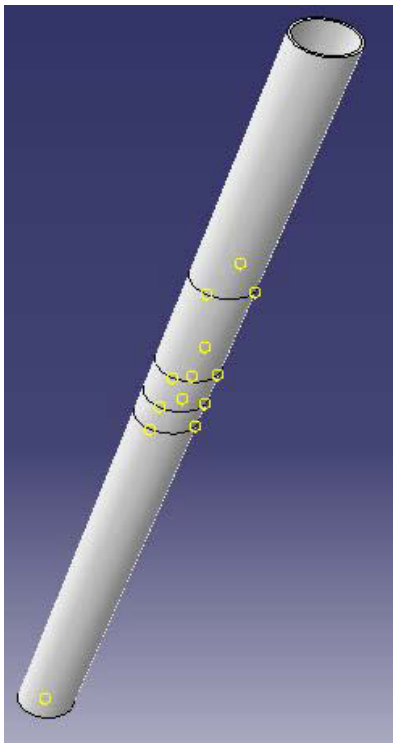

Figure 5-17. The pile/tower constructed for the numerical models

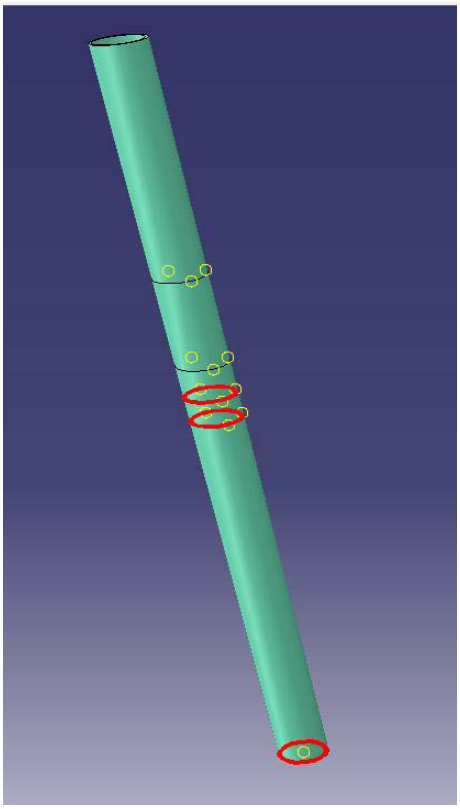

Figure 5-18. The material property adopted for the section below the water table in the numerical model

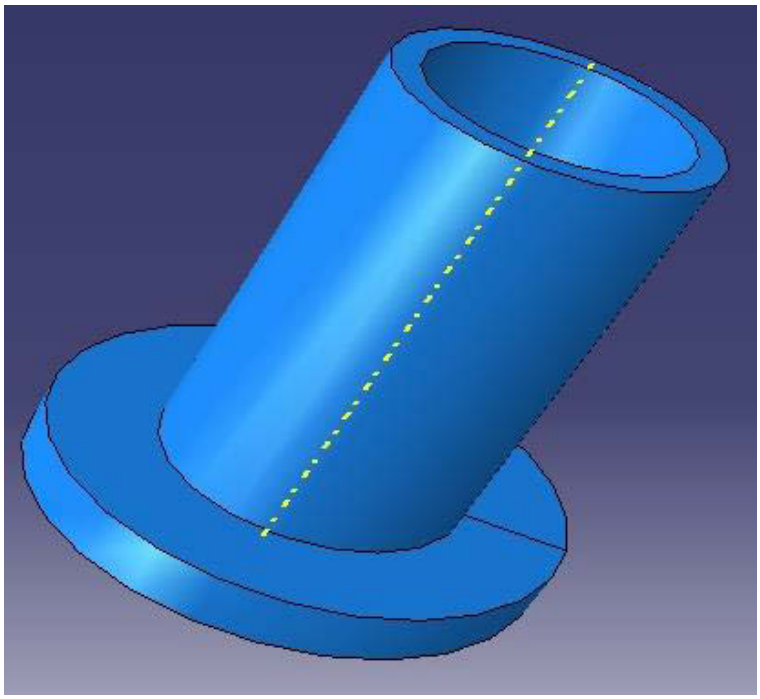

Figure 5-19. The collar constructed for the numerical models

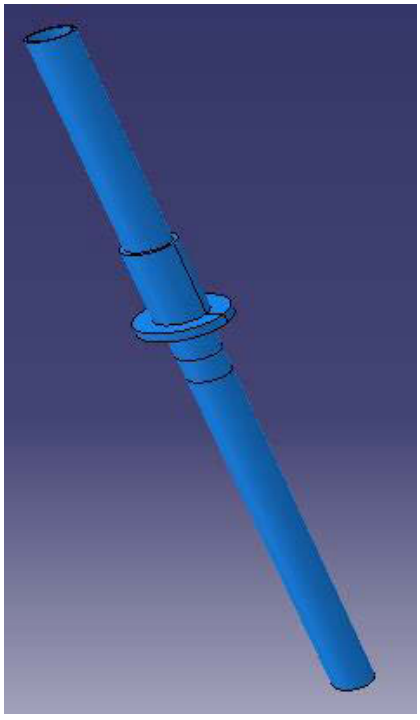

Figure 5-20. The pile/tower and the attached collar

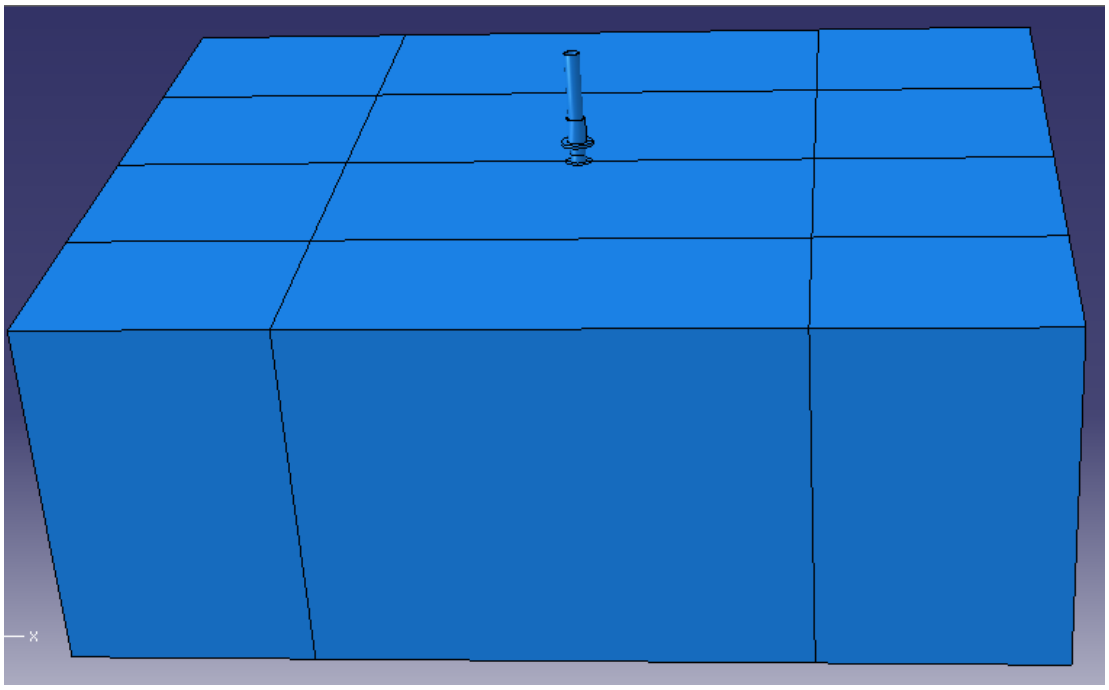

Figure 5-21. The monopile and the collar located within the soil block

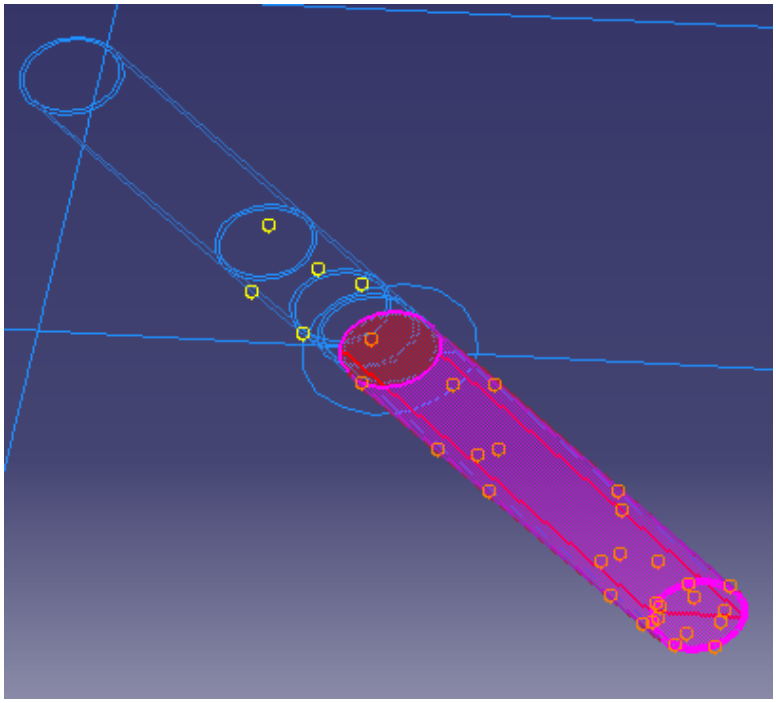

Figure 5-22. The pile and soil interaction

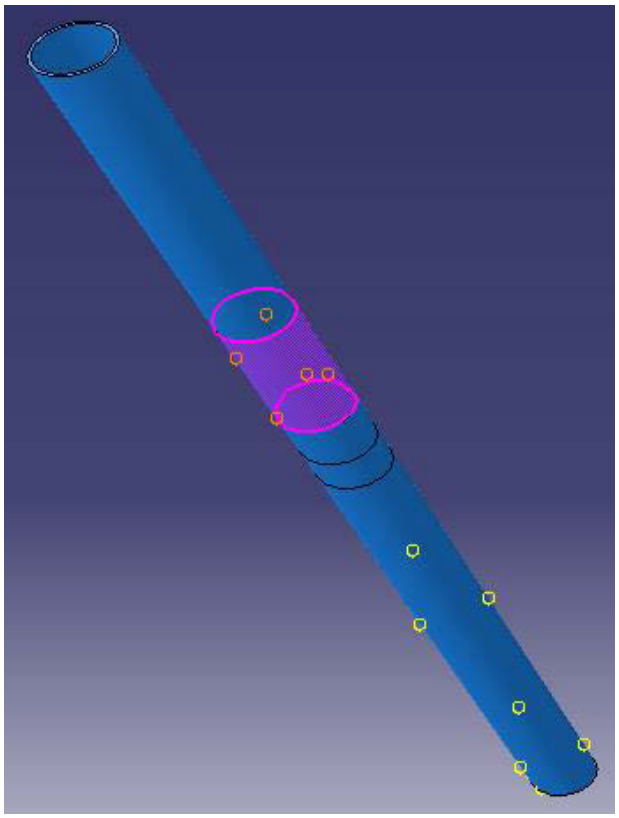

Figure 5-23. The region selected on the pile/tower to interact with the collar

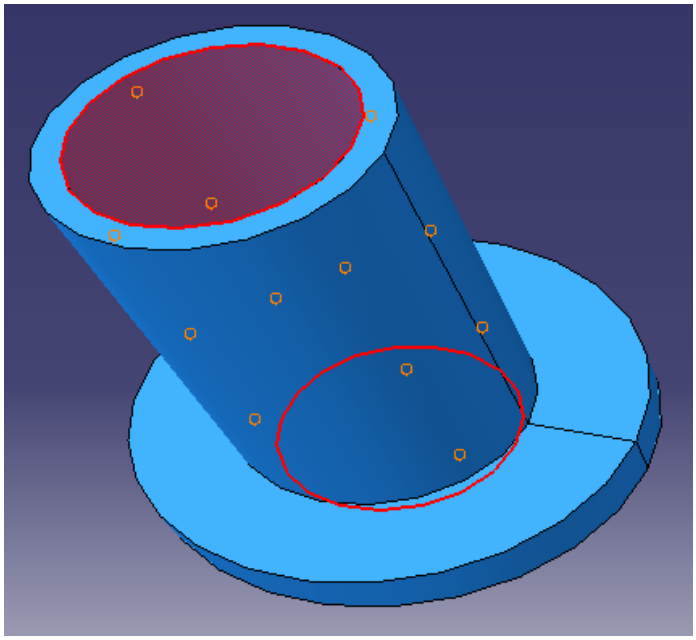

Figure 5-24. The region selected on the collar to interact with the pile/tower

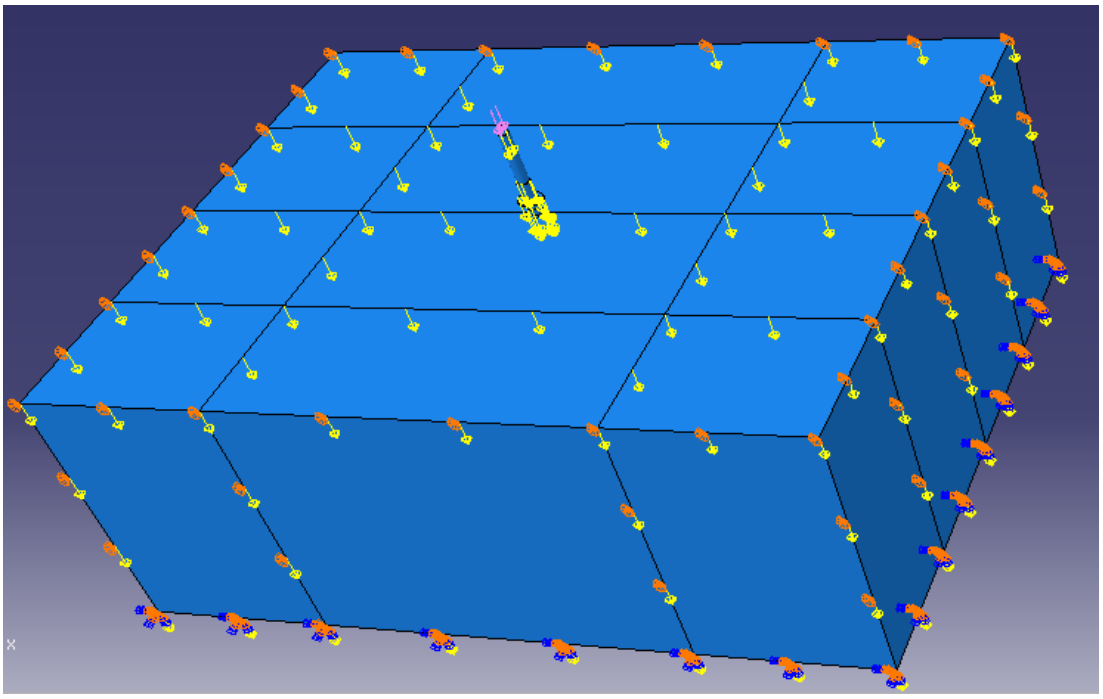

Figure 5-25. The gravity and pressure applied to model number one (monopile)

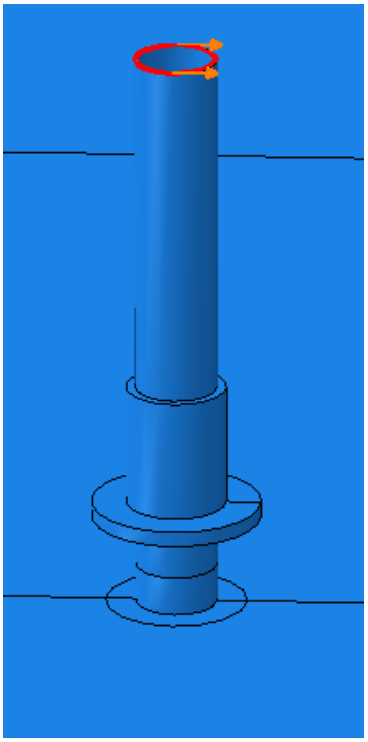

Figure 5-26. The boundary condition acting on the pile/tower's head for model number one (monopile)

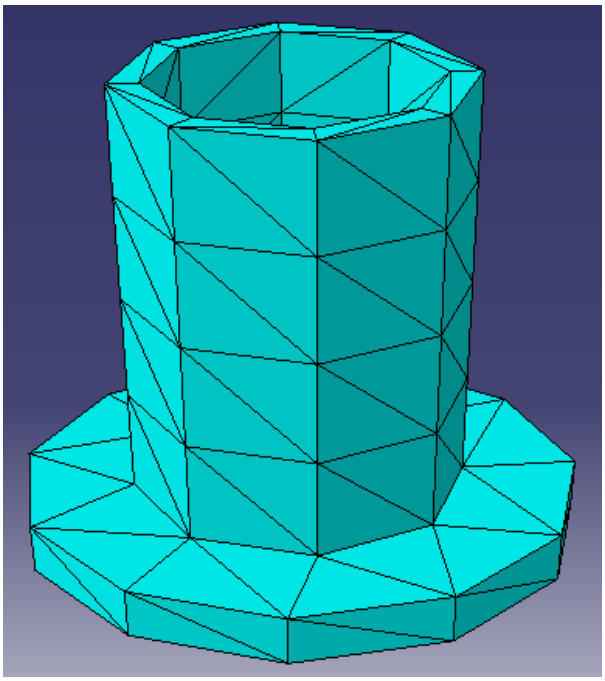

Figure 5-27. The mesh generated on the collar

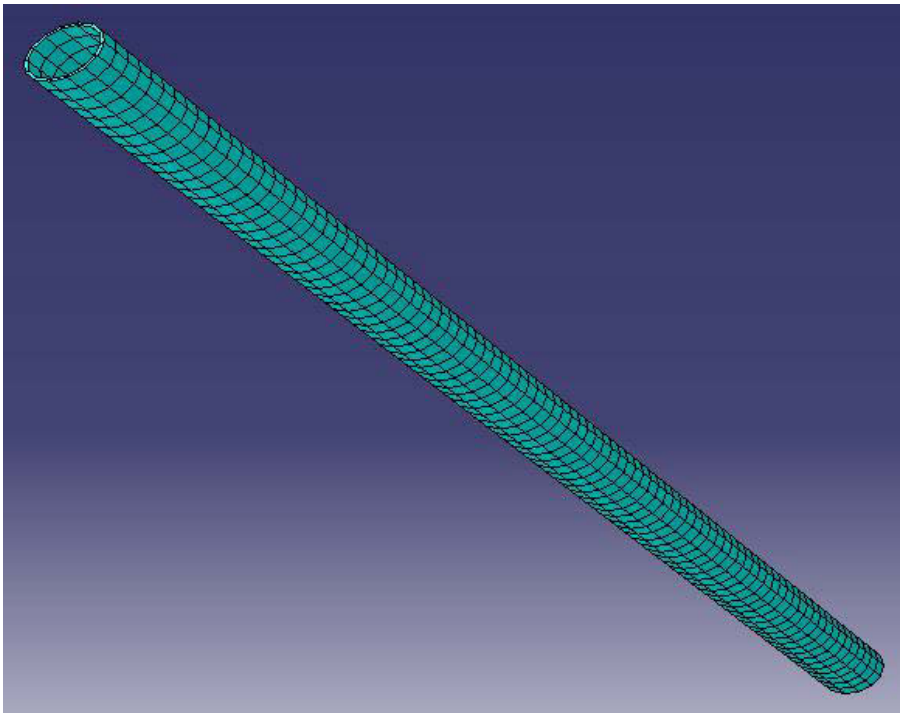

Figure 5-28. The mesh generated on the pile/tower

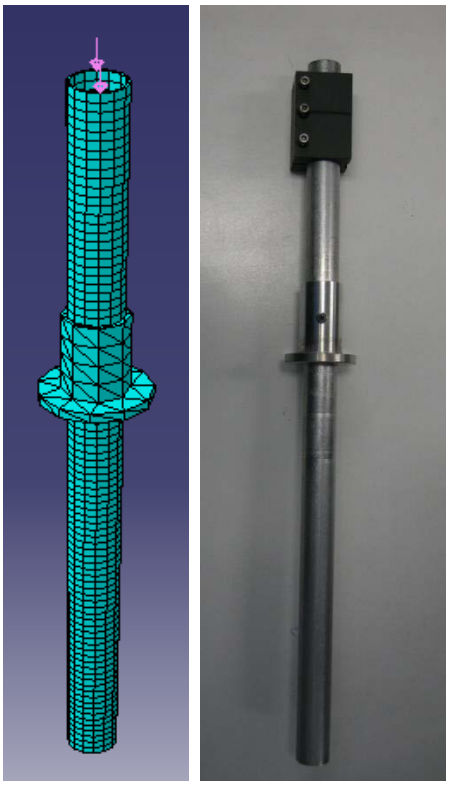

Figure 5-29. The pile/tower and the collar in the numerical and the centrifuge test

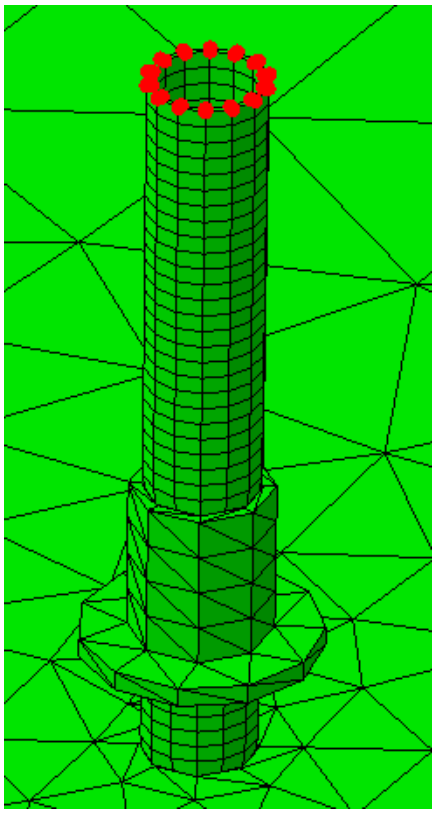

Figure 5-30. The tower's nodes used for extracting the reaction forces

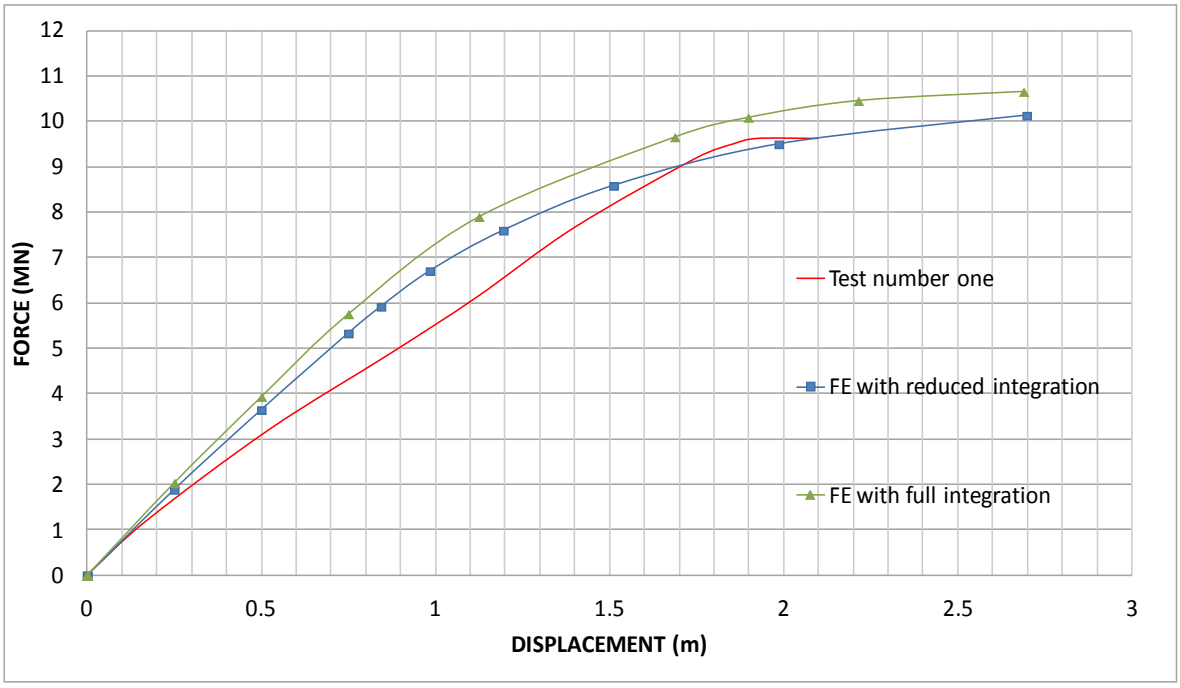

Figure 5-31. The numerical results for a linear increase in the soil modulus compared with the results of test number one (monopile structure, VL = 5.3 MN)

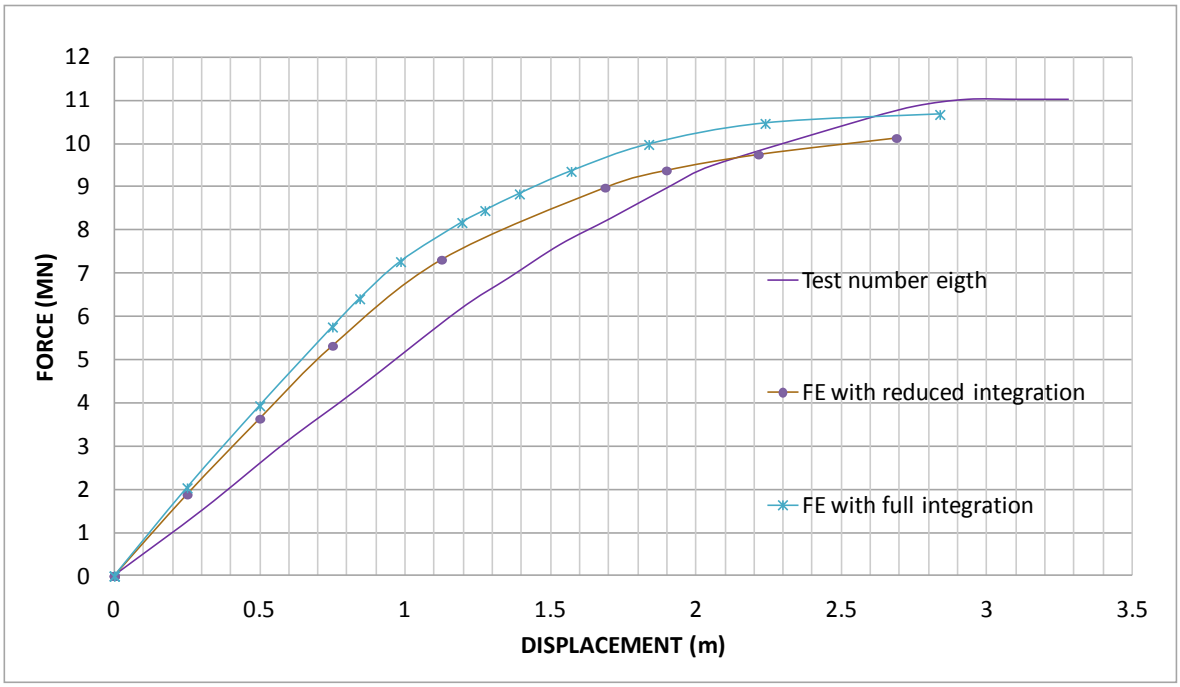

Figure 5-32. The numerical results for a linear increase in the soil modulus with the results of test number eight (monopile structure, VL = 6.5 MN)

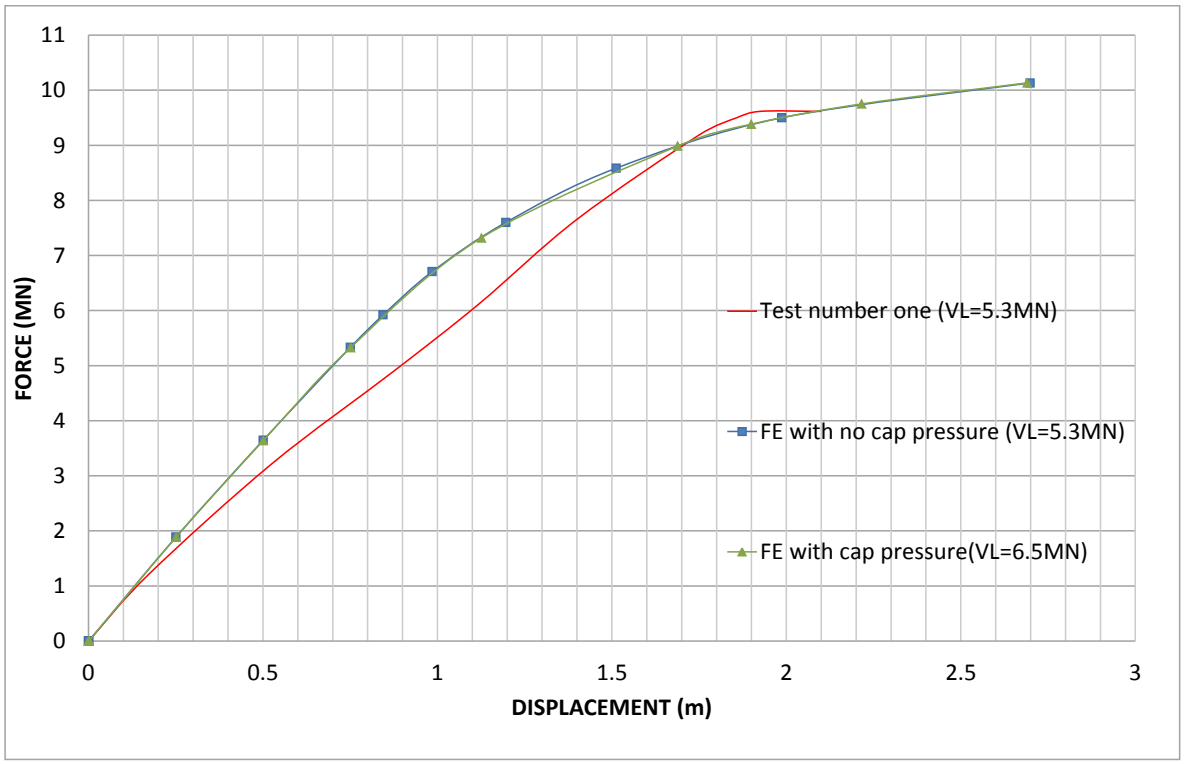

Figure 5-33. The FE results with a reduced integration scheme and a linear increase in the soil modulus

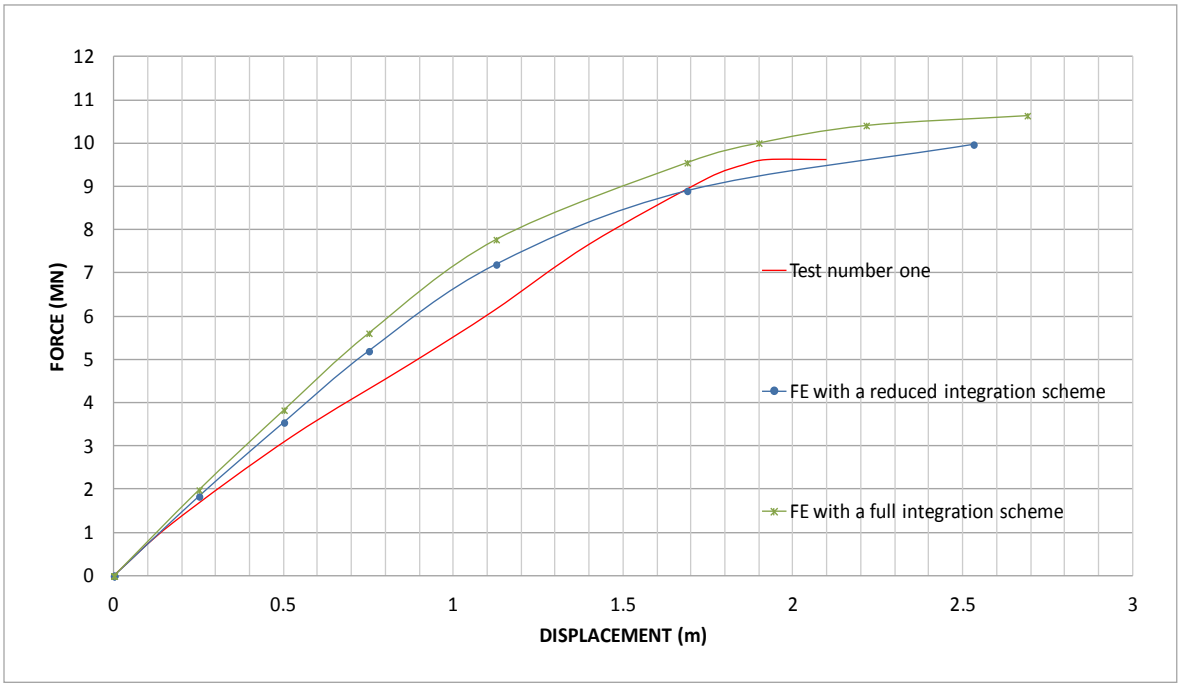

Figure 5-34. The FE results with a parabolic increase in the soil's modulus with different integration schemes (test number one, VL=5.3 MN)

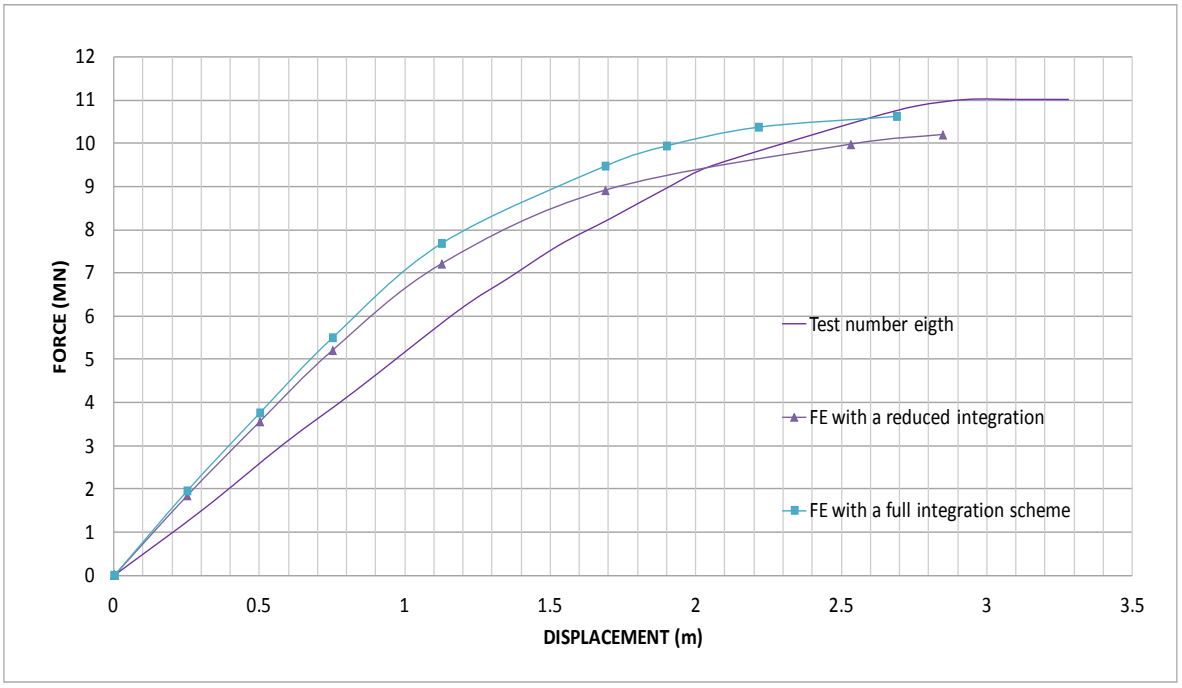

Figure 5-35. The numerical results with a parabolic increase in the soil modulus for test number eight (monopile, VL=6.5 MN)

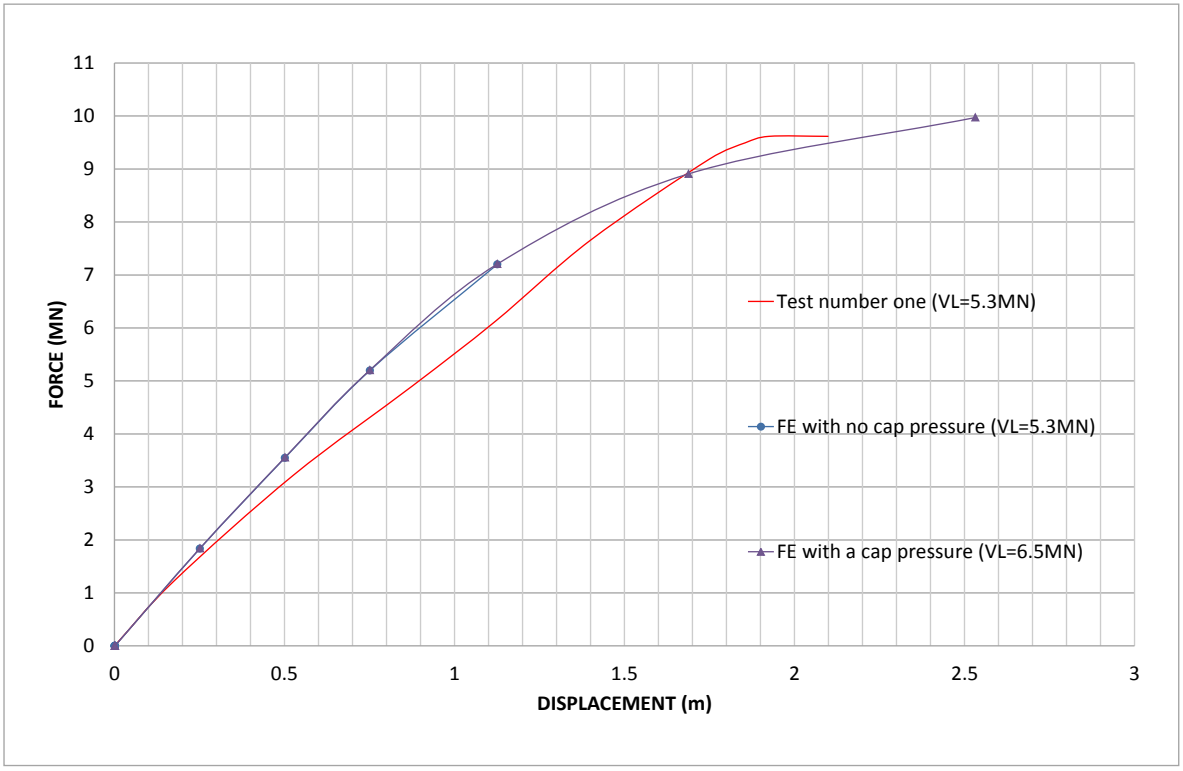

Figure 5-36. The FE results with a reduced integration scheme and a parabolic increase in the soil modulus compared to the results of test number one (monopile, VL=5.3 MN)

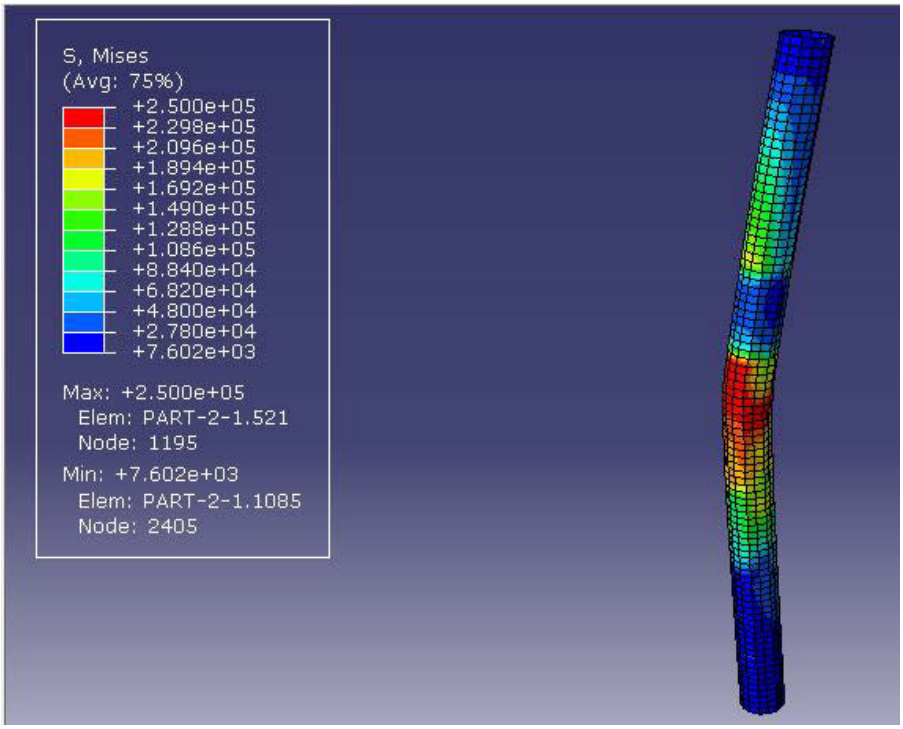

Figure 5-37. The Von Mises stresses acting on the pile/tower (without the cap pressure) for a linear increase in the soil modulus

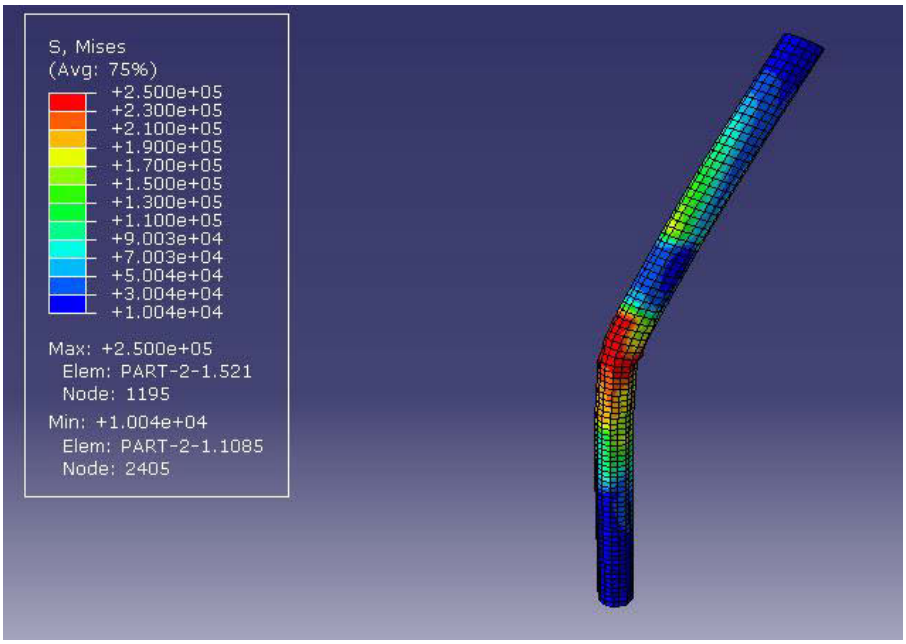

Figure 5-38. The Von Mises stresses acting on the pile/tower (with the cap pressure) for a linear increase in the soil modulus

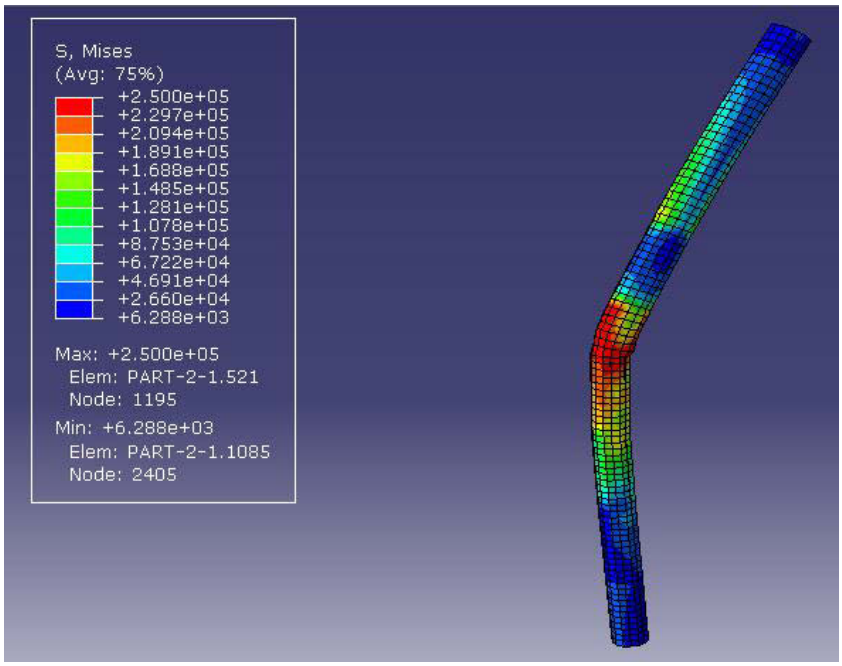

Figure 5-39. The Von Mises stresses acting on the pile/tower (without the cap pressure) for a parabolic increase in the soil modulus

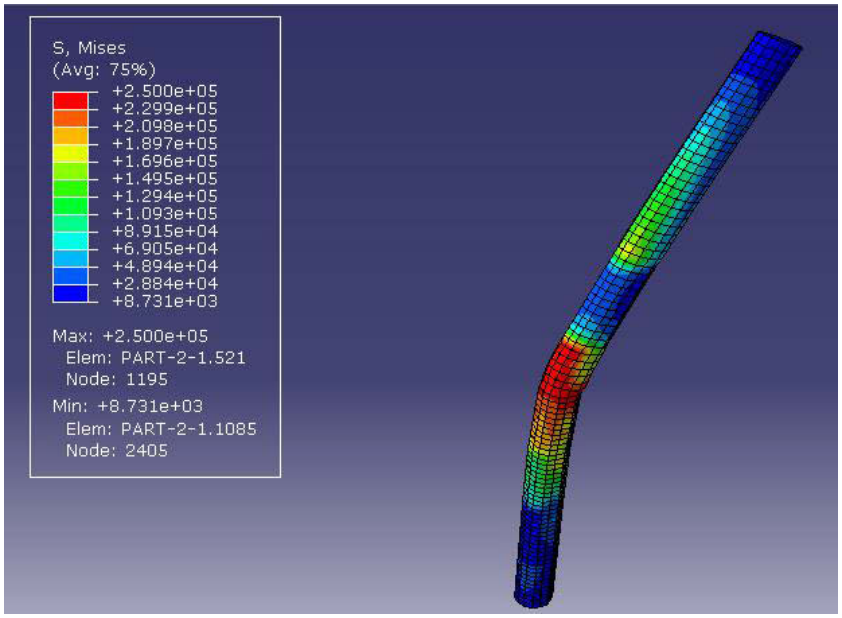

Figure 5-40. The Von Mises stresses acting on the pile/tower (with the cap pressure) for a parabolic increase in the soil modulus

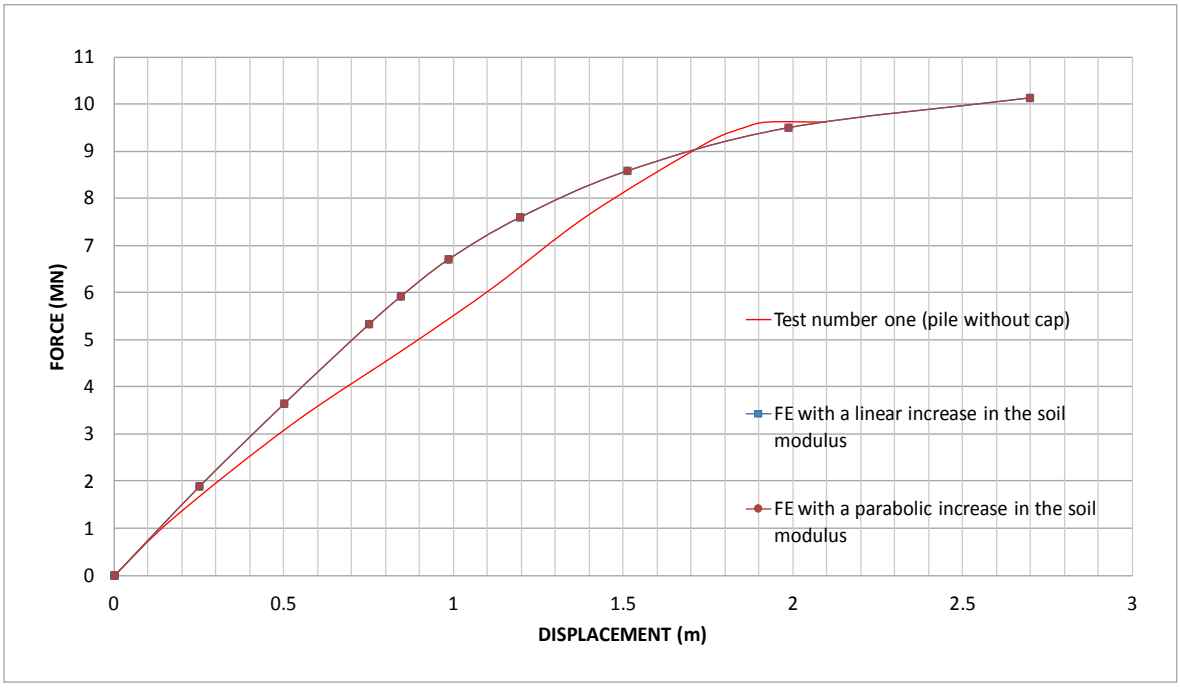

Figure 5-41. Comparing the FE results with different soil moduli with a reduced integration scheme (monopile, VL=5.3 MN)

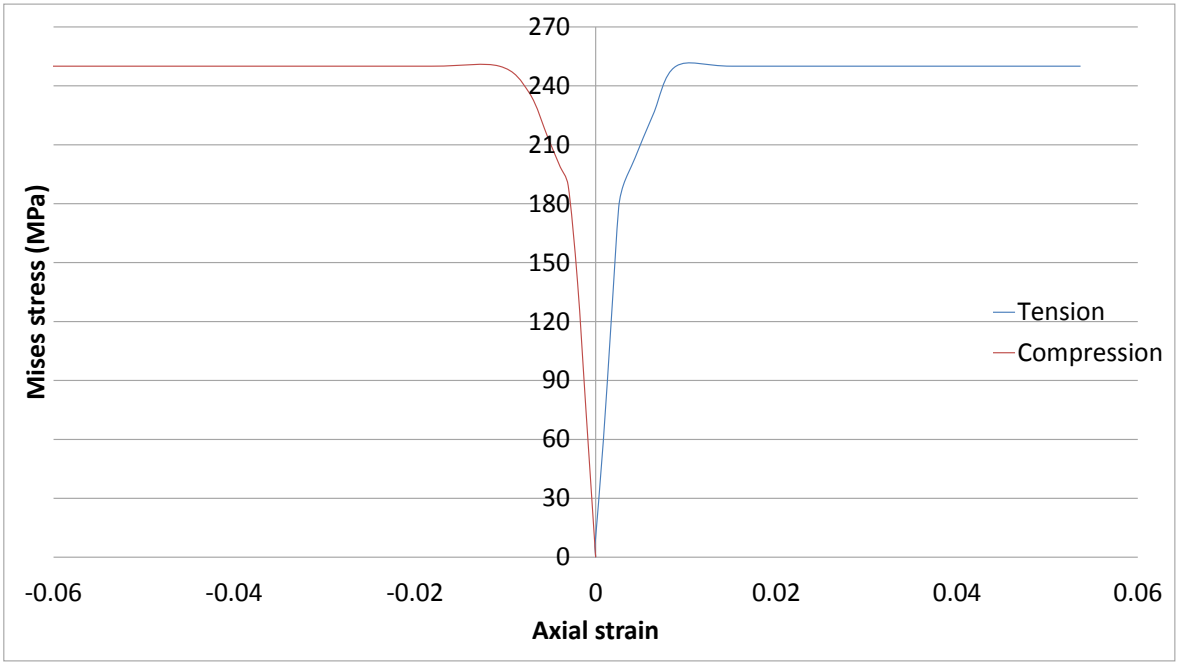

Figure 5-42. The strain hardening of the Aluminium pipe for model number one (monopile, VL=5.3 MN)

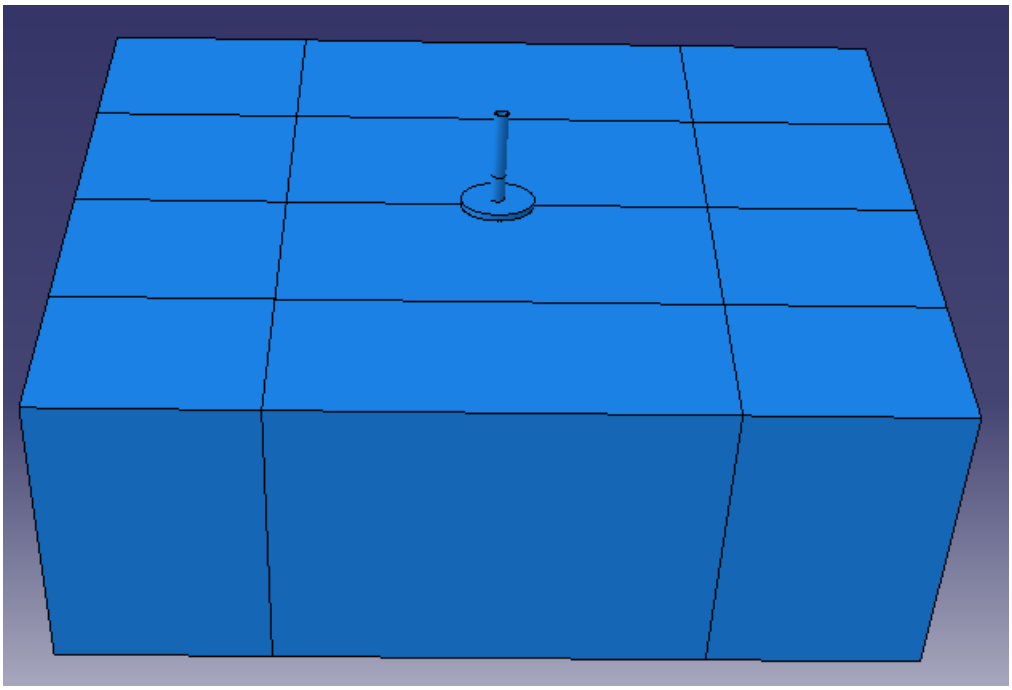

Figure 5-43. The soil block and the footing assembled for the numerical model

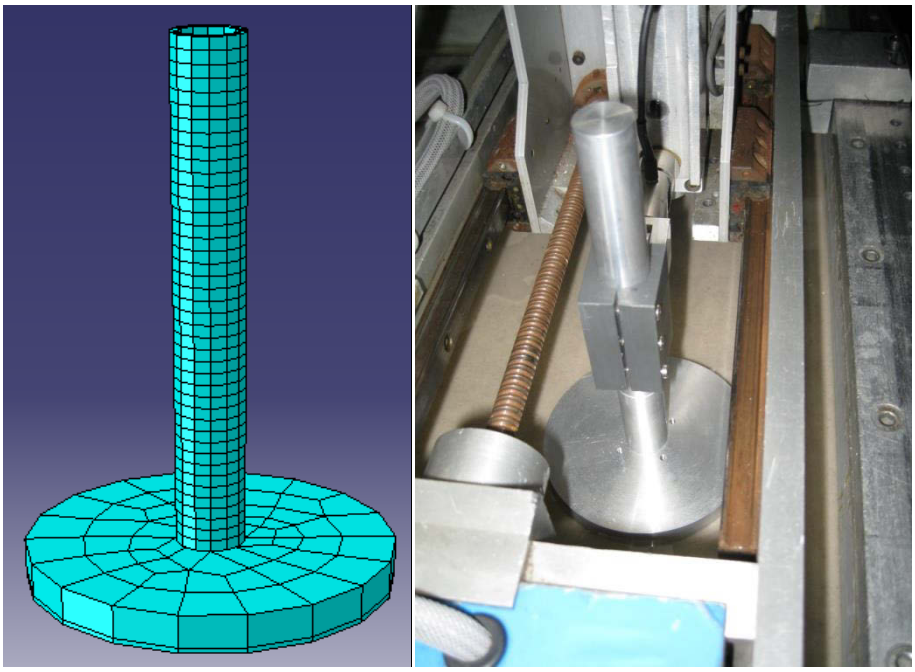

Figure 5-44. Model and test number two (un-piled footing)

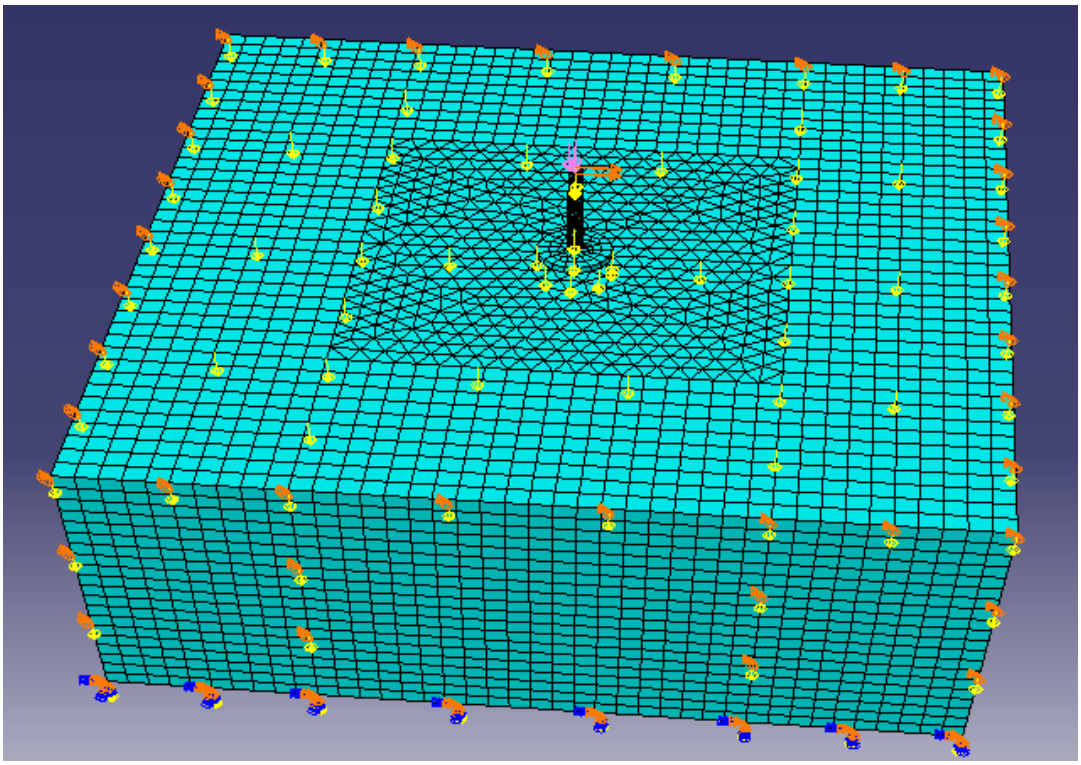

Figure 5-45. The footing structure embedded in the soil block for model number two (un-piled footing)

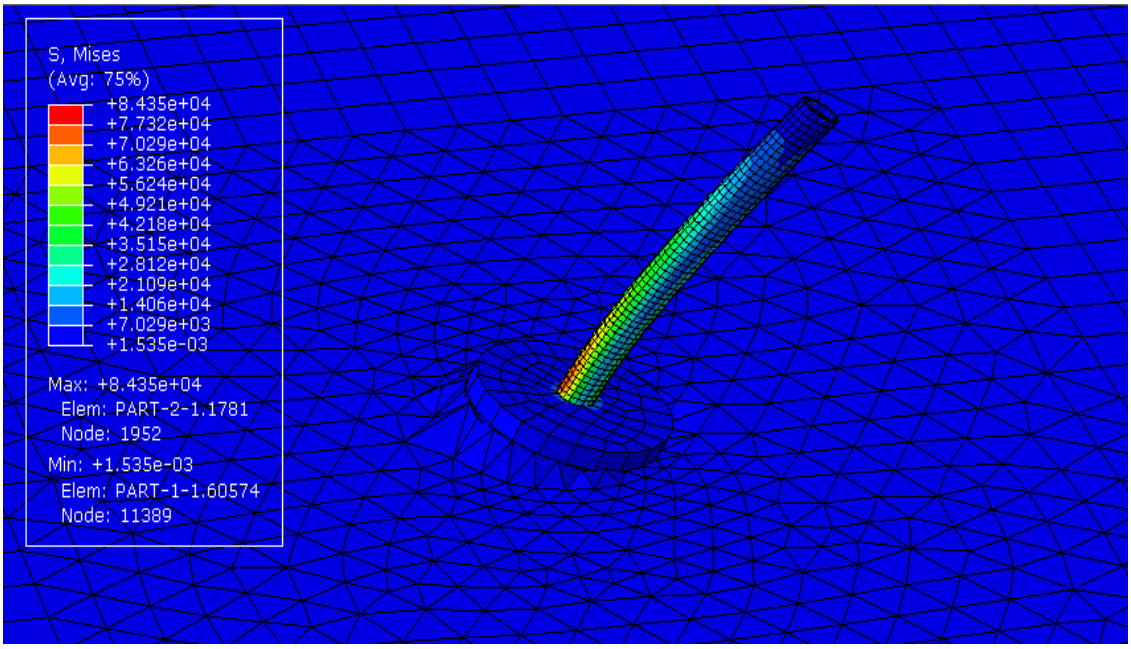

Figure 5-46. The Von Mises stresses acting on model number two with a linear increase in the soil modulus (un-piled footing)

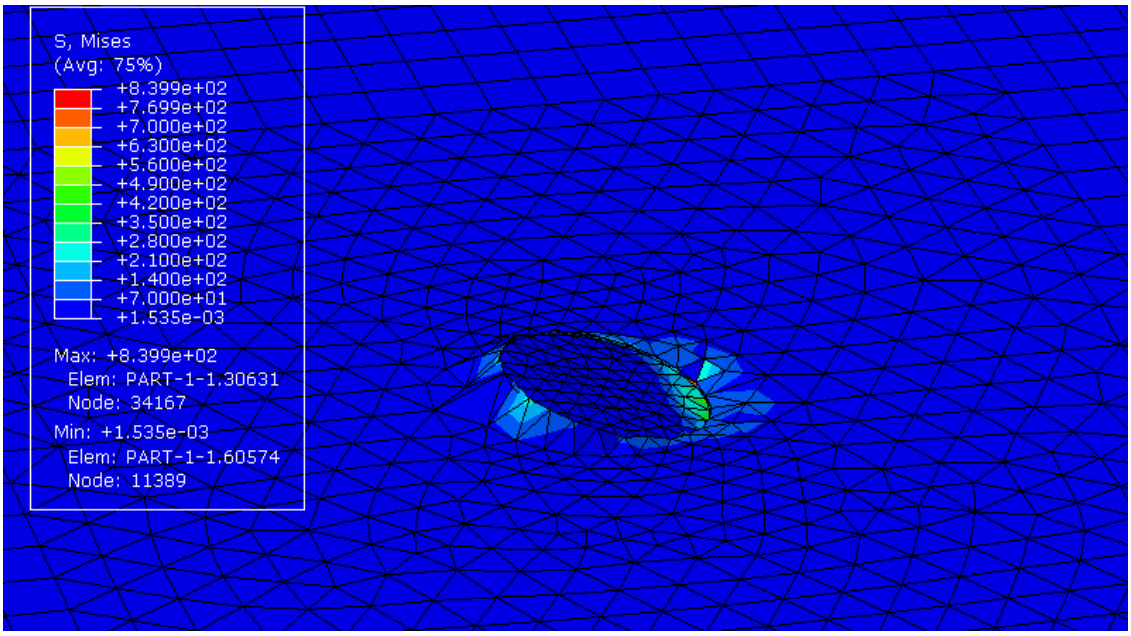

Figure 5-47. The Von Mises stresses acting on the soil block for model number two with a linear increase in the soil modulus (VL=9.3 MN)

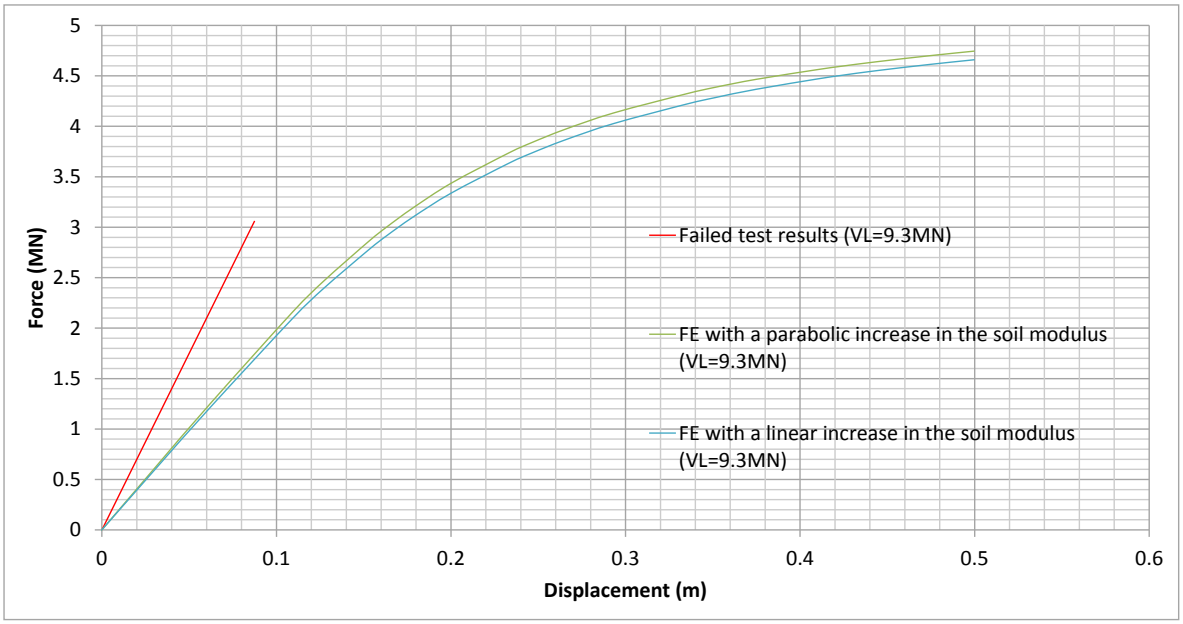

Figure 5-48. The FE predictions for model number two (un-piled footing)

Figure 5-49. The piled footing structure constructed for model number three (piled footing, VL=6.5 MN)

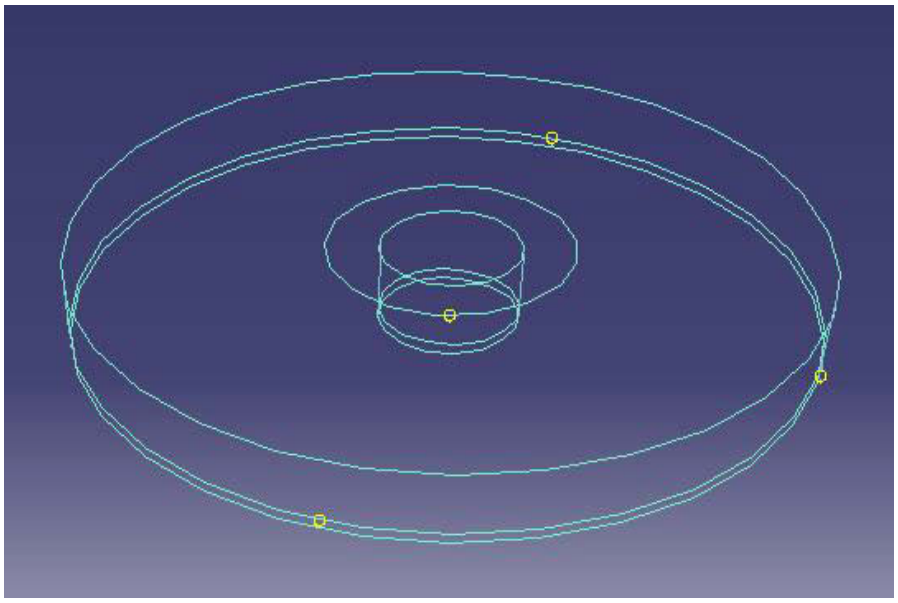

Figure 5-50. The bearing plate used at the base of the piled footing structure with its datum points

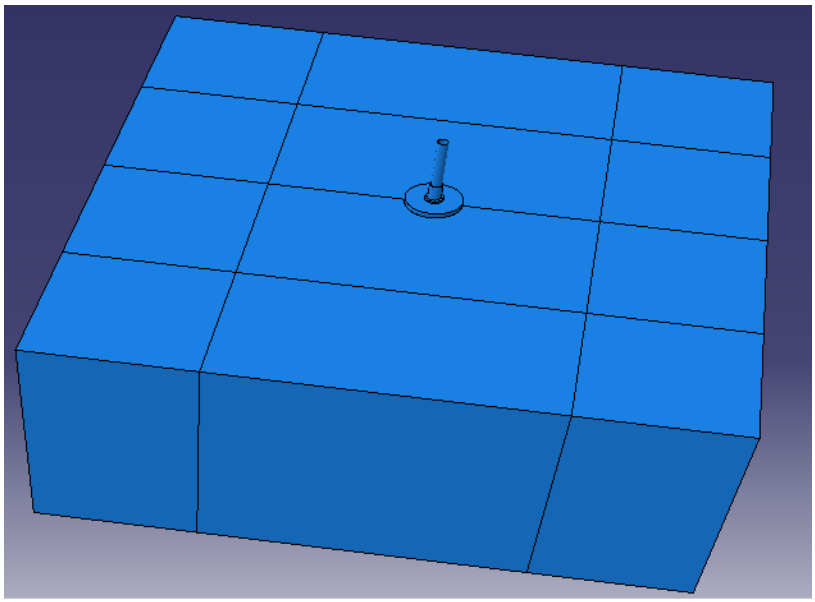

Figure 5-51. The piled footing structure assembled for model number three

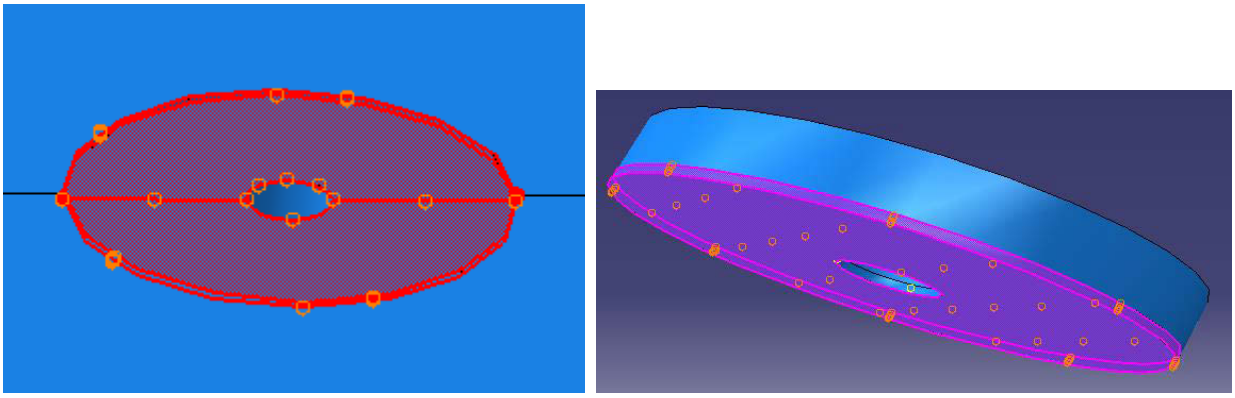

Figure 5-52. The zone of interaction between the soil block and the bearing plate

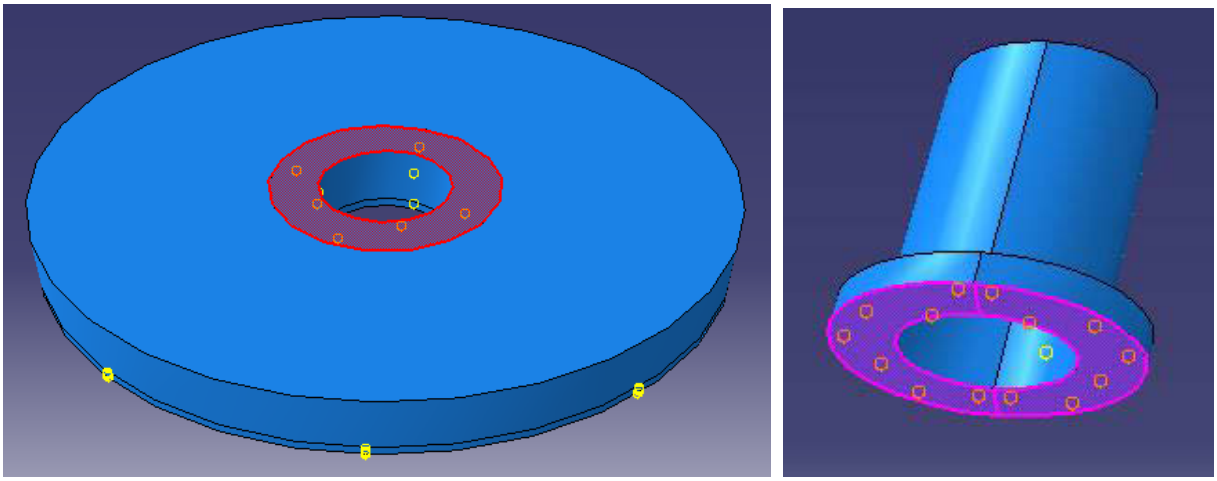

Figure 5-53. The zone of interaction between the bearing plate and the collar

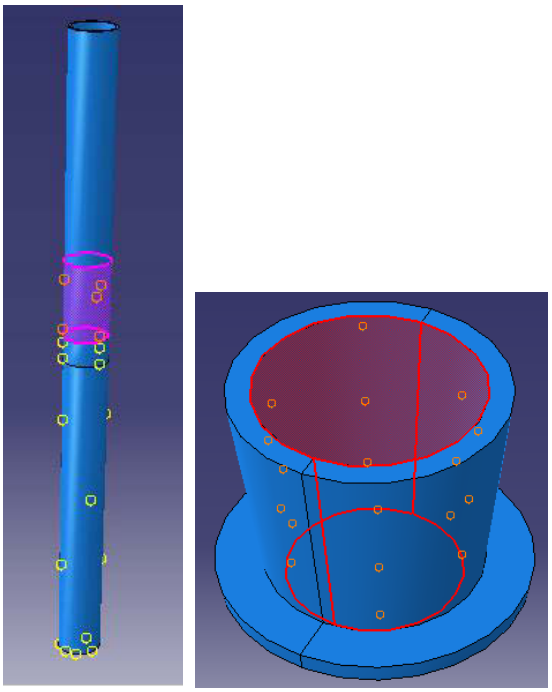

Figure 5-54. The interaction zone between the pile/tower and the collar

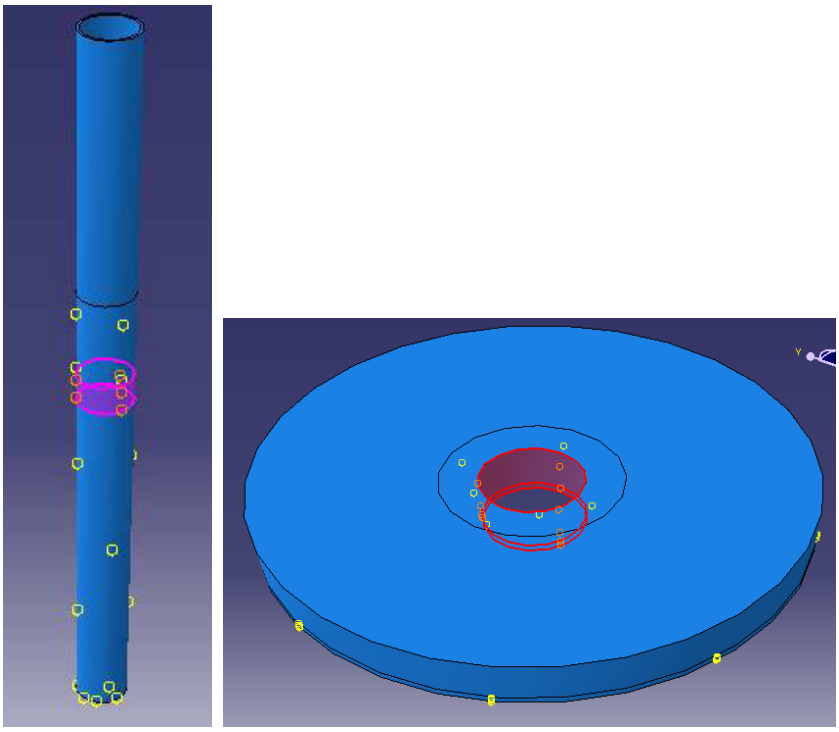

Figure 5-55. The interaction zone between the footing and the pile/tower

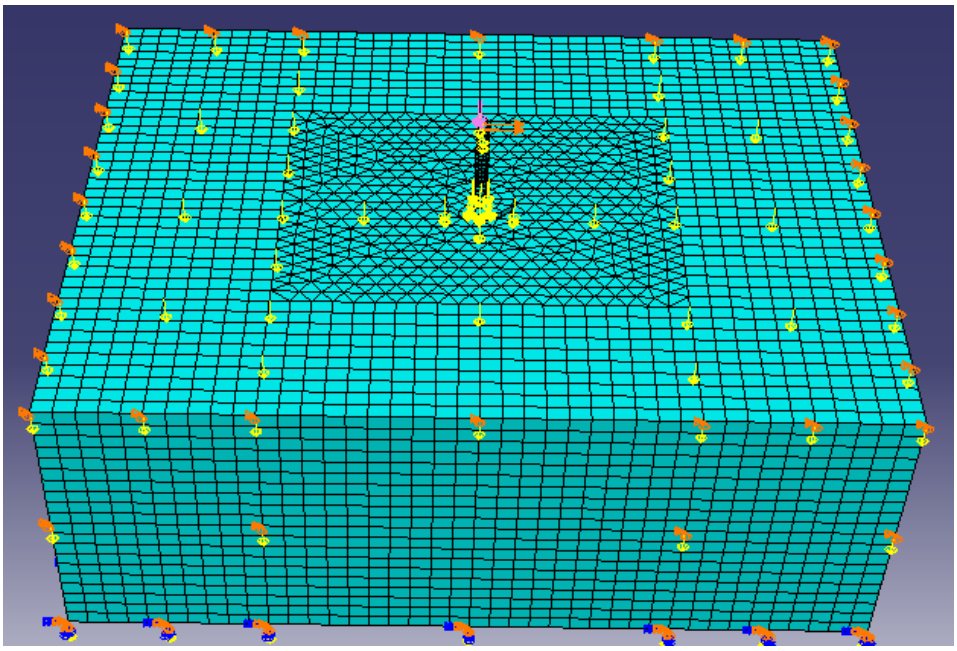

Figure 5-56. All components of model number three with their generated mesh

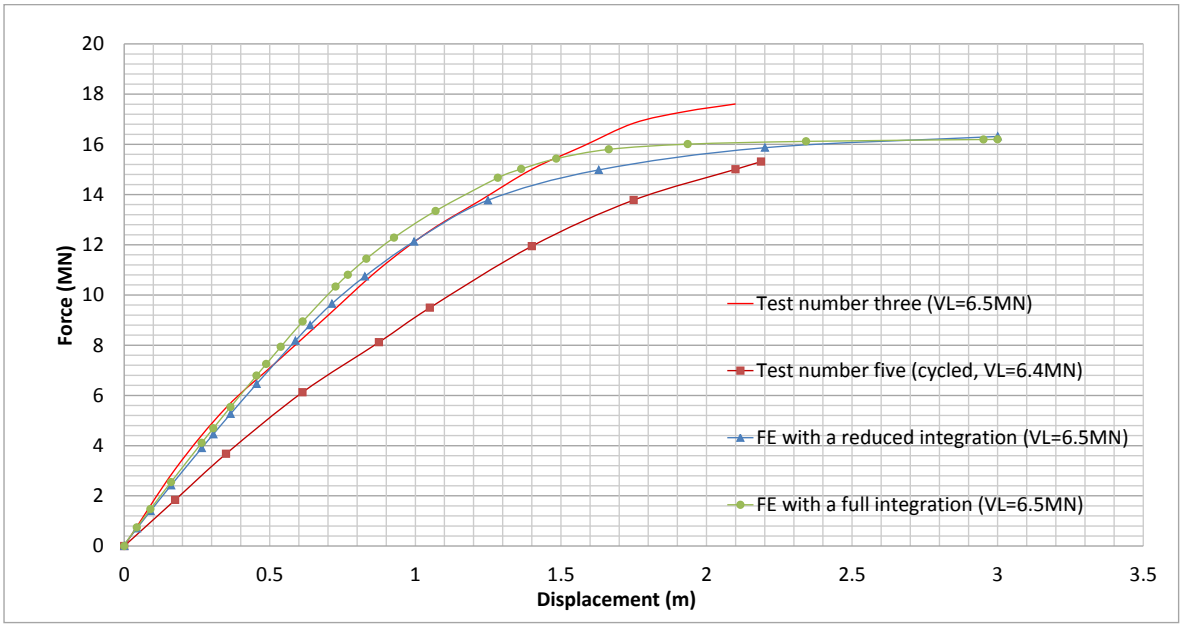

Figure 5-57. The piled footing tests and the FE results for a linear increase in the soil modulus

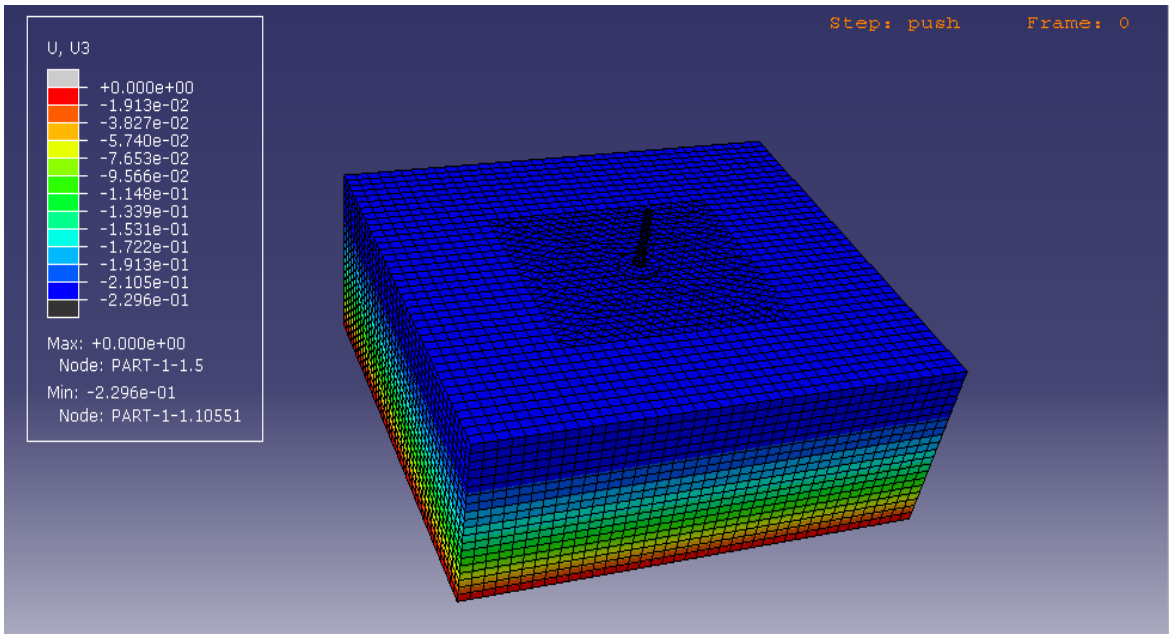

Figure 5-58. The vertical displacement after applying the gravity to model number three with a linear increase in the soil modulus

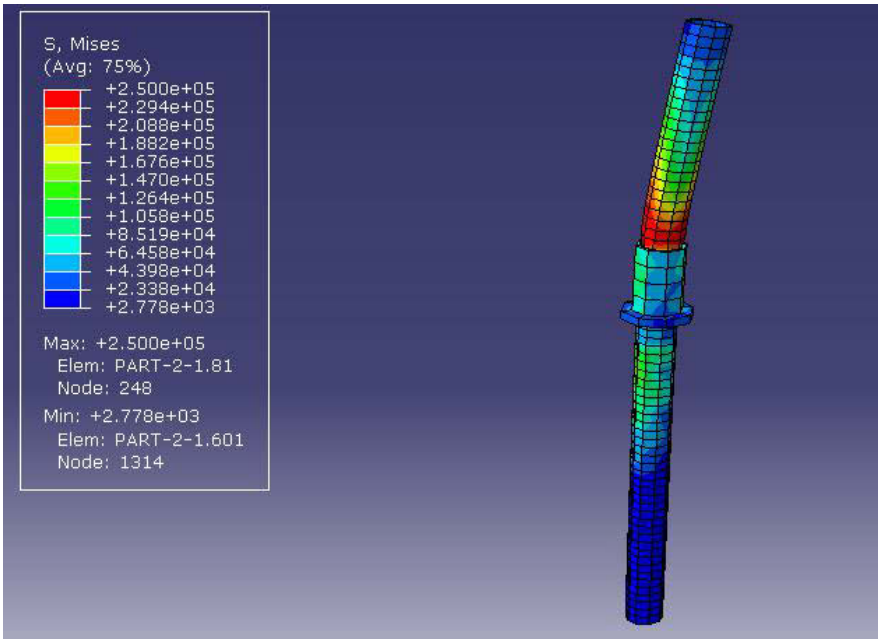

Figure 5-59. The Mises stresses acting on the pile/tower for model number three (piled footing)

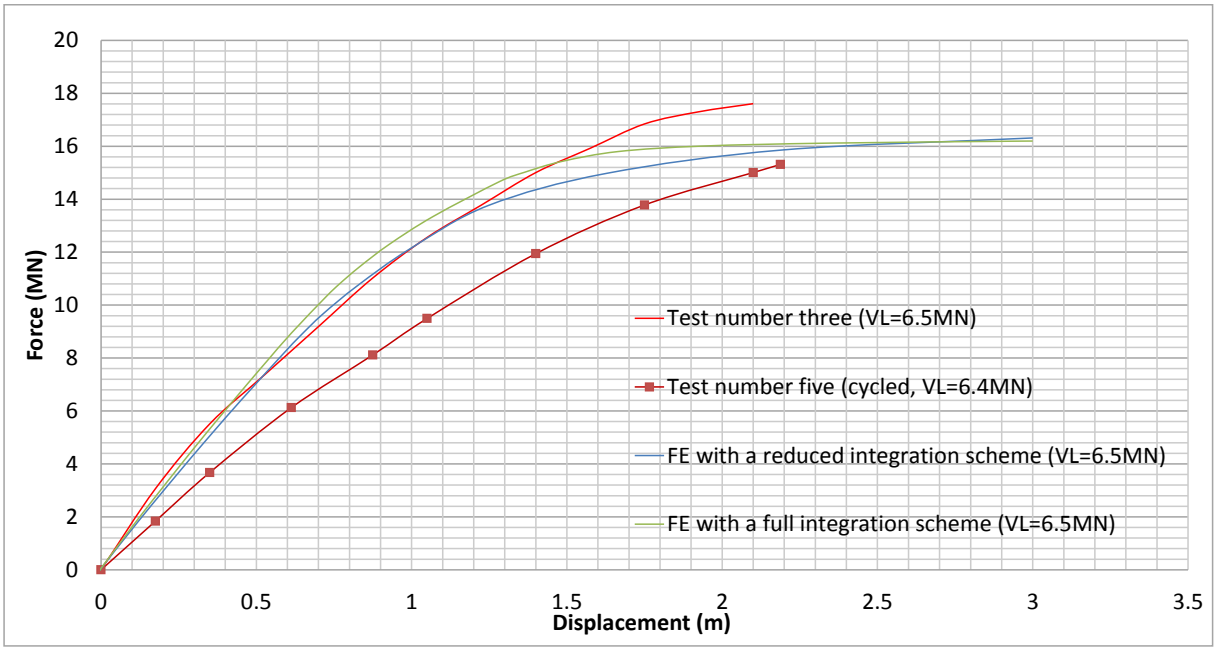

Figure 5-60. The tests and the FE results for a parabolic increase in the soil modulus (piled footing structure)

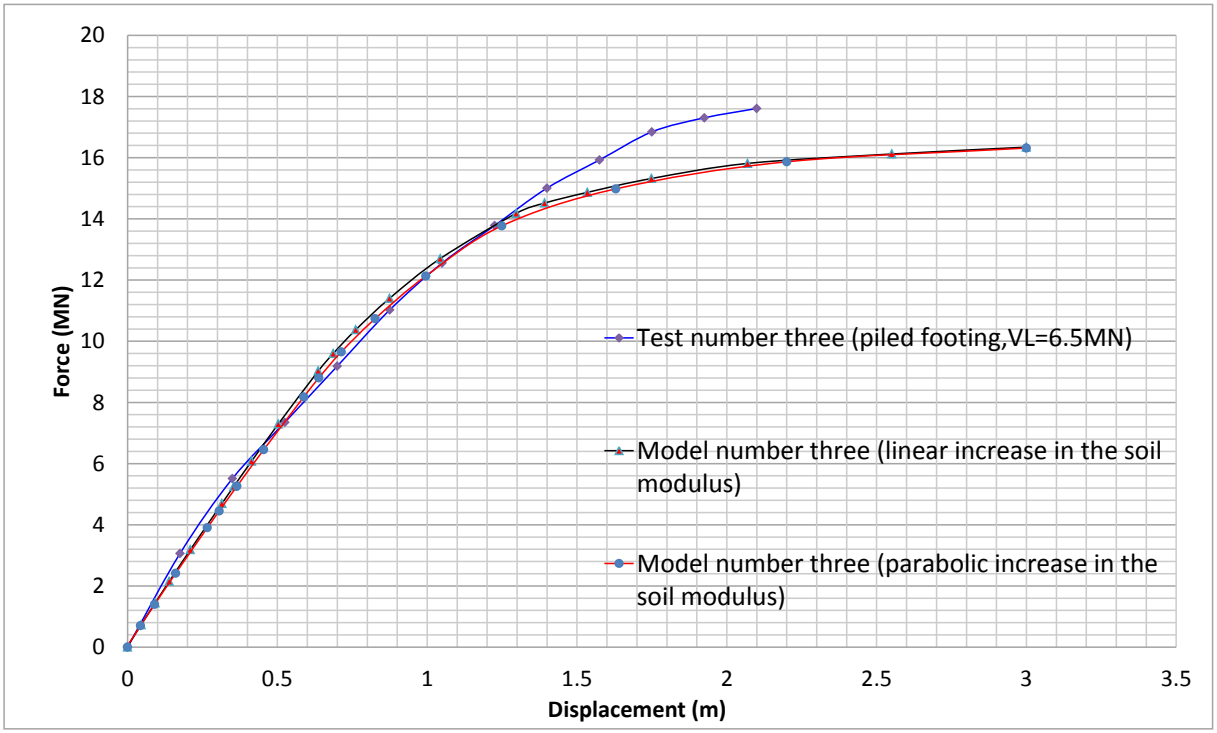

Figure 5-61. The FE results with a reduced integration scheme for different soil moduli (piled footing structure)

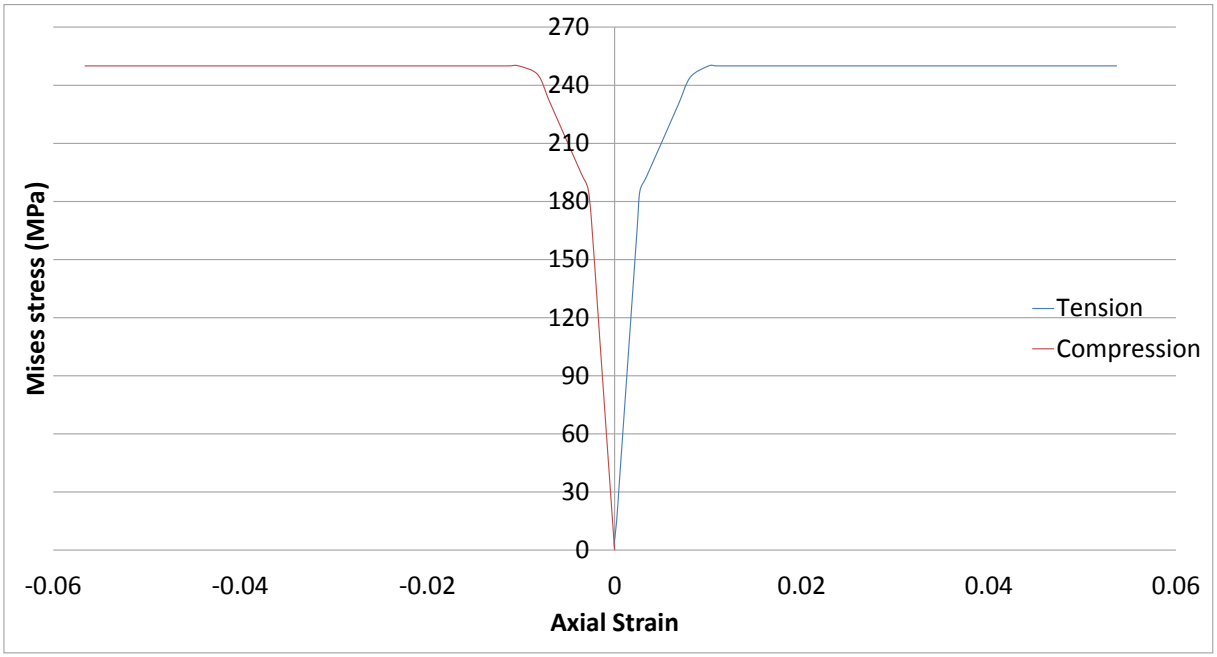

Figure 5-62. The stress versus strain graph from the FE results (model number three)

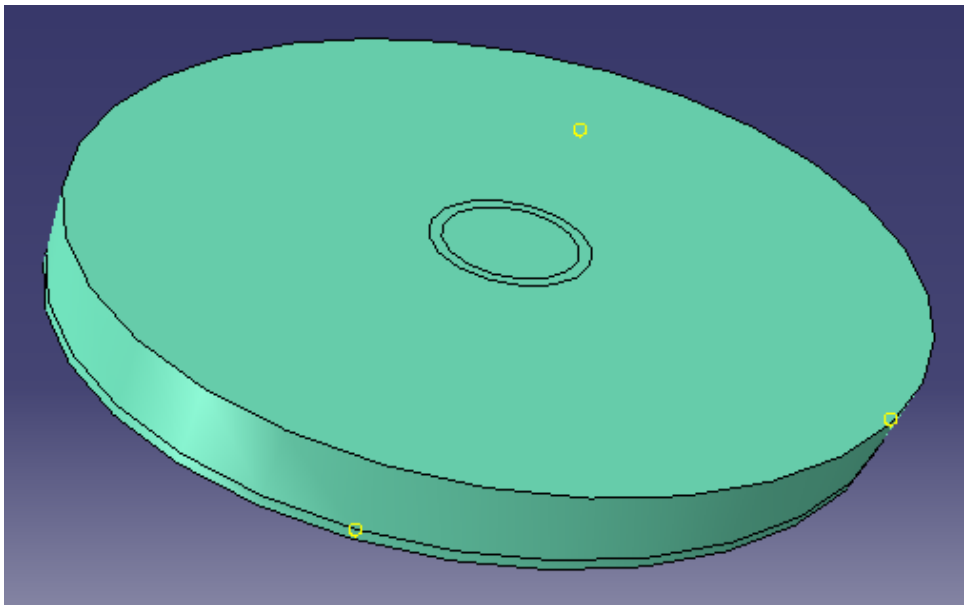

Figure 5-63. The solid footing with its datum points used for model number four

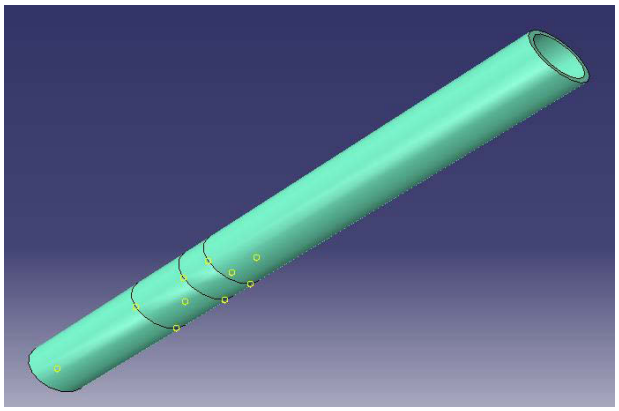

Figure 5-64. The tower used for model number four

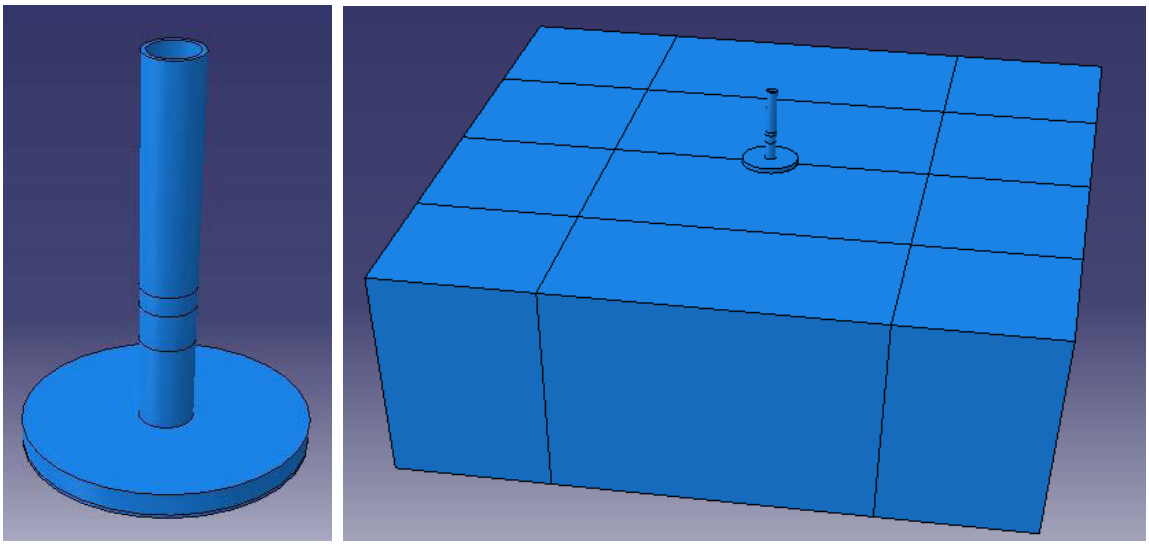

Figure 5-65. The tower and footing used for model number four

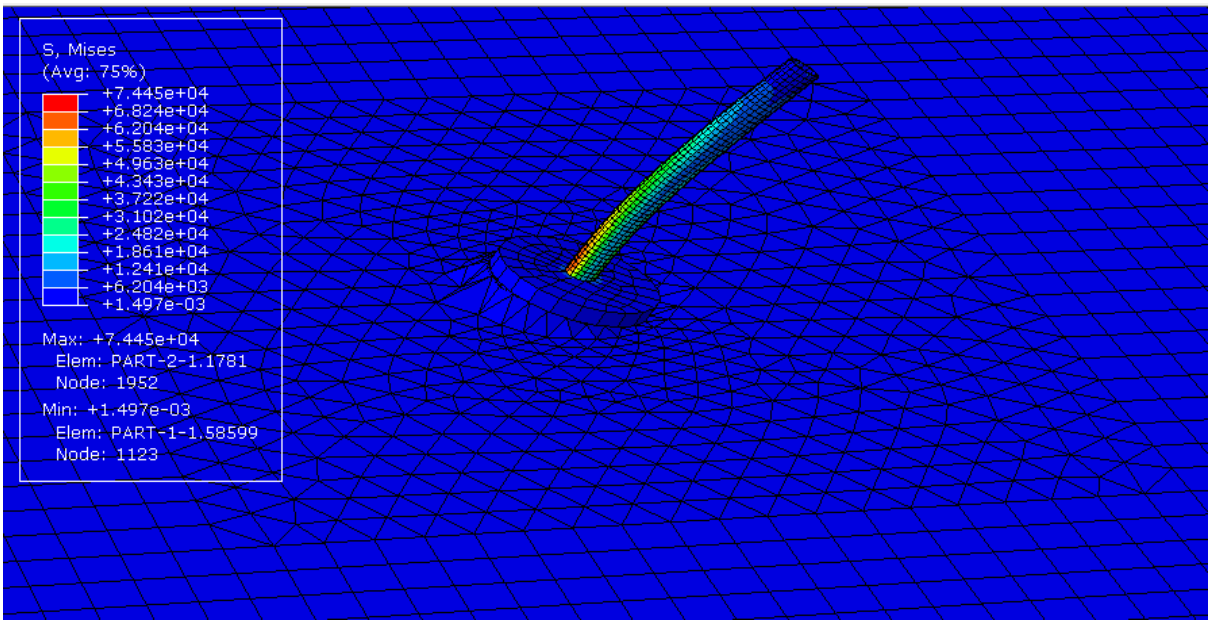

Figure 5-66. The Mises stresses acting on model number four for a linear increase in the soil modulus

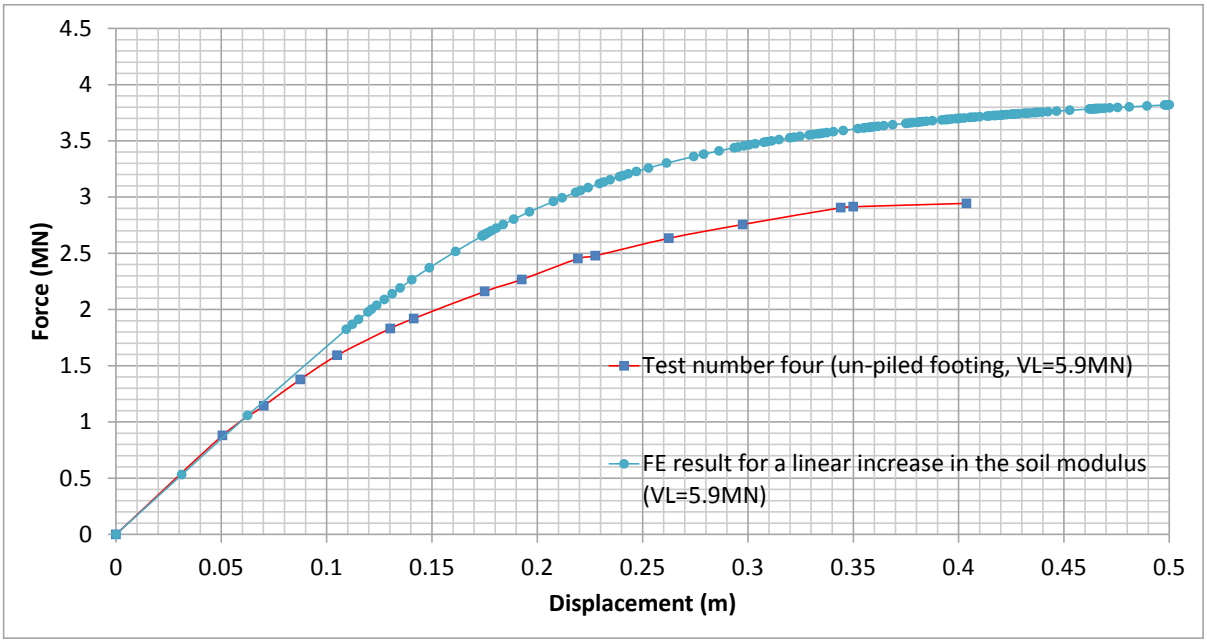

Figure 5-67. The results of test and model number four for a linear increase in the soil modulus (un-piled footing structure)

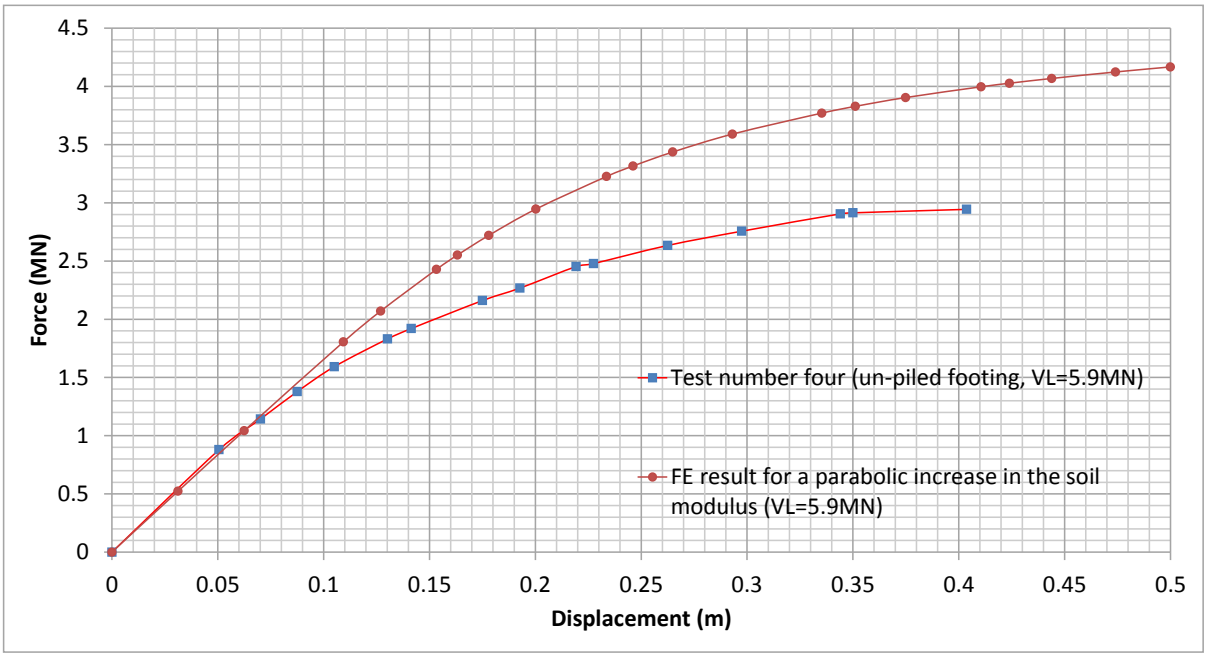

Figure 5-68. The results of test and model number four for a parabolic increase in the soil modulus (un-piled footing structure)

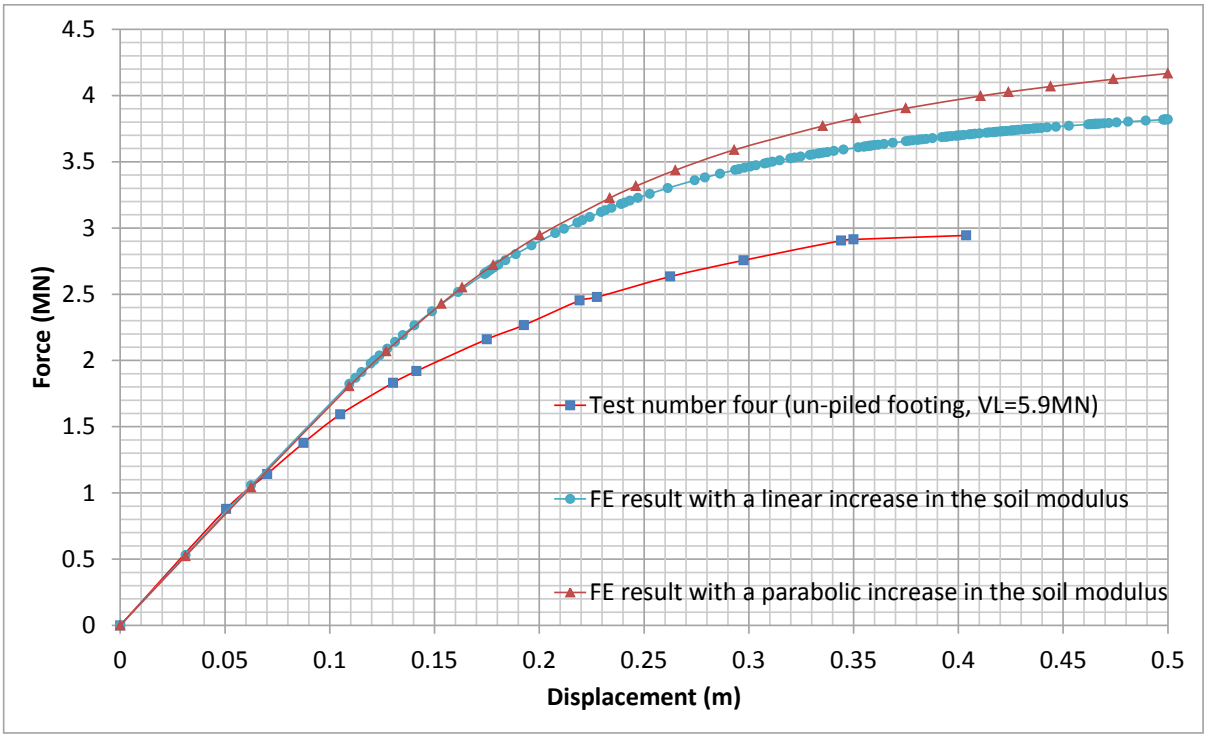

Figure 5-69. Comparing the results of test number four with the FE results with different soil moduli (un-piled footing structure)

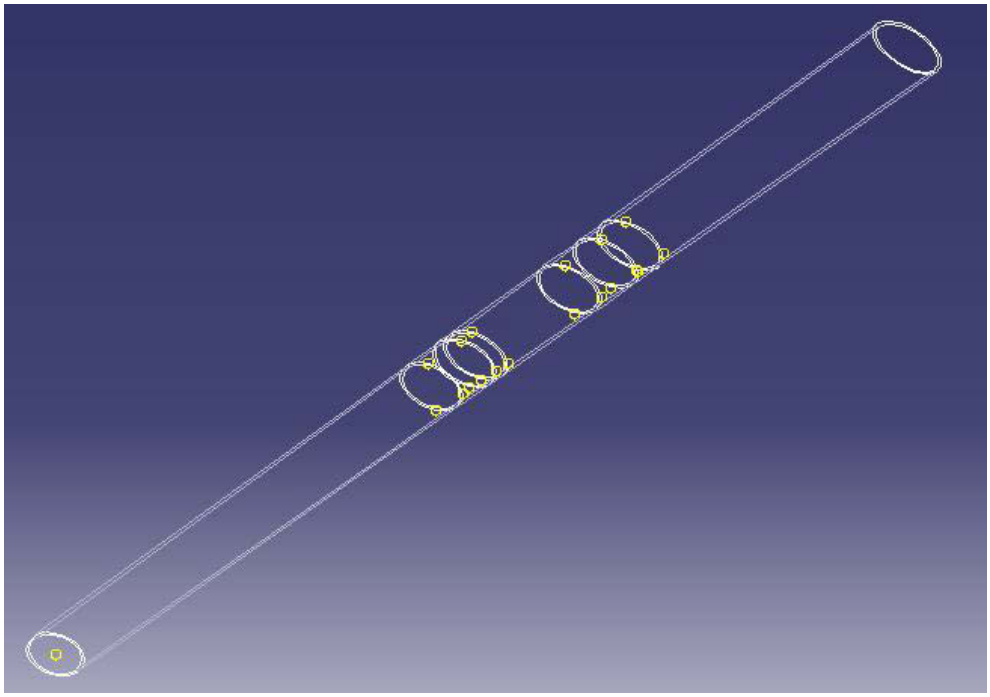

Figure 5-70. The pile/tower used for model number five (piled footing, VL=13.2 MN)

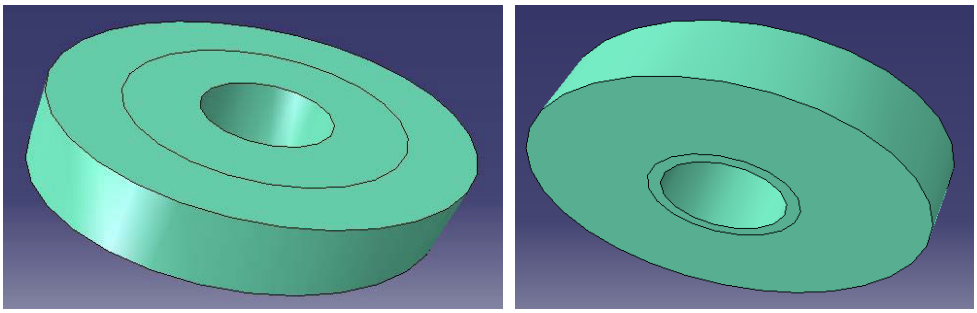

Figure 5-71. Footing number two used in model number five with its partitions

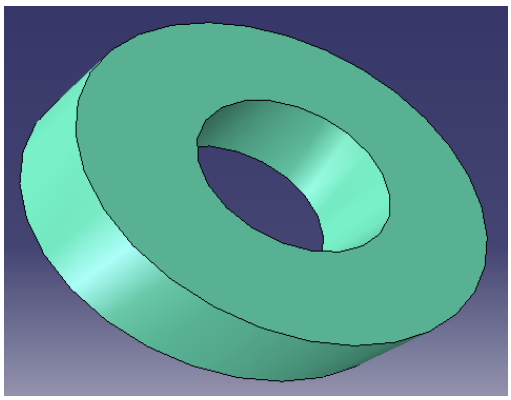

Figure 5-72. Footing number three used in model number five

Figure 5-73. The assembled structure for model number five (piled footing)

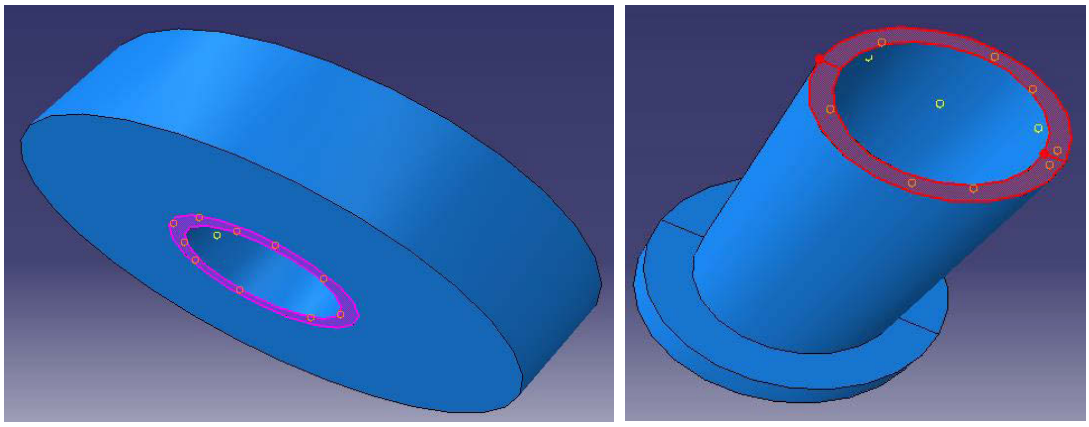

Figure 5-74. The tie constraint generated between the collar and footing number two

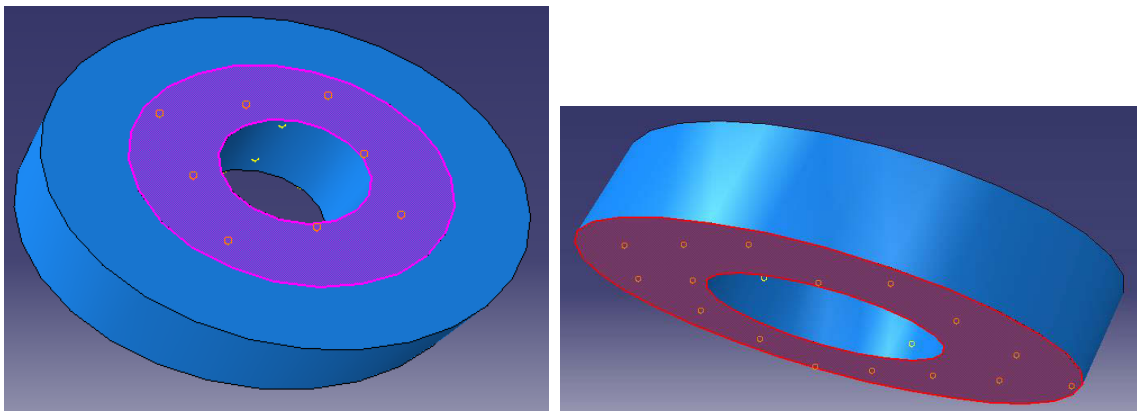

Figure 5-75. The tie constraint generated between the two footings

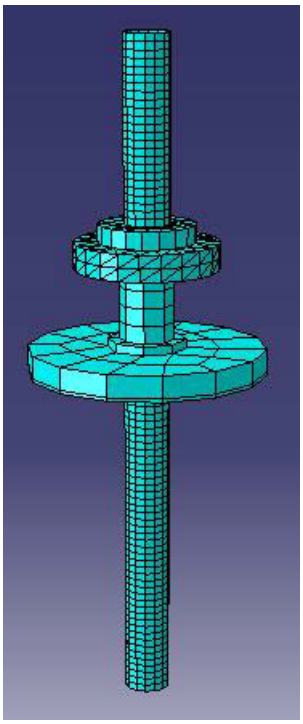

Figure 5-76. The mesh generated for model number five

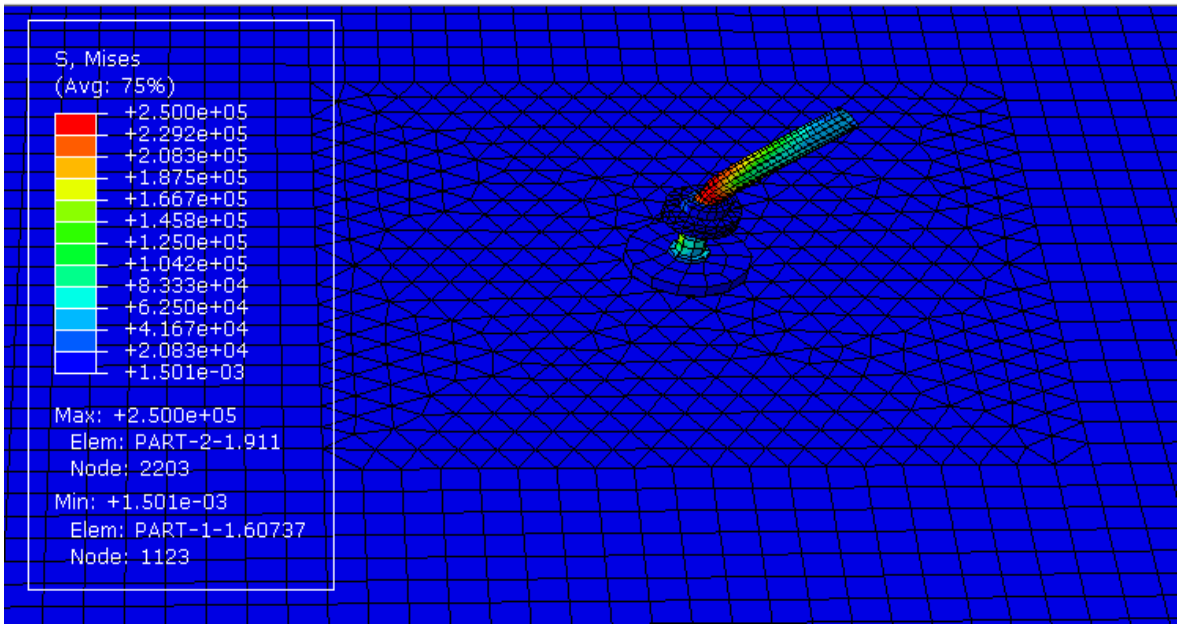

Figure 5-77. The Mises stresses acting on the piled footing structure located in the soil block with a reduced integration scheme (VL=13.2 MN)

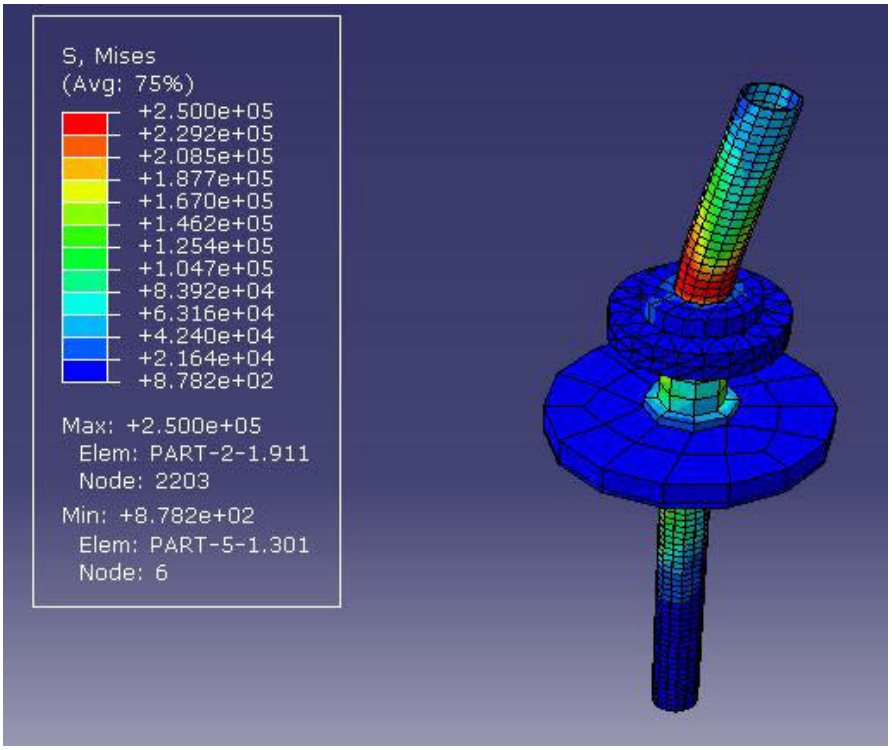

Figure 5-78. The location of the maximum Mises stresses acting on the pile/tower with a reduced integration scheme (VL=13.2 MN)

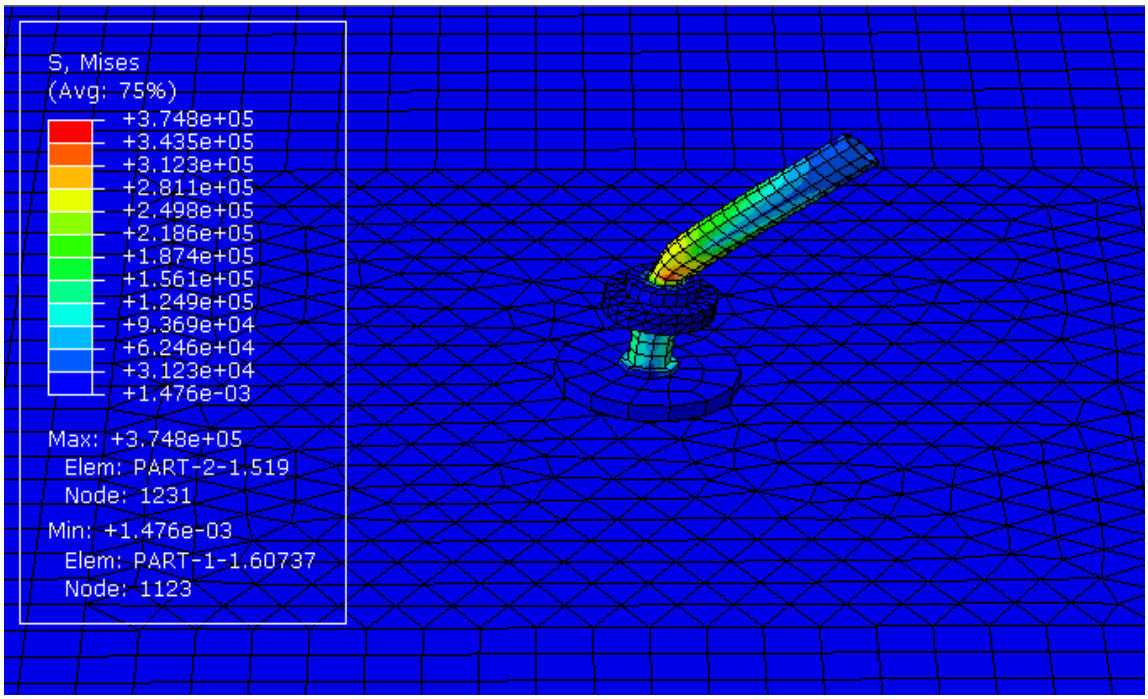

Figure 5-79. The Mises stresses acting on model number five with a full integration scheme adopted

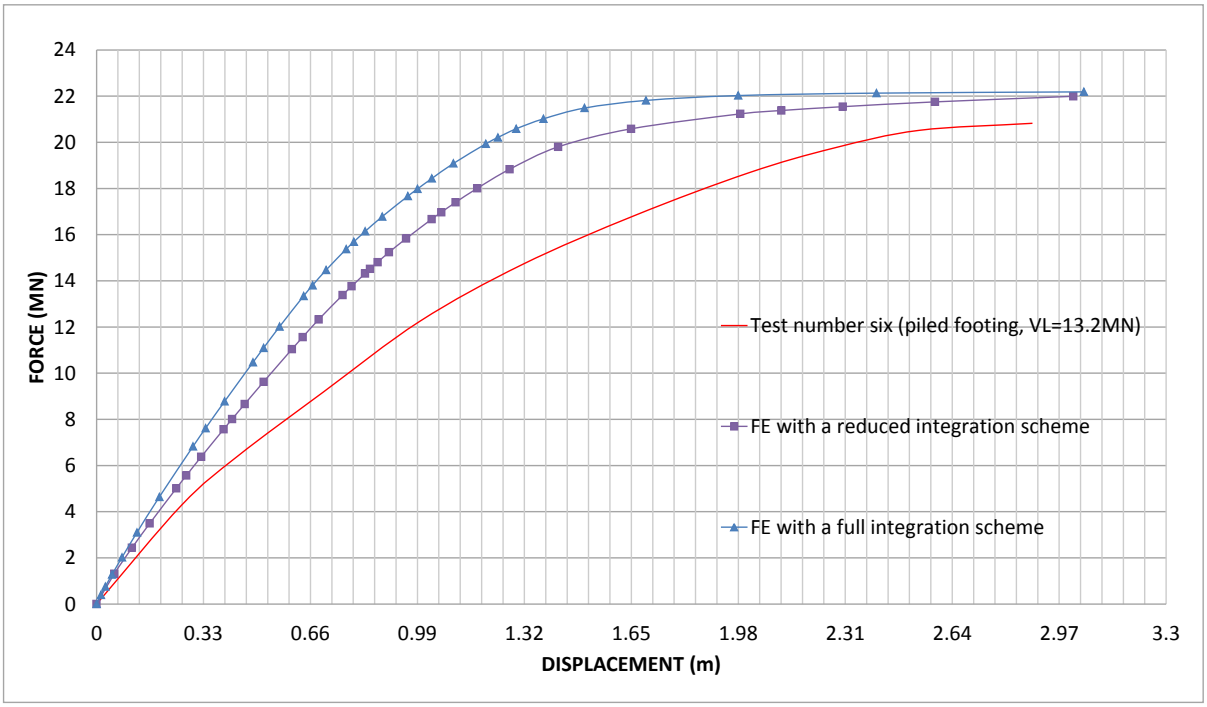

Figure 5-80. The results of model number five compared with the test result for a linear increase in the soil modulus (piled footing structure, VL=13.2 MN)

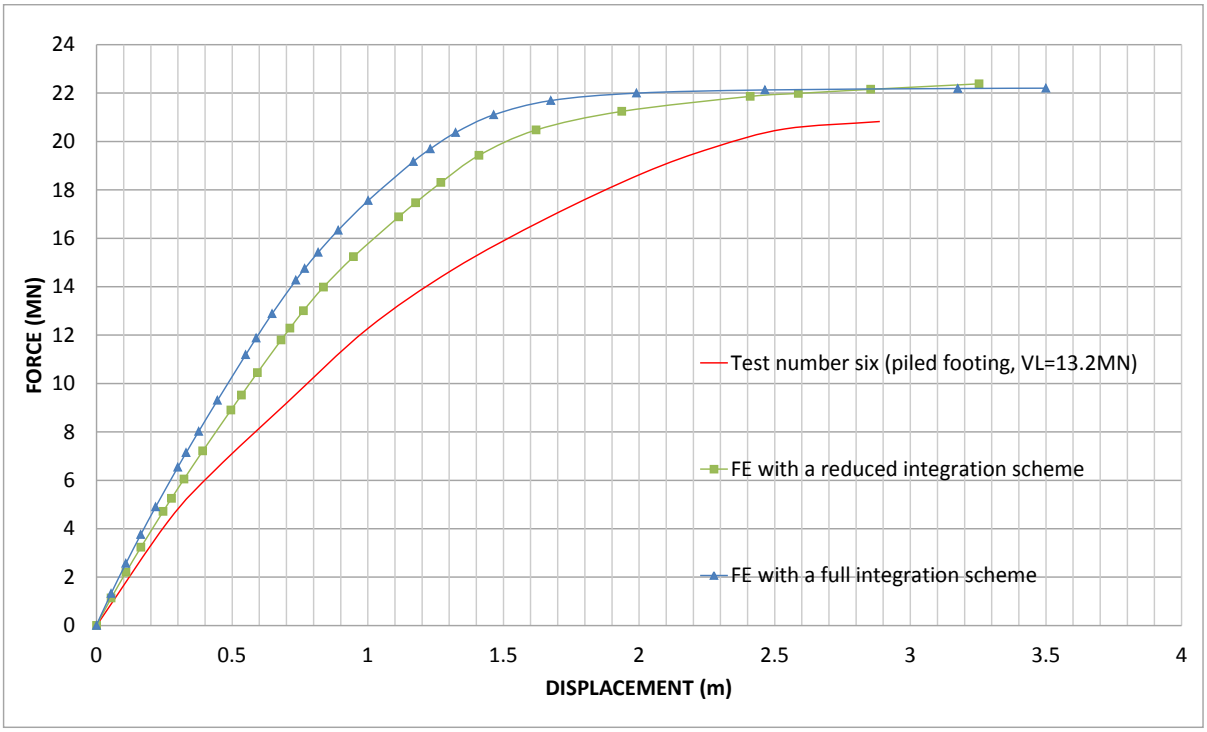

Figure 5-81. The results of model number five compared to the test results with a parabolic increase in the soil modulus (piled footing structure, VL=13.2 MN)

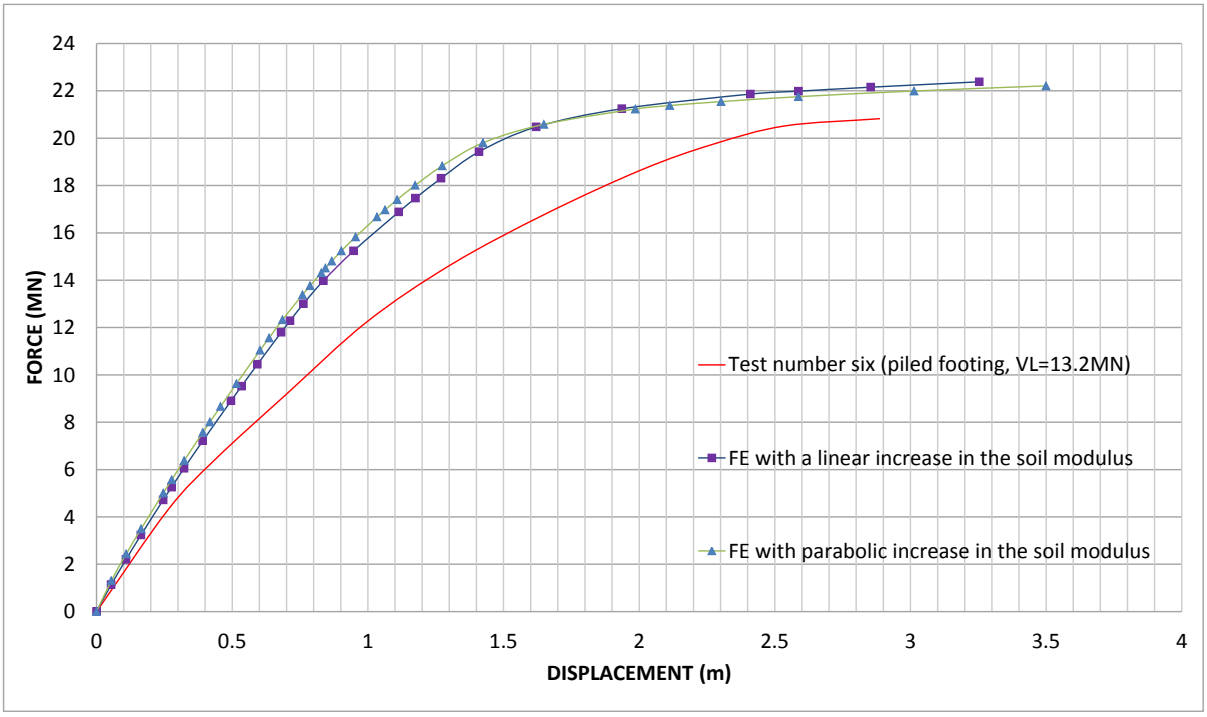

Figure 5-82. The results of model number five with different soil moduli with a reduced integration scheme on the pile/tower structure

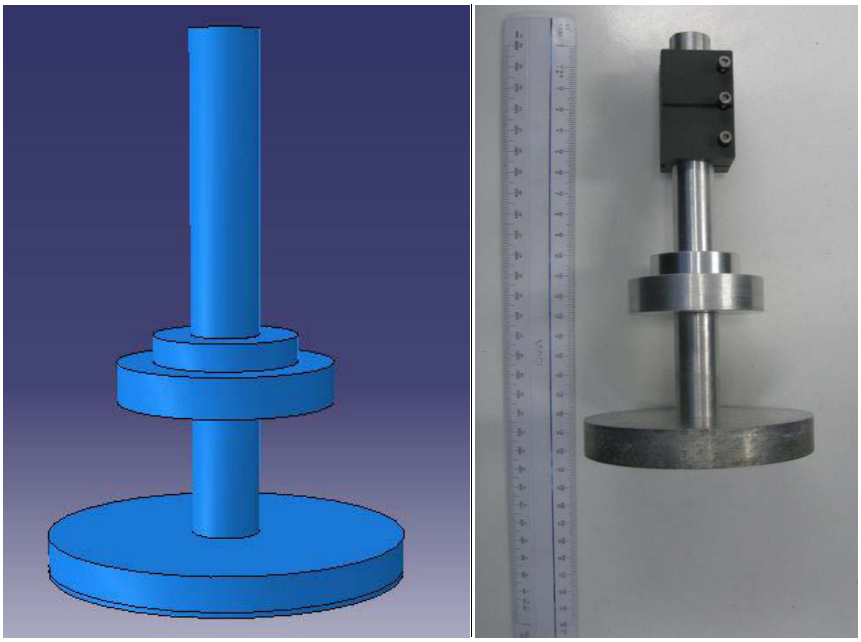

Figure 5-83. Model number six and test number seven (un-piled footing)

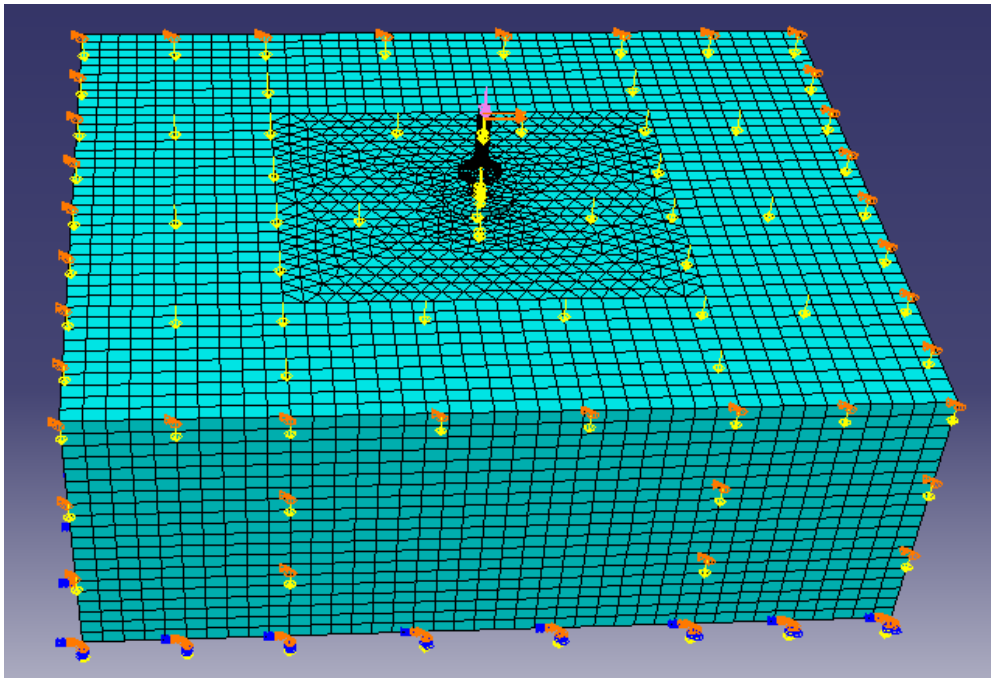

Figure 5-84. The loads and boundary conditions acting on model number six (un-piled footing)

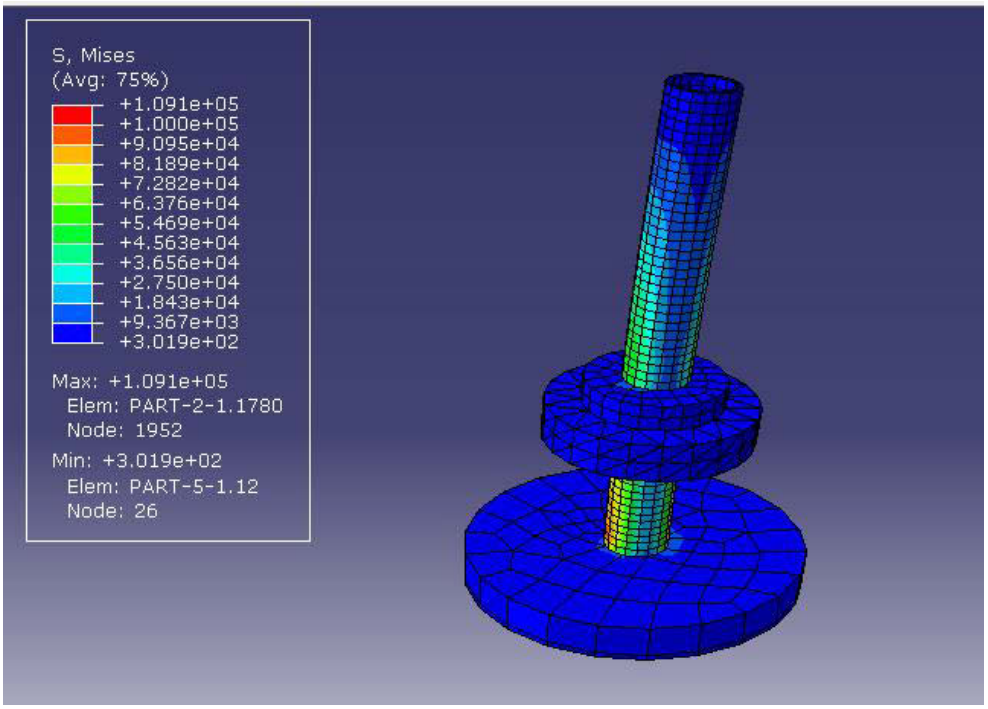

Figure 5-85. The Von Mises stresses acting on the structure for a linear increase in the soil modulus

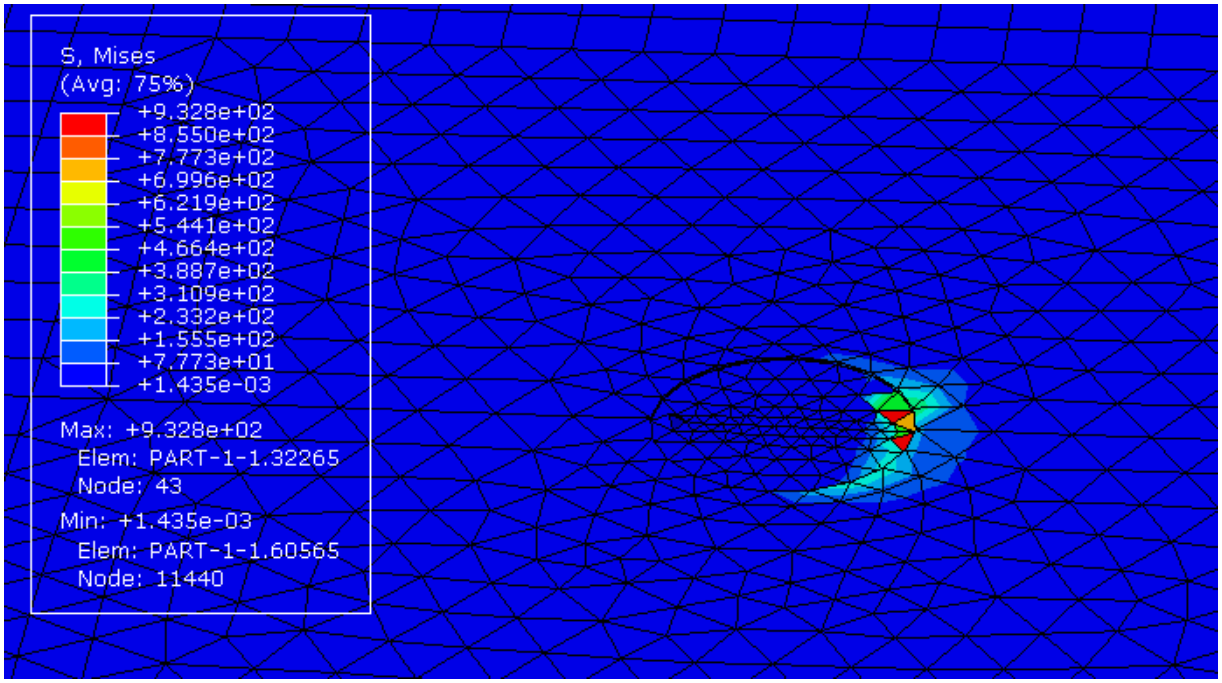

Figure 5-86. The Mises stresses acting on the soil block with a linear increase in the soil modulus

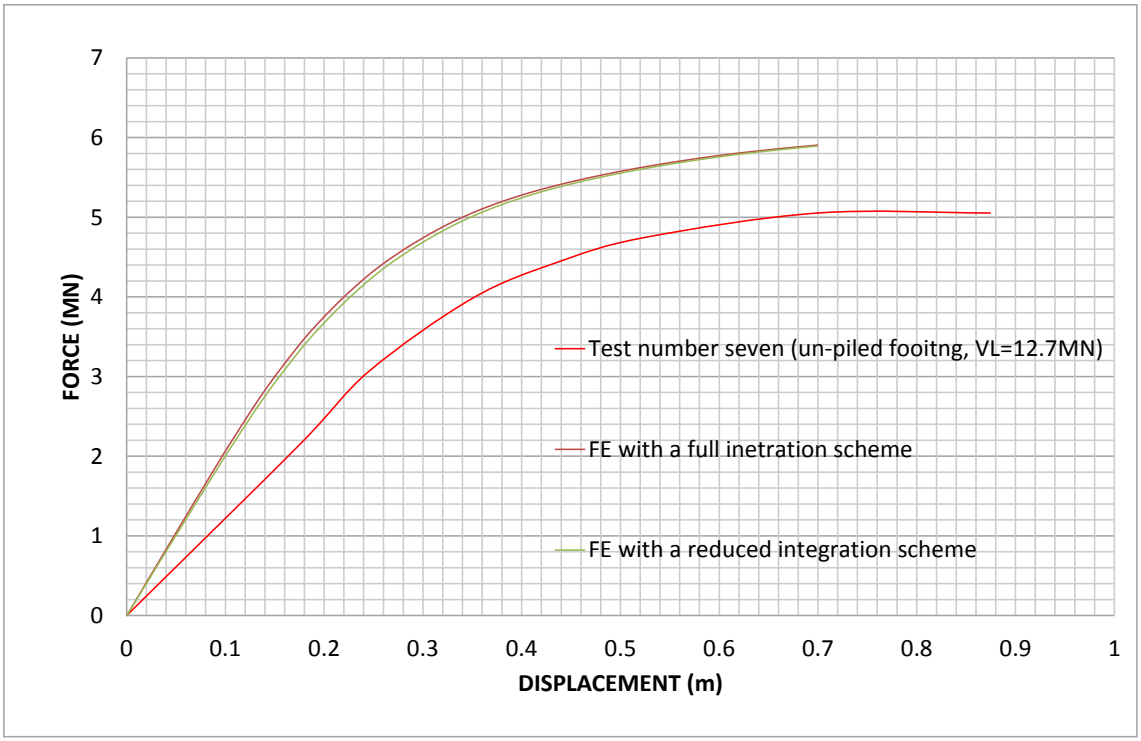

Figure 5-87. The test and the FE results for a linear increase in the soil modulus (un-piled footing, VL=12.7 MN)

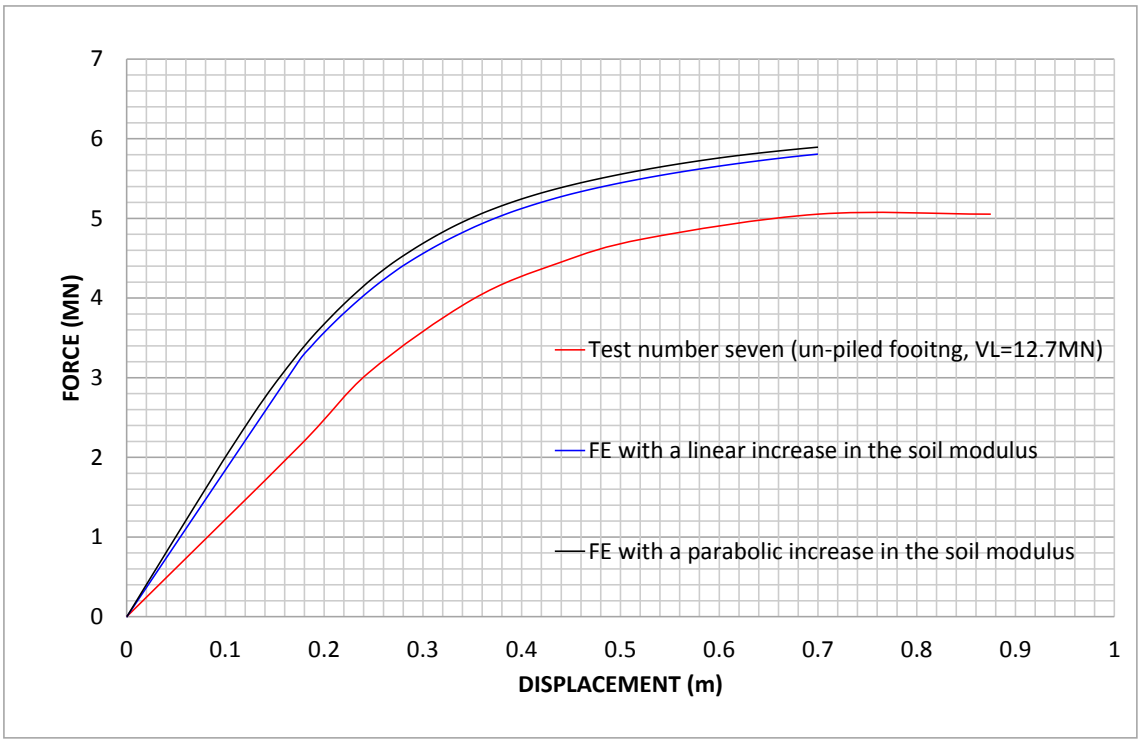

Figure 5-88. Test number seven compared to the FE results with different soil moduli (un-piled footing, VL=12.7 MN)

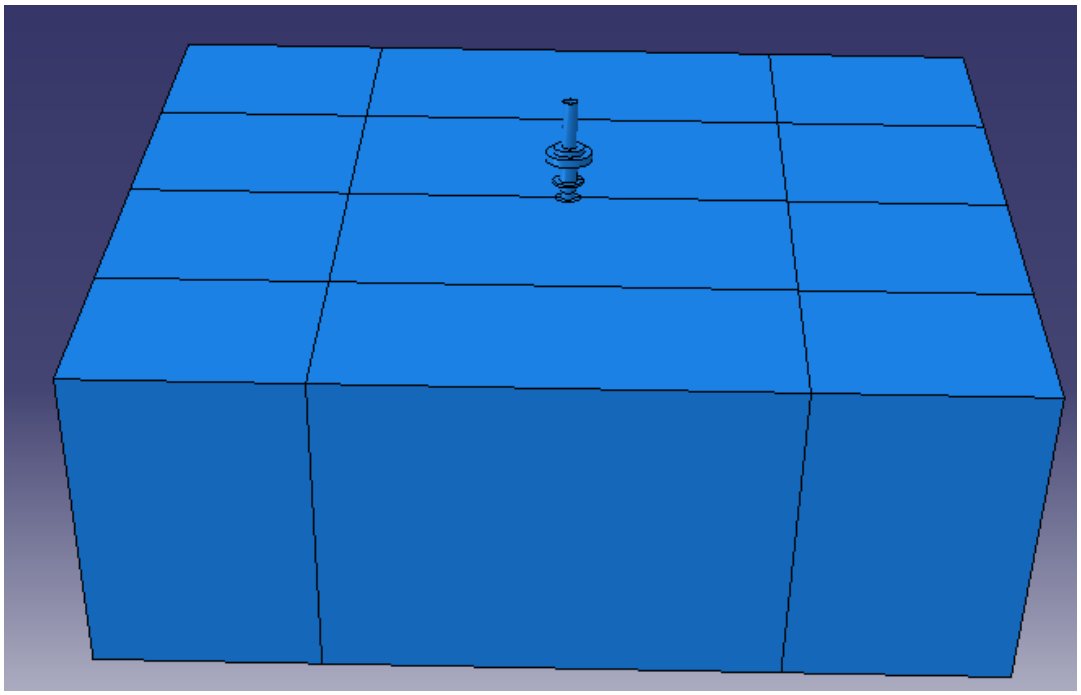

Figure 5-89. The monopile structure with two extra weights attached to it

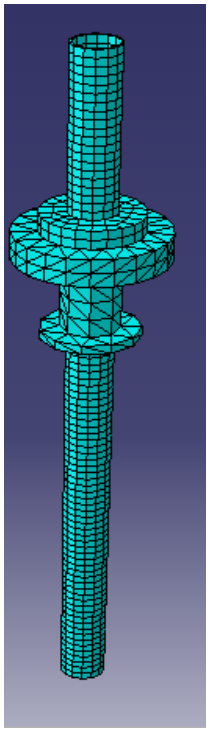

Figure 5-90. The pile/tower with extra weights used for the numerical model

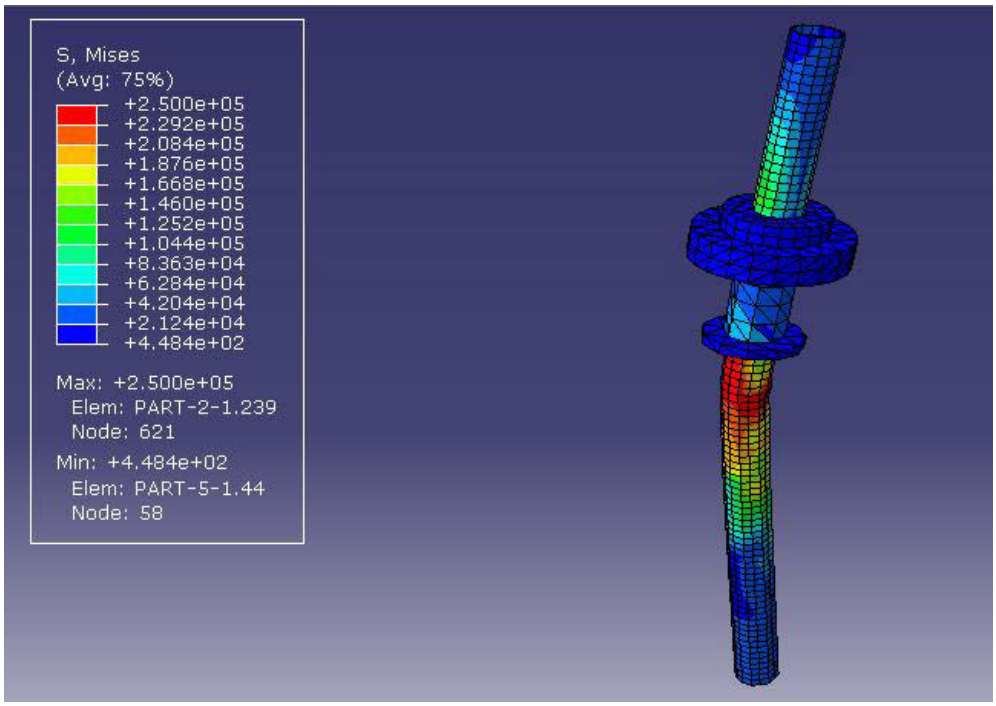

Figure 5-91. The Von Mises stresses acting on the pile/tower with weights

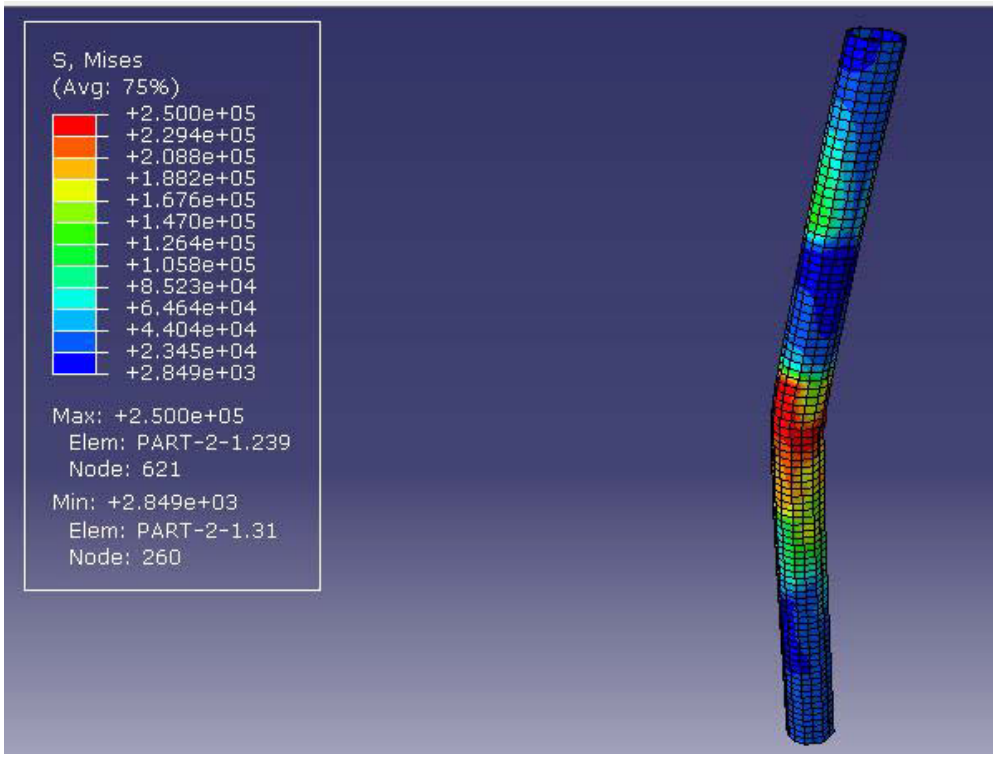

Figure 5-92. The Von Mises stresses acting on the pile/tower

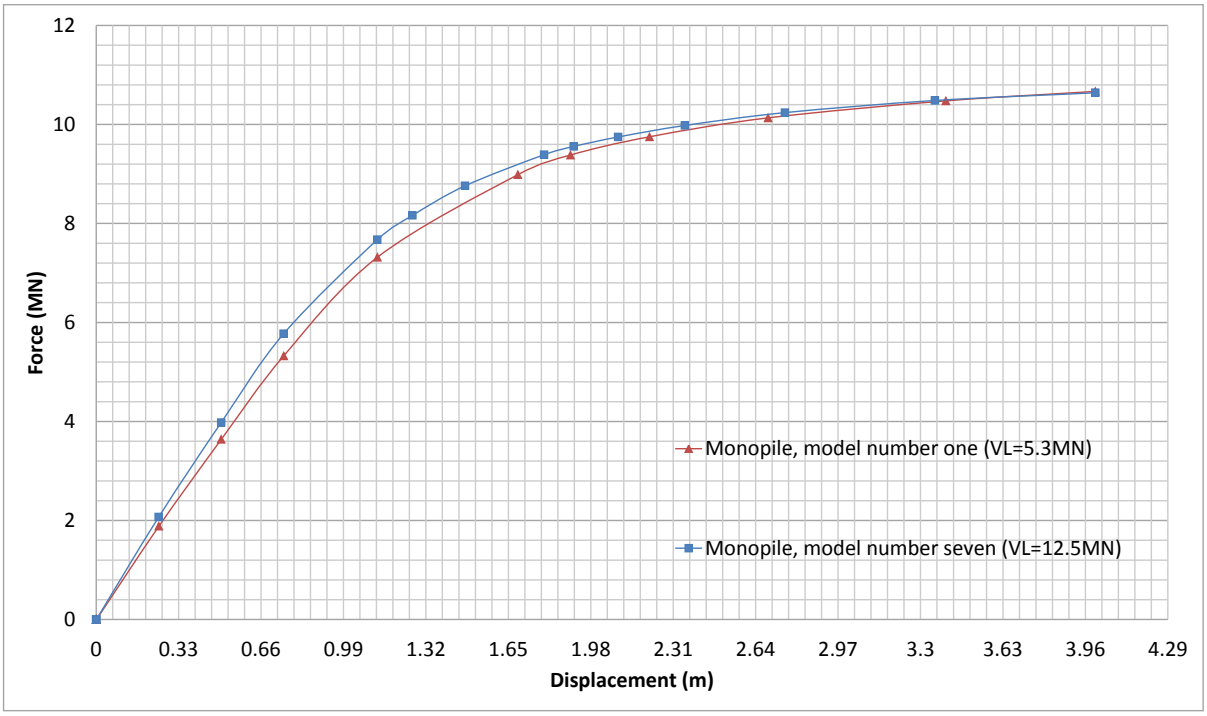

Figure 5-93. The results of model number one and seven with a reduced integration scheme for a linear increase in the soil modulus

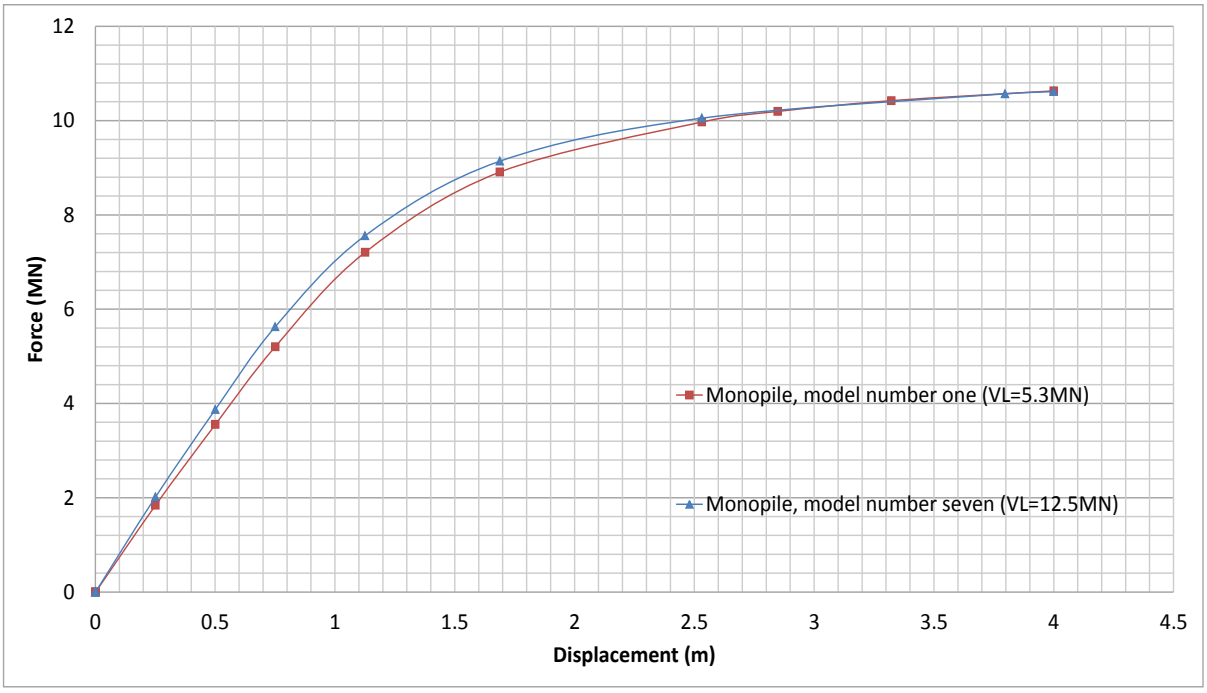

Figure 5-94. The results of model number one and model number seven with a reduced integration scheme and a parabolic increase in the soil modulus

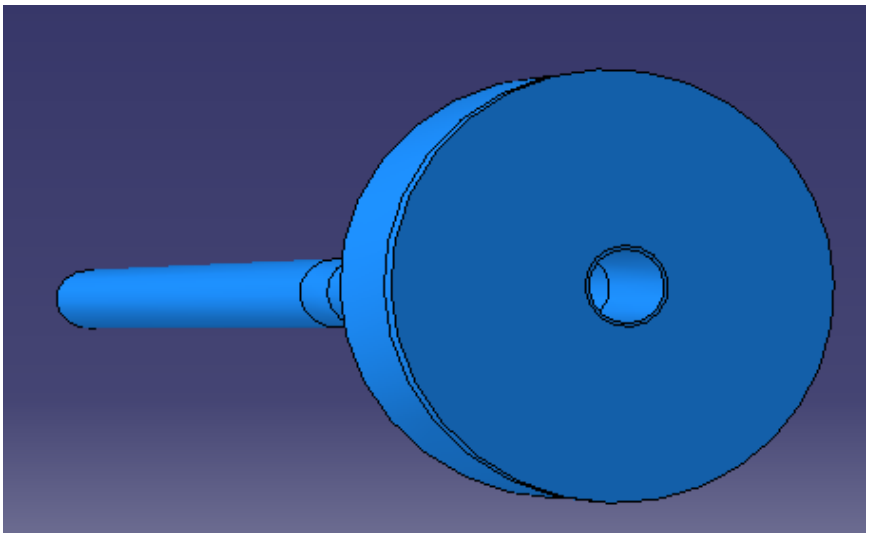

Figure 5-95. The tower and footing used for model number eight (un-piled footing)

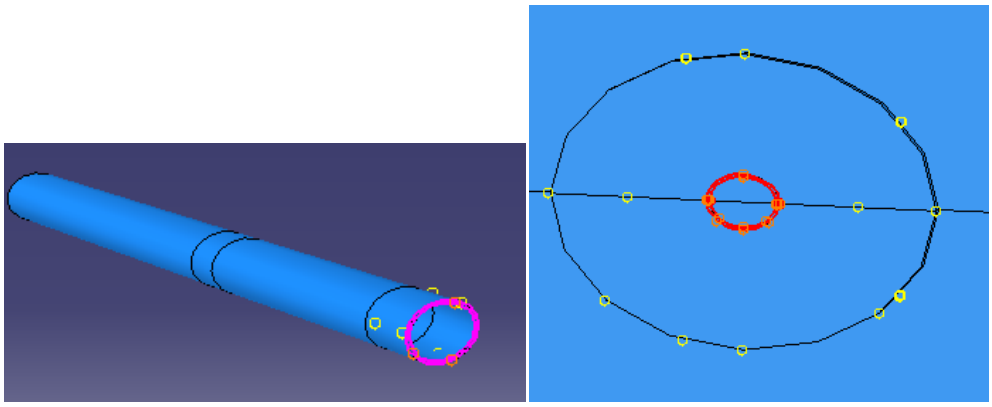

Figure 5-96. The tie constraint between the tower and the soil block for model number eight

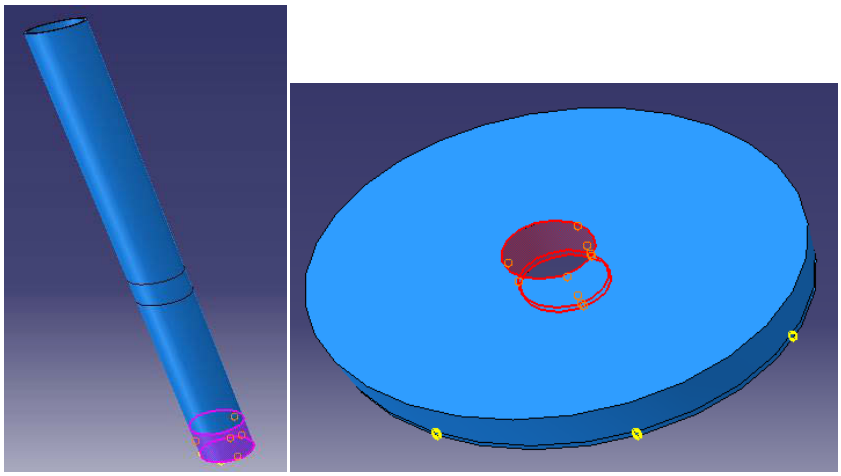

Figure 5-97. The tie constraint between the tower and the footing for model number eight

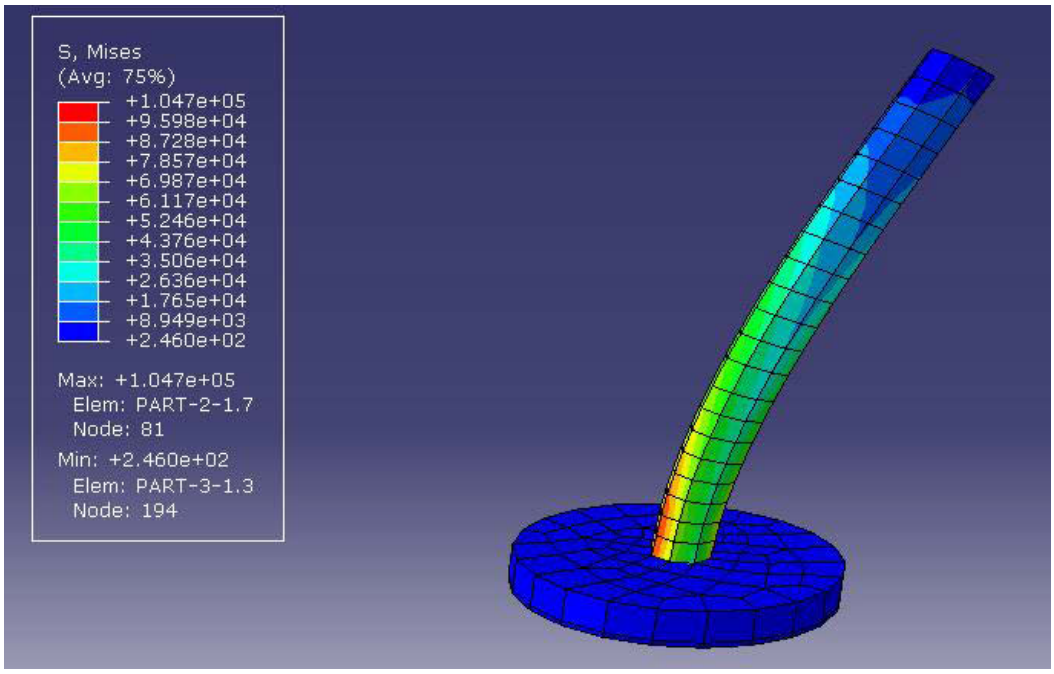

Figure 5-98. The Mises stresses acting on the hollow tower and the bearing plate for model number eight

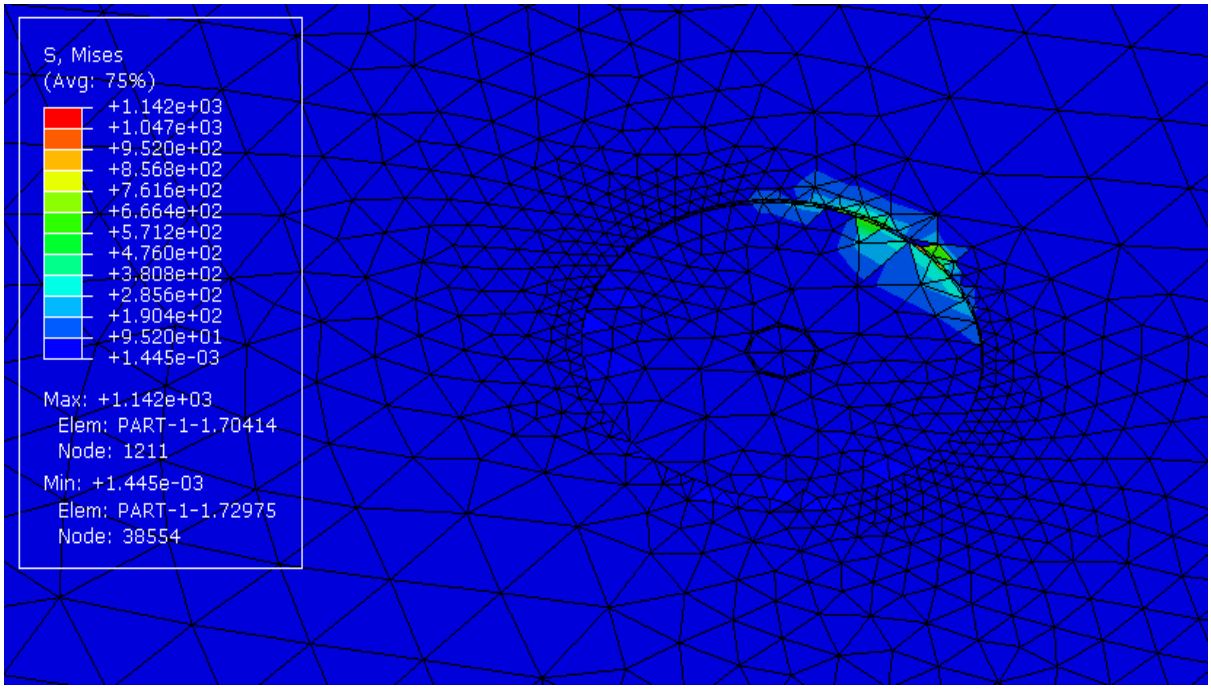

Figure 5-99. The Mises stresses acting on the soil block for model number eight (un-piled footing)

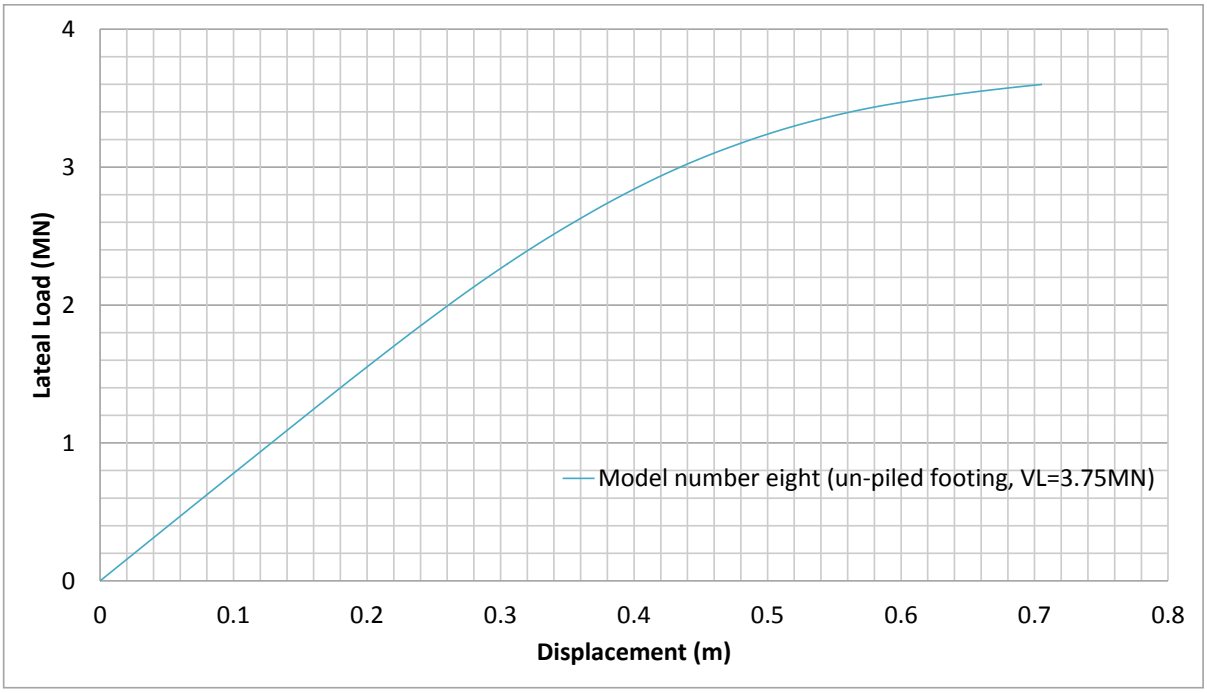

Figure 5-100. The results of model number eight (un-piled footing)

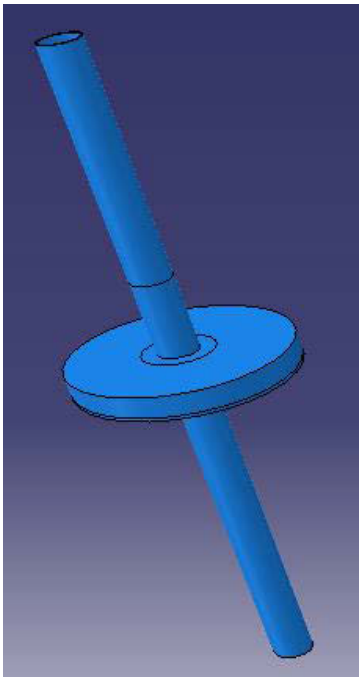

Figure 5-101. The assembled structure for model number nine (piled footing)

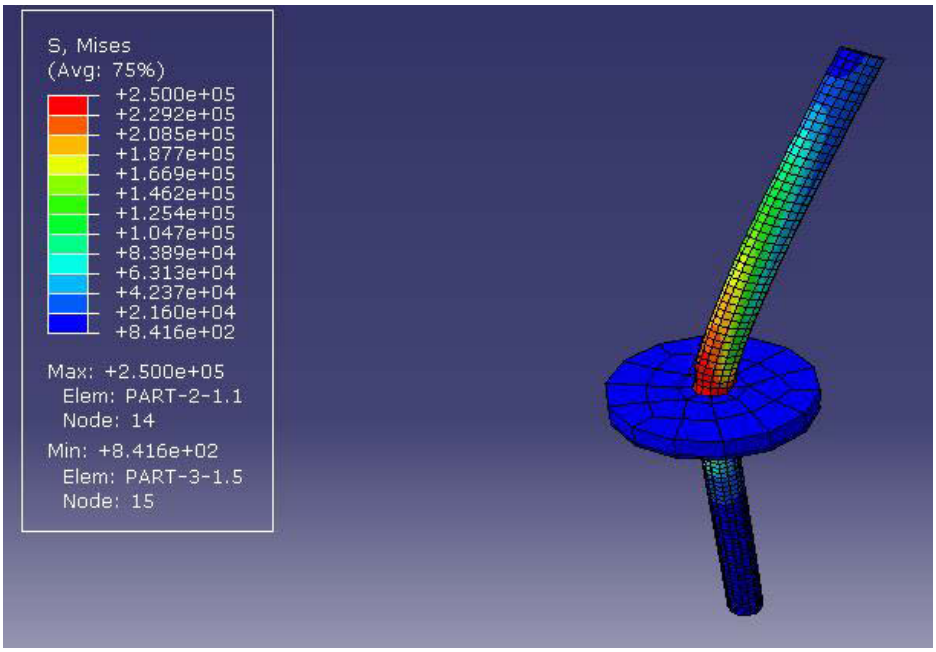

Figure 5-102. The results of model number nine illustrating the Mises stresses (piled footing, VL=3.75 MN)

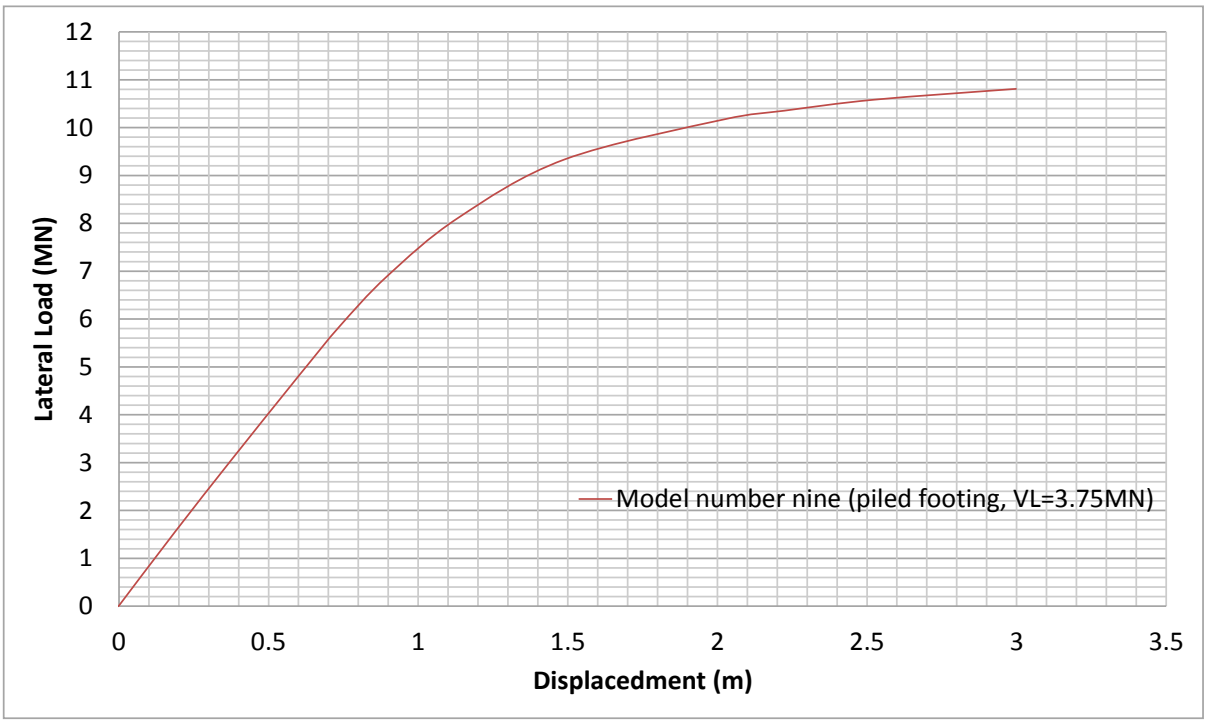

Figure 5-103. The FE results for model number nine (piled footing structure)

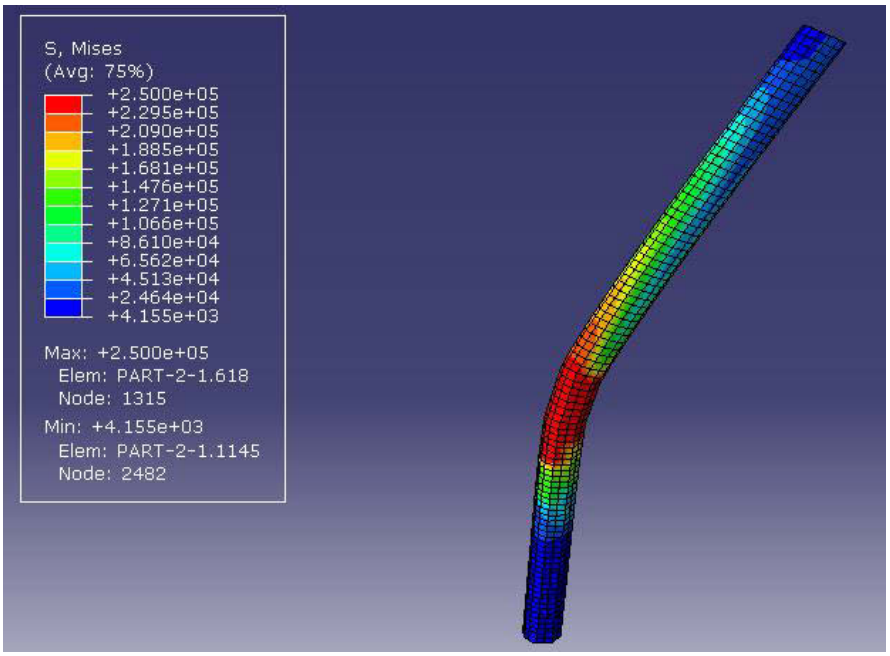

Figure 5-104. The Mises stresses acting on model number ten (monopile, VL=3.8 MN))

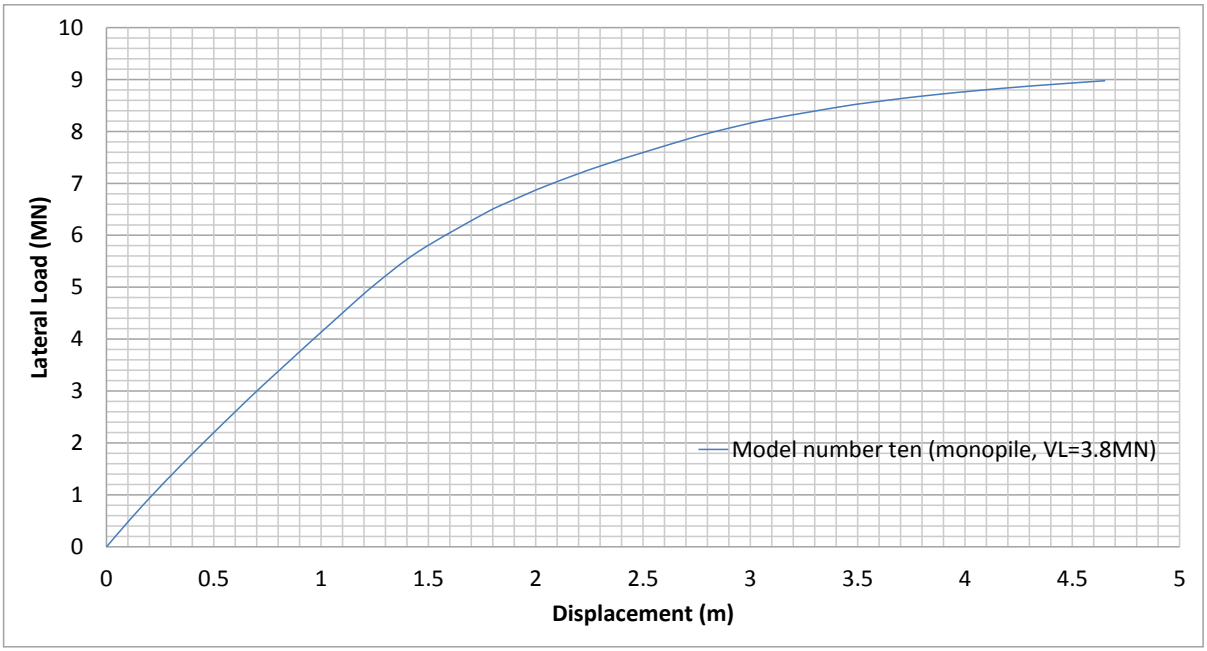

Figure 5-105. The results of test number ten (monopile without a collar, VL = 3.8 MN)

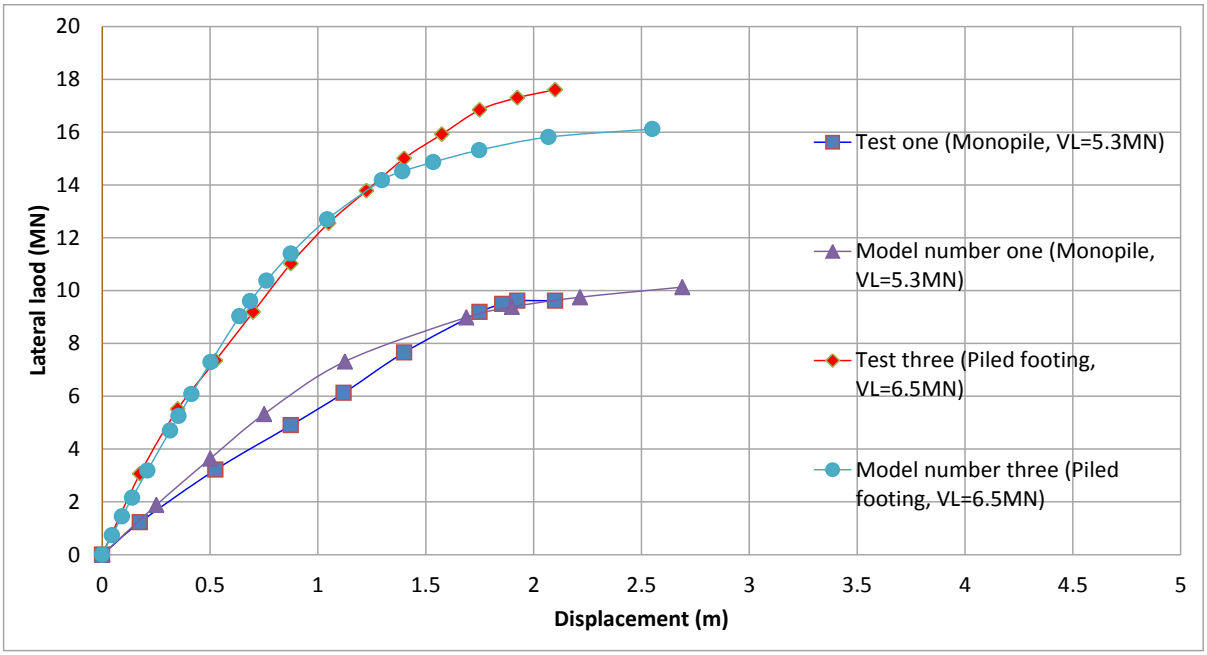

Figure 5-106. The test and the FE results for the monopile and the piled footing structures under a vertical load of 5 to 6.5 MN

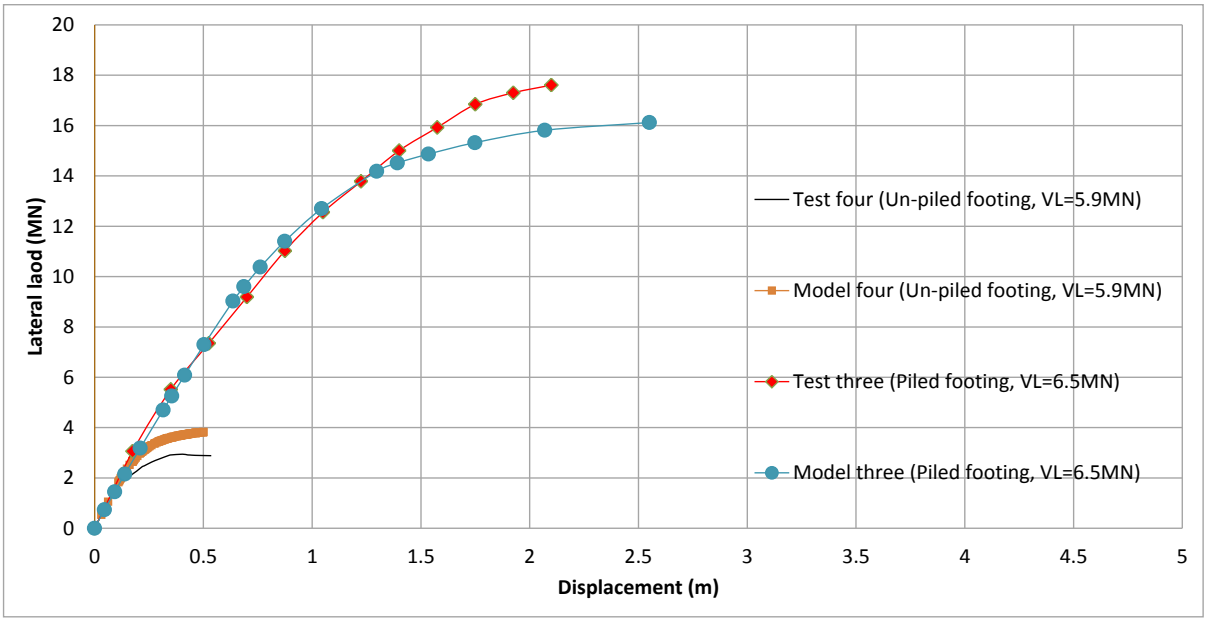

Figure 5-107. The un-piled footing and piled footing results under a vertical load of 5.9 to 6.5 MN

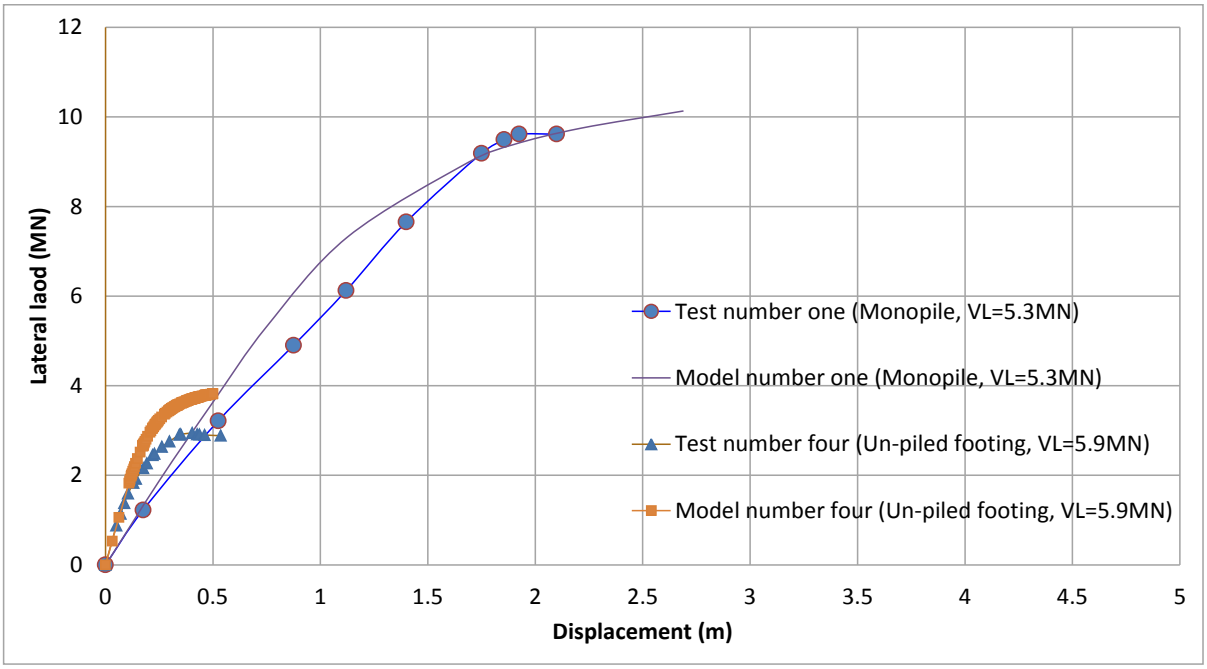

Figure 5-108. The results of the monopiles and the un-piled footings under a vertical load of 5 to 6 MN

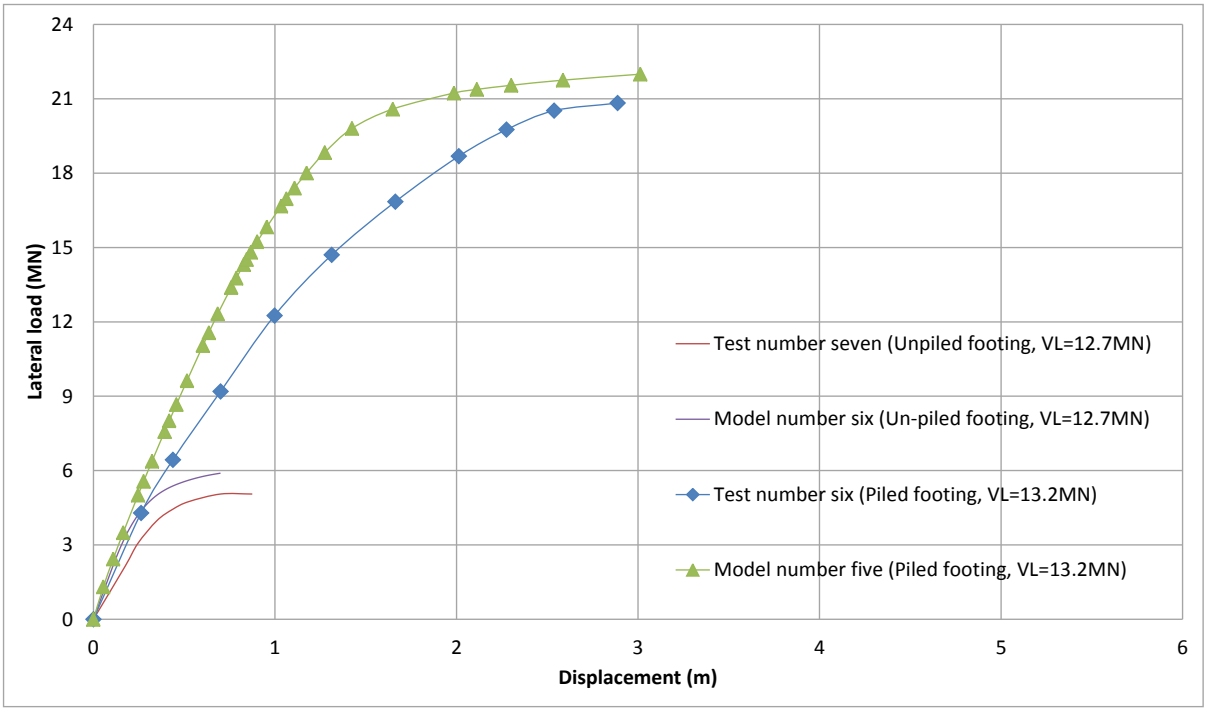

Figure 5-109. The un-piled footing and piled footing results under a vertical load of 12.7 to 13.2 MN

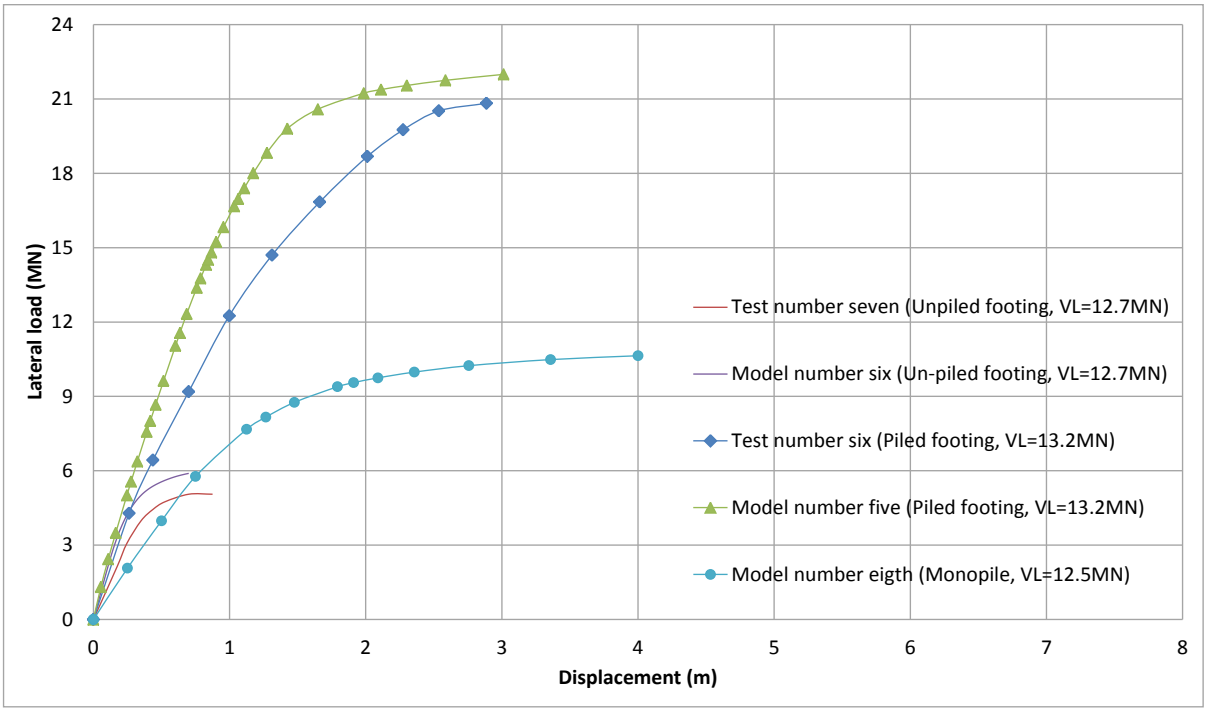

Figure 5-110. Comparing the results under a vertical load of 12.5 to 13.2 MN

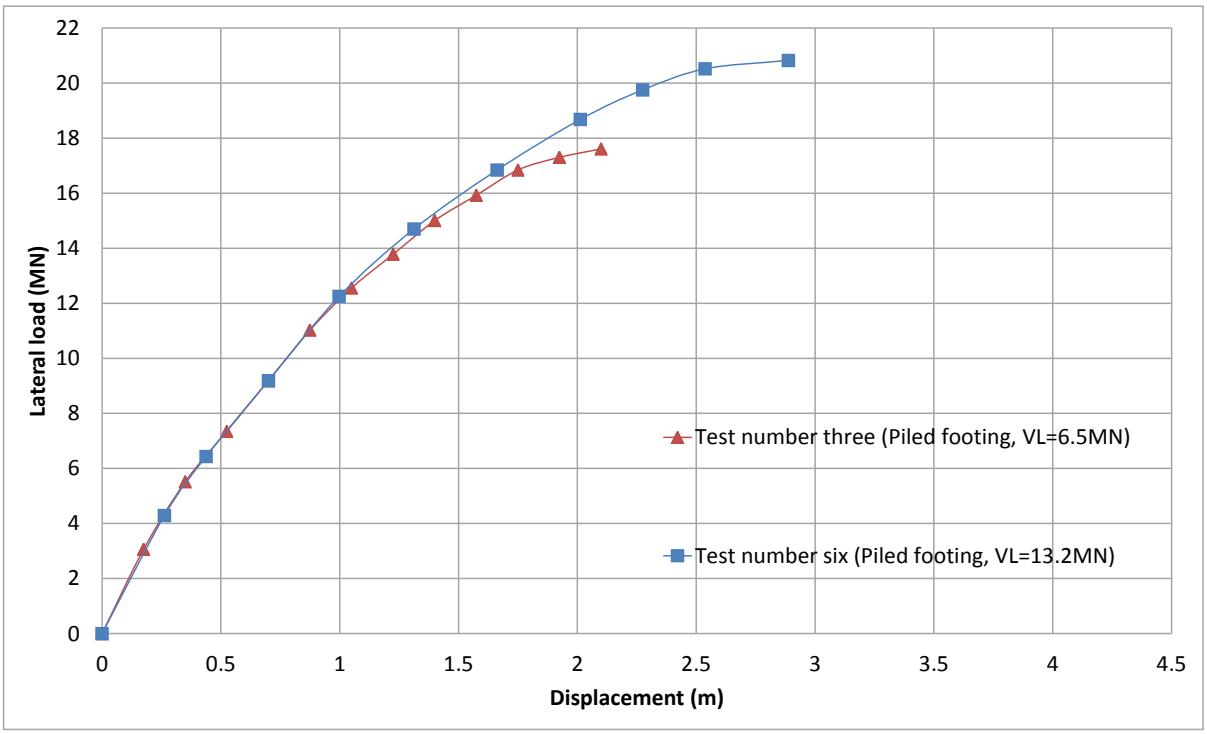

Figure 5-111. The centrifuge test results for the piled footing structures

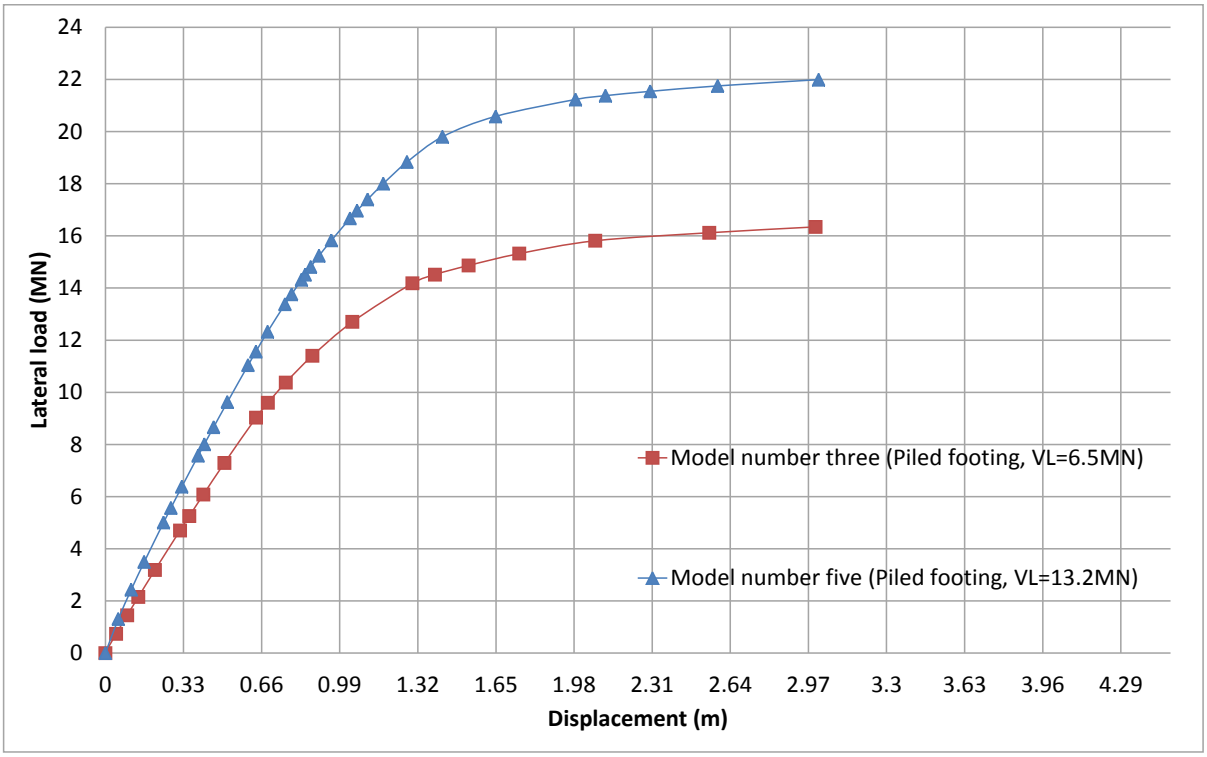

Figure 5-112. The FE results for the piled footing structures

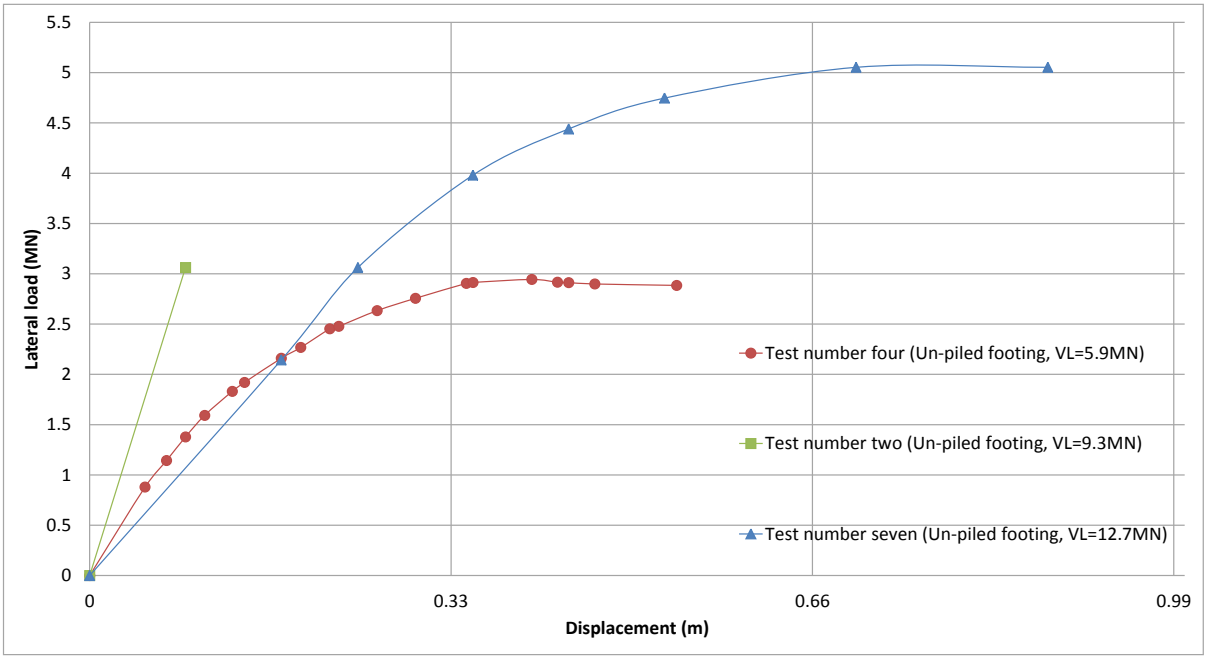

Figure 5-113. The centrifuge test results for the un-piled footing structures

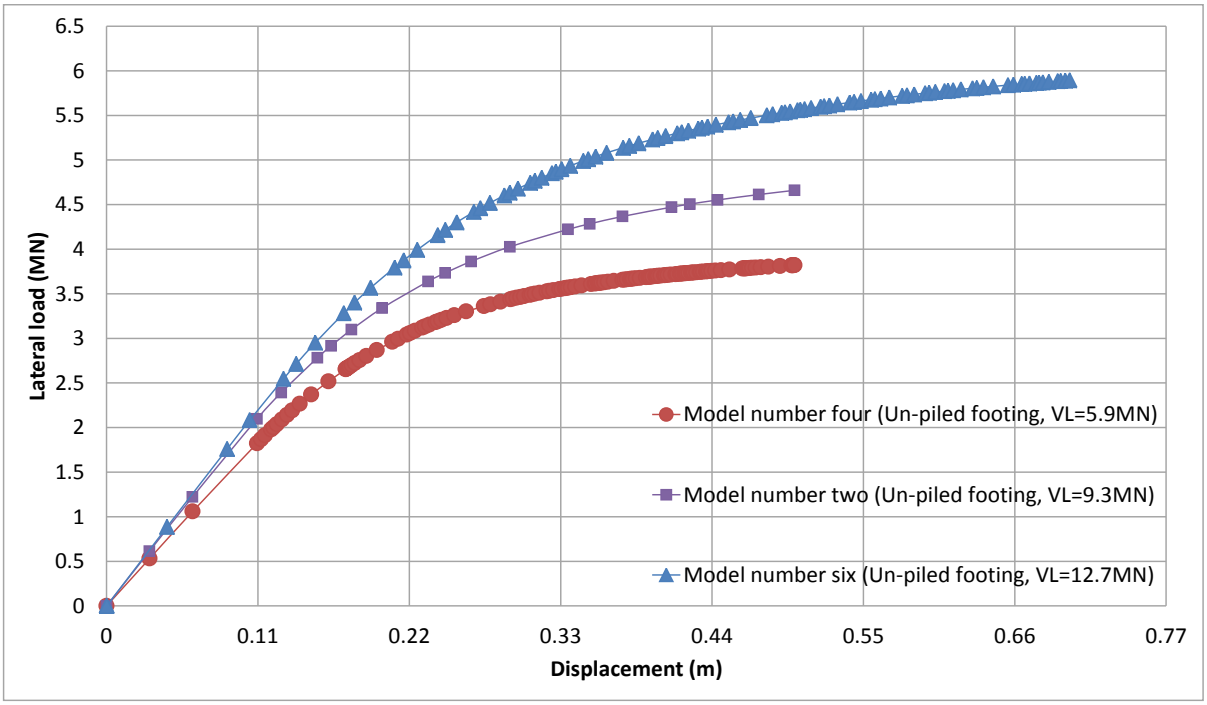

Figure 5-114. The FE results for the un-piled footings with different vertical loads

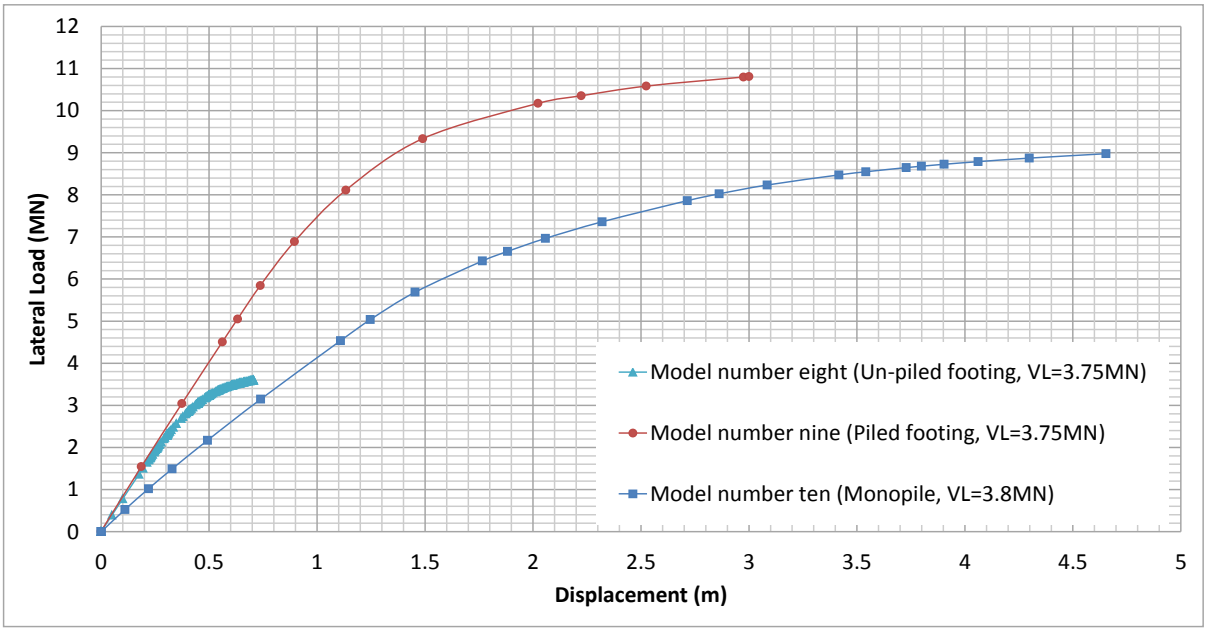

Figure 5-115. The FE results for the un-piled footing, piled footing and the monopile structure

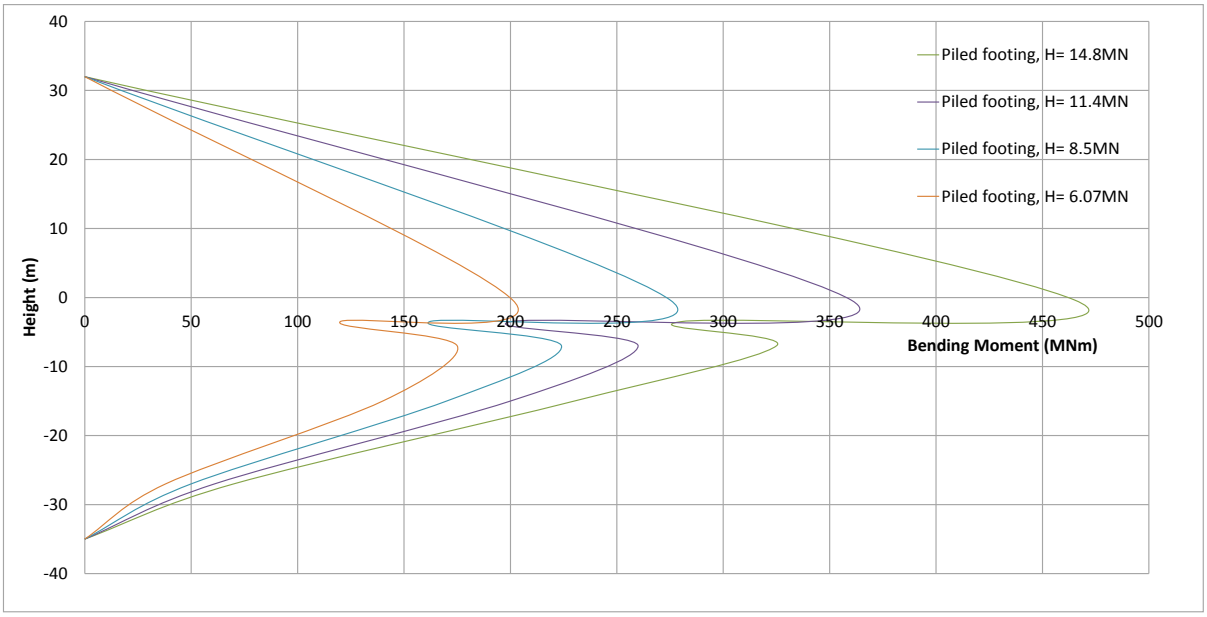

Figure 5-116. The bending moments generated for the piled footing structure (model number three, VL=6.5 MN)

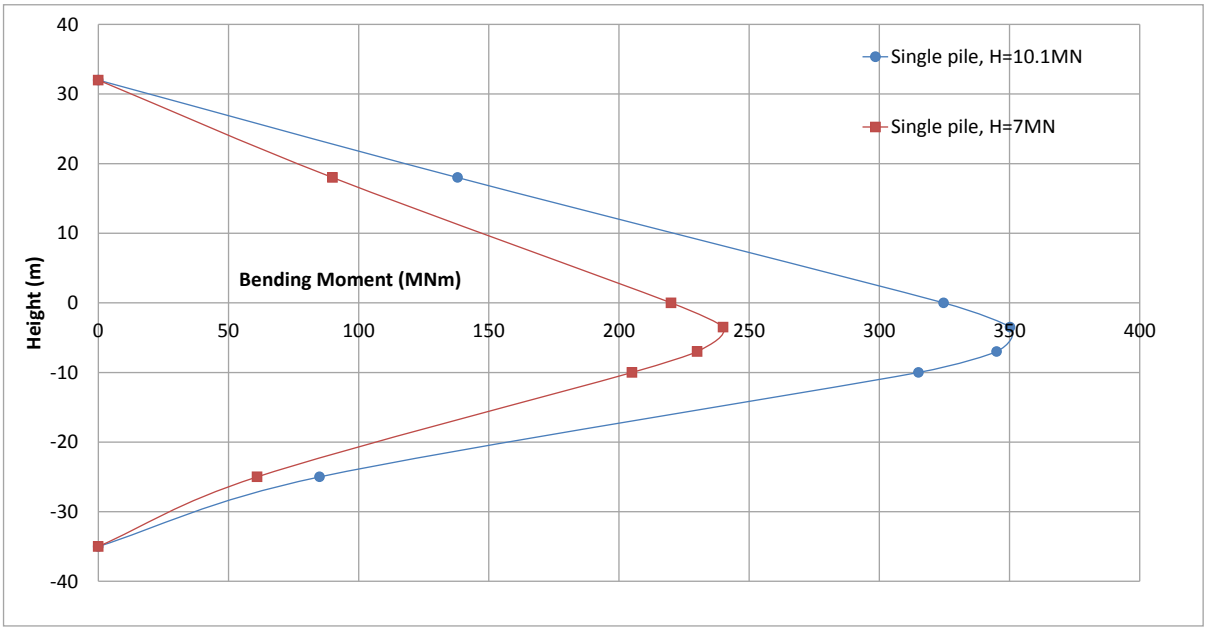

Figure 5-117. The bending moments generated on the monopile structure (model number one, VL=5.3 MN)

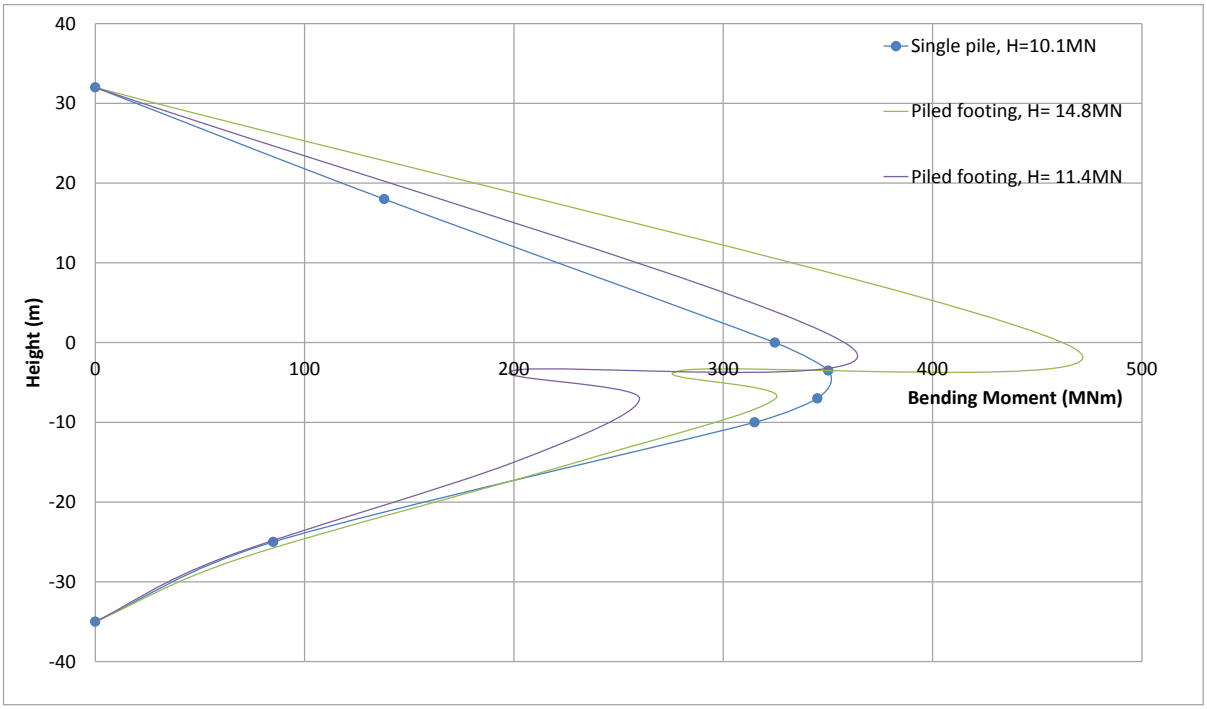

Figure 5-118. Comparing the bending moments generated from the piled footing (model number three, VL=6.5 MN) and the monopile structures (model number one, VL=5.3 MN)

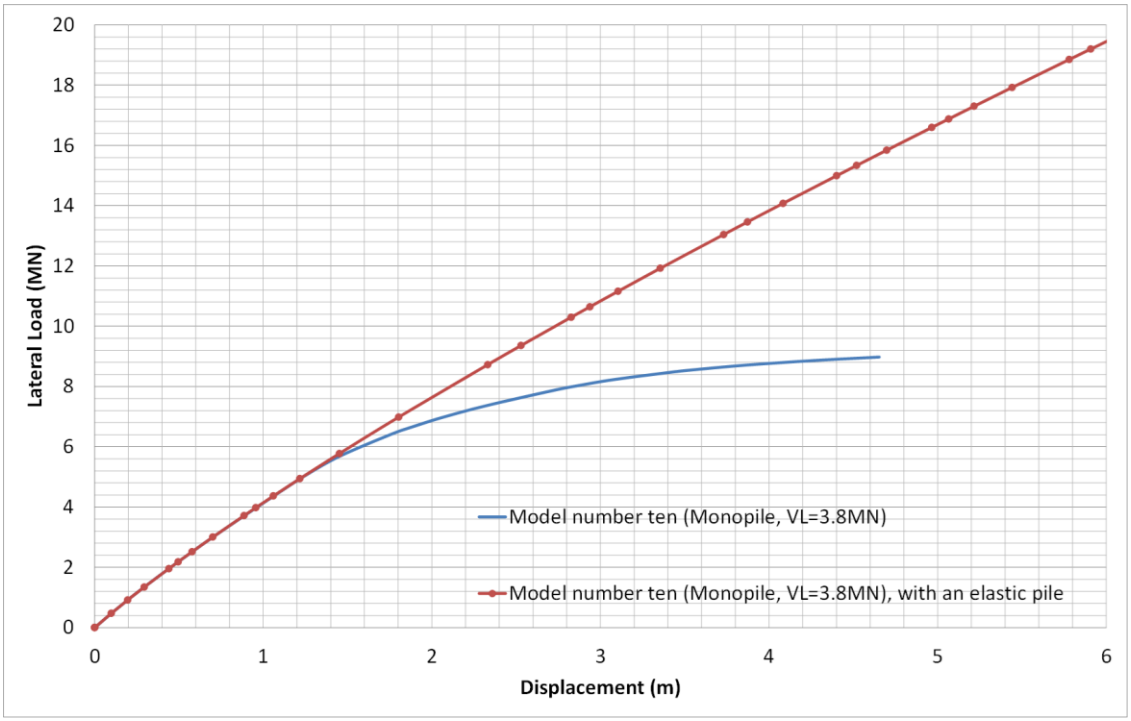

Figure 5-119. The results of model number ten with and without considering the yield point for the pile materail

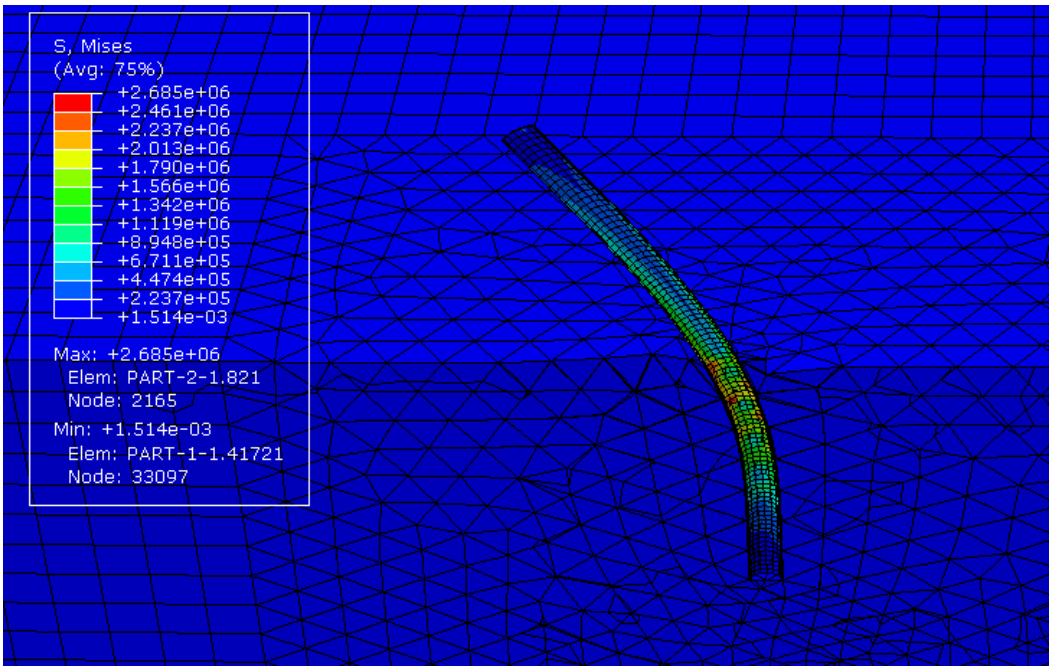

Figure 5-120. The Mises stresses acting on model number ten with an elastic pile (without a yield point)

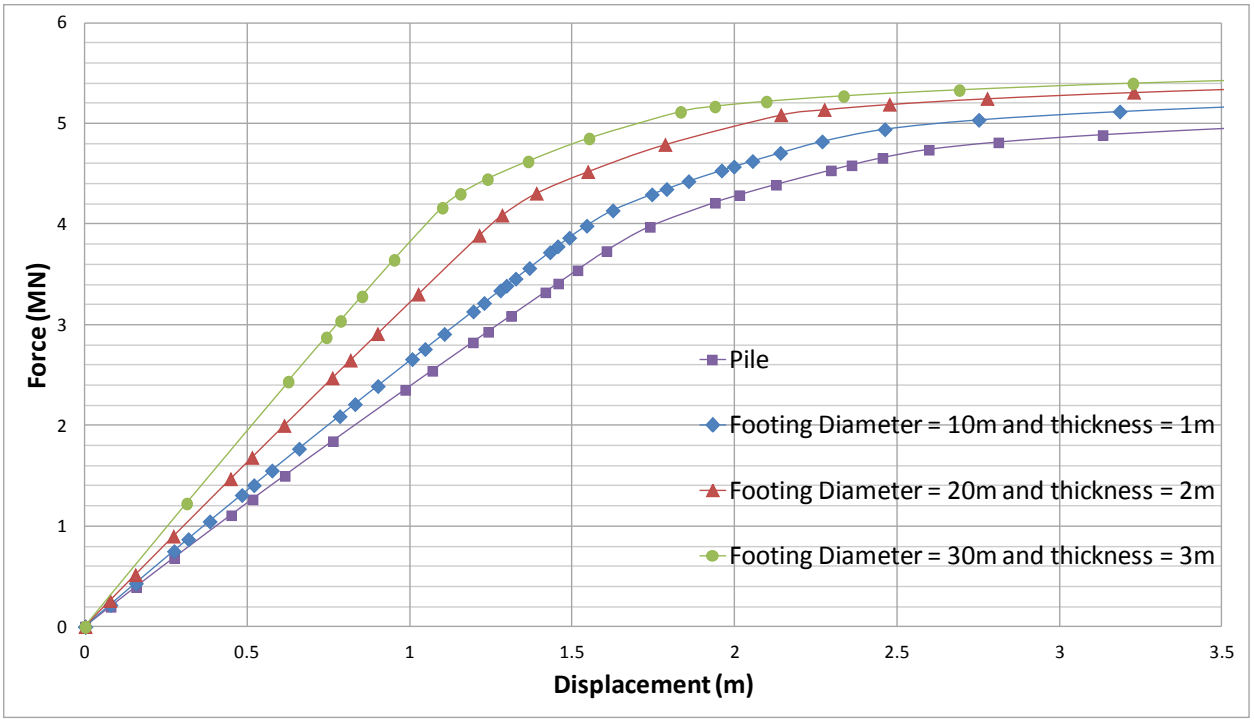

Figure 5-121. The displacement versus force graph for the loose sand

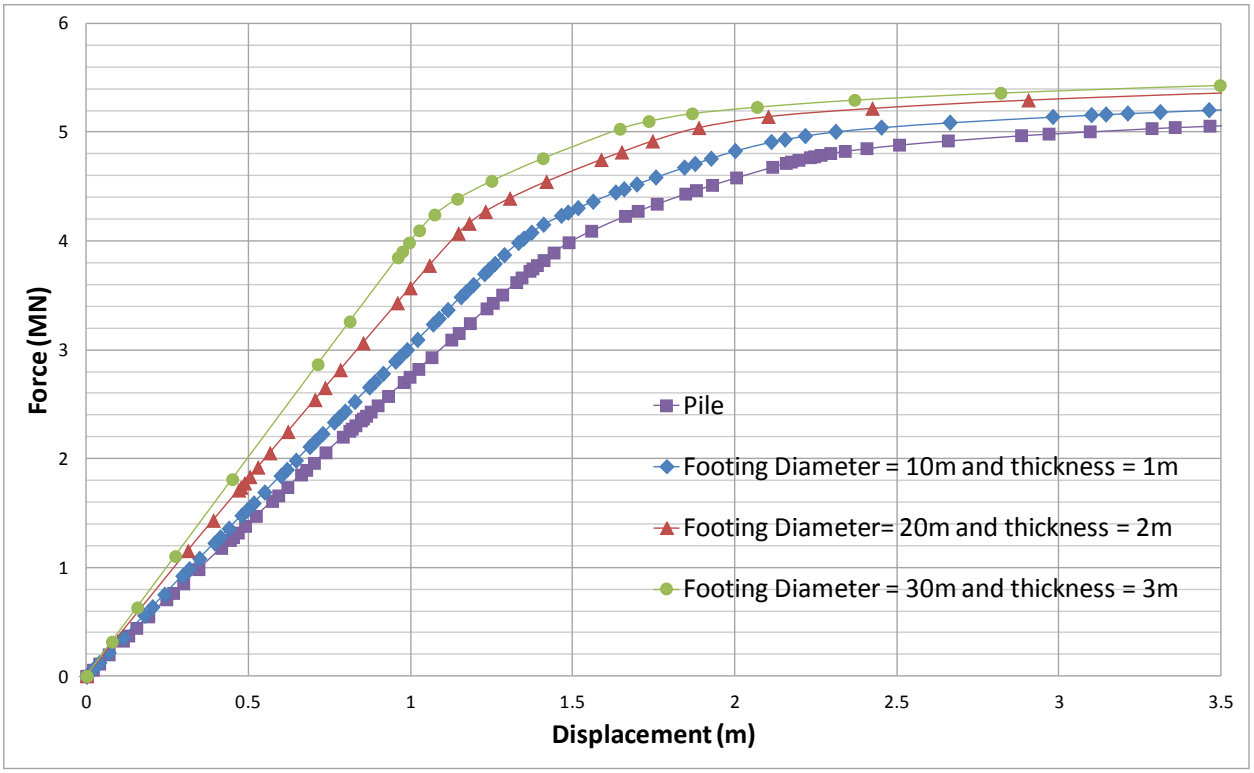

Figure 5-122. The displacement versus force graph for the dense sand

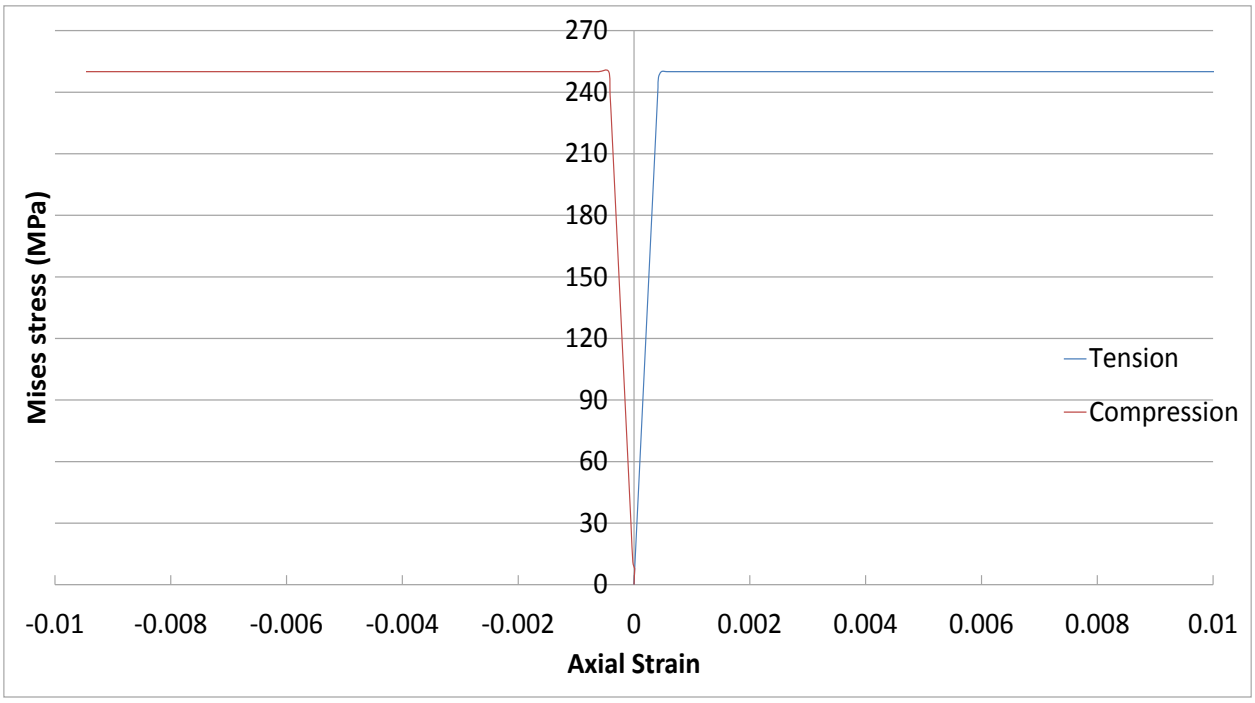

Figure 5-123. The stress versus strain graph

CHAPTER 6 FACTORS INFLUENCING THE LATERAL BEHAVIOUR OF MONOPILES AND MONOPILED FOOTING STRUCTURES

6.1 INTRODUCTION

In this chapter, a parametric study is conducted by constructing numerical models, which consist of monopiles, un-piled footings and piled footing structures. The goal was to investigate the influence of different footing dimensions, the embedment depth of the footing, the soil's friction angle, and the soil's modulus of elasticity on the lateral behaviour of a piled footing structure. In addition, the influence of the pile dimensions was investigated for both the monopile and the piled footing structures.

As discussed in Section 2.2, the Egmond aan zee and the Horns Rev wind farms constructed in Europe are considered as the largest offshore wind farms to the date. To conduct a parametric study on monopiles and piled footing structures the dimensions used in this study were adapted from these wind farms.

The Egmond aan zee wind farm consisted of monopiles with a diameter of 4.6 m, which were driven 30 m into the seabed. The hub for each tower was around 80 m above the ground level, the thickness of each pile was 50 mm to 60 mm and they were constructed out of steel. The transition piece, which was installed on the pile's head, had a diameter of 4.3 m and a length of 25 m. The transition piece was slightly smaller in diameter so that it could be grouted to the pile at the sea level.

To conduct a parametric study the dimensions of a monopile used in the Egmond aan zee wind farm were considered as the initial design parameters. The parameters under investigation were then altered in respect to the initial design to investigate how much the lateral capacity might vary due to the changes made to the structure. The initial tower's height from the ground level was considered 70 m and its value was changed during the parametric study to investigate the effects of the eccentricity for monopiles and the piled footing structures in different sand deposits.

It must be pointed out that the lateral displacements versus lateral force graphs have been investigated for all structures in this chapter and all piles were considered hollow (as in the case of offshore wind turbines).

6.2 DIMENSIONS AND MATERIAL PROPERTIES USED FOR THE PARAMETRIC STUDY

The monopiles in all numerical models were constructed out of structural steel (ASTM-A36) with no strain hardening. The mechanical properties of the steel are illustrated in Table 6-1. It must be noted that in Chapter 5 the pile/tower was constructed out of Aluminium (as in the case of the centrifuge tests) but at this stage by considering the structure to be constructed out of steel, two different alloys have been considered for checking the reliability of the hybrid structure in this research.

Pile/ Tower- Structural steel ASTM-A36	
Unit weight	78 kN/m^3
Modulus of Elasticity	200 GPa
Poisson's ratio	0.32
Yield strength	250 MPa

Table 6-1. The material properties used for the pile structure in the numerical models

The footings constructed for the piled footing structures were all constructed out of concrete (similar to grade M25) with the material properties illustrated in Table 6-2.

The footing's material properties	
Unit weight	23.8 kN/m^3
Modulus of Elasticity	25 GPa
Poisson's ratio	0.15

Table 6-2. The material properties for the footings used in the numerical models

The pile/tower in the numerical models had an outer diameter of 4.6 m with a thickness of 60 mm. The pile's length underground was 30 m and the tower's height was 70 m, which makes a total length of 100 m. These dimensions are in line with the pile/towers used in the Egmond aan zee wind farm.

A surplus of 2.5 MN was applied to the tower's head for all numerical models to take account of the weight of the nacelle, rotor and hub. The force applied by the nacelle on the pile/tower's head is usually in the range of 1.5-2 MN while the rotor and hub apply a load of around 0.6-1 MN (Sender 2009 & Vestas report - V120).

As the piles and the piled footing structures are to be installed offshore, a constant water depth of 10 m was considered for all numerical models constructed in this chapter. This water depth was important for the analysis, as the buoyant unit weight of steel had to be considered for a height of 10 m above the ground level. This was the case for all monopiles and piled footing structures constructed in this chapter. In addition, the buoyant unit weight of concrete was considered for all piled footing structures.

As discussed in Chapter 1 monopiles used as wind turbines have failed under their ultimate lateral capacities in practice (Figures 1-5 and 1-6) and so in this chapter the serviceability and the ultimate lateral capacities of all structures have been investigated.

Two soil groups were chosen for the parametric study. The first group, which is group A, had the following properties:

Soil Group A (loose soil)	
Effective unit weight	7 kN/m^3
Modulus of Elasticity (kPa)	1000 Z(m)
Poisson's ratio	0.33
Dilatation angle	0°
Effective friction angle	30°

Table 6-3. The soil properties adopted for soil Group A

The properties of the second soil group, which is soil group B, are illustrated in Table 6-4. In these soil groups (A & B), the soil Young's modulus increased linearly with depth but this increase was higher for soil group B, so it is clear that soil group B can be considered as a stiff soil. The linear increase in the soil Young's modulus for all numerical models was adjusted by a Python script, which worked with MATLAB (the Python script is attached in Appendix A).

As discussed in Chapter 2, wind turbines are driven into position by driving them into the surrounding soil on site and so a critical soil friction angle would be more suitable for such cases in dense sands. As discussed by Bolton et al. (1986) critical friction angles of sands higher than 37° are for cohesionless material with a significant amount of feldspar. Therefore, in-group B the critical friction angle was chosen as 37° and not higher.

Soil Group B	
Effective unit weight	7 kN/m^3
Modulus of Elasticity (kPa)	2500 Z(m)
Poisson's ratio	0.28
Dilatation angle	10°
Effective critical friction angle	37°

Table 6-4. The soil properties adopted for soil Group B

The soil Poisson's ratio in soil groups A & B were calculated from the adopted friction angles through Equation 5-3.

The first step in the parametric study was to determine an efficient footing dimension for the piles used in the parametric study and then to investigate how the hybrid structure would behave under changes made to the soil properties and the pile dimensions.

It must be highlighted that the ultimate lateral capacity of the monopiles in this study will be checked in respect to the methods adopted by Broms (1964), Fleming et al. (1992) and Zhang et al. (2005) to illustrate the accuracy of those methods in respect to the FE results.

The numerical models constructed for this study are similar to the models constructed in Chapter 5. For this study, the collar present on the monopile and the piled footing structures were removed and the dimensions were adjusted in respect to the Egmond aan zee wind farm monopiles. Figures 6-1 and 6-2 illustrates the loads, boundary conditions and the mesh generated for a monopile and a piled footing structure respectively.

To ensure that the mesh generated for the structures were accurate enough, a purely elastic model (pile and soil) was constructed and the horizontal displacement of the pile/tower at the ground level was checked in respect to the solutions provided by Poulos (1971a) (discussed in Section 3.4.1). For the constructed elastic model the modulus of elasticity of the pile was equal to 200 GPa, the soil's modulus was equal to 50 MPa and the soil Poisson's ratio was equal to 0.49. Using Equation 3-16 for the pile dimensions, which were provided, in this section, the lateral displacement at the ground level was calculated to be equal to 0.0067 m and the predicted value from the FE calculation was equal to 0.0065 m. This illustrated that the adopted mesh was accurate for the analysis.

6.3 EFFECTS OF FOOTING DIMENSIONS

To study the effects of the footing dimensions (radius and thickness) a procedure similar to the method adopted by Powrie and Chandler (1998) was used. In this method, the required thickness or radius will be varied to a point where the benefit gained from increasing that particular dimension under investigation would be very small.

Figure 6-3 illustrates the FE predictions for the lateral displacement of a retaining wall with and without a stabilising platform embedded in a clay layer. As Powrie and Chandler (1998) discuss, only a very small benefit was achieved by increasing the length of the platform beyond 7.8m. This method is mainly an economical approach, as it will provide a cost efficient design for the proposed structure.

For the hybrid structure under investigation, the radius and thickness of the footings were varied separately to illustrate how they individually increase the lateral capacity of the proposed structure.

The adopted procedure and the obtained results will be further discussed in the following sections.

6.3.1 Effect of footing thickness

To investigate the effect of the footing thickness a bearing plate with a small radius of 2.53 m was attached to a single pile. The single pile's dimensions constructed in the numerical model were similar to the Egmond aan zee wind turbines. The footing's radius was small so that the effects of the footing thickness would be pronounced.

The initial thickness of the footing was equal to 1.15 m and its value was sequentially increased by $0.2D_p$ (D_p is the pile diameter = 4.6 m) as illustrated in Table 6-5.

Footing thickness (m)	Footing Radius (m)
1.15	2.53
2.07	2.53
2.99	2.53
3.91	2.53
4.83	2.53

Table 6-5. The footing dimensions used in the numerical models for investigating the effects of the footing thickness

The changes made to the thickness of the footings with a constant footing radius were considered for both soil groups, that is groups A & B. In addition, the piled footing results obtained for each soil group were compared with the results obtained for a monopile case embedded within each soil group.

Figure 6-4 illustrates the results of the lateral displacement versus lateral force for soil group A. As can be seen from the figure, the ultimate capacity and the stiffness of the piled footing structures were higher than the capacity and stiffness of the monopile structure.

The ultimate capacity of the monopile in Figure 6-4 can be validated against solutions provided by Broms 1964 (Figure 2-34a) and Fleming et al. 1992 (Figure 2-40b) for long piles embedded in a sand deposit. For Broms solutions Figure 2-34a can be used, as the maximum moment acting on the pile section was higher than of the yield moment of the pile ($M_{max} > M_{yield}$). Moreover, in Section 6.5 it will be illustrated that for the monopile embedded in soil group A (the loose soil) the pivot point is nowhere close the pile's toe and so the pile can be considered as a long pile. By considering the latest points, Broms (1964) solution provides an ultimate lateral capacity equal to 3.27 MN, which is in a very close agreement with the FE predictions illustrated in Figure 6-4.

The procedure adopted to calculate the ultimate lateral capacity of a monopile embedded in soil group A by Broms chart will be illustrated at this point. In addition, as discussed in Section 2.6.2 the method adopted by Broms (1964) can be checked by solving Equations 2-52 & 2-53 with considering the yield stress of the material, the latest process was adopted in a MATLAB script (Appendix B) to confirm the results obtained from the charts for this chapter.

From Figure 2-34a, the abscissa is equal to:

$$\frac{M_y}{D^4 K_p \gamma'} = \frac{250\times10^6\times0.25\times3.14\times(2.3^4-2.24^4)/2.3}{4.6^4\times3\times7\times10^3} = 25.47$$

e/D = 70/4.6 = 15.2

Therefore, $Q_{u\,(g)}$ or the ultimate lateral force will be equal to $K_P \times \gamma' \times D^3 \times 1.6$ and that is equal to $3 \times 7 \times 10^3 \times 4.6^3 \times 1.6 = 3.27$ MN. The FE model predicts a value of 4.1 MN. The difference

between the adopted method by Broms (1964) and the FE result is -20.24%. The difference in this chapter will be calculated as in Equation 6-1.

$$\%\text{Difference} = \frac{\text{Adopted Method} - \text{FE result}}{\text{FE result}} \quad \textbf{6-1}$$

Using the charts produced by Fleming et al. (1992), that is Figure 2-40(b) the ultimate lateral capacity of the monopile was equal to 6 MN, which has a difference of +46.34% with the FE prediction.

The method adopted by Zhang et al. (2005) discussed in Section 2.6.5 can also be used for calculating the ultimate lateral capacity of the monopile. As they discuss, their equations are suitable for long and short piles in cohesionless material. Using Equations 2-79 and 2-80 with considering a value of 0.6ϕ for δ (Table 2-6) and a value of $1.5K_0$ (Table 2-5) for K the ultimate capacity was calculated to be equal to 4.8 MN, which has a difference of +17.0% with the FE result.

Figures 6-5 and 6-6 are a close up illustration of the results of Figure 6-4 (without considering t = 2.07 m). It is clear that the ultimate capacities of the piled footings are slightly increasing from a footing thickness of 1.15 m (Figure 6-4). This might be because the footing thickness provides a support around the pile structure and as its value increases, the ultimate capacity of the entire structure is affected.

It is apparent that transporting or constructing a footing with a thickness of around 5 m for an offshore case is not economical. In addition, the difference in the stiffness between a footing thickness of 2.99 m and 4.83 m at a displacement of $0.2D_p$ was only +4.0%, as illustrated in Figure 6-6. Therefore, considering a thickness of 2.99 m would be preferable from a design application point. In addition, the increase in the ultimate lateral capacity and the stiffness between a footing thickness of 2.99 m and 3.91 m is not significant, as illustrated in Figures 6-4 and 6-5.

Figure 6-7 illustrates the results of soil group B with considering different footing thicknesses. Figures 6-8 and 6-9 illustrates the same results up to a displacement of $0.2D_p$ (without considering t = 2.07 m). Similar to the results of soil group A the stiffness's of all piled footing structures were higher than the stiffness of a monopile from the initial point. In addition, a footing with a thickness of 2.99 m seems to be a reasonable choice (this choice considers the high costs of transporting and constructing a large and heavy footing for a very small gain in the stiffness of the structure).

The results of the monopiles and the piled footing structures embedded in soil groups A & B can be used for comparison purposes. From Figures 6-4 and 6-7, it is clear that the ultimate lateral capacity of a single pile/tower and a piled footing structure does not increase as the soil becomes stiffer. For instance, it is evident that the ultimate lateral capacity of the single pile embedded in both soil groups is equal to 4.1 MN regardless of the soil type. On the other hand, from Figures 6-5, 6-6, 6-8 and 6-9 it is clear that the stiffness of both structures (that is the monopile and the piled footing structures) increases as the soil becomes stiffer. For instance, the ultimate lateral

capacity of the monopile in soil group A and B was equal to 4.1 MN but the difference between the stiffness of the two structures at $0.2D_p$ was equal to +10.5%. This illustrates that the ultimate capacity of the monopiles and the piled footing structures were entirely controlled by their structural capacity, while the surrounding soil only affected the stiffness of the structures at small displacements.

The ultimate lateral capacity of the monopile in soil group B can also be checked in respect to Broms (1964) chart for long piles embedded in sands. By using Figure 2-34a the ultimate lateral capacity of the monopile was calculated to be equal to 3.29 MN which is consistent with the FE results obtained in Figure 6-7. This clearly illustrates that by increasing the stiffness of the surrounding soil the ultimate lateral capacity of the structure (monopiles with high eccentricities) does not change.

For a piled footing structure with a footing radius of 2.53 m and a thickness of 2.99 m at a lateral displacement of $0.2D_p$, the gain in the stiffness due to the stiffer surrounding soil (comparing the results of soil groups A & B, Figures 6-6 and 6-8) was +11.3%.

6.3.2 Effects of the footing radius

The effect of the footing radius was investigated in a similar way to that adopted for studying the effects of the footing thickness conducted in the previous section.

A small thickness of 0.23 m was considered for all footings embedded in soils group A & B. This modest thickness was considered so that it would not significanlty influence the effects of chaning the footing's radius (mainly the stiffness). With considering a small thickness for the footings involved in the piled footing structures, the radius of the footing was increased and the lateral load versus lateral displacement graphs for the hybrid structures were investigated.

Table 6-6 illustrates the dimensions used in the constructed numerical models.

Footing Radius (m)	Footing Thickness (m)
5.29	0.23
7.13	0.23
10	0.23
15	0.23

Table 6-6. The footing dimensions used in the numerical models to investigate the effects of the footing thickness

By considering a small thickness for the footings involved in the hybrid structures, the effects of increasing the footing radius will be pronounced.

Figures 6-10 and 6-11 illustrate the results of the piled footing structures embedded in soil group A. From Figure 6-11 it is clear that at a lateral displacement of $0.2D_p$ the difference in stiffness between a footing with a radius of 10 m and 15 m was +1.42% while at $0.1D_p$ their stiffness's

were equal. The maximum difference between the two mentioned radiuses was +6% at a displacement of $0.3D_p$.

Figures 6-12 and 6-13 illustrate the results of the piled footing structures embedded in soil group B. Similar to the previous case; at a lateral displacement of $0.2D_p$, the difference in the stiffness between a 10 m and a 15 m footing radius was+3.63%.

By comparing Figures 6-10 and 6-12, it is clear that by changing the footing's radius for the two soil groups (groups A & B) the ultimate lateral capacities of the structures were not affected. In addition, from Figures 6-11 and 6-13 it is clear that for a piled footing structure with a footing radius of 10 m with a small thickness (0.23 m) the gain in the stiffness for the structure at $0.2D_p$ between the two soil types was +4.76%.

As discussed in Chapter 2 a single design which is appropriate for different soil types is more economical and allows for construction simplicity. This seems to be the case for a piled footing structure with a radius of 10 m, as this structure provides almost an equal stiffness and ultimate capacity for both soil types. Moreover, it is clear that the costs of constructing or transporting a concrete footing with a radius of 10 m for an offshore scenario will be much less compared to a 15 m footing radius.

6.3.3 Defining an efficient footing size for the monopile structure

It can be concluded that by changing the thickness and the diameter of the footing in two different soil types for the piled footing structures, their ultimate lateral capacities did not alter (the soil type did not affect the ultimate capacities). This was also the case for the monopile structures. In addition, the stiffness of all piled footing structures were higher compared to the stiffness of the monopiles from the initial point. It was also illustrated that by changing the footing's thickness, the ultimate lateral capacity of the structures slightly increased and this was the case for both soil groups.

As previously discussed, Powrie and Chandler (1998) concluded that an optimized length for the stabilising platform in their study was around 50% of the embedment depth of the retaining wall (Section 2.9). Their study was conducted on a clay layer and their proposed retaining wall had a depth of only 5.06 m.

For this study, a piled footing with a thickness of 2.99 m and a radius of 10 m was selected to investigate the effects of the embedment depth of the footing, soil properties and the changes in the pile dimensions for the piled footing structure.

Figures 6-14 and 6-15 compare the results of the monopile with the piled footing structures embedded in soil groups A and B respectively. The thickness and radius of the footing for the piled footing structures in these figures were 2.99 m and 10 m respectively. At a lateral displacement of $0.1D_p$, the difference in the stiffness between the monopile and the piled footing structure was +55.5% and +45% for soil groups A and B respectively. Moreover, at a displacement of $0.2D_p$, the differences in the stiffness between the two structures was +43.8% and 40.2% for soil groups A and B respectively.

In the sections that follow the effects of the embedment depth for the footing, the soil type, the pile thickness and the pile diameter will be investigated. It must be emphasised that for all piled footing structures in the following sections the footings have a radius of 10 m and a thickness of 2.99 m.

6.4 EFFECTS OF FOOTING EMBEDMENT FOR THE HYBRID STRUCTURE

To study the effects of embedding the footing into the soil for a piled footing structure, the nominated hybrid structure was embedded to a depth of 1m and its lateral capacity was compared to a piled footing structure, which its footings was resting at the ground level. The results of this comparison are illustrated in Figures 6-16 and 6-17 for soil groups A and B respectively. As can be seen from the latest figures, there was no significant improvement in the ultimate lateral capacity or the stiffness of the piled footing structures by embedding their footings to a depth of 1m below the ground surface, and that was the case for both soil groups.

From the results of Figures 6-16 and 6-17, it is clear that the footings should not have had a significant horizontal displacement and so embedding the footing did not influence the lateral capacity of the hybrid structures. If the soil in front of the footing was to resist the horizontal load, the footing in both soil groups must move sufficiently horizontally so that the effects of the sidewalls would be pronounced. The average displacement of the footing sitting at the ground level for soil group A was 15 mm while for soil group B that was 4.7 mm. When the footings were embedded 1m in to the ground level, the average horizontal displacements of the footings in both soil groups were unchanged.

To further investigate the effects of the embedment depth, a single footing with a tower (un-piled footing) was constructed. The footing had a radius of 10 m and a thickness of 2.99 m and was constructed from concrete (Table 6-1). The tower was constructed from steel (Table 6-2) with considering a water head of 10 m above the ground level. The height of the tower from the ground level was 70 m and had a diameter of 4.6 m and a thickness of 600 mm, as in the case of the monopiles and the hybrid structures.

The results obtained for the un-piled footing installed at the ground surface for soil group A is illustrated in Figure 6-18. In Figure 6-18, the results of the monopile and the hybrid structures with the bearing plate installed at the ground level are also shown. Using the bearing capacity equations discussed in Section 2.8 with N_γ taken from Table 2-10 (Vesic 1973) for a soil with a friction angle of 30°, the ultimate vertical load was calculated to be equal to 279.4 MN (for the structure located at the ground level). With the weight of the structure equal to 19.51 MN the equation provided by Gottardi et al. (1993) and Butterfield et al. (1994) (Equation 2-108) can be used to calculate the ultimate lateral capacity of the un-piled footing. The ultimate horizontal capacity provided by Equation 2-108 was equal to 2.07 MN. The value calculated by the FE analysis was 1.3 times the value calculated by the equation provide by Gottardi et al. The horizontal load, which causes overturing of the structure, was calculated by Equation 5-13 and it

was equal to 2.78 MN. The value calculated by Equation 5-13 has a difference of -0.71% with the FE analysis for the structure located at the ground level.

The average horizontal displacement of the un-piled footing at the ultimate load was equal to 46 mm. This shows that the average displacement of the un-piled footing installed at the ground level was three times higher than of a piled footing structure with its footing installed at the ground surface (or embedded 1m below the ground surface) for soil group A.

To illustrate how the un-piled footing would behave if it were embedded into the soil, the constructed footing was buried to a depth of 1 m below the ground surface and laterally loaded to failure. Figure 6-19 illustrates the FE predictions for soil group A. As can be seen, the ultimate lateral capacity has increased with increasing the embedment depth for the un-piled footing case, while the stiffness has not been effected. The difference in the ultimate lateral capacity of the structure with different embedment depths was +17.8%. Using the bearing capacity equations with N_γ taken from Vesic (1973) and the equation provided by Gottardi et al. (Equation 2-108) for the un-piled footing structure embedded at a depth of 1m below the ground surface the ultimate lateral capacity was calculated to be equal to 2.1 MN. The value calculated by the FE analysis is 1.5 times greater than the value calculated by Gottardi et al. equation. Moreover, the average horizontal displacement of the footing with an embedment depth of 1m was 30 mm (when the footing was at the ground level the average displacement was 46 mm). This clearly illustrates that by embedding the un-piled footing structure, the ultimate lateral capacity of the structure can be increased and the soil surrounding the footing decreases the footing's displacement.

The results of soil group B for an un-piled footing with different embedment depths is illustrated in Figure 6-20. Similar to the previous case, embedding the un-piled footing increased the ultimate capacity of the structure by +20.68%. Moreover, the average displacement of the footing was reduced to 0.03 mm from 11 mm when the un-piled footing was embedded 1 m below the ground surface.

Using the bearing capacity equations discussed in Section 2.8 with N_γ taken from Table 2-10 (Vesic 1973) for a soil with a friction angle of 37° the ultimate vertical load was calculated to be equal to 825.6 MN (for the structure located at the ground level). With consideration of the weight of the structure to be equal to 19.51 MN the equation provided by Gottardi et al. (1993) and Butterfield et al. (1994) (Equation 2-108) was used to calculate the ultimate lateral capacity of the un-piled footing. The ultimate horizontal capacity provided by Equation 2-108 was equal to 2.17 MN. The value calculated by the FE analysis was 1.3 times the value calculated by the equation provided by Gottardi et al. For the un-piled footing structure embedded 1m below the ground surface, the equations provided a lateral capacity of 2.18 MN, which is 1.6 times the FE result. The horizontal load, which causes overturing of the structure, was calculated by Equation 5-13 and it was equal to 2.78 MN as in for soil group A. The value calculated by Equation 5-13 has a difference of -4.13% with the FE analysis for a structure located at the ground level. It must be reminded that as discussed by Gourvenec et al. (2008) the moments calculated by the FE analysis stand higher than the equations provided by Gottardi et al. (1993) and this was clear for

the un-piled footing structures embedded in to the soil for both groups. In addition, the values calculated through the equations provided by Gottardi et al. and Butterfield et al. might be higher for the embedded structures because in their tests, the footings were sitting at the ground level and none were embedded into the surrounding soil.

From the results of Figures 6-19 and 6-20, it is evident that for an un-piled footing structure with its footing located at the ground level the ultimate lateral capacity has not been significantly affected by the changes made to the soil properties. The difference between the ultimate lateral capacities of the un-piled footings for soil groups A and B with their footings at the ground level was +3.57%. This clearly illustrates that for un-piled footing structures located at the ground level the over turning capacity can provide a simple and accurate estimate for the maximum lateral capacity of such structures.

From the above discussions, it is clear that embedding an un-piled footing into the soil will increase the ultimate lateral capacity of the structure but embedding the piled footing structure does not make any changes to the ultimate lateral capacity. As the average horizontal displacement of the footing was not changed for the piled footing structures with different embedment depths for the two soil groups, it can be concluded that in the case of the piled footing structures, the pile prevents the horizontal movement of the footing. Therefore, embedding the footing will not change the ultimate lateral capacity of the hybrid structure.

It is obvious that by installing the footing at the ground level for the hybrid structure, the costs of installation will be reduced while a high stiffness and ultimate capacity can be sustained by the proposed structure.

6.5 LATERAL SOIL STRESSES AND DISPLACEMENTS

To investigate the lateral soil displacements along the pile's length for the monopile and the piled footing structures installed in both soil groups, nodes in the soil along the sidewall of the pile's shaft were selected in the direction of the applied displacement, which was acting on the tower's head at the ultimate capacity of each structure.

Figure 6-21 illustrates the results of the monopile and the hybrid structure embedded in soil group A. It is clear that the footing has significantly reduced the soil displacements along the sidewalls of the pile. The results of soil group B are illustrated in Figure 6-22.

From Figures 6-21 and 6-22, it is clear that as the soil becomes stiffer the lateral soil displacements for the monopile and the piled footing structures have reduced, but in both cases, the lateral soil displacements along the pile's shaft for the hybrid structures are smaller than of a monopile for both soil groups. In addition, the pivot point for the monopile in the dense sand was higher (closer to the ground surface) than that of loose sand while for the piled footing structure those points are even closer to the ground surface compared to a monopile structure. It is also clear that the pivot point for the piled footing structure in the dense sand is also higher than of loose sand.

As discussed in Section 2.9 the bearing pressure on the underside of the footing provides a surcharge on the soil in front of the wall, and this in turn increases the passive force and thus it reduces the total displacement.

The horizontal stresses in the soil along the sidewalls of the pile's shaft were plotted for the monopile structure for both soil groups at the ultimate lateral capacity. Figrues 6-23 and 6-24 illustrate the results.

From Figures 6-21 and 6-23 it is clear that the point of rotation of the monopile structure embedded in soil group A (worst-case scenario) was nowhere close to its toe, as discussed by Broms (1964) and so the monopile can be considered as a long pile.

Figures 6-25 and 6-26 illustrates the Von Mises stresses acting on the monopile and the hybrid structure at their ultimate lateral capacity embedded in soil group A respectively. From Figure 6-25, it is clear that for the monopile structure, the high stress zone starts from around 12 m above the ground level and it was continued up to around 8 m below the ground level. Moreover, for the piled footing structure embedded in soil group A, the high stress zone starts from around 14 m above the ground level and it is continued up to around 5 m below the ground level.

6.6 THE EFFECTS OF SOIL FRICTION ANGLE AND THE SOIL'S MODULUS OF ELASTICITY

In Chapter 5, it was illustrated that for the monopiles and the hybrid structures adopting a linear or a parabolic increase in the soil's modulus of elasticity would not significantly affect the lateral capacity of both structures.

At this point, for both soils groups (A & B), the soil's friction angle was altered and the lateral capacity of the structures were investigated. For soil group A only the friction angle was increased to 37° while for soil group B the friction angle was decreased to 30° (the stiffness of the soils were unchanged). The changes were made for both the monopiles and the piled footing structures. It must be remembered that as the friction angles varied, the Poisson's ratio was adjusted in respect to Equation 5-3 for each constructed model.

The results of the monopiles and the piled footing structures are illustrated in Figures 6-27 and 6-28 for soil groups A and B respectively. It is clear that changing the soil's friction angle does not significantly affect the ultimate lateral capacity and the stiffness of a monopile and the piled footing structure.

The ultimate lateral capacity of the monopile embedded in soil group A with a friction angle of 37° can be validated in respect to Broms solutions for long piles embedded in sands (Figure 2-34a). With considering the pile's material properties, the calculation will be as follows:

$$\frac{M_y}{D^4 K_p \gamma'} = \frac{250\times10^6\times0.25\times3.14\times(2.3^4-2.24^4)/2.3}{4.6^4\times4\times7\times10^3} = 19$$

e/D = 70/4.6 = 15.2

Therefore, $Q_{u\,(g)}$ or the ultimate lateral force will be equal to $K_P \times \gamma' \times D^3 \times 1.207$ and that is equal to $4 \times 7 \times 10^3 \times 4.6^3 \times 1.207 = 3.29$ MN. The FE model predicts a value of 4.1 MN. This confirms that the friction angle of the soil does not significantly contribute to an increase in the ultimate lateral capacity of a monopile embedded in a sand deposit.

Using the chart produced by Fleming et al. (1992), that is Figure 2-40(b) the ultimate lateral capacity of the monopile was calculated to be equal to 10.9 MN, which is significantly higher than the values calculated by Broms and the FE analysis. The difference between the result of the chart produced by Fleming et al. (1992) and the FE result is +165.85%.

The method adopted by Zhang et al. (2005) discussed in Section 2.6.5 was also used to calculate the ultimate lateral capacity of the monopile too. Using equations 2-79 and 2-80 with considering a value of 0.6ϕ for δ (Table 2-6) and a value of $1.5K_0$ (Table 2-5) for K the ultimate lateral capacity was calculated to be equal to 8.5 MN which has a difference of +107.31% with the FE result.

The above discussion illustrates that Broms charts are in a very close agreement with the FE results while the chart produced by Fleming et al. and the method adopted by Zhang et al. illustrate higher discrepancies with the FE results. It was also clear that the difference between the results becomes significant for sands with high friction angles.

The soil's Young modulus was also changed for both soil groups to illustrate its effect on the monopiles and the piled footing structures. The results are illustrated in Figures 6-29 and 6-30 for soil groups A & B respectively. From the figures, it is clear that the soil's modulus of elasticity does not seriously affect the results too. For the monopile cases in soil group A the maximum difference in the stiffness by increasing the soil modulus was +6.7% while for the piled footing cases that was +5.55%. For the monopiles embedded in soil group B the maximum difference in the stiffness by increasing the soil modulus was +9.0% while for the piled footing structures that was +7.7%. Moreover, for each structure the ultimate lateral capacities within each soil group were not changed as the soil's modulus of elasticity was altered.

From the above results, it can be concluded that the soil properties do not have a great influence on the behaviour of the pile/towers used as wind turbines embedded in sands. This point is related to the very high eccentricities in these structures. In addition, the ultimate capacities of the monopiles and the piled footing structures were both controlled by their structural capacity. If this is the case, changing the pile's thickness and diameter must have a great influence on the stiffness and the ultimate capacity of the pile/towers embedded in sands. These points will be further investigated in the upcoming sections.

6.7 THE EFFECTS OF PILE WALL THICKNESS

The pile wall thickness for the monopile and the piled footing structures were changed to investigate their effects on the stiffness and the ultimate lateral capacity of both structures. The pile thickness was changed from 60 mm to 30 mm and 85 mm for both the monopiles and the piled footing structures.

Figure 6-31 illustrates the results of changing the pile thickness for soil group A. As can be seen, changing the thickness affects the stiffness and the ultimate capacity of the monopiles. The ultimate lateral capacity of the monopiles with a thickness of 30 mm illustrated in Figure 6-31 can be validated in respect to Broms solutions for long piles embedded in sands (Figure 2-34a). The following calculation is for the ultimate lateral capacity of a monopile with a thickness of 30 mm embedded in soil group A by Broms (1964) chart.

$$\frac{M_y}{D^4 K_p \gamma'} = \frac{250\times10^6\times0.25\times3.14\times(2.3^4-2.27^4)/2.3}{4.6^4\times3\times7\times10^3} = 13$$

e/D = 70/4.6 = 15.2

Therefore, $Q_{u\,(g)}$ or the ultimate lateral load will be equal to $K_P \times \gamma' \times D^3 \times 1$ and that is equal to $3 \times 7 \times 10^3 \times 4.6^3 \times 1 = 2.04$ MN. The FE model predicts a value of 2.1 MN.

Using the charts produced by Fleming et al. (1992), Figure 2-40(b) the ultimate lateral capacity of the single pile/tower was calculated to be equal to 6 MN, which is higher than the values calculated by Broms chart and the FE results. It is interesting to note that by changing the pile's thickness the results obtained from the chart produced by Fleming et al. did not change, while the FE results and Broms results obtained from his chart changed accordingly (this was because of the very high eccentricity value of the structure).

The method adopted by Zhang et al. (2005) discussed in Section 2.6.5 was also used to calculate the ultimate lateral capacity of the monopile. Using Equations 2-79 and 2-80 with considering a value of 0.6ϕ for δ (Table 2-6) and a value of $1.5K_0$ (Table 2-5) for K the ultimate lateral capacity was calculated to be equal to 4.8 MN. This method also does not correspond accurately in regards to the changes made to the pile thickness similar to the charts produced by Fleming et al. (1992).

The difference between the results of Broms (1964), Fleming et al. (1992, their chart) and Zhang et al. (2005) with the FE predictions were -2.85%, +185.7% and +128.5% for a monopile with a thickness of 30 mm embedded in soil group A.

For a pile thickness of 85 mm, using Broms solutions for long piles embedded in sand deposit the ultimate lateral capacity was calculated to be equal to 4.53 MN for the monopile embedded in soil group A. The FE analysis predicts a value of 5.6 MN.

The chart produced by Fleming et al. (1992) and the method adopted by Zhang et al. (2005) provide a value of 6 MN and 4.8 MN respectively for the ultimate lateral capacity of the monopile embedded in soil group A. As previously mentioned, in these methods the thickness of the pile was not affecting the results, which is indeed a drawback to these methods.

From the above results and graphs, it is clear that the ultimate lateral capacity and the stiffness of a monopile were significantly influenced by the thickness of the pile structure (this was clear from the FE and Broms calculations).

From the FE results for the changes made to the monopile thickness in soil group A it was clear that, at a displacement of $0.2D_p$ the difference between the stiffness of a monopile with a

thickness of 60 mm and 85 mm was +33.8% while this difference was +36.58% for their ultimate capacity.

For soil group B the results of changing the monopile thickness is illustrated in Figure 6-32. The results of the pile/tower with a thickness of 85 mm can be checked in respect to Broms chart for long piles embedded in sands, the calculation is as follows:

$$\frac{M_y}{D^4 K_p \gamma'} = \frac{250\times10^6\times0.25\times3.14\times(2.3^4-2.215^4)/2.3}{4.6^4\times4\times7\times10^3} = 26.6$$

e/D = 70/4.6 = 15.2

Therefore, $Q_{u\,(g)}$ or the ultimate lateral force will be equal to $K_P \times \gamma' \times D^3 \times 1.67$ and that is equal to $4 \times 7 \times 10^3 \times 4.6^3 \times 1.67 = 4.56$ MN. The FE model predicts a value of 5.6 MN.

The chart produced by Fleming et al. (1992) provides a value of 10.9 MN for the ultimate lateral capacity of the structure while Zhang et al. (2005) provides a value of 8.5 MN. The difference between the solutions provided by Broms, Fleming et al. (their chart) and Zhang et al with the FE results for soil group B with a pile thickness of 85 mm were equal to -18.57%, +94.64% and +51.78%. This again illustrates that Broms chart are in a closer agreement with the FE predictions and are conservative.

For a monopile thickness of 30 mm embedded in soil group B the difference between the solutions provided by Broms (1964), Fleming et al. (1992) and Zhang et al. (2005) with the FE result were -19.52%, +419.0% and +304.76% respectively. This clearly illustrates that for monopiles used as wind turbines the ultimate lateral capacity of the structure is significantly overestimated by Fleming et al. (1992) chart and the method adopted by Zhang et al. (2005) for stiff sand mediums.

To investigate the effects of the pile thickness for the piled footing structures, the pile thickness was changed from 60 mm to 30 mm and 85 mm for the hybrid structure, similar to the monopile cases. The results are illustrated in Figure 6-33 for soil group A. The piled footing results for soil group B are also illustrated in Figure 6-34. From the latest figures, it is clear that the soil properties are insignificant in affecting the ultimate lateral capacity of the hybrid structures while the thickness of the piles significantly affect the results.

Form Figures 6-33 and 6-34 it is clear that the difference between the ultimate lateral capacities of a piled footing structure with a thickness of 60 mm and 85 mm was +38.7% for both soil groups.

Figure 6-35 illustrates the lateral displacement versus lateral force for a monopile and a piled footing structure with a pile thickness of 30 mm embedded in soil group A. Figure 6-36 illustrates the results of a monopile and a piled footing structure with a pile thickness of 85 mm embedded in soil group A. For a pile thickness of 85 mm embedded in soil group A at a displacement of $0.2D_p$, the difference in the stiffness between the monopile and the piled footing structure was +41.5%.

As previously discussed, the soil behaviour does not have a significant role in changing the stiffness or the ultimate lateral capacity of the monopiles and the piled footing structures. For the case of illustration, the results of the monopile and the piled footing structures with different thicknesses for soil group B are illustrated in Figures 6-37 and 6-38.

6.8 THE EFFECTS OF PILE DIAMETER

In practice, it is customary to increase the pile diameter if an increase in the stiffness and the ultimate lateral capacity of a monopile is required. In this section, the monopile's diameter has been varied to investigate its effects on the stiffness and the ultimate lateral capacity of monopiles and the piled footing structures embedded in both soil groups.

To study the effects of the monopile diameter, the thickness of the monopile was maintained while the pile diameter was changed to 3 m and 6 m. All other dimensions and material properties were kept constant (L_{pile} = 30 m, pile thickness = 60 mm and eccentricity = 70 m). To date, the largest pile diameter used for an offshore wind turbine is around 6 m and that is why the maximum pile diameter was chosen as 6 m in this section.

Figure 6-39 illustrates the results of changing the pile diameter for the monopiles embedded in soil group A. As expected, the stiffness and the ultimate lateral capacity of the monopiles were influenced by the changes made to the pile diameter. Similar to the changes made to the pile thickness the ultimate lateral capacities in Figure 6-39 can be checked in respect to Broms (1964) solution for long piles embedded in sands (Figure 2-34a).

For a pile diameter equal to 3 m embedded in soil group A, the lateral capacity using Broms (1964) chart for long piles was calculated as follows:

$$\frac{M_y}{D^4 K_p \gamma'} = \frac{250\times10^6\times0.25\times3.14\times(1.5^4-1.44^4)/1.5}{3^4\times3\times7\times10^3} = 58.6$$

e/D = 70/3 = 23

Therefore, $Q_{u\,(g)}$ or the ultimate lateral force will be equal to $K_P \times \gamma' \times D^3 \times 2.41$ and that is equal to $3 \times 7 \times 10^3 \times 3^3 \times 2.41$ = 1.37 MN. The FE model predicts a value of 1.68 MN.

Fleming et al. (1992) chart for long piles provides a value equal to 1.7 MN, while the method adopted by Zhang et al. (2005) provides a value equal to 3.1 MN with considering a value of 0.6ϕ for δ (Table 2-6) and a value of $1.5K_0$ (Table 2-5) for K.

For the monopile with a diameter of 6m embedded in soil group A, the calculation is as follows:

$$\frac{M_y}{D^4 K_p \gamma'} = \frac{250\times10^6\times0.25\times3.14\times(3^4-2.94^4)/3}{6^4\times3\times7\times10^3} = 15$$

e/D = 70/6 = 11.6

Therefore, $Q_{u\,(g)}$ or the ultimate lateral force will be equal to $K_P \times \gamma' \times D^3 \times 1.23$ and that is equal to $3 \times 7 \times 10^3 \times 6^3 \times 1.23$ = 5.59 MN. The FE model predicts a value of 7.3 MN.

Fleming et al. (1992) chart provides a value of 13.6 MN while Zhang et al. (2005) method provides a value equal to 6.2 MN with considering a value of 0.6ϕ for δ (Table 2-6) and a value of $1.5K_0$ (Table 2-5) for K.

From Figure 6-39 it is clear that at a displacement of $0.1D_p$, the difference between the lateral capacity of a monopile with a diameter of 6 m and 4.6 m was +85% and at $0.2D_p$, that value was +100%. On the other hand, when the pile diameter was reduced from 4.6 m to 3 m at a displacement of 0.1D the difference in the lateral capacity was equal to +200% while at 0.2D that value was +210.3%. This clearly illustrates that by increasing the pile diameter the lateral capacity of the structure significantly increases but as discussed in Chapter 2, there are limitations to the size of the monopiles as transporting them and hammering them into their required position will be very expensive.

The results of changing the pile diameter for the monopiles embedded in soil group B are illustrated in Figure 6-40. As expected the ultimate lateral capacity was not influenced by the soil properties in FE predictions (that is comparing Figures 6-39 and 6-40).

Broms (1964) chart for long piles embedded in sand (group B) provides a lateral capacity equal to 1.38 MN and 5.62 MN for a pile diameter of 3 m and 6m respectively. The FE results for pile diameters equal to 3 m and 6 m for soil group B were 1.68 MN and 7.3 MN respectively.

Fleming et al. (1992) chart provides an ultimate lateral capacity equal to 3 MN for a pile diameter of 3 m embedded in soil group B while for a pile diameter equal to 6 m the ultimate capacity was equal to 24 MN, which is completely out of line compared to the results obtained from the FE analysis and Broms solution.

Zhang et al. (2005) method predicted the ultimate lateral capacity of a monopile embedded in soil group B as 5.5 MN and 11 MN for the monopile's with diameters equal to 3 m and 6 m respectively (with considering a value of 0.6ϕ for δ (Table 2-6) and a value of $1.5K_0$ (Table 2-5) for K).

From the above discussion, it is clear that the discrepancies between the FE results and the predicted values by Fleming et al. (1992) (their chart) and Zhang et al. (2005) increases as the soil becomes stiff. For example in soil group A, the difference between the FE results and the results obtained by Fleming et al. (1992) chart for a pile diameter of 3 m and 6 m were +1.19% and +86.3% respectively, while for soil group B the difference was equal to +78.5% and +228.76% for a pile diameter of 3 m and 6 m respectively. In Section 6.9, this point will be further discussed.

The results of the piled footing structures with different pile diameters embedded in soil group A are illustrated in Figure 6-41. From this figure, it is clear that at a displacement of $0.1D_p$ the difference in the lateral capacity between a piled footing structure with a pile diameter of 6m and 4.6 m was +95% while at a displacement of $0.2D_p$ that value was +100%. This result clearly illustrates the importance of the pile diameter used for piled footing structures but as previously mentioned; there are limitations to the size of a pile and this is clearly due to the costs of transportation and hammering the pile to its required location.

Figures 6-42 and 6-43 compares the results of a monopile with a piled footing structure for pile diameters equal to 3 m and 6 m respectively installed in soil group A. It is clear that the bearing plate has had an influence on both the stiffness and the ultimate lateral capacity of the structure.

As in other cases, the soil properties did not significantly increase the stiffness or the ultimate capacity of the piled footing structures. The results of the piled footing structures for soil group B are illustrated in Figure 6-44. Figures 6-45 and 6-46 compares the results of the piled footing structures with the monopiles embedded in soil group B.

At a displacement of $0.2D_p$, the difference in stiffness of a monopile and a piled footing structure for soil group B were +38.3%, +40.2% and +40.19% for pile diameters of 3 m, 4.6 m and 6 m respectively. It is interesting to note that although a pile diameter of 4.6 m was used to find a suitable footing dimension in Section 6.3, the differences were not significantly affected when the monopile diameter was changed to 3m and 6m from its original value.

6.9 THE EFFECTS OF ECCENTRICITY

As offshore wind structures have high eccentricities, to investigate the effects of the eccentricity on the stiffness and the ultimate lateral capacity of the monopiles and the hybrid structures, two pile eccentricities were examined, 70 m and 100 m while the pile diameter and the thickness were kept constant (D_p = 4.6 m, pile thickness = 60 mm and L_{pile} = 30 m). The mechanical properties of the pile/towers were as in Table 6-1.

The finite element results of the monopiles and the hybrid structures embedded in soil groups A & B are illustrated in Figures 6-47 and 6-48 respectively. It is expected that as the eccentricity increased the ultimate lateral capacity and the stiffness of the structures both decreased.

The finite element results obtained for the monopiles embedded in both soil groups can be validated with respect to the methods adopted by Broms (1964), Fleming et al. (1992) and Zhang et al. (2005).

For the monopile with an eccentricity value of 100 m embedded in soil group A, Broms chart predicts a value equal to 2.33 MN while the chart produced by Fleming et al (1992) and the method adopted by Zhang et al. (2005) provide a value of 6 MN and 3.57 MN respectively. The FE analysis provided a value of 2.8 MN. It is interesting that similar to the changes made to the pile thickness (Section 6.7) the chart produced by Fleming et al. did not correspond to the changes made to the eccentricity and that was the case for both soil groups. This is a serious drawback of the produced chart by Fleming et al (2009) as offshore wind turbines have very high eccentricities and these charts can significantly overestimate the ultimate lateral capacity of such structures.

For the monopile with an eccentricity value of 100 m embedded in soil group B, the FE analysis calculated the ultimate lateral capacity of the monopile to be equal to 2.8 MN. The methods adopted by Broms (1964), Fleming et al. (1992, their chart) and Zhang et al. (2005) provided values of 2.34 MN, 10.9 MN and 6.3 MN respectively.

From the above discussion, it is clear that if a stiff soil is considered for a monopile used as a wind turbine, the accuracy of the produced chart by Fleming et al. (1992) and the method adopted by Zhang et al. (2005) will significantly decrease. For example for a eccentricity value of 100 m embedded in soil group A the difference between the FE results and the values calculated by Broms, Fleming et al. (using their charts) and Zhang et al. are -16.78%, +114.28% and +27.5% respectively. For the same monopile embedded in soil group B the differences between the FE result and the calculated values by Broms (1964), Fleming et al. (1992) and Zhang et al (2005) are -16.42%, +289.28% and +125.0% respectively. This clearly illustrates that the chart provided by Fleming et al. (1992) and the method adopted by Zhang et al. (2005) can significantly overestimate the ultimate lateral capacity of wind turbines embedded in a dense sand, while the chart provided by Broms (1964) is well suited for such structures in both loose and dense sand deposits.

From Figures 6-47 and Figure 6-48, it was also clear that as the eccentricity value increased for each structure (monopiles and the piled footings) the difference between the stiffness obtained for each soil group A & B decreased. For example, for the monopiles with an eccentricity of 70 m and 100 m the difference in the stiffness at a displacement of $0.2D_p$ between the two soil groups (that is groups A & B) for each eccentricity value was +9.34% and +5.8% respectively. This clearly illustrates that as the eccentricity increases the effects of the soil parameters decreases too. This was also the case for the piled footing structures embedded in soil groups A & B. For the piled footing structures with an eccentricity of 70 m and 100 m the difference in the stiffness at a displacement of $0.2D_p$ between the two soil groups for each piled footing structure was +9.26% and +5.5% respectively.

6.10 THE EFFECTS OF PILE LENGTH

To investigate the effects of the pile length for the monopile and the hybrid structures, the pile diameter and the eccentricity were kept constant (D_p = 4.6 m, eccentricity = 70 m and pile thickness = 60 mm) while the pile length was changed for both soil groups.

For the monopile structures, embedded in both soil groups the pile lengths were changed to 60 m and 5 m to investigate the pile's length influence on the stiffness and the ultimate lateral capacities. Figures 6-49 and 6-50 illustrate the results obtained for the monopiles embedded in soil groups A & B respectively. As discussed by Broms (1964) it is clear that by doubling the pile's length from 30 m to 60 m the ultimate lateral capacity of the monopiles in both soil groups have not been affected. In fact, the results of the monopiles with a pile length of 30 m and 60 m for each soil group are identical. On the other hand, the ultimate capacities of the short piles (5 m) have significantly decreased in respect to the monopiles with lengths of 30 m and 60 m.

Following the discussion in Section 6.5 and the results obtained from Figures 6-49 and 6-50 it is clear that the monopiles in both soil groups with a length of 30 m are behaving as long piles. This point was also evident in all above investigated cases as the maximum moment (M_{max}) acting on the piles were higher than the yield moment of the pile section (M_{yield}) and this clearly demonstrated that the piles must be considered as long piles for Broms analysis. It is interesting

to note that the method adopted by Zhang et al. (2005) was sensitive towards changes made to the pile's length. Zhang's method predicts an ultimate capacity of 8.5 MN and 56.5 MN for the piles embedded in soil group B with a length of 30 m and 60 m respectively. The value obtained by Zhang's method for a pile length of 60 m embedded in soil group B was significantly over estimated the ultimate lateral capacity of the monopile structure, as they have considered the pile's length in their equation (the soil failure was considered in their calculations and not the pile failure).

It was discussed that the initial stiffness of the hybrid structure was controlled by the footing and not by the pile structure and that was discussed in Chapter 5. This indicates that if a hybrid structure is adopted in practice a shorter pile with an appropriate footing size must provide a higher stiffness compared to a monopile structure. To further investigate the stiffness and the ultimate lateral capacity of the hybrid structures, the pile's length was varied to 5 m and 15 m from their original value of 30 m for both soil groups.

Figures 6-51 and 6-52 illustrate the results of the piled footing structures for soil groups A and B respectively. In Figures 6-51 and 6-52, the results of the monopiles with a length of 30 m have been considered too. It is clear that the ultimate lateral capacity and the stiffness of the piled footing structures in both soil groups have not changed as the pile length was halved. In addition, it is evident that for both soil groups the stiffness of the short piled footing structures (length = 5 m) is higher than of a 30 m monopile.

It is apparent that by decreasing the pile's length for the hybrid structure the high costs of pile driving for offshore environments can be significantly reduced while a high stiffness and ultimate capacity can still be sustained by the aid of the proposed hybrid structure.

6.11 REMARKS AND CONCLUSION

Based on the results obtained in this investigation, the following conclusions can be made in respect to the behaviour of the monopiles and the hybrid structures.

It was demonstrated that a footing with a radius and thickness of 10 m and 2.99 m respectively was capable of increasing the stiffness of a monopile in excess of 40% for a soft and stiff soil deposit. Although the footing dimensions were adjusted for a certain pile structure (D_p = 4.6 m) it was clear that changing the pile dimensions did not seriously affect the difference between the stiffness of a monopile and a piled footing structure at a tower displacement of $0.2D_{pile}$.

It was clear that the initial behaviour of the nominated hybrid structure was controlled by the footing and not by the pile structure. It was also demonstrated that the initial behaviour of the piled footing structure was higher than of a monopile from the very initial point and this was also the case for the un-piled footing structures installed in a soft and stiff soil medium with the same footing dimensions used for the hybrid structure.

For the hybrid structure, it was evident that embedding the footing to a depth of 1 m below the ground surface would not increase the stiffness or the ultimate capacity of the proposed structure. This was because the pile structure prevented the lateral displacement of the footing and so the

soil surrounding the footing would not make any contribution to the stiffness or the ultimate capacity of the hybrid structure. On the other hand, the ultimate capacities of the un-piled footings were increased by +17.8% and +20.68% when the footings were embedded to a depth of 1m below the ground surface for a loose and dense sand respectively.

For the nominated hybrid structure (footing thickness = 2.99 m and footing radius = 10 m), the installed footing at the ground level significantly reduced the soil displacements along the pile's shaft at the ultimate capacity for a dense and loose sand compared to a monopile structure.

It was evident that the ultimate lateral capacity of the monopiles and the hybrid structures with high eccentricities were controlled by their structural capacity. The ultimate lateral capacity of the monopiles and the hybrid structures were not sensitive towards changes made to the soil parameters while their stiffness slightly increased as the soil became stiffer. The increase in the stiffness for the monopile and the nominated hybrid structure embedded in two different soil types was less than +15% for changes made to the soil parameters (friction angle and modulus of elasticity).

The difference in the stiffness of a monopile in two different soils at a displacement of $0.2D_{pile}$ rose as the pile thickness and diameter were individually increased. The increase in the stiffness for the monopile structures at a displacement of $0.2D_{pile}$ in two different soils was less than +15% for changes made to the pile thickness and diameter.

It was apparent that as the eccentricity value increased, the difference between the stiffness at $0.2D_{pile}$ for each individual structure embedded in the soft and stiff sand deposit decreased. This clearly demonstrated that as the eccentricity value increases the significance of the soil parameters decrease.

The method and chart produced by Broms (1964) was well suited for calculating the ultimate lateral capacity of monopiles with high eccentricities. It was illustrated that for wind turbines, which have high ratios of eccentricity to pile diameter the chart provided by Fleming et al. (1992) and the method adopted by Zhang et al. (2005) can significantly over estimate the ultimate lateral capacity of a monopile structure embedded in dense sand. The discrepancy between the adopted methods and the FE results could be up to +419% for a monopile embedded in dense sand. It was also demonstrated that the stiffness and the ultimate lateral capacity of a long pile embedded in a sand deposit was not affected when the pile's length was increased.

As the footing controlled the initial stiffness of the hybrid structure, it was evident that by adopting this structure in practice it is possible to reduce the pile's length and still sustain a high stiffness and ultimate capacity for the hybrid structure. This could significantly decrease the costs of pile driving in an offshore environment.

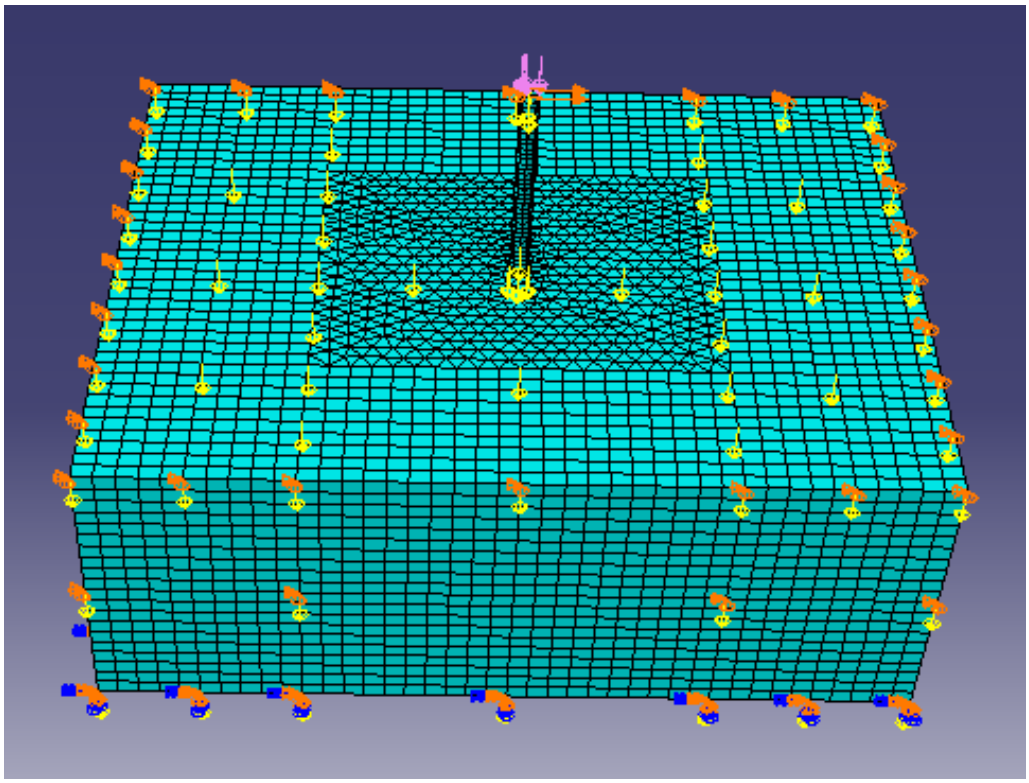

Figure 6-1. The numerical model constructed for the monopile foundation

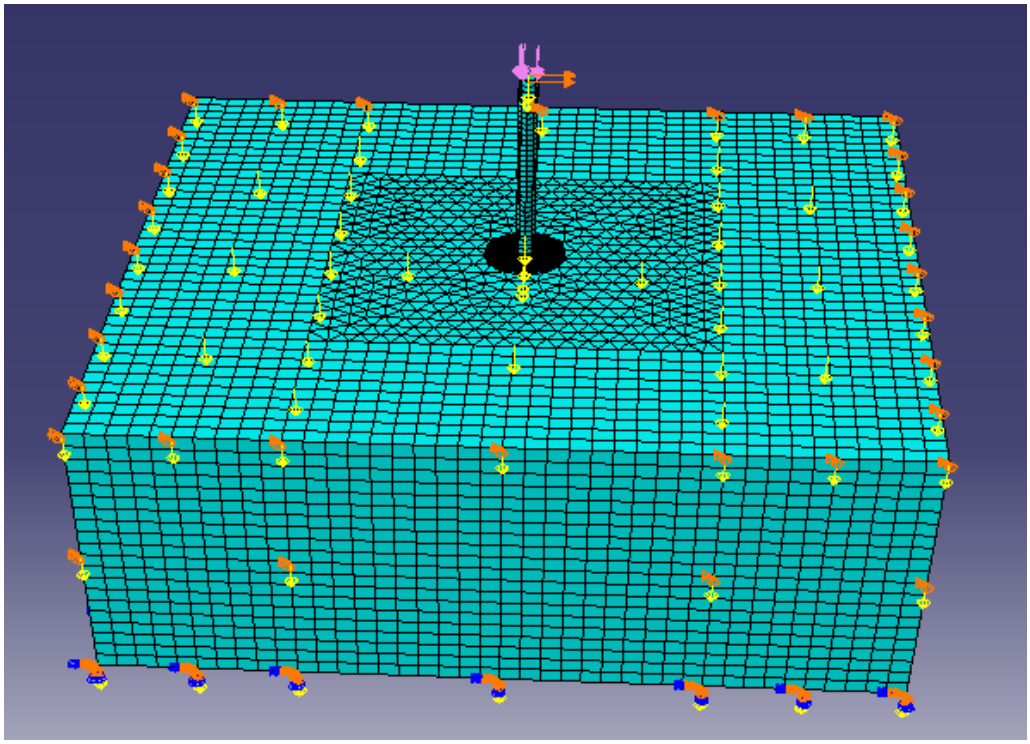

Figure 6-2. The numerical model constructed for the piled footing foundation

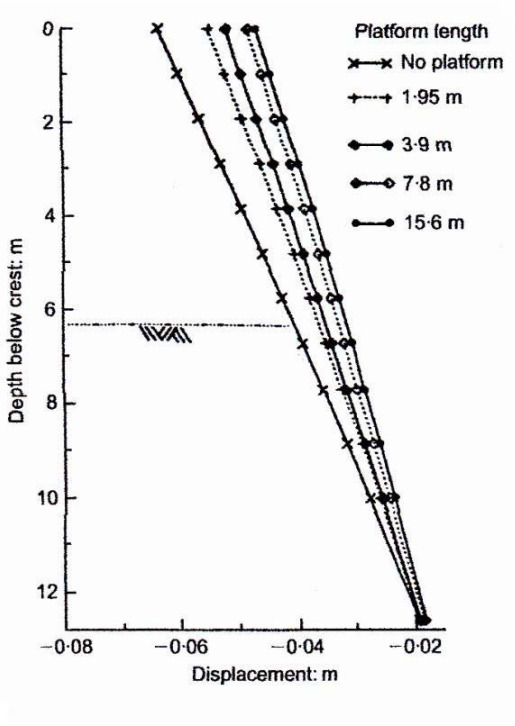

Figure 6-3. Displacement profile for a 7.06 m wall with different platform lengths (after Powrie and Chandler 1998)

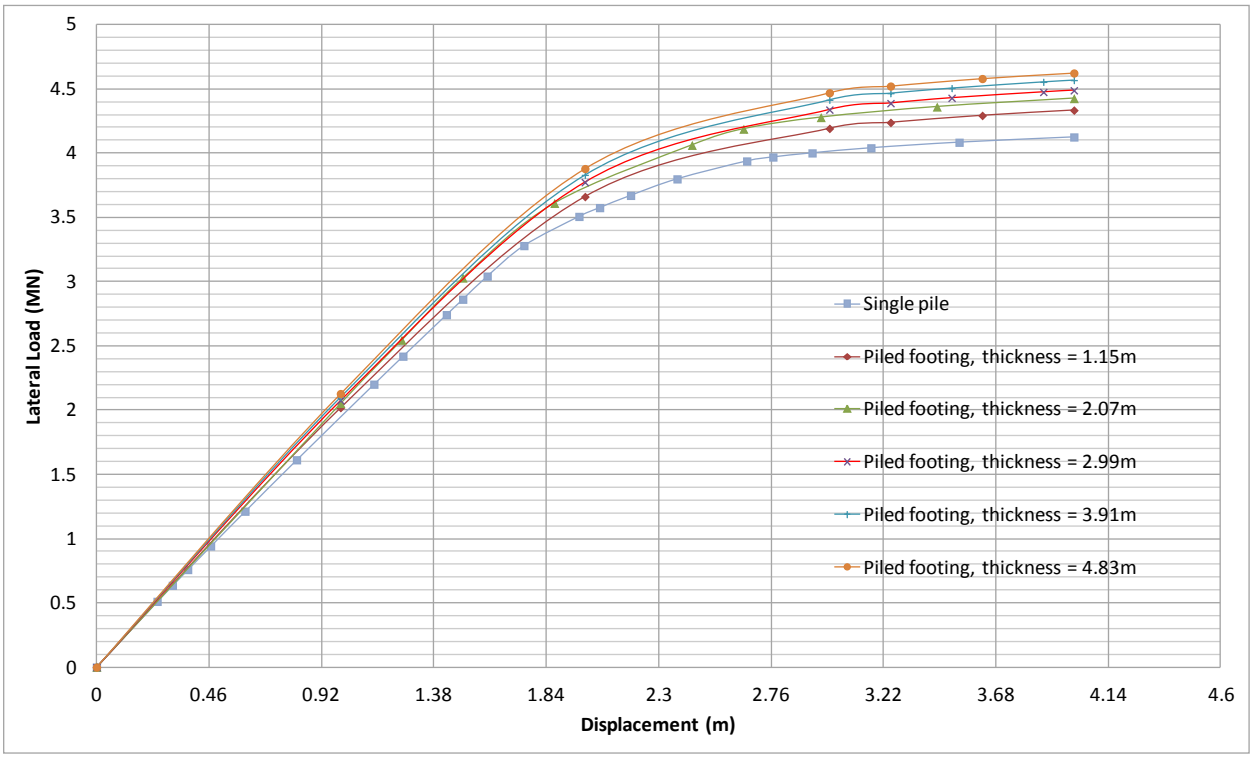

Figure 6-4. The lateral load versus lateral displacement graph for structures embedded in soil group A (changes in the footing thickness for a constant radius equal to 2.53 m for all piled footings)

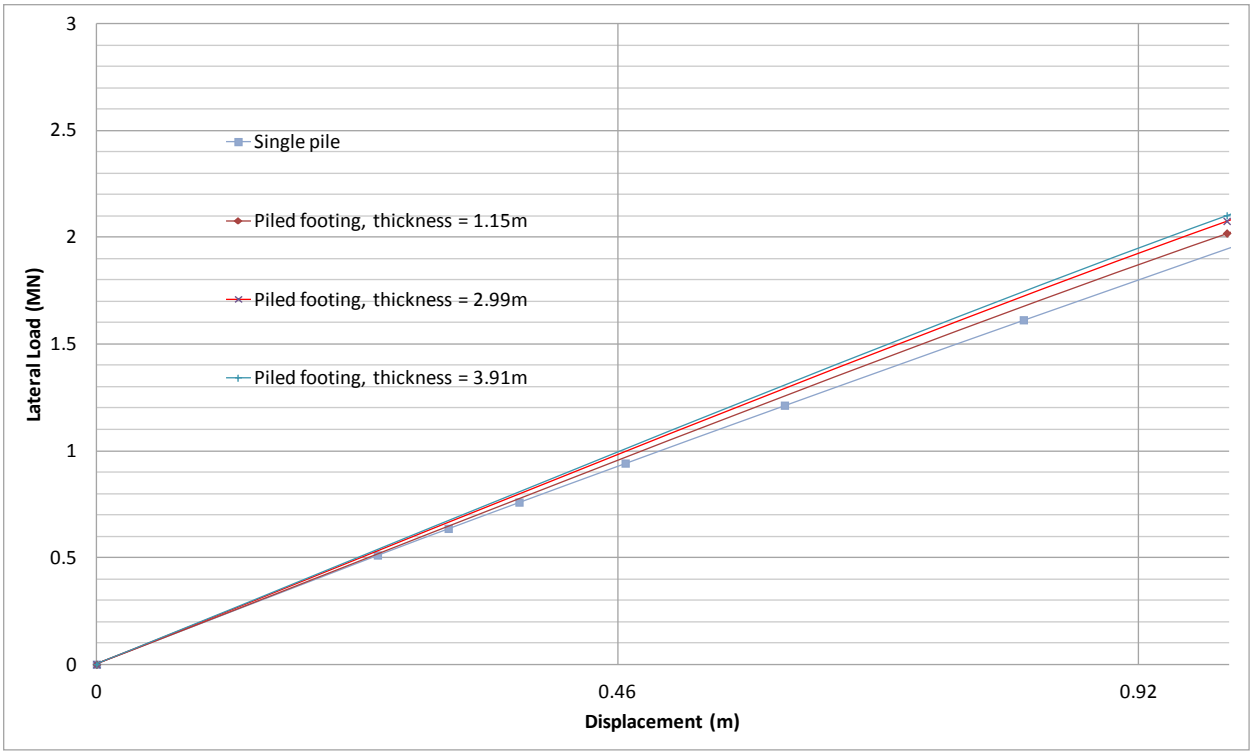

Figure 6-5. The lateral load versus lateral displacement graph for soil group A (up to a displacement of $0.2D_{pile}$)

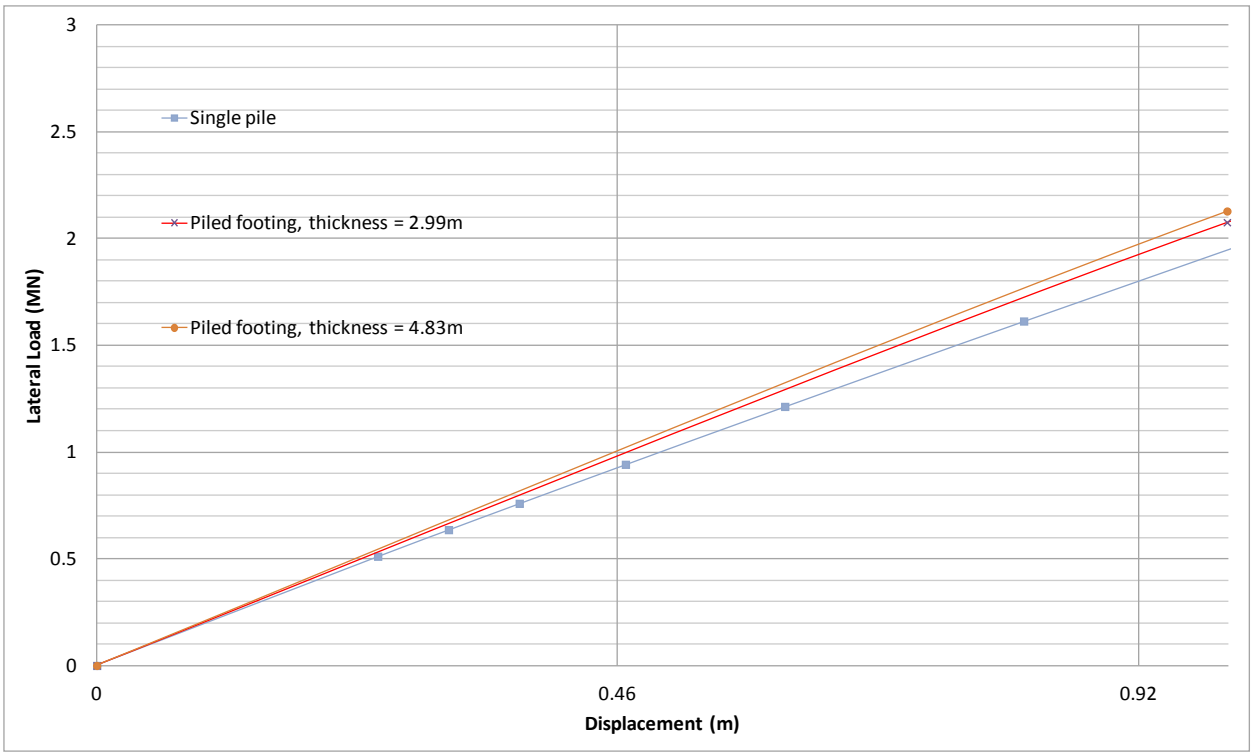

Figure 6-6. The lateral load versus lateral displacement graph for soil group A (up to a displacement of $0.2D_{pile}$)

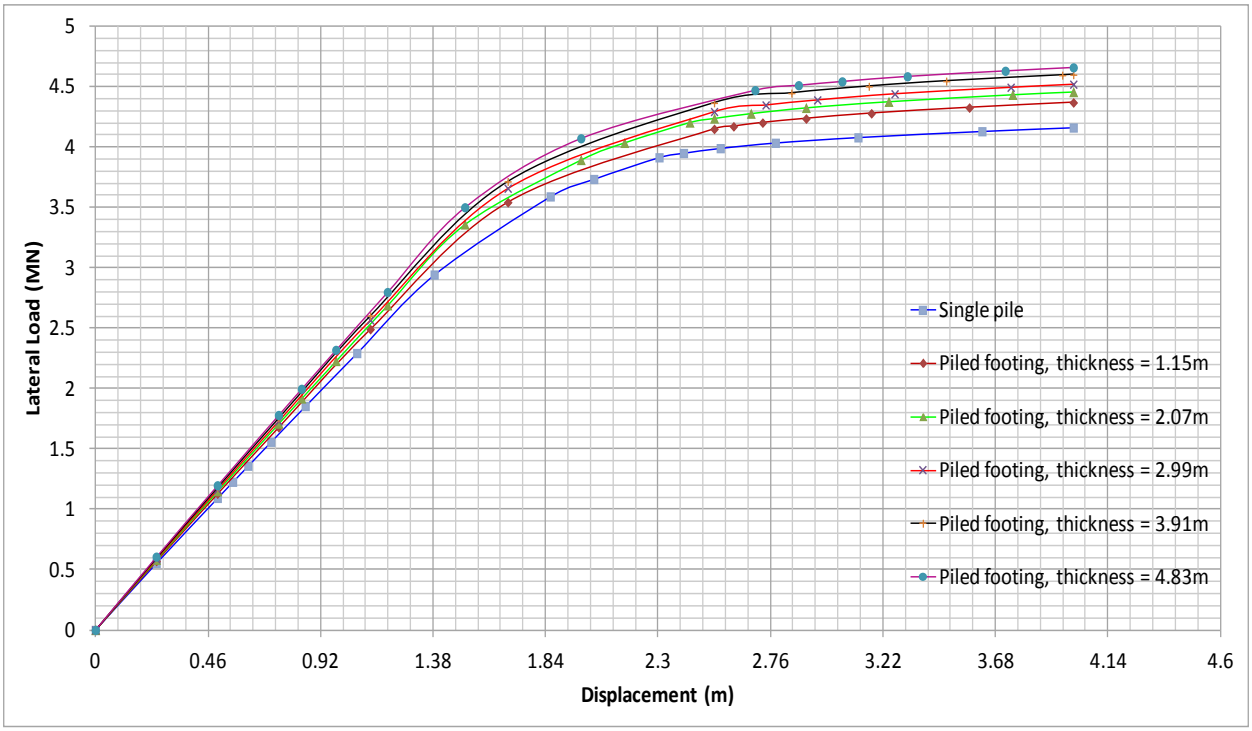

Figure 6-7. The lateral load versus lateral displacement graphs for structures embedded in soil group B (changes in the footing thickness for a constant radius equal to 2.53 m for all piled footings)

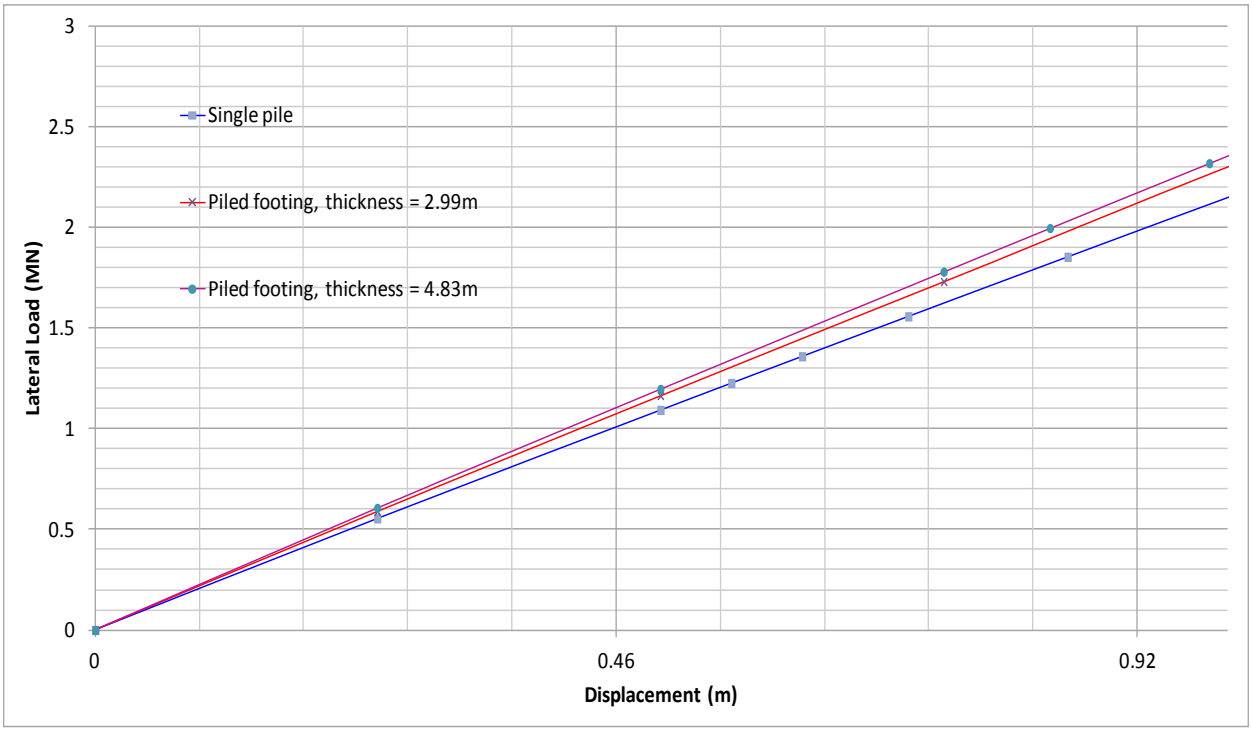

Figure 6-8. The lateral load versus lateral displacement graph for soil group B (up to a lateral displacement of $0.2D_{pile}$)

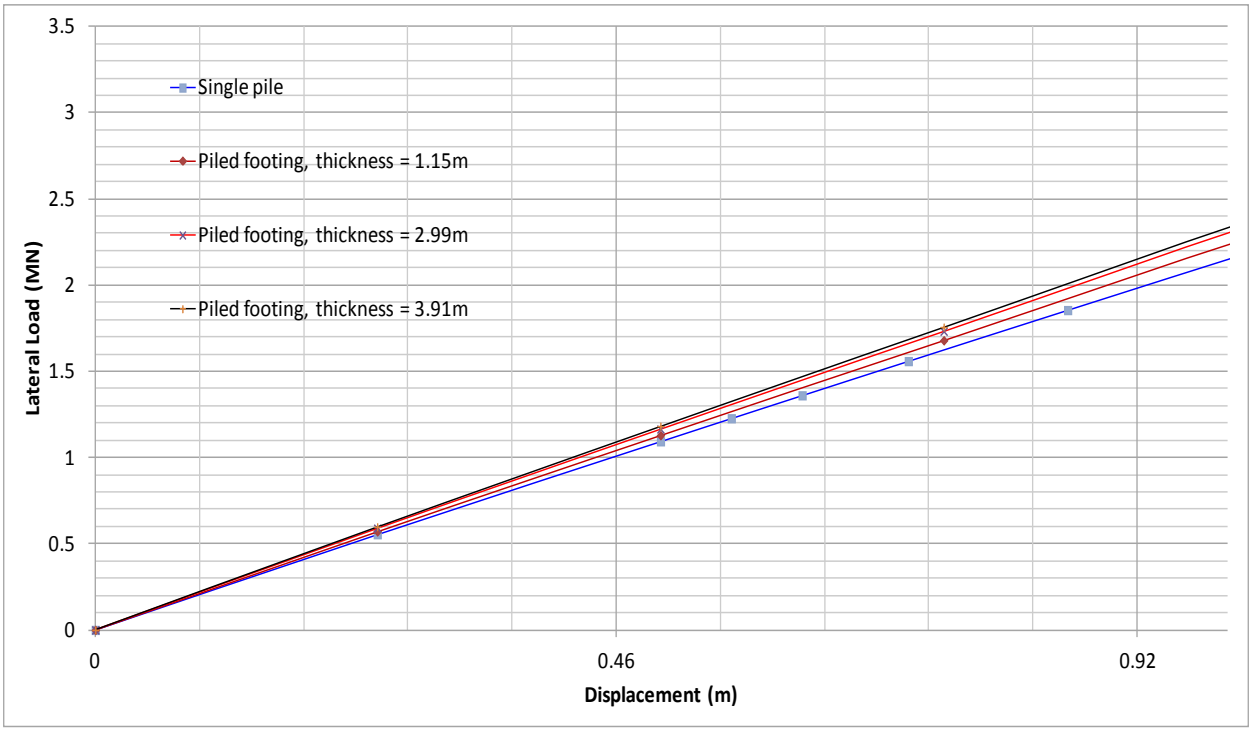

Figure 6-9. The lateral load versus lateral displacement graph for soil group B (up to a lateral displacement of $0.2D_{pile}$)

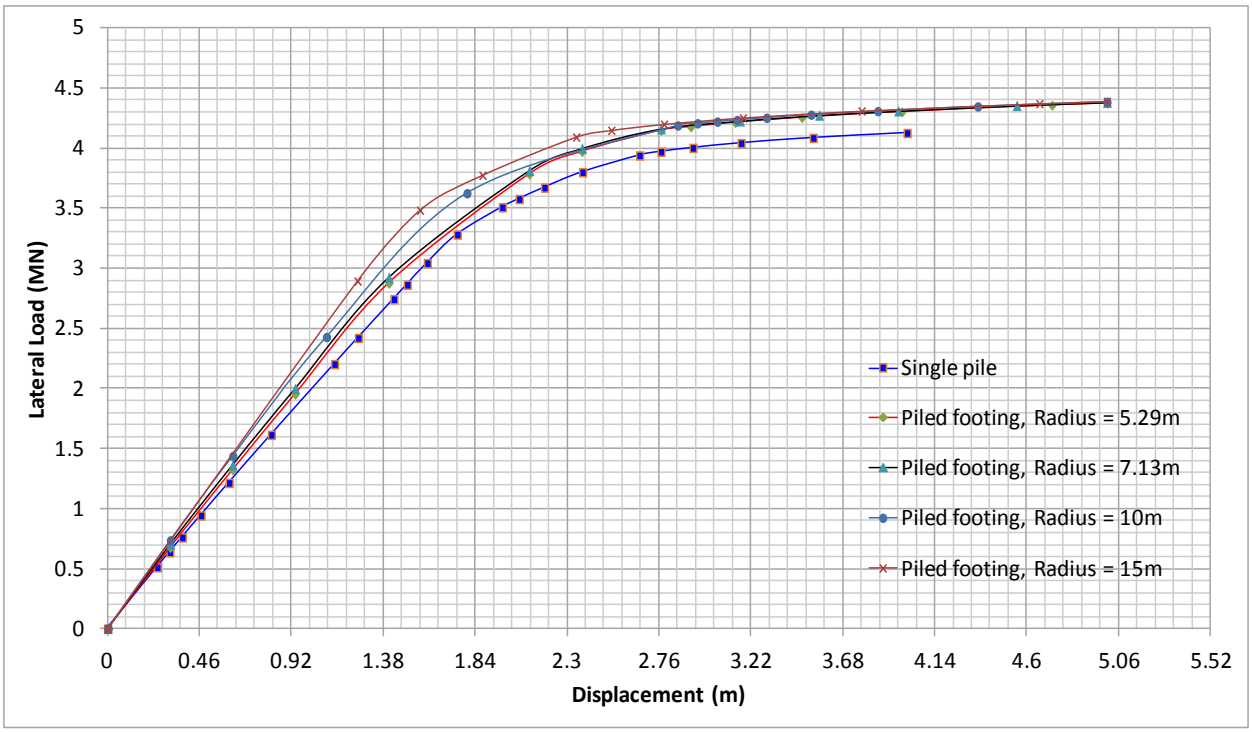

Figure 6-10. The lateral load versus lateral displacement graphs for structures embedded in soil group A (changes in the footing radius with a constant thickness)

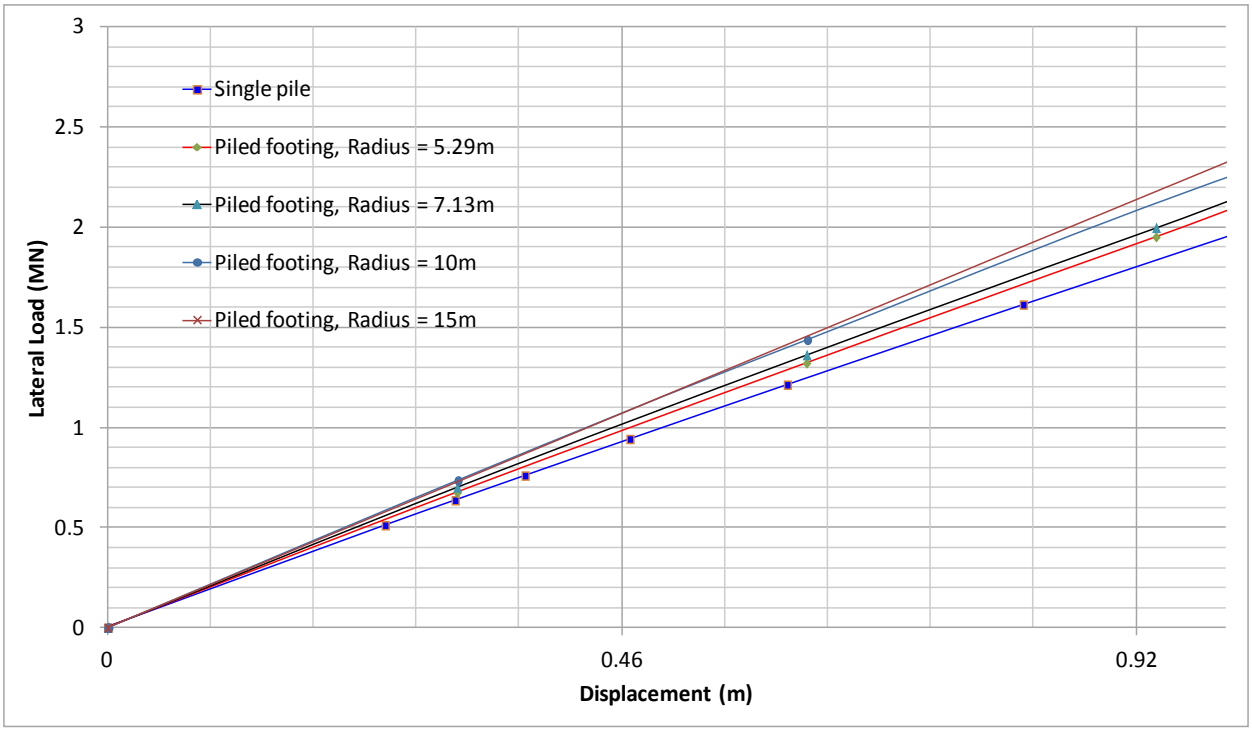

Figure 6-11. The lateral load versus lateral displacement graphs for structures in soil group A (up to a lateral displacement of $0.2D_{pile}$)

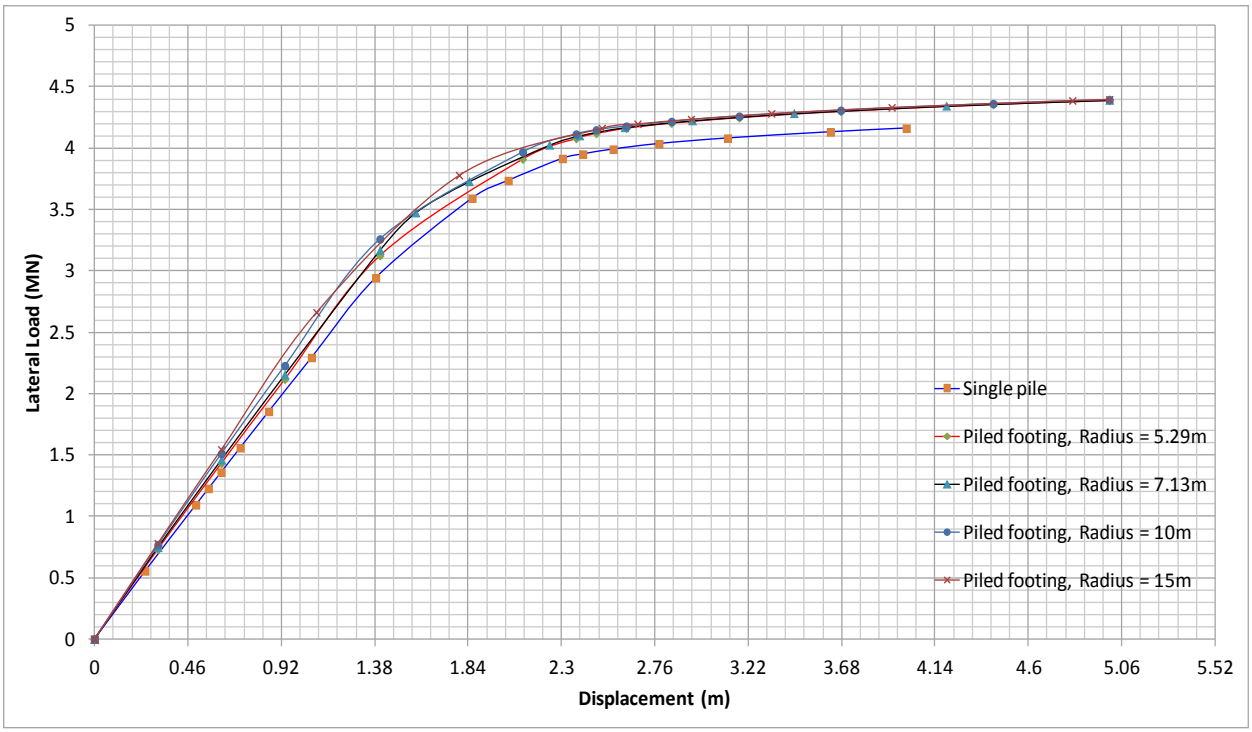

Figure 6-12. The lateral load versus lateral displacement graph for soil group B (change in footing radius with a constant thickness)

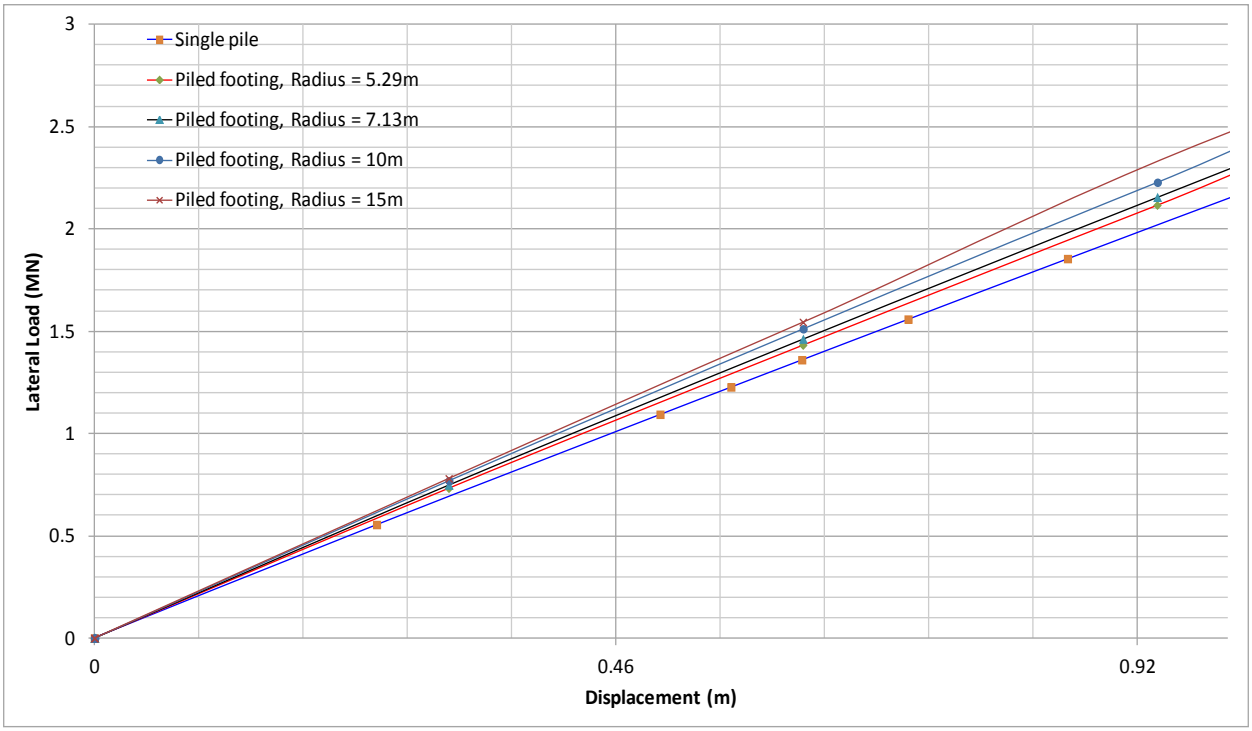

Figure 6-13. The lateral load versus lateral displacement graph for soil group B (up to a displacement of $0.2D_{pile}$)

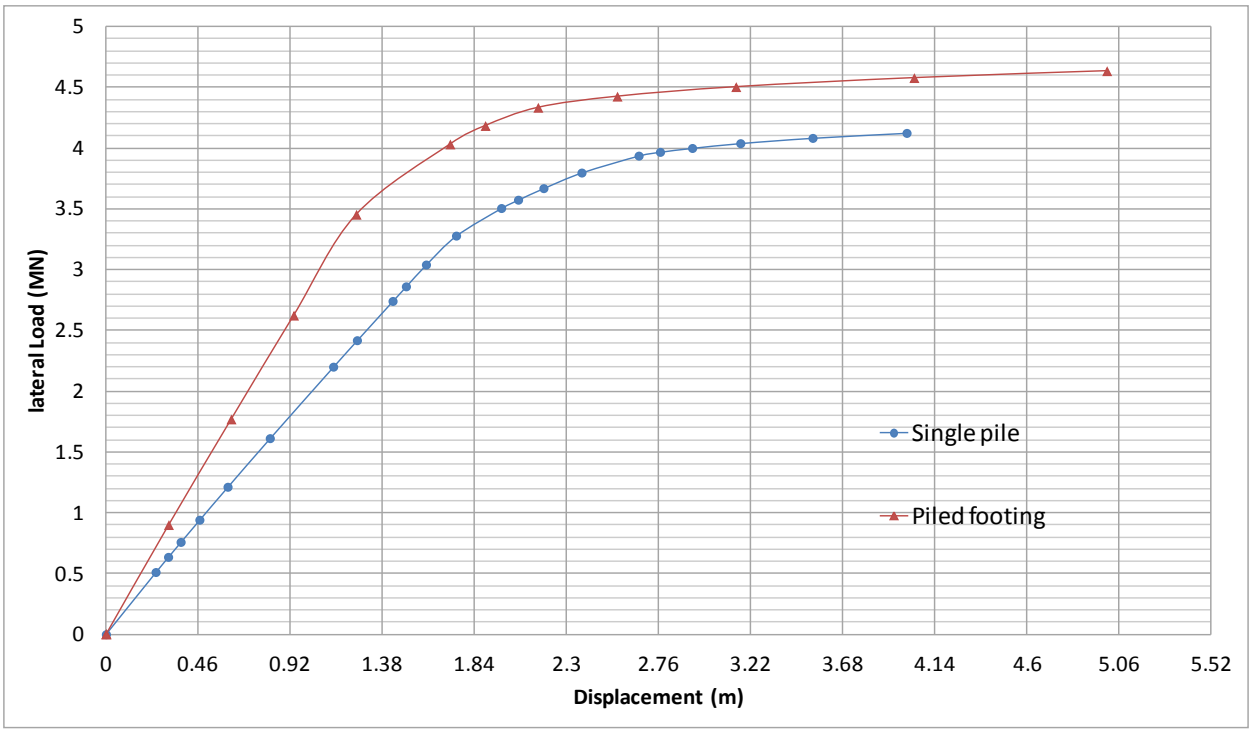

Figure 6-14. Comparing the lateral capacity of a monopile with a piled footing structure (soil group A)

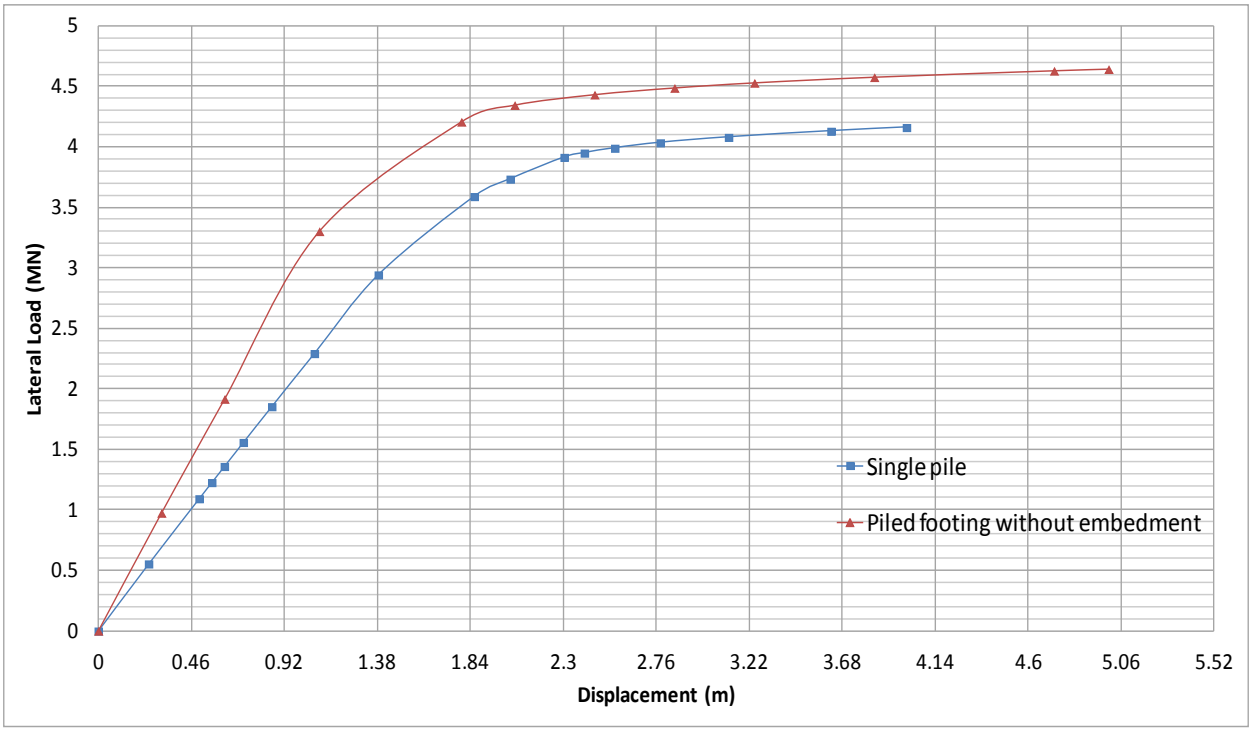

Figure 6-15. Comparing the lateral capacity of a monopile with a piled footing structure (soil group B)

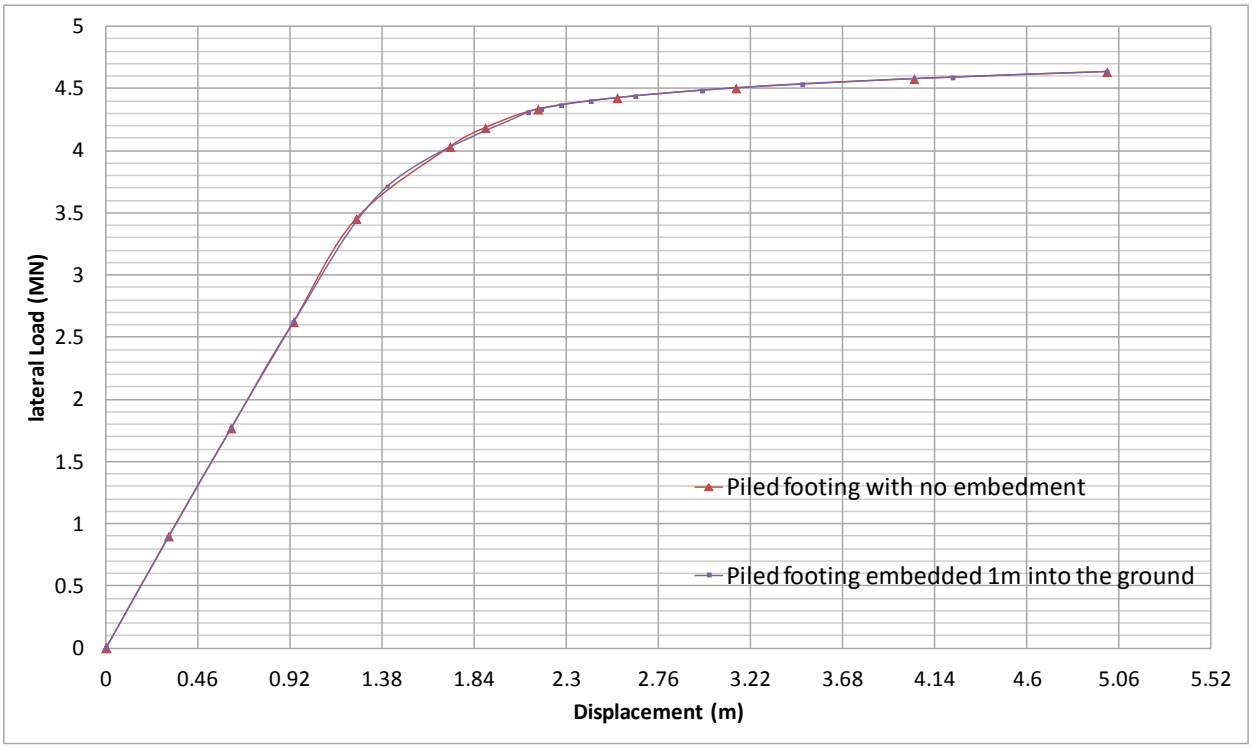

Figure 6-16. Comparing the lateral capacity of piled footings with their footings at the ground level and embedded 1 m below the ground surface (soil group A)

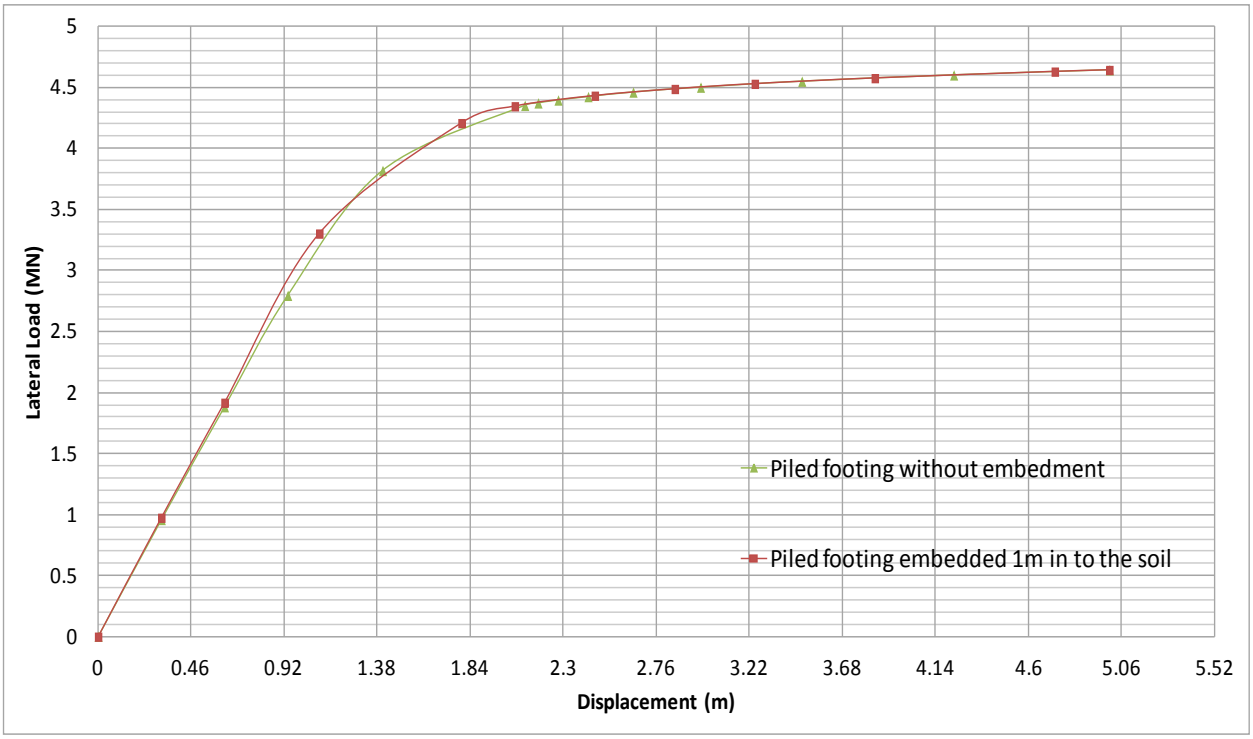

Figure 6-17. Comparing the lateral capacity of piled footings with their footings at the ground level and embedded 1 m below the ground surface (soil group B)

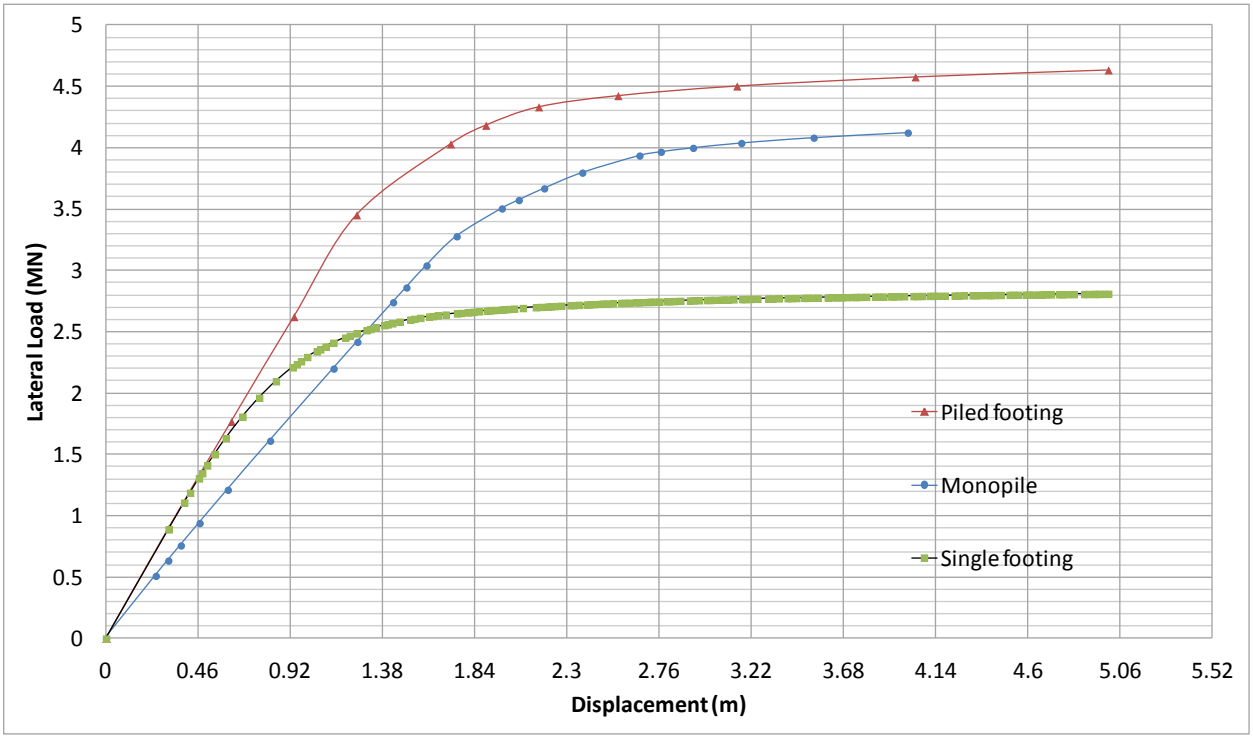

Figure 6-18. Comparing the lateral capacity of the proposed structures embedded in soil group A

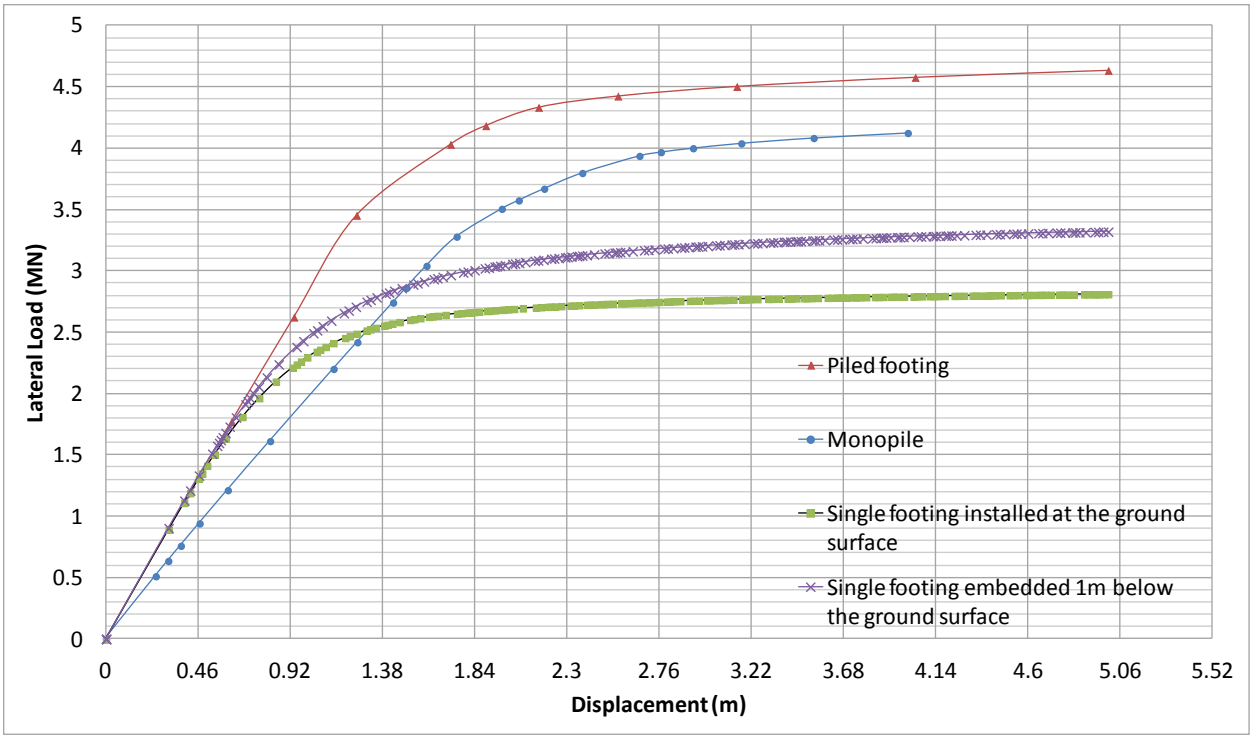

Figure 6-19. The affects of embedment depth on an un-piled footing structure embedded in soil group A

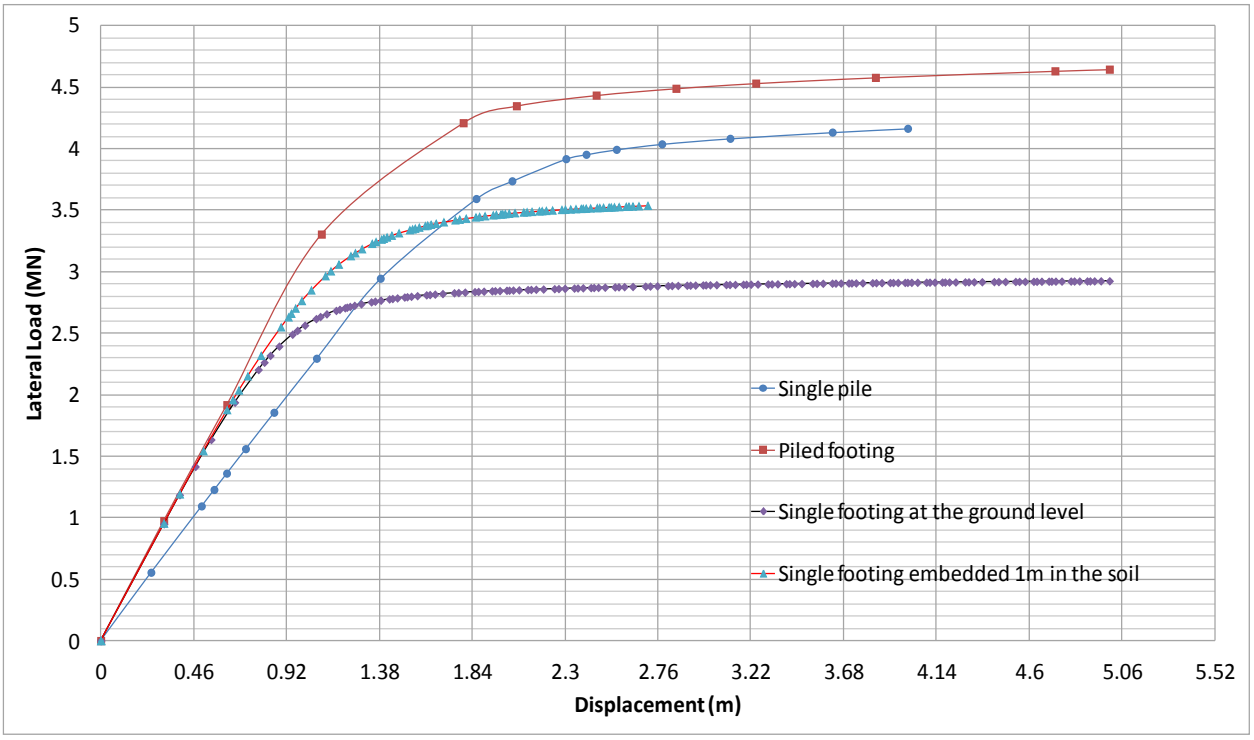

Figure 6-20. The affects of embedment depth on an un-piled footing structure embedded in soil group B

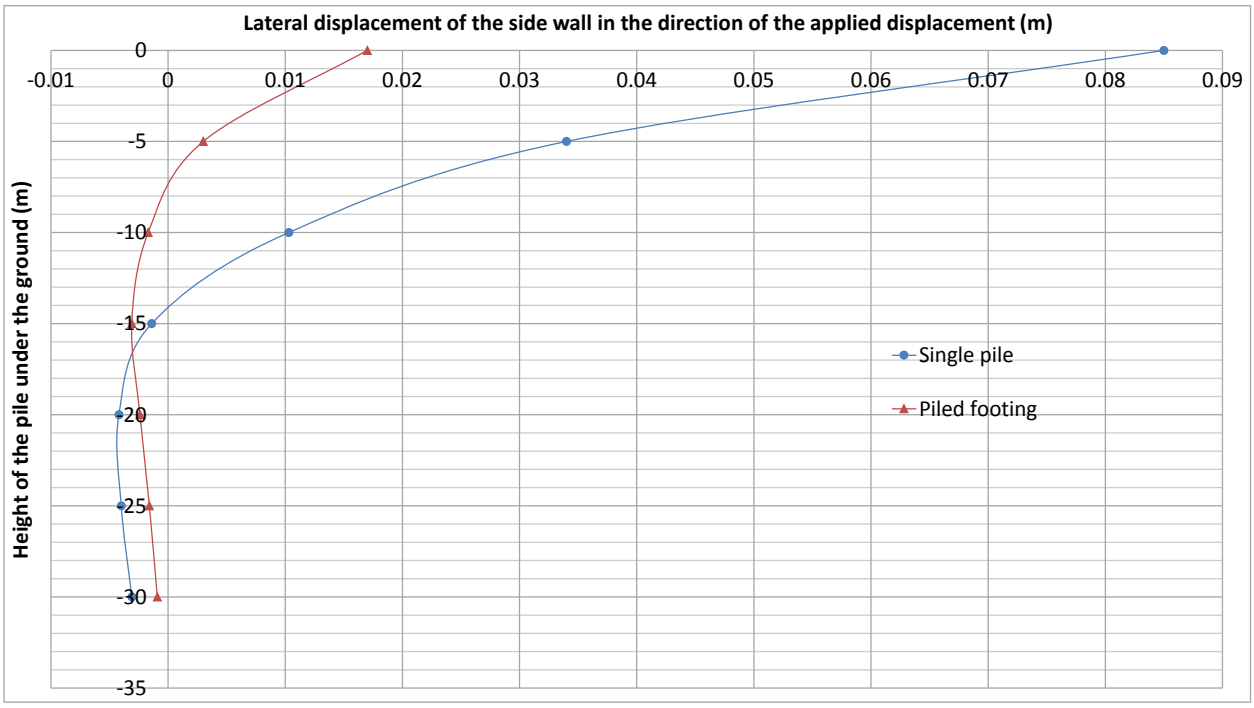

Figure 6-21. The lateral displacement of the soil in the direction of the applied load for soil group A

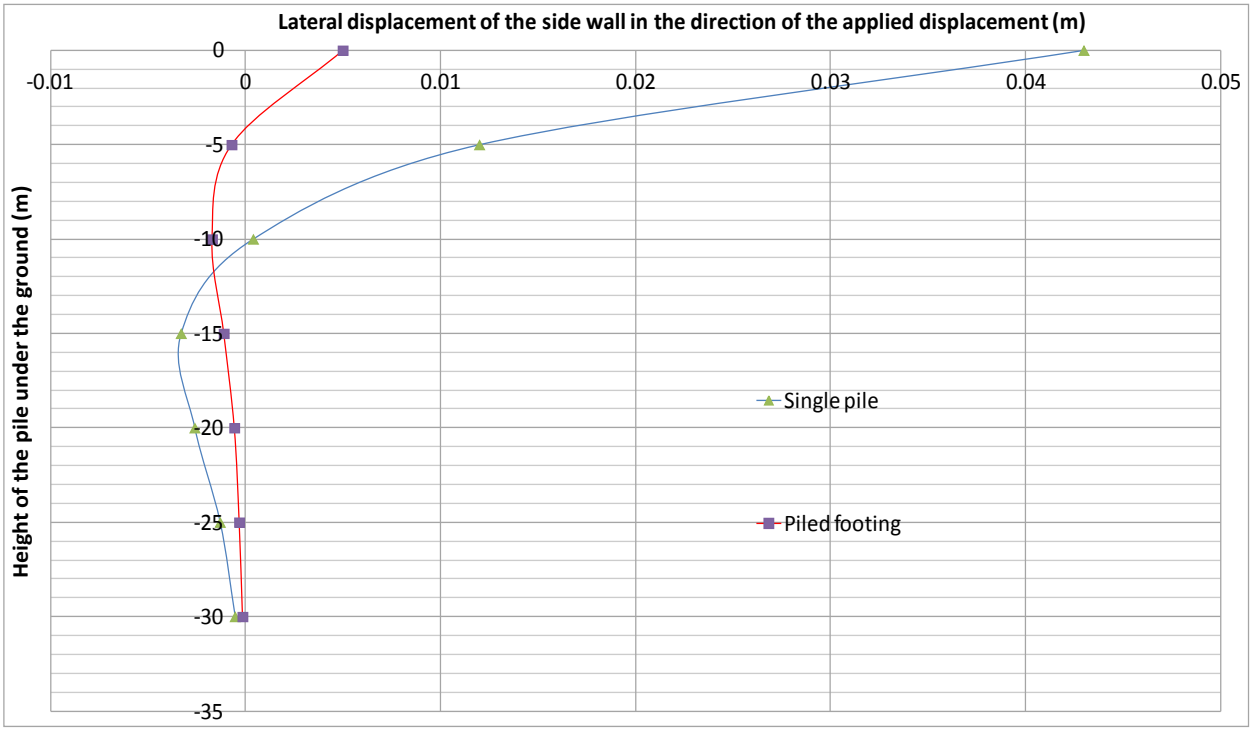

Figure 6-22. The lateral displacement of the soil in the direction of the applied load for soil group B

Figure 6-23. Lateral stresses generated on the soil for the monopile case (soil group A)

Figure 6-24. Lateral stresses generated on the soil for the monopile case (soil group B)

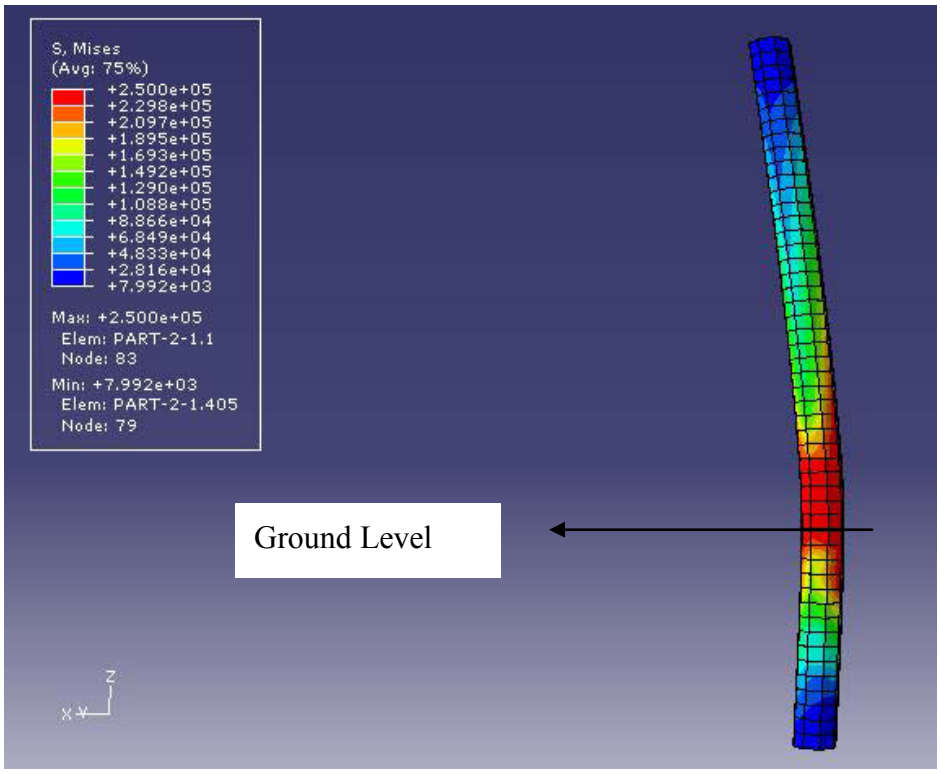

Figure 6-25. The Mises stresses acting on the monopile installed in soil group A

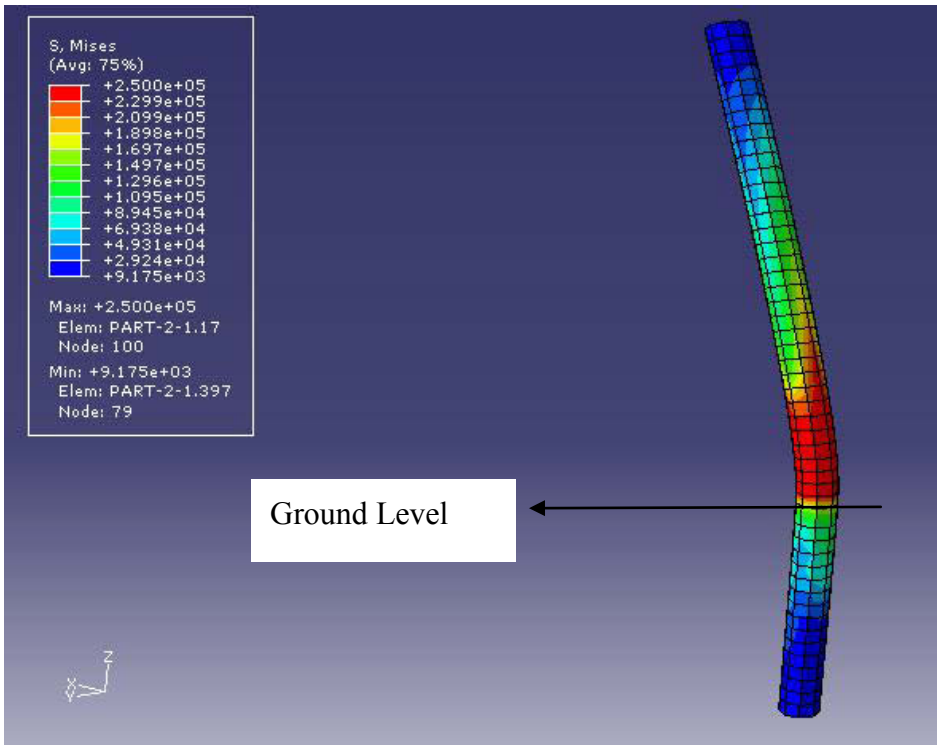

Figure 6-26. The Mises stresses acting on the hybrid structure installed in soil group A

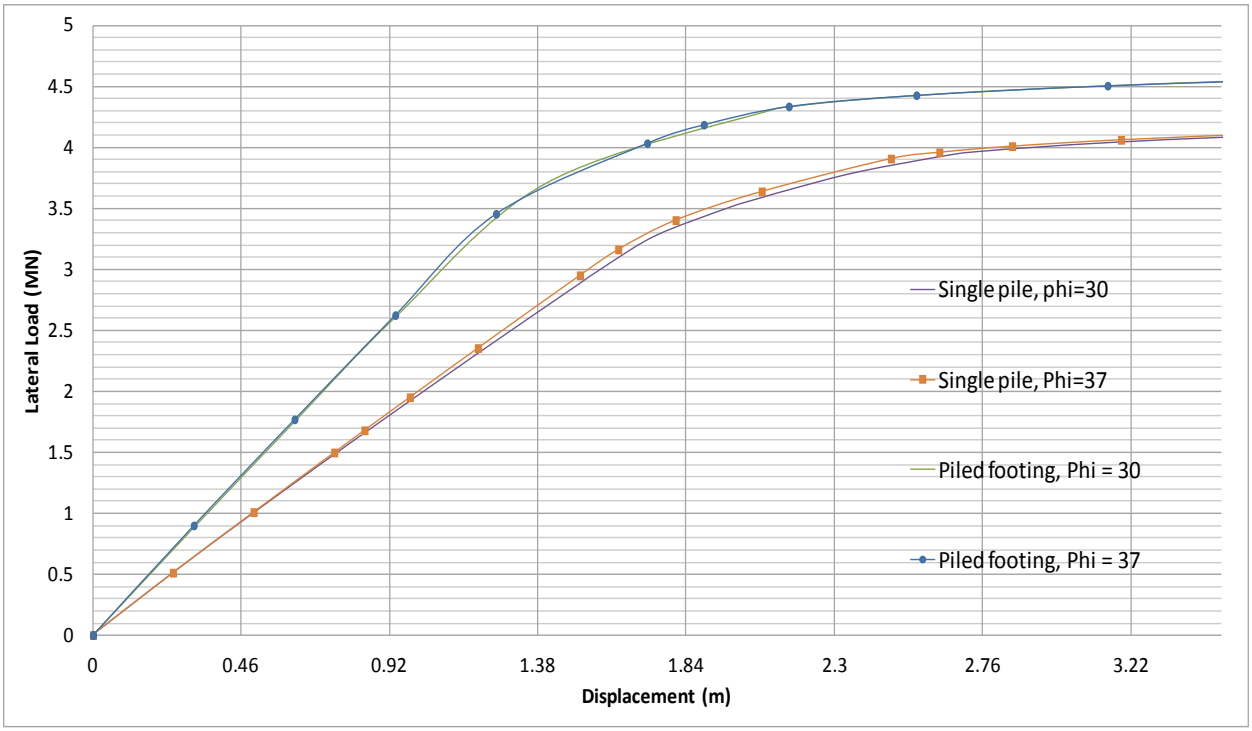

Figure 6-27. Changes in the soil's friction angle for monopiles and piled footing structures (soil group A)

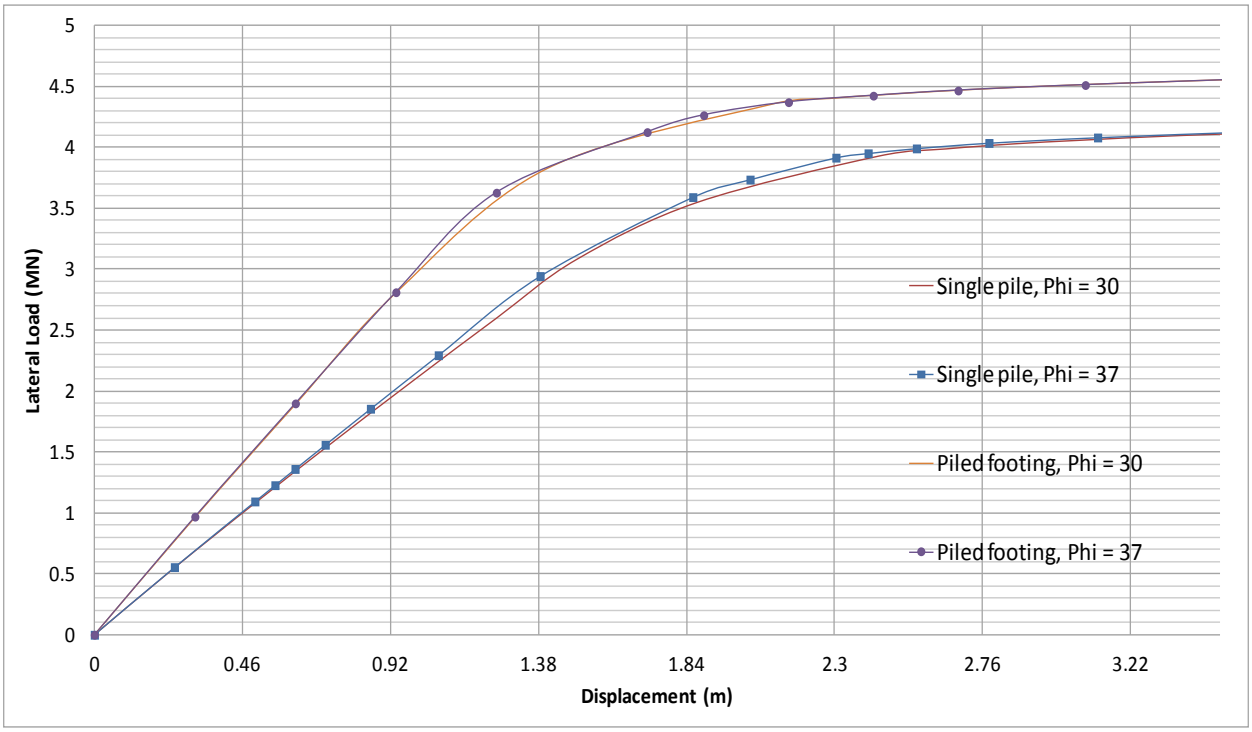

Figure 6-28. Changes in the soil's friction angle for monopiles and piled footing structures (soil group B)

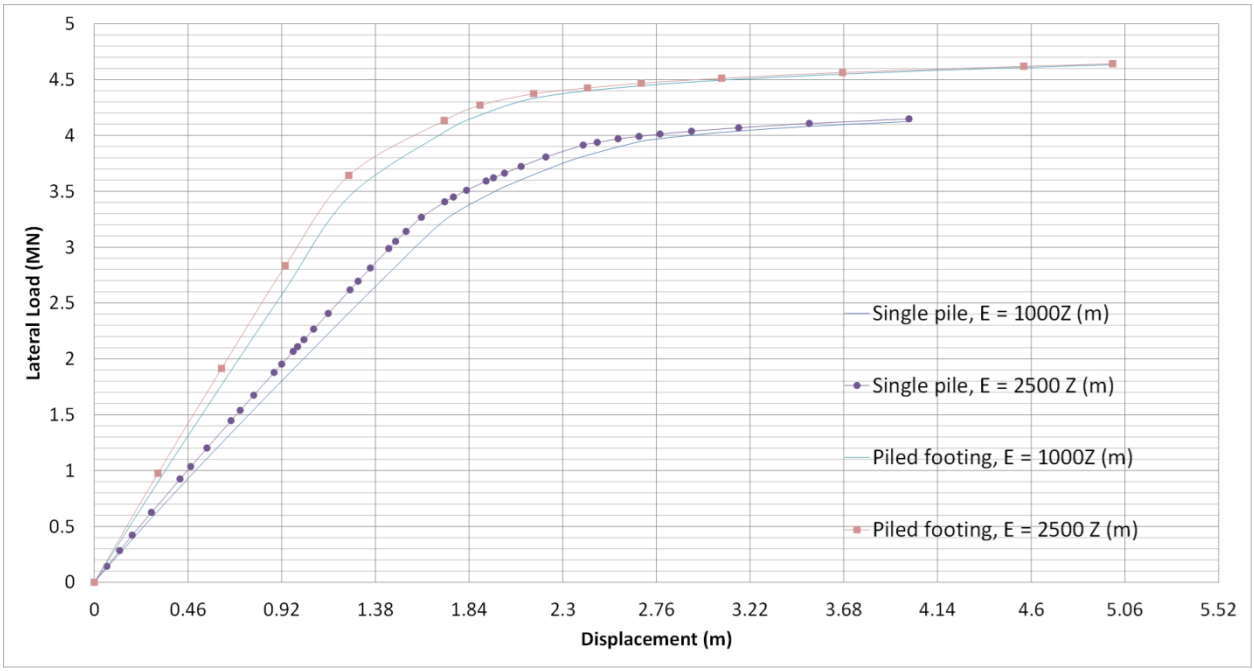

Figure 6-29. Changes in the soil Young's modulus for single piles and piled footing structures (soil group A)

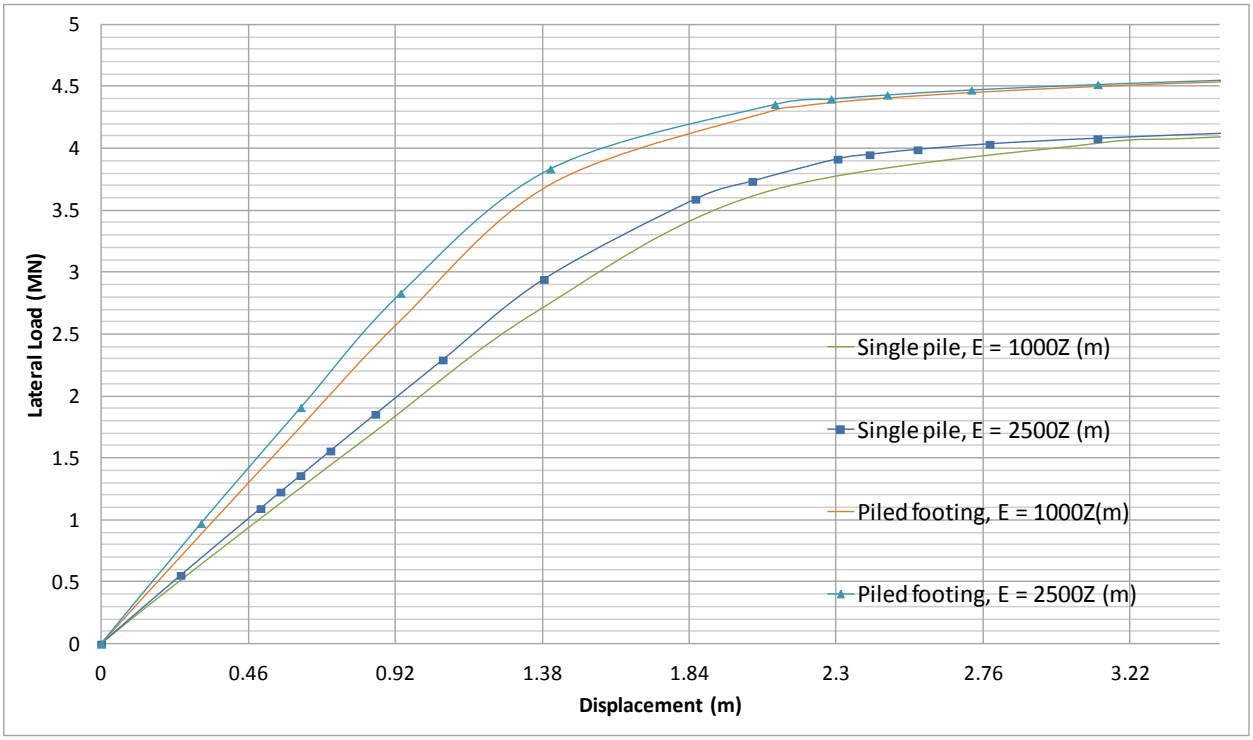

Figure 6-30. Changes in the soil Young's modulus for single piles and piled footing structures (soil group B)

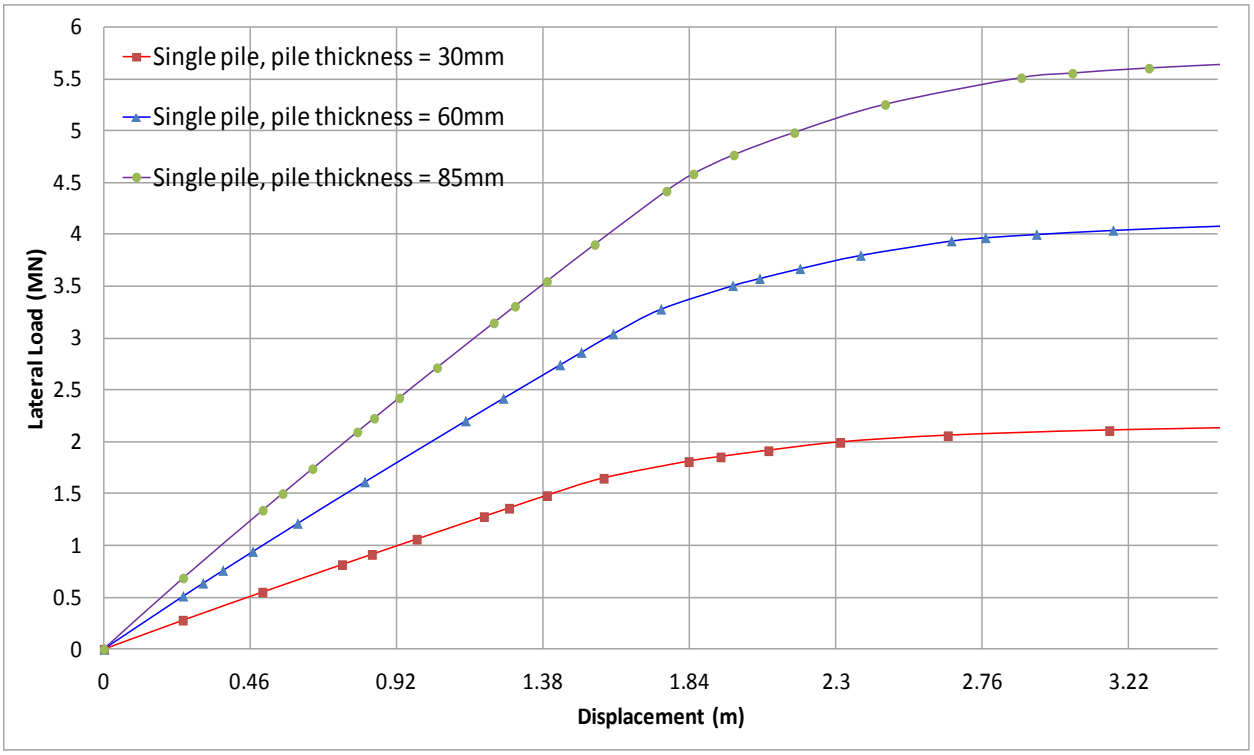

Figure 6-31. Change in the pile thickness for soil group A

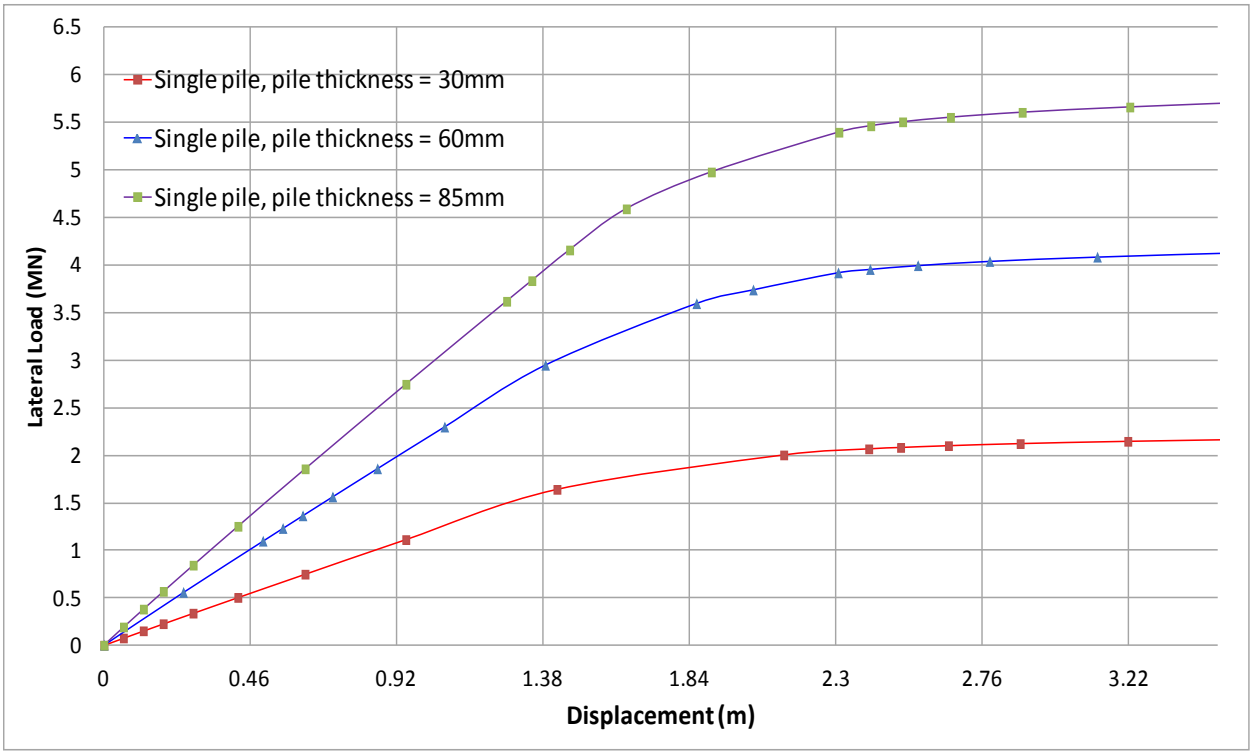

Figure 6-32. Change in the pile thickness for soil group B

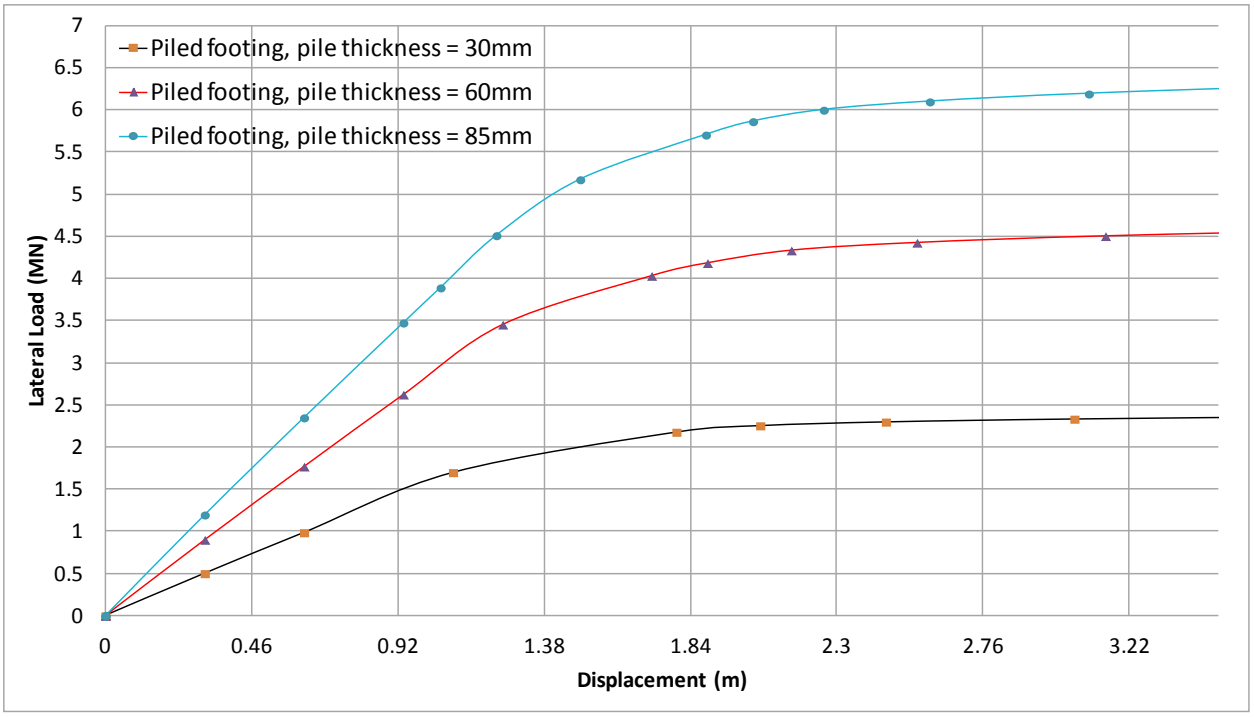

Figure 6-33. The results of changing the pile thickness for the piled footing structures embedded in soil group A

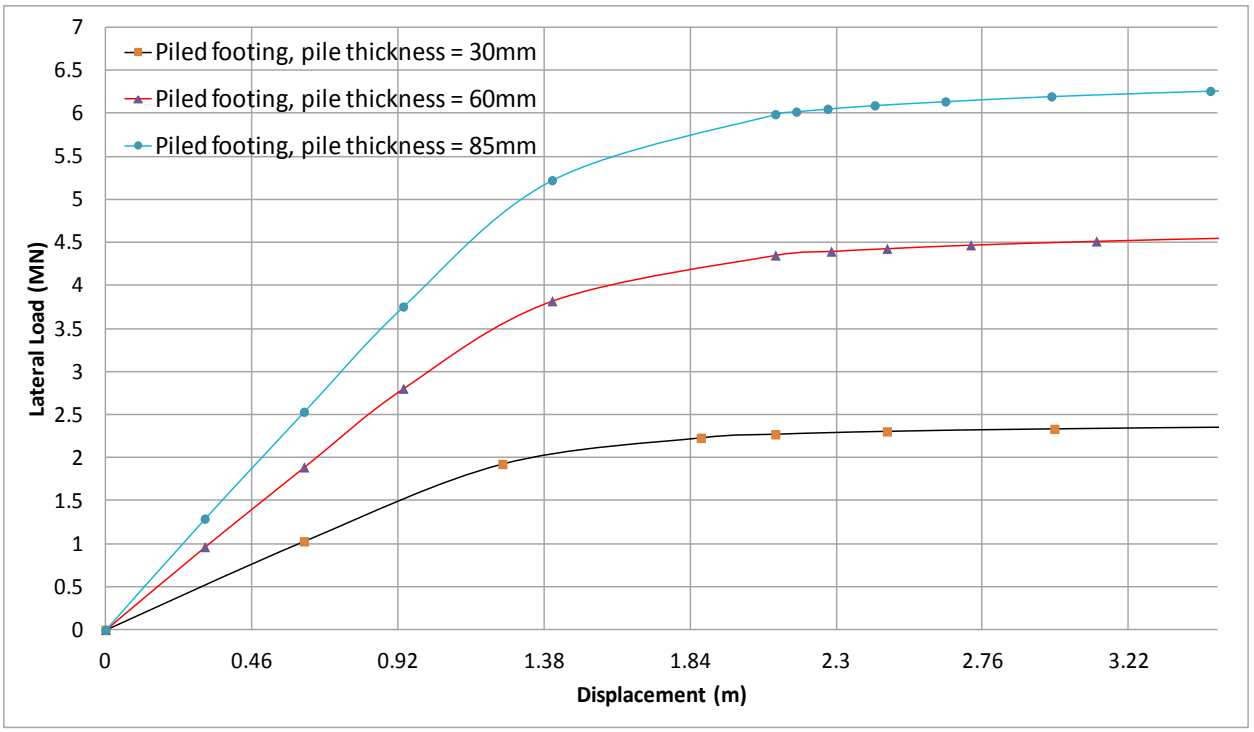

Figure 6-34. The results of changing the pile thickness for the piled footing structures embedded in soil group B

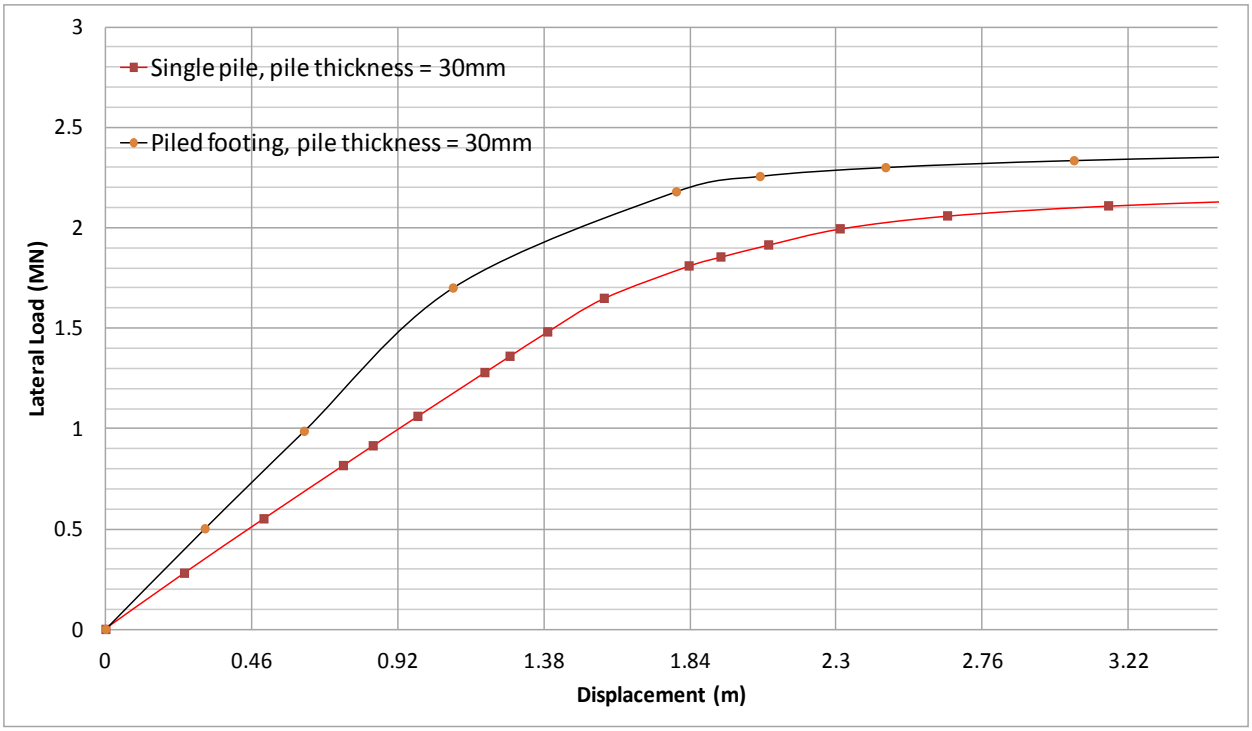

Figure 6-35. The results of changing the pile thickness for the monopile and the hybrid structure (soil group A)

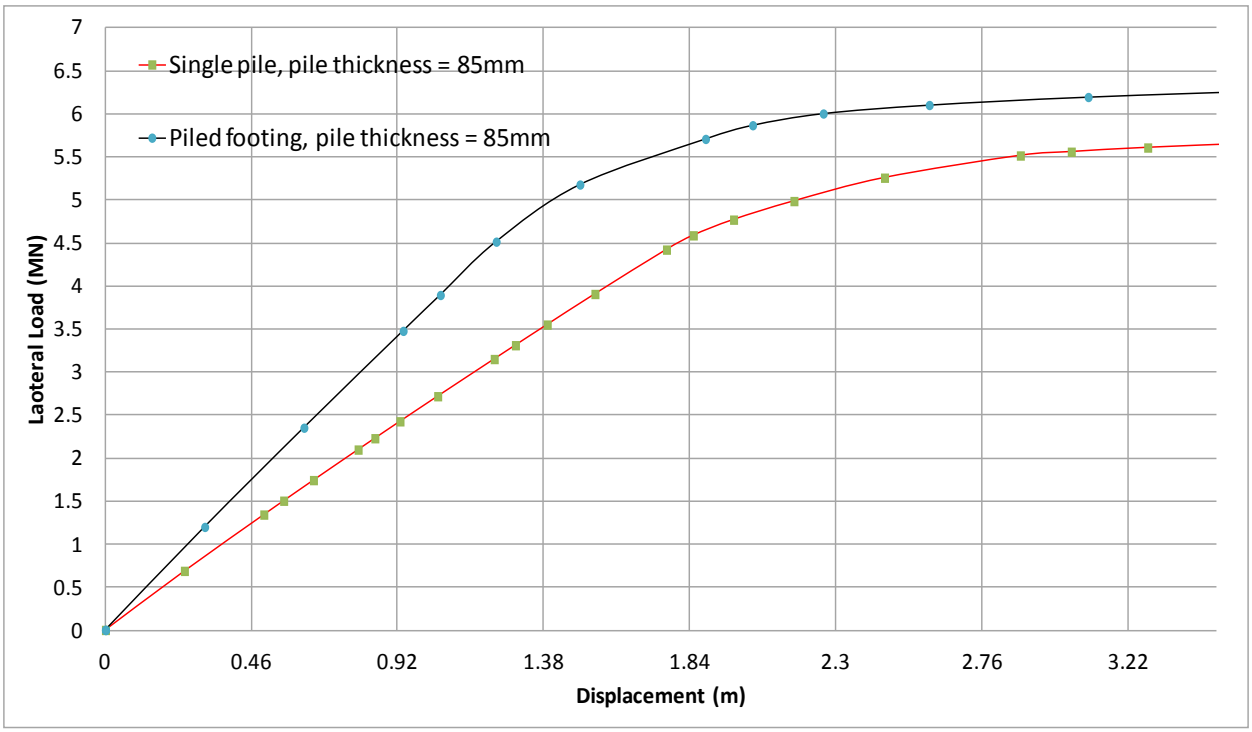

Figure 6-36. The results of changing the pile thickness for the monopile and the hybrid structure (soil group A)

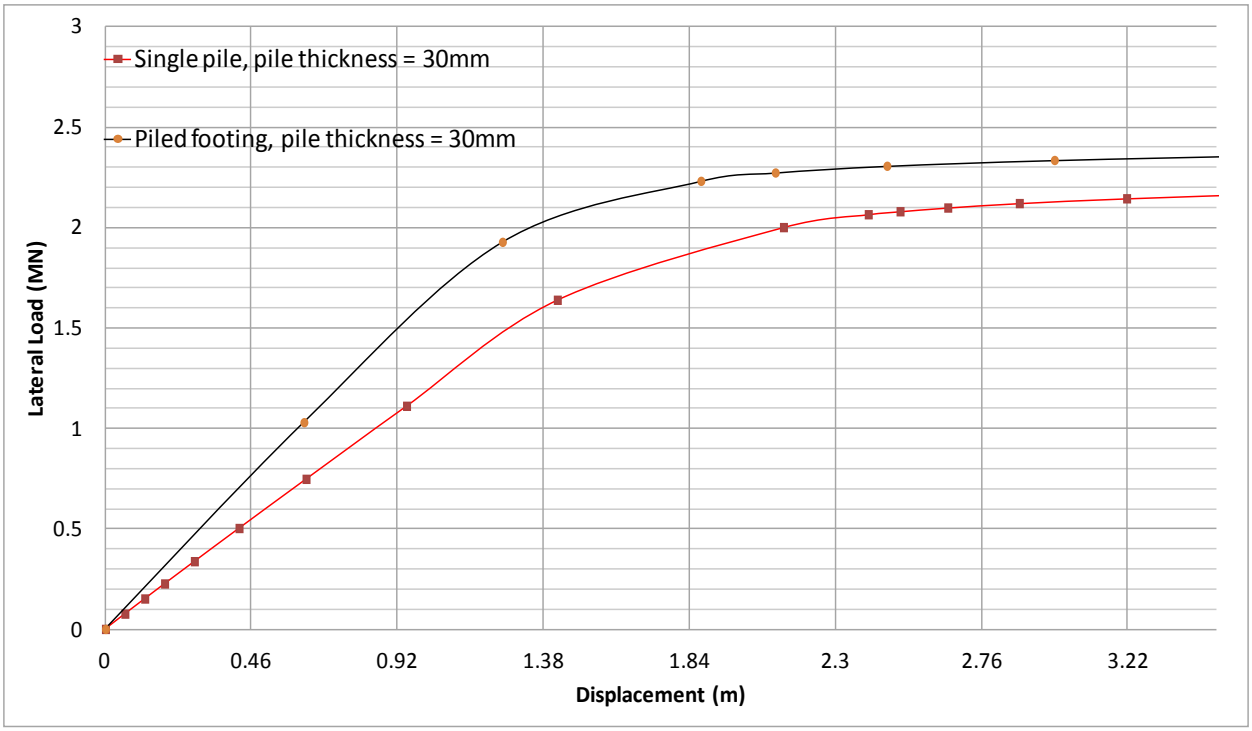

Figure 6-37. The results of changing the pile thickness for the monopile and the hybrid structure (soil group B)

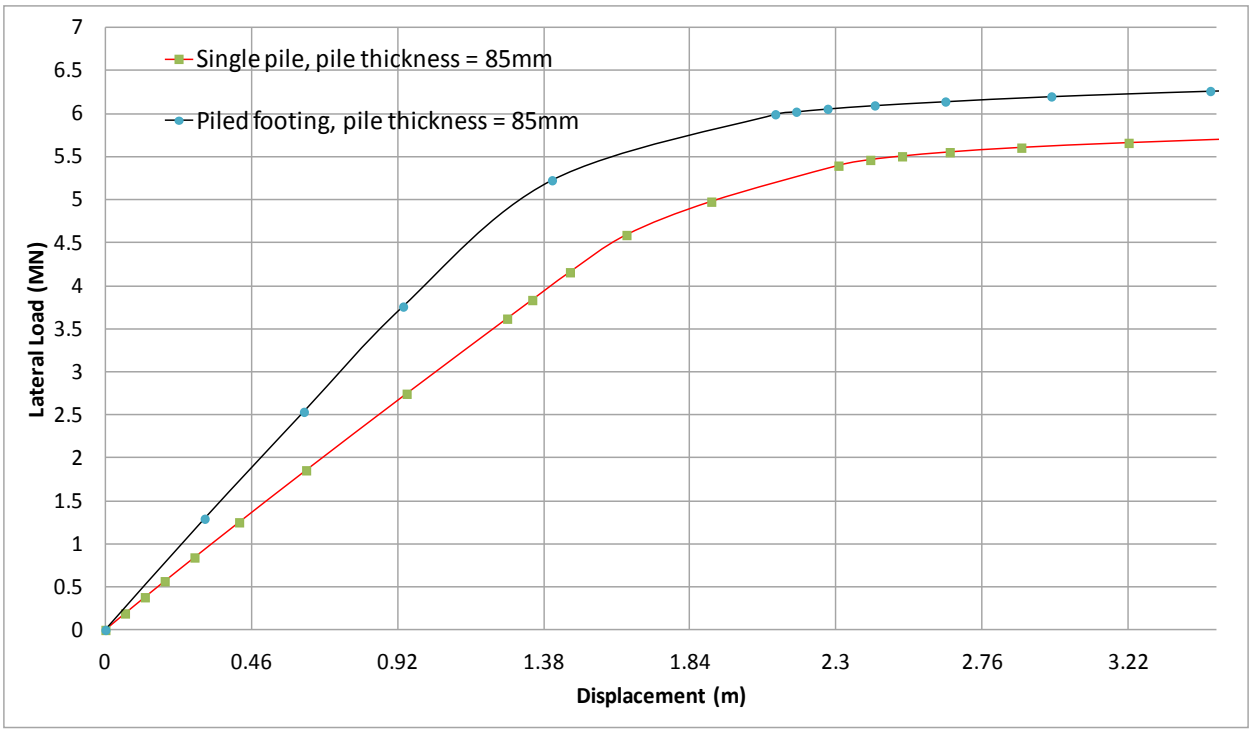

Figure 6-38. The results of changing the pile thickness for the monopile and the hybrid structure (soil group B)

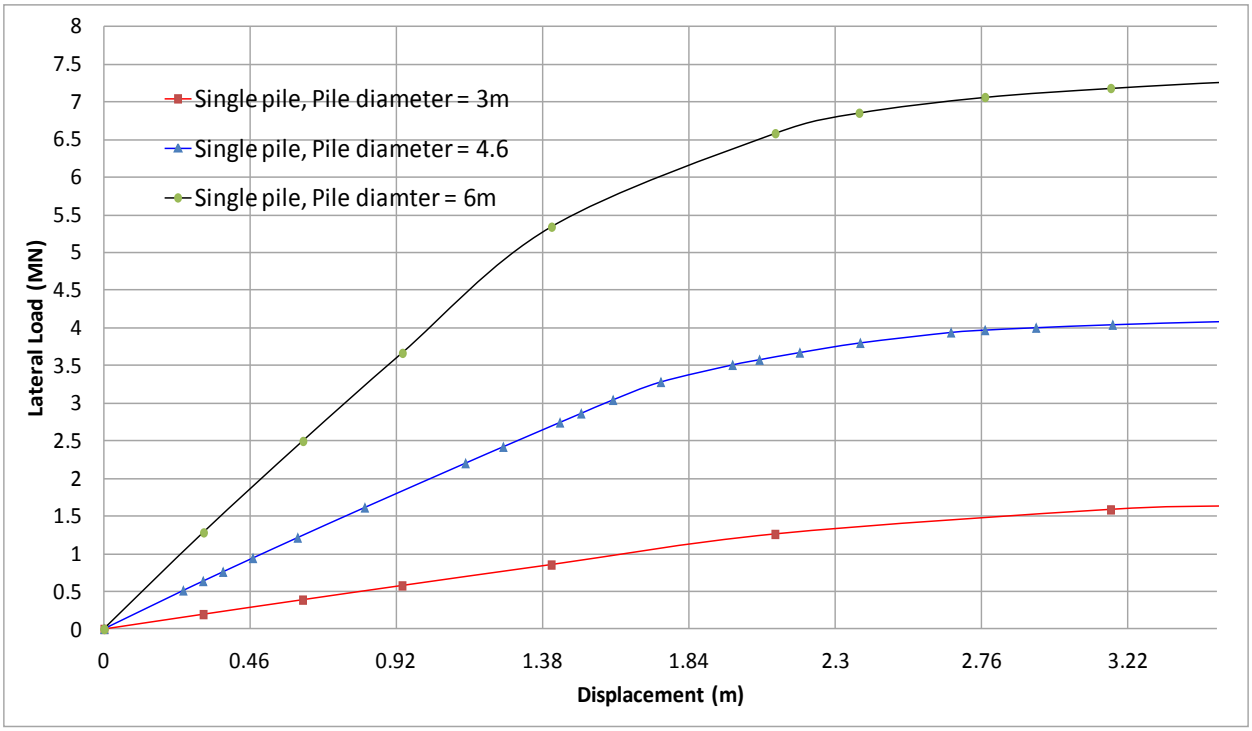

Figure 6-39. Changes in the pile diameter for soil group A

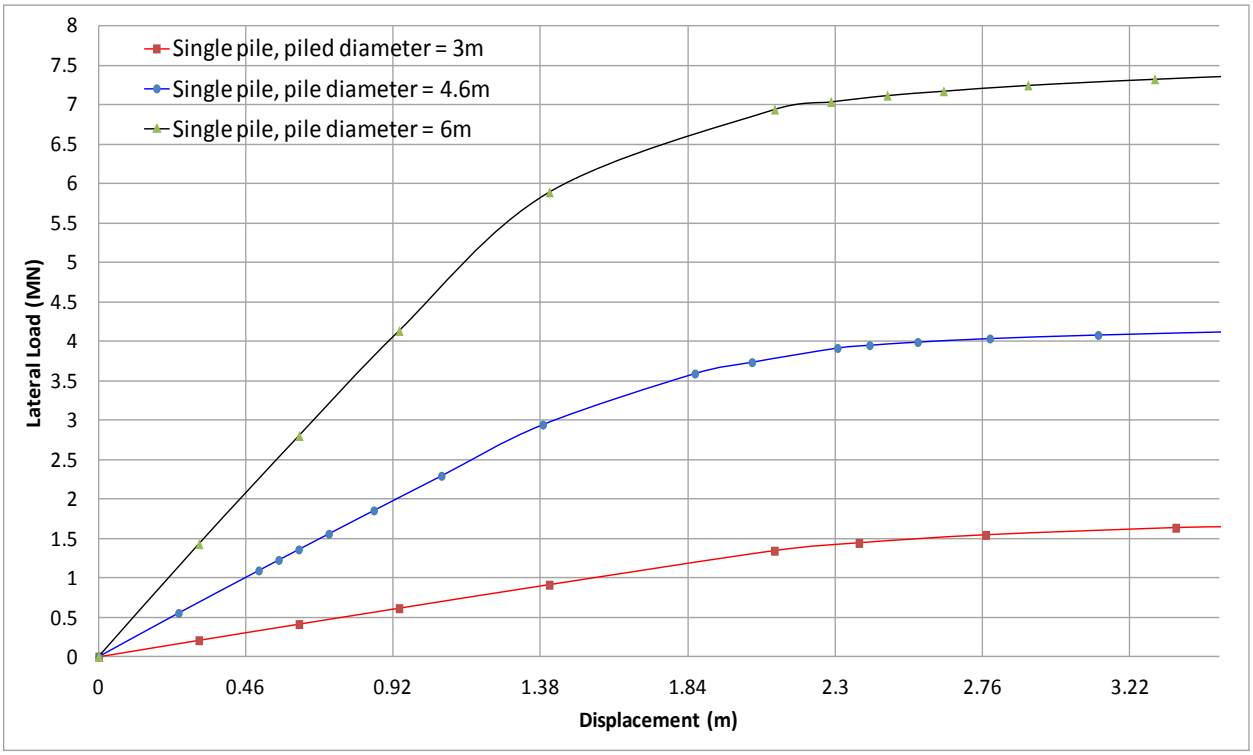

Figure 6-40. Changes in the pile diameter for soil group B

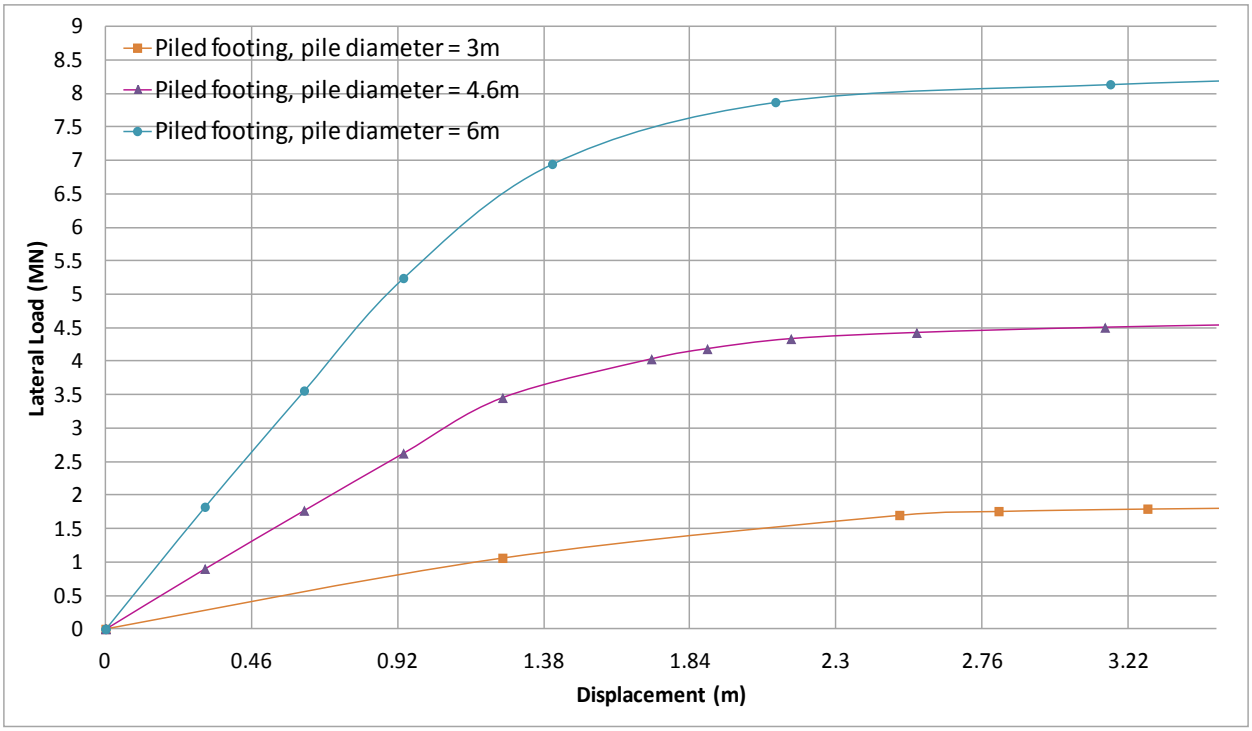

Figure 6-41. Changes in the pile diameter for the piled footing structures (soil group A)

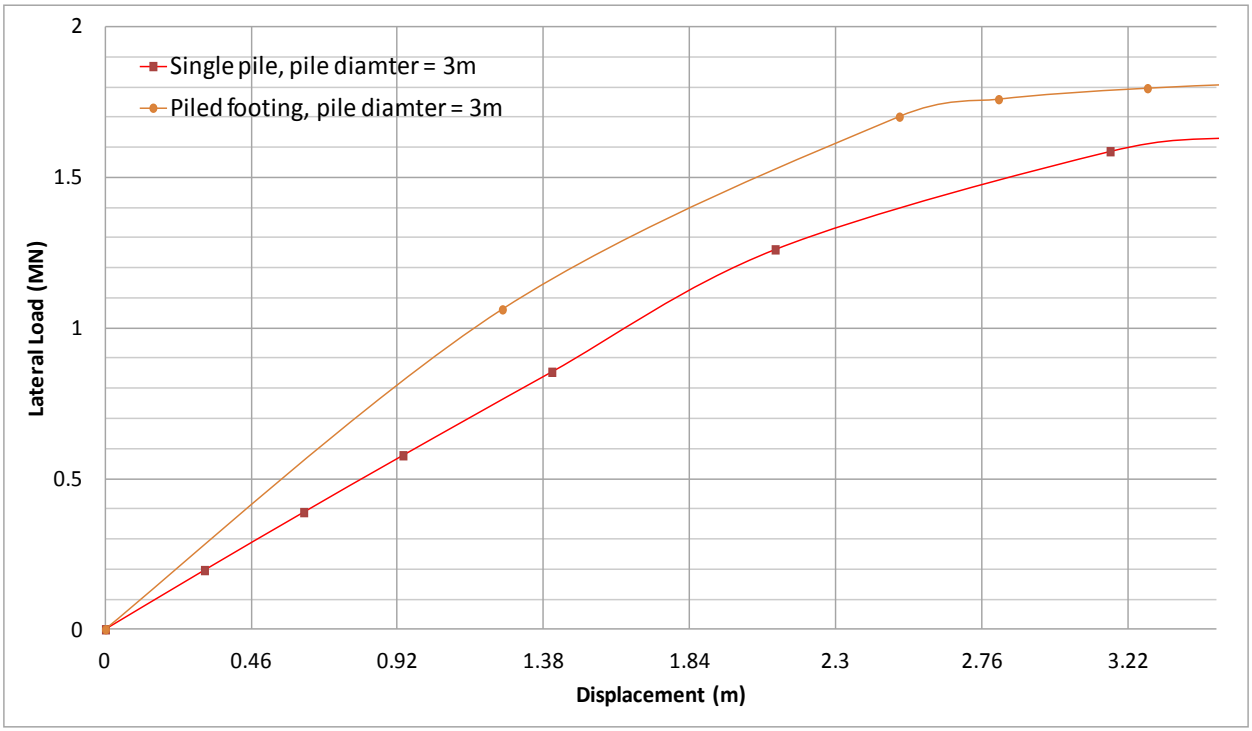

Figure 6-42. The results of changing the pile diameter for the monopile and the hybrid structure (soil group A)

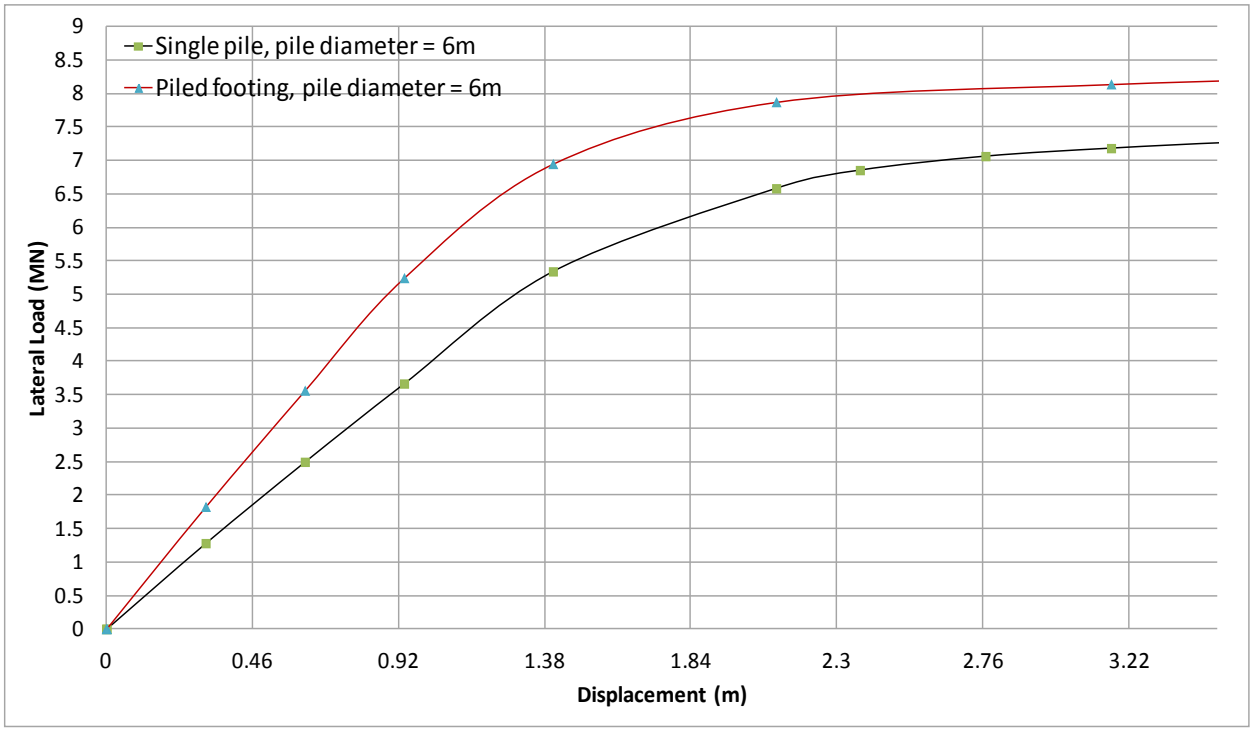

Figure 6-43. The results of changing the pile diameter for the monopile and the hybrid structure (soil group A)

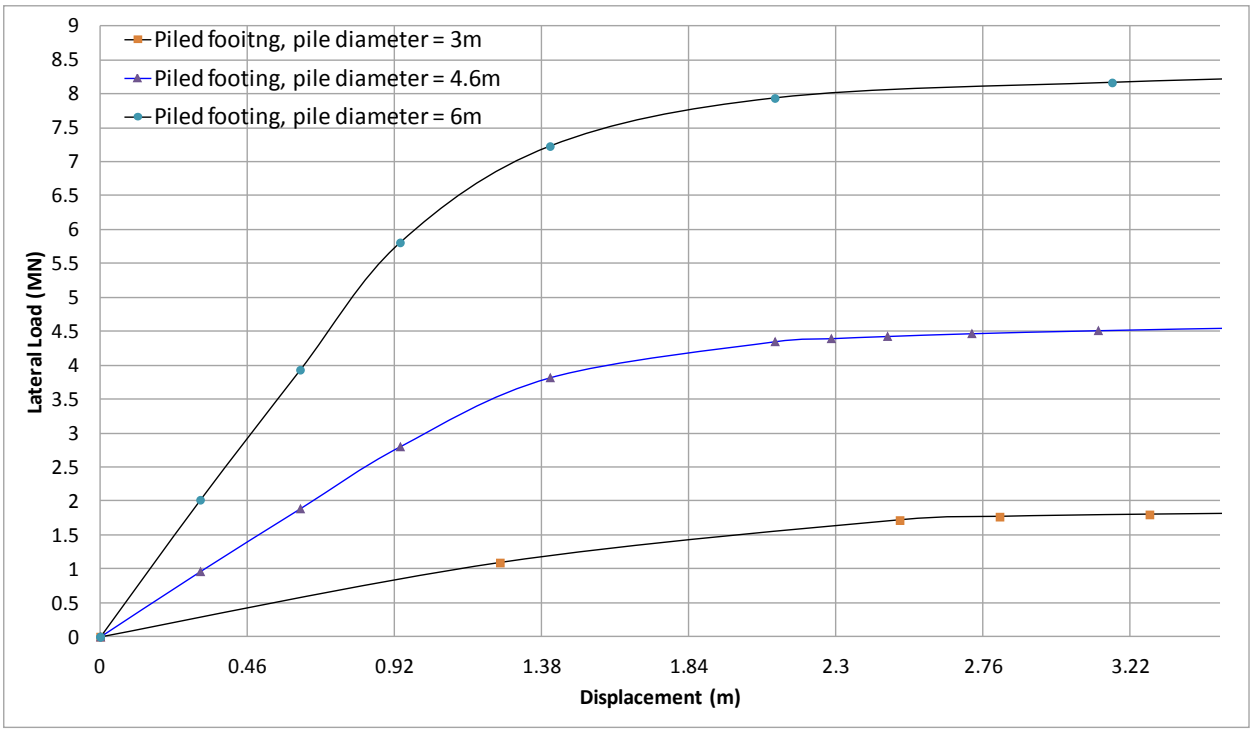

Figure 6-44. Changes in the pile diameter for the piled footing structures (soil group B)

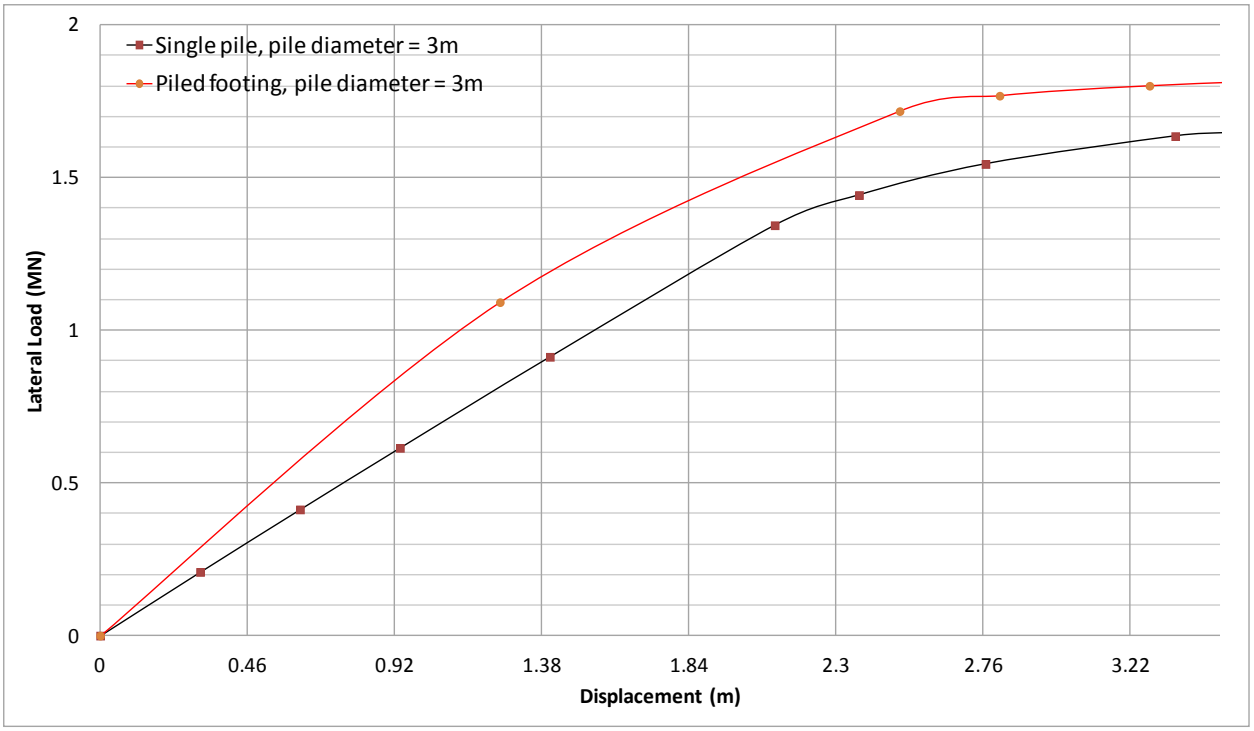

Figure 6-45. The results of changing the pile diameter for the monopile and the hybrid structure (soil group B)

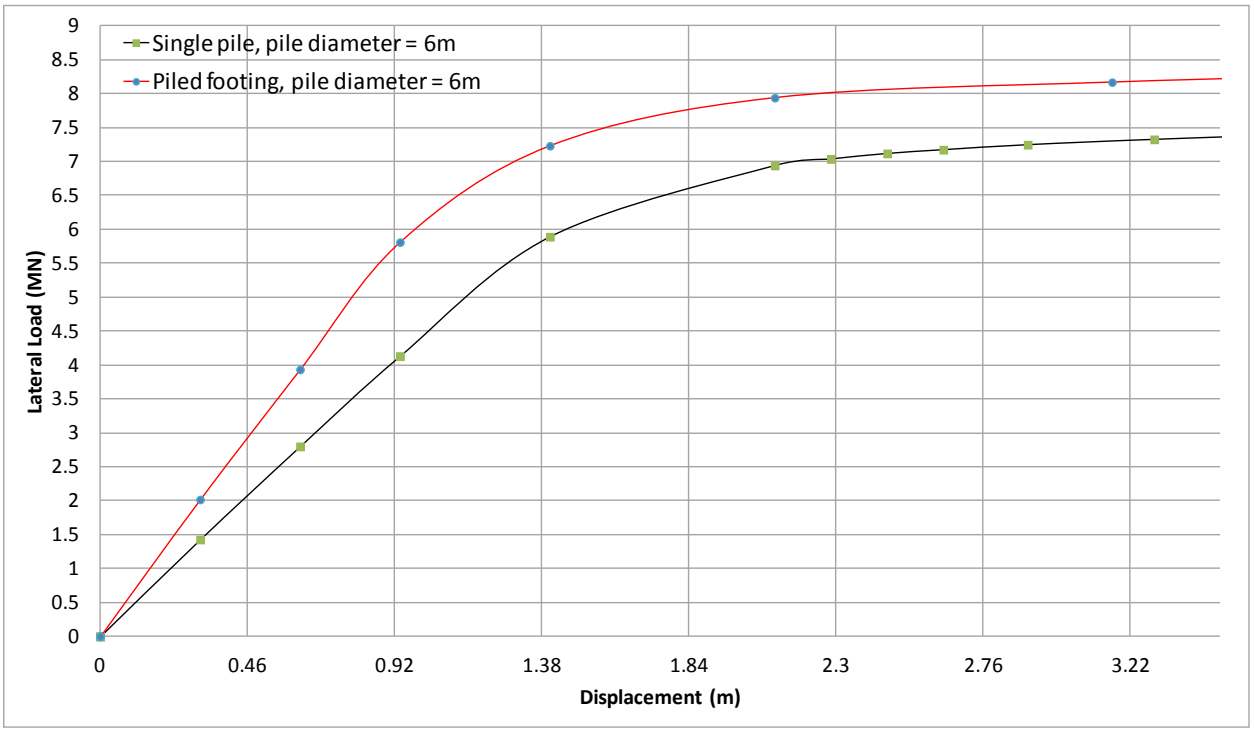

Figure 6-46. The results of changing the pile diameter for the monopiles and the hybrid structures (soil group B)

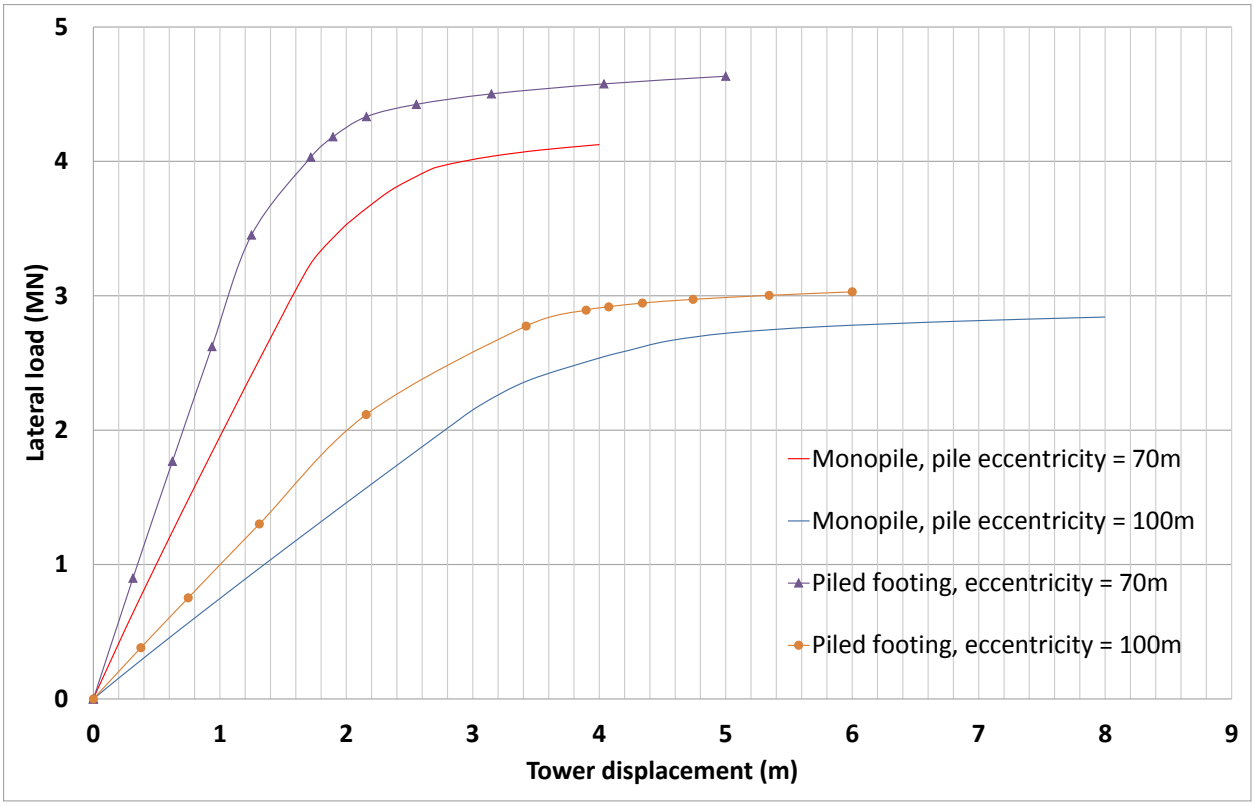

Figure 6-47. The results of changing the eccentricity for the monopiles and the hybrid structures (soil group A)

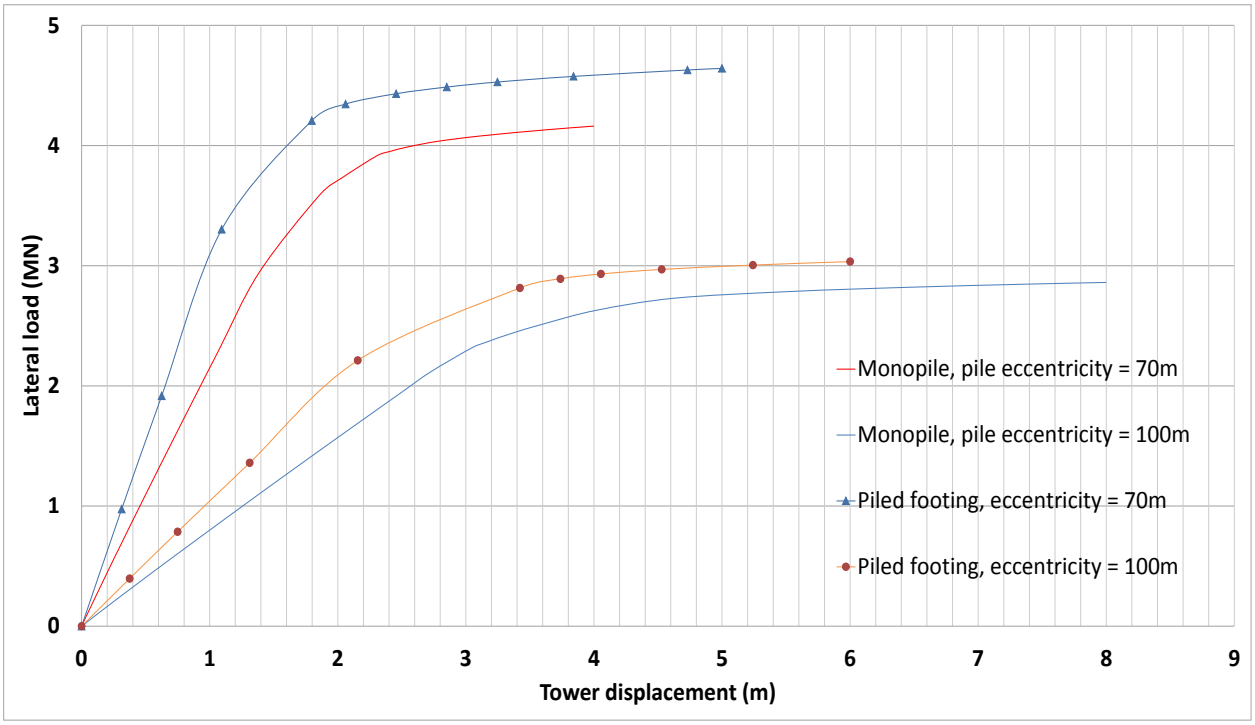

Figure 6-48. The results of changing the eccentricity for the monopiles and the hybrid structures (soil group B)

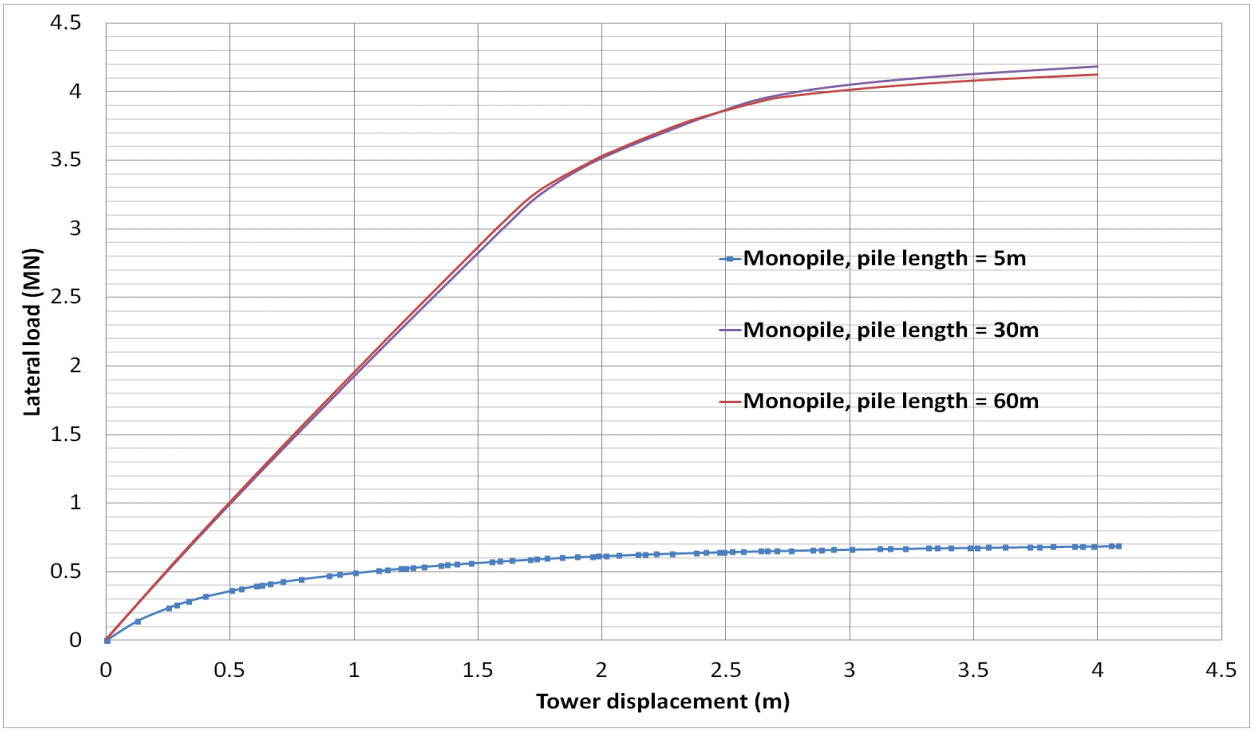

Figure 6-49. The results of changing the pile length for the monopiles (soil group A)

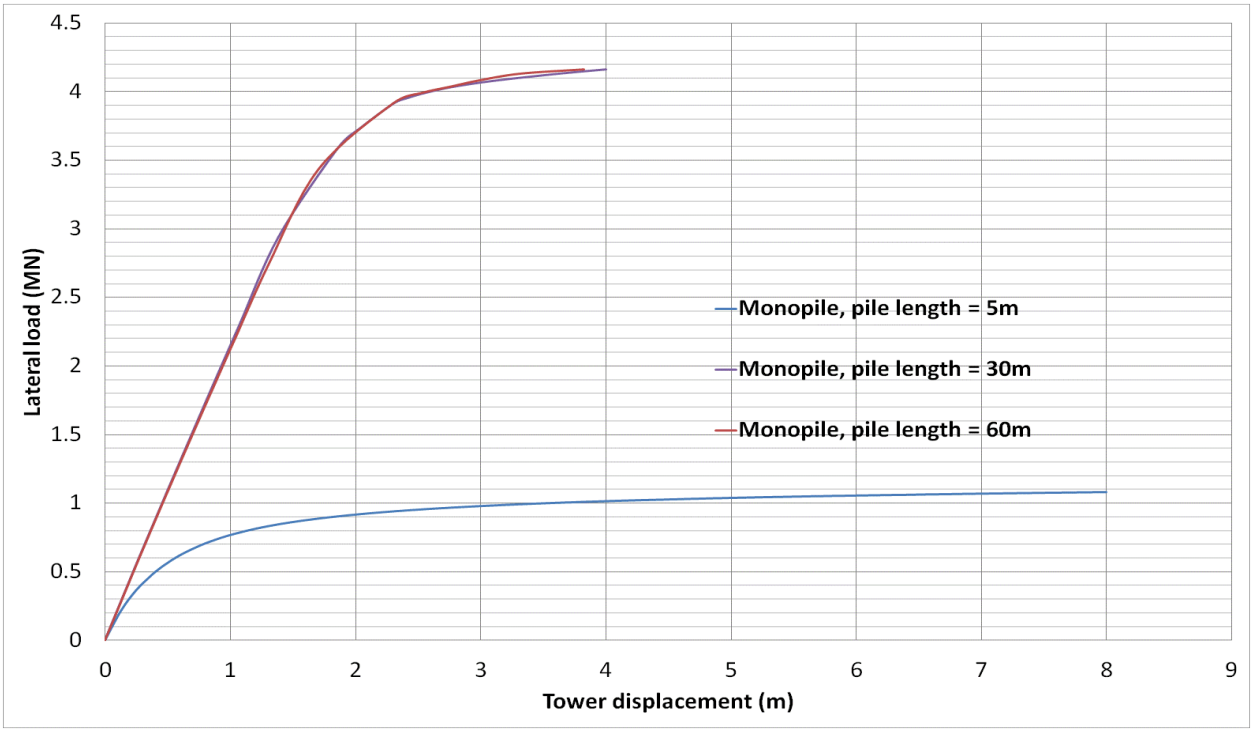

Figure 6-50. The results of changing the pile length for the monopiles (soil group B)

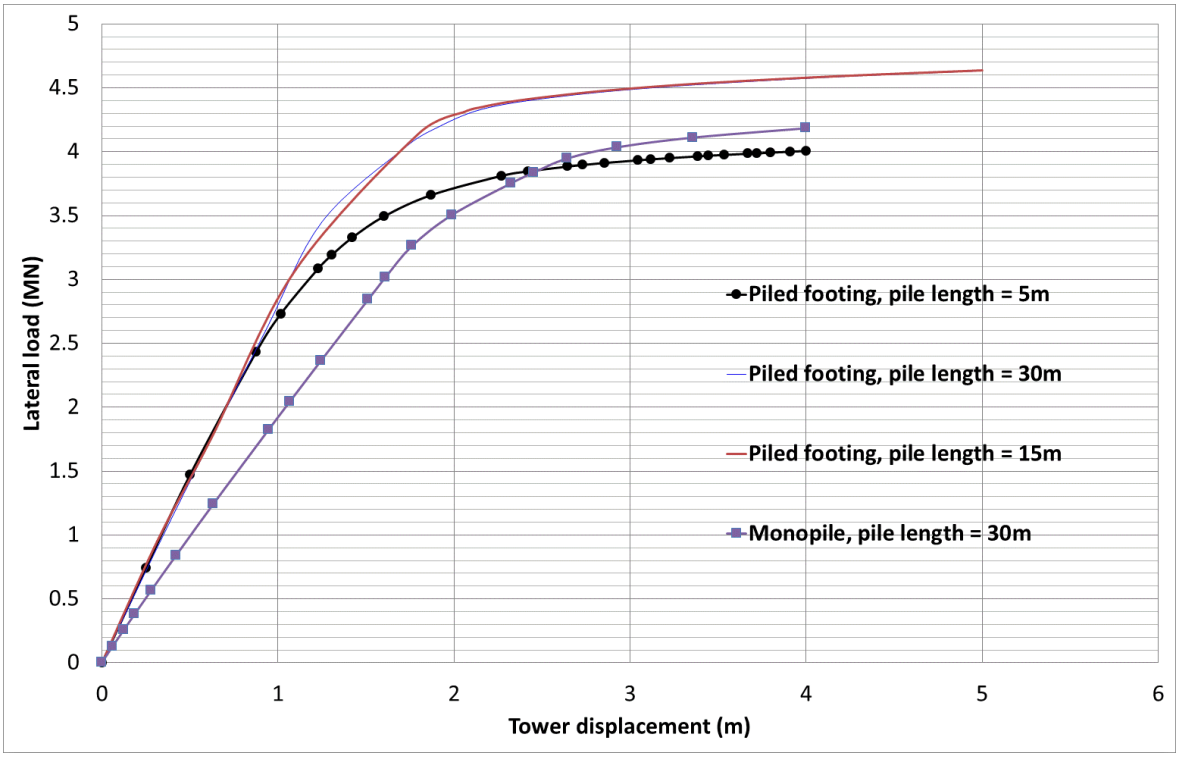

Figure 6-51. The results of changing the pile length for the piled footing structures (soil group A)

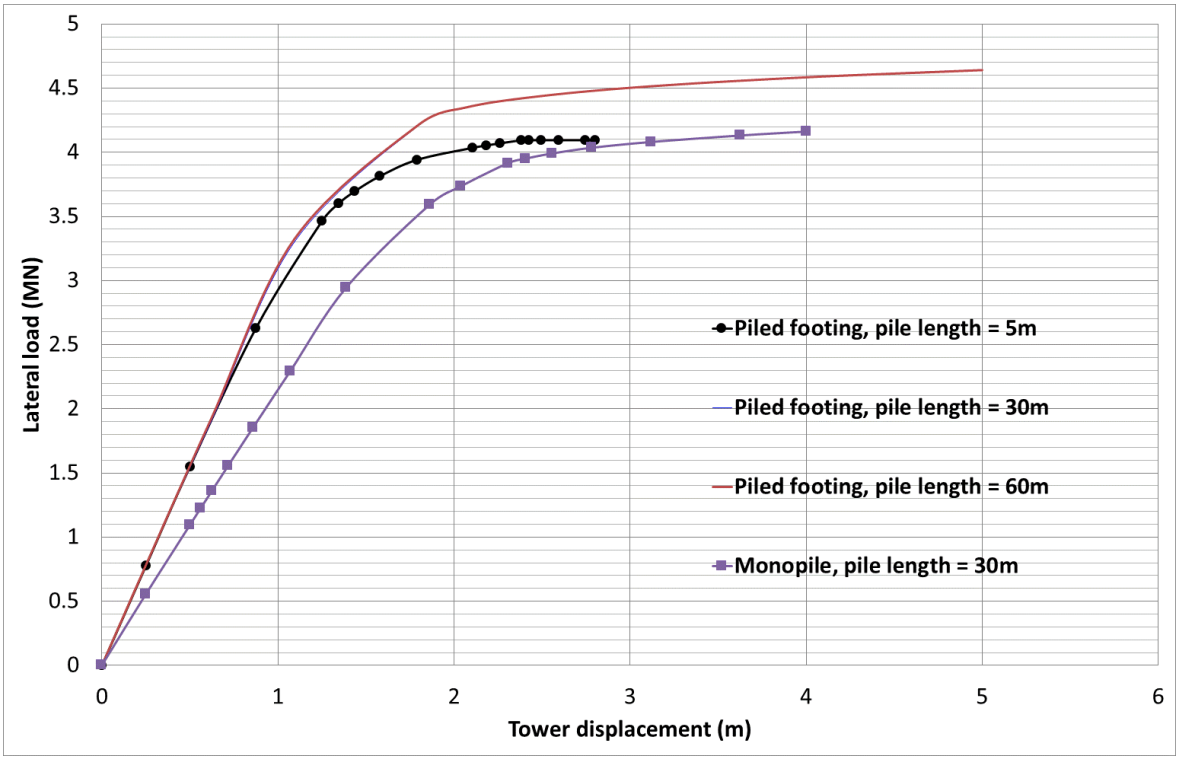

Figure 6-52. The results of changing the pile length for the piled footing structures (soil group B)

CHAPTER 7 CONCLUSIONS AND FURTHER RESEARCH

7.1 SUMMARY

The focus of this thesis was investigating the behaviour of monopiled footings embedded in sands for offshore wind turbines. The research was conducted on the background of finite element analysis and a series of small-scale centrifuge tests. In this chapter, the main conclusisons are summarised and recommendations are made for further research.

7.2 CONCLUSION AND MAIN FINDIGS

7.2.1 Development of new equations for elastic piles embedded in an elastic soil medium

Using 20-noded elements and a model with reflective symmetry the equations for short and long elastic piles embedded in an elastic soil medium were improved. In these equations, the pile head was at the ground level and the horizontal and moments were acting on it. Moreover, an equation was developed for calculating the lateral displacement of a restrained pile's head embedded in an elastic soil medium. The provided equations were validated against the equations adopted by previous scholars and the FE predictions to illustrate their accuracy. In these models, the soil's modulus of elasticity was considered as a constant value.

7.2.2 Comparison of the centrifuge tests with the FE results for piled footings, monopiles and un-piled footing structures

The small-scale centrifuge tests conducted on monopiles, piled footings and un-piled footings embedded in silica sand were modelled with the aid of finite element analysis. It was demonstrated that the stiffness of a piled footing structure was more than 40% greater than that of a monopile structure used as a wind turbine.

It has been discussed by a few scholars that the initial behaviour of the piled footing structure was controlled by the pile's stiffness. This research was conducted with the aid of the centrifuge tests conducted by Harloe (2010) and finite element analysis. In the FE models a Mohr-Coulomb soil criteria and an elasto- plastic material with strain hardening was considered for the pile structure. From the centrifuge tests, and the numerical models it was clear that the stiffness of a piled footing structure was higher compared to a monopile structure. This point was evident as the initial stiffness of the piled footing was higher than of a single pile/tower structure at all times for a medium dense sand deposit.

It was clearly demonstrated that the initial behaviour of the piled footing structure was controlled by the footing and not by the monopile. This was evident because at low displacements the stiffness of the un-piled footing structure was higher than of a monopile and this was confirmed by the FE and the centrifuge tests.

From the FE models constructed for the tests, adopting a linear or a parabolic increase in the soil modulus did not significantly affect the results. The linear increase in the soil's modulus of elasticity was adopted in respect to the CPT results obtained from the centrifuge tests. The parabolic increase was adopted in respect to the tests conducted by Gourvenec et al. (2008) on the same silica sand used in the centrifuge tests and it was in line with the conducted CPT tests in this study too.

With the aid of the FE models, it was clearly demonstrated that by adopting an appropriate friction angle and a soil modulus accurate results could be obtained for all three structures, which were monopiles, piled footings and un-piled footings embedded in a sand deposit.

With the aid of the FE models, it was demonstrated that the bending moments generated on the piled footing structure were smaller than those of a monopile for the segment embedded under the ground. This was important because if a piled footing structure is to be used instead of a monopile not only its stiffness must be higher than of a monopile structure but also its bending moments must be smaller too. This point was clearly demonstrated for the monopiles and the piled footing structures in the FE models for different horizontal loads applied to the tower's head.

From the FE analysis, it was clear that not only the stiffness of the piled footing structure was higher than of a monopile but also its ultimate lateral capacity was also higher. This point was also confirmed by the tests conducted in the centrifuge.

From the FE results, it was clear that the stiffness and the ultimate capacity of a monopile used as a wind turbine is not significantly enhanced with increasing the vertical load on the tower's head. It was also clear that the structural capacity controls the stiffness and the ultimate capacity of a monopile used as a wind turbine. By constructing, an elastic monopile embedded in a sand deposit (FE analysis) it was illustrated that the sidewalls containing the monopile were remote from collapse and this clearly confirmed that the yield strength of the pile controlled the ultimate capacity of the structure. This latest point was discussed by Powrie et al. (2007), which conducted tests on a sand deposit in the centrifuge with retaining walls and a stabilizing platform, in a plain strain situation this structure is similar to half a piled footing structure.

With the aid of the FE models, it was clearly illustrated that for un-piled footing structures the vertical load acting on them controlled their ultimate lateral capacity. Moreover, it was demonstrated that the bearing capacity equations in combination with the equations provided by Gottardi et al. (1993) and Butterfield et al. (1994) provided close results to the tests and the FE predictions. These agreements were achieved using the values of N_γ adopted from Vesic (1973) for calculating the maximum vertical load that the soil could sustain for a footing, which had a shallow embedment depth (0.35 m).

By conducting a parametric study, it was illustrated that if a piled footing structure is to be used instead of a monopile a radius and thickness of 10 m and 2.99 m is necessary if a pronounced increase in the stiffness is to be achieved. These dimensions were adopted for a piled dimension of 4.6 m but it was illustrated that for other pile dimensions these values were also acceptable.

It was demonstrated that by embedding, the piled footing structure in the sand deposit there would be no increase in the stiffness of the structure; this was a point, which was debated by a few researchers over the last few years. The reason that there was no increase in the stiffness of the structure by embedding it into the sand was because the lateral displacement of the structure was very small due to the resistance of the pile structure and so the effect of the sidewalls were negligible. This suggests that if a piled footing structure is to be used instead of a monopile structure the footing can be directly installed at the ground level and this is definitely cheaper than embedding the footing into the sand layer for offshore purposes.

With the aid of the finite element analysis, it was illustrated that changes in the soil modulus of elasticity did not affect the ultimate lateral capacity of the monopiles and the piled footing structures with high eccentricities, although there was an increase in the stiffness of the structures as the soil became stiffer. Further, it was demonstrated that an increase in the soil friction angle did not significantly change the stiffness of a monopile and a piled footing structure used as a wind turbine in a sand deposit too. The charts provided by Broms (1964) for long piles embedded in a sand deposit confirmed the latest point.

As the structural capacity of the pile/tower controlled the ultimate lateral capacity of a monopile embedded in a sand deposit the effects of the pile's diameter and its thickness were investigated in this research. Broms (1964) chart for calculating the ultimate lateral capacity of long piles embedded in a sand deposit illustrated a very close agreement with the FE results. On the other hand, the methods adopted by Fleming et al. (1992) and Zhang et al. (2005) were not very well suited for monopiles used as wind turbines in a sand deposit as these structures have very high eccentricities and the effect of the soil on the structure is minimal. Moreover, the methods adopted by Fleming et al. (1992) and Zhang et al. (2005) for calculating the ultimate capacities did not change as the pile thickness was changed during the parametric study while the method adopted by Broms (1964) changed accordingly with the pile's thickness. This is a serious draw back of the methods adopted by Fleming et al. (1992) and Zhang et al. (2005) as the pile thickness can significantly enhance the ultimate lateral capacity and the stiffness of a monopile structure. As discussed by Fleming et al. (1992) their calculated results must be similar to the results obtained by Broms (1964) for the range of friction angles adopted in this investigation. It seems that their produced chart is not well suited for pile tower structures with high eccentricities. In regards to the method adopted by Zhang et al. (2005), their method is not acceptable, as they do not consider the yield point of the pile material at any point in their original paper. It can be concluded that if the method adopted by Fleming et al. (1992) is to be considered for pile towers with high eccentricities, generating a script is essential.

It was demonstrated that as the footing controlled the initial stiffness of the piled footing structures a shorter pile length (half the size of the monopile's length) with a suitable footing size was able to provide a higher stiffness and ultimate lateral capacity compared to a monopile structure. It was also evident that when the pile's length was increased in the parametric study there were no changes made to the stiffness or the ultimate capacity of the monopile structure as discussed by Broms (1964). This was a problem for the method adopted by Zhang et al. (2005) as they have considered the pile's length in their equation for calculating the ultimate lateral

capacity of a monopile structure. On the other hand, the method adopted by Broms (1964) was again well suited for design purposes.

In regards to the analyses conducted in Chapter 6, a piled footing structure with a footing radius and thickness of 10 m and 3 m respectively, would be suitable for practical application with a pile/tower structure, with a diameter, length, thickness and eccentricity of 4.6 m, 20 m, 60 mm and 70 m respectively. This structure would be suitable for medium to dense sand deposits in a shallow offshore environment.

7.3 FURTHER RESEARCH

It would be constructive to investigate how this hybrid structure (monopiled footing) would behave when embedded in a very loose to loose sand deposit. This investigation must include tests and numerical modelling to illustrate the structure's behaviour when embedded in such a sand deposit. Furthermore, a few topics for futher research are introduced below.

7.3.1 Investigation into the behaviour of piled footing structures under cyclic loading

Further research can be conducted on the behaviour of piled footing structures under cyclic loading regimes. If such a study is to be conducted, centrifuge tests must be accompanied with finite element analysis.

This study can be important because the soil degrades under cyclic loading regimes and these structures must be able to withstand daily impacts from waves and currents. Usually platforms are designed for severe storms with a maximum 100-year wave in excess of 30 m and so in such cases, the soil failure might dominate the behaviour of the structure and not the pile material. Further, if this point is to be investigated by the aid finite element analysis the endurance or fatigue limit of the metal must be used. The latest point is because the yield strength of metals decreases after they have been subjected to a certain number of cyclic loads.

Such a study must include piled footings, monopiles and un-piled footings so that their results can be compared for comparison purposes similar to this research.

7.3.2 Micro piles

As the soil around the footing rim in a piled footing scenario is unable to sustain tension when it is under a moment loading, micro piles can be used around the rim of the footing instead of using one single long pile located at the centre of the footing, as illustrated in the Figure 7-1.

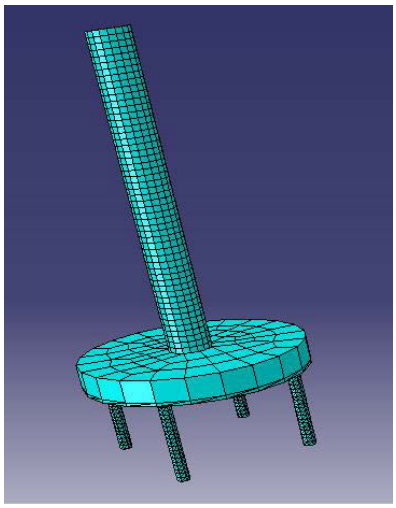

Figure 7-1. An illustration of a footing structure with micro piles

If this structure is to be investigated, its stiffness and ultimate lateral capacity is strongly recommended to be compared with a monopile and a piled footing structure under a monotonic and cyclic lateral loading regime by centrifuge tests and FE analysis.

If this structure is compared with a piled footing structure, the amount of steel used under the ground for a piled footing structure is strongly recommended to be compared with the sum of the material used as micro piles around the rim of the footing. The latter will ensure that both structures have the same amount of material used in constructing the piles; this is an economical view to the problem.

APPENDIX A

```
from odbAccess import *
import sys

# Open an output data file
odb1=session.openOdb('D:/Plastic models with Collar/footing.odb')

out1=open('D:/Plastic models with Collar/nodalCoords.dat','w')

# identify the odb file you want to access

# now the step in the odb file that you want to access
loadStep=odb1.steps['push']

# indentify the part you want to access
#myInstance=odb1.rootAssembly.instances['PART_1-1']

# then identify the node set within the part
#ns=myInstance.nodeSets['SOIL']

#_____________________________________________________________________
#
#
#  The above will need to be changed depending on the the
#  .odb file name and location
#  the step name in the model
#  the part name in the model
#  and the node set name in the model
#
#_____________________________________________________________________

# specify the frame number
i=1
# set current frame
currentFrame=loadStep.frames[1]
# set stress
coords=currentFrame.fieldOutputs['RF']
for Values in coords.values:
     out1.write(str(Values.instance.name))
     out1.write(str('.'))
     out1.write(str(Values.nodeLabel))
     out1.write(str(','))
     out1.write(str(Values.data[2]))
     out1.write('\t')

     out1.write('\n')
out1.close()
```

APPENDIX B

Broms (1964) solution for circular piles embedded in a sand deposit

```
clear all %this line clears the workspace

s=input('enter the yield stress of the material in MPa: ');

y1=input('enter the outer radius of the pile section in meters: ');

y2=input('enter the inner radius of the pile section in meters: ');

u=input('enter the effective unit weight of the soil in kN/m3: ');

sf=input('enter the soil friction angle in degrees: ');

e=input('enter the eccentricity value in meters: ');

l=input('enter the pile length under the ground in meters: ');

I=0.25*pi*((y1^4)-(y2^4));                %this line calculates the moment of
inertia of the pile section

My=(s*I)/(y1);                            %this line calculates the yield
stress of the pile section using the flexure equation

Kp=(1+sind(sf))/(1-sind(sf)); %this line calculates the passive earth pressure

Hu=(0.5*u*2*y1*l^3*Kp)/(e+l); %this line is equal to equation 2.50 in the
thesis

f=0.82*sqrt(Hu/(2*y1*Kp*u)); %this line equal to equation 2.52 in the thesis

Mmax=Hu*(e+((2/3)*f));     %this line is equal to equation 2.53 in the thesis

if Mmax<My  %if this condition is satisfied the pile is considered to be short

    t=Hu/10^3;  %dividing the value of Hu by a thousand

    fprintf('The maximum yield force of the short pile calculated by Brom''s
solution is equal to: %f kN\n\n',t); %this line prints the results for the
short pile

else        %if this condition is satisfied the pile is considered to be long

syms Hu     %this line considers a symbolic value for Hu

f=0.82*sqrt(Hu/(2*y1*Kp*u)); %this line is equivalent to equation 2.52 in the
thesis but with a symbolic value for Hu

g=My-Hu*(e+0.66*f); %this line prepares the equation to be solved with the
yield stress of the material, equation 2.53 in the thesis

b=solve(g,'Hu');        %this line solves the equation
```

```
a=round(b);                 %this line changes the result to an integer

c=a/1e6;                    %this line is a division

d=double(c);                %this line changes the result to a numerical value

fprintf('The maximum yield force of the long pile calculated by Brom''s
solution is equal to: %f MN\n\n',d); %this line prints the result

end
```

REFERENCES

ABAQUS User's Manual, 2009, Dassault Systems Simulia Corp., Providence, RI, USA.

Abdel-Rahman, K., and Achmus. M. (2005). Finite element modelling of horizontally loaded monopile foundations for offshore wind energy converters in Germany. *Proc. International symposium "Frontiers in offshore Geotechnics"*. Perth, Australia.

American Petroleum Institute (API) (2007). Recommended practice for planning, designing and constructing fixed offshore platforms-working stress design.

Anderson, K.H. and Lauritzsen, R. (1988). Bearing capacity for foundation with cyclic loads. Journal of Geotechnical and Geoenvironmental Engineering (ASCE), Vol. 119, 1532-1549.

Anderson, K.H., Jostad, H.P. and Dyvik, R. (2008). Penetration resistance of offshore skirted foundations and anchors in dense sand. Journal of Geotechnical and Geoenvironmental Engineering (ASCE). Vol. 134, No. 1.

Attaway, S. (2012). *MATLAB a practical introduction to programming and problem solving*. 2th Ed., Butterworth-Heinemann, United states.

Barton, Y.O., and Finn, W.D.L. (1983). Lateral pile response and p-y curves from centrifuge tests. *Proc., 15th Annual Offshore Technology Conf.*, Houston, Vol. 4502, 503–508.

Berezartzev, V.G., Khirstoforv, V.S. and Golubkov, V.N. (1961). Load bearing capacity and deformation of piled foundation. *Proc. Of the 5th International conference on soil mechanics and foundation engineering*, Paris, Vol. 2, 11-15.

Bienen, B., Byrne, B.W., Houlsby, G.T. and Cassidy, M.J. (2006). Investigating six degree-of-freedom loading of shallow foundations on sand. *Géotechnique*, Vol. 56, No. 6, 367-379.

Bolton, M.D. (1986). The strength and dilatancy of sands. *Géotechnique*, Vol. 36, No.1, 65-78.

Booker, J.R., Balaam, N.P. and Davis, E.H. (1985). The behaviour of an elastic non-homogeneous half-space. International Journal Numerical and Analytical Methods in Geomechanics, Vol. 9, 353-367.

Boresi, A.P. and Schmidt R.J. (2003). *Advance mechanics of materials*. 6th Ed., John Wiley & Sons, United States.

Borgard, D., and Matlock, H. (1980). Simplified calculation of p-y curves for laterally loaded piles in sand, *Earth Technology Corporation, Inc*., Houston.

Braiaud, J.L., and Smith, T.D. (1983). Using the pressuremeter curve to design laterally loaded piles. *Proc. 15th offshore technology Conf.*, Houston, Vol. 4501, 495-502.

Brich Hansen, J. (196). The ultimate resistance of rigid piles against transversal forces. Geoteknisk Institute, Copenhagen, Bull. No. 12.

Brinch-Hansen, J. (1970). A revised and extended formula for bearing capacity. The Danish Geotechnical Institute, Copenhagen, Bulletinno. 98, 5-11.

Broms, B.B. (1964). Lateral resistance of piles in cohesionless soils. Journal of the Soil Mechanics and the Foundations Division (ASCE), Vol. 90, No. SM3, 123-156.

Budhu, M. (2007). *Soil mechanics and foundations*. 2th Ed., John Wiley & Sons, United States.

Budhu, M. (2008). *Foundations and earth retaining structures*. 1th Ed., John Wiley & Sons, United States.

Budhu, M. and Davis, T.G. (1987). Non-linear analysis of laterally loaded piles in cohesionless soils. Canadian Geotechnical Journal, Vol. 24, 289-296.

Budhu, M., and Davies, T.G. (1988). Analysis of laterally loaded piles in soft clays. Journal of Geotechnical and Geoenvironmental Engineering (ASCE), Vol. 114, No. 1, 21-39.

Butterfield, R. and Gottardi G. (1994). A complete three-dimensional failure envelope for shallow footings on sand. *Géotechnique*, Vol. 44, No. 1, 181-184.

Byrne, B.W., Houlsby, G.T. (2003). Foundations for offshore wind turbines. *Philosophical Transactions of the Royal Society London, Series A (Mathematical, Physical and Engineering Sciences)*, Vol. 361, No. 1813, 2909-2930.

Byrne, B.W., Houlsby, G.T. and Martin, C.M. (2002). Cyclic loading of shallow offshore foundations on sand. *Proc. 1th Int. Conf. on Physical Modelling in Geotechnics (ICPMG)*, Newfoundland, 277-282.

Carter, J.P. and Kulhawy, H. (1992). Analysis of laterally loaded shafts in rock. Journal of Geotechnical and Geoenvironmental Engineering (ASCE), Vol. 118, No. 6, 839-855.

Chun, W.J. (2007). *Core PYTHON programming*. 2th Ed., Pearson Education, United States.

Comodromos, E.M. (2003). Response prediction for horizontally loaded pile groups. Journal of Geotechnical Engineering, Southeast Asian Geotech Soc. 33-123.

Cook, R.D., Malkus, D.S., Plesha, M.E. and Witt, R.J (2002). *Concepts and application of finite element analysis*. 4th Ed., John Wiley & Sons, United States.

Coyle, H.M. and Castello, R.R. (1981). New design correlations for piles in sand. Journal of the Geotechnical Engineering Division (ASCE), Vol. 107, 965-986.

Das, B.M. (1999). *Bearing capacity and settlement.* CRC Press LLC. United States.

Das, B.M. (1999). *Principles of foundation engineering.* 4th Ed., Brooks/Cole, United States.

Davis, E.H. and Booker, J.R. (1973). The bearing capacity of strip footings from the standpoint of plasticity theory. *Proc. 1th Australian and New Zealand Conf. on Geomechanics*, Vol. 1, 276-282.

Davis, T. G. and Budhu, M. (1986). Nonlinear analysis of laterally loaded piles in heavily overconsolidated clays, *Géotechnique*, Vol. 36, No. 4, 527-538.

Davison, M.T. and Gill, H.L. (1963). Laterally loaded piles in layered soil system. Journal of soil Mechanic and Foundation Engineering (ASCE), Vol. 89, No. SM3, 63-94.

DeBeer, E.E. (1970). Experimental determination of the shape factors and the bearing capacity factors of sand. *Géotechnique*, Vol. 20, No. 4, 347-411.

Dixon, R.K. (2005). Marine Foundations. Wo 2005/038146.

DNV (2004). Draft design of offshore wind turbine structures. Offshore standard DNV –OS-J101 Det Norske Veritas.

DNV (2007). Design of offshore wind turbine structures, *Offshore Standard DNV-OSJ101*, Det Norske Veritas. Available from: DNV Webshop Online [20 June 2010].

DTI (2001). Monitoring and evaluation of Blyth offshore wind farm – Projected capital costs of UK offshore wind farms based on experience at Blyth. DTI/Pub URN 01/1524, London.

Dyson, G.J. (1999). Lateral loading of piles in calcareous sediments. PhD thesis, The University of Western Australia.

Fleming, W., and Thorburn, S. (1983). Recent piling advances. State of the art report in *Proc. Conf. On advances in piling and ground treatment for foundations*, ICE, London.

Fleming, W.G.K., Weltman, A.J., Randolph, M.F. and Elson, W.K. (1992). *Piling engineering*. 2th Ed., University Press, UK.

Gazetas, G., and Stokoe, K.H. (1991). Free vibration of embedded foundations: theory versus experiments. Journal of Geotechnical and Geoenvironmental Engineering (ASCE). Vol. 117, No. 9, 1362-1381.

Gottardi, G, and Butterfield, R. (1995). The displacement of a model rigid surface footing on dense sand under general planar loading. Japanese Geotechnical Society. Vol. 35, No. 3, 71-82.

Gottardi, G, Houlsby, G.T. and Butterfield, R. (1999). Plastic response of circular footings on sand under general planar loading. *Géotechnique*, Vol. 49, No.4, 453-469.

Gottardi, G. and Butterfield, R. (1993). On the bearing capacity of surface footings on sand under general planar loads. Japanese society of soil mechanics and foundation engineering. Vol. 33, No. 3, 68-79.

Gottardi, G., Houlsby, G.T., and Butterfield, R. (1999). Plastic response of circular footings on sand under general planar loading, *Géotechnique*, Vol. 49, No. 4, 453-469.

Gourvenec, S., Govoni, L. and Gottardi, G. (2008). An investigation of shallow foundations on sand under moment loading. *Proc. 2th British International Conference on Foundations (ICOF),* U.K., 873 – 884.

Govoni, L., Gourvenec, S., Gottardi, G. and Cassidy, M.J. (2006). Drum centrifuge tests of surface and embedded footings on sand. Physical Modelling in Geotechnics – 6th ICPMG, London, 651-657.

Hansen, B. (1961). The bearing capacity of sand, tested by loading circular plates. *5th International conference on soil mechanics and foundation engineering*. Paris, France. Vol. 1, 659-664.

Harloe, S.A. (2010). Investigation of a new offshore wind turbine foundation. Thesis. The University of Western Australia.

Hibbeler, R.C. (2005). *Mechanics of Materials*. 6th Ed., Prentice-Hall, United States.

HKS. *ABAQUS Manual*, *V.6.4*, Hibbit, Karlsson and Sorensen, Inc.2006.

Houlsby G.T. and Purzin, A.M. (1999). The bearing capacity of strip footing on clay under combined loading. *Proc. Royal Society*, 455A, 893-916.

Houlsby, G.T. and Byrne, B.W. (2005). Calculation procedures for installation of suction caissons in sand. *Geotechnical Engineering*, Vol. 158, 135-144.

Houlsby, G.T., Ibsen, L.B. and Byrne, B.W. (2005a). Suction caissons for wind turbines. *Proc. International symposium "Frontiers in offshore Geotechnics"*. Perth, Australia.

Houlsby, G.T., Kelly, R.B. and Byrne, B.W. (2005b). The tensile capacity of suction caissons in sand under rapid loading. *Proc. International symposium "Frontiers in offshore Geotechnics"*. Perth, Australia.

Jaky, J. (1948). The coefficient of earth pressure at rest. Journal Soc. Hungarian Architects Eng. Vol. 7, 355-358.

Jamiolkowski. M., and Garassino, A. (1977). Soil modulus for laterally loaded piles. *Proc. 9th Int. Conference on soil mechanics and foundation engineering*. Tokyo, 87-92.

Janbu, N. (1976). Static bearing capacity of friction piles. *Proc. of the 6th European Conf. on Soil Mechanics and Foundation Engineering.* Vol. 1, No.2, 479-488.

Jardin, R.J., Overy, R.F. and Chow, F.C. (1998). Axial capacity of offshore piles in dense North Sea sands. Journal of Geotechnical and Geoenvironmental Engineering, Vol. 124, 171-178.

Karasev, O.V., Talanov, G.P. and Benda, S.F. (1977). Investigation of the work of single situ-cast piles under different load combinations. Journal of Soil Mechanics and Foundation Engineering, Vol. 14, No. 3, 7-173.

Karthigeyan, S., Ramakrishna, V.V.G.S.T. and Rajagopal, K., (2006). Influence of vertical load on the lateral response of piles in sand. Computers and Geotechnics, Vol. 33, 121-131.

Karthigeyan, S., Ramakrishna, V.V.G.S.T. and Rajagopal, K., (2007). Influence of vertical load on the lateral response of piles in sand. Journal of Geotechnical and Geoenvironmental Engineering (ASCE), Vol. 133, No. 5, 512-521.

Kishida, H. (1967). Ultimate bearing capacity of piles driven into loose sand. Journal of Soil and Foundations. Vol. 7, No. 3, 20-29.

Ko, H. Y., and Davidson, L. W. (1973). Bearing capacity of footings in plane strain. Journal of soil Mechanics and Foundations Division (ASCE), Vol. 99, No. 1, 1.

Krohn, S. (2002). Offshore wind energy: full speed ahead Danish Wind Industry Association.

Kuhlemeyer, R.L. (1979). Static and dynamic laterally loaded floating piles. Soil Mechanics and Foundation Division (ASCE), Vol. 105, No. GT2, 289-304.

Kulhawy, F.H. (1984). Limiting tip and side resistance: Fact or fallacy. *Proc. Symp. On design and analysis of pile foundations*, New York, 80-98.

Kulhawy, F.H. (1991). Drilled shaft foundations. *Foundation engineering handbook*, 2th Ed, United states.

Kulhawy, F.H., Trautmann, C.H., Beech, J.F., O'Rourke, T.D., McGuire, W., Wood, W.A. and Capano, C. (1983). Transmission line structure foundations for uplift compression loading. *No. EL-2870*, Electrical Power Research Institute, Palo Alto, Calif.

Lehane, B.M., Powrie, W. and Doherty, J.P. (2010). Centrifuge model tests on piled footings in clay for offshore wind turbines. *Proc. Int. Symp. on Frontiers in offshore Geotechnics (ISFOG),* Perth.

Lehane, B.M., Schneider, J.A. and Xu. X. (2005). A review of design methods for offshore driven piles in siliceous sand. Research Report Geo: 05358, Geomechanics Group, The University of Western Australia.

Logan, D.L., Chaudhry, K.K. and Singh, P. (2011). *A first course in the finite element method*. 4th Ed., Global Engineering, United States.

Malhorta, S. (2011). Selection, design and construction of offshore wind turbine foundations. Chapter 10, Wind turbines, I. Al-Bahadly, ed., InTech, Rijeka, Croatia.

Meyerhof, G.G. (1951). The ultimate bearing capacity of foundations. *Géotechnique*, Vol. 2, No. 4, 301-332.

Meyerhof, G.G. (1953). The bearing capacity of foundations under eccentric and inclined loads. *3th International Conf. on Soil Mech. and Foundation Eng*., Zurich, 440-445.

Meyerhof, G.G. (1963). Some recent research on the bearing capacity of foundations. Journal of Canadian Geotech, Vol. 1, No. 1, 16-26.

Meyerhof, G.G. (1976). Bearing capacity and settlement of pile foundations. Journal of Geotechnical and Geoenvironmental Engineering, Vol. 102, No. GT3, 195-228.

Meyerhof, G.G. (1995). Development of geotechnical limit state design. Canadian Geotechnical Journal, Vol. 32, No.1, 128-136.

Moaveni, S. (2008). *Finite element analysis theory and application with ANSYS*. 3th Ed., Pearson international edition, United States.

Mokwa, R.L. & Duncan J.M. (2001). Rotational restraint of pile caps during lateral loading. Journal of Geotechnical and Geoenvironmental Engineering (ASCE), Vol. 127, No. 2, 185-192.

Murff, J.D. (1996). The geotechnical centrifuge in offshore engineering. *Proceedings of Offshore Technology Conference*, Houston, OTC 8265.

Nordlund, R.L. (1963). Bearing capacity of piles in cohesionless soils. Journal of soil Mechanics and Foundation Engineering (ASCE), Vol. 89, No. SM3, 1-35.

Ochi, M.K. (1979). A series of JONSWAP wave spectra for offshore structure design. *Proc. 2th Int. Conference on the Behaviour of offshore structures (BOSS),* London.

Patel, S.N. (2009). Investigation of a new foundation type for wind turbines. Honours Thesis. University of Western Australia.

Pender, M. J. (1993). Aseismic pile foundation design analysis. *Bulletin of New Zealand National Society for Earthquake Engineering*, Wellington, Vol. 26 No. 1 49-161.

Poulos, H.G. (1971a). Behaviour of laterally loaded piles: Part I - single piles. Soil Mechanics and Foundation Division (ASCE), Vol. 97, No. SM5, 711-731.

Poulos, H.G. (2009). Handbook, The University of Sydney.

Poulos, H.G., and Davis E.H. (1980). *Pile foundation analysis and design*. John Wiley & Sons, United States.

Poulos, H.G., Carter, J.P. and Small, J.C (2002). Foundations and retaining structures. Research and Practice. *Proc. 15th International Conf. on Soil Mech. and Foundation Engineering, Istanbul*, Vol. 4, 2527-2606.

Powrie, W. & Chandler, R.J. (1998). The influence of a stabilizing platform on the performance of an embedded retaining wall: a finite element study. *Géotechnique*, Vol. 48, No. 3, 403-409.

Powrie, W. (1997). *Soil mechanics: Concepts and Application*. 1th Ed., E & FN Spon, UK.

Powrie, W., and Daly, M.P. (2007). Centrifuge modelling of embedded retaining walls with stabilizing bases. *Gèotechnique,* Vol. 57, No. 6, 485-497.

Prandtl, L. (1920). Über die Härte plastischer Körper, Nachrichten von der Königlichen Gesellschaft der Wissenschaften zu Göttingen (Mathematics-physikalische Klasse aus dem Jahre), Berlin, 74-85.

Prasad, Y.V.S.N., and Chari, T.R. (1999). Lateral capacity of model rigid piles in cohesionless soils. Journal of Soils and Foundation, Vol. 39, No. 2, 21–29.

Randolph, M.F. (1981). The response of flexible piles to lateral loading. *Géotechnique*, Vol. 31, No. 2, 247-259.

Randolph, M.F. (2003). RATZ-Load transfer analysis of axially loaded piles. User manual, University of Western Australia, Perth.

Randolph, M.F. and Houlsby, G.T. (1984). The limiting pressure on a circular pile loaded laterally in cohesive soil. *Géotechnique*, Vol. 34, No. 4, 613-623.

Randolph, M.F., Jewell, R.J., Stone, K.J.L. and Brown, T.A. (1991). Establishing a new centrifuge facility. Boulder, Colorado, A.A., Balkema.

Reese, L.C., Cox, W.R. and Koop, F.D. (1974). Analysis of laterally loaded piles in sand. *Proc. 6th Offshore Technology Conf.*, Houston, Vol. 2, 473-483.

Sa'don, N.M., Pender, M.J., Orense, R.P. and Abdul Karim, A.R. (2008). Lateral Dynamic response of a single pile model. Australian Earthquake Engineering Conference AEES, Ballarat, Victoria.

Schneider, J.A. and Lehane, B.M. (2006). Effects of width for square centrifuge displacement piles in sand. *Proc. Int. Conf. on Physical Modelling in Geotechnics*, Hong Kong, Vol. 1, 867-73.

Senders, M. (2009). Suction caissons in sand as tripod foundations for offshore wind turbines, Ph.D. Thesis, University of Western Australia.

Skempton, A.W. (1959). Cast-in-situ bored piles in London clay. *Geotechnique*, Vol. 9, No.7, 153-173.

Smith, T.D. (1987). Pile horizontal modulus values. Journal of Geotechnical Engineering, Vol. 113, No. 9, 1040-1044.

Soulsby, R. (1997). *Dynamics of marine sands*. Thomas Telford Publications.

Stone, K.J.L., Newson, T.A, El Marassi, M. El Naggar, H. Taylor, R.N. and Goodey, R.J. (2010). An investigation of the use of bearing plate to enhance the lateral capacity of monopile foundations. *Proc. Int. Symp. on Frontiers in offshore Geotechnics (ISFOG),* Perth.

Stone, K.J.L., Newson, T.A. and Sandon, J. (2007). An investigation of the performance of a hybrid monopile-footing foundation for offshore structures. *Proc. Int. Conf. on Offshore Site Investigation*, London.

Taiebat, H., and Carter, J.P. (2000). Bearing capacity of strip and circular foundations on undrained clay subjected to eccentric loads. *Géotechnique*, Vol. 52, No. 1, 61-64.

Taylor, R.N. (1995). *Geotechnical centrifuge technology*. Blackie academic & professionals, UK.

Terzaghi, K. (1943). *Theoretical soil mechanics*. John Wiley and Sons, United States.

Terzaghi, K. and Peck, R.B. (1948). *Soil Mechanics in engineering practice.* John Wiley & Sons, United States.

Ueno, K., Miura, K. and Maeda, Y. (1998). Prediction of ultimate bearing capacity of surface footings with regard to size effects. Journal of Soils and Foundations, Vol. 38, No. 3, 165-178.

Ugural, A.C. (2008). *Mechanics of materials*. 1th Ed., John Wiley & Sons, United States.

Ugural, A.C., Fenster S.K. (2003). *Advanced strength and applied elasticity*. 4th Ed., Pearson education, United States.

Vesic, A. (1961). Bending of beams resting on isotropic solid. Journal of Engineering Mechanics Division (ASCE), Vol. 87, No. 2, 35-53.

Vesic, A.S. (1973). Analysis of ultimate loads of shallow foundations. Journal of Geotechnical and Geoenvironmental Engineering, Vol. 99, No. SM1, 45-73.

Vesic, A.S. (1975). Bearing capacity of shallow foundations. *Foundation Engineering Handbook*. New York, P121.

Vesic, A.S. (1977). Design of pile foundations. National cooperative highway research program. Synthesis of highway practice, No. 42, TRB, National Research Council, Washington DC.

Vestas wind systems report A/S (2004). V120-4.5 MW Leadership in offshore. Ole Gunneskov.

Wind Turbine - Materials and Manufacturing Fact Sheet (2011). Prepared for the Office of Industrial Technologies, US Department of Energy by Princeton Energy Resources International, LLC. Dan Ancona and Jim McVeigh.

Zadroga, B. (1994). Bearing capacity of shallow foundations on noncohesive soils. Journal of Geotechnical Engineering, Vol. 120, No. 11, 1991-2008.

Zhang, L., Silva, F. and Grismala, R. (2005). Ultimate lateral resistance of piles in cohesionless soils. Journal of Geotechnical and Geoenvironmental Engineering (ASCE), Vol. 131, No. 1, 78-83.